

An Electrochemical Framework to Study the Corrosion Behavior of Model Metals and Alloys in Molten LiF-NaF-KF Salts

A
Dissertation
Presented to
the faculty of the School of Engineering and Applied Science
University of Virginia

in partial fulfillment
of the requirements for the degree

Doctor of Philosophy

by

Ho Lun Chan

August 2025

APPROVAL SHEET

This
Dissertation
is submitted in partial fulfillment of the requirements
for the degree of
Doctor of Philosophy

Author: Ho Lun Chan

This Dissertation has been read and approved by the examining committee:

Advisor: John R. Scully

Advisor:

Committee Member: Robert G. Kelly

Committee Member: Ji Ma

Committee Member: Bi-Cheng Zhou

Committee Member: Christopher Paolucci

Committee Member:

Committee Member:

Accepted for the School of Engineering and Applied Science:



Jennifer L. West, School of Engineering and Applied Science

August 2025

Dissertation Abstract

Molten salt is becoming an integral part of tomorrow's energy. Notably, it offers a combination of heat capacity, vapor pressure, and thermal stability that makes the development of Generation IV molten salt reactor (MSR) technology possible. The MSR reactor utilizes a molten fluoride salt between 500°C and 700°C as the medium for nuclear fission, heat storage, and transfer. Examples of molten fluorides are eutectic mixtures of LiF-NaF-KF (46.5-11.5-42 mol%), LiF-BeF₂ (66-34 mol%), and NaF-ZrF₄ (59.5–40.5 mol%) salts. These molten fluorides are prone to containing dissolved hydrofluoric acid (HF) due to moisture and/or metallic cation impurities (e.g., Fe, Cr) that drive the corrosion of candidate structural containment alloys, which include 316SSH, Hastelloy N, and Inconel 600, and may possibly form a damage morphology that is susceptible to the loss of engineering function. Corrosion in molten fluorides remains a critical challenge today. The underlying factors that regulate the corrosion process must be well understood to prevent materials failures and ensure the overall sustainability of MSR development.

A key knowledge gap in understanding molten salt corrosion is the inadequacy of mechanistic insights and interpretations that target the fundamental principles of electrode reactions, such as the identification of reaction rate factors at the electrode-salt interface or transport through metallic or ionic conductor phases when alloys are exposed to molten fluorides. Particularly for alloy systems, it is unknown whether there exists a “window of corrosion susceptibility” where select metals and alloys are immune or susceptible to a particular form of corrosion damage, e.g., bicontinuous dealloying, uniform corrosion, grain boundary attack, or a mixture of them. Current progress has been limited primarily by capsule or flow-loop types of time-based exposures followed by surface characterization after periods of exposure. This approach often lacks diagnostics, does not assess rates except by serial exposure, and makes it difficult to separate variables critical to the corrosion process, leaving questions such as: (1) What is the valence of metal dissolution? (2) What are the rate-determining steps governing corrosion rate? (3) What is the role of microstructure and salt chemistry? The real challenge remains that these experiments are often high fidelity. Therefore, investigation into the corrosion behavior of structural metals should begin with model materials (such as pure metal or high-purity binary alloys), with a focus on targeting the fundamental principles of corrosion thermodynamics and kinetics.

The objective of this work is to develop a mechanistic understanding of the corrosion process of model metals and alloys (Cr, Ni, Ni-Cr) in molten LiF-NaF-KF (or FLiNaK) salts using the principles of electrochemical thermodynamics and kinetics. As a foundation, the spontaneity and thermodynamic driving force for metal dissolution in molten fluorides were first assessed by developing potential-activity diagrams for Cr in molten fluorides (akin to Pourbaix Diagrams), which were verified by experimental cyclic voltammetry measurements (CV) for Cr(II) and Cr(III) in molten FLiNaK at 600°C. The thermodynamic predictions were then utilized to understand the dissolution kinetics and possible rate-determining steps (RDS) for Cr dissolution using linear sweep voltammetry. Results showed that at low potentials, Cr dissolution is charge-transfer controlled and resulted in a faceted surface morphology; at high potentials, Cr dissolution is mass-transport controlled due to the formation of alkali metal-Cr-salt films leaving behind a smooth plan view-morphology. These phenomena allow for the fate of Cr—whether dissolved as ions or retained in the metal—to be tracked and used to quantify corrosion rates. This insight inspires the development of an in-situ electrochemical method to calculate Cr mass loss in real time by measuring the concentrations of Cr(II) and Cr(III) species using CV with a secondary Pt working electrode.

This framework was subsequently utilized to understand the corrosion and dealloying behavior of model Ni-20Cr alloys (wt.%) in molten LiF-NaF-KF at 600°C. Here, Cr is the less noble element and Ni is the more noble element. The RDS and corrosion morphology were examined over the electrode potentials from 1.75 $V_{K+/K}$ to 2.75 $V_{K+/K}$. Between 1.75 $V_{K+/K}$ and 2.10 $V_{K+/K}$, Cr was selectively dissolved under an initial charge-transfer controlled behavior at a significantly faster rate than Ni. This process left behind a micron-scale bicontinuous structure characterized by a network of interconnected pores and ligaments rich in Ni driven by Ni surface diffusion, which undergo further surface coarsening until 2.30 $V_{K+/K}$. Cr bulk solid outward diffusion, consisting of lattice and grain boundary diffusion of Cr, was calculated to play a major role in regulating the rate of Cr dealloying in molten FLiNaK due to the high homologous temperature (T_h : 0.53) corresponding to the 600°C test environment. To identify the RDS controlling molten fluorides dealloying, the rates of Cr oxidation ($J_{electric}$), Cr(III) ionic diffusion ($J_{Cr(III)}$), Cr solid bulk outward diffusion (J_{bulk}) were calculated over the duration of dealloying. It was found that over time J_{bulk} (consisting of both lattice and grain boundary diffusions) is insufficient to support $J_{electric}$, suggesting that molten fluoride dealloying can be bulk diffusion limited. To validate this hypothesis cold working was performed on Ni-20Cr alloy (10%, 30%, 50%) to ameliorate this effect by providing a high density of dislocation structures, serving as short-circuit diffusion pathways to accelerate Cr bulk diffusion. Results revealed that dealloying of cold-worked Ni20Cr (wt%) was found to be controlled by charge-transfer mechanism instead.

In summary, this work contributes to the fundamental understanding of metal and alloy corrosion, particularly the Ni-Cr systems, in molten fluorides, establishing a systematic framework that relates species electrode potential—a readily measurable parameter—to the corrosion rate and possible damage morphology of the metal and alloy. This framework is transferable for studying compositionally complex alloys considered as candidates for MSR applications. It can also guide the discovery of new alloy compositions or material structures designed to resist corrosion or cracking. Ultimately, the successful development of modular molten salt reactors can be the basis for the democratization of relatively clean, abundant energy in both rich and poor countries.

Table of Contents

Abstract.....	2
Acknowledgements.....	8
List of Tables	9
List of Figures.....	11
Bibliography	19
Chapter 1: Background.....	20
The Development of Molten Salt Reactor.....	20
Structural Materials Corrosion in Molten Salt Reactor	23
Progress in Molten Fluoride Salt Corrosion Research	24
Critical Knowledge Gap: The Window of Corrosion Susceptibility	27
Overall Objective & Hypothesis.....	28
Approach & Thesis Organizations.....	29
References.....	30
Chapter 2 Task 1: Corrosion Thermodynamics of Pure Cr in Molten LiF-NaF-KF Salts	33
Abstract.....	33
Introduction	33
Materials and Methods	36
Setup, sample and salt preparation	36
Reference potential determination.....	37
Thermodynamic Calculations.....	38
Assumption & Limitations	40
Potentiostatic polarization of pure Cr and X-Ray Diffraction.....	41
Results and Discussions.....	41
Cyclic Voltammograms of Pt in FLiNaK-CrF ₃ salts.....	41
Calculating the Concentration of CrF ₂ and CrF ₃ in FLiNaK.....	42
Estimating the Gibbs free energy of solvated chromium fluoride Ions.....	44
Stability of Cr(II) and Cr(III) in Molten Fluorides.....	47
Ramification towards spontaneous corrosion of Cr in FLiNaK.....	51
Conclusions	51
References	52
Chapter 3 Task 2: Electrochemical Corrosion Kinetics of Pure Cr in Molten FLiNaK Salts	55
Abstract.....	55
Introduction	55
Materials and Methods	57
Materials and electrolytes.....	57
Molten salt electrochemical cell	58
Impurity analysis using electrochemical diagnostics	59
Molten salt corrosion electrochemical methods	59
Approach to analyze electrochemical results	59
Post-exposure characterization: XRD, SEM, EBSD.....	59

Results	61
Diagnostics of FLiNaK salts using electrochemical methods	61
Identifying the rate-controlling kinetic regimes of Cr corrosion in FLiNaK	64
Oxidation states for Cr dissolution	66
Validation of rate-controlling kinetic regimes.....	67
Effect of CrF ₃ on corrosion behavior	69
Electrodes kinetics of cathodic and anodic reactions	71
Effects of scan rates on the potentiodynamic polarization behavior	72
Description of the transient corrosion process at OCP	73
Morphological dependence on rate-controlling corrosion regimes.....	74
Current-time relationship during potentiostatic hold.....	76
Corrosion morphology through multiple corrosion regimes	77
Corrosion morphology after exposure at OCP condition	79
Discussion	80
Analysis of polarization curves and electrode kinetics	80
Microstructural implication of charge-transfer and mass-transport controlled regimes ...	83
Conclusions	85
References	86

Chapter 4 Task 3: An *In Situ*, Multi-Electrodes Electrochemical Method to Assess the Open Circuit Potential Corrosion of Cr in Unpurified Molten FLiNaK Salts

Abstract.....	91
Introduction	91
Materials and Methods	94
Metal and salts preparation.....	94
Multi-electrodes molten salt electrochemical cell	94
Electrochemical methods with dual working electrodes	95
Estimation of dissolved corrosion product concentration	96
Corrected half-cell oxidation and reduction potential	97
Static or open-circuit immersion tests	97
ICP-OES analysis	97
X-ray diffraction analysis	98
Estimation of total Cr mass loss	98
Results	99
<i>In-situ</i> corrosion product detection.....	99
Assessment of total Cr(II) and Cr(III) supplied by electrodisolution	102
Discussion	108
Conclusions	111
References	111

Chapter 5 Task 4: Morphological Evolution and Dealloying During Corrosion of Ni₂₀Cr (wt.%) in Molten LiF-NaF-KF Salts, 600°C

Abstract.....	115
Introduction	115

Materials and Methods	119
Materials preparation.....	119
Salt preparation.....	119
Molten salt electrochemistry experiments.....	120
Scanning electron microscopy (SEM) and energy dispersive spectroscopy (EDS).....	121
Electron backscattered diffraction (EBSD)	122
X-ray diffraction analysis	122
Inductively coupled plasma-mass spectrometry (ICP-MS) analysis.....	122
Results	123
Thermodynamic and kinetics for Ni20Cr dissolution	123
Morphological evolution with applied potential	124
Dealloying at +1.75V _{K+/K}	126
Dealloying at +1.90V _{K+/K}	129
Dealloying at +2.10V _{K+/K}	132
XRD of as-solidified salts.....	134
Discussion	135
Applied potential effect on surface diffusions.....	138
Applied potential effect on electrolytic dissolution.....	138
Effect of bulk diffusion on dissolution	140
Conclusions	145
References	146
Supplemental Tables, Chapter 5 Task 4	151
Supplemental Figures, Chapter 5 Task 4.....	153

Chapter 6 Task 5: Dealloying of Cold-Worked Ni-20Cr (wt.%) Alloy in Molten LiF-NaF-KF Salts at 600°C.....

Abstract.....	159
Introduction	160
Materials and Methods	162
Materials preparation.....	162
Salt preparation.....	162
X-ray diffraction analysis	163
Molten salt electrochemistry	164
Scanning electron microscopy (SEM) and energy dispersive spectroscopy (EDS).....	165
Electron backscattered diffraction (EBSD)	165
Optical microscopy & electrolytic etching.....	165
Kinetic analysis of potentiostatic dealloying.....	166
Results	170
Microstructural characterization of as-cold worked Ni20Cr alloys	172
Effect of cold work on dealloying at +1.75V _{K+/K}	172
Morphological evolution vs. %CW at +1.75V _{K+/K}	172
Electrochemistry of dealloying at +1.75V _{K+/K}	174
Effect of cold work on dealloying at +1.90V _{K+/K}	175

Morphological evolution vs. %CW at +1.90V _{K+/K}	175
Electrochemistry of dealloying at +1.90V _{K+/K}	178
Dealloying at +1.90V _{K+/K} overtime	179
Discussion	182
Conclusions	188
References	189
Supplemental Tables, Chapter 6 Task 5	195
Supplemental Figures, Chapter 6 Task 5.....	198
Chapter 6: Conclusions and Suggested Future Work	213
Summary of Findings	213
Suggested future work for molten salt fundamental studies	216
Suggested future work for molten salt dealloying studies.....	216
Suggested future work for molten salt alloy developments.....	217
Appendix 1: Deciphering when Metal Corrosion is Spontaneous in Molten Fluorides Using Potential-Activity Diagrams	218
Abstract.....	218
Introduction	218
Experimental Procedures	219
Results and Discussions.....	221
Conclusions	225
References	225
Appendix 2: Uncovering Accurate Values of the Polarization Resistance in Molten Fluorides Using Electrochemical Impedance Spectroscopy	226
Abstract.....	226
Introduction	226
Theory.....	231
Quantifying the geometrically induced NUCP effects in R _{ct} and C _{dl} measurements	231
Simulating impedance responses using ECM models.....	233
Sensitivity analysis of fitting errors.....	235
Materials and methods.....	236
Results	238
Simulating impedance under charge-transfer controlled regime.....	238
Simulated and experimental impedance under charge-transfer controlled regime	239
Impedance under mass-transport controlled regime.....	243
Discussions	244
Conclusions	248
Glossary	249
References	250
Supplemental A Tables, Appendix #2	258
Supplemental A Figures, Appendix #2.....	259
Supplemental B, Equation Derivations.....	263

Acknowledgements

This may be a lengthy and likely incomplete list of acknowledgments, but I find it necessary to express my gratitude. I was raised in a single-parent household with very limited financial resources or perspectives on future. Statistically, the likelihood of someone growing up staying out of trouble, immigrating to the U.S., pursuing college, earning a doctorate, becoming an engineer, and being recognized as an emerging technical leader may perhaps be less than 1%. This journey wasn't mine alone. Over the past 25 years, countless family members, mentors, and friends have made this possible. **I dedicate this thesis to them.**

First and foremost, I would like to express my sincerest gratitude to my family members, notably my grandmother (Ms. Linh Ly), my mother (Ms. Ally Yeung), my siblings (C.H. Chan, Y.H. Chan, H.P. Chan), my uncles, aunts, and my deceased dog Melo. For without their love, support and tenacity in surmounting years of adversities, I would never have been able to come to the U.S., pursue an advanced education in engineering, nor have the strength to follow my dream to this very day. Their belief in me, even in moments when I doubted myself, has been my constant source of strength. I will be forever in debt to their sacrifices.

Following that, I would like to extend my heartfelt thanks to my Ph.D. advisor, Professor John R. Scully, for the privilege of pursuing a doctorate at the University of Virginia under his guidance, for believing in my abilities, for always pushing my boundary to succeed, and for supporting my scholarship and fellowship pursuits. His mentorship goes beyond the transaction nature of academic learning. I am forever grateful for his personal or professional guidance, which are undoubtedly instrumental to the next stage in life.

Moving forward, I am deeply thankful to my undergraduate advisor, Professor Vilupanur Ravi at Cal Poly Pomona, for taking a risk to recruit an unskilled, know-nothing 1st year undergraduate student (me) to his research group. Without his mentorship, friendship, and contagious passion in materials science and engineering, I would have never discovered my passion in materials science or corrosion, considered pursuing graduate school, or recognized that I can also become a future technical leader.

Moreover, I am profoundly indebted to several of my elementary school, high school teachers and college mentors. Ms. Angel Yim instilled in me the values of morality and ethics, how to face adversities and take responsibilities to be better person. Mr. William Choi opened my eyes to science, product development, and spending days to each me how to skillfully present complex ideas. Mr. Thomas VanWinkle helped me with my educational and cultural transition as an American immigrant.

It is of absolutely necessity to recognize my best friends, in no particular order: Nazanin Shalviri, Dr. Elena Romanovskaia***, Dr. Juan Carlos Nava, Kevin Guo, Roberto Herrera del Valle, CheukYiu Ip, Kenneth Hirscht, Debashish Sur, Desmon Lau, Ryan Grimes, Harjot Singh, Thu Nguyen, Armando Shehi, Milena McCarthy, Victor Wong, Marina Wittig, Kyle Wang, Rogine Gomez, Meice Hamad. They have supported me through nearly every dilemma over the last eight years, offering companionship, advice, and unwavering encouragement. I also need to extend my heartfelt thanks to more friends and colleagues who shaped my path: Prof. Peter Hoseman, Dr. Blas Uberuaga, Dr. Toni Maurechax, Dr. Valentin Romanovski, Won Choi, Dr. Suketu Bhavsar (along with the Kellogg Honors College), Dr. Abby Ganas, Dr. Angela Y. Gerald, Dr. Lauren Singer, Michael Kloesel, Mary Benice, Minh Tran, Dr. Alen Korjenic, Dr. Winny Dong, Dr. Everado Baraza (along with the CPP Office of Undergraduate Research), SM Lee, and Dr. Junsoo Han.

I would be remiss not to acknowledge the instrumental supports from the staffs of the UVA materials science and engineering department, notably Ms. Tonya Reynolds and Dr. Bryana Amador, for ensuring my well-being personally, financially, and professionally. Thank you my thesis committee: Prof. Robert Kelly, Prof. Bi-Cheng Zhou, Prof. Giovanni Zangari, and Prof. Chris Paolucci for their feedback and review! Additionally, I would like to thank my 30+ collaborators from the Department of Energy Basic Science Office FUTURE EFRC projects for the last 5 years of continuous intellectual stimulation and learning experiences that I will always cherish. Thank you to ASM and AMPP Internationals for providing me with invaluable opportunities to grow as a leader and contribute to the materials and corrosion engineering community! Last but not least, a big thank you to the NSF Graduate Research Fellowship for their support!

List of Tables (Notation: Chapter/Appendix# – Figure #)

Table 1 – 1. Structural alloys considered for molten salt reactor applications

Table 2 – 1. Standard Gibbs free energy of formation (ΔG_f^0) of potassium fluoride and chromium fluoride compounds at 600°C.

Table 2 – 2. Equilibrium redox reactions and their thermodynamic expression utilized for the construction of potential-concentration diagrams in molten fluoride salts

Table 2 – 3. Standard Gibbs free energy of formation (ΔG_f^0) of potassium fluoride and chromium fluoride compounds at T=0 Kelvin obtained from various thermodynamic databases

Table 2 – 4. Calculated standard Gibbs free energy of formation (ΔG_f^0) of solvated chromium fluoride compounds based on cyclic voltammetry results at 600°C

Table 3 – 1. Electrochemical kinetic parameters obtained from graphical analysis of LSV scans of Cr in FLiNaK salts at 600 °C with various wt% addition of CrF₃

Table 3 – 2. True anodic current density of Cr in FLiNaK salts at 600 °C recorded between 1 and 10 mV relative to E_{oc} at various wt% addition of CrF₃

Table 3 – 3. Electrochemical parameters used for the construction of Evan's Diagram. Noted that the CrF₃⁻ and CrF₆³⁻ represent the Cr(II) and Cr (III) species, respectively

Table 4 – 1. Chemical composition of as-solidified FLiNaK salts before and after 50 h of Cr immersion, mg/kg

Table 4 – 2. Concentration (mol/L) of dissolved Cr in FLiNaK salts determined through CV and ICP-OES methods

Table 4 – 3. Salt film layer thickness and Cr mass in the film determined microscopically, gravimetrically and by XRD

Table 4 – 4. Mass loss measured by gravimetric method and calculated from electrochemical CV method (with and without diffusion profile correction)

Table 5 – 1. Plan-view EDS point analysis on Ni20Cr (wt.%) upon potentiostatic hold at +1.75 V_{K+/K}, +1.90 V_{K+/K}, and +2.10V_{K+/K} for 10 ks in molten FLiNaK, 600 °C.

Table 5 – 2. Correlation between applied potential, total charge consumed, and select morphological properties in Ni20Cr (wt.%) alloys post 10ks of potentiostatic dealloying in FLiNaK at 600 °C.

Table 5 – 3. Plan view measurements of ligament Width for Ni20Cr potentiostatically polarized at +1.90 V_{K+/K} for 1, 3, 5 and 10 ks in molten FLiNaK at 600 °C

Table 5 – S1. Elemental composition of bulk FLiNaK salts measured using ICP-MS technique: as-prepared vs. subjected potentiostatic hold of Ni20Cr alloy at 600 °C

Table 5 – S2. Weighted fractional elemental composition (in ppm) of LiF, NaF, and KF salts according to supplier's certificates of analysis

Table 5 – S3. The EEC fitting parameters for impedance spectra of Ni20Cr potentiostatically held at +1.75 V_{K+/K} for 10 ks in molten FLiNaK salts at 600°C

Table 5 – S4. The EEC fitting parameters for impedance spectra of Ni20Cr potentiostatically held at +1.90 V_{K+/K} for 10 ks in molten FLiNaK salts at 600°C.

Table 5 – S5. The EEC fitting parameters for impedance spectra of Ni20Cr potentiostatically held at +2.10 V_{K+/K} for 10 ks in molten FLiNaK salts at 600 °C

Table 5 – S6. Charge-transfer resistance (R_{ct}) calculated from eec fitting of impedance spectra for Ni20Cr potentiostatically held at +1.75 V_{K+/K}, +1.90 V_{K+/K}, and +2.10 V_{K+/K} from 1 to 10 ks

Table 6 – 1. The calculated dislocation densities and lattice parameters from the X-ray diffractogram of Ni20Cr 10%, 30% and 50% CW samples

Table 6 – 2. Plan view measurements of pore width (l_{pore}) and ligament (λ_{ligament}), and cross-sectional measurements of dealloying depth (h_{dealloyed}) for CW and dealloyed Ni20Cr

Table 6 – 3. Time-dependent changes in l_{pore}, λ_{ligament}, and h_{dealloyed} of 50% CW Ni20Cr alloy dealloyed in FLiNaK, 600 °C at +1.90 V_{K+/K}

Table 6 – S1. Weighted fractional elemental composition (in ppm) of LiF, NaF, and KF salts according to supplier's certificates of analysis

Table 6 – S2. The EEC fitting parameters for impedance spectra of 10%, 30% and 50% CW Ni20Cr alloy potentiostatically dealloyed in FLiNaK, 600 °C at +1.75 V_{K+/K} and +1.90 V_{K+/K}

Table 6 – S3. Ionic diffusivity (D_{Ox}) of corrosion products calculated from the Warburg diffusion coefficient from Table 4 using Eq. 12

Table 6 – S4. Calculation of cathodic correction factors

Table 6 – S5. Results of digital image porosity analysis for Ni20Cr at varying % CW dealloyed in molten FLiNaK at 600 °C for 10 ks at the E_{applied} of 1.75 and 1.90 V_{K+/K}. The porosity of post-test specimen surfaces was estimated using digital image processing techniques applied to the cross-sectional SEM micrographs. First, the region of interest (ROI), which was the porous, dealloyed surface, was manually isolated from the bulk substrate. Open-source image analysis software was then used to binarize the remaining alloy and voids within the ROI via a global thresholding algorithm. The porosity was calculated as the ratio of the void area to the total image area

Table 6 – S5. Ni surface diffusivities reported at 600 °C

Table A1 – 1. Gibbs free energy of fusion and formation for select chemical compounds at 600°C

Table A1 – 2. A list of half-cell redox reactions, their nernst potential equation and formal potentials (E°) calculated at 600°C utilized in this work

Table A2 – 1. Collected electrochemical impedance spectroscopy data in molten salts

Table A2 – 2. Parameters for ECM simulations

Table A2 – 3. EIS fitting parameters for pure Cr in Molten FLiNaK salts + 1 wt% EuF3 at 600 °C for 1hr under open-circuit condition

Table A2 – 4. EIS fitting parameters for pure cr corroded in molten FLiNaK salts + 1 wt% Euf3 at 600 °C for 24 h under open-circuit condition

List of Figures (Notation: Task# – Figure #)

Figure 1 – 1. Figure of merit displaying of the electrical power density (MW/m^3) and primary operating pressure (MPa) for different reactor coolants, including Liquid Metal (red), Molten Salt (yellow), Helium (purple), and Water (blue). The operating pressure range and power density for each coolant are represented by ellipses, with data points showing specific reactors or designs.

Figure 1 – 2. Schematic diagram of an example Molten Salt Reactor (MSR) system, showcasing the reactor core, control rods, and purified salt circulation through heat exchangers to generate steam, which powers a turbine connected to an electrical generator. The system also includes a chemical processing plant and emergency dump tanks equipped with a freeze plug for safety in case of emergencies. Noted that a reactor design can differ among developers.

Figure 1 – 3. The number of scholastic publications, including journal articles, technical reports, book chapters, conference abstracts, in the past 7 decades based on Google scholar data

Figure 1 – 4. Comparison of half-cell Nernst potential of redox metal/metal fluoride couples relative to a F_2/F^- reference as a function of temperature in fluoride salts constructed by Guo et al.²⁹

Figure 1 – 5. Compiled plots displaying the reported mass loss of Hastelloy N, alloy 800H, stainless steel, and other Ni-based alloys at different times in molten fluorides and chlorides by Raiman et al.⁴³

Figure 2 – 1. Schematics of the molten salt electrochemical cell

Figure 2 – 2. Cyclic voltammogram of Pt wire in a FLiNaK salt at 600°C . (a) shows the cyclic voltammogram before and after the addition of (b) 1.0 wt% and (c) 0.42 wt% of CrF_3 at 600°C . (a), (b) indicate the equilibrium potential of KF reduction ($E_{\text{KF}/\text{K}}$). The red dotted lines in (b) and (c) show the approximate experimentally determined equilibrium redox potential of Cr/Cr(II) redox couples ($E_{\text{Cr}/\text{Cr(II)}}$).

Figure 2 – 3. The concentration of Cr calculated using cyclic voltammetry. (a) Concentration of Cr(II) and Cr(III) species. (b) The percent conversion from CrF_3 to Cr(II) species at a various weight fraction of CrF_3 added to FLiNaK. The red line marks the reported solubility limit of CrF_3 in FLiNaK at 600°C .

Figure 2 – 4. The Nernst potentials associate with $\text{Cr}^0/\text{Cr(II)}$ redox reaction at different calculated concentrations of Cr(II) ions in FLiNaK at 600°C . The left y-axis shows the potential relative to the pseudo KF/K potential and the right y-axis shows that calculated potential referenced to the F_2/F^- potential.

Figure 2 – 5. $E - \log(a_{\text{F}^-})$ equilibrium diagram for Cr. (a) considers the CrF_3^- and CrF_6^{3-} , and (b) the CrF_4^{2-} and CrF_5^{2-} solvated states. The red, blue, and green dots at $\log(a_{\text{F}^-}) = 1.693$ mark the results presented in Fig. 6. The gray vertical line at $\log(a_{\text{F}^-}) = 1.693$ indicates the fluoride activity corresponding to the FLiNaK salts. $a_{\text{Cr(II)}}$ and a_{KF} were assumed to be 10^{-6} and 20.3M, respectively. The ratio of $a_{\text{Cr(III)}}/a_{\text{Cr(II)}}$ of 0.082 was used based on Fig. 2. The ratio of $a^{1/2}_{\text{H}}/a_{\text{HF}}$ used was be 0.1, 1 and 10.

Figure 2 – 6. X-Ray diffractogram of the solidified FLiNaK salt in (a) baseline condition, and with Cr potentiostatically polarized to (b) $-5 V_{\text{F}_2/\text{F}^-}$ for 1h, (c) $-4 V_{\text{F}_2/\text{F}^-}$ for 50h, (d) $-3.2 V_{\text{F}_2/\text{F}^-}$ for 50h

Figure 2 – 7. $E - \log(a_{\text{CrF}_3^-})$ equilibrium diagram for Cr in FLiNaK salts ($\log(a_{\text{F}^-}) = 1.693$) at 600°C . The blue dot indicates the equilibrium redox potential of Cr/Cr(II) reported in Fig 5.

Figure 3 - 1. Schematics of molten salt electrochemical cells 5-electrodes set up

Figure 3 – 2. Electrochemical diagnostics of the FLiNaK molten salt at 600°C using a Pt wire. (a) Cyclic voltammogram, (b) potential-time relationship during the 60 s galvanostatic hold of Pt wire at -2, -40, and -100 mA/cm^2 , and (c) square wave voltammogram.

Figure 3 – 3. Potential-time relationship of Pt wire working electrode (red curve), Pt mesh counter electrode (blue curve), and cell voltage (purple) galvanostatically held at (a) 40 and (b) -40 mA/cm²

Figure 3 – 4. Linear sweep voltammogram curve of Cr in FLiNaK at 600 °C corrected with solution resistance, cathodic current density, and limiting current density

Figure 3 – 5. (a) Linear sweep voltammogram of Cr in FLiNaK at 600 °C measured at a scan rate of 1 mV/s. The E-log(*i*) curve was colored to distinct the cathodic, charge-transfer, and mass-transport regimes. The plot was shaded with colors to show the field of thermodynamic stability of Cr, CrF₃⁻, and CrF₆³⁻ species as a function of potential (dashed line shows the phase boundary). The green and blue dotted lines show the half-cell redox potential for HF/H₂ and Cr(III)/Cr reduction, respectively. The activities of Cr(II) and Cr(III) were assumed to be 10⁻³ M; F⁻ to be 49.3 M; HF to be 100 ppm. (b) and (c) shows the current-time relationship of Cr potentiostatically polarized at 0.95 and 1.20 V_{pseudo K+/K} for 700 s and 1000 s, respectively.

Figure 3 – 6. The potential range for rapid CV sweeping was highlighted in (a) and (b), representing a charge-transfer (0 and 30 mV vs. OCP) and a mixed charge-transfer, and mass-transport regimes (0 and 600 mV relative to OCP), respectively. Cr oxidation kinetic regimes are shown in the cyclic voltammograms in (c) and (d) recorded with a scan rate of 10 mV/s. (e) shows the uniform thickness of K₃CrF₆ salt film formed from the cycling in (b) using Faraday's Law and (f) shows the boundary layer thickness calculated using limiting current densities measured in (d)

Figure 3 – 7. Linear sweep voltammogram of Cr in FLiNaK salts at 600 °C with the additions of 0.14 wt%, 0.28 wt%, and 1.00 wt% of CrF₃ recorded at a 0.5 mV/s scan rate

Figure 3 – 8. Relationship between true anodic current densities and CrF₃ concentration

Figure 3 – 9. (a) shows the linear sweep voltammogram measured at scan rates of 0.5, 1.0, 2.5, and 10 mV/s. (b) shows the anodic limiting current densities and transition time for salt film formation calculated using the Sand Equation.

Figure 3 - 10. (a) Open circuit potential measurements of Cr in FLiNaK salts at 600 °C for 50 h. (b) shows the LSV curve performed after 1 h and 50 h of static immersion. The dotted lines in (b) indicate the phase boundary between Cr, Cr(II), and Cr(III) species with their activities assumed to be 10⁻⁶ M. The green dotted line shows the phase boundary of Cr(III)/Cr(II) at saturated conditions.

Figure 3 – 11. Plan view and X-ray diffractogram of residual salts for Cr potentiostatically polarized in FLiNaK salts at 600 °C at (a,d) +0.18 for 1 h, (b,e) +1.08 for 50 h and (c,f) +1.80 V_{pseudo K+/K} for 50 h

Figure 3 – 12. Plan view surface morphology of Cr potentiostatically polarized in FLiNaK salts at 600 °C at (a) 1.08 and (b) 1.80 V_{pseudo K+/K} for 1ks

Figure 3 – 13. Current-time relationship of Cr potentiostatically polarized in FLiNaK salts at 600 °C at (a) 0.18 for 1 h, (b) 1.08 and (c) 1.80 V_{pseudo K+/K} for 50 h.

Figure 3 – 14. Plan view surface micrograph of Cr upon completion of the LSV scan. (b) shows the overlapped elemental maps of (a). The color orange, blue, and red, yellow correspond to Cr, F, K, Na respectively. (c) shows the surface topography colormap of the dashed yellow rectangle. The black arrow in (c) shows the relative height measurement and the result is displayed in (d)

Figure 3 – 15. Plan view SEI micrograph of Cr subjected to LSV scan in 1 wt% CrF₃ + FLiNaK salts at 600 °C measured at (a) 1500x, (b) 5000x, and (c) 7000x magnifications

Figure 3 – 16. (a,b) Cross-sectional SEM micrograph of Cr immersed in 50 h at 600 °C in FLiNaK. (c) EBSD orientation map of (d). shows the surface of the as-corroded Cr sample

Figure 3 – 17. Macrophotographs of Cr embedded in residual FLiNaK salts after exposure at 600 °C for (a) 10 h, (b) 20 h, (c) 30 h, (d) 40 h, and (e) 50 h, respectively. Selected regions in (e) were analyzed with XRD shown in (f)

Figure 3 – 18. Evan's diagram constructed for pure Cr in molten FLiNaK salts at 600 °C. The red curves show the E-log(*i*) curves consisting of charge-transfer and mass-transport controlled regimes for the anodic Cr/Cr(II)/Cr(III) reactions. (a) shows the cathodic polarization curves for the HF/H₂ reactions with [HF] assumed between 10 and 1000 ppm. (b) shows cathodic polarization curves for the Cr(III)/Cr(II) reactions at various concentration of Cr(II) and Cr(III).

Figure 3 – 19. Evan's diagrams highlight the conditions under which Tafel slopes determination via linear fittings in the anodic CT regimes is (a) valid or (b) compromised. (a) shows an example of a valid scenario with cathodic reactions being HF/H₂ at 100 ppm of HF. In contrast, (b) illustrates a scenario where Tafel slope determination is impossible when the K₃CrF₆ salt film is present on the surface. The semi-transparent orange rectangles in both (a) and (b) represent the typical, experimentally expected anodic region for Tafel slope determination.

Figure 4 – 1. Schematics of the multi-electrode molten salt electrochemical cell

Figure 4 – 2. Cyclic voltammogram of Pt in unpurified FLiNaK salts at 600 °C 8 mm away from the Cr metal at 100 mV/s. (a) shows the baseline CV curve before Cr immersion. The orange box highlighted the CV potential scan range for (b) through (f) shows the Pt-CV curve from 0 to 50 h of Cr exposure. The current peaks pertaining to the half-cell redox reactions of Cr/Cr(II), Cr(II)/Cr(III), Cr(III)/Cr(II), and Cr(II)/Cr were marked on the CV curves with the black arrows

Figure 4 – 3. X-Ray diffractogram of residual unpurified FLiNaK salts after 50 h of Cr corrosion at 600 °C (cooling rate ~20 °C/min)

Figure 4 – 4. X-Ray diffractogram of the salt film formed on the Pt foil after 50 h of Cr exposure in unpurified FLiNaK salts

Figure 4 – 5. Cyclic voltammograms of a platinum wire (a) that was continuously exposed to or (b) separately inserted into the FLiNaK salts at 50 h at various scan rates. (c) shows the peak current densities plotted versus the square root of scan rates

Figure 5 – 6. (a) Calculated concentrations of CrF₃⁻, CrF₆³⁻ species and their combined value from cyclic voltammetry results are shown in Figure 2. (b) shows the semi-infinite diffusion profile for Cr species reconstructed using results from (a) between 10 and 50 h

Figure 5 – 7. (a) Photograph of post-exposure FLiNaK salts fractured to reveal the location of Cr metal, bulk salt "Region (a)", salt film "Region (b)", and the location of a Pt electrode; (b) shows the schematics illustrating the development of a corrosion product concentration profile; (c) shows the X-Ray diffractogram of the different regions highlighted in (a) and unpurified FLiNaK before corrosion (black line) for comparison.

Figure 5 – 8. Mass loss measured by the static immersion method and calculated from the electrochemical CV method (with and without diffusion profile correction).

Figure 5 – 9. The open-circuit potential of Cr in FLiNaK for 50 h overlaid with square, circular, and triangular symbols representing the half-cell redox potentials of Cr/Cr(II), Cr(II)/Cr(III) and Cr(II)/Cr couples, respectively. The filled symbols represent surface concentration corrected potential values.

Figure 6 – 1. (a) The one-dimensional phase stability diagram for Cr, Ni, Cr(II), Cr(III), and Ni(II) species calculated assuming a F⁻ ion activity (*a*_{F⁻}) of 49.3 M at 600 °C and using the activity of Cr and Ni in Ni₂₀Cr

(wt%). Horizontal black arrows on the diagram represent phase boundaries based on an assumed species concentration, while the double-headed vertical arrow highlights the range of phase boundary conditions, extending from 10^{-3} M to bulk saturation. (b) and (c) display the experimental polarization curves for pure Ni, Cr, and the Ni20Cr alloy in the form of linear sweep voltammograms at 1 mV s^{-1} . (c) illustrate the polarization curve for the Ni20Cr alloy, both in its as-measured state and after corrections for iR and cathodic current density

Figure 6 – 2. Representative backscattered electron micrographs depicting the top-view surfaces of Ni20Cr (wt.%) subjected to potentiostatic polarization conditions: (a) at $+1.75 V_{K+/K}$, (b) at $+1.90 V_{K+/K}$, (c) at $+2.1 V_{K+/K}$, (d) at $+2.3 V_{K+/K}$, (d) at $+2.5 V_{K+/K}$, and (e) at $+2.7 V_{K+/K}$. The alloys were exposed to molten FLiNaK salts at a temperature of $600 \text{ }^\circ\text{C}$ for a duration of 10 ks

Figure 6 – 3. Ni20Cr (wt.%) subjected to potentiostatic hold in molten FLiNaK at $600 \text{ }^\circ\text{C}$ at $+1.75 V_{K+/K}$. (a) display the current-time relationship, (b) shows the cyclic voltammogram measured the secondary Pt WE before (black) and after 10 ks of potentiostatic hold of Ni20Cr. The redox peaks of possible Cr/Cr(II) and Cr(II)/Cr(III) reactions are labeled. The inset in (b) highlights the potential range in which the Ni/Ni(II) half-cell redox reactions are possible (c) shows the Nyquist plots measured at each 2 ks time increment containing the EEC used for fitting analysis and fitting results (black lines)

Figure 6 – 4. Ni20Cr (wt.%) potentiostatically polarized at $+1.75 V_{K+/K}$ for 10 ks. (a) Plan-view SEM image showing surface morphology. (b) Composite EDS elemental maps overlaid on SEM image, highlighting Ni (red) and Cr (green) distribution. Specific locations were marked for point analysis. (c) Cross-sectional SEM image of the sample. (d) and (e) EDS maps for Ni (red) and Cr (green), respectively. The semi-transparent rectangle in (c) indicates the area subjected to EDS line scan analysis, with corresponding elemental profiles for Ni and Cr presented in (f). EBSD analysis is shown via the inverse pole figure (IPF) plot of a separate cross-sectional surface in (g). The stereographic triangle in (h) marks the orientation of the grains present in (g)

Figure 6 – 5. Ni20Cr (wt.%) subjected to potentiostatic hold in molten FLiNaK at $600 \text{ }^\circ\text{C}$ at $+1.90V_{K+/K}$. (a) display the current time relationship, (b) shows the cyclic voltammogram measured the secondary Pt WE before (black) and after 10 ks of potentiostatic hold of Ni20Cr. The redox peaks of possible Cr/Cr(II), Cr (II)/Cr(III), Ni/Ni(II) reactions are labeled. The inset in (b) highlights the potential range in which the Ni/Ni(II) half-cell redox reactions are possible (c) shows the Nyquist plots measured at each 2 ks time increment containing the EEC used for fitting analysis and fitting results (black lines)

Figure 6 – 6. Ni20Cr (wt.%) potentiostatically polarized at $+1.90 V_{K+/K}$ for 10 ks. (a) Plan-view SEM image showing surface morphology. (b) Composite EDS elemental maps overlaid on (a), highlighting Ni (red) and Cr (green) distribution. Specific locations were marked for point analysis. (c) Cross-sectional SEM image of the sample. (d), (e), (f) are EDS maps for Ni (red), Cr (green), and F (blue) respectively. The semi-transparent rectangle in (c) indicates the area subjected to EDS line scan analysis, with corresponding elemental profiles for Ni and Cr presented in (g). EBSD analysis is shown via the inverse pole figure (IPF) plot of a separate cross-sectional surface in (h). The stereographic triangle in (i) marks the orientation of the grains present in (h)

Figure 6 – 7. Backscattered electron micrographs of Ni20Cr potentiostatically held at $+1.90V_{K+/K}$ for (a) 1ks, (b) 3ks, (c) 5ks, and (d) 10ks in molten FLiNaK salts, $600 \text{ }^\circ\text{C}$ taken at $2,000\times$ magnification. (e), (f), (g), and (h) display the $10,000\times$ magnified region of (a), (b), (c), and (d), respectively

Figure 6 – 8. Ni20Cr (wt.%) subjected to potentiostatic hold in molten FLiNaK at $600 \text{ }^\circ\text{C}$ at $+2.10 V_{K+/K}$. (a) display the current time relationship, (b) shows the cyclic voltammogram measured the secondary Pt WE before (black) and after 10 ks of potentiostatic hold of Ni20Cr. The redox peaks of possible Cr/Cr(II) and Cr(II)/Cr(III) reactions are labeled. The inset in (b) highlights the potential range in which the Ni/Ni(II)

half-cell redox reactions are possible (c) shows the Nyquist plots measured at each 2 ks time increment containing the EEC used for fitting analysis and fitting results (black lines).

Figure 6 – 9. Ni₂₀Cr (wt.%) potentiostatically polarized at +2.10 V_{K+/K} for 10 ks. (a) Plan-view SEM image showing surface morphology. (b) Composite EDS elemental maps overlaid on (a), highlighting Ni (red) and Cr (green) distribution. Specific locations were marked for point analysis. (c) Cross-sectional SEM image of the sample. (d), (e), (f) are EDS maps for Ni (red), Cr (green), and F (blue) respectively. The semi-transparent rectangle in (c) indicates the area subjected to EDS line scan analysis, with corresponding elemental profiles for Ni and Cr presented in (g). EBSD analysis is shown via the inverse pole figure (IPF) of a separate cross-sectional surface in (h). The stereographic triangle in (i) marks the orientation of the grains present in (h)

Figure 6 – 10. X-ray diffractogram of as-solidified salt mixture subjected to Ni₂₀Cr potentiostatic hold at (a) +1.75 V_{K+/K}, (b) +1.90 V_{K+/K}, and (c) +2.10 V_{K+/K} in FLiNaK, 600 °C for 10 ks

Figure 6 – 11. Plan view measurements of ligament width between 1 and 10 ks for Ni₂₀Cr (wt.%) for Ni₂₀Cr potentiostatically polarized in Molten FLiNaK at 600 °C. The inset displays a simplified schematic of Ni-rich ligament coarsening process

Figure 6 – 12. Cumulative charge consumed (Q_{consumed}) during the potentiostatic hold of Ni₂₀Cr in molten FLiNaK salts, 600 °C at +1.75 V_{K+/K}, +1.90 V_{K+/K}, and +2.10 V_{K+/K} for 10 ks

Figure 6 – 13. Charge transfer resistance (R_{ct}) of Ni₂₀Cr in molten FLiNaK salts, 600 °C potentiostatically held at +1.75 V_{K+/K}, +1.90 V_{K+/K}, and +2.10 V_{K+/K} from 1 ks to 10 ks

Figure 6 – 14. Schematics displaying a simplified mechanism of molten fluoride dealloying

Figure 6 – 15. J_{electric} vs.time for Ni₂₀Cr (wt.%) potentiostatically held at (a) +1.75 V_{K+/K}, (b) +1.90 V_{K+/K}, and (c) +2.10 V_{K+/K} for 10 ks. The solid grey line represents the calculated effective bulk diffusion flux (J_{Bulk}^{Cr}) and the dashed line shows the ionic diffusion flux of Cr(III), J_{FLiNaK}^{Cr(III)}, in FLiNaK at 600 °C

Figure 7 – 1. EBSD analysis on Ni₂₀Cr CW samples before corrosion. (left) Inverse pole figure (IPF) maps and (right) GND maps taken for the (a) 0% CW, (b) 10% CW, (c) 30% CW, and (d) 50% CW conditions

Figure 7 – 2. Plan view backscattered scanning electron (BSE) micrographs of Ni₂₀Cr alloys subjected to an E_{applied} at +1.90 V_{K+/K} for 10 ks in molten FLiNaK at 600°C. Panels (a) through (d) depict the samples after 0%, 10%, 30%, and 50% CW, respectively, all captured at 2,500× magnification. Panels (e) through (h) present the corresponding micrographs at 10,000× magnification

Figure 7 – 3. BSE micrographs displaying cross sectional view of Ni₂₀Cr alloys subjected to (a) 0% CW, (b) 10% CW, (c) 30% CW, and (d) 50% CW dealloyed at +1.75 V_{K+/K} for 10 ks in molten FLiNaK at 600 °C. The insets display regions analyzed with EDS line scan

Figure 7 – 4. The relationship between J_{Bulk}^{Cr} (w/ & w/o CW), J_{electric}^{Cr}, J_{FLiNaK}^{Cr(III)}, h_{dissolved} and time of Ni₂₀Cr with (a,b) 10%, (c,d) 30%, and (e,f) 50% CW dealloyed at 1.75 V_{K+/K} for 10ks

Figure 7 – 5. Plan view BSE micrographs of Ni₂₀Cr alloys subjected to an E_{applied} at +1.75 V_{K+/K} for 10 ks in molten FLiNaK at 600°C. Panels (a) through (d) depict the samples after 0%, 10%, 30%, and 50% CW, respectively, all captured at 2,500× magnification. Panels (e) through (h) present the corresponding micrographs at 10,000× magnification

Figure 7 – 6. BSE micrographs displaying cross sectional view of Ni₂₀Cr alloys subjected to (a) 0% CW, (b) 10% CW, (c) 30% CW, and (d) 50% CW dealloyed at +1.90 V_{K+/K} for 10 ks in molten FLiNaK at 600 °C. The insets display regions analyzed with EDS line scan

Figure 7 – 7. The relationship between $J_{\text{Bulk}}^{\text{Cr}}$ (w/ & w/o CW), $J_{\text{electric}}^{\text{Cr}}$, $J_{\text{FLiNaK}}^{\text{Cr(III)\&Ni(II)}}$, $h_{\text{dissolved}}$ and time of Ni20Cr with (a,b) 10%, (c,d) 30%, and (e,f) 50%CW dealloyed at $1.90V_{\text{K+K}}$ for 10ks

Figure 7 – 8. Cross sectional morphology of 50% CW Ni20Cr subjected to an E_{applied} at +1.90 in molten FLiNaK salts, 600 °C for (a,e) 0.5 ks, (b,d) 1 ks, (c,g) 5 ks, and (d,h) 10 ks. Panels (e-h) show overlaid EDS elemental maps with Ni in red, Cr in green, F in blue, and K in purple, corresponding to panels (a-d), respectively. Panels (e-h) also a semi-transparent grey arrow representing the region analyzed with compositional line profile (wt.%)

Figure 7 – 9. EBSD analysis on 50% CW Ni20Cr sample potentiostatically polarized in molten FLiNaK salts, 600 °C at +1.90 $V_{\text{K+K}}$ for (a,b) 0.5 ks, (c,d) 1 ks, and (e,f) 5 ks, (g,h) 10 ks. (left) IPF maps and (right) GND maps

Figure 7 – 10. Schematic Illustration of diffusion fluxes, and their interaction during Cr dealloying in Ni20Cr alloy at different CW levels 0%, 10% CW, 30% CW, and 50% CW

Figure 7 – 11. SEM cross section analysis of 30% CW Ni20Cr sample potentiostatically polarized in molten FLiNaK salts, 600 °C at +1.90 $V_{\text{K+K}}$. (a) Secondary electron image and corresponding (b) IPF maps and (c) GND maps. EDS elemental maps of (d) Ni, (e) Cr, (f) F, and (h) K

Figure 7 – 12. Magnified SEM cross section analysis at the dealloyed grain boundary triple point shown towards the bottom of Fig. 12. (a) BSE micrograph, and corresponding (b) GND map, (c) grain orientation spread map, and (d) IPF map

Figure 7 – 13. Effective diffusion coefficients (D_{eff}) as a function of grain size (d) calculated using Eq.7 with and without considering dislocation density. Parameters are $D_l = 10^{-15} \text{ cm}^2/\text{s}$, $D_{GB} = 10^{-10} \text{ cm}^2/\text{s}$, $D_{dis} = 10^{-9} \text{ cm}^2/\text{s}$, $\rho = 10^{11} \text{ cm}^{-2}$, and $b = 2.51 \cdot 10^{-8} \text{ cm}$. The transitions of factors that govern D_{eff} are marked for two types of recrystallized grains and the grain size of the 0%CW or as-homogenized alloy

Figure 7 – S1. (a) displays the X-ray diffraction patterns for both the as-homogenized and the CW samples at 10%, 30%, and 50%. (b) shows the calculated dislocation density ($\rho_{\text{dislocation}}$) and lattice parameter (a_{Ni20Cr}) at different cold work levels.

Figure 7 – S2. Cyclic voltammogram of a Pt wire measure at a scan rate of 100 mV/s in FLiNaK at 600 °C relative to the K^+/K potential. Scans were recorded prior to the dealloying of Ni20Cr (grey), and after potentiostatic hold +1.75 $V_{\text{K+K}}$ and (green) +1.90 $V_{\text{K+K}}$ for 10 ks (orange). The red and blue boarder insets show the potential window for Cr/Cr(II)/Cr(III) and Ni/(II) redox reactions, respectively. (a), (b), and (c) shows the results measured at 10%, 30%, and 50% CW, respectively

Figure 7 – S3. (a) and (b,c) display the Nyquist and Bode plots of Ni20Cr (wt.%) dealloyed at +1.75 $V_{\text{K+K}}$ measured at the 10ks mark. The inset in (d) displays the electrical equivalent circuits (EECs) used for fitting

Figure 7 – S4. (a) and (b,c) display the Nyquist and Bode plots of Ni20Cr (wt.%) dealloyed at +1.90 $V_{\text{K+K}}$ measured at the 10ks mark. The inset in (d) displays the electrical equivalent circuits (EECs) used for fitting analysis

Figure 7 – S5. Electrochemical characterization of Ni20Cr in the as-homogenized and 10%, 30%, and 50% CW. (a) displays the linear sweep voltammogram (LSV) measured at a scan rate of 1 mV/s in molten FLiNaK, 600 °C. (b) and (c) display the current-time relationships of the CW samples potentiostatically held at +1.75 $V_{\text{K+K}}$ and +1.90 $V_{\text{K+K}}$ for 10 ks, respectively

Figure 7 – S6. Analysis of LSV results shown in Fig. S3. As-measured LSV plots (black squares) are first IR-corrected (red rhombus). The cathodic Tafel regions are then fitted and plotted as i_{cathodic} (orange triangle). The anodic current density (i_{anodic}) is then calculated and fitted with a linear line representing the anodic Tafel region (solid blue lines)

Figure 7 – S7. Microstructural characterization of Ni20Cr alloys, subjected to varying degrees of cold work. Panels (a), (b), (c), and (d) show the BSE images, maps of GNDs, IPF and its corresponding stereographic triangle and for the samples with 10% CW, respectively. Similarly, panels (d), (e), (f), (g) as well as panels (i), (j), (k), (l) are organized in the same order for the 30% and 50% CW samples, respectively.

Figure 7 – S8. Optical micrographs of (a) 10% CW and (b) 30% CW Ni20Cr samples. The same samples subjected to electrolytic etching in 1M H₂SO₄ at +6 V for ~15 s as displayed in (c) and (d), respectively

Figure 7 – S9. Optical micrographs of (a) 50% CW Ni20Cr sample. (b), (c), (d), and (e) show the electrolytically etched surface (1M H₂SO₄ at +6 V for ~15 s) of a 50% CW sample annealed in Ar gas at 600 °C for 0.5 ks, 1 ks, 5 ks, and 10 ks, respectively.

Figure 7 – S10. Bar chart comparing the average grain interior area of as-homogenized, 10%, 30%, and 50% CW samples annealed in Ar gas, 600 °C for various duration

Figure 7 – S11. Morphological and compositional analysis of the 0%CW Ni20Cr alloy subjected to a potentiostatic hold at +1.75 V_{K+/K} for 10 ks: (a) reveals the dealloyed porous surface; (b) shows the corresponding elemental distribution highlighting the predominance of Ni (red) over Cr (green); (c) provides a cross-sectional view; while (d) and (e) present the Ni and Cr elemental maps, respectively. The white semi-transparent rectangle in (c) indicates the region subjected to EDS line scan, the results of which are depicted in (f). Figures S12 through 19 share this caption format, with additional variations specified for each figure.

Figure 7 – S12. 10% CW Ni20Cr alloy subjected to the potentiostatic hold at +1.75 V_{K+/K} for 10 ks in molten FLiNaK at 600 °C (See Figure 7 – S11 for full captions)

Figure 7 – S13. 30% CW Ni20Cr alloy subjected to the potentiostatic hold at +1.75 V_{K+/K} for 10 ks in molten FLiNaK at 600 °C

Figure 7 – S14. 50% CW Ni20Cr alloy subjected to the potentiostatic hold at +1.90 V_{K+/K} for 10 ks in molten FLiNaK at 600 °C

Figure 7 – S15. 0% CW Ni20Cr alloy subjected to the potentiostatic hold at +1.9 V_{K+/K} for 10 ks in molten FLiNaK at 600 °C

Figure 7 – S16. 10 % CW Ni20Cr alloy subjected to the potentiostatic hold at +1.90 V_{K+/K} for 10 ks in molten FLiNaK at 600 °C

Figure 7 – S17. 10 % CW Ni20Cr alloy subjected to the potentiostatic hold at +1.90 V_{K+/K} for 10 ks in 30% CW Ni20Cr alloy subjected to the potentiostatic hold at +1.90 V_{K+/K} for 10 ks in molten FLiNaK at 600 °C

Figure 7 – S18. 50% CW Ni20Cr alloy subjected to the potentiostatic hold at +1.90 V_{K+/K} for 10 ks in molten FLiNaK at 600 °C

Figure 7 – S19. (a) Cross-sectional BSE images of 10% CW Ni20Cr alloy subjected to the potentiostatic hold at +1.90 V_{K+/K} for 10 ks in molten FLiNaK at 600 °C, demonstrating the occurrence of percolation dealloying within the alloy substrate . (b), (c), (d) and (e) display the elemental maps of Ni, K, Cr, and F, respectively

Figure 7 – S20. Large field of view EBSD analysis on 10% CW Ni20Cr sample potentiostatically polarized in molten FLiNaK salts, 600 °C at +1.75 V_{K+/K} 10 ks. (a) shows the IPF and (b) shows the GND map.

Figure A1 – 1. Potential-fluoride activity diagrams at 600°C (a) shows the potential stability window defined by the fluorine gas evolution (F₂/F⁻) and stability in the oxidized state for Li⁺, K⁺, and Na⁺ cation constituents. The vertical dashed line indicates the F⁻ activity in FLiNaK salt at a_{F⁻} = 49.3 M and (b) displays the Nernst potentials of O₂/O²⁻ and HF/H₂ reactions assuming the oxidant concentration of 10 ppm,

100 ppm, and 1,000 ppm. The diagram was shaded with different colors to indicate the type of gas evolution and/or plating of salt cations within the phase stability map

Figure A1 – 2. Potential-fluoride activity diagrams displaying the Nernst potentials of F_2/F^- , O_2/O^{2-} , $Eu(II)/Eu(III)$, $Ni/Ni(II)$, HF/H_2 , $Fe/Fe(II)$, $Cr/Cr(II)$, $Cr(II)/Cr(III)$, K^+/K , and half-cell redox reactions calculated at 600°C. The concentration of O^{2-} and HF was assumed to be 1,000 ppm (corresponding to the molar concentration of 1.00×10^{-1} M and 1.25×10^{-1} M), $Cr(II)$ in $Cr(II)/Cr(III)$ and $Eu(II)$ are taken to be 10^{-6} M, while that of $Eu(III)$, $Ni(II)$, $Fe(II)$, and $Cr(II)$ in $Cr/Cr(II)$ are assumed to be 10^{-3} M

Figure A2 – 1. The different equivalent electrical circuits (ECMs) selected for EIS simulation in a molten salt system [87]. (a) shows an ideal and simplified Randles circuit, (b) a simplified Randles circuit with a CPE, (c) shows two-time constants in series, termed “Two-time constants”, (d) a Randles circuit with a diffusional impedance (ZW), and (e) a Randles circuit in series with a second-time constant also containing a diffusional element

Figure A2 – 2. Cross-sectional and plan view schematics and optical micrographs of Cr working electrodes of different areas fabricated for molten FLiNaK electrochemistry

Figure A2 – The errors of (a) polarization resistance, R_{ct} and (b) double layer capacitance, C_{dl} calculated as a function of frequency at different disk electrode areas (A_{disk}) and a baseline C_{dl} of 13 mF/cm². The vertical arrows mark the ohmic effect critical frequency ($f_{critical}^{dispersion}$)

Figure A2 – 4. Simulated impedance spectra representing charge-transfer controlled interfacial dissolution of Cr in FLiNaK, 600 °C. The Bode modulus and phase angle plots of the (a,b) simplified Randles circuit and (c,d) two-time constant ECM models are displayed with the disk area of 10^0 , 10^{-1} and 10^{-2} cm². The dashed line shows a baseline case of 10^0 cm² with no k_f^i factors correction, labeled as “ref”. The grey vertical lines identify the frequency regime, 10^{-2} to 10^4 Hz, in which experimental measurement is routinely obtained. All simulation parameters are referenced in Table 1.

Figure A3 – 5. Experimental impedance spectra of Cr exposed in FLiNaK+1wt.% EuF_3 , 600 °C for 1 h. The Cr geometries are macroelectrode (1.9cm²) and two disk electrodes (Disk A: $1.96 \cdot 10^{-1}$ & Disk B: $1.29 \cdot 10^{-2}$ cm²). The Bode modulus plots are shown in (a), (b), and (c), representing the raw, area corrected, and R_s and area corrected curves, respectively. The phase angle plots are shown in (d) and (e) displaying the raw and R_s corrected results, respectively. Symbols are the data and the solid lines are the fits.

Figure A3 – 6. Simulated impedance spectra representing mass transport controlled interfacial dissolution of Cr in FLiNaK, 600 °C. The Bode impedance and phase angle plots in (a,b) are simulated spectra based on an ECM comprising of two-time constants containing diffusional impedance of a disk (Figure 1e) with an assumed area of 10^0 , 10^{-1} and 10^{-2} cm², and those in (c,d) are experimental measurements of Cr exposed in molten FLiNaK + 1 wt.% EuF_3 for 24h with different electrode geometries and areas. The dashed line reveals a baseline case of 10^0 cm² with no k_f^i factors correction, labeled as “ref”. The grey vertical lines the frequency regime, 10^{-2} to 10^4 Hz, in which experimental measurement is feasible

Figure A3 – 7. Percent variation as a function of lower termination frequency (f_{cutoff}) selected for ECM fitting analysis. The fitting processes are performed on the simulated impedance spectra constructed based on the (a) simplified Randles circuit (Figures 4a & 4b) and (b) two-time constants (Figure 4c and 4d) ECM models for both bulk rectangular (Bulk R) and disk geometries. The down arrow on (a) and (b) indicates the f_{trans}^{RCT} with and without k_f correction

Bibliography

Publications that resulted from this dissertation and other relevant work are listed below:

1. *H. L. Chan**, E. Romanovskaia, V. Romanovski, H. Singh, M. Tran. Scully. “The Effect of Cr Composition in the Molten Salt Dealloying Behavior of Ni-Cr ” (*Under preparation*)
2. *H. L. Chan**, E. Romanovskaia, S. Mills, V. Romanovski, X. Wang, AM. Minor, P. Hosemann, J.R. Scully. “Dealloying of Cold-Rolled Ni₂₀Cr (wt.%) Alloy in Molten FLiNaK Salts” *Acta Materialia*. (Submitted Dec 2024)
3. S. H. Mills, *H. L. Chan**, N. Biederdorf, M. Hong, E. Romanovskaia, C. Peddetti, L. Capolungo, M. Asta, J. R. Scully, A. M. Minor, P. Hosemann. “Uncovering the re-distribution mechanism of Ni in a de-alloyed Ni-Cr alloy in molten fluorinated salts” *Acta Materialia*, (Submitted Nov. 2024)
4. J. Qiu, R. Hayes, H. Williams, H.L. Chan, D.D. Macdonald, R. Scarlat, D. Kaoumi, John R Scully, Peter Hosemann. “Effect of cold forging on the microstructure and corrosion behavior of type 316L stainless steel in molten FLiNaK salt” *Journal of Nuclear Materials*, 155624–155624. <https://doi.org/10.1016/j.jnucmat.2025.155624>
5. *H. L. Chan**, *H. Singh*, *V. Romanovski*, *E. Romanovskaia*, *J. Han*, *J.R. Scully*, Uncovering accurate values of the polarization resistance in molten fluorides using electrochemical impedance spectroscopy, *Journal of Electroanalytical Chemistry*. (2024) 118619. <https://doi.org/10.1016/j.jelechem.2024.118619>.
6. *H. L. Chan**, E. Romanovskaia, S. Mills, V. Romanovski, M.S. Hong, C. Peddetti, N. Biederdorf, AM. Minor, P. Hosemann, M. Asta, J.R. Scully. Morphological Evolution and Dealloying Behavior of Ni₂₀Cr in Molten FLiNaK. *Journal of the Electrochemical Society*. 171 (2024) 081501. <https://doi.org/10.1149/1945-7111/ad6037>.
7. **H.L. Chan*, J.R. Scully. Deciphering when Metal Corrosion is Spontaneous in Molten Fluorides Using Potential-Activity Diagrams. *Corrosion*, 79(11), 1236–1240. <https://doi.org/10.5006/4401>
8. **H.L. Chan*, E. Romanovskaia, V. Romanovski, F. Garfias, M. Hong, S. Mastromarino, P. Hosemann, Raluca Scarlat, J.R. Scully, An In Situ, multi-electrode electrochemical method to assess the open circuit potential corrosion of Cr in unpurified molten FLiNaK, *Corrosion Science*. 222 (2023) 111389–111389. <https://doi.org/10.1016/j.corsci.2023.111389>.
9. M. Hong, *H. L. Chan**, P. Hosemann, J. R. Scully. “Corrosion property of Alloy 625 in Molten FLiNaK salt according to the Tellurium Concentrations”. *Journal of Nuclear Materials*. 212:110913. <https://doi.org/10.1016/j.jnucmat.2023.154548>
10. H. L. Chan, E. Romanovskaia, V. Romanovski, D. Sur, M. Hong, P. Hosemann, J.R. Scully. Corrosion Electrochemistry of Chromium in Molten FLiNaK Salts at 600 °C. *Journal of the Electrochemical Society*. 170, 081502. <https://doi.org/10.1149/1945-7111/ace8c0>.
11. *H. L. Chan**, E. Romanovskaia, A. L. Morales, F. Schmidt, V. Romanovski, C. Winkler, J. Qiu, Y. Wang, D. Kaoumi, F. A. Selim. B. P. Uberuaga, P. Hosemann, J.R. Scully. Multi-length scale characterization of point defects in thermally oxidized proton irradiated iron oxides. *Materialia*, 28, 101762, 2023. <https://doi.org/10.1016/j.elecom.2020.106900>.
12. M. Hong, *H. L. Chan**, Y. Xie, E. Romanovskaia, P. Hosemann, J. R. Scully. “Effect of Tellurium Concentration on the Corrosion and Mechanical Properties of 304 Stainless Steel in Molten FLiNaK Salt”. *Corrosion Science*, 110913, 2022. <https://doi.org/10.1016/j.corsci.2022.110913>
13. H. L. Chan, E. Romanovskaia, J. Qiu, P. Hosemann, J.R. Scully. Insights on the corrosion thermodynamics of Cr in molten LiF-NaF-KF eutectic salts. *Npj Materials Degradation*, 6(1), 2022. <https://doi.org/10.1038/s41529-022-00251-3>.
14. R. Auguste, *H. L. Chan**, E. Romanovskaia, Wagner, F. Selim, D. Kaoumi, B. P. Uberuaga, P. Hosemann, J. Scully. “A multimodal approach to revisiting oxidation defects in Cr₂O₃. *Npj Materials Degradation*, 6(61), 2022. <https://doi.org/10.1038/s41529-022-00269-7>.
15. J. Han, M.G. Wartenberg, *H.L. Chan**, B.K. Derby, N. Li, J.R. Scully, Electrochemical stability, physical, and electronic properties of thermally pre-formed oxide compared to artificially sputtered oxide on Fe thin films in aqueous chloride, *Corrosion Science*. 186 (2021) 109456–109456. <https://doi.org/10.1016/j.corsci.2021.109456>.
16. J. Han, *H. L. Chan**, M.G. Wartenberg, H.H. Heinrich, J.R. Scully. “Distinguishing interfacial double layer and oxide-based capacitance using gold and pre-oxidized Fe-Cr in room temperature ionic liquid,” *Electrochemistry Communication*. 122, 106900, 2021. <https://doi.org/10.1016/j.elecom.2020.106900>.

Chapter 1: Background

The Development of Molten Salt Reactor

Dr. Nikolai Kardashev famously proposed the concept of Kardashev scale in the late 1960s, correlating that the progress of a civilization to its technical capability to harness and utilize energy.¹ This concept cannot be more relevant to today's world. The International Energy Agency predicts that the global demand of energy will experience a 2-fold increase by 2030². Such demand is exacerbated by the rising developments of artificial intelligence which have considerable energy consumption at their data centers³, electric vehicles and consumer electronics.⁴ Coupled with the societal need to reduce carbon footprints, the production of clean energy is a high priority to transform the traditionally fossil fuel dependent economy.

Nuclear power is an alternative and promising source of energy to fulfill this demand. To-this-date, 18% of U.S. domestic energy is generated by nuclear power alone⁵, notably using industrial, gigawatt scale GW-scale light water reactors (LWRs). In LWR, water is pressurized to steam above 10 MPa operating near $\sim 300^{\circ}\text{C}$ in the primary coolant, including both the reactor core and primary heat exchange loop⁶. Enthalpy produced from the primary loop transfers to the second heat exchange loop connected to a steam turbine generator. LWR has broadly applied for both military and civilian applications since the 1950s, whether it is designed to deploy at industrial/GW or at modular/MW scales. However, major public and political concerns remain regarding the possibility of a loss-of-coolant accident triggered by material failures, potentially leading to a nuclear reactor meltdown. Such an accident will have a catastrophic impact on human health and environmental safety based on the lessons learned from the Chernobyl and Fukushima incidents⁶ (not to mention the radioactive nuclear wastes produced that last thousands of years). Consequentially, in the last two decades the nuclear industry has constantly been seeking alternative reactor concepts with enhanced safety and maneuverability during an emergency, reduced radioactive waste without compromising the reactor performance.

In present, small modular reactor (SMR) has been proposed as an alternative safe and efficient reactor concept.^{7,8} Despite being designed to only generate MW-scale of thermal and/or electrical power, SMR offers a higher dispatchability (i.e. reactor core can be designed to fit and be transported in a truck) and opportunities to utilize both aqueous (water/steam) and non-aqueous medium (liquid metal, molten salt, or helium gas) as a reactor coolant. The latter is also referred to as Generation IV reactor concept⁹. Fig. 1 displays the electrical power density versus the primary operating pressure of available SMR data.⁷ An ideal scenario is a reactor that operates at near ambient pressure (thus reducing the risk of explosion, or materials failure leading to loss of coolant and lowering structural materials constraints) and at high power density. From Fig. 1, molten salt reactor (MSR) and liquid metal reactor (LMR) fall into this opportunistic regime.¹⁰

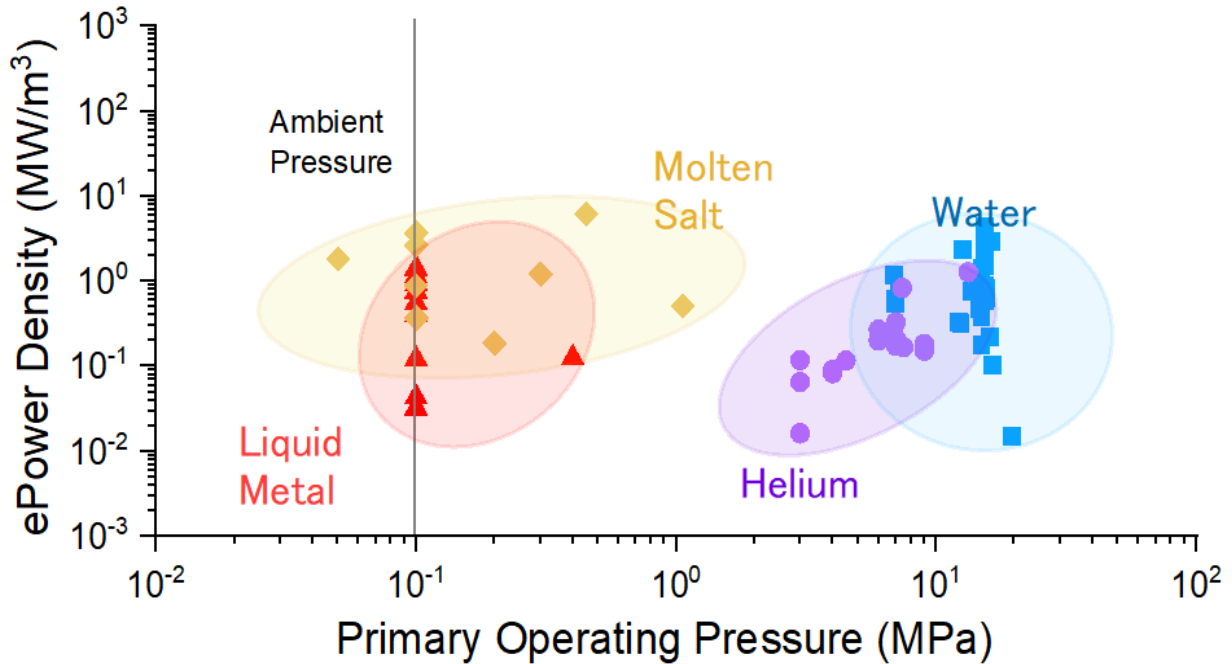


Figure 1. Figure of merit displaying of the electrical power density (MW/m^3) and primary operating pressure (MPa) for different reactor coolants, including Liquid Metal (red), Molten Salt (yellow), Helium (purple), and Water (blue). The operating pressure range and power density for each coolant are represented by ellipses, with data points showing specific reactors or designs. ⁷

MSRs utilize a molten fluoride salt blend as the primary fuel for nuclear fission (referred as primary salt) and as a high temperature fluid for heat storage and exchange (referred as secondary salt) to a tertiary power module. Fig. 2 displays a schematics of a molten salt reactor displaying these compartments. The use of molten salt offers several key advantages that distinguish them as promising candidates for SMR¹⁰⁻¹², including but not limited to, (i) *low melting but high boiling points*, (ii) *chemical stability under neutron irradiation*, (iii) *near ambient pressure at high temperature up to 900°C (vs. 218 atm in LWR)*, (iv) *ability to serve as fuels*, (v) *capable of utilizing U-233/Thorium fuel cycle (vs. 4 times more abundant than U-235 used in LWR¹³)*, and (vi) *closed fuel cycles limiting long-lived actinides waste¹⁴*.

Features (i) through (iii) enable inherent safety (eliminating the possibility of steam explosion, which is a major cause for both the Chernobyl and Fukushima disasters^{6,15,16}) and more efficient reactor operation with an ideal thermodynamic efficiency of 50% (vs. 30% in LWR)⁷, whereas (iv) and (vi) allow simpler fuel design, waste handling, and potentially a more resilient fuel supply chain. Candidate fuel and coolant salts identified include, LiF-NaF-KF (46.5-11.5-42 mol %), LiF-BeF₂ (66-34 mol%), and NaF-ZrF₄ (59.5–40.5 mol%)¹⁷. Due to its promising properties, MSR has become a popular global thrust for clean energy development through a collaborative effort between academia, government laboratories, and industries⁷.

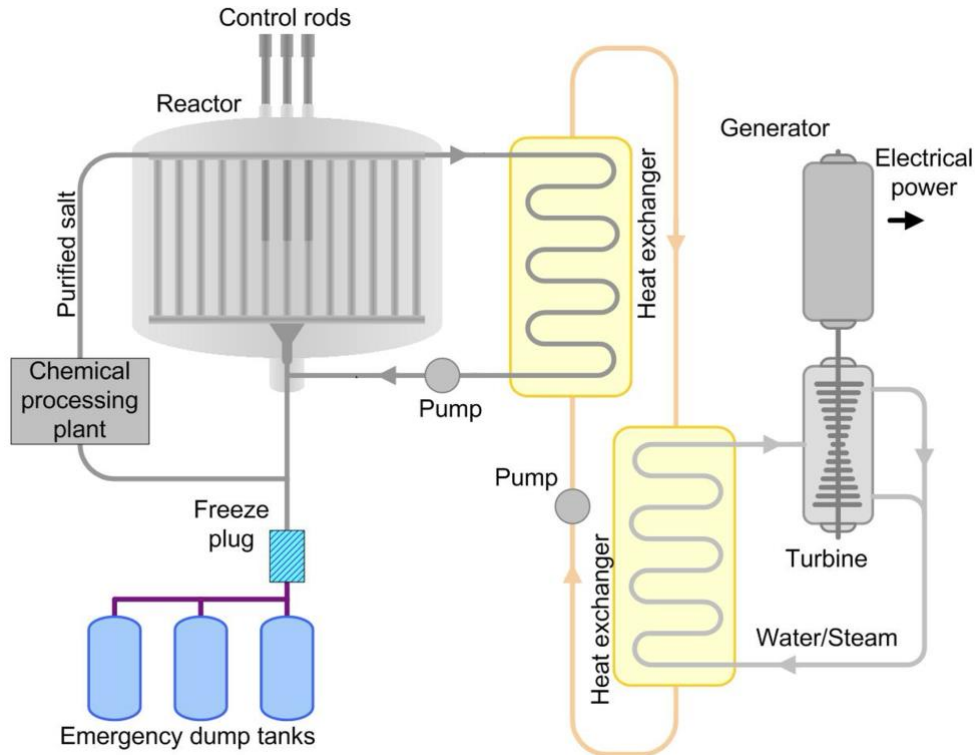


Figure 2. Schematic diagram of an example Molten Salt Reactor (MSR) system, showcasing the reactor core, control rods, and purified salt circulation through heat exchangers to generate steam, which powers a turbine connected to an electrical generator. The system also includes a chemical processing plant and emergency dump tanks equipped with a freeze plug for safety in case of emergencies. Noted that a reactor design can differ among developers.

To understand the scientific principles and objectives proposed in this work, conducting a brief review of the history of MSR materials and corrosion development is vital. Fig. 3 shows the number of scholastic publications per year compiled by the authors using Google Scholar Database include, but not limited to, journal publications, book chapters, conference abstracts and proceedings. Two key words: “Molten Salt Reactor”, “Corrosion in Molten Fluorides” were searched. The pioneering research work began in the 1950s initiated by aircraft propulsion project at the Oak Ridge National Laboratory (ORNL)¹⁹. Between 1950s and 1980s, most literature work were driven by technical reports published by ORNL^{19–26}. These earlier work seek to explore and/or develop suitable salt-facing structural alloys that offers a combination of (1) corrosion resistance & compatibility with fission products, (2) resistance to high temperature creep deformation, (3) tolerance of radiation damage coupled with (4) good weldability and formability^{27,28}. Within this period, published reports center on post-mortem forensic characterizations of structural components (e.g. reactor vessels, flow loops for salt transport and heat exchanges) after service (typically radioactive, high temperature, corrosive reactor environments¹⁹). For instances, components fabricated by conventionally high-temperature legend alloys such as Hastelloy W (Ni-24Mo-6Fe-5Cr, wt.%) was found

to corrode by the mechanism of thermal gradient mass transport coupled with Cr selective dissolution within several months of service in a modular MSR reactor¹⁹. Poor performance was often attributed to the impurity-driven corrosion attack, including hydrofluoric acid that is formed due to the absorption and reaction of moisture with F⁻ ion ($\text{H}_2\text{O} + 2\text{F}^- \rightarrow 2\text{HF} + \text{O}^{2-}$) coupled with creep failure and their synergetic effects with radiation²⁰⁻²². These results inspire civilian and national laboratories to perform miniature-scale experiments that study the corrosion of metallic materials in simulated MSR environments, such as high-temperature static molten salt. Therefore, as shown in Fig. 3, it wasn't until the early 2000s to present days when a rising number of literatures was published by civilian laboratories.

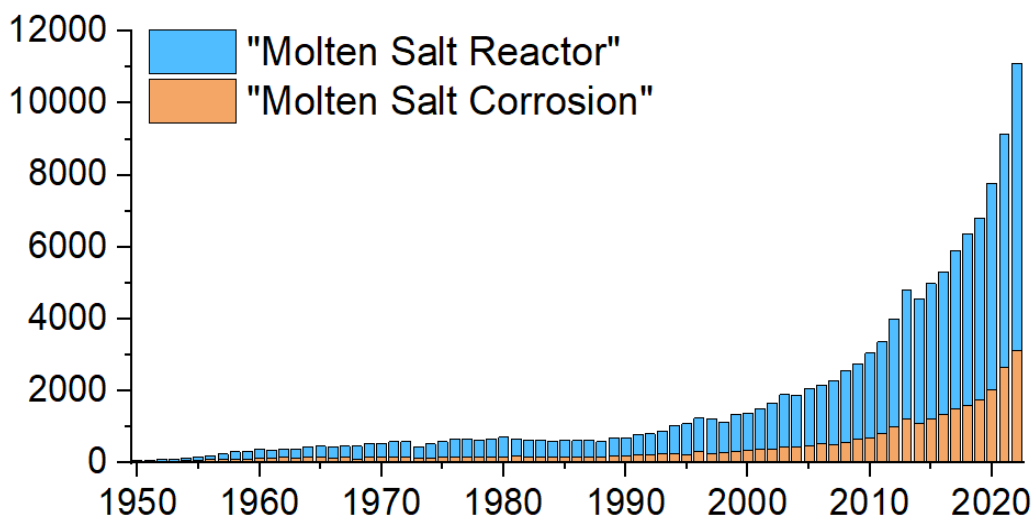


Figure 3. The number of scholastic publications, including journal articles, technical reports, book chapters, conference abstracts, in the past 7 decades based on Google scholar data ¹⁸

Structural Materials Corrosion in Molten Salt Reactor

Table 1 shows a list of structural alloys considered and being extensively evaluated for MSR harsh environments. Commercial Ni-based superalloys or their derivatives, such as Hastelloy N and Inconel 600, are recommended for MSR applications considering their machineability, creep resistance, and corrosion resistance^{27,28}. Nevertheless, when impurities are present in molten fluorides, the less noble elements in the alloy such as Cr ^{29,30} remains susceptible to be selectively dissolved via the path of least resistance, e.g. grain boundary, and has been observed in all alloys shown in Table 1. This is due to the fact that the Gibbs energy of formation (ΔG_f^0) of chromium difluorides (CrF_2) is lower than those of iron and nickel fluorides (other major alloying elements)^{31,32}, and therefore Cr is predicted to exhibit the highest thermodynamic driving force to dissolve at a given impurity level. Therefore, Cr as an alloying element is detrimental to the corrosion resistance in the context of molten fluorides corrosion. However, the addition of Cr is still

necessary to form a protective Cr₂O₃ passive film to protect oxidation on the external surface of structural components²⁷. Coupled with the fact that molten fluoride is a non-oxide forming environment with high solubility for most oxides³³⁻³⁵, the use of a protective Cr₂O₃ film is undermined for the internal surface of reactor materials³⁶. These factors contribute to the difficulty of corrosion protection in high temperature molten fluorides. Recent efforts explore the use of ASME Section III Division 5 alloys³⁷, such as Alloy 800H and 316HSS²⁷. However, the fundamental understanding of the corrosion of these materials is poor and factors that control the corrosion morphologies are uncertain.

Table 1. Structural materials considered for molten salt reactor components.

-	Hastealloy N	Hastealloy W	Inconel 600	Incoloy 800H	SS316	SS304
Ni	Bal.	Bal.	Bal.	30-35	10-14	8-10.5
Cr	7	4-6	16.2	19-23	16-18	18-20
Fe	<4	4-7	6.3	>39.5	Bal.	Bal.
Mo	16	23-26	8	-	2-3	-
C	0.06	0.5	0.016	0.05-0.10	0.08	0.08
Si	<1	<1	0.002	-	0.75	1
Mn	<0.8	<1	-	-	2	2
V	<0.5	<0.6	-	-	-	-
Al+Ti	<0.5	<0.6	-	0.30-1.20	-	-
Cu	<0.35	<0.5	0.006	-	-	-
Co	<0.2	<2.5	-	-	-	-
W	<0.5	<1.0	-	-	-	-
Others	-	<0.04	0.09	-	0.045	0.045

Progress in Molten Fluoride Salt Corrosion Research

Published literature adopt a phenomenological approach toward MSR corrosion studies. The approach centers on performing laboratory scale crucible- and/or capsule-based immersion tests on candidate materials and correlating their mass loss to independent variables such as (i) crucible materials^{38,39}, (ii) different types of salt impurities⁴⁰⁻⁴⁴, (iii) radiation^{30,45-47}, (iv) alloy composition^{43,48,49}, and (v) microstructural modification²⁹. Impurities in molten fluorides causes rapid early-stage corrosion. The four major types of impurities are (1) moisture-induced hydrofluoric acid ($H_2O(g) + F^-(salt) \rightarrow HF(salt) + O^{2-}(salt)$), (2) metallic cations such as Ge, Ag, Cr and Fe in the ppm levels⁴⁰, (3) dissolved native oxides releasing Cr(III) such as Cr₂O₃³⁶, and (4) fission products such as Te⁵⁰. Among them, HF is highly oxidizing as even 10 to 100 ppm can cause the structural alloy to exhibit a corrosion potential in which the dissolution of Cr to Cr(III) is thermodynamically favorable⁵¹, generating soluble Cr(III) product which is also oxidizing itself⁵². In NiFeCr and 316SS alloy systems, soluble Fe(II) and Ni(II) corrosion products are also expected²⁹. Figure 4 displays the half-cell Nernst potentials calculated by Guo et al.²⁹ comparing the driving forces of several redox couples of interests between 550°C and 850°C. Figure 4 is a convenient approach to compare

and identify spontaneous corrosion. For instance, the red dotted HF/H₂ (=0.1) line sits above the purple solid Cr/CrF₂ lines. This suggests that if cathodic HF/H₂ reaction (1) and anodic Cr/CrF₂ reaction (2) are coupled, this redox reaction is spontaneous. It is therefore suggested that HF/H₂ has a high oxidizing power²⁹. Depending on the HF/H₂ ratios, the HF/H₂ may spontaneously oxidize Fe, Cr, Mn, Al depending on the activity of the alloy systems, which will be further discussed in Chapter 2 and Appendix 1. The coupled reactions will thermodynamically and kinetically yield a corrosion potential (E_{corr}) and thus a corrosion current density (i_{corr}) to the material, which will also be further illustrated in Chapters 3 and 4.

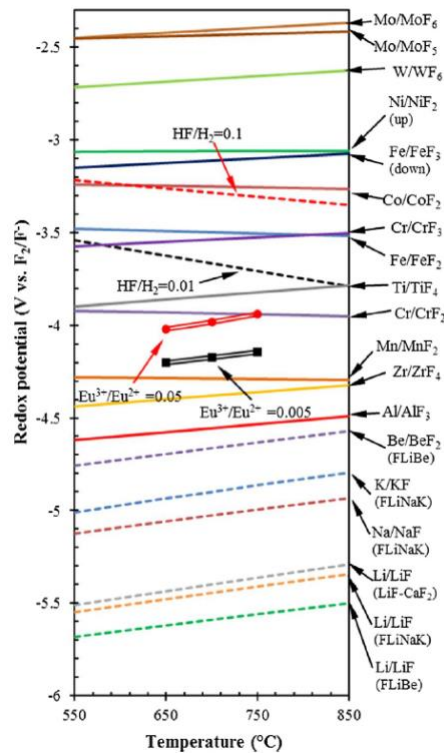
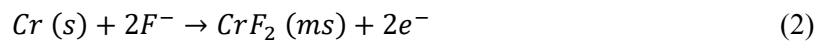
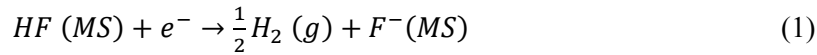


Figure 4. Comparison of half-cell Nernst potential of redox metal/metal fluoride couples relative to a F₂/F⁻ reference as a function of temperature in fluoride salts constructed by Guo et al.²⁹

In a realistic condition, the corrosive environment is constantly changing, e.g. *in-situ* impurity consumption and production, which also manifests as a change in corrosion potential and its rate. It is thus important to understand the relationships between impurity type, concentration, and the corrosion potential of candidate alloy systems. Such understanding will enable the development of MSR corrosion mitigation strategies—such as identifying dealloying susceptibility conditions, redox control³², corrosion modeling⁵³,

and alloy development⁵⁴. The current popular approach of laboratory study is “cook-and-look” by principle – which an alloy is statically immersed in a molten salt for an extended period, followed by an examination of its plan-view and cross-sectional corrosion morphology. This approach, while straightforward, lacks instantaneous potential/rate information critical to understand materials evolution in molten salts, especially at the early stage of exposure. The replicability of laboratory-scale immersion tests is also controversial. Raiman et al.⁴³ compiled the mass loss results of materials tested in molten chloride and fluoride salts in different environments, crucible materials, duration, and impurity levels as shown in Figure 5.

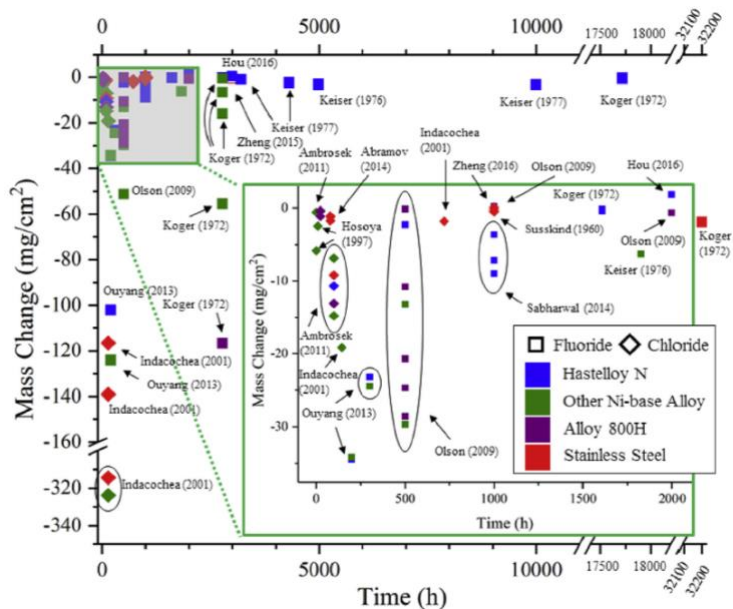


Figure 5. Compiled plots displaying the reported mass loss of Hastelloy N, alloy 800H, stainless steel, and other Ni-based alloys at different times in molten fluorides and chlorides by Raiman et al.⁴³

As shown in Table 5, published results were found to exhibit large statistical scattering due to the lack of standard experimental practice and uncontrolled impactful variables. If the impurity level is not controlled, the mass loss as well as corrosion morphology can also be affected^{40,55,56}. Not to mention, due to the complexity of variables involved with each experiment, it is challenging to utilize forensic analysis alone to isolate critical attributes that regulate these corrosion processes or develop theories and conceptual frameworks to predict degradation rates. The data presented in Figure 5 implies that the corrosion potential of the alloy was not controlled but could experience gradual changes in potential and/or salt chemistry. As a result, the alloy may have undergone multiple corrosion modes throughout exposure, with the final corrosion mode prevailing in appearance while earlier stages of degradation could have been erased.

Electrochemical techniques provide an *in-situ* and diagnostical approach to characterize the corrosion behavior of candidate materials real-time either in open-circuit (static immersion) or under polarized conditions⁵⁷. However, electrochemical methods alone cannot capture every corrosion mode and should be complemented with other experimental techniques. One also needs to understand the system constraints

when performing electrochemistry in molten salts or other non-aqueous media. These concerns include but, not limited to, the choice of reference electrodes, the species that support the cathodic/anodic reactions on both the working and counter electrodes during a scan, the role of double layer, stability of electrolytes under applied potential etc. These concerns are well-summarized by the reviews by Fredrickson et al⁵⁸ and Nishikata et al⁵⁹. The past five years have seen a rising number of studies that compare the electrochemical corrosion behavior of nickel-based superalloys^{36,41,60,61} and stainless steels^{36,41} in molten fluoride salts; often using electrochemical metrics, such as the relative difference in corrosion potential (E_{corr}), corrosion current density (i_{corr}) at varying impurities level (e.g. H₂O and CrF₃^{62,63}), alloy composition and microstructure^{61,64–66}. However, data analysis is comparative, quantitative, and does not fully leverage the advantages offered by electrochemistry. For instances, potentiodynamic polarization (PD) method (also referred to as Linear Sweep Voltammetry (LSV)) may be used to estimate reaction/corrosion rates of corrosion reactions at the impose potential or potential range^{61,64–66}. Moreover, PD can also inform possible rate-limiting steps at the metal/electrolyte interface by analyzing the current-potential relationship.

Critical Knowledge Gap: The Window of Corrosion Susceptibility

A key knowledge gap is the inadequacy of mechanistic insights and interpretation that target the fundamental principles of electrode reactions, such as the identification of reaction rate limiting factors whether at the electrode-salt interface, transport through metallic or ionic conductor phases due to salt films and deposit of differing chemical identity, or on a dealloyed nanoporous front when alloys are exposed to molten fluorides. Current progress has been limited primarily by capsule or flow loop type of time-based exposures followed by surface characterization after periods of exposure; often using complex alloys which lack separation of variables. Hence most corrosion studies are long term look-and-see exposure studies with time-based exposures unable to provide rate information, lacking in systematic variation in variables, lack of *in operando* or instantaneous measurements, lack understanding of corrosion in 4-dimensional (multiple probes using multiple techniques over the same time), and lack of diagnostics. It is unknown whether there exists a “windows of corrosion susceptibility” in molten salts where select metals and alloy are immune or susceptible to a particular form of corrosion damage, e.g. bicontinuous dealloying⁶⁷, uniform corrosion⁵¹, grain boundary attack²⁹, or a mixed of them? These phenomena is well-documented in aqueous systems, where dealloying occurs within a specific potential range—determined by conditions in which the dealloying rate exceeds that of uniform attack. This concept will be further explored in Chapters 5 and 6. Nevertheless, such “window of corrosion susceptibility” remains exclusive in molten salts.

Corrosion is an interfacial phenomenon dictated by the electrolyte chemistry, the electrolyte fluid dynamics, electrochemical reaction thermodynamics and kinetic, materials composition, microstructure, surface conditions and many more factors⁵⁷. Molten salt also operates at a high homologous temperature

(T_H : 0.4-0.6), which suggests the role of solid-state bulk diffusion, which is often neglected in room temperature corrosion studies. The major consequence of a corrosion process is transition a morphology that may be susceptible to catastrophic failure, e.g., stress-corrosion cracking⁶⁸. These factors work in concert to yield several defined electrochemical parameters that enable assessment of the nobility and rate of a corrosion process, notably the corrosion potential (E_{corr}) and corrosion current density (i_{corr}), respectively⁵⁷. E_{corr} is a mixed potential that is thermodynamically and kinetically determined. In an industrial environment (particularly in the pipeline and cathodic protection industry⁶⁹), i_{corr} is difficult to measure and E_{corr} can be correlated with an electrode potential measured with a voltmeter relative to a reference electrode. Hence, these considerations yield three key motivating scientific questions: **(1) Is it possible to relate the electrode potential of a metal or alloy to a certain damage morphology in molten salts? (2) What are the windows of corrosion susceptibility for different alloy/salt systems? (3) What regulates the corrosion rate? (4) If windows of corrosion susceptibility exists in molten salts, then how are these windows be affected by the salt impurity, alloy composition, microstructure, and operating temperature?** Given that electrode potentials can be imposed by either an applied potential or naturally by impurity cathodic reactants, answering these questions are highly relevant in the context of molten salt corrosion for reactor developments.

A technical whitespace exists in defining the windows of corrosion susceptibility and its attendant damage morphology as a function of electrode potential (both through an applied potential or impurity as a chemical potentiostat; also dictate the interfacial rate-controlling dissolution mechanism, i.e. charge-transfer vs. mass-transport controlled dissolution), alloy composition for elemental immunity, impurity concentration, temperature etc. Given sufficient information, scientific understanding can enable the development of models of corrosion processes and can enable the prediction of damage evolution or degradation rates as well as an understanding of alloy and physical attributes. Ideally such insights which can guide alloy design and corrosion mitigation strategies.

Overall Objective & Hypothesis

This **overall objective** of this thesis to advance a fundamental understanding of corrosion processes in molten fluorides, with a focus on elucidating rate-regulating mechanisms and the morphological evolution of materials. By applying electrochemical thermodynamics and kinetics, this work integrates multi-modal experimental characterization and analysis to provide deeper mechanistic insights. Consequently, a model corrosion system consisting of pure metals and binary alloys (Cr, Ni, Ni-20Cr wt.%) in a molten LiF-NaF-KF (or FLiNaK) salt electrolyte at 600°C is selected as the focus of this thesis. The **overall hypothesis** is that there exists a specific window of susceptibility, defined by electrode potential for a salt and material

system, within which metals and alloys are vulnerable to different forms of morphological damage due to differences in corrosion driving forces and rate-regulating interfacial charge-transfer mechanisms.

Approach & Thesis Organizations

This thesis is organized to 5 chapters and 2 appendices:

- *Chapter 2, Task 1* aims to identify the thermodynamic phase stabilities of metals, and their cation oxidation states in molten fluorides using potential-activity diagrams. The thermodynamic predictions are verified with experimental methods, including cyclic voltammetry and X-Ray Diffraction, performed on a model system consisting of pure Cr in molten LiF-Na-KF (or FLiNaK) salts at 600°C.
 - Supporting *Task 1, Appendix 1* delves further to explain how the presented potential-activity diagrams may be used to illustrate the spontaneity of metal corrosion in molten fluorides.
- *Chapter 3, Task 2* seeks to identify the rate-regulating phenomenon that governs the interfacial charge-transfer behavior for Cr oxidation in molten FLiNaK at 600°C at different electrode potentials. The attendant thermodynamic phase stability of Cr (and its species) as well as the morphological damage at different electrode potentials are also studied, enabling different “corrosion regimes” to be categorized.
- *Chapter 4, Task 3* aims to provide a time-based description of the Cr corrosion process in molten FLiNaK by designing and implementing an *in-situ*, multi-electrodes technique, which enables the electrochemical studies of two working electrodes (WEs) simultaneously. On the primary WE (e.g. Cr), DC and/or AC measurement techniques are performed, whereas on the secondary WE, cyclic voltammetry is performed on a blocking electrode (e.g. Pt) to capture corrosion products real time.
 - Supporting *Tasks 2 &3, Appendix 2* explores and evaluates the use of flush-mounted disk electrodes, as the working electrode geometry, to accurately measure the charge-transfer resistance of Cr in molten FLiNaK using electrochemical impedance spectroscopy technique.
- *Chapter 5, Task 4* aims to leverage the techniques developed from Tasks 1 through 3 to investigate the corrosion and dealloying behavior of Ni₂₀Cr (wt.%) alloys in molten FLiNaK, 600°C at high homologues temperature. The thermodynamic stability of Ni and Cr, morphological evolution, and possible rate-determining step for Cr dissolution at different electrode potentials are studied. The role of interfacial Cr dissolution, bulk (lattice & grain boundary), and surface diffusions are elucidated.
- *Chapter 6, Task 5* investigates the effect of cold working on the morphological evolution of Ni₂₀Cr (wt.%) alloy in molten FLiNaK, 600°C. Cold working was performed to study the effect of accelerated Cr solid diffusion on molten salt dealloying by introducing a high density of point and line defects, which serve as short-circuit diffusion pathways.

Lastly, Chapter 7 provides a comprehensive summary and a list of future works. It is noted that the effects of Cr composition, temperature, and oxidizer concentration on the dealloying behavior of Ni-Cr alloys were also examined in this thesis, but their discussion remains beyond its scope.

References

1. N. S. Kardashev, Transmission of Information by Extraterrestrial Civilizations, *Soviet Astronomy* 8 (1964) 217.
2. World Energy Outlook – Topics. IEA. <https://www.iea.org/topics/world-energy-outlook>.
3. Q. Zhang, et al., A survey on data center cooling systems: Technology, power consumption modeling and control strategy optimization, *J. Syst. Archit.* 119 (2021) 102253. <https://doi.org/10.1016/j.sysarc.2021.102253>.
4. International Energy Agency, Electricity Market Report, July 2021, OECD (2021). <https://doi.org/10.1787/f4044a30-en>.
5. U.S. Energy Information Administration (EIA), Frequently Asked Questions (FAQs). <https://www.eia.gov/tools/faqs/faq.php>.
6. G. Steinhauser, A. Brandl, T.E. Johnson, Comparison of the Chernobyl and Fukushima nuclear accidents: A review of the environmental impacts, *Sci. Total Environ.* 470–471 (2014) 800–817. <https://doi.org/10.1016/j.scitotenv.2013.10.029>.
7. IAEA (International Atomic Energy Agency). *Advances in Small Modular Reactor Technology Developments: A Supplement to IAEA Advanced Reactors Information System (ARIS), 2022 Edition*. IAEA, 2022.
8. L.M. Krall, A.M. Macfarlane, R.C. Ewing, Nuclear waste from small modular reactors, *Proc. Natl. Acad. Sci.* 119 (2022) e2111833119. <https://doi.org/10.1073/pnas.2111833119>.
9. Generation IV Nuclear Reactors - World Nuclear Association. <https://world-nuclear.org/information-library/nuclear-fuel-cycle/nuclear-power-reactors/generation-iv-nuclear-reactors>.
10. J. Serp, et al., The molten salt reactor (MSR) in generation IV: Overview and perspectives, *Prog. Nucl. Energy* 77 (2014) 308–319. <https://doi.org/10.1016/j.pnucene.2014.02.014>.
11. T.J. Dolan, *Molten Salt Reactors and Thorium Energy*, Elsevier (2017) 841.
12. A.S. Benn, Molten Salt Reactor Fuel Qualification Considerations and Challenges, 19.
13. M.B. Schaffer, Abundant thorium as an alternative nuclear fuel: Important waste disposal and weapon proliferation advantages, *Energy Policy* 60 (2013) 4–12. <https://doi.org/10.1016/j.enpol.2013.03.030>.
14. T. Kamei, Recent Research of Thorium Molten-Salt Reactor from a Sustainability Viewpoint, *Sustainability* 4 (2012) 2399–2418. <https://doi.org/10.3390/su4092399>.
15. F.J. Bonte, Chernobyl retrospective, *Semin. Nucl. Med.* 18 (1988) 16–24.
16. J. Yanez, M. Kuznetsov, A. Souto-Iglesias, An analysis of the hydrogen explosion in the Fukushima-Daiichi accident, *Int. J. Hydrog. Energy* 40 (2015) 8261–8280. <https://doi.org/10.1016/j.ijhydene.2015.04.111>.
17. R.R. Romatoski, L.W. Hu, Fluoride salt coolant properties for nuclear reactor applications: A review, *Ann. Nucl. Energy* 109 (2017) 635–647. <https://doi.org/10.1016/j.anucene.2017.05.051>.
18. Google Scholar. <https://scholar.google.com/>.
19. Aircraft Nuclear Propulsion Project Quarterly Progress Report.
20. R.E. Thoma, Chemical Aspects of MSRE Operations, ORNL--4658, 4675946 (1971). <https://doi.org/10.2172/4675946>.
21. J.H. DeVan, Effect of Alloying Additions on Corrosion Behavior of Nickel-Molybdenum Alloys in Fused Fluoride Mixtures. <https://www.osti.gov/biblio/4789147>.
22. J.H. DeVan, R.B. Evans III, Corrosion Behavior of Reactor Materials in Fluoride Salt Mixtures, ORNL-TM-328, 4774669 (1962). <https://doi.org/10.2172/4774669>.
23. J.H. Shaffer, Preparation and Handling of Salt Mixtures for the Molten Salt Reactor Experiment, ORNL--4616, 4074869 (1971). <https://doi.org/10.2172/4074869>.
24. W.H. Jordan, S.J. Cromer, A.J. Miller, Aircraft Nuclear Propulsion Project Quarterly Progress Report For Period Ending September 10, 1956. ORNL Report No. 2157, (1956) p. 105, Oak Ridge, Tennessee, US.
25. L.S. Richardson, D.C. Vreeland, W.D. Manly, Corrosion by Molten Fluorides, Interim Report, (1952). <https://doi.org/10.2172/4127448>.
26. H.E. McCoy Jr., Status of Materials Development for Molten Salt Reactors, ORNL/TM-5920, 5195742 (1978). <https://doi.org/10.2172/5195742>.
27. R.N. Wright, T.-L. Sham, Status of Metallic Structural Materials for Molten Salt Reactors, (2018). <https://doi.org/10.2172/1467482>.

28. J. Busby, et al., Technical Gap Assessment for Materials and Component Integrity Issues for Molten Salt Reactors, 156.
29. S. Guo, J. Zhang, W. Wu, W. Zhou, Corrosion in the molten fluoride and chloride salts and materials development for nuclear applications, *Prog. Mater. Sci.* 97 (2018) 448–487. <https://doi.org/10.1016/j.pmatsci.2018.05.003>.
30. W. Zhou, et al., Proton irradiation-decelerated intergranular corrosion of Ni-Cr alloys in molten salt, *Nat. Commun.* 11 (2020) 3430. <https://doi.org/10.1038/s41467-020-17189-2>.
31. Yoo, J. H. Thermodynamic DataBase for Metal Fluorides, Technical Report Number: TR-1824, (Korea Atomic Energy Research Institute) KAERI, (2001). J. Zhang, et al., Redox potential control in molten salt systems for corrosion mitigation, *Corros. Sci.* 144 (2018) 44–53. <https://doi.org/10.1016/j.corsci.2018.08.002>.
32. C.F. Baes, The chemistry and thermodynamics of molten salt reactor fuels, *J. Nucl. Mater.* 51 (1974) 149–162. [https://doi.org/10.1016/0022-3115\(74\)90079-5](https://doi.org/10.1016/0022-3115(74)90079-5).
33. H. Ai, et al., Effects of O₂⁻ additive on corrosion behavior of Fe–Cr–Ni alloy in molten fluoride salts, *Corros. Sci.* 150 (2019) 175–182. <https://doi.org/10.1016/j.corsci.2019.02.017>.
34. Y. Song, et al., Solubility of Cr₂O₃ in Molten Fluorides with Different ZrF₄ Contents and Fluoroacidities, *J. Electrochem. Soc.* 167 (2020) 023501. <https://doi.org/10.1149/2.0232002JES>.
35. J. Qiu, et al., Electrochemical study of the dissolution of oxide films grown on type 316L stainless steel in molten fluoride salt, *Corros. Sci.* 186 (2021) 109457. <https://doi.org/10.1016/j.corsci.2021.109457>.
36. American Society of Mechanical Engineers (ASME). ASME Boiler and Pressure Vessel Code, Section III, Division 5: High Temperature Reactors. ASME (2023).
37. W.C. Phillips, et al., Design and performance of high-temperature furnace and cell holder for in situ spectroscopic, electrochemical, and radiolytic investigations of molten salts, *Rev. Sci. Instrum.* 91 (2020) 083105. <https://doi.org/10.1063/5.0017043>.
38. L.C. Olson, et al., Impact of Corrosion Test Container Material in Molten Fluorides, *J. Sol. Energy Eng.* 137 (2015) 061007. <https://doi.org/10.1115/1.4031475>.
39. D. Sulejmanovic, J.M. Kurley, K. Robb, S. Raiman, Validating modern methods for impurity analysis in fluoride salts, *J. Nucl. Mater.* 553 (2021) 152972. <https://doi.org/10.1016/j.jnucmat.2021.152972>.
40. W.H. Doniger, et al., Investigation of impurity-driven corrosion behavior in molten 2LiF-BeF₂ salt, *Corros. Sci.* 174 (2020) 108823. <https://doi.org/10.1016/j.corsci.2020.108823>.
41. W. Ding, J. Gomez-Vidal, A. Bonk, T. Bauer, Molten chloride salts for next generation CSP plants: Electrolytical salt purification for reducing corrosive impurity level, *Sol. Energy Mater. Sol. Cells* 199 (2019) 8–15. <https://doi.org/10.1016/j.solmat.2019.04.019>.
42. S.S. Raiman, S. Lee, Aggregation and data analysis of corrosion studies in molten chloride and fluoride salts, *J. Nucl. Mater.* 511 (2018) 523–535. <https://doi.org/10.1016/j.jnucmat.2018.09.033>.
43. K.M. Sankar, P.M. Singh, Effect of oxide impurities on the corrosion behavior of structural materials in molten LiF-NaF-KF, *Corrosion Science* 206 (2022) 110473. <https://doi.org/10.1016/j.corsci.2022.110473>.
44. H.E. McCoy, R.E. Gehlbach, Influence of Irradiation Temperature on the Creep-Rupture Properties of Hastelloy-N, *Nucl. Technol.* 11 (1971) 45–60. <https://doi.org/10.13182/NT71-A28952>.
45. G.W. Keilholtz, J.G. Morgan, W.E. Browning, Effect of Radiation on Corrosion of Structural Materials by Molten Fluorides, *Nucl. Sci. Eng.* 5 (1959) 15–20. <https://doi.org/10.13182/NSE59-A28953>.
46. Z. Zhu, et al., Synergistic effect of irradiation and molten salt corrosion: Acceleration or deceleration?, *Corros. Sci.* 185 (2021) 109434. <https://doi.org/10.1016/j.corsci.2021.109434>.
47. G. Zheng, K. Sridharan, Corrosion of Structural Alloys in High-Temperature Molten Fluoride Salts for Applications in Molten Salt Reactors, *JOM* 70 (2018) 1535–1541. <https://doi.org/10.1007/s11837-018-2985-2>.
48. K. Sridharan, T.R. Allen, Corrosion in Molten Salts, in: F. Lantelme, H. Groult (Eds.), *Molten Salts Chemistry*, Elsevier, Oxford, 2013, pp. 241–267. <https://doi.org/10.1016/B978-0-12-398538-5.00012-3>.
49. M. Hong, et al., Effect of tellurium concentration on the corrosion and mechanical properties of 304 stainless steel in molten FLiNaK salt, *Corros. Sci.* 212 (2023) 110913. <https://doi.org/10.1016/j.corsci.2023.110913>.
50. H.L. Chan, et al., Corrosion Electrochemistry of Chromium in Molten FLiNaK Salt at 600 °C, *J. Electrochem. Soc.* (2023). <https://doi.org/10.1149/1945-7111/acf026>.
51. E. Romanovskaia, et al., An In Situ, multi-electrode electrochemical method to assess the open circuit potential corrosion of Cr in unpurified molten FLiNaK, *Corros. Sci.* 222 (2023) 111389. <https://doi.org/10.1016/j.corsci.2023.111389>.
52. R. Pillai, D. Sulejmanovic, T. Lowe, S.S. Raiman, B.A. Pint, Establishing a Design Strategy for Corrosion Resistant Structural Materials in Molten Salt Technologies, *JOM* 75 (2023) 994–1005. <https://doi.org/10.1007/s11837-022-05667-w>.

53. B. Goh, et al., Nobility vs. mobility: Insights into molten salt corrosion mechanisms of high-entropy alloys via high-throughput experiments and machine learning, *Matter* 7 (2024) 2313–2335. <https://doi.org/10.1016/j.matt.2023.12.017>.
54. F.-Y. Ouyang, C.-H. Chang, B.-C. You, T.-K. Yeh, J.-J. Kai, Effect of moisture on corrosion of Ni-based alloys in molten alkali fluoride FLiNaK salt environments, *J. Nucl. Mater.* 437 (2013) 201–207. <https://doi.org/10.1016/j.jnucmat.2013.01.303>.
55. S.S. Sawant, et al., High Temperature Corrosion Studies in Molten Salt Using Salt Purification and Alloy Coating, *Indian Chem. Eng.* 59 (2017) 242–257. <https://doi.org/10.1080/00194506.2017.1349045>.
56. R.G. Kelly, J.R. Scully, D. Shoesmith, R.G. Buchheit, *Electrochemical Techniques in Corrosion Science and Engineering*, CRC Press (2002).
57. G.L. Fredrickson, et al., Review—Electrochemical Measurements in Molten Salt Systems: A Guide and Perspective, *J. Electrochem. Soc.* 166 (2019) D645–D659. <https://doi.org/10.1149/2.0341913jes>.
58. A. Nishikata, H. Numata, T. Tsuru, Electrochemistry of molten salt corrosion, *Mater. Sci. Eng. A* 146 (1991) 15–31. [https://doi.org/10.1016/0921-5093\(91\)90077-6](https://doi.org/10.1016/0921-5093(91)90077-6).
59. Y. Wang, H. Liu, G. Yu, J. Hou, C. Zeng, Electrochemical study of the corrosion of a Ni-based alloy GH3535 in molten (Li,Na,K)F at 700°C, *J. Fluor. Chem.* 178 (2015) 14–22. <https://doi.org/10.1016/j.jfluchem.2015.07.003>.
60. S. Fabre, et al., Use of electrochemical techniques to study the corrosion of metals in model fluoride melts, *J. Nucl. Mater.* 441 (2013) 583–591. <https://doi.org/10.1016/j.jnucmat.2013.06.035>.
61. G. Yamazaki, et al., Corrosion of pure Cr and W in molten FLiNaK with hydrogen fluoride solution, *Fusion Eng. Des.* 172 (2021) 112741. <https://doi.org/10.1016/j.fusengdes.2021.112741>.
62. Y.L. Wang, Q. Wang, H.J. Liu, C.L. Zeng, Effects of the oxidants H₂O and CrF₃ on the corrosion of pure metals in molten (Li,Na,K)F, *Corros. Sci.* 103 (2016) 268–282. <https://doi.org/10.1016/j.corsci.2016.01.008>.
63. D. Cao, et al., Performance of protective oxide films on Fe–Ni alloy anodes in molten KF–AlF₃–Al₂O₃ salts at 700°C, *Electrochim. Acta* 347 (2020) 136275. <https://doi.org/10.1016/j.electacta.2020.136275>.
64. Y.L. Wang, Q. Wang, H.J. Liu, C.L. Zeng, Effect of grain refinement on the corrosion of Ni–Cr alloys in molten (Li,Na,K)F, *Corros. Sci.* 109 (2016) 43–49. <https://doi.org/10.1016/j.corsci.2016.03.003>.
65. W.H. Doniger, A. Couet, K. Sridharan, Potentiodynamic Polarization of Pure Metals and Alloys in Molten LiF–NaF–KF (FLiNaK) Using the K/K⁺ Dynamic Reference Electrode, *J. Electrochem. Soc.* 169 (2022) 071502. <https://doi.org/10.1149/1945-7111/ac7d3b>.
66. T. Ghaznavi, S.Y. Persaud, R.C. Newman, Electrochemical Corrosion Studies in Molten Chloride Salts, *J. Electrochem. Soc.* 169 (2022) 061502. <https://doi.org/10.1149/1945-7111/ac6b50>.
67. G. Young, J. Quincey, A. Brittan, P. Schulze, E. Tsotsos, L. Parrington, J. Parrington, A. Demma, M. Hackett, S. Briggs, J. Tucker, Assessing Environmentally Assisted Cracking of Structural Alloys in Molten Salts, *Proceedings of the 20th Conference on Environmental Degradation of Materials in Nuclear Power Systems-Water Reactors* (2022).
68. E. Macero, *An Introduction to Cathodic Protection*, (2009).

Chapter 2 Task 1: Corrosion Thermodynamics of Cr in Molten LiF-NaF-NF Salts

Ho Lun Chan^{1,2}, Elena Romanovskaia^{1,2}, Jie Qiu³, Peter Hosemann³, John R. Scully^{1,2}

¹Department of Materials Science and Engineering, University of Virginia, Charlottesville, VA, 22904

²Center for Electrochemical Science and Engineering, University of Virginia, Charlottesville, VA, 22904

³Department of Nuclear Engineering, University of California, Berkeley, CA, 94150

Abstract

The thermodynamic stability of chromium (Cr) in the Cr⁰, Cr(II) and Cr(III) oxidation states considering various F⁻ ion coordination compounds was investigated in molten LiF-NaF-KF (FLiNaK) eutectic salt. Potential-fluoride ion activity (F⁻ and CrF₃⁻) diagrams were constructed to predict the most stable Cr oxidation states as a function of anion activity, solvation state of chromium ions and potential at 600°C. The Gibbs free energies of these compounds were estimated by utilizing a combined cyclic voltammetry - Nernst theory analysis approach in FLiNaK salt. To verify the constructed diagrams, X-Ray Diffraction was utilized after exposure of Cr at various applied potentials to determine whether compounds detected in solidified FLiNaK salts agreed with thermodynamic calculations. The present work aims to identify key thermodynamic factors that are significant to the chromium corrosion for molten salt nuclear reactor applications. The F⁻ stability region spans the entire region where spontaneous corrosion of Cr occurs. Cr may be oxidized to Cr(II) and Cr(III) in the presence HF (due to moisture as an impurity) spontaneously except some conditions of $p^{1/2}H_2/a_{HF}$ etc. This situation is not changed qualitatively for various states of solvation between oxidized Cr solute in F⁻ solvent and this aspect is substantially similar for the two cases (pair 1: Cr⁰/CrF₃⁻/CrF₆³⁻; pair 2: Cr⁰/CrF₄²⁻/CrF₅²⁻) considered in this work.

Introduction

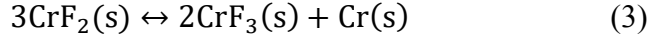
Molten salt reactor (MSR) has been recognized as a promising system for generation IV nuclear reactor with improved safety and performance¹. Compared to the conventional light-water reactor (LWR), molten fluoride salts (e.g. LiF-NaF-KF, LiF-BeF₂ eutectic) operate in the temperature range between 600°C and 900°C and replace water as the medium to dissolve dissolved fissile materials¹ and transfer heat; in other words, molten fluoride salts can serve as both the solvents for the reactor fuel and coolant^{2,3}. The research and commercial development of MSR reactor center on solving technical problems that are deleterious to the safety and sustainability of this technology including reactor materials; and thus, the corrosion of metallic structural components should be addressed^{4,5}.

Fundamentally, the corrosion of metallic elements in MSRs has been posited to occur by electrochemical processes governed by mixed potential theory where the thermodynamic driving force for oxidative corrosion is determined by the difference in the Gibbs free energies of reaction between the reduction half-cell or cathodic reactions of the oxidants in the molten fluoride salts, coupled with anodic half-cell reactions associated with transition metals used in structural materials. Herein, we consider the Cr⁰ oxidation half-cell reactions producing oxidized chromium-fluoride compounds⁶. These are in turn based on the free energy of formation (ΔG_f^0) of the relevant reactants and products. However, these free energies may vary depending upon the specific Cr oxidation states and possible F⁻ coordination complexes that may form (e.g., CrF₂, CrF₃, FeF₂)⁷⁻⁹. For instance, it has recently been argued that Cr(II) can exist as CrF₃⁻ or CrF₄²⁻ and Cr(III) may exist as CrF₅²⁻, CrF₆³⁻, and Cr₃F₁₇²⁻ states in molten fluorides at 700°C¹⁰.

The origins of the oxidants can range from moisture impurities¹¹ (the cause of the dissolved hydrofluoric acid corrosion¹²), dissolved cations associated with metallic elements that originally were contained in air pre-formed oxides¹³, to the corrosion products themselves¹¹, such as reduction of Cr in CrF₃ or CrF₂ compounds originally generated from Cr metal corrosion^{11,14,15}. In technological applications, corrosion may result from differences in mixed potentials established by cold legs relative to hot legs¹⁶⁻¹⁹. Chromium is a common alloying element for various candidate MSR reactor materials including alloys which exhibit good corrosion resistance in aqueous systems⁴. Since molten fluoride salt is a non-oxide forming environment with high solubility for oxygen and most oxides^{9,13,20}, the use of a protective Cr₂O₃ barrier layer is not suitable for this application²¹. This is further exacerbated by the fact that the ΔG_f^0 of chromium difluorides (CrF₂) is lower than those of iron and nickel fluorides (other major alloying elements)^{1,8}, and therefore Cr is predicted to exhibit the highest thermodynamic driving force for corrosion relative to candidate oxidizers discussed above. This is evidenced by phenomena such as selective Cr dissolution along grain boundaries^{7,22,23}.

Nevertheless, our understanding on the electrochemical corrosion process involved with Cr metal and its alloys in molten salt is limited. The question remains open which oxidation state (Cr(II) or Cr(III)) is pertinent during Cr containing alloy corrosion. Thermodynamic predictions⁸ suggests that Cr has a high driving force to dissolve to the Cr(II) state due to the lower Gibbs free energy of the reaction producing CrF₂ (reaction 1). Direct dissolution to the Cr(III) state (reaction 2) has not been reported as a predominant reaction step⁶. Moreover, it is posited that the resultant Cr(II) state will then be converted to the Cr(III) state through the disproportionation reaction (reaction 3) in which Cr metal is redeposited on its surface²⁴.

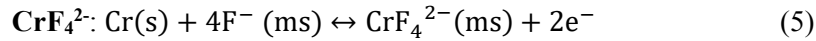
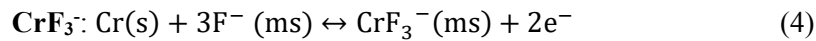




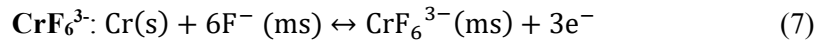
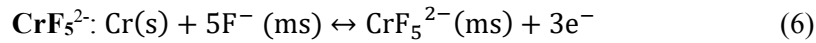
Where (MS) indicates a dissolved species in molten salt:

Recent progress in molten fluoride electrochemistry offers additional insights that help to interpret the corrosion mechanism of Cr. Wang et al. performed a detailed electrochemical study on a Pt wire electrode in a LiF-NaF-KF eutectic salt with the addition of CrF₂ at 600°C²⁵. The X-ray diffractogram of salt mixture quenched from 600 °C revealed the presence of crystalline CrF₃⁻ and CrF₆³⁻ phases, corresponding to the chromium oxidation state of Cr(II) and Cr(III) ions, respectively²⁵. A recent computational study by Winner et al. shows the solvated states of CrF₃⁻ and CrF₄²⁻ are possible for Cr(II). Moreover, CrF₅²⁻, CrF₆³⁻, and Cr₃F₁₇²⁻ are possible for Cr(III) in molten fluorides at 700°C¹⁰. However, it is unclear which solvated structure will form naturally during the spontaneous corrosion process. Nevertheless, fluoride solvation should be considered in understanding the mechanism of Cr corrosion. Thus, reactions (1) – (3) can be modified to the reactions (4) - (9) through the following. It is noted that only reaction steps that involve the transfer of 1 mole of e⁻ is the Cr(II)/Cr(III) conversion reaction:

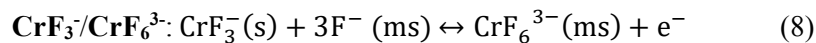
Oxidation from Cr⁰ to Cr(II):



Oxidation from Cr⁰ to Cr(III):



Oxidation from Cr(II) to Cr(III):



Based on the literature, the prior approach to understand the thermodynamics of molten fluoride salt corrosion centers on (1) systematically ranking the Gibbs free energies of possible half-cell reactions (ΔG_r^0) and associated half-cell reaction potentials (E)⁸, and (2) developing predominance diagrams, which depict regions of stable phases as a function of chemical compound activities (e.g. a_{CrF_2} , a_{CrF_3} , $a_{\text{Li}_2\text{O}}$), partial

pressures of oxygen (P_{O_2}) and/or fluorine gas (P_{F_2}), and/or potential (E)^{7,11,13,26,27}. While the goal is to predict the most favorable reaction, both approaches have not considered the Cr-F solvation phenomenon reported in recent literature¹⁰, which is critical since it affects the potential range over which thermodynamic stability of Cr⁰, Cr(II) and Cr(III) is obtained. This in turn affects corrosion. Additionally, predominance diagrams are calculated and constructed based on chemical reactions (e.g. $Cr + F_2 \rightarrow CrF_2$) rather than electrochemical reactions ($Cr + 2F^- \rightarrow CrF_2 + 2e^-$), which may possibly affect the accuracy of the phase stability prediction. Although easy to construct especially with the help of modern thermodynamic calculation software, predominance diagrams also have limited flexibility since the oxidizing chemical potential is sometimes expressed as gaseous partial pressure (e.g. P_{O_2}). In molten salt corrosion, it is a thermodynamic variable rather than measurable or quantitative property, making it difficult to determine the exact point which Cr locates in a phase stability, or predominance, diagram. This provides a literature gap and an opportunity to develop potential-activity diagrams that can be utilized to predict under what conditions Cr is oxidized or immune to dissolution as a function of electrode potential and fluoride ion activities (two measurable, quantitative properties) analogous to a classical Pourbaix diagram²⁸.

The objective of this work is to understand and predict the conditions for oxidative Cr corrosion in molten fluorides. This work aims to investigate Cr corrosion in LiF-NaF-KF (FLiNaK) eutectic salt, applicable to a MSR reactor²⁹. Thermodynamic analysis was carried out using the Nernst theory to predict the predominance phase of charged, solvated ions as a function of fluoride ions activity and potential (the theory is discussed in detail in Materials and Methods section). Electrochemical measurement coupled with X-Ray Diffraction (XRD) were utilized to verify the predicted thermodynamic stability regions for Cr⁰, Cr(II) and Cr(III) stability in FLiNaK salts at 600°C.

Materials and Methods

Setup, sample and salt preparation

High purity Cr rectangular sheet (99.995%, Alfa Aesar) with the dimension 20 mm x 1.5 mm x 3 mm were used. Coupons were metallographically prepared to 1200 grit surface finish using silicon carbide polishing papers. The FLiNaK salt was prepared by weighting LiF (99.85%, Fisher Scientific), NaF (99.99%, Fisher Scientific), KF (99.9%, Fisher Scientific) into the stoichiometric ratio of 46.5, 11.5, and 42 mol%, respectively. Prior to mixing, these salts were dried in a vacuum furnace for 48 hours at 100°C, and then transferred to a N₂-filled glove box with controlled O₂ and H₂O level below <0.1 ppm. During this transfer process, it is expected that the salts could absorb water from moist air during transfer (relative humidity of the laboratory is about 30%). 30 grams of FLiNaK salt were used for each experiment. The mass ratio of salt to Cr coupon is approximately equivalent to 0.03 g of FLiNaK/g of Cr.

The setup to perform electrochemical measurement is shown in Fig. 1. All measurement was carried out in a N₂ filled glove box in a modified muffle furnace at 600°C. A glassy carbon crucible (99.999%, Fisher Scientific) was used as both the salt container and counter electrode, and a Pt wire was used as a Pt/PtO/O²⁻ quasi-reference electrode based on a controlled oxygen level. The working electrode was either a Cr coupon spot welded to a Ni200 wire or a platinum wire (99.997%, Alfa Aesar™). All the electrodes were fed through an alumina tube and placed in a quartz tube to ensure sturdy connections. A Gamry interface 1000 potentiostat was used to perform electrochemical tests. To minimize impurities pertaining to residual water moisture or oxygen, prior to the insertion of test electrodes, the salt mixture was heated to 600°C for 3 h under the flow of ultra-high purity N₂ gas (99.999%).

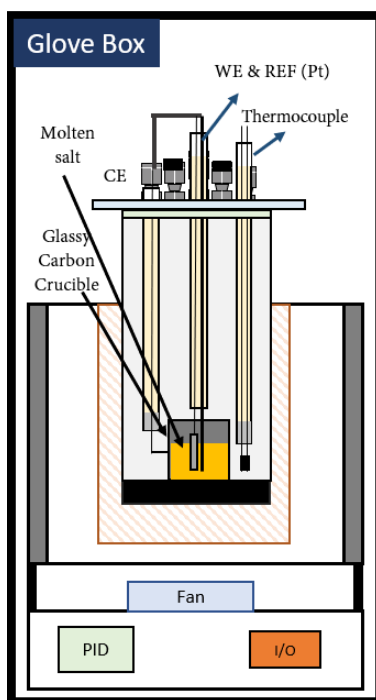
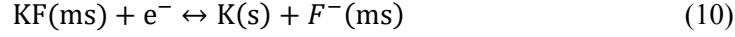


Figure 1. Schematics of the molten salt electrochemical cell

Reference potential determination

For a more meaningful and reliable comparison between thermodynamic calculation and electrochemistry results, the electrode potential was represented relative to both the reduction of potassium ions (K^+/K) and the evolution of fluorine gas (reaction (11), F_2/F^-). However, due to the lack of thermodynamic data regarding the activity coefficient and Gibbs free energy of K^+ in molten fluorides, the half-cell redox potential of K^+/K was calculated instead via the KF to K (or reaction(10)) the Gibbs free energy of formation of KF is known. All potentials calculated in this chapter were also calculated relative to the evolution of fluorine gas (reaction (11), F_2/F^-). Reactions (10) and (11) define the electrochemical potential window in molten FLiNaK salts.



The redox potential for reaction (10) can be experimentally measured using a cyclic voltammetry technique performed on a Pt wire in molten fluoride salts²⁷. This method has also been utilized by Massot et al²⁷, Shay et al⁴⁰, and Wang et al⁴¹. The technique involves polarizing the Pt wire to a cathodic (negative) direction until a sharp increase in reduction current corresponding to KF reduction is detected, and the scan is reversed to oxidize the K deposited on the Pt wire surface. An example cyclic voltammogram is shown in Fig. 2a. The equilibrium potential of reaction (10) was estimated at the position between the oxidation peak (KF/K)^{27, 40, 41}. Once the KF/K potential was known, the F₂/F⁻ potential was calculated using the Nernst equation as shown in the next section.

Thermodynamic Calculation

In this work, a systematic thermodynamic analysis was carried out to predict the most favorable reaction for Cr dissolution as a function of potential and fluoride ion activities. Firstly, consider a general, reversible, half-cell electrochemical reaction in molten fluorides as shown in reaction (12):



where x describes the number of fluoride ions reacted per atom of Cr. The Nernst Equation for reaction (12) can be represented by the Nernst equations as Eq. (13) and Eq. (14)⁴²:

$$E_{\text{M}/\text{MF}_x^{n-x}} = E_{\text{M}/\text{MF}_x^{n-x}}^0 + \frac{2.303RT}{nF} \log\left(\frac{a_{\text{MF}_x^{n-x}}}{a_{\text{F}^-}^x a_{\text{M}}}\right) \quad (13)$$

$$E_{\text{M}/\text{MF}_x^{n-x}} = E_{\text{M}/\text{MF}_x^{n-x}}^0 + \frac{0.173}{n} \log\left(\frac{a_{\text{MF}_x^{n-x}}}{a_{\text{F}^-}^x a_{\text{M}}}\right) \quad (14)$$

where $E_{\text{M}/\text{MF}_x^{n-x}}$ is the Nernst potential, R is universal gas constant, T is temperature in K, n is the number of electrons transferred to complete the reaction shown one time, F is the Faraday's constant of 96500 coulombs/mol e⁻, a_i ($= \gamma_i C_i$) is the ion activity, and $E_{\text{M}/\text{MF}_x^{n-x}}^0$ is the standard electrode potential of the half-cell reaction. The $E_{\text{M}/\text{MF}_x^{n-x}}^0$ can be related to ΔG_f^0 through Eq. (15) and (16):

$$\Delta G_{rxn}^0 = -nF\Delta E_{\text{Cr}/\text{Cr}^{(II)}}^0 \quad (15)$$

$$\Delta G_{rxn}^0 = \Delta G_f^0(\text{Cr}^{(II)}) - \Delta G_f^0(\text{Cr}) \quad (16)$$

where ΔG_f^0 represents the standard Gibb's free energy of formation and ΔG_{rxn}^0 represents the Gibb's free energy of reaction (12). Table 1 shows the ΔG_f^0 of potassium and chromium fluoride compounds obtained from Barin et al³⁸ at 600°C (with a reference state relative to the enthalpy of 298K). Since the melting point of KF, CrF₂, CrF₃ is higher than 600°C, the ΔG_f^0 at supercooled state was used. This is calculated by the summation of their solid state ΔG_f^0 and the fusion energy (ΔG_F^0)^{6,43} obtained by Eq. (17):

$$\Delta G_F^0 = (H_{l,F}^0 - H_{s,F}^0) - T(S_{l,F}^0 - S_{s,F}^0) \quad (17)$$

where the subscript “l” is liquid phase and “s” is solid phase. The values of $H_{l,F}^0$, $H_{s,F}^0$, $S_{l,F}^0$, $S_{s,F}^0$ values were obtained from the FactSage 8.0 SGTE pure substances database (v13.1)⁴⁴. It is also noted that as metal fluorides compounds dissolve in FLiNaK, a free energy due to dissolution (ΔG_{diss}^0) will arise. Yet, ΔG_{diss}^0 has yet to be theoretically predicted and will not be estimated here. The ΔG_f^0 of fluoride ion (F⁻) is assumed to be 0 and the partial pressure of fluorine gas (F₂) is assumed to be 1 atm so reaction 11 can be a reference for other electrochemical reactions.

Table 1. Standard Gibbs free energy of formation (ΔG_f) of potassium fluoride and chromium fluoride compounds at 600°C. The reference state is relative to enthalpy at 600°C.

Compound	KF	CrF ₂	CrF ₃	Ref	Note
ΔG_f^0	-484.3	-674.6	-954.8	[Barin,1977] ³⁸	Uncorrected
[kJ/mole]	-477.9	-666	-885	-	Supercooled corrected

To ensure the reliability of the ΔG_f^0 values used in this work, the ΔG_f^0 values from various thermodynamic database are listed in Table 2. It is noted that these values represent the condition at T = 0 K. The ΔG_f^0 values from Barin et al.³⁸ are consistent with Yoo¹ and with two open source thermodynamic databases: Open Quantum Materials Database (OQMD)^{45,46} and Materials Project (MP)⁴⁷. The method to convert the formation energy reported in OQMD and MP, from eV/atom to the standard unit of kJ/mol, can be found in the work of Lany et al⁴⁸. To predict the thermodynamic stability of Cr, the equilibrium redox reactions that are possible involving the Cr⁰, CrF₃, CrF₃⁻, CrF₄²⁻, CrF₅²⁻, CrF₆³⁻ species must be considered. Table 3 lists the possible redox reactions and their Nernst equations. The potential window offered by molten fluorides can be defined by the reduction of potassium fluoride, reaction (10), and fluorine gas evolution, or reaction (11). The Nernst potentials of possible redox reactions pertaining to the Cr metal and its species are computed as a function of electrochemical potential and fluoride ion activity. These results are presented in the form of a potential-activity diagram (vs. log(a_{F⁻}) and log(a_{CrF₃⁻})) applicable for molten fluoride salt, which is analogous to Pourbaix diagram developed for aqueous systems²⁸.

Table 2. Equilibrium redox reactions and their thermodynamic expression utilized for the construction of potential-concentration diagrams in molten fluoride salts

<i>Description</i>	<i>Reaction #</i>	<i>Chemical Equation</i>	<i>Nernst Equation / Gibbs free energy expression</i>
Potential Window for Molten Fluorides	10	$\text{KF} + \text{e}^- \leftrightarrow \text{K} + \text{F}^-$	$E = E^0 - \frac{2.303RT}{F} \log\left(\frac{a_{\text{F}^-}}{a_{\text{KF}}}\right)$
	11	$\text{F}_2 + 2\text{e}^- \leftrightarrow 2\text{F}^-$	$E = -\frac{2.303RT}{2F} \log(a_{\text{F}_2}^2)$
Direct Dissolution from Cr ⁰ to Cr(II)	4	$\text{Cr} + 3\text{F}^- \leftrightarrow \text{CrF}_3^- + 2\text{e}^-$	$E = E^0 + \frac{2.303RT}{2F} \log\left(\frac{a_{\text{CrF}_3^-}}{a_{\text{F}^-}^3}\right)$
	5	$\text{Cr} + 4\text{F}^- \leftrightarrow \text{CrF}_4^{2-} + 2\text{e}^-$	$E = E^0 + \frac{2.303RT}{2F} \log\left(\frac{a_{\text{CrF}_4^{2-}}}{a_{\text{F}^-}^4}\right)$
Direct Dissolution from Cr ⁰ to Cr(III)	6	$\text{Cr} + 6\text{F}^- \leftrightarrow \text{CrF}_6^{3-} + 3\text{e}^-$	$E = E^0 + \frac{2.303RT}{3F} \log\left(\frac{a_{\text{CrF}_6^{3-}}}{a_{\text{F}^-}^6}\right)$
	7	$\text{Cr} + 5\text{F}^- \leftrightarrow \text{CrF}_5^{2-} + 3\text{e}^-$	$E = E^0 + \frac{2.303RT}{3F} \log\left(\frac{a_{\text{CrF}_5^{2-}}}{a_{\text{F}^-}^5}\right)$
Disproportionation RXN between Cr(II) and Cr(III)	8	$\text{CrF}_3^- + 3\text{F}^- \leftrightarrow \text{CrF}_6^{3-} + \text{e}^-$	$E = E^0 + \frac{2.303RT}{F} \log\left(\frac{a_{\text{CrF}_6^{3-}}}{a_{\text{CrF}_3^-} a_{\text{F}^-}^3}\right)$
	9	$\text{CrF}_4^{2-} + \text{F}^- \leftrightarrow \text{CrF}_5^{2-} + \text{e}^-$	$E = E^0 + \frac{2.303RT}{F} \log\left(\frac{a_{\text{CrF}_5^{2-}}}{a_{\text{CrF}_4^{2-}} a_{\text{F}^-}}\right)$
Solvation of chromium fluorides	-	$\text{CrF}_3 + 3\text{F}^- \leftrightarrow \text{CrF}_6^{3-}$	$\Delta G = \Delta G^0 + 2.303RT \log\left(\frac{a_{\text{CrF}_6^{3-}}}{a_{\text{F}^-}^3 a_{\text{CrF}_3}}\right)$
	-	$\text{CrF}_3 + 2\text{F}^- \leftrightarrow \text{CrF}_5^{2-}$	$\Delta G = \Delta G^0 + 2.303RT \log\left(\frac{a_{\text{CrF}_5^{2-}}}{a_{\text{F}^-}^2 a_{\text{CrF}_3}}\right)$
Reduction of hydrofluoric acid	12	$\text{HF} + \text{e}^- \leftrightarrow \frac{1}{2}\text{H}_2 + \text{F}^-$	$E = E^0 - \frac{2.303RT}{F} \log\left(\frac{p_{\text{H}_2}^{1/2} a_{\text{F}^-}}{a_{\text{HF}}}\right)$

To perform a complete thermodynamic analysis, the Gibbs free energy of formation (ΔG_f^0) of various chromium fluoride compounds (e.g. CrF_3^- , CrF_4^{2-} , CrF_5^{2-} , CrF_6^{3-}) needs to be known. However not all these values were reported or verified in literature. In this work, an electrochemical method was used to estimate the ΔG_f^0 values of these compound²⁷. The redox electrode potentials ($E_{\text{M}/\text{MF}_x^{n-x}}$) of Cr redox reactions (4)–(9) was determined from cyclic voltammetry performed on a platinum wire inserted in FLiNaK salts with the addition between 0.11 and 1 wt% of CrF_3 (97%, Fisher Scientific) at 600°C. The standard electrode potential ($E_{\text{M}/\text{MF}_x^{n-x}}^0$) was obtained by the extrapolation of $E_{\text{M}/\text{MF}_x^{n-x}}$ to 1M MF_x^{n-x} in the FLiNaK salts. The ΔG_f^0 of possible chromium fluoride compounds were calculated using Eq. (15)²⁷.

Assumptions & Limitations

It is important to point out the ΔG_f^0 values calculated from the experimental CV results are relative to our thermodynamic assumptions used in this chapter. These include that (1) the literature ΔG_f^0 used in this work have a reference state relative to the enthalpy of 873.15K, (2) F^- participates in the half-cell redox

reactions, (3) $\Delta G_f^0(F^-) = 0$ at 600°C, (4) the reduction of K^+ ions to K involves that of KF to K, (5) the activity of F^- is assumed to be 49.M, (6) pure metal activity to be 1, and (7) the activity coefficients of metal fluoride species calculated are assumed unity. These assumptions were selected to facilitate analytical simplification and methodological consistency. Any modification to these assumptions, regardless of the intended purpose, will inevitably affect the results derived from the thermodynamic analysis, including the calculated ΔG_f^0 values for CrF_3^- , CrF_4^{2-} , CrF_5^{2-} , CrF_6^{3-} , and their corresponding half-cell redox potentials.

Table 3. Standard Gibbs free energy of formation (ΔG_f^0) of potassium fluoride and chromium fluoride compounds at T=0 Kelvin obtained from various thermodynamic databases

Compound	KF	CrF ₂	CrF ₃	Ref
ΔG_f^0 [kJ/mole]	-569.8	-777.7	-1172.7	[Barin,1977] ³⁸
	-570.1	-777.1	-	[Yoo, 2001] ¹
	-562.1	-721.0	-1120.7	[OQMD] ⁴⁵⁻⁴⁶
	-566.5	-817.4	-1174.0	[MP] ⁴⁷

Potentiostatic polarization of pure Cr and X-Ray Diffraction

To access the validity of some predictions, a pure Cr coupon was potentiostatically polarized to $-3.2 V_{F_2/F^-}$ for 50 h, $-4 V_{F_2/F^-}$ for 50 h, $-5 V_{F_2/F^-}$ for 1 h in FLiNaK salts at 600°C using a Pt quasireference electrode and a glassy carbon crucible as a counter electrode. The potential values selected will be justified in the result section. The phase composition of solidified salts was analyzed by XRD using the Malvern-Panalytical Empyrean diffractometer [wavelength Cu K α (1.5405 Å)]. The PDF4+ database was used as the reference data. The software HighScore Plus was used for Rietveld refinements. The peak profile was refined by pseudo-Voigt function.

Results and Discussion

Cyclic Voltammograms of Pt in FLiNaK-CrF₃ salts

Fig. 2 show the cyclic voltammograms on a Pt wire in FLiNaK salts with the additions of 1.0wt% and 0.42wt% of CrF₃ at 600°C. In Fig. 2a, no Cr was present and the potassium ion reduction (K^+) reaction was observed at the cathodic terminal of the scan, and its equilibrium potential ($E_{K^+/K}$) was marked in both Fig. 2a and 2b. All potential reported in this work will be referenced from this measured $E_{KF/K}$ potential value. It is noted that the $E_{KF/K}$ potential is referred as the $E_{K^+/K}$ in literature²⁷. Hence, the reference potential used in this study is a quasi-reference $E_{K^+/K}$ potential. In Fig. 2c, two redox couples were observed pertaining to the Cr/Cr(II) and Cr(II)/Cr(III) redox reactions. It is noted that no particular species (e.g. CrF₂, CrF₃, CrF₃⁻, CrF₆³⁻) were assigned to describe the Cr(II) or Cr(III) oxidation state. The electrochemical behavior of the Pt wire in FLiNaK salts with either CrF₂ or CrF₃ additions have been extensively studied by multiple

authors^{14,15,25,27,30}. It was reported that both redox reactions exhibit quasi-reversibility. The Nernst potential of Cr/Cr(II) ($E_{Cr/Cr(II)}$) and Cr(II)/Cr(III) ($E_{Cr(II)/Cr(III)}$) pairs may be approximated at the midpoints between the oxidation and reduction peaks^{31,32}, which are marked the red dotted lines in both Figs. 2b and 2c.

However, in Fig. 2c, it can be seen that the Cr(III)/Cr(II) reduction peak was very shallow. This peak cannot be clearly distinguished for a given weight percent of CrF_3 added^{41,47} (such as in Fig. 2b), making it difficult to precisely determine its peak potential and current. The smaller peak current and shallower peak shape may be due to the combined effects of the lower diffusivity of Cr(III) (an order of magnitude lower than that of Cr(II) at 600°C in FLiNaK salts²⁵), and if the reduction reaction occurs not only on the Pt surface but elsewhere in the bulk molten salt²⁴.

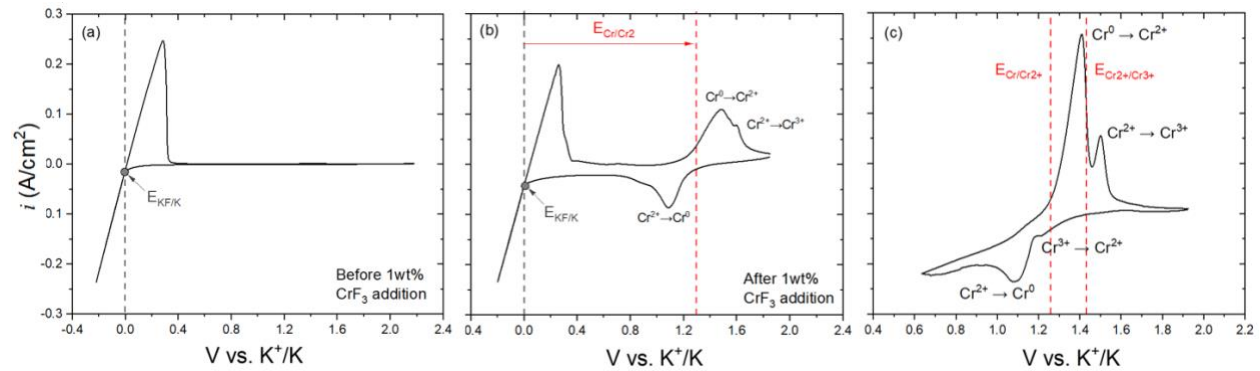


Figure 2. Cyclic voltammogram of Pt wire in a FLiNaK salt at 600°C. (a) shows the cyclic voltammogram before and after the addition of (b) 1.0 wt% and (c) 0.42 wt% of CrF_3 at 600 °C. (a), (b) indicate the equilibrium potential of KF reduction ($E_{KF/K}$). The red dotted lines in (b) and (c) show the approximate experimentally determined equilibrium redox potential of Cr/Cr(II) redox couples ($E_{Cr/Cr(II)}$).

Calculating the Concentration of CrF_2 and CrF_3 in FLiNaK

Upon the addition of CrF_3 in FLiNaK salts, it was expected that deposited Cr particles and CrF_2 would be formed by the disproportionation reaction, or reaction (3), as observed by Liu et al.²⁴ Determining the activity of CrF_2 and CrF_3 in FLiNaK salts is important to the thermodynamic analysis. Given that the Cr/Cr(II) and Cr(II)/Cr(III) reactions are quasi-reversible^{14,25,30,33–36}, the Randles-Ševcik relation (Eq. (18)) was used to estimate the concentration of ionic species at a known scan rate and peak current densities:

$$i_p = 0.4463nFAC_b D^{1/2} \left(\frac{nFv}{RT} \right)^{1/2} \quad (18)$$

where i_p is the peak current density; n is the moles of electrons transferred; A is the area; C_b is bulk concentration; v is the scan rate; D is the diffusivity; R is the universal gas constant $8.314 \text{ J}\cdot\text{K}^{-1}\cdot\text{mol}^{-1}$; T is temperature. To approximate the concentration of Cr(II) species in our FLiNaK- CrF_3 salt, the ratio of peak current densities associated with Cr/Cr(II) and Cr(II)/Cr(III) reactions were determined, yielding Eq. (19):

$$\frac{C_{\text{Cr(II)}}}{C_{\text{Cr(III)}}} = \frac{i_{\text{Cr/Cr(II)}}^{\text{peak}}}{i_{\text{Cr(II)/Cr(III)}}^{\text{peak}}} \left(\frac{D_{\text{Cr(III)}}}{D_{\text{Cr(II)}}} \right)^{1/2} \quad (19)$$

where $i_{\text{Cr/Cr(II)}}^{\text{peak}}$ and $i_{\text{Cr(II)/Cr(III)}}^{\text{peak}}$ are the peak current densities in the CV associated with the Cr/Cr(II) and Cr(II)/Cr(III) oxidation peaks, and $D_{\text{Cr(II)}}$ and $D_{\text{Cr(III)}}$ are the diffusivities of Cr(II) and Cr(III) related species, which were reported by Wang and Zhang²⁵ to be $2.55 \cdot 10^{-5}$ and $7.74 \cdot 10^{-6} \text{ cm}^2\text{s}^{-1}$ in FLiNaK salts at 600°C . Using the disproportionation reaction (3) as the basis for stoichiometric conversion, the resulting ratio of Cr(II) to Cr(III) concentration when Cr(III) is added can also be expressed as:

$$\frac{C_{\text{Cr(II)}}}{C_{\text{Cr(III)}}} = \frac{3x}{C_{\text{CrF}_3}^0(\text{M}) - 2x} \quad (20)$$

where x represents the moles reacted. Using Eqs. (19) and (20), the concentration of Cr(II) and Cr(III) species as a function of initial CrF_3 concentration ($C_{\text{CrF}_3}^0$) can be obtained as shown in Fig. 3a. Both Cr(II) and Cr(III) species follow a linear relationship with $C_{\text{CrF}_3}^0$ as shown in Eq. (21) and (22):

$$C_{\text{Cr(II)}}(\text{M}) = 0.0152 C_{\text{CrF}_3}^0(\text{wt}\%) \quad (21)$$

$$C_{\text{Cr(III)}}(\text{M}) = 0.173 C_{\text{CrF}_3}^0(\text{wt}\%) \quad (22)$$

The percent conversion of initial CrF_3 to Cr(II) species was computed and shown in Fig. 3b. The red line marks the solubility limit of CrF_3 in FLiNaK, which was calculated to be 0.3 wt% by Yin et al³⁷. Prior to CrF_3 saturation, the percent conversion increased and plateaued when 0.42 wt% of CrF_3 was introduced, which is consistent with thermodynamic prediction³⁷. Upon saturation, it was determined that about 7.71% of CrF_3 was converted to CrF_2 , close to the percent conversion value reported by Peng et al³⁴.

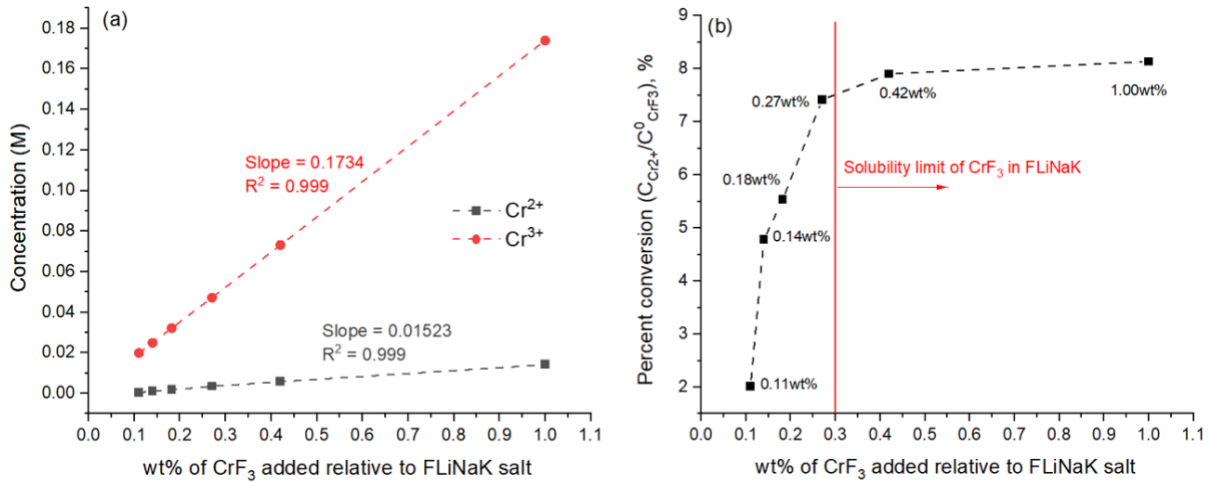


Figure 3. (a) Concentration of Cr(II) and Cr(III) species. (b) The percent conversion from CrF_3 to Cr(II) species at a various weight fraction of CrF_3 added to FLiNaK. The red line marks the reported solubility limit of CrF_3 in FLiNaK at 600°C .

Estimating the Gibbs Free Energy of Formation of Solvated Chromium Fluorides

Fig. 4 shows the experimental Cr/Cr(II) Nernst potential ($E_{\text{Cr/Cr(II)}}$) indicated by symbols versus the calculated Cr(II) concentration (Eq. (21)) on a logarithmic scale. The solid line is a best fit to the data that can be fitted against Eq. (23). Between 0.11 and 0.27wt% CrF_3 addition, the $E_{\text{Cr/Cr(II)}}$ potential exhibits a positive linear relationship with the log-scale concentration, which is consistent with the general Nernst expression of the ($\text{Cr} \rightleftharpoons \text{Cr(II)} + 2e^-$) half-cell redox reaction:

$$E_{\text{Cr/Cr(II)}} = E_{\text{Cr/Cr(II)}}^0 + \frac{2.303RT}{2F} \log(a_{\text{Cr(II)}}) \quad (23)$$

$$E_{\text{Cr/Cr(II)}} = E_{\text{Cr/Cr(II)}}^0 + \frac{2.303RT}{2F} \log(\gamma_{\text{Cr(II)}}) + \frac{2.303RT}{2F} \log(C_{\text{Cr(II)}}) \quad (24)$$

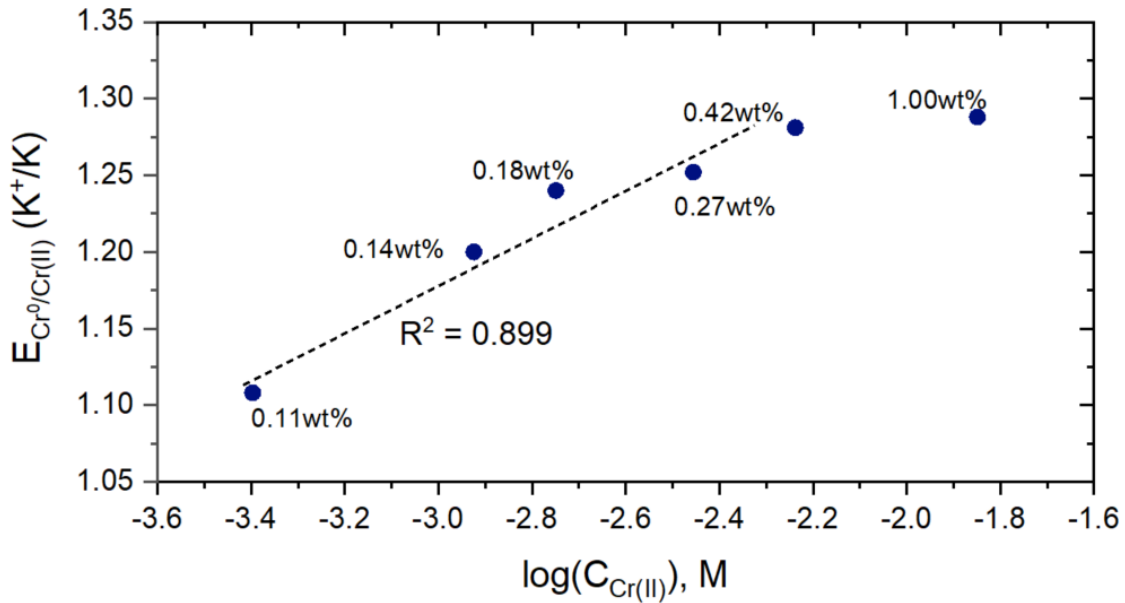


Figure 4. The Nernst potentials associate with $\text{Cr}^0/\text{Cr(II)}$ redox reaction at different calculated concentrations of Cr(II) ions in FLiNaK at 600 °C. The left y-axis shows the potential relative to the pseudo KF/ K potential and the right y-axis shows that calculated potential referenced to the F_2/F^- potential.

At 0.42 and 1.00 wt%, the measured $E_{\text{Cr/Cr(II)}}$ values were similar likely due to the saturation of CrF_3 in FLiNaK when concentrations greater than the solubility limit of 0.3 wt% of CrF_3 was introduced³⁷, resulting in the formation of distinct K_2CrF_5 or K_3CrF_6 phases in FLiNaK³⁷. When the solubility limit is exceeded, the FLiNaK salt remains at a constant relative concentration of Cr(II) and Cr(III) in the FLiNaK salts, which limits the measured $E_{\text{Cr/Cr(II)}}$ potential values since the equilibrium value of Cr(II) was present.

The linear region in Fig. 4 can be fitted and extrapolated to determine the standard electrode potential ($E_{\text{Cr/Cr(II)}}^0$) using the y-intercept of Eq. (24). Using a similar electrochemical approach²⁷, Massot et al. reported that $\gamma_{\text{Cr(II)}}$ (activity coefficient of Cr(II)) to be close to unity in LiF-NaF salts at 700°C²⁷. In this

work, $E_{\text{Cr/Cr(II)}}^0$ (with Cr(II) exists as CrF_2 , CrF_3^- , or CrF_4^{2-}) was found to be $1.66\text{V}_{\text{K}^+/\text{K}}$ or $-3.02\text{V}_{\text{F}_2/\text{F}^-}$, which is similar to $-3.16\text{V}_{\text{F}_2/\text{F}^-}$ computed from Table 1²⁷. Nevertheless, without knowing the actual species involve in the Cr/Cr(II) redox reaction and the activities coefficient of Cr(II) and F^- (both are assumed in this work), it is difficult to utilize this experimentally extracted value to estimating the ΔG_f^0 value of Cr(II).

In molten fluorides, the Cr(II) oxidation state can also possibly exist in the forms of CrF_3^- or CrF_4^{2-} species¹⁰. To approximate their ΔG_f^0 values, the half-cell redox reactions of Cr/ CrF_3^- and Cr/ CrF_4^{2-} were first separately considered. To approximate the Cr/ CrF_3^- ($E_{\text{Cr}/\text{CrF}_3^-}^0$) and Cr/ CrF_4^{2-} ($E_{\text{Cr}/\text{CrF}_4^{2-}}^0$) formal potentials, the $E_{\text{Cr}/\text{CrF}_2}^0$ computed from Table 1 was utilized. Firstly, consider the Nernst expression for reactions (4) and (5) as Eqs. (25) and (26), respectively:

$$E_{\text{Cr}/\text{CrF}_3^-} = E_{\text{Cr}/\text{CrF}_3^-}^0 + \frac{2.303RT}{2F} \log \left(\frac{a_{\text{CrF}_3^-}}{a_{\text{F}^-}^3} \right) \quad (25)$$

$$E_{\text{Cr}/\text{CrF}_4^{2-}} = E_{\text{Cr}/\text{CrF}_4^{2-}}^0 + \frac{2.303RT}{2F} \log \left(\frac{a_{\text{CrF}_4^{2-}}}{a_{\text{F}^-}^4} \right) \quad (26)$$

Assuming that (i) the activity coefficient of Cr(II) ions in FLiNaK salts is unity^{8,27}, (ii) the activity coefficient of F^- ions is unity in FLiNaK salt since the F^- ions do not form complexes or a separate phase with Li^+ , Na^+ and K^+ ions^{8,9,39}, (iii) and the concentration of F^- ions is 49.3 M based on stoichiometric calculation (i.e. $\log(a_{\text{F}^-}) = 1.693$). The intercept of Eq. (24) can be related to that in Eqs. (25) and (26), resulting in the relations Eqs. (27) and (28), respectively:

$$E_{\text{Cr}/\text{CrF}_3^-}^0 = E_{\text{Cr}/\text{Cr(II)}}^0 - 0.435 \quad (27)$$

$$E_{\text{Cr}/\text{CrF}_4^{2-}}^0 = E_{\text{Cr}/\text{Cr(II)}}^0 - 0.580 \quad (28)$$

Using these relations, the standard electrode potentials of each Cr(II) solvated species may be estimated. The integers presented in Eqs. (27) and (28) are a function of the stoichiometric moles of F^- ions consumed, which is different depending on the solvated structure. For clarity purposes, the calculation of these standard potentials assumes that only one solvated state contributes to the Cr/Cr(II) redox reaction. In this work, the $E_{\text{Cr}/\text{CrF}_3^-}^0$ and $E_{\text{Cr}/\text{CrF}_4^{2-}}^0$ are found to be -3.896 and $-4.190\text{V}_{\text{F}_2/\text{F}^-}$, which are equivalent to the ΔG_f^0 values of -751.8 and -808.7kJ/mol , respectively. It is noted that the calculated ΔG_f^0 values are not absolute values and will change relative to the thermodynamic assumptions used for calculations.

The method presented relies on identifying both the oxidation and reduction potentials of a redox reaction. However, it was previously mentioned that the reduction peak of Cr(III)/Cr(II) was shallow and could yield erroneous Nernst potentials. Therefore, the experimental-theoretical method utilized above may not yield reliable result in estimating the ΔG_f^0 of CrF_5^{2-} and CrF_6^{3-} species.

An alternative approach was used. From UV-Vis absorption spectroscopy²⁴ to cyclic voltammetry measurements³⁴, it was reported that the Cr(II) and Cr(III) states can coexist in equilibrium, saturated condition, upon the addition of CrF₂ or CrF₃ salts in FLiNaK. In Fig. 3b, it was found that 7.71% of Cr(III) was converted to Cr(II) species, which is similar to the value reported by Peng et al³⁴ and Zhang et al²⁵. Upon CrF₃ saturation, it is fair to assume that the ratio of Cr(II)/Cr(III) activities (i.e. $a_{\text{CrF}_3^-}/a_{\text{CrF}_6^{3-}}$ or $a_{\text{CrF}_4^{2-}}/a_{\text{CrF}_5^{2-}}$) were 0.0814. Consider the Nernst equations for reactions (10) and (11):

$$E = E^0 + \frac{2.303RT}{F} \log\left(\frac{a_{\text{CrF}_6^{3-}}}{a_{\text{CrF}_3^-} a_{\text{F}^-}^3}\right) \quad (29)$$

$$E = E^0 + \frac{2.303RT}{F} \log\left(\frac{a_{\text{CrF}_5^{2-}}}{a_{\text{CrF}_4^{2-}} a_{\text{F}^-}}\right) \quad (30)$$

With a Cr(II)/Cr(III) equilibrium activity ratio of 0.0814 and $\log(a_{\text{F}^-})$ of 1.693, Eqs. (29) and (30) can be simplified to Eqs. (31) and (32), respectively :

$$E_{\text{CrF}_6^{3-}/\text{CrF}_3^-}^0 = E_{\text{CrF}_6^{3-}/\text{CrF}_3^-} + 0.690 \quad (31)$$

$$E_{\text{CrF}_5^{2-}/\text{CrF}_4^{2-}}^0 = E_{\text{CrF}_5^{2-}/\text{CrF}_4^{2-}} + 0.104 \quad (32)$$

In this case, the standard electrode or formal potentials of reactions (8) and (9) can be experimentally determined by measuring the redox potential of $E_{\text{Cr(II)/Cr(III)}}$ when FLiNaK salt is saturated with CrF₃. In this work, $E_{\text{Cr(II)/Cr(III)}}$ was found to be +1.43 V_{KF/K} or -3.26 V_{F₂/F⁻}. $E_{\text{CrF}_6^{3-}/\text{CrF}_3^-}^0$ and $E_{\text{CrF}_5^{2-}/\text{CrF}_4^{2-}}^0$ were found to be -2.57 and -3.15 V_{F₂/F⁻}, respectively. Using Eq. (16) and the ΔG_f^0 values of CrF₃⁻ and CrF₄²⁻ previously determined, the ΔG_f^0 of CrF₅²⁻ and CrF₆³⁻ were calculated to be -999.7 and -1113.1 kJ/mol, respectively. The summary of the ΔG_f^0 of solvated chromium fluorides is shown in Table 4. It is noted that Eqs. (27) and (28) were used to calculate the ΔG_f^0 in the case of solvated CrF₃⁻ or CrF₄²⁻ species using data presented by Massot et al²⁷. The result shows a similar value as compared in Table 4.

Table 4. Calculated standard Gibbs free energy of formation (ΔG_f) of solvated chromium fluoride compounds based on cyclic voltammetry results at 600°C in

Solvated state	CrF ₃ ⁻ (Cr(II))	CrF ₄ ²⁻ (Cr(II))	CrF ₅ ²⁻ (Cr(III))	CrF ₆ ³⁻ (Cr(III))	Ref
ΔG_f^0	-751.8	-808.7	-1113.1	-999.7	This work
[kJ/mole]	-733.4 ¹	-761.7 ¹	-	-	[Massot et al] ²⁷

1) The Gibbs free energy of solvated chromium fluorides reported here were derived from the formal potential ($E_{\text{CrF}_2/\text{Cr}}$) reported by Massot, 2021 using Eq. (17) and (18) in this work.

Stability of Cr(II) and Cr(III) in Molten Fluorides

The Nernst equations for key redox reactions involving CrF_3 , CrF_3^- , CrF_4^{2-} , CrF_5^{2-} , CrF_6^{3-} , and Cr species are listed in Table 3. The predominance region of each possible reaction product considered in Table 4 is plotted as a function of potential versus the F^- activity (Fig. 5) and the CrF_3^- (Fig. 7) activities a logarithmic scale. The solid lines indicate equilibrium boundaries between the species considered. Given the complexity arising from the consideration of all solvated states, two pairs of solvated species (pair 1: $\text{Cr}^0/\text{CrF}_3^-/\text{CrF}_6^{3-}$; pair 2: $\text{Cr}^0/\text{CrF}_4^{2-}/\text{CrF}_5^{2-}$) were first independently considered.

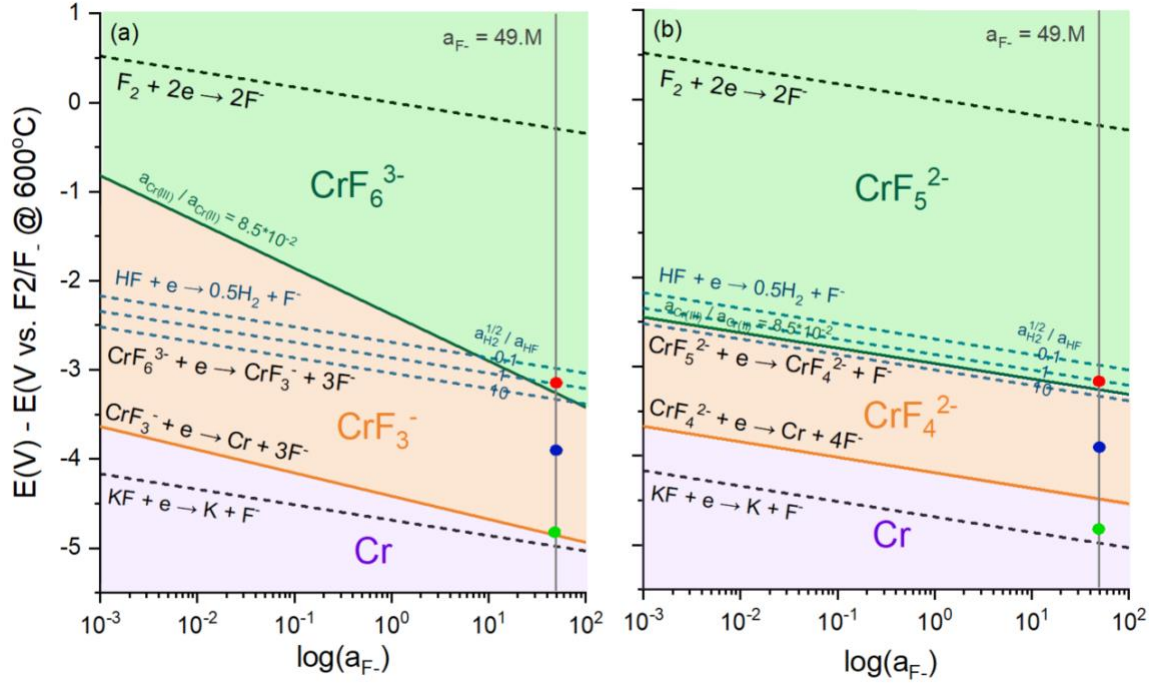
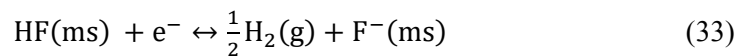


Figure 5. $E - \log(a_{\text{F}^-})$ equilibrium diagram for Cr. (a) considers the CrF_3^- and CrF_6^{3-} , and (b) the CrF_4^{2-} and CrF_5^{2-} solvated states. The red, blue, and green dots at $\log(a_{\text{F}^-}) = 1.693$ mark the results presented in Fig. 6. The gray vertical line at $\log(a_{\text{F}^-}) = 1.693$ indicates the fluoride activity corresponding to the FLiNaK salts. $a_{\text{Cr(II)}}$ and a_{KF} were assumed to be 10^{-6} and 20.3M, respectively. The ratio of $a_{\text{Cr(III)}}/a_{\text{Cr(II)}}$ of 0.082 was used based on Fig. 2. The ratio of $a_{\text{H}_2}^{1/2}/a_{\text{HF}}$ used was be 0.1, 1 and 10.

Figs. 5a and 5b illustrate the potential- $\log(a_{\text{F}^-})$ diagrams for pair 1: $\text{Cr}^0/\text{CrF}_3^-/\text{CrF}_6^{3-}$ (Fig. 5a) and for pair 2: $\text{Cr}^0/\text{CrF}_4^{2-}/\text{CrF}_5^{2-}$ (Fig. 5b) at 600 °C. Unless otherwise specified, the activities of all Cr ionic species were assumed be 10^{-6} M. All potentials displayed are with respect to the potential for fluorine gas (F_2/F^-) evolution at 600°C calculated from its Nernst equation (Table 2). The blue and orange dashed line indicates the potential window of molten FLiNaK salts defined by reactions (10) and (11). The black dotted-dash line indicates the HF reduction reaction, or reaction (33), at various ratio of $p^{1/2}_{\text{H}_2}/a_{\text{HF}}$:



In Fig. 5a, the CrF_3^- ion exists in a relatively narrow stability region, approximately ~ 120 mV wide at the FLiNaK salt composition (gray line). Above $-2.966 V_{\text{F}_2/\text{F}^-}$, the CrF_6^{3-} species (+2 oxidation state) is predicted to be most thermodynamically stable. This behavior remains consistent in the range of $\log(a_{\text{F}^-})$ studied. It is also noted that the equilibrium potential given by the Nernst potential for hydrogen evolution (reaction (33)) exists at potentials above that $\text{CrF}_3^-/\text{CrF}_6^{3-}$ oxidation, indicating the oxidizing power of HF towards spontaneous anodic dissolution of Cr leading to formation of solvated Cr(II) and Cr(III).

In Fig. 5b, the stability regions of Cr, CrF_4^{2-} , and CrF_5^{2-} species are shown. As the $\log(a_{\text{F}^-})$ increases, the stability region of CrF_4^{2-} species widens, and then converted to CrF_5^{2-} though reaction (9). To verify which one of these situations actually exists when Cr is exposed to FLiNaK systems at 600°C , high purity Cr was potentiostatically polarized to -4.8 , -3.9 , $-3.18 V_{\text{F}_2/\text{F}^-}$ in FLiNaK salts at the same temperature (marked as the green, blue, red dots in Fig. 5). The composition of the solidified residual salts was analyzed with XRD. This will be discussed in the next section. Fig. 5 predicts that Cr would remain as the Cr^0 state (in the “immunity” region) when it is polarized at or below $-4.8 V_{\text{F}_2/\text{F}^-}$, and undergo active corrosion to either CrF_3^- or CrF_5^{2-} state at $-3.9 V_{\text{F}_2/\text{F}^-}$, and either CrF_5^{2-} or CrF_6^{3-} state at $-3.18 V_{\text{F}_2/\text{F}^-}$. Potentiostatic hold experiments coupled with XRD were used to verify these predictions. Fig. 6 shows the XRD of FLiNaK salts after Cr was potentiostatically polarized to $-3.18 V_{\text{F}_2/\text{F}^-}$ for 50 h, $-3.9 V_{\text{F}_2/\text{F}^-}$ for 50 h, and $-4.8 V$ for 1 h.

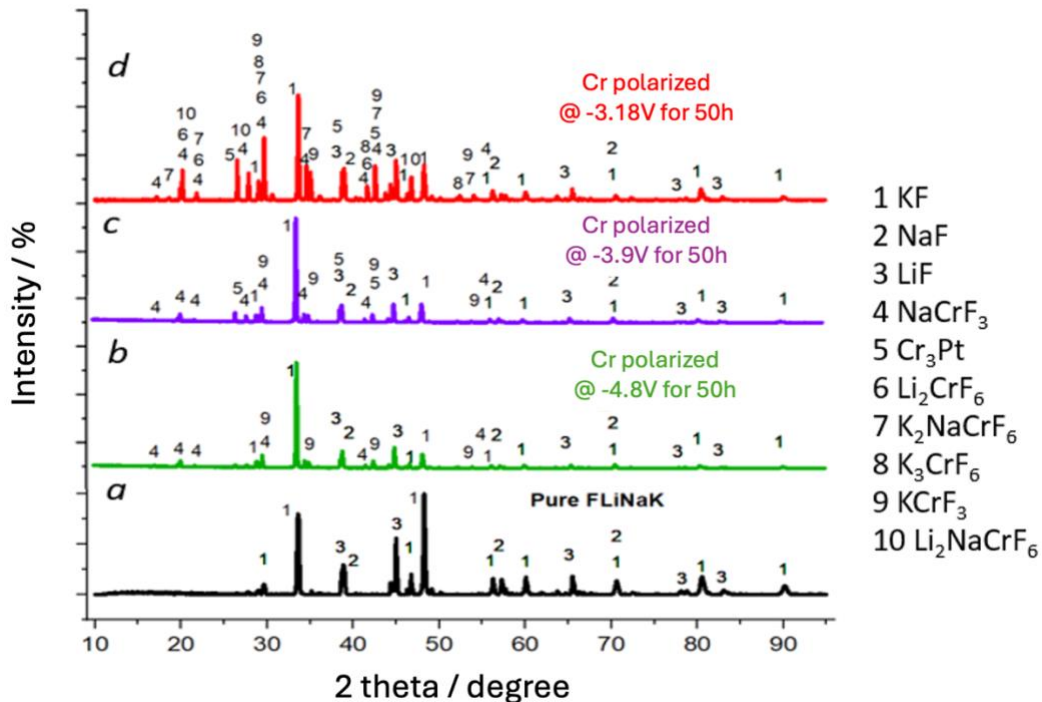


Figure 6. X-Ray diffractogram of the as-solidified of (a) baseline FLiNaK salt and with Cr potentiostatically polarized to (b) $-4.8 V_{\text{F}_2/\text{F}^-}$ for 1h, (c) $-3.9 V_{\text{F}_2/\text{F}^-}$ for 50h, (d) $-3.18V_{\text{F}_2/\text{F}^-}$ for 50h

In the pure solidified FLiNaK (Fig. 6a), the XRD patterns reveal diffraction peaks of KF, LiF and NaF with KF peaks sharing the highest percent intensity. When Cr metal was held at $-4.8 V_{F_2/F^-}$ for 1 h, no significant mass loss of Cr was observed. However, the XRD pattern (Figure 6b) of the tested salts shows low intensity diffraction peaks corresponding to the presence of NaCrF_3 (peak 4) and KCrF_3 (peak 9) species. The presence of Cr may be attributed to the dissolution of the native Cr_2O_3 oxide film at the beginning of the experiment. It is noted that large cathodic reduction current density ($>1\text{A}/\text{cm}^2$) was observed after 1h of potentiostatic hold (not shown) at this potential. This may either be due to formation of H_2 bubbles from HF reduction or the reduction of potassium on the Cr surface.

Figs. 6c and 6d show the XRD patterns of FLiNaK salts where a Cr coupon was potentiostatically polarized at $-3.9V_{F_2/F^-}$ for 50 h, respectively. In Fig. 6c, the presence of NaCrF_3 (peak 4) and KCrF_3 (peak 9) species were identified, corroborating with thermodynamic prediction. In Fig. 6d, the NaCrF_3 (peak 4), KCrF_3 (peak 9), K_2NaCrF_6 (peak 7), K_3CrF_6 (peak 8), $\text{Li}_2\text{NaCrF}_6$ (peak 10) compounds were identified, confirming the existence of both CrF_3^- and CrF_6^{3-} states. The CrF_3^- likely formed during the solidification of FLiNaK and maintained a thermodynamic equilibrium with the CrF_6^{3-} state²⁴. The K_2NaCrF_6 , K_3CrF_6 , $\text{Li}_2\text{NaCrF}_6$ compounds suggest that the Cr(III)ion has a coordination number 6 at the temperature studied. Here we acknowledge that XRD result alone is not sufficient to conclude the actual molecular structure of the fluorinated Cr(II) species as that may change in molten state or fluoride activity. The assumption here is that the melting of KCrF_3 or others salts with form K^+ and CrF_3^- species with no addition reaction with the F^- salt. There are limited experimental results in the existing body of literature to suggest otherwise and requires further investigation.

Nevertheless, results obtained are in a good correlation with literature data and previous work on compound prediction reported in Ab-initio simulations¹⁰. In all potentials studied, no CrF_5^{2-} related compounds were detected. This indicates that the Cr/Cr(II) and Cr(II)/Cr(III) seen in Fig. 2 likely correspond to the Cr/ CrF_3^- and $\text{CrF}_3^-/\text{CrF}_6^{3-}$ redox couples. During the corrosion of Cr, the activities of CrF_3^- and CrF_6^{3-} species in the FLiNaK salts are expected to increase over an exposure period. Therefore, it is useful to consider the change in thermodynamic driving forces (Table 2) with respect to the activities of CrF_3^- and CrF_6^{3-} ions under a defined constant of $\log(a_{\text{F}^-})$ where $(\log(49.3) = 1.693$ for FLiNaK).

Fig. 7 shows the potential-activity diagrams considering the predominant phases of Cr, CrF_3^- , and CrF_6^{3-} species as a function of $\log(a_{\text{CrF}_3^-})$ and potential. The equilibrium potential between Cr and CrF_3^- ions was computed from reaction (4) and exhibits a linear relationship with $\log(a_{\text{CrF}_3^-})$. The blue circle symbols shown in Fig. 7 are the experimental half-cell Nernst potential reported in Fig. 4, which are closely following but slightly different from the thermodynamic prediction. Nevertheless, the boundary of these stability regions is sensitive to the ΔG_f^0 of solvated chromium fluorides (Table 2) utilized to construct these potential-activity diagrams. The use of cyclic voltammetry provides a relatively straightforward method to estimate these

ΔG_f^0 values, but the method is sensitive to errors. For example, the uncertainties could be related to the use of quasi $E_{KF/K}$ potential, temperature distributions or natural convection effects during molten salt electrochemistry measurement or because the Nernst potential theory cannot completely describe the potential for the quasi-reversible reactions³¹.

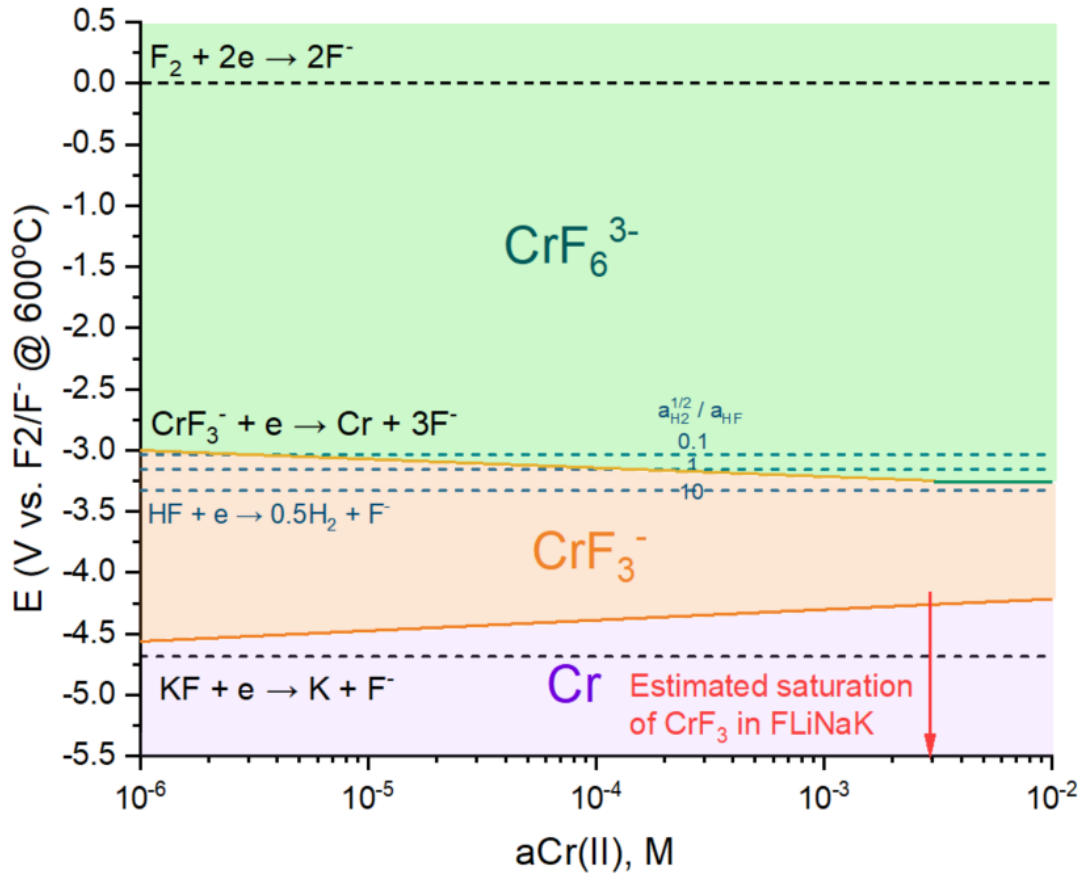


Figure 7. $E - \log(a_{CrF_3^-})$ equilibrium diagram for Cr in FLiNaK salts ($\log(a_{F^-}) = 1.693$) at 600°C. The blue dot indicates the equilibrium redox potential of Cr/Cr(II) reported in Fig 5.

Before reaching the CrF_3 solubility limit in FLiNaK salts, the CrF_3^-/CrF_6^{3-} equilibrium line shows a linearly decreasing potential consistent with the prediction of the Nernst equation. When the solubility limit is reached, the ratio of CrF_3^- to CrF_6^{3-} activities is assumed to be 0.0814 calculated assuming the 7.71% conversion shown in Fig. 3b. Therefore, the Nernst potential is a straight horizontal line since an equilibrium ratio was enforced. It is noted that the equilibrium potential of CrF_3^-/CrF_6^{3-} reactions in Fig. 7 is lower than that in Fig. 5a. This is because the CrF_3^-/CrF_6^{3-} activity ratio (Fig. 3b) was considered when constructing the potential- $\log(a_{CrF_3^-})$ diagram; whereas all Cr ion activities were assumed to be $10^{-6}M$ in Figs. 4a and b.

One observation is that as the $p^{1/2}_{H_2}/a_{HF}$ ratio increases, the equilibrium potential of HF/ H_2 reaction decreases and approaches to that of the CrF_6^{3-}/CrF_3^- reduction. As the CrF_3^- activity increases, the stability region of CrF_3^- E - $\log(a_{CrF_3^-})$ phase space becomes smaller. Practically, based on the estimated ΔG_f^0 , the Cr/ CrF_3^-

boundary will not intersect with that of the $\text{CrF}_3^-/\text{CrF}_6^{3-}$. Therefore, thermodynamic prediction indicates that the corrosion of Cr may take place first through the direct dissolution to Cr(II) state in the form of CrF_3^- , and CrF_6^{3-} will then be formed electrochemically in either within the FLiNaK salts or Cr surface.

Ramifications towards spontaneous corrosion of Cr in FLiNaK

The diagrams (Figs. 5 and 7) indicate that the KF is oxidized at all potentials where Cr is oxidized to Cr(II) and Cr(III). The F^- stability region spans the entire region where spontaneous corrosion of Cr occurs. Cr may be oxidized to Cr(II) and Cr(III) in the presence HF (due to moisture impurity) spontaneously except some combinations of $p^{1/2}_{\text{H}_2}/a_{\text{HF}}$ etc. This situation is not changed qualitatively for different solvation of oxidized Cr with F^- and this aspect is substantially similar for the two cases (pair 1: $\text{Cr}^0/\text{CrF}_3^-/_\text{CrF}_6^{3-}$; pair 2: $\text{Cr}^0/\text{CrF}_4^{2-}/\text{CrF}_5^{2-}$) considered in this work. Cr may be oxidized by HF and may be oxidized by other sufficiently noble metal impurities. It is therefore crucial to consider the spontaneity of Cr corrosion by systematically comparing the driving force of Cr/Cr(II) with possible oxidizing reactions, such as HF/ H_2 , Eu(III)/Eu(II) and many others. Appendix 1 further explores this topic by deciphering when metal corrosion is spontaneous in molten fluorides using potential-activity diagrams.

It is important to note that Fig. 5 and 7 are conventional thermodynamic stability fields that assume full reversibility of electrochemical reactions, uniform distribution of concentration, and chemical equilibrium between species. Readers must take caution when applying these principles to analyze actual complex corrosion system involving both kinetic and thermodynamic factors. Work is still ongoing to further verify and optimize the accuracy of potential- activity diagrams in molten fluoride salts, for example to theoretically calculate the Gibbs free energy of formation of solvated compounds in molten fluorides. The thermodynamic prediction presented here are consistent with literature the experimental findings of Liu et al.²⁴ and an ample number of electrochemical studies in FLiNaK salts^{14,25,30,35–38}. The potential-activity diagram developed in this work is also useful to help understanding the corrosion thermodynamics and kinetics of metallic alloys in molten fluoride salts, which will be illustrated in the next chapter.

Conclusions

The Gibbs free energy of formation of CrF_3^- , CrF_4^{2-} , CrF_5^{2-} , and CrF_6^{3-} solvated chromium compounds were extracted from analysis of cyclic voltammetry data on a Pt wire in FLiNaK salts with CrF_3 addition at 600°C. Based on classical thermodynamics including the Nernst equation, a potential- $\log(a_{\text{F}^-})$ analogous to a Pourbaix diagram was constructed for two systems: (i) $\text{Cr}/\text{CrF}_3^-/\text{CrF}_6^{3-}$ (ii) $\text{Cr}/\text{CrF}_4^{2-}/\text{CrF}_5^{2-}$ pertinent to Cr exposure in molten fluoride salts. To validate the prediction, a Cr coupon was potentiostatically held at selected potentials corresponding to the different thermodynamic stability regions, and the solidified salts were analyzed using X-Ray Diffraction. Experimental XRD results confirmed that the $\text{Cr}/\text{CrF}_3^-/\text{CrF}_6^{3-}$

described Cr corrosion thermodynamics in FLiNaK salts at 600°C, while CrF_4^{2-} or CrF_5^{2-} compounds were not detected by XRD.

A potential- $\log(a_{\text{CrF}_3^-})$ diagram based on the $\text{Cr}/\text{CrF}_3^-/\text{CrF}_6^{3-}$ system was developed to predict the most thermodynamically favorable oxidation state for Cr corrosion. Prediction shows that the direct dissolution from Cr to CrF_3^- via a +2 charge is favored over all reasonable values of a_{HF} . F^- complexation assuming $\text{Cr}/\text{CrF}_3^-/\text{CrF}_6^{3-}$ compared to CrF_4^{2-} or CrF_5^{2-} produces E - a_{HF} diagrams which are similar but have distinct differences. The E - $\log(a_{\text{F}^-})$ activity diagrams indicate that the KF is oxidized at all potentials where Cr is oxidized to Cr(II) and Cr(III). The F^- stability region spans the entire region where spontaneous corrosion of Cr occurs. Cr may be oxidized to Cr(II) and Cr(III) in the presence HF (due to moisture impurity) spontaneously except some conditions of $p^{1/2}_{\text{H}_2}/a_{\text{HF}}$ etc. This situation is not changed qualitatively for various states of solvation between oxidized Cr solute in F^- solvent and this aspect is similar for the two cases (pair 1: $\text{Cr}^0/\text{CrF}_3^-/\text{CrF}_6^{3-}$; pair 2: $\text{Cr}^0/\text{CrF}_4^{2-}/\text{CrF}_5^{2-}$) considered in this work.

References

1. Yoo, J. H. Thermodynamic DataBase for Metal Fluorides, Technical Report Number: TR-1824, (Korea Atomic Energy Research Institute) KAERI, (2001).
2. Dolan, T. J. Molten Salt Reactors and Thorium Energy (Woodhead Publishing, 2017).
3. Serp, J. et al. The molten salt reactor (MSR) in generation IV: overview and perspectives. *Prog. Nucl. Energy* 77, 308–319 (2014). <https://doi.org/10.1016/j.pnucene.2014.02.014>
4. Wright, R. N. & Sham, T. L. Status of Metallic Structural Materials for Molten Salt Reactors. Technical Report INL/EXT-18-45171; Argonne National Laboratory & Idaho National Laboratory (2018).
5. Busby, J. et al. Technical Gap Assessment for Materials and Component Integrity Issues for Molten Salt Reactors. Technical Report ORNL/SPR-2019/1089; Oak Ridge National Laboratory (2019).
6. Guo, S. et al. Corrosion in the molten fluoride and chloride salts and materials development for nuclear applications. *Prog. Mater. Sci.* 97, 448–487 (2018). <https://doi.org/10.1016/j.pmatsci.2018.05.003>
7. Sridharan, K. & Allen, T. Molten Salts Chemistry from Lab to Application - Chapter 12: Corrosion in Molten Salts (Elsevier, 2013).
8. Zhang, J. et al. Redox potential control in molten salt systems for corrosion mitigation. *Corros. Sci.* 144, 44–53 (2018). <https://doi.org/10.1016/j.corsci.2018.08.035>
9. Baes, C. F. The chemistry and thermodynamics of molten salt reactor fuels. *J. Nucl. Mater.* 51, 149–162 (1974). [https://doi.org/10.1016/0022-3115\(74\)90124-X](https://doi.org/10.1016/0022-3115(74)90124-X)
10. Winner, N. et al. Ab-initio simulation studies of chromium solvation in molten fluoride salts. *J. Mol. Liq.* 335, 116351 (2021). <https://doi.org/10.1016/j.molliq.2021.116351>
11. Wang, Y. et al. Effects of the oxidants H_2O and CrF_3 on the corrosion of pure metals in molten (Li,Na,K)F. *Corros. Sci.* 103, 268–282 (2016). <https://doi.org/10.1016/j.corsci.2015.11.032>
12. Pizzini, S. & Morlotti, R. Oxygen and hydrogen electrodes in molten fluorides. *Electrochim. Acta* 10, 1033–1041 (1965). [https://doi.org/10.1016/0013-4686\(65\)80015-9](https://doi.org/10.1016/0013-4686(65)80015-9)
13. Ai, H. et al. Effects of O_2 —additive on corrosion behavior of Fe–Cr–Ni alloy in molten fluoride salts. *Corros. Sci.* 150, 175–182 (2019). <https://doi.org/10.1016/j.corsci.2019.01.040>

14. Wu, W. et al. Electrochemical behaviors of Cr(III) in molten LiF-NaF-KF eutectic. *Int. J. Electrochem. Sci.* 13, 225–234 (2018). <https://doi.org/10.20964/2018.01.21>
15. Yoko, T. & Bailey, R. A. Electrochemical studies of chromium in molten LiF - NaF - KF (FLINAK). *J. Electrochem. Soc.* 131, 2590–2595 (1984). <https://doi.org/10.1149/1.2115363>
16. Jordan, W. H. et al. Aircraft Nuclear Propulsion Project Quarterly Progress Report. Technical Report Number: ORNL-2221; Oak Ridge National Laboratory (1957).
17. Koger, J. W. Effect of FeF₂ Addition on Mass Transfer in A Hastelloy N: LiF-BeF₂-UF₄ Thermal Convection Loop System. Technical Report Number: ORNL-TM-4188; Oak Ridge National Laboratory (1972).
18. DeVan, J. H. & Evans, III, R. B. Corrosion Behavior of Reactor Materials in Fluoride Salt Mixtures. Technical Report ORNL-TM-328; Oak Ridge National Laboratory (1962).
19. Jordan, W. H. et al. Aircraft Nuclear Propulsion Project Quarterly Progress Report for Period Ending Sept. 10, 1956. Technical Report Number: ORNL-2157; Oak Ridge National Laboratory (1956).
20. Song, Y. et al. Solubility of Cr₂O₃ in molten fluorides with different ZrF₄ contents and fluoroacidities. *J. Electrochem. Soc.* 167, 023501 (2020). <https://doi.org/10.1149/1945-7111/ab6984>
21. Qiu, J. et al. Electrochemical study of the dissolution of oxide films grown on type 316L stainless steel in molten fluoride salt. *Corros. Sci.* 186, 109457 (2021). <https://doi.org/10.1016/j.corsci.2021.109457>
22. Wang, Y., Liu, H., Yu, G., Hou, J. & Zeng, C. Electrochemical study of the corrosion of a Ni-based alloy GH3535 in molten (Li,Na,K)F at 700 °C. *J. Fluor. Chem.* 178, 14–22 (2015). <https://doi.org/10.1016/j.jfluchem.2015.06.014>
23. Zhou, W. et al. Proton irradiation-decelerated intergranular corrosion of Ni-Cr alloys in molten salt. *Nat. Commun.* 11, 3430 (2020). <https://doi.org/10.1038/s41467-020-17244-y>
24. Liu, Y. et al. Corrosion of Cr in molten salts with different fluoroacidity in the presence of CrF₃. *Corros. Sci.* 169, 108636 (2020). <https://doi.org/10.1016/j.corsci.2020.108636>
25. Wang, Y. & Zhang, J. Electrochemical properties of CrF₂ in FLiNaK molten salt and the new analytical methods for their determination. *J. Electrochem. Soc.* 167, 086503 (2020). <https://doi.org/10.1149/1945-7111/ab8923>
26. Cramer, S. D. & Covino Jr., B. S. ASM Handbook Volume 13A: Corrosion: Fundamentals, Testing, and Protection (ASM International, 2003).
27. Massot, L. et al. Corrosion products electrochemical behaviour into molten lif-naf: investigation of Cr(II) system. *J. Electrochem. Soc.* 168, 026510 (2021). <https://doi.org/10.1149/1945-7111/abe088>
28. Pourbaix, M. Atlas of Electrochemical Equilibria in Aqueous Solutions (National Association of Corrosion Engineers, 1974).
29. Sohal, M. S. et al. Engineering Database of Liquid Salt Thermophysical and Thermochemical Properties. Technical Report Number: INL/EXT-10-18297; Idaho National Laboratory (2010).
30. Ludwig, D. et al. High temperature electrochemistry of molten fluoride salt for measurement of dissolved chromium. *Corros. Eng., Sci. Technol.* 46, 360–364 (2011). <https://doi.org/10.1179/147842209X12579401586645>
31. Elgrishi, N. et al. A practical beginner's guide to cyclic voltammetry. *J. Chem. Educ.* 95, 197–206 (2018). <https://doi.org/10.1021/acs.jchemed.7b00361>
32. Hamman, C. H. et al. *Electrochemistry*, 2nd edition. (Wiley, 2007).
33. Wang, Y. Species Chemistry and Electrochemical Separation in Molten Fluoride Salt. PhD's thesis, Virginia Polytechnic Institute and State University (2019).
34. Jain, A. et al. The materials project: a materials genome approach to accelerating materials innovation. *APL. Materials* 1, 011002 (2013).

35. Zakharova, V. V. et al. Electrochemistry of iron, nickel and chromium in LiF–NaF–KF (FLiNaK) eutectic melt: a cyclic voltammetry study. AIP Conf. Proc. 2313, 050039 (2020). <https://doi.org/10.1063/5.0032424>
36. Peng, H. et al. Electrochemical investigation of the stable chromium species in molten FLiNaK. RSC Adv. 5, 76689–76695 (2015). <https://doi.org/10.1039/C5RA09919F>
37. Zheng, G. & Sridharan, K. Corrosion of structural alloys in high-temperature molten fluoride salts for applications in molten salt reactors. JOM 70, 1535–1541 (2018). <https://doi.org/10.1007/s11837-018-2981-2>
38. Doniger, W. H. & Sridharan, K. Application of voltammetry for quantitative analysis of chromium in molten 2LiF–BeF₂ (FLiBe) salt. J. Electrochem. Soc. 838, 73–81 (2019). <https://doi.org/10.1016/j.jelechem.2019.02.048>
39. Yin, H. et al. Thermodynamic modeling of LiF–NaF–KF–CrF₃ system. J. Fluor. Chem. 209, 6–13 (2018). <https://doi.org/10.1016/j.jfluchem.2018.02.005>
40. Barin, I., Knacke, O. & Kubaschewski, O. Thermochemical Properties of Inorganic Substances (Springer Berlin Heidelberg, 1977).
41. Bieber, A. L. et al. Fluoroacidity evaluation in molten salts. Electrochim. Acta 6, 5022–5027 (2011). <https://doi.org/10.1016/j.electacta.2011.03.099>
42. Shay, N. W. Electrochemical Sensor Development for Fluoride Molten Salt Redox Control. Master's thesis, Ohio State University (2017).
43. Jones, D. A. Principles and Prevention of Corrosion (Prentice Hall, 1996).
44. Guo, S., Shay, N., Wang, Y., Zhou, W. & Zhang, J. Measurement of europium (III)/ europium (II) couple in fluoride molten salt for redox control in a molten salt reactor concept. J. Nucl. Mater. 496, 197–206 (2017). <https://doi.org/10.1016/j.jnucmat.2017.09.027>
45. Bale, C. W. et al. FactSage thermochemical software and databases—recent developments. CALPHAD 33, 295 (2009).
46. Saal, J. E. et al. Materials design and discovery with high-throughput density functional theory: the open quantum materials database (OQMD). JOM 65, 1501–1509 (2013). <https://doi.org/10.1007/s11837-013-0755-4>.
47. Kirklin, S. et al. The open quantum materials database (OQMD): assessing the accuracy of DFT formation energies. npj Comput Mater. 1, 1–15 (2015). <https://doi.org/10.1038/npjcompumats.2015.10>
48. Stevanović, V. et al. Correcting density functional theory for accurate predictions of compound enthalpies of formation: fitted elemental-phase reference energies. Phys. Rev. B 85, 115104 (2012). <https://doi.org/10.1103/PhysRevB.85.115104>

Chapter 3 Task 2: Electrochemical Corrosion Kinetics of Pure Cr in Molten LiF-NaF-KF salts

Ho Lun Chan^{1,2}, Elena Romanovskaia^{1,2}, Valentin Romanovski^{1,2}, Debashish Sur^{1,2}, Minsung Hong³, Peter Hosemann^{3,4}, John R. Scully^{1,2}

¹Department of Materials Science and Engineering, University of Virginia, Charlottesville, VA, 22904

²Center for Electrochemical Science and Engineering, University of Virginia, Charlottesville, VA, 22904

³Department of Nuclear Engineering, University of California, Berkeley, CA, 94150

⁴Materials Science Division, Lawrence Berkeley National Laboratory, Berkeley, CA, 94720, USA

Abstract

The chapter revisits the corrosion behavior of pure Cr in molten LiF-NaF-KF salts (FLiNaK) salt at 600 °C from the perspective of corrosion electrochemistry. In this work, the potential-dependent, rate-limiting charge-transfer, and salt film-mediated mass-transport controlled regimes of Cr corrosion in FLiNaK at 600 °C are investigated. The kinetic and thermodynamic parameters that limit electrodisolution and the consideration of grain orientation on these regimes are elucidated. At low Cr(III) concentrations, the corrosion process is governed by charge transfer control at low overpotentials and is crystal orientation dependent. However, when Cr(III) concentrations are high or when there is a high overpotential, the formation of a metal fluoride salt film on the Cr surface shifts the kinetic behavior to be governed by mass transport control at all anodic potentials with a surface morphology controlled by salt film deposition location and identity. Evans' diagrams were developed to consolidate and elucidate these observations. These findings were supported by an examination of the post-corrosion microstructure, X-ray diffraction of solidified salts, and thermokinetics analysis in each corrosion regime.

Introduction

Candidate molten salts, such as LiF-BeF₂ (66–34 mol%), provide multiple key advantageous properties as molten salt reactor coolant, such as chemical stability at high-temperature and upon neutron irradiation, near moisture-free, and low volatility.^{1,2} These properties are the basis for the development of nuclear reactor concepts with enhanced safety and engineering performance. Concerns over structural material corrosion led to work at Oak Ridge National Laboratory (ORNL) starting with an aircraft propulsion project at the ORNL.³ In these studies, post forensic characterizations of corrosion damage to structural components (e.g. reactor vessels, flow loops for salt transport, and heat exchanges) after exposures to various service conditions (typically radioactive, high temperature, corrosive reactor environments³) were examined.

In the past 5 years, there were a growing number of studies that compared the corrosion behavior of microstructurally and compositionally complex commercial alloys (e.g. Ni-based superalloys⁴⁻⁷ and

stainless steels^{4,7}) in molten fluoride salts. Some of these have extended from exposure studies to those utilizing electrochemical methods.^{6,8–10,73–75} Electrochemical methods provide an *in situ* and diagnostical approach to characterize the corrosion behavior of candidate materials in real-time either in the case of open-circuit (static immersion) or under polarized conditions.¹¹ For example, potentiodynamic polarization (PD) or linear sweep voltammetry (LSV) can (i) provide a straightforward approach to rank the relative stability of alloys in the molten salts over a range of potentials often representative of open circuit potentials (OCP) with oxidants,⁶ (ii) enable the determination of corrosion potential (E_{corr}) and corrosion current density (i_{corr}) for quantitative analysis,^{4–7} and (iii) identify the rate-determining steps (RDS) that controls the materials dissolution process as a function of driving force (i.e., electrode potential) at the metal/electrolyte interface. However, mechanistic insights that elucidate the electrochemical and material factors governing electrode reactions and properties of the electrode-salt interface are limited in molten salt corrosion studies. Nevertheless, the elucidation of electrochemical corrosion behavior (e.g. polarization curve measured using LSV) of structural alloys in nonaqueous, aggressive media, such as molten LiF-NaF-KF salts, is challenging since they may be impacted by a large array of factors (e.g. microstructure, impurity, potential).

An essential first step toward resolving the complexities of alloys corrosion is to understand the dissolution mechanism of their most vulnerable alloying constituent (i.e. most favorable thermodynamically to dissolve) and to describe the RDS of this process using the principles of electrochemical thermodynamics, kinetics, and materials science. In molten fluorides research, Cr is often described as a vulnerable alloying element in candidate molten salt reactor (MSR) structural alloys (such as Ni-based superalloys and stainless steels^{12,13}) due to its high thermodynamic driving force to dissolve as a Cr(II) and/or Cr(III) types species relative to other alloying elements.¹⁴ To understand the corrosion behavior of Fe–Cr, Ni–Cr, and Fe–Ni–Cr alloys, as well as Ni-based superalloys, it is essential to establish such solid foundation.

An early work by Fabre et al. carried out a series of LSV measurements on a number of pure metals (Cr, Fe, Ni, Ag, Au, Mo, W) in FLiNaK salts at 900 °C.⁶ The oxidation potential of each metal was measured against a Pt pseudo-reference electrode. Direct dissolution (i.e., activation-controlled) of pure metals to their fluoride complexes was proposed as the primary mechanism based on ~200 mV of overpotential vs OCP when anodically polarized in LSV. Wang et al.¹⁵ carried out LSV substantiated by electrochemical impedance spectroscopy (EIS) measurements on Cr, Ni, and Fe in FLiNaK at 700 °C with varying H₂O and CrF₃ concentrations. Wang et al.¹⁵ extended the anodic polarization range up to ~400 mV vs OCP and observed an anodic limiting current density on the order of 10 mA cm⁻². The ionic diffusion of Cr(III) was postulated as the reason for this rate-limiting behavior (i.e. mass-transport controlled). Recently, Doniger et al.¹⁰ performed LSV (or PD) measurements on pure Cr, Ni, Ni–Cr alloys, and others in FLiNaK salts at 700 °C.¹⁰ The authors did not observe rate-limiting mass transport control in their anodic scan (up to 300 mV overpotential with respect to the corrosion potential) and postulated that uniform corrosion was likely the

predominant oxidation mechanism and appeared to be activation controlled. This was not consistent with the polarization behavior and corrosion morphology reported by Wang et al.¹⁵ who also showed the corrosion front contained localized attack and was not uniform.

The above-mentioned discrepancy may be attributed to the difference in oxidizer concentration or experimental parameters used and will be further investigated in this work. Nevertheless, it was clear that Cr corrosion is given by a set of thermodynamic and kinetic factors and that its RDS may be a function of electrochemical potentials. For example, a lower overpotential may result in activation-controlled dissolution while the polarization behavior at a more positive potential may be mass-transport controlled. Moreover, the corrosion kinetic features and coupled morphological dependence on potential have not been interrogated in literature previously. This connection is a foundational concept necessary to describe the corrosion behavior. Recent work¹⁶ developed potential-activity diagrams (analogous to Pourbaix diagrams) to describe the electrochemical thermodynamics of Cr redox reactions in FLiNaK. These diagrams provided a map of phase stability regions of Cr, its corrosion products (such as Cr(III) in the form of CrF_6^{3-}), and included oxidants as a function of potential and ion activities, providing predominant anodic/cathodic reaction identification as a function of potential and activity. As a continuation of our recent thermodynamic study¹⁶, the objective of this work is to understand and elaborate upon the processes governing Cr dissolution across various rate-limiting potential regimes in molten FLiNaK salts at 600 °C. Various electrochemical methods including cyclic voltammetry (CV) on Pt were used to interrogate the reaction kinetic and corrosion morphological dependence of these regimes. A key outcome is to understand the origin of experimental polarization behavior/curve of Cr in molten FLiNaK salts.

Materials and Methods

Materials and electrolytes

A high-purity polycrystalline Cr rectangular plate (99.995%, supplied from Alfa Aesar) with the dimensions 20 mm × 1.5 mm × 5 mm was used. The Cr coupon was polished to 1200 grit surface finish using silicon carbide polishing papers at all faces. Electrochemical studies were carried in molten LiF-NaF-KF (46.5–11.5–42 mol%) eutectic salt at 600 °C. For salt preparation steps, LiF (99.85%, Fisher Scientific), NaF (99.99%, Fisher Scientific), KF (99.5%, Fisher Scientific) were weighed and mixed into the FLiNaK stoichiometric ratio in a nitrogen(N_2)-filled glove box (O_2 & H_2O controlled below <0.1 ppm). Additionally, 0.14 wt%, 0.28 wt%, and 1 wt% of CrF_3 (99.98%, Fisher Scientific) were introduced in the salt to investigate the effects of CrF_3 on Cr corrosion. Approximately 30 g of FLiNaK salt was used for each experiment. The salt-to-metal working electrode mass ratio was maintained at 38.6 ± 7.1 g/g for all experiments. All salts were dried in a vacuum furnace for 48 h at 100 °C. Some moisture and oxygen impurities were expected during the salt transfer process in the open air and the dissolution of Cr native passive film,⁷ respectively.

To reduce impurities pertaining to trapped moisture or oxygen, the salt mixture was heated to 600 °C for 3 h under the flow of ultra-high purity (UHP) N₂ gas (99.999%) prior to the test. Prior to each experiment, a CV analysis was performed on a Pt electrode to identify possible redox-active impurities.^{4,17,18,73}

Molten salt electrochemical cell

Figure 1 shows the electrochemical cell developed to carry out electrochemical tests in molten salts. The experiment was performed in a N₂-filled glove box. A boron nitride crucible (>99.9%, supplied from MSE Supplies LLC.) was used as the salt container. A high-surface area platinum mesh was used as a counter electrode (CE). This apparatus contained two working electrodes (WE). The first WE (WE#1) was a Cr coupon spot welded to a pure Ni wire. The welded spot was coated with boron nitride paste to avoid contact with the molten salt. The second WE (WE#2) was a 1 mm diameter Pt wire (99.997%, supplied from Alfa Aesar™). These electrodes were inserted through an alumina tube for insulation and mechanical supports. An additional Pt wire was inserted adjacent to the second WE as a Pt/PtO/O²⁻ quasi-reference electrode. A Gamry Interface 1000 potentiostat was used to perform electrochemical tests.

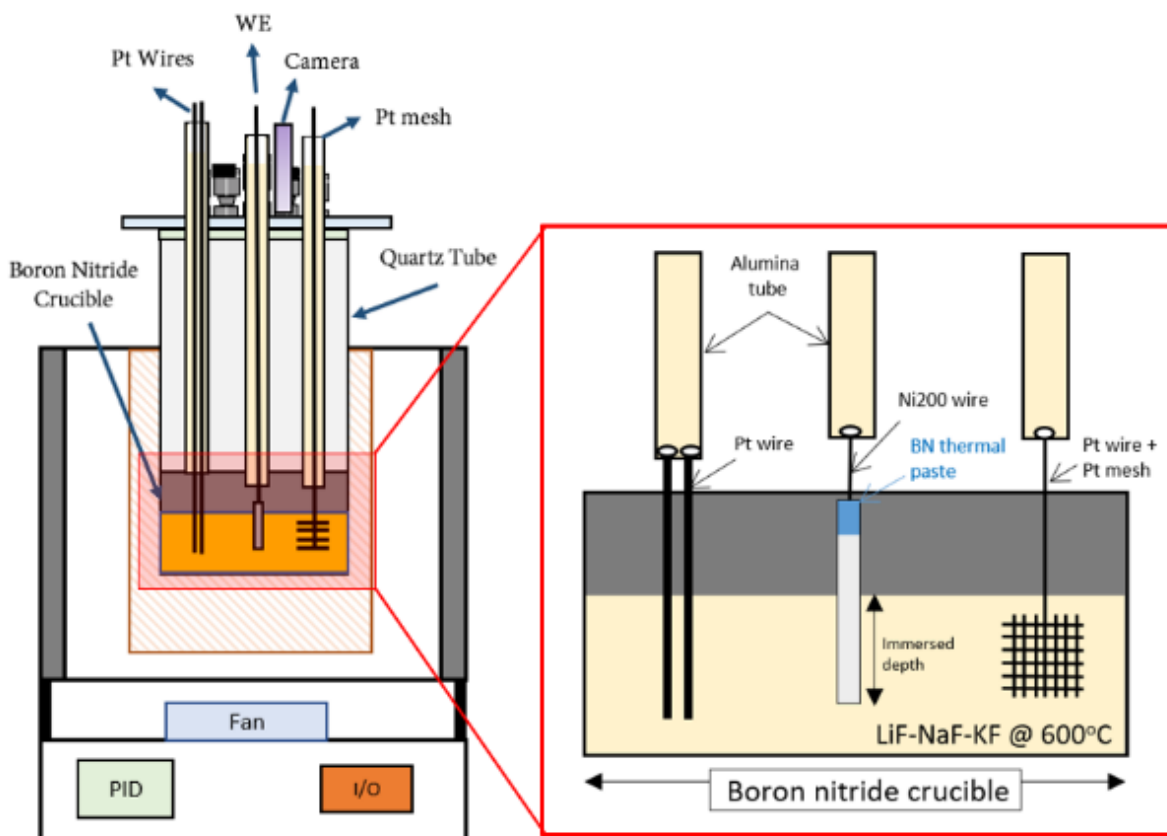


Figure 1. Schematics of molten salt electrochemical cells 5-electrodes set up

Impurity analysis using electrochemical diagnostics

Several electrochemical diagnostics techniques were performed on a Pt wire to screen for possible impurities and to detect and assay cations by their redox reactions in the molten salt. To establish a pseudo-reference potential, CV and galvanostatic hold (i.e. chronopotentiometry) techniques were employed to identify the equilibrium half-cell redox potential for potassium reduction in FLiNaK. This pseudo K⁺/K reference potential is often referred to as a dynamic reference potential and is often used to calibrate electrochemical measurements in molten salts.^{10,16,19–21} Firstly, a CV scan was performed on the Pt wire at a 100 mV s⁻¹ toward the negative/cathodic terminal until a sharp increase in cathodic current was observed. At this point, the potential was reversed to its initial starting potential. This scan was measured only once prior to the insertion and testing of Cr (WE#1). Secondly, a galvanostatic hold was performed on the Pt wire at several current densities to identify the CE potential. The cell voltage (i.e. the potential difference between the working and counter electrode) was simultaneously measured to elaborate the possible reactions occurring at the counter electrode. Lastly, square-wave voltammetry (SWV) was performed on the Pt wire to estimate the concentration of oxyanions following Shen et al. and Massot et al.^{22,23}

Molten salt corrosion electrochemical methods

A series of electrochemical techniques were performed to assess the electrochemical corrosion behavior of pure Cr in molten FLiNaK salts. The experiments are summarized as follows. It is noted that the choices of test parameters will be elaborated on in the results section.

–1 h and 50 h OCP exposure of Cr was followed by LSV scan from –0.4 V to 1 V vs. OCP at 1 mV s⁻¹ scan rate. The LSV scans were also performed at scan rates at 0.5, 2.5, and 10 mV s⁻¹.

–A successive CV scan was performed on Cr in the potential range between 0 and 30 mV vs OCP as well as between 0 and 600 mV vs OCP at a scan rate of 10 mV s⁻¹.

–Potentiostatic hold (pstat) of Cr was carried out 0.18, 1.08, and 1.80 V_{Pseudo K⁺/K} for 1 ks and 50 h. The mass of samples pre- and post-exposure was recorded.

Approach to analyze electrochemical results

The LSV curve (i.e. E-log(i) plot) was graphically and numerically analyzed to obtain certain electrochemical parameters critical to the understanding of electrode kinetics. These parameters included the Tafel slope (β), moles of electrons transferred per mole of species reactant or product (n), and charge-transfer coefficient (α).²⁴ n was determined using Faraday's Law by comparing the mass and charge consumed during the potentiostatic hold experiments. The apparent cathodic Tafel slope (β_c) constant was directly obtained from the linear fitting of the E-log(i) plot. Additional steps were used to obtain the anodic Tafel slope (β_a).

To correct for the ohmic resistance effect (i.e. iR drop), the electrolyte resistance (R_e) was measured with the high-frequency EIS technique before the polarization scan, and the measured potential was corrected using Eq. 1. The anodic current density (i_a) was then calculated using Eq. 2 since the net current density (i_{net}) consists of both the cathodic (i_c) and anodic (i_a) current contributions. The anodic regime of Cr in FLiNaK at 600 °C also exhibited an anodic limiting current density (i_L), which was corrected using Eq. 3. Upon performing these corrections, β_a was obtained through linear regressions of E- i_a data in the true anodic regions.²⁴ The α for this regime could then be subsequently calculated using equation when $2.303RT/F$ is Eq. 4.

$$V_{true} = V_{mea} - i_{net}R_e \quad (1)$$

$$i_{net}(E_{app}) = i_a - |i_c| \quad (2)$$

Here i_{true} is the true anodic current density given i_a describes the anodic charge transferred controlled current density while i_L describes the anodic mass transport current density.

$$\frac{1}{i_{true}} = \frac{1}{i_a} + \frac{1}{i_L} \quad (3)$$

$$\beta_a = \frac{2.303RT}{nF\alpha} \quad (4)$$

Post-exposure characterization: XRD, SEM, EBSD

The phase composition of the remaining salt was analyzed employing X-ray Diffraction (XRD) technique using the Malvern-Panalytical Empyrean diffractometer [wavelength Cu $K\alpha$ (1.5405 Å)]. The PDF4+ database was used as the reference data. The software HighScore Plus was used for Rietveld refinements. The peak profile was refined by the pseudo-Voigt function. It is worth noting the XRD results obtained from residual salts may not be indicative of the exact molecular structure of species present in the molten state, as rapid cooling can potentially cause phase transformations upon solidification and thereafter.²⁵ Nonetheless, analyzing these results can offer insight into the oxidation state of Cr species and molecular identities based on their corresponding compounds.

To analyze the post-corrosion morphology of test coupons, scanning electron microscopy (SEM) coupled with elemental analysis via energy dispersive spectroscopy (EDS) (Thermo Phenom XLG2 SEM) was utilized. Additionally, electron backscatter diffraction (EBSD) (Scios 2, FEG, Thermo Fischer) was performed to indicate the position of grain boundaries and to analyze the relationship between crystallographic orientation and corrosion morphology. The specimen was polished to 0.05 μm using Al₂O₃ suspension and sonicated in ethanol for 10 min. For EBSD characterization, the sample was mounted on

45° of pre-tilted holder and totally tilted to 70° holder. A 20 kV of acceleration voltage was selected while and the vacuum pressure was maintained below 1×10^{-5} torr. EBSD analysis with a step size of $0.5 \mu\text{m}$ was conducted in the $50 \times 8 \mu\text{m}^2$ analyzed area. The AztecCrystal S/W (Aztec, Oxford Instruments, High Wycombe, UK) was used to analyze and refine the data.

Results

Diagnostics of FLiNaK salts using electrochemical methods

Figure 2 shows the cyclic voltammogram of Pt wire in molten FLiNaK salts at 600°C . The equilibrium potential for K^+ reduction⁵ could be approximated at the mid-point between the rapid increase in cathodic current densities from $-1.0 \text{ V}_{\text{Pt}}$ to $-1.3 \text{ V}_{\text{Pt}}$ (due to the reduction of K^+) and an anodic peak seen at $\sim -1.1 \text{ V}_{\text{Pt}}$ (attributing to the oxidation of electro-reduced K). The K^+/K reduction/oxidation potential value was found to be $-1.2 \text{ V}_{\text{Pt}}$ with a current density of -37 mA cm^{-2} .

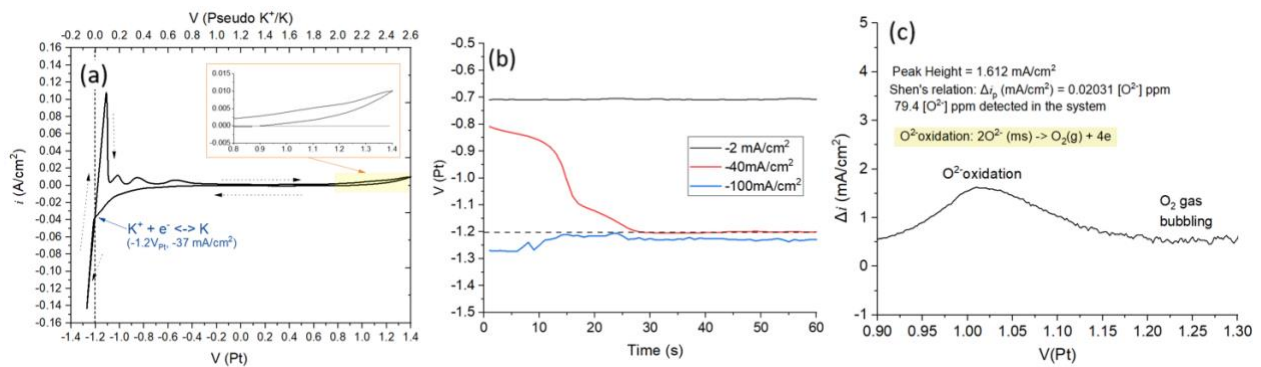
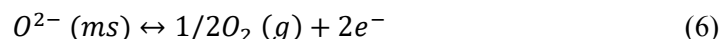


Figure 2. Electrochemical diagnostics of the FLiNaK molten salt at 600°C using a Pt wire. (a) Cyclic voltammogram, (b) potential-time relationship during the 60 s galvanostatic hold of Pt wire at -2 , -40 , and -100 mA cm^{-2} , and (c) square wave voltammogram.

The FLiNaK salts did not exhibit additional current peaks between -0.8 and $+1.4 \text{ V}_{\text{Pt}}$. This suggests the absence of a significant amount of oxidizing and/or reducing species electrochemically active over the potential range where $\text{Cr}/\text{Cr(II)}$ and $\text{Cr(II)}/\text{Cr(III)}$ will be studied.¹⁶ The K^+/K potential value can also be obtained by applying a sufficient cathodic current density via a galvanostatic hold technique as shown in the potential-time relationship in Figure 2b. In the result shown, a minimum of -40 mA cm^{-2} rapidly shifted the electrode potential negative to reach a steady potential of $\sim -1.2 \text{ V}_{\text{Pt}}$ in 20 s consistent with the CV. An increase in the applied cathodic current density caused a faster shift but did not appear to significantly shift the final potential value, only creating a $\sim 10 \text{ mV}$ shift. This potential herein is referred to as a pseudo K^+/K potential. Based on our prior work, the K^+/K potential was estimated to be $-4.68 \text{ V}_{\text{F2/F}^-}$ based on available thermodynamic data¹⁶.

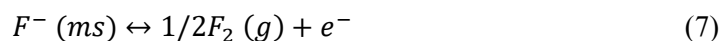


Furthermore, SWV was performed to estimate the oxyanions concentration in the molten FLiNaK salts as shown in Figure 2c. The voltammogram displayed a peak attributed to the oxidation of oxyanions via reaction (6) at +1.025 V_{Pt} followed by small differential-current fluctuations characterized as oxygen gas bubbling.^{22,23,26} Using the linear correlation established by Shen et al.²³ for the exact same salt composition and temperature, the oxyanions concentration was estimated to be 79.4 ppm. Reaction (6) is an irreversible reaction and O₂ gas generated could quickly escape from the corrosion cell to the glove box environment. Therefore, the CV curve in Figure 2a could not quantify the reaction (6) despite some anodic current densities could be found between +1.0 and +1.4 V_{Pt}, which was consistent with Massot's earlier observation.²²

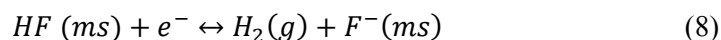


The alkali metal cations and environmental impurities, such as Li⁺, Na⁺, K⁺, HF, and O²⁻, provide a half-cell reaction at the CE which was theoretically limited by their concentration but practically infinite compared to the Cr dissolved electrochemically in this study. An upward polarization scan on Cr may require 100 C cm⁻² which can be accommodated by alkali metal cation reduction at the CE as seen in 2b. To verify this concept, the Pt WE#2 electrode was subjected to a galvanostatic hold at either -40 mA cm⁻² (cathodic) or +40 mA cm⁻² (anodic) up to 130 s while the cell voltage (i.e., the potential difference between the working and counter electrode) was measured.

Figure 3 shows the cell voltage and potential measured at the working and counter electrodes. At +40 mA cm⁻², the WE#2 potential situated between +2.0 and +2.3 V_{Pt} (i.e. +3.2 and +3.5 V_{K+/K}) for the first 70 s, which may be attributed to the oxidation of O₂ and/or the Pt wire. F₂ gas evolution via reaction (7) was not likely since a potential of +4.681 V_{K+/K} was required.



The CE potential initially started at -0.6 V_{Pt} and gradually declined to a steady potential of -1.2 V_{Pt} after 70 s. The reduction of HF (formed by moisture) via reaction (8) may occur over this potential range.



If the cathodic currents in the first 70 s were attributed to HF reduction, then 19.3 ppm of HF would be consumed using Faraday's Law⁹:

$$m = \frac{itM}{nF} \quad (9)$$

where i is current density in A/cm^2 , t is time, M is molar mass in g/mol , F is the Faraday constant of 96500 C mol^{-1} . Between 70 and 130 s, K^+ reduction was possible and 0.0248 mmol of K^+ ions would have been reduced on CE, which is insignificant relative to the concentration of K^+ in FLiNaK (i.e. 304.5 mmol). Fig 3b shows the potential-time relationship on both the WE#2 and CE electrodes, where the WE#2 electrode was polarized under a constant current of $-40 \text{ mA}\cdot\text{cm}^{-2}$ for 65 s. The potential of the WE#2 electrode fluctuated around $-1.2 \text{ V}_{\text{Pt}}$, which again may be related to K^+ reduction. The potential of the CE electrode initially started at $-0.5 \text{ V}_{\text{Pt}}$ and stabilized between $+1$ and $+1.5 \text{ V}_{\text{Pt}}$ for approximately 55 s, indicating a potential range where O_2 evolution could occur.

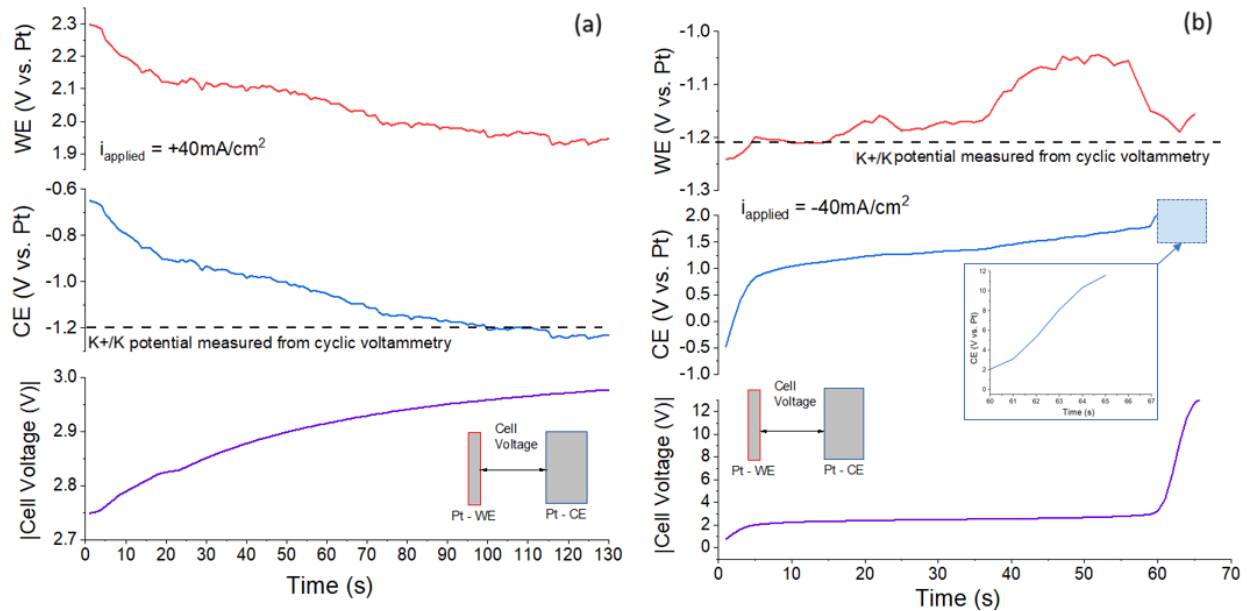


Figure 3. Potential-time relationship of Pt wire working electrode (red curve), Pt mesh counter electrode (blue curve), and cell voltage (purple) galvanostatically held at (a) 40 and (b) $-40 \text{ mA}/\text{cm}^2$

Using Faraday Law 9, 7.73 ppm of O^{2-} would be consumed by O_2 evolution for this period of charge accumulation. After 60 s, a rapid increase in CE potential and cell voltage was observed. This may be attributed to the exhaustion of available impurity-related redox agents (e.g. O^{2-}), which facilitate the oxidation of 2F^- to F_2 gas via reaction (7) and caused the shift in CE potential. Production and stagnation of gas bubbles on the CE electrode surface could block current flow in the ionic circuit, raising the cell voltage beyond the potentiostat specification.

This result demonstrates that electrochemistry experiments may lead to the oxidation of O^{2-} anions that shift the quasi Pt/PtOx/ O^{2-} reference potential. This shifting effect may be significant depending on the

experimental control of test environments. In this work, the LSV (Figure S1a) and select potentiostatic hold experiments on Cr metals can result in a reference potential shift of approximately 100 mV. This K+/K potential value shift is not significant for Cr statically immersed in FLiNaK for 50 h. Despite this behavior, this shift does not impact the interpretation of the Cr corrosion behavior addressed in this work as our discussion focuses on the anodic polarization of Cr (WE), where the ionic current flow at the CE is supported by K^+ reduction rather than oxygen (Figure 3). For future studies, it is essential to ensure enough oxidizing and reducing species (e.g. by introducing a buffering agent) in the salt.

Identifying the rate-controlling kinetic regimes of Cr corrosion in FLiNaK

Figure 4 shows the as-measured anodic LSV curve, the linear fittings, and after each step of correction using Eqs. (1) through (4). The inset shows the region that was fitted with linear regression to approximate the Tafel slopes, which are shown in Table 1.

Table 1. Electrochemical kinetic parameters obtained from graphical analysis of LSV scans of Cr in FLiNaK salts at 600 °C with various wt% addition of CrF_3

CrF ₃ wt%	OCP		β_a	β_c	$i_{0,a}$	$i_{0,c}$	α_a	n
	V_p KF/K	V_p F ₂ /F						
0	0.977	-3.704	54.2	-974	0.304	0.110	1.38	2.39
0.14	1.103	-3.578	57.3	-676	0.468	0.176	1.31	2.33
0.28	1.341	-3.340	67.2	-425	0.197	0.147	0.934	2.46
1	1.412	-3.269	64.1	-321	0.431	0.060	1.174	2.33

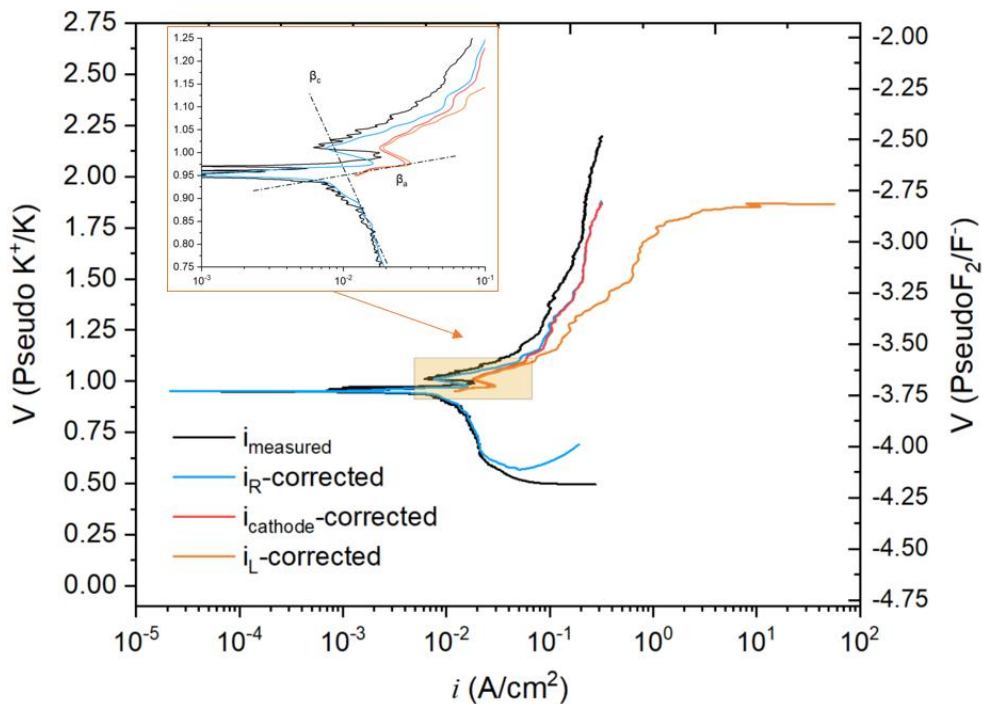


Figure 4. Linear sweep voltammogram of Cr in FLiNaK at 600 °C corrected with solution resistance, cathodic current density, and limiting current density

After correction, the E-log(i) behavior of Cr in FLiNaK, 600 °C is displayed in the polarization curve shown in Figure 5a, which is represented by two different reference potential scales. Portions of the polarization plot were shaded with different colors to indicate the potential regimes in which Cr, Cr(II), and Cr(III), possibly in the forms of Cr^0 , CrF_3^- , CrF_6^{3-} species, were predicted to be thermodynamically stable.¹⁶ It was noted that the Cr(II) and Cr(III) oxidation states were referred to as the CrF_3^- and CrF_6^{3-} compounds for the following reasons: (i) Molecular dynamic simulation demonstrated that Cr metallic cation has the tendency to be solvated with F^- ions;²⁷ (ii) Simulation has yet to be performed in FLiNaK salts at 600°C. The CrF_3^- and CrF_6^{3-} species were first selected because there are existing thermodynamic and kinetic data available for these complexes.^{16,25,28–30} Both were proposed as possible fluoride-solvated species^{16,25,28,29}; (iii) While other solvated complexes, such as CrF_4^{2-} and CrF_5^{2-} are possible, they do not constitute a significant shift in the redox potential for Cr/Cr(II), Cr (III) /Cr(II), and Cr/Cr(III).¹⁶

The LSV polarization curve in Figure 5a displays three kinetic regimes with differing E-log(i) behavior that are potential dependent. The curve was highlighted with a different color to indicate these kinetic regimes. From +0.56 $V_{\text{pseudo K+/K}}$ to OCP of +0.92 $V_{\text{pseudo K+/K}}$, the measured negative current density was attributed to cathodic reactions on the Cr surface. The origin of these oxidants may be attributed to commercial metallic cation impurities,³¹ environmental impurities (e.g. HF, H₂O, O₂), reduction of the remnant native passive film, and cations released by corrosion that took place during the first hour of OCP measurement. Between +0.92 and +1 $V_{\text{pseudo K+/K}}$, Cr was anodically polarized within a regime where *i* is exponentially dependent on applied potential suggesting a charge-transfer controlled behavior (CT regime). The dissolution of Cr may be interfacially controlled limited by the kinetics of Cr oxidation (i.e. charge transfer at the metal-salt interface). The E-log(i) behavior up to a current peak potential (denoted E_{peak}) was also fit using the Butler-Volmer equation (after *i*R and limiting current density corrections) to interpret the Cr electrode kinetics behavior in the later sections.

Moreover, E_{peak} was observed near +1 $V_{\text{pseudo K+/K}}$ which may be a result of Cr metal ions accumulating and supersaturating the surface with Cr-F-K salt.⁵ Beyond the saturation peak, it was shown that the anodic polarization curve lies within the stability field of Cr (III) and gradually transitioned to a region where *i* is relatively independent of potential, suggesting anodic mass transport controlled dissolution behavior (MT regime). Oxide-based passivation was not likely in FLiNaK salts.⁷ Instead, the E-*i* behavior resembled the behavior of salt film precipitation on a corroding metal surface as seen in some aqueous corrosion studies (e.g., chloride salt films on Ni-Cr alloy and stainless steel surfaces^{32–36}). The formation of a salt film on the Cr corroding surface may also occur in this case especially due to the low solubility limit of CrF₃ in FLiNaK salts (0.3 wt. % or $5.51 \times 10^{-2} \text{ mol l}^{-1}$ calculated by Yin et al.^{28,37}). This was a post mortem observation in our static immersion experiments (See Figure 18) and will be discussed later. This type of anodic mass-transport controlled polarization was also observed in the LSV scans of Cr in FLiNaK at 700 °C reported

by Wang et al.¹⁵ The authors stated that the origin of mass-transport was attributed to the ionic diffusion of Cr(III) species but did not mention the role of salt film.

Oxidation states for Cr dissolution

Figure 5 shows the potential range over which Cr, Cr(II), and Cr(III) may be thermodynamically stable.¹⁶ The dashed lines indicate the Nernst potentials for selected possible half-cell redox reactions, including reactions $\text{CrF}_3^- (\text{Cr(II)})/\text{Cr}$ (10), $\text{CrF}_6^{3-} (\text{Cr(III)})/\text{Cr}$ (11), $\text{CrF}_6^{3-} ((\text{Cr(III)})/\text{CrF}_3^- (\text{Cr(II)})$ (12), and HF/H_2 (13). Except for HF and $\text{KF}(\text{K}^+)$, the ion activities were assumed to be 10^{-3} M which corresponds to roughly 54.5 ppm of CrF_3 . Based on the literature that utilized the ICP-MS or ICP-OES technique to identify metallic cation impurities in FLiNaK, it was expected that a commercial salt mixture may contain between 10 and 60 ppm of Cr ions along with Fe, Ni, Rh etc.^{31,38-41} This validates the ionic activity assumption.

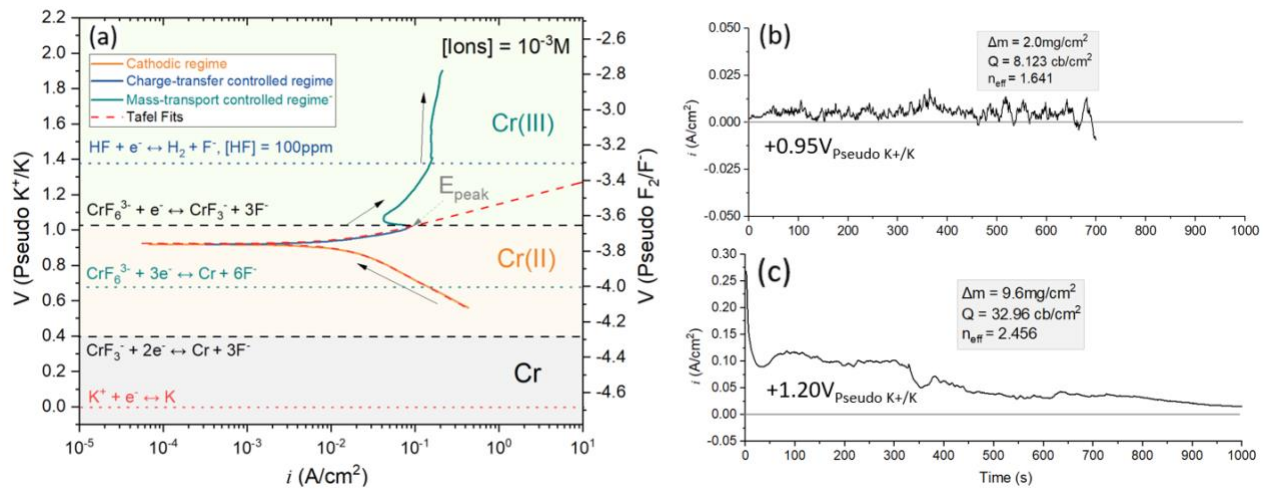
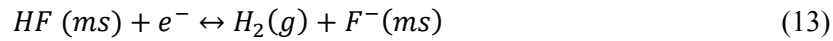
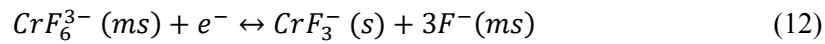
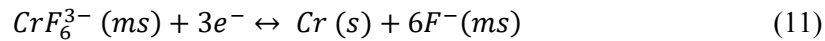
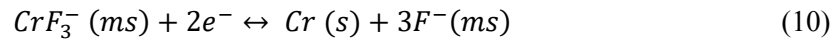


Figure 5. (a) Linear sweep voltammogram of Cr in FLiNaK at 600 °C measured at a scan rate of 1 mV/s. The E-log(*i*) curve was colored to distinct the cathodic, charge-transfer, and mass-transport regimes. The plot was shaded with colors to show the field of thermodynamic stability of Cr, CrF_3^- , and CrF_6^{3-} species as a function of potential (dashed line shows the phase boundary). The green and blue dotted lines show the half-cell redox potential for HF/H_2 and $\text{Cr(III)}/\text{Cr}$ reduction, respectively. The activities of Cr(II) and Cr(III) were assumed to be 10^{-3} M; F^- to be 49.3 M; HF to be 100 ppm. (b) and (c) shows the current-time relationship of Cr potentiostatically polarized at 0.95 and 1.20 V_{Pseudo K+/K} for 700 s and 1000 s, respectively

The Nernst potential of Cr(II)/Cr is more negative than that of Cr(III)/Cr, implying that Cr may be more thermodynamically favorable dissolve first to Cr(II) via reaction (10), then possibly be oxidized to Cr(III) via reaction (12).¹⁶ Moreover, the possibility that Cr is dissolving directly into Cr(III) via reaction (11) cannot be considered fully because the activation barriers for reactions (10) and (11) are not known. They are a function of the molecular structure and bonding thermodynamics associated with forming these solvated chromium fluoride species. Nevertheless, to verify the hypotheses regarding the charge state, Cr was potentiostatically held at +0.95 V_{pseudo K+/K} for 700 s (Figure 5b) and +1.20 V_{pseudo K+/K} for 1000 s (Figure 5c), corresponding to polarization in the Cr(II) and Cr(III) stability fields, respectively. The mass loss and total charge consumed per unit area were recorded, which was used to calculate n using Faraday's Law⁹.

Noting that the potentiostatic hold duration was selected to ensure that currents remained net positive (anodic) and no reduction reaction could take place. The n values for potentiostatic hold at +0.95 and +1.20 V_{pseudo K+/K} were 1.64 and 2.46, respectively. These values support not only the thermodynamic phase stability maps (based on the n transferred for corrosion in each regime) but also imply that the total anodic reaction may involve some combination of half-cell reactions (10) and (12). While literature have demonstrated that Cr(III) is more favorable in molten fluorides, electrochemical studies of FLiNaK salts containing CrF₂ or CrF₃ species on a Pt wire have shown that 88–92% of Cr(II) can be oxidized to Cr(III)^{16,17,29,42–45} with some Cr(II) remain when a sufficient driving force is present, either controlled by applied potential or varying the concentration of oxidizers.

Validation of rate-controlling kinetic regimes

To verify and interrogate the CT and MT-controlled regimes of Cr dissolution, cyclic voltammetry was performed on Cr over a selective range of potentials ($\Delta\eta$) with a scan rate of 10 mV s⁻¹ (in comparison to 1 mV s⁻¹ shown in Figure 5). Cr was cycled between 0 and 30 mV vs OCP (Figure 6a) and between 0 and 600 mV vs OCP (Figure 6b), corresponding to the CT and MT-controlled regimes, respectively. In Figure 6c, the E- i behavior showed linear i - ΔE relationship during both forward and backward scans, implying a CT-controlled polarization where $i_{\text{anodic}} \propto \exp(\Delta\eta/\beta)$ when Cr(III) and Cr(II) concentrations are low and constant.⁴⁶ Theoretically, the low overpotential range that gives rise to the E- i linearity is likely to occur defined by Eq. 14:^{47,48}

$$\frac{\Delta\eta}{\beta_a} < 0.1 \quad (14)$$

where $\Delta\eta = E - \text{OCP}$ is the overpotential. The β_a constant was estimated to be 54.3 mV decade⁻¹ in this work (Table I) after iR correction.⁴⁹ The linear overpotential range based on low-field approximation was only about ~5.4 mV before a deviation from linearity. The experimental E- i curve deviated from the theoretical linear relationship (i.e., Tafel fits from Figure 5a) at about ~10 mV vs OCP as depicted in Figure 6c.

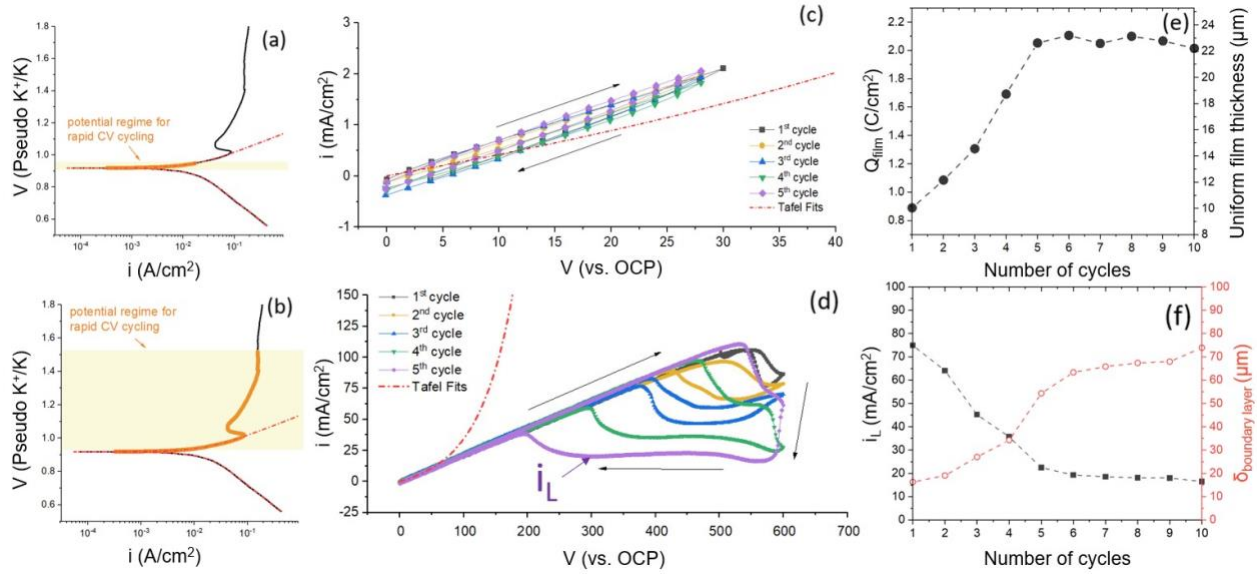


Figure 6. The potential range for rapid CV sweeping was highlighted in (a) and (b), representing a charge-transfer (0 and 30 mV vs. OCP) and a mixed charge-transfer, and mass-transport regimes (0 and 600 mV relative to OCP), respectively. Cr oxidation kinetic regimes are shown in the cyclic voltammograms in (c) and (d) recorded with a scan rate of 10 mV/s. (e) shows the uniform thickness of K_3CrF_6 salt film formed from the cycling in (b) using Faraday's Law and (f) shows the boundary layer thickness calculated using limiting current densities measured in (d)

Fig 6d shows the CV profile cycled between 0 and 600 mV vs OCP within the proposed MT-controlled regime. The E-i behavior deviates significantly from the CT-controlled low-field approximation at ~ 30 mV vs OCP. Continuous cycling results in a potential independent E-i region appearing after an upward linear E-i regime, which is likely controlled by charge transfer control with the ohmic resistance. The suggestion is that the salt film first formed at the current apex and then behavior on the downward scan was also MT controlled until the salt film dissolved. A hysteresis was observed similar to the behavior seen in metal pits under salt films and experiencing MT-controlled dissolution.^{50,51} The increasing difference between the forward and backward scan currents can be attributed to the formation and thickening of a salt film. Although up to 10 cycles were performed, the E-i curve remained identical after the 5th cycle, indicating the sluggish dissolution of the salt film.

The maximum salt film thickness formed during the successive CV scan can be approximated by calculating the total charge consumed during the CV scan using Eq. 15:^{52,53}

$$Q_{film} = \int_{t_1}^{t_2} i dt \quad (15)$$

where Q_{film} is the charge in C/cm^2 and i is the measured current density in A/cm^2 . Q_{film} can be used to approximate the mass and thickness of an assumed K_3CrF_6 salt film formed using Faraday's law (Eqs. 9 and

16) assuming that K^+ and F^- remain unchanged in valence state. It is also postulated that all Cr(III) produced from Cr dissolution will chemically convert to the salt film upon reaching the current apex:

$$h = \frac{Q_{film} M}{nF\rho} \quad (16)$$

where M represents the molar mass of K_3CrF_6 , which is $283.28 \text{ g mol}^{-1}$. The value of n was assumed to be 2.5 based on Figure 5c, and ρ denotes the theoretical density of cubic K_3CrF_6 at $600 \text{ }^\circ\text{C}$, found to be 2.66 g cm^{-3} .^{30,54} Fig 6e shows the calculated Q and h for each cycle, as an upper bound and it demonstrates that the salt film thickness stabilized upon the 5th cycle at $23 \text{ }\mu\text{m}$ assuming a uniform layer. This thickness value varied depending on the scan rate and range of the potential excursion.

During the backward scan, an i_L regulated by the salt film was observed over the MT-controlled regime indicated by the purple arrow in Figure 6d. The boundary layer thickness ($\delta_{\text{boundary layer}}$) was calculated using Eq. 17⁵⁵ to better understand the length scale pertinent to ionic transport in molten FLiNaK salts.

$$\delta_{\text{boundary layer}} = nFD \frac{C_{\text{sat}} - C_{\text{bulk}}}{i_L} \quad (17)$$

C_{sat} is a saturated concentration of Cr(III) (assumed to be $5.06 \cdot 10^{-2} \text{ mmol} \cdot \text{cm}^{-3}$ from prior calculation¹⁶); C_{bulk} is a bulk concentration of Cr(III) assumed to be 0; n is assumed to be 2.5; D is the diffusivity of Cr(III) in FLiNaK estimated to be $10^{-5} \text{ cm}^2 \text{ s}^{-1}$.²⁹ As the cycling proceeds, the i_L dropped from 74.9 to 16.5 mA cm^{-2} with the $\delta_{\text{boundary layer}}$ increases from 16.3 to $73.9 \text{ }\mu\text{m}$, which are large compared to typically expected values in aqueous corrosion studies.^{33,35} Nevertheless, Figure 6 validates the presence of assigning CT and salt film-regulated MT-controlled regimes to describe the Cr polarization behavior in FLiNaK salts.

Effects of CrF_3 on Corrosion Behavior

It has been suggested that the addition of the CrF_3 compound may promote further oxidation of Cr metal and its alloys in FLiNaK salts.^{5,15,56-60} Fig 7 shows the LSV plot of Cr in FLiNaK at 600°C with additions of 0.14 wt%, 0.28 wt%, and 1.00 wt% of CrF_3 salts relative to the initial mass of salt melted.

Table 2. True anodic current density of Cr in FLiNaK salts at $600 \text{ }^\circ\text{C}$ recorded between 1 and 10 mV relative to E_{oc} at various wt% addition of CrF_3

wt.% CrF_3	$[CrF_3^-]$, M	i_{anodic} (A/cm^2)					
		1 mV _{oc}	2 mV _{oc}	3 mV _{oc}	4 mV _{oc}	5 mV _{oc}	10 mV _{oc}
0	$1.0 \cdot 10^{-3}$	$1.3 \cdot 10^{-2}$	$1.3 \cdot 10^{-2}$	$1.3 \cdot 10^{-2}$	$1.4 \cdot 10^{-2}$	$1.4 \cdot 10^{-2}$	$1.5 \cdot 10^{-2}$
0.14	$2.1 \cdot 10^{-3}$	$3.5 \cdot 10^{-2}$	$3.7 \cdot 10^{-2}$	$4.0 \cdot 10^{-2}$	$4.6 \cdot 10^{-2}$	$4.8 \cdot 10^{-2}$	$6.6 \cdot 10^{-2}$
0.28	$4.3 \cdot 10^{-3}$	$8.4 \cdot 10^{-2}$	$8.4 \cdot 10^{-2}$	$9.0 \cdot 10^{-2}$	$9.7 \cdot 10^{-2}$	$1.1 \cdot 10^{-1}$	$1.2 \cdot 10^{-1}$
1.00	$1.5 \cdot 10^{-2}$	$1.1 \cdot 10^{-1}$	$1.2 \cdot 10^{-1}$	$1.3 \cdot 10^{-1}$	$1.4 \cdot 10^{-1}$	$1.4 \cdot 10^{-1}$	$1.8 \cdot 10^{-1}$
Slope		0.435	0.446	0.453	0.460	0.487	0.488
R^2		0.942	0.947	0.962	0.964	0.988	0.989

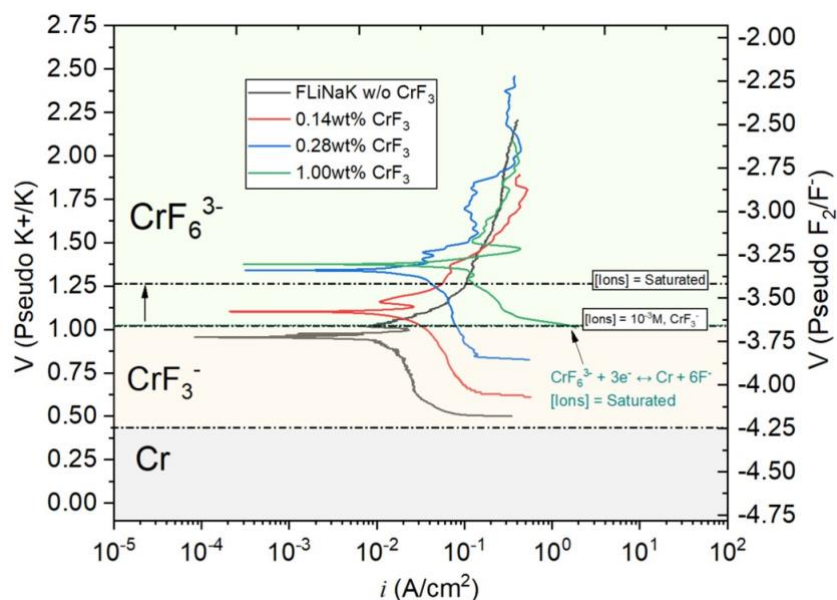


Figure 7. Linear sweep voltammogram of Cr in FLiNaK salts at 600 °C with the additions of 0.14 wt%, 0.28 wt%, and 1.00 wt% of CrF₃ recorded at a 0.5 mV/s scan rate

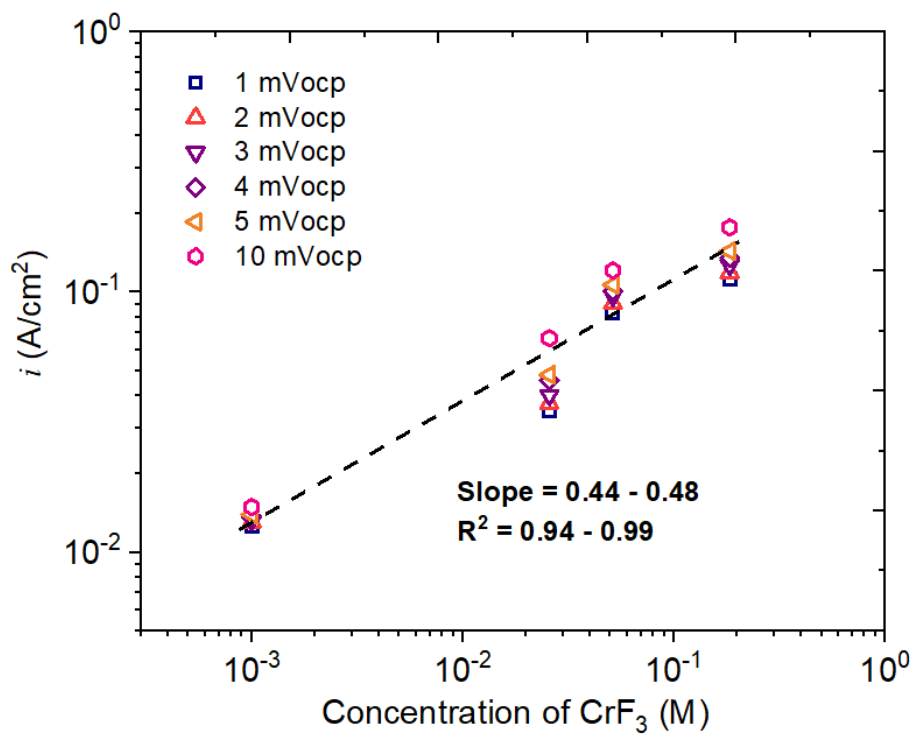


Figure 8. Relationship between true anodic current densities and CrF₃ concentration

The result indicates that the OCP value was shifted toward a more positive and noble value, increasing from approximately +0.977 to +1.412 V_{pseudo K+/K} as more CrF₃ was introduced into the salt. All anodic curves display a CT controlled regime coupled with a saturation peak, but not all exhibit a stable i_L , especially for 0.14 wt% and 0.28 wt% CrF₃ additions. The i_L also did not exhibit an expected linear relationship with the amount of CrF₃ added based on Eq. 17. Cr(III) may be reduced to Cr (II) during the cathodic scan at a scan rate of 0.5 mV s⁻¹. The cathodic potential scan range falls within the stability range of Cr (II). Thus, adding more CrF₃ introduces another cathodic reaction that increases the cathodic current densities and modifies the kinetics of the cathodic reaction. Similar effects can be expected from the initial dissolution of the air-formed Cr₂O₃ oxide ($\rho = 5.22 \text{ g cm}^{-3}$) which typically has a thickness of about 1–3 nm. In this case, the contribution of Cr(III) is negligible.

Electrodes kinetics of cathodic and anodic reactions

The results of electrochemical parameters, such as corrosion current, Tafel slopes, and the concentration of chromium fluorides, are shown in Table I. The addition of CrF₃ did not significantly modify the β_a values which were between 50 and 70 mV decade⁻¹. This is in agreement with the β_a values reported by Wang et al. who performed a similar series of LSV experiments on pure Cr with controlled concentrations of H₂O and CrF₃ in FLiNaK at 700 °C.¹⁵ Moreover, a recent work by Doniger et al. also carried out LSV measurements on pure Cr, Ni, and Ni-Cr alloys in FLiNaK at 700 °C.¹⁰ The authors reported β_a values of Cr at about 12.9 mV decade⁻¹ but their reported E-log(i) curve indicated otherwise (based on linear fitting of their data, the β_a values of Cr should be close to 92 mV decade⁻¹).¹⁰ Additionally, the n determined was between 2 and 3 for all four cases with an α coefficient slightly higher than 1, suggesting that the oxidation from Cr to Cr(III) may be a multi-step reaction.⁴⁸

Without CrF₃, the β_c value was fitted to be -974 mV decade⁻¹, which is considerably higher than β_a . A high β_c value indicates that the oxidizer (assumed to be predominantly HF) was also limited by mass-transport.^{15,61} This value has been shown to decrease to -378 mV decade⁻¹ in highly purified FLiNaK salts.¹⁰ With the increasing amount of CrF₃, the β_c value was observed to decrease to -676 mV decade⁻¹ at 0.14 wt.% CrF₃, -597 mV decade⁻¹ at 0.28 wt.% CrF₃, and further decrease to -321 mV decade⁻¹ at 1.00 wt.% CrF₃. This suggests that the cathodic reactions involving Cr(III)/Cr(II) contributed to the cathodic scans, in addition to mixed or mass transport limited HF/H₂.

Moreover, it is also possible to estimate the reaction order (ρ) of the anodic electro-dissolution of Cr to Cr(III) reaction. This analysis was carried out with respect to the concentration of CrF₃ using Eq. (18) on the true anodic current densities recorded at identical overpotential.⁴⁸ The current densities within first 10 mV vs. E_{oc} were used since the E-i relationship was linear and avoiding Cr surface saturation (Table II). Fig 8 displays a linear relationship with a slope between 0.44 – 0.48 with CrF₃⁻, corresponding to an overall

reaction order. Although this work proposed that the dissolution of Cr in FLiNaK may proceed via 2-step reactions involving the oxidation from Cr(0) to Cr(II) followed by Cr(II) to Cr(III), Cr(II) carrying a +2 oxidation state is not regarded as stable unless an externally applied potential is present.¹⁶ XRD evidence also suggested the addition of CrF₂ to FLiNaK results in the formation of crystalline KCrF₃ and K₃CrF₆ in as-solidified salts.²⁹

$$\rho = \left(\frac{\log(i)}{\log(C)} \right)_{E,T,P} \quad (18)$$

Effects of scan rate on the potentiodynamic polarization behavior

Figure 9a shows the LSV polarization curve at scan rate (ν) between 0.5 and 10 mV/s and shows a similar polarization behavior with that shown in Fig 5a; however, at 10 mV/s, the i_L is not clearly distinct. Two saturation peaks were detected at 1.1 and 1.65 V_{pseudo K+/K} with the second peak exhibiting an order of magnitude higher in peak current density. This was followed by a rapid drop in current density (defined as i_L) for about 250 mV. The fast scan rate freezes the surface chemistry, limiting ionic diffusion of CrF₆³⁻ species and possibly the stabilization of the salt film⁶², contributing the current instability in the anodic polarization regime. A slower scan rate may mitigate this effect.

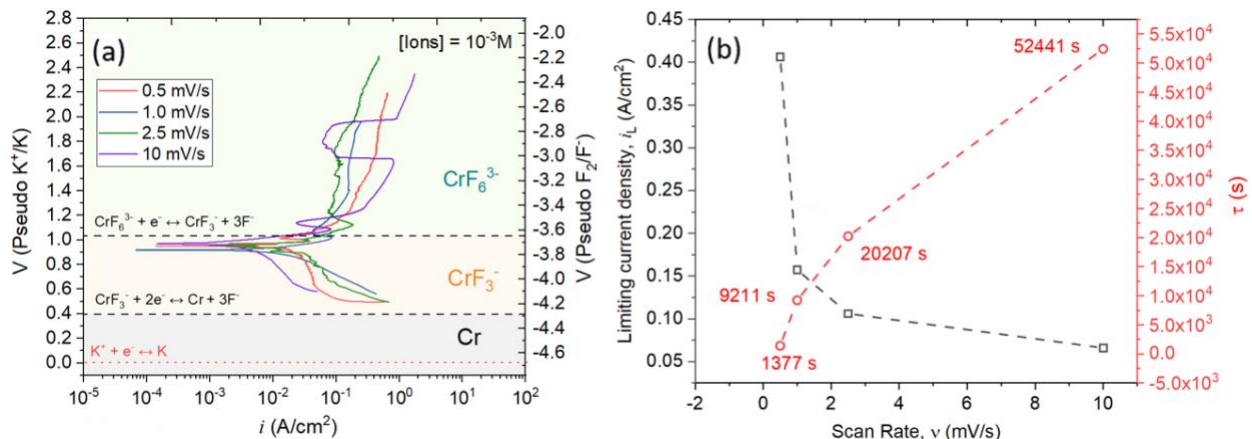


Figure 9. (a) shows the linear sweep voltammogram measured at scan rates of 0.5, 1.0, 2.5, and 10 mV/s. (b) shows the anodic limiting current densities and transition time for salt film formation calculated using the Sand Equation.

It is challenging to use Eq. (17) to qualitatively describe i_L since molten salts were unstirred and electrolyte movements were dictated by natural convection (i.e. with attendant uncertainty in boundary layer thickness) and the surface concentration at oversaturated conditions was unknown. Nevertheless, these experimental conditions enable the use of Sand Equation, or Eq. (19), to

analytically approximate the transition time required for CrF_6^{3-} concentration to reach saturation C_{sat} (be 5.06 mmol/cm^3) at the electrode surface (i.e., limiting current condition)⁵³, and is used to predict the time required to form a stable salt film:

$$i_L \tau^{1/2} = \frac{nFAD^{1/2}\pi^{1/2}C_{\text{sat}}}{2} \quad (19)$$

where τ is the transition time in sec. Fig 9b also displays the calculated transition time (τ) based on the i_L obtained in the LSV curve at each scan rate. At 0.5 mV/s , 1377 s was predicted as the onset for limiting current conditions. τ was shown to increase significantly with v and could reach up to $52,441 \text{ s}$ at 10 mV/s . Thus, the scan over the potential range of interest could occur before salt film formation. In general, a higher scan rate can lead to a higher non-faradaic current from double layer charging⁴⁷, freezing the surface structure and chemistry^{47,63}, and contribute to errors in determining Tafel slopes^{47,63}. The charging current for interfacial capacitance (C_{dl}) was neglected in our analysis since the experimental C_{dl} in molten fluorides was in order of mF/cm^2 so change in mV scale of v used will not significantly contribute to mA -scale measured current density.^{8, 64-66}

Description of the transient corrosion process at OCP

Fig 10 shows the OCP measurement of Cr statically immersed in FLiNaK salts at $600 \text{ }^\circ\text{C}$ for 50 h. As Cr corroded, the OCP gradually raised from $+0.955 \text{ V}_{\text{Pseudo K+/K}}$ and stabilized to near $+1.50 \text{ V}_{\text{Pseudo K+/K}}$ starting near 20 h. The transient rise in potential can be attributed to the production of Cr(II) and Cr(III) species by Cr oxidation.⁶² which directly impacts the details of the coupled corrosion half-cell reactions. The rise in potential is consistent with Figure 7 and with a mixed potential theory where the OCP is located at potentials between the rising reduction-oxidation potential for Cr electrochemical dissolution and a cathodic half-cell reaction such as HF reduction. Fig 10a is also highlighted with orange and cyan showing whether CT or MT dominates Cr corrosion under OCP conditions brought about by Cr(III). The finding here is based on LSV at 1 mV s^{-1} . Using this approach, it is posited that the first 5.3 h likely corresponds to CT-controlled Cr dissolution while that between 5.3 and 50 h was by salt-film mediated MT. It was noted that the duration of CT and MT regimes dissolution can be modified by factors such as temperature, the concentration of oxidizers present in the salt, and/or the ratio between salt volume and exposed surface area.

Moreover, the horizontal dashed lines in Figure 10a indicate the Nernst potentials for various half-cell reactions at different ion activities. In a corrosion couple, the cathodic half-cell reactions indicated can form a spontaneous corrosion couple at an OCP, such as HF/H₂ in a wide range of concentration, that is more positive than the oxidation potential of Cr. These Nernst potentials can be compared with OCP as a function

of time to understand (a) the effect of a rising Cr(III) concentration and (b) the predominant cathodic reactions that led to the spontaneity of Cr corrosion since these reactions are coupled. At the early stage, the HF/H₂ potential between 10 ppm and 550 ppm [HF] sits above the initial OCP, suggesting the presence of HF impurity-driven spontaneous corrosion.⁶³ On the other hand, the K⁺/K reduction reaction has the lowest potential of all and will likely not participate in the spontaneous corrosion process of Cr even when salt is highly purified.¹² The question remains open whether it is possible for *in situ* formed Cr(III) species to become an oxidizer with respect to Cr.

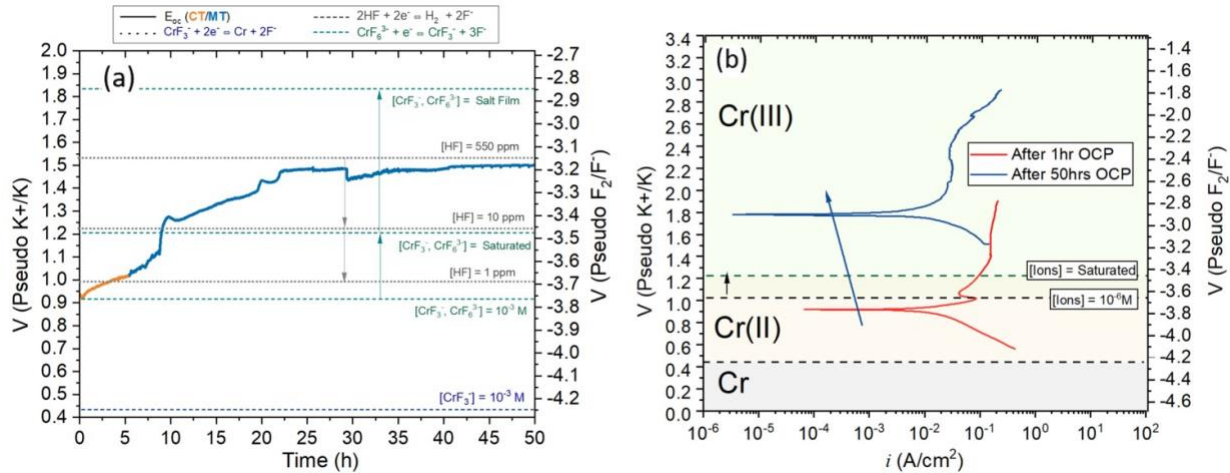


Figure 10. (a) Open circuit potential measurements of Cr in FLiNaK salts at 600 °C for 50 h. (b) shows the LSV curve performed after 1 h and 50 h of static immersion. The dotted lines in (b) indicate the phase boundary between Cr, Cr(II), and Cr(III) species with their activities assumed to be 10⁻⁶ M. The green dotted line shows the phase boundary of Cr(III)/Cr(II) at saturated conditions.

Fig 10a shows the reduction potential values for Cr(III)/Cr(II) reactions (grey short dashed lines) assuming that all ions are 10⁻³ M (simulating initial condition) and at saturated conditions. At the initial exposure period, the Cr(III)/Cr(II) potential was located slightly above the OCP and was likely not a strong oxidant for cathodic reactions compared to HF impurities. Undersaturated bulk conditions ([Cr(II)] = 4.40·10⁻³ M and [Cr(III)] = 5.06·10⁻² M stoichiometrically calculated from 0.3 wt.% CrF₃ saturation in FLiNaK), the Cr(III)/Cr(II) potential was increased to +1.19 V_{K+/K} and was above OCP until 10 h of exposure. If HF impurities were exhausted at this point (below 10 ppm), it was likely that Cr (III) generated by initial Cr corrosion would serve as a cathodic reactant, explaining the sudden rise in potential between 8.5 and 10 h. This is also consistent with the LSV plots shown in Figure 10b in which the OCP was shifted toward a positive direction after 50 h of exposure. As salt film forms, the surface concentration of Cr(III) will become saturated. The Cr(III)/Cr(II) potential was determined to be +1.82 V_{pseudo K+/K} assuming [Cr(II)] = 10⁻⁶ M and [Cr(III)] = 5.06·10⁻² M. This suggests that Cr(III) species may exhibit the thermodynamic driving force necessary to oxidize Cr spontaneously in the case where HF is depleted.

Morphological dependence on rate-controlling corrosion regimes

Figure 11 shows the plan-view surface morphology and XRD of the solidified salt for Cr potentiostatically maintained at $+0.18 V_{\text{pseudo K+/K}}$ for 1 h, $+1.08 V_{\text{pseudo K+/K}}$ for 50 h, and $+1.80 V_{\text{pseudo K+/K}}$ for 50 h. Based on Figure 5, these potential values should fall in the cathodic, CT, and MT-controlled regimes, corresponding to the stable regions of Cr, Cr(II), and Cr(III) phases.

In the cathodic regime of $+0.18 V_{\text{pseudo K+/K}}$, the 1 h hold time was the maximum duration as continued polarization led to current overload to be detailed in the next section. Nevertheless, no major sign of corrosion attack was observed as seen in Figure 11a. Some CrF_2 products were detected by XRD as shown in Figure 11b. In the CT regime of $+1.08 V_{\text{pseudo K+/K}}$, the dissolution process resulted in a highly faceted surface morphology containing crystallographic facets displayed in Figure 11b. At this potential and duration, $27.9 \mu\text{m}$ was expected to dissolve equivalent to about a grain diameter. This was a clear indication that the Cr dissolution in this regime was interfacially CT controlled and may be dependent upon crystallographic orientation. The XRD in Figure 11e confirms the presence of Cr(II) based compounds, such as CrF_2 and KCrF_3 , compounds. In the MT regime of $+1.80 V_{\text{pseudo K+/K}}$, the Cr surface after the potentiostatic hold was relatively smooth as seen in Figure 11c. The smooth morphology may serve as another piece of evidence that the Cr was dissolving beneath a salt film.^{32–36}

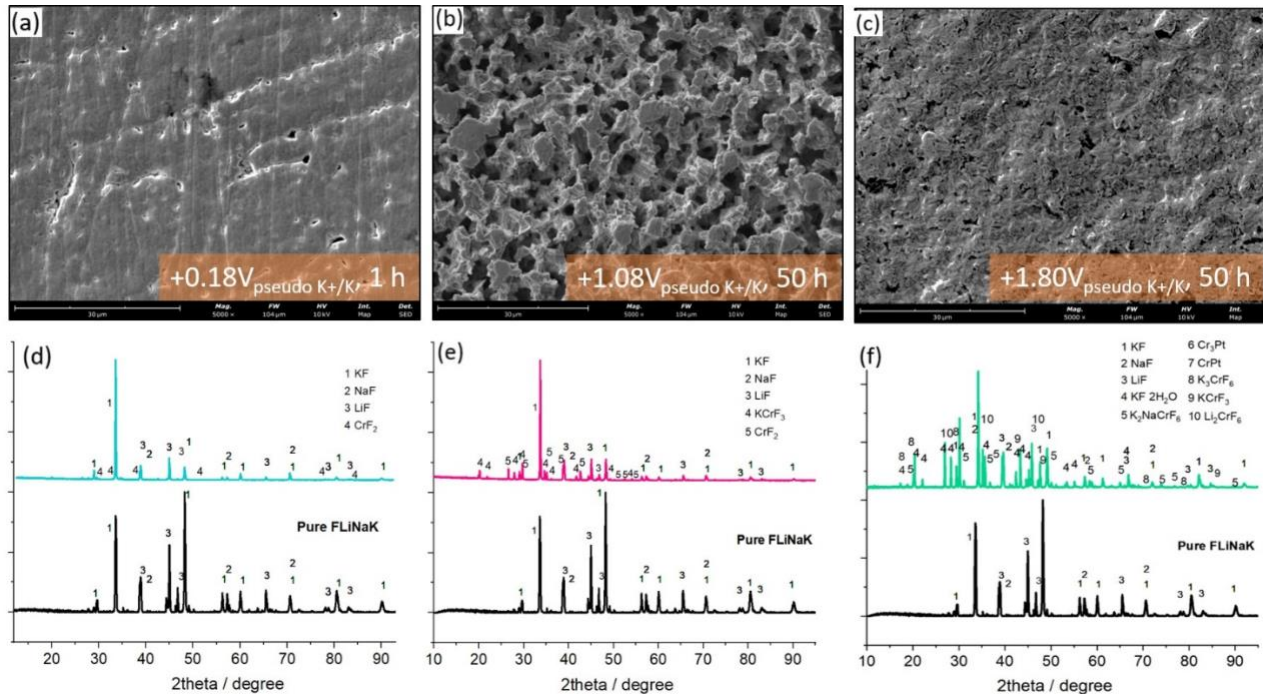


Figure 11. Plan view and X-ray diffractogram of residual salts for Cr potentiostatically polarized in FLiNaK salts at 600°C at (a,d) $+0.18$ for 1 h, (b,e) $+1.08$ for 50 h and (c,f) $+1.80 V_{\text{pseudo K+/K}}$ for 50 h

An additional potentiostatic hold was carried out at $+1.08$ and $+1.80 V_{\text{pseudo K+/K}}$ for 1 ks to examine the short-term morphological evolution and to avoid the salt film effect on corrosion morphology, as shown in

Figure 12. A shorter hold duration in the CT regime resulted in a faceted corrosion attack that was similar to the morphology shown in Figure 11a. In the MT regime, the Cr surface exhibited individual grain facets resembling matchstick and step-edge morphologies,⁶⁴ which was likely defined by the underlying grain orientation. It was noted that the grain facets presented in Figure 12b were not as visually clear as those in Figure 11b despite both dissolution processes were interfacial controlled. It was hypothesized that at +1.80 $V_{\text{pseudo K+K}}$, the anodic current density may be sufficient to relatively, uniformly dissolve the polycrystalline Cr in contrast to that observed at 1.08 $V_{\text{pseudo K+K}}$, which appeared to be more localized.

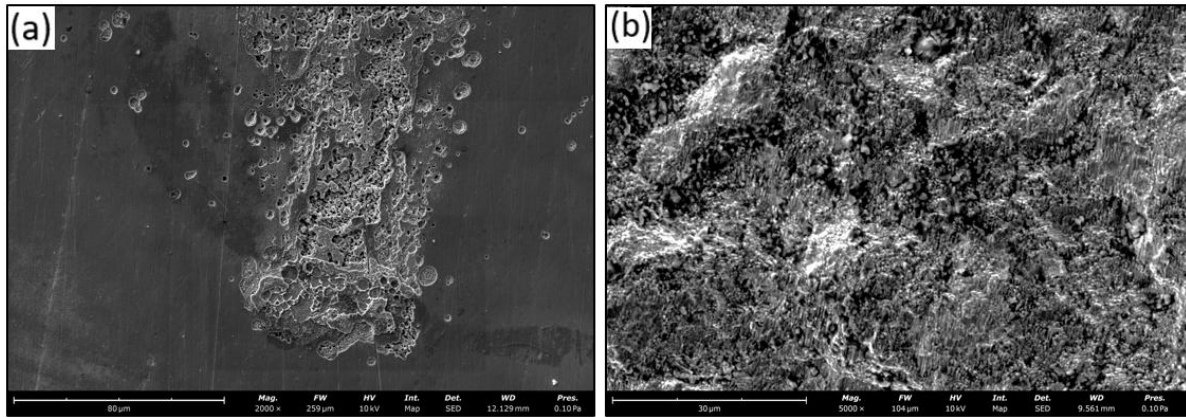


Figure 12. Plan view surface morphology of Cr potentiostatically polarized in FLiNaK salts at 600 °C at (a) 1.08 and (b) 1.80 $V_{\text{pseudo K+K}}$ for 1ks

Current-time relationship during potentiostatic hold

Figure 13 shows the current-time (i - t) relationships of Cr potentiostatically held at 0.18 for 1 h, 1.08, and 1.80 $V_{\text{pseudo K+K}}$ for 50 h. In the cathodic regime of 0.18 $V_{\text{pseudo K+K}}$, a reducing (negative) current density was measured for the first hour (~3600 s) followed by a sharp increase in current density leading to current overload. A reasonable explanation of this sharp current rise can again be attributed to the exhaustion of oxidizers (e.g. O^{2-}) as illustrated in Fig 3a. the 1 h hold time was the maximum duration as continued polarization led to current overload to be detailed in the next section. This may be attributed to the oxidation of O^{2-} at the CE that led to a shift in Pt/PtO_x/O²⁻ pseudo reference potential, leading to a condition in which K^+ was being reduced on Cr. This behavior limits the ability to perform stable pstat study in this regime.

In the CT regime, Cr exhibited a large initial oxidizing (positive) current density and it gradually dropped and transitioned into cathodic regimes at ~14000 s (Fig 13b). Current spikes were detected starting at 100 s. As seen in Figs. 7 and 10, loading the FLiNaK salts with CrF₃ can shift the polarization curve upward. In other words, maintaining the Cr potential at 1.08 $V_{\text{pseudo K+K}}$ could first produce CrF₃⁻ species that accumulated to a point where the Nernst potential became more positive and was subsequently reduced on the Cr metal surface. To approximate the depth of attack, Eq. (9) and (16) were utilized to estimate the

uniform thickness of Cr dissolved using the anodic current densities. Prior to the transition to cathodic regime, an average thickness of 30 μm was expected to dissolve (close to one grain size).

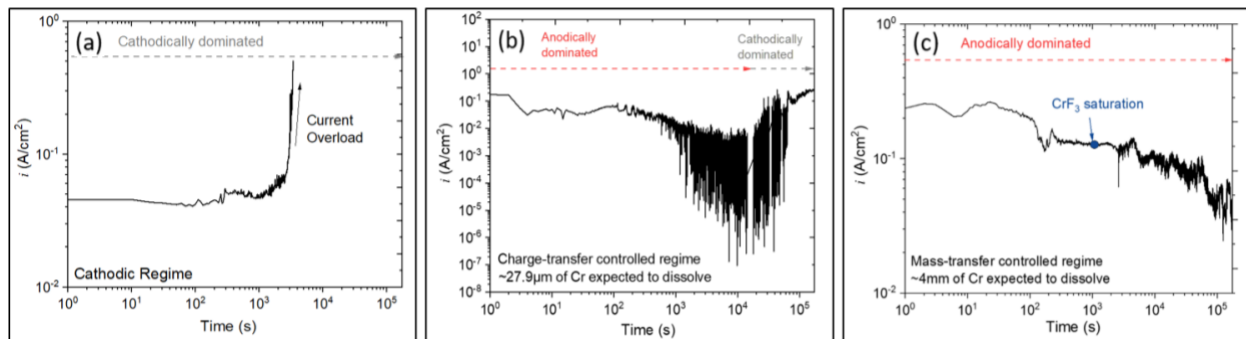


Figure 13. Current-time relationship of Cr potentiostatically polarized in FLiNaK salts at 600 °C at (a) 0.18 for 1 h, (b) 1.08 and (c) 1.80 $V_{\text{pseudo K}^+/\text{K}}$ for 50 h.

Figure 13c shows that the i - t relationship of Cr potentiostatically held in the mass-transport controlled regime at 1.80 $V_{\text{pseudo K}^+/\text{K}}$. A large but slowly declining anodic current was detected, indicating that Cr was continuously oxidized over the course of pstat hold. Toward the end of the scan, close to 4 mm of thickness of Cr metal was expected to dissolve using Eq. (9) and (16). Coupling with stoichiometric calculation, the amount of Cr dissolved would reach a saturation point at $t = 1173$ s (0.3 wt.% CrF_3) in which salt film formation should begin. The predicted onset time was very close to the one calculated using the Sand Equation ($t = 1377$ s). The current after $t = 1173$ s remained anodic until 18000 s suggesting that the salt film formed did not retard the oxidation of Cr. Beyond 1173 s, the current density decays at a slope of ~ 0.5 , suggesting that the polarization behavior at this potential is mass-transport controlled. Using Faraday's Law, it was calculated that up to 4 mm of Cr would have been dissolved assuming uniform attack. Compounds containing CrF_3^- (Cr(II)) and CrF_6^{3-} (Cr(III)) were detected from XRD (Figure 11f).

Corrosion morphology through multiple corrosion regimes

The importance of elucidating the corrosion morphology individually for each transport regime can be highlighted by Figure 14, which reveals the SEM and surface roughness analysis of Cr subjected to LSV sweep from -0.4 to $+1.5$ V vs. OCP. The potential sweep range indicates that the Cr was subjected to corrosion through cathodic, CT, and MT regimes. In Figure 14a, the Cr surface exhibits both step-like facets and smooth morphologies. The faceted surface (toward the left of the micrograph) also contains residual molten salts which was confirmed by the EDS element map analysis in Figure 14b. It was noted that the Cr sample was removed immediately from the molten salt after LSV scan to avoid the deposition of Cr due to the occurrence of Cr(III)/Cr (II) disproportionation reaction.

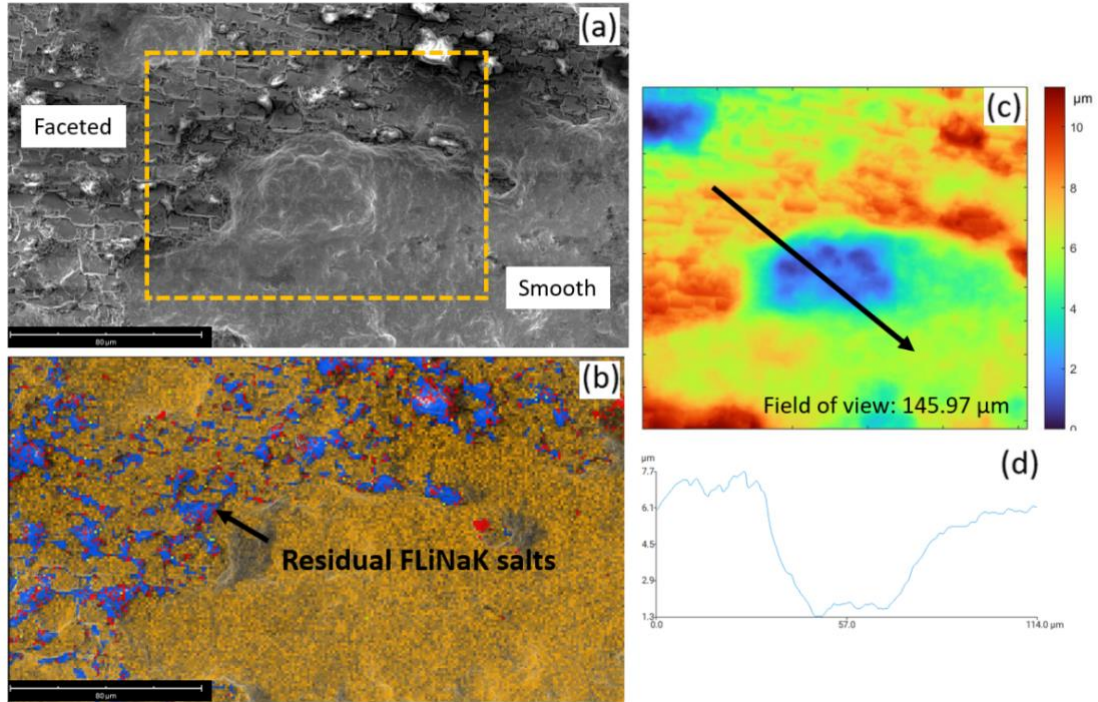


Figure 14. Plan view surface micrograph of Cr upon completion of the LSV scan. (b) shows the overlapped elemental maps of (a). The color orange, blue, and red, yellow correspond to Cr, F, K, Na respectively. (c) shows the surface topography colormap of the dashed yellow rectangle. The black arrow in (c) shows the relative height measurement and the result is displayed in (d)

The dashed orange rectangular in Figure 14a was analyzed with a micro-scale surface topological scan and the results are shown in Figs. 14c and 14d. The blue region in Figure 14c highlights the area with a relatively lower depth/position, which corresponds to the smooth corrosion surface. In other words, during the potential sweep, it can be postulated that the faceted surface was first formed in the CT regime and then subsequently transitioned into a smoothly dissolving surface under a salt film in the MT regime. Figs 15a-15c also reveal other types of corrosion morphologies observed after the LSV scan, notably locally dissolving areas with contours following the shape of the residual salt with a rock-salt crystal structure.

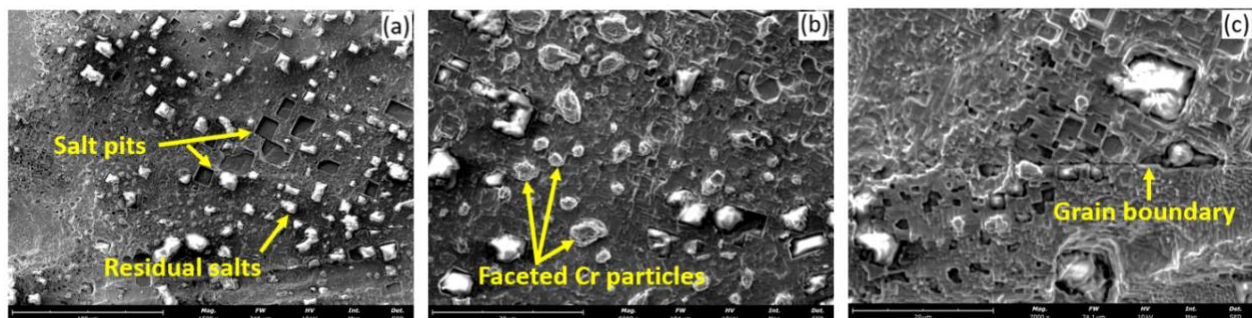


Figure 15. Plan view SEI micrograph of Cr subjected to LSV scan in 1 wt% CrF_3 + FLiNaK salts at 600 °C measured at (a) 1500x, (b) 5000x, and (c) 7000x magnifications
Corrosion morphology after exposure at OCP condition

The cross-section of immersed (i.e. open-circuit condition) Cr in FLiNaK for 50 h was examined using SEM and EBSD analysis. The backscattered electron micrograph in Figure 16a shows that the grain size of Cr ranged between 5.6 and 47.2 μm with subgrains sized about $6.8 \pm 4.6 \mu\text{m}$. Both Figs. 16a and 16b did not reveal any evidence of grain boundary attack as seen in most alloys¹² and pure Ni.^{15,62} Micro-voids were observed near the surface possibly due to vacancy injection to the Cr metal substrate during dissolution. The EBSD orientation maps (Figure 16c) show that the surface grains exhibit orientations close to (001) and (101). Additionally, as shown in Figure 16d, the Cr surface exhibited a highly faceted surface similar to the features observed in Figs. 14a and 15.⁶⁴

Corrosion morphology after exposure at OCP condition

To provide a time-based description of the salt film development, static immersion tests of Cr were separately carried out between 10 and 50 h of exposure and examined. The as-solidified salt was removed from the test crucible after testing. The salts were carefully fractured to reveal the location of Cr as indicated by the macrophotographs shown in Figure 17. Over the course of immersion, a thin dark green layer of the surface film was found adjacent to the Cr metal surface (Figs. 17a, 17b) from 10 to 20 h. Upon further exposure, the thickness of this layer increased to approximately 1.1 mm at 30 h and remain macroscopically identical up until 50 h. Regions described as “salt” and “film” were analyzed with XRD.

Fig 17f shows the X-ray diffractogram of an as-prepared FLiNaK salt (control), film, and salt regions. As expected, the as-prepared FLiNaK salts contained three salt constituents including cubic KF— peak#1, NaF—peak#2, and LiF—peak#3 compounds. The “film” region also exhibited both KCrF_3 (peak#4) and K_3CrF_6 (peak#5) compounds and that peak #5 was not distinct in the “salt” region. This suggested that K_3CrF_6 was likely the primary constituent of the salt film. Based on XRD, the salt film with different cation constituents or their mixture, such as Li_2CrF_6 , $\text{Na}_2\text{LiCrF}_6$, and K_2CrF_5 , were also observed.²⁸ This result also justifies the earlier discussion on the effect of K_3CrF_6 salt film.

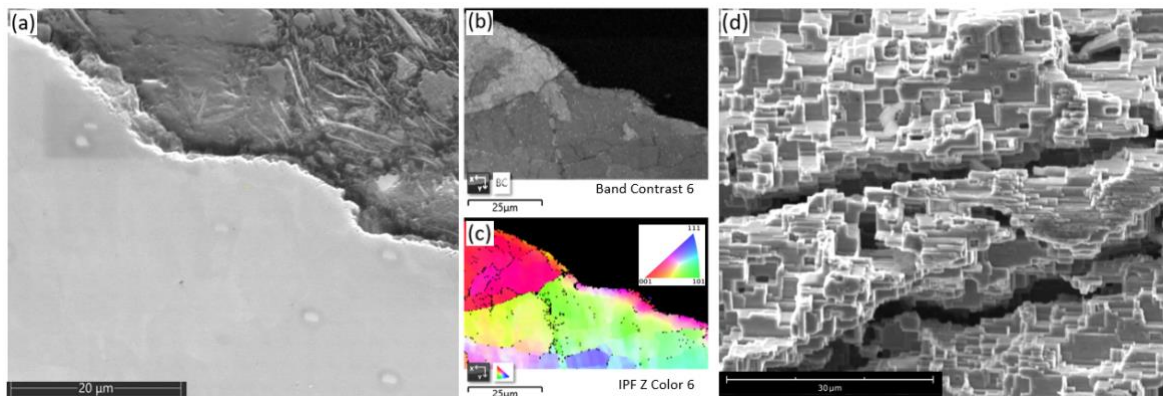


Figure 16. (a,b) Cross-sectional SEM micrograph of Cr immersed in 50 h at 600 °C in FLiNaK. (c) EBSD orientation map of (d). shows the surface of the as-corroded Cr sample

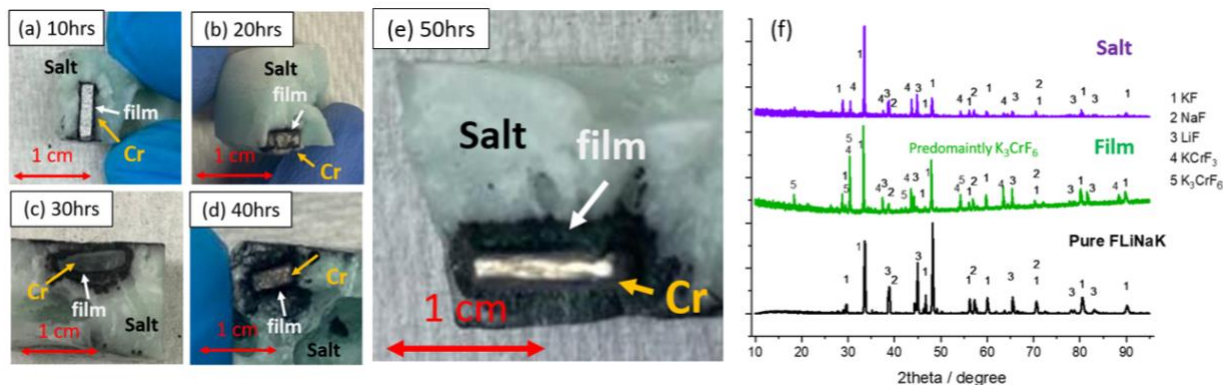


Figure 17. Macrophotographs of Cr embedded in residual FLiNaK salts after exposure at 600 °C for (a) 10 h, (b) 20 h, (c) 30 h, (d) 40 h, and (e) 50 h, respectively. Selected regions in (e) were analyzed with XRD shown in (f)

Discussions

Analysis of polarization curves and electrode kinetics

The corrosion of Cr in FLiNaK occurs at a mixed potential that is thermodynamically and kinetically established by the details of the anodic Cr/Cr(II) and/or Cr(II)/Cr(III) oxidation half-cell reactions coupled with cathodic reactions such as HF/H₂ and Cr(III)/Cr(II) reduction. The kinetic properties of each of these redox reactions can be interrogated by electrochemical methods.^{11,72} However, the complexity of interpreting experimental polarization curves (i.e., LSV) arises from the presence of multiple oxidation paths and rate regulating phenomena (e.g., salt film formation, MT limitation, etc.) that are dependent upon potential, experiment conditions and salt chemistry.

To construct a foundational framework towards understanding polarization curves measured in molten fluorides, Evan's diagrams were constructed taking account of the finding above. Fig 18 shows the E-log(i) behavior of multiple half-cell reactions constructed using the electrochemical parameters shown in Table II. The assumption made is that HF and Cr(III) are the predominant cathodic reactants although this is not proven. Parameter selection, such as diffusivity and exchange current densities, were based on electrochemical data previously reported in Table I and approximated to within an order of magnitude. Eq. 3 was used to simulate the half-cell E-i relationship containing a CT and MT regime. The CT or activation-controlled current was calculated using Eqs. 4 and 18. The i_L for the possible cathodic reactions (i.e. Cr(III)/Cr(II) and HF/H₂) were calculated using Eq. 17 with different Cr(III) and Cr(II) concentrations shown in Table 3. It should be noted that the current of the cathodic half-cell reactions is described by i_c , the anodic by i_a , and the open circuit potential occurs at a potential where $i_c = i_a$. which is where $i_a = -i_c = i_{corr}$. When $i_a > i_c$ then the potential necessary to drive such current must be supplied by the potentiostat.

$$\eta = \pm \beta_{a/c} \log\left(\frac{i_a/c}{i_{corr}}\right) \quad (20)$$

Based on Figure 18a, due to its high reduction potential, HF/H₂ (blue curve) remains a predominant cathodic reaction during Cr corrosion in a wide range of possible HF concentrations between 10 and 1000 ppm. It is not until HF falls below 10 ppm (either through consumption from corrosion or rigorous salt purification processes^{10,65}) and the FLiNaK salt saturates with chromium fluoride that the Cr(III)/Cr(II) reaction may dominate the cathodic polarization curve. Between 10 and 1000 ppm, the HF/H₂ polarization curve (blue) intersects with the half-cell reaction in the CT regime for Cr dissolution (red). The overall polarization behavior follows Figure 5a (Cathodic → CT → Saturation Peak → MT) for Cr in molten fluoride containing high HF concentration.¹⁵ This remains true even if the Cr(III)/Cr(II) cathodic polarization curves (orange curve) dominate in the concentration range between “unpurified” and “bulk saturated” conditions and is experimentally proven in Figure 7. A key insight is that the cathodic polarization curves of HF/H₂ (between 10 and 100 ppm) and Cr (III)/Cr(II) reactions (between unpurified and bulk saturated conditions) still intersect with the anodic CT polarization regime of Cr/Cr(II)/Cr(III) curves. As a result, it is still possible to extract an anodic Tafel slope for E-i data when under these conditions, as shown in Figure 19a. However, as the oxidizer concentration increases, the CT regime for linear E-log(i) fitting becomes narrower as shown in Figure 19, making it challenging to accurately define a Tafel slope. To ensure reliable analysis, it is also crucial to correct for contributions from cathodic and limiting current densities (e.g. Figure 4) from the experimentally measured anodic CT regime.

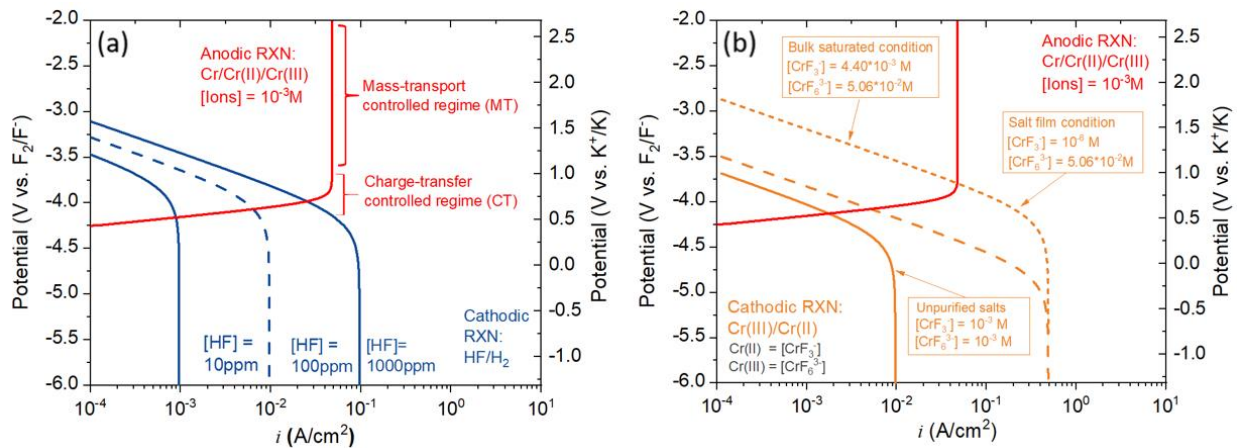


Figure 18. Evans’ diagram constructed for pure Cr in molten FLiNaK salts at 600 °C. The red curves show the E-log(*i*) curves consisting of charge-transfer and mass-transport controlled regimes for the anodic Cr/Cr(II)/Cr(III) reactions. (a) shows the cathodic polarization curves for the HF/H₂ reactions with [HF] assumed between 10 and 1000 ppm. (b) shows cathodic polarization curves for the Cr(III)/Cr(II) reactions at various concentration of Cr(II) and Cr(III).

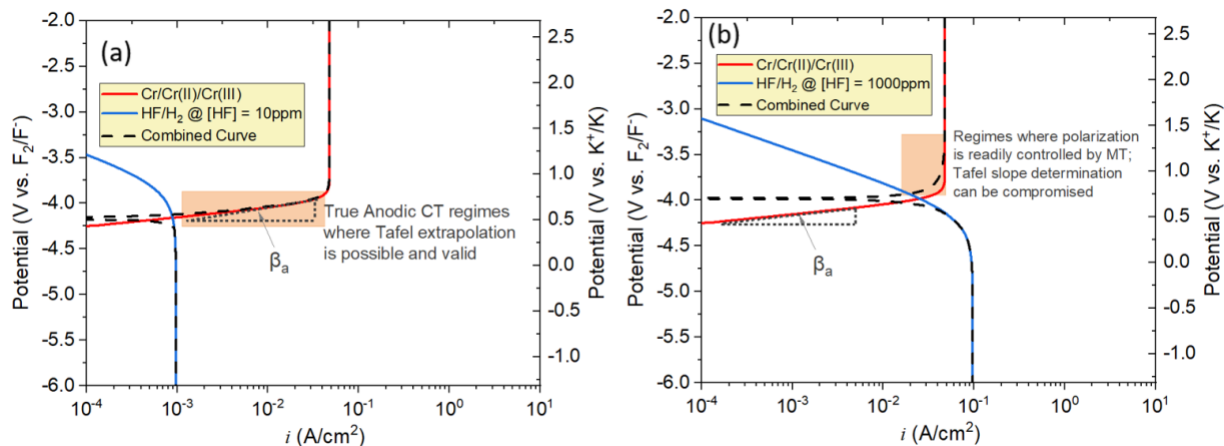


Figure 19. Evan’s diagrams highlight the conditions under which Tafel slopes determination via linear fittings in the anodic CT regimes is (a) valid or (b) compromised. (a) shows an example of a valid scenario with cathodic reactions being HF/H₂ at 100 ppm of HF. In contrast, (b) illustrates a scenario where Tafel slope determination is impossible when the K₃CrF₆ salt film is present on the surface. The semi-transparent orange rectangles in both (a) and (b) represent the typical, experimentally expected anodic region for Tafel slope determination.

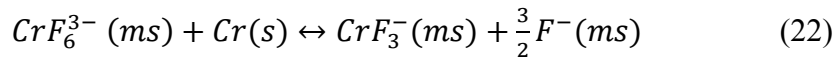
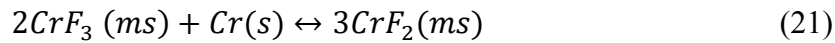
Erroneous determination of the Tafel slope can occur when the cathodic polarization curves intersect with and/or are very close to the anodic MT-controlled regime (highlighted in Figure 18b). At this potential intersection, the i_L , i_a , and i_c become identical. Based on this simulation, a HF/H₂ reduction reaction with 1000 ppm of HF can lead to this condition. Another possible scenario may also be the formation of a K₃CrF₆ salt film present on the surface of the material, which can be the case for various Cr-containing alloys.^{9,66,67} Many studies overlook this point and try to force a fit of E- i_{meas} data to an anodic Tafel slope (not possible when $i_a = i_L$) in a “false” CT regime that is actually controlled by mass transport as pointed out in Figure 18b. The occurrence of this condition depends on factors such as the thermokinetic properties of both anodic and cathodic reactions (e.g., i_o , i_L , E) and it may not be the only possible scenario in which an interpretation of the CT regime is compromised. The cathodic reactions of HF/H₂ and CrF₆³⁻(Cr(III))/CrF₃(Cr(II)) can also be limited by ionic diffusion in the molten salt phase.⁵⁹ The cathodic mass-transport limitation becomes significant when the oxidizer concentration is low and is practically analogous to highly purified salts. In this scenario, low oxidizer concentration may undermine the potential range of a linear E-log(i) region that can be used for Tafel extrapolation (leading to inaccurate kinetic analysis). The MT limitation for cathodic polarization scan is more prominent for HF/H₂ than Cr(III)/Cr(II) reactions unless at sufficiently high overpotential. This also informs us that at open-circuit conditions, the Cr(III) produced by Cr corrosion will likely not be limited by MT and may immediately be consumed (reduced) at the salt/metal interface.

Table 3. Electrochemical parameters used for the construction of Evan’s Diagram. Noted that the CrF_3^- and CrF_6^{3-} represent the Cr(II) and Cr (III) species, respectively

Reaction	Concentration	E_{Nernst}	i_0	i_L
	M	$V_{\text{F}_2/\text{F}^-}$	A/cm ²	A/cm ²
$\text{Cr}(s) + 3\text{F}^- \leftrightarrow \text{CrF}_3^-(ms) + 2e^-$	$[\text{CrF}_3^-] = 10^{-3} \text{ M}$	-4.254	10 ⁻⁴	$4.79 \cdot 10^{-2}$
$\text{CrF}_3^- + 3\text{F}^- \leftrightarrow \text{CrF}_6^{3-}(ms) + e^-$	$[\text{CrF}_3^-] = 10^{-3} \text{ M},$ $[\text{CrF}_6^{3-}] = 10^{-3} \text{ M}$	-3.668		$9.65 \cdot 10^{-4}$
	$[\text{CrF}_3^-] = 4.40 \cdot 10^{-3} \text{ M},$ $[\text{CrF}_6^{3-}] = 5.06 \cdot 10^{-2} \text{ M}$	-3.484		$4.88 \cdot 10^{-2}$
	$[\text{CrF}_3^-] = 10^{-6} \text{ M}$ $[\text{CrF}_6^{3-}] = 5.06 \cdot 10^{-2} \text{ M}$	-2.853		
$\text{HF}(ms) + e^- \leftrightarrow \text{H}_2(g) + \text{F}^-(ms)$	$[\text{HF}] = 5 \cdot 10^{-4} \text{ M}$ or 10 ppm	-3.452		$9.65 \cdot 10^{-4}$
	$[\text{HF}] = 5 \cdot 10^{-2} \text{ M}$ or 100 ppm	-3.279		$9.65 \cdot 10^{-3}$
	$[\text{HF}] = 5 \cdot 10^{-3} \text{ M}$ or 1000 ppm	-3.106		$9.65 \cdot 10^{-2}$

*[F⁻] was stoichiometrically calculated to be 49.3 M. The diffusivity of HF and CrF_6^{3-} was assumed to be 10⁻⁵ cm² s⁻¹. Boundary layer thickness ($\delta_{\text{boundary layer}}$) was assumed to be 10 μm for all reactions.

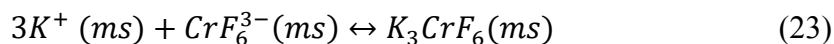
Nevertheless, diffusion of Cr(III) from the Cr surface to the bulk electrolyte would require ~19,000 s using estimates of the characteristic diffusion length $x = \sqrt{Dt}$. There are three possible pathways in which Cr(III) in the form of CrF_6^{3-} may be reduced: (i) at the metal surface and supporting the oxidation of Cr metal, (ii) by Cr (II) ions at the salt/metal interface, leading to the production of Cr particles akin to the disproportionation reaction commonly referred to as reactions (21) or (22) when F⁻ solvation is considered. If this is the case, corrosion of Cr may be limited; and/or (iii) by other environmental impurities, such as metallic cation impurities.



Microstructural implication of charge-transfer and mass-transport controlled regimes

Results suggest that Cr can dissolve by charge-transfer (or activation-controlled) in FLiNaK at 600 °C at low overpotential (i.e. lower driving force) and can transition to dissolution regulated by a salt-film induced mass-transport process. As discussed in Figure 18, it appears that a wide array of HF and Cr(III) oxidizer concentrations can result in this behavior. Each regime also has an underlying microstructural effect. Surface faceting was observed in Figs. 11b and 12b in both CT and MT regimes prior to salt film formation. Since the dissolution of each grain involves the creation of new solid/liquid (S/L) interfaces, it is reasonable

to suggest that crystallographic orientation may have a sizeable impact on Cr oxidation since different grain surfaces present surfaces with different S/L interfacial energy. Further work will be carried out to interrogate the effect of crystallographic orientation on molten salt corrosion. The electrochemical potential in which the mass transport regime is rate-limiting falls within the phase stability field where Cr(III) species dominates, leading to the formation of a K_3CrF_6 salt film possibly via reaction (23) either directly on or adjacent to the Cr metal surface. Both scenarios have been observed experimentally.^{57,68}



The existence of a salt film requires the metal/salt interface to be kinetically stable in which the rate of salt film formation (i_{form}) at the metal/film interface is at least identical to that of dissolution (i_{diss}) at the film/molten salt interface.^{35,69} Only the former is controlled by applied potential and the latter is diffusion controlled. The anodic dissolution of Cr in the MT-controlled regime was likely not solely determined by the diffusion of CrF_6^{3-} species in the liquid phase electrolyte and possibly requires the transport of metallic cations through the K_3CrF_6 salt film.³³ This may be an explanation for linear E-i behavior in Figure 6d. The mechanism of salt film formation should follow a series of redox and chemical reactions shown in reactions (10), (12), and (23). Formation of the salt film also depends on the availability of K^+ cations on the salt/metal interface, which should not be rate-limiting due to its large concentration.

It was noted the salt film may be not a pure K_3CrF_6 compound. It may contain other salt compounds, in which CrF_6^{3-} is the anion constituent, such as K_2NaCrF_6 and Li_2CrF_6 , which may also be deposited as defective salt crystals. It is challenging to use XRD alone to distinguish these compounds due to the similarities in their crystal structures. These salts possibly have different solubility limits, and may precipitate at different times during LSV and potentiostatic holds. The compositional heterogeneity in the salt film may lead to MT-controlled dissolution not occurring uniformly on the Cr surface as expected with a homogeneous salt film. It is reasonable to state that the dissolution under salt crystals varies with crystal identity giving the false impression of a cubic crystal orientation etch pit that can instead be explained by locally varying mass transport control under a cubic salt crystal. Furthermore, it is possible that the precipitated salt film is porous, compact, or a mixture of both. For compact salt film deposited adjacent to Cr, the growth of K_3CrF_6 may be governed by the outward Cr(III) cation migration through the film. K_3CrF_6 is a cubic compound highly packed with Cr(III) ions occupying the FCC framework with 3 basis atoms of K^+ ions and 6 of F^- ions fully occupying both tetrahedral and octahedral interstitial sites,³⁰ a high population of thermal vacancies at 600 °C is expected that enhances the mobility of cation migration. The salt film can be thickened up to 1 mm at a 20 h exposure period, becoming a “thick” dielectric layer that limits ionic migration and activity-driven diffusion across the salt compound.

From thermodynamic prediction, the solubility of CrF_3 in FLiNaK would be increased to 0.8 wt.% and 1.6 wt.% at 700 °C and 800 °C, respectively.²⁸ This was observed in higher temperatures by multiple authors.^{6,9,10,15} This phenomenon is certainly of practical concern for MSR performance since reactor pressure vessels and secondary heat exchanger tubes, both of which may be exposed to FLiNaK or other molten fluoride salts, operating between 500 °C and 700 °C.⁷⁰ In fact, the formation of a metal fluoride salt film was first reported in 1962 by DeVan and Evan on Ni–Mo–Cr alloys after 5000 h of loop corrosion tests,⁷¹ and then by Holcomb and Sacit in 2010 on Inconel 600 alloy as a mm-scale film that hinders heat transports.⁶⁸ Although not investigated in this work, it is also of the community interest to investigate possible salt film precipitation in other candidate MSR salts especially LiF–BeF₂ (FLiBe) salts.

Conclusions

The corrosion regimes of Cr in FLiNaK at 600 °C were defined as a function of potential based on in situ, real-time electrochemical measurements. Cr dissolution in molten fluorides can be rate-limited by the interfacial reaction (i.e., charge-transfer controlled) involving a series of Cr/Cr(II)/Cr(III) half-cell reactions or salt film induced mass-transport controlled processes. Both processes are dependent upon the applied potential, Cr cation content, and the electrochemical driving force for corrosion. A regime of thermodynamic immunity can also be found, defined by the Cr/Cr(II) half-cell reaction, in which Cr can be cathodically protected and undergoes limited corrosion. Caution is warranted that the routine aqueous assumption of an infinite cathode is not the case in FLiNaK. During polarization, cathodic limitations may arise. These potential-dependent polarization regimes were interrogated diagnostically using multiple scan rates, scan potential range, Cr(III) concentration, and scan cycles as diagnostics.

The Evans diagram constructed herein establishes the regimes set forth above and identifies factors and half-cell reactions that regulate corrosion reactivity. In a few situations, the accurate determination of Tafel slopes from E-i behavior is complicated and cannot be accessed graphically. The presence of an unidentified salt film on the Cr surface, possibly consisting of K_3CrF_6 and other K–Cr–F compounds, combined with a sufficiently high oxidizer concentration enables rate-limited anodic mass transport control. Oxidizers may include but are not limited to Cr(III) produced during Cr corrosion and HF formed by environmental moisture impurities. With this framework, radiation effects may be considered.

The OCP behavior of Cr during a 50 h static immersion provides insights into the time-dependent transitions between the charge transfer and mass transport-controlled potential regimes during spontaneous corrosion. Specifically, the OCP of Cr lies within the CT regime at the early exposure times. As the exposure time progresses, the concentrations of Cr(II) and Cr(III) increase, resulting in the transition of corrosion into the MT regime. This transition is accompanied by the formation of a salt film, which occurs approximately 10 h into the exposure period. Lastly, corrosion stifling may operate when the concentrations of Cr(III) rise

sufficiently during corrosion. These observations are all supported by a post in situ exposure analysis. Multiple salt precipitation routes are possible to mediate the rate of MT-controlled electro-dissolution kinetics depending on salt identity. Further research is needed to investigate the formation, growth mechanism, and stability of the K_3CrF_6 salt film in molten fluorides.

References

1. J. Serp, M. Allibert, O. Beneš, S. Delpech, O. Feynberg, Véronique Ghetta, D. Heuer, D. Holcomb, V. Ignatiev, J. L. Kloosterman, L. Luzzi, E. Merle-Lucotte, J. Uhlíř, R. Yoshioka, Dai Zhimin, The molten salt reactor (MSR) in generation IV: Overview and perspectives, *Progress in Nuclear Energy*. 77 (2014) 308–319. <https://doi.org/10.1016/j.pnucene.2014.02.014>.
2. D. F. Williams & K. T. Clarno, Evaluation of Salt Coolants for Reactor Applications. *Nuclear Technology*, 163(3) (2008) 330–343. <https://doi.org/10.13182/NT08-A3992>
3. W.H. Jordan, S. J. Cromer & A.J. Miller. Aircraft Nuclear Propulsion Project Quarterly Progress Report. ORNL-2387, (1957). Oak Ridge National Laboratory, TN. (<http://moltensalt.org/references/static/downloads/pdf/ORNL-2387.pdf>)
4. W.H. Doniger, C. Falconer, M. Elbakhshwan, K. Britsch, A. Couet, K. Sridharan, Investigation of impurity driven corrosion behavior in molten $2LiF\text{-}BeF_2$ salt, *Corrosion Science*. 174 (2020) 108823–108823. <https://doi.org/10.1016/j.corsci.2020.108823>.
5. Y. Wang, H. Liu, G. Yu, J. Hou, C. Zeng, Electrochemical study of the corrosion of a Ni-based alloy GH3535 in molten (Li,Na,K)F at 700°C, *Journal of Fluorine Chemistry*. 178 (2015) 14–22. <https://doi.org/10.1016/j.jfluchem.2015.06.014>.
6. S. Fabre, C. Cabet, L. Cassayre, P. Chamelot, S. Delepech, J. Finne, L. Massot, D. Noel, Use of electrochemical techniques to study the corrosion of metals in model fluoride melts, *Journal of Nuclear Materials*. 441 (2013) 583–591. <https://doi.org/10.1016/j.jnucmat.2013.03.055>.
7. J. Qiu, D.D. Macdonald, R. Schoell, J. Han, S. Mastromarino, J.R. Scully, Djamel Kaoumi, P. Hosemann, Electrochemical study of the dissolution of oxide films grown on type 316L stainless steel in molten fluoride salt, *Corrosion Science*. 186 (2021) 109457–109457. <https://doi.org/10.1016/j.corsci.2021.109457>.
8. D. Cao, Y. Ma, Z. Shi, J. Xu, X. Hu, Z. Wang, Performance of protective oxide films on Fe–Ni alloy anodes in molten $KF\text{-}AlF_3\text{-}Al_2O_3$ salts at 700 °C, *Electrochimica Acta*. 347 (2020) 136275–136275. <https://doi.org/10.1016/j.electacta.2020.136275>.
9. Y. L. Wang, Q. Wang, Hui Jun Liu, Chao Liu Zeng, Effect of grain refinement on the corrosion of Ni-Cr alloys in molten (Li,Na,K)F, *Corrosion Science*. 109 (2016) 43–49. <https://doi.org/10.1016/j.corsci.2016.03.027>.
10. W.H. Doniger, A. Couet, K. Sridharan, Potentiodynamic Polarization of Pure Metals and Alloys in Molten $LiF\text{-}NaF\text{-}KF$ (FLiNaK) Using the K/K^+ Dynamic Reference Electrode, *Journal of the Electrochemical Society*. 169 (2022) 071502–071502. <https://doi.org/10.1149/1945-7111/ac7a66>.
11. R.G. Kelly, J. R. Scully, D. Shoosmith, R. G. Buchheit. *Electrochemical Techniques in Corrosion Science and Engineering*, 2002 (Boca Raton, FL: CRC Press). <https://doi.org/10.1201/9780203909133>.
12. S. Guo, J. Zhang, W. Wu, W. Zhou, Corrosion in the molten fluoride and chloride salts and materials development for nuclear applications, *Progress in Materials Science*. 97 (2018) 448–487. <https://doi.org/10.1016/j.pmatsci.2018.05.003>.
13. W. Zhou, Y. Yang, G. Zheng, K.B. Woller, P.W. Stahle, A.M. Minor, M.P. Short, Proton irradiation-decelerated intergranular corrosion of Ni-Cr alloys in molten salt, *Nature Communications*. 11 (2020). <https://doi.org/10.1038/s41467-020-17244-y>.
14. J. Zhang, C.W. Forsberg, M.F. Simpson, S. Guo, S.T. Lam, R.O. Scarlat, F. Carotti, K.J. Chan, P.M. Singh, W. Doniger, K. Sridharan, J.R. Keiser, Redox potential control in molten salt systems for corrosion mitigation, *Corrosion Science*. 144 (2018) 44–53. <https://doi.org/10.1016/j.corsci.2018.08.035>.

15. Y. L. Wang, Q. Wang, Hui Jun Liu, Chao Liu Zeng, Effects of the oxidants H₂O and CrF₃ on the corrosion of pure metals in molten (Li,Na,K)F, *Corrosion Science*. 103 (2016) 268–282.
<https://doi.org/10.1016/j.corsci.2015.11.032>.
16. H. L. Chan, E. Romanovskaia, J. Qiu, P. Hosemann, J.R. Scully, Insights on the corrosion thermodynamics of chromium in molten LiF-NaF-KF eutectic salts, *Npj Materials Degradation*. 6 (2022).
<https://doi.org/10.1038/s41529-022-00251-3>.
17. L. Massot, M. Gibilaro, D. Quaranta, P. Chamelot, Corrosion Products Electrochemical Behaviour into Molten LiF-NaF: Investigation of Cr(II) System, *Journal of the Electrochemical Society*. 168 (2021) 026510–026510.
<https://doi.org/10.1149/1945-7111/abe088>.
18. W.H. Doniger, K. Sridharan, Application of voltammetry for quantitative analysis of chromium in molten 2LiF-BeF₂ (FLiBe) salt, *Journal of Electroanalytical Chemistry*. 838 (2019) 73–81.
<https://doi.org/10.1016/j.jelechem.2019.02.048>.
19. T. Ghaznavi, S.Y. Persaud, R.C. Newman, Electrochemical Corrosion Studies in Molten Chloride Salts, *Journal of the Electrochemical Society*. 169 (2022) 061502–061502. <https://doi.org/10.1149/1945-7111/ac735b>.
20. S.W. McAlpine, N.C. Skowronski, W. Zhou, Guiqiu (Tony) Zheng, M.P. Short, Corrosion of commercial alloys in FLiNaK molten salt containing EuF₃ and simulant fission product additives, *Journal of Nuclear Materials*. 532 (2020) 151994–151994. <https://doi.org/10.1016/j.jnucmat.2020.151994>.
21. N.W. Shay. Electrochemical Sensor Development for Fluoride Molten Salt Redox Control. Master Thesis. The Ohio State University, 2017.
22. L. Massot, L. Cassayre, P. Chamelot, P. Taxil, On the use of electrochemical techniques to monitor free oxide content in molten fluoride media, *Journal of Electroanalytical Chemistry*. 606 (2007) 17–23.
<https://doi.org/10.1016/j.jelechem.2007.04.005>.
23. M. Shen, H. Peng, M. Ge, Y. Zuo, L. Xie, Use of square wave voltammeter for online monitoring of O₂–concentration in molten fluorides at 600°C, *Journal of Electroanalytical Chemistry*. 748 (2015) 34–39.
<https://doi.org/10.1016/j.jelechem.2015.04.023>.
24. R. Guidelli, R.G. Compton, J.M. Feliu, Eliezer Gileadi, Jacek Lipkowski, Wolfgang Schmickler, S. Trasatti, Defining the transfer coefficient in electrochemistry: An assessment (IUPAC Technical Report), *Pure and Applied Chemistry*. 86 (2014) 245–258. <https://doi.org/10.1515/pac-2014-5026>.
25. T. Dumaire, Rudy, Anna Louise Smith, Thermodynamic Assessment of the AF–CrF₃ (A = Li, Na, K) and CrF₂–CrF₃ Systems, *Thermo*. 1 (2021) 205–219. <https://doi.org/10.3390/thermo1020014>.
26. A. Saïla, M. Gibilaro, L. Massot, P. Chamelot, P. Taxil, A.M. Affoune, Electrochemical behaviour of dysprosium(III) in LiF–CaF₂ on Mo, Ni and Cu electrodes, *Journal of Electroanalytical Chemistry*. 642 (2010) 150–156. <https://doi.org/10.1016/j.jelechem.2010.03.002>.
27. N. Winner, H. Williams, R.O. Scarlat, M. Asta, Ab-initio simulation studies of chromium solvation in molten fluoride salts, *Journal of Molecular Liquids*. 335 (2021) 116351–116351.
<https://doi.org/10.1016/j.molliq.2021.116351>.
28. H. Yin, P. Zhang, X. An, J. Cheng, X. Li, S. Wu, X. Wu, W. Liu, L. Xie, Thermodynamic modeling of LiF-NaF-KF-CrF₃ system, *Journal of Fluorine Chemistry*. 209 (2018) 6–13.
<https://doi.org/10.1016/j.jfluchem.2018.02.005>.
29. Y. Wang, J. Zhang, Electrochemical Properties of CrF₂ in FLiNaK Molten Salt and the New Analytical Methods for their Determination, *Journal of the Electrochemical Society*. 167 (2020) 086503–086503.
<https://doi.org/10.1149/1945-7111/ab8923>.
30. The Materials Project 2020 Materials data on K₃CrF₆ by materials project (<https://osti.gov/dataexplorer/biblio/dataset/1676629>)
31. D. Sulejmanovic, J. Matthew Kurley, K. Robb, S. Raiman, Validating modern methods for impurity analysis in fluoride salts, *Journal of Nuclear Materials*. 553 (2021) 152972–152972.
<https://doi.org/10.1016/j.jnucmat.2021.152972>.

32. G. Gao, B. Yuan, C. Wang, L. Li, S. Chen, The Anodic Dissolution Processes of Copper in Sodium Fluoride Solution, *International Journal of Electrochemical Science*. 9 (2014) 2565–2574. [https://doi.org/10.1016/s1452-3981\(23\)07948-8](https://doi.org/10.1016/s1452-3981(23)07948-8).
33. M.J. Danielson, Transport Properties of Salt Films on Nickel in 0.5N HCl, *Journal of the Electrochemical Society*. 135 (1988) 1326–1332. <https://doi.org/10.1149/1.2095974>.
34. J. Han, M.G. Wartenberg, Ho Lun Chan, B.K. Derby, N. Li, J.R. Scully, Electrochemical stability, physical, and electronic properties of thermally pre-formed oxide compared to artificially sputtered oxide on Fe thin films in aqueous chloride, *Corrosion Science*. 186 (2021) 109456–109456. <https://doi.org/10.1016/j.corsci.2021.109456>.
35. R.D. Grimm, D. Landolt, Salt films formed during mass transport controlled dissolution of iron-chromium alloys in concentrated chloride media, *Corrosion Science*. 36 (1994) 1847–1868. [https://doi.org/10.1016/0010-938x\(94\)90023-x](https://doi.org/10.1016/0010-938x(94)90023-x).
36. T. Rayment, A.J. Davenport, A.J. Dent, J.-P. Tinnes, Richard J.K. Wiltshire, C. Martin, G. Clark, P. Quinn, F.W. Mosselmanns, Characterisation of salt films on dissolving metal surfaces in artificial corrosion pits via in situ synchrotron X-ray diffraction, *Electrochemistry Communications*. 10 (2008) 855–858. <https://doi.org/10.1016/j.elecom.2008.03.018>.
37. H. Yin, K. Wang, L. Xie, H. Han, W. Wang, Thermodynamic modeling of KF-CrF₃ binary system, *Chemical Research in Chinese Universities*. 31 (2015) 461–465. <https://doi.org/10.1007/s40242-015-4319-8>.
38. J. Busby, L. Garrison, L. Lin, S. Raiman, S. Sham, C. Silva, H. Wang. Technical assessment of materials compatibility in molten salt reactors, ORNL/SPR-2019/1089, March 2019, Oak Ridge National Laboratory, TN.
39. Y. Gu, W. Zhang, Y. Xu, Y. Shi, Korzhyk Volodymyr, Stress-assisted corrosion behaviour of Hastelloy N in FLiNaK molten salt environment, *Npj Materials Degradation*. 6 (2022). <https://doi.org/10.1038/s41529-022-00300-x>.
40. M. Rose, J. Krueger, T. Lichtenstein, E. Wu, L. Gardner. Precision of Property Measurements with Reference Molten Salts. ANL/CFCT-21/20; 170664; TRN: US2301832. Argonne National Lab. (ANL), Argonne, IL. <https://doi.org/10.2172/1823476>
41. R. Lan, Y. Liu, L. Han, J. Yang, H. Yin, M. Ge, X. Fu, H. Liu, Y. Qian, Probing the ionic structure of FLiNaK–ZrF₄ salt mixtures by solid-state NMR, *RSC Advances*. 11 (2021) 23846–23850. <https://doi.org/10.1039/d1ra04629b>. b
42. T. Yoko, R.A. Bailey, Electrochemical Studies of Chromium in Molten LiF - NaF - KF (FLiNaK), *Journal of the Electrochemical Society*. 131 (1984) 2590–2595. <https://doi.org/10.1149/1.2115363>.
43. W. Wu, S. Guo, J. Zhang, Electrochemical Behaviors of Cr(III) in Molten LiF-NaF-KF Eutectic, *International Journal of Electrochemical Science*. 13 (2018) 225–234. <https://doi.org/10.20964/2018.01.21>.
44. A. Robin, Jacques De Lépinay, Electrochemical study of the anodic dissolution of iron and nickel in the molten LiF-NaF-KF eutectic at 600°C using convolutional voltammetry, *Electrochimica Acta*. 37 (1992) 2433–2436. [https://doi.org/10.1016/0013-4686\(92\)87079-f](https://doi.org/10.1016/0013-4686(92)87079-f).
45. D. Ludwig, L. Olson, K. Sridharan, M. Anderson, T. Allen, High temperature electrochemistry of molten fluoride salt for measurement of dissolved chromium. *Corrosion Engineering, Science and Technology*, 46(4) (2011) 360–364. <https://doi.org/10.1179/147842209X12579401586645>
46. E. McCafferty. *Introduction to Corrosion Science* (Berlin: Springer). 2011. <https://doi.org/10.1007-978-1-4419-0455-3>.
47. J.R. Scully, Polarization Resistance Method for Determination of Instantaneous Corrosion Rates, *CORROSION*. 56 (2000) 199–218. <https://doi.org/10.5006/1.3280536>.
48. E. Gileadi. *Electrode Kinetics for Chemists, Chemical Engineers and Materials Scientists* (New York: Wiley). VCH Verlagsgesellschaft, Weinheim. 1993.
49. D. A. Jones. *Principles and Prevention of Corrosion* (Upper Saddle River, New Jersey: Prentice Hall). 1996.
50. T. Li, J.R. Scully, G.S. Frankel, Localized Corrosion: Passive Film Breakdown vs Pit Growth Stability: Part V. Validation of a New Framework for Pit Growth Stability Using One-Dimensional Artificial Pit Electrodes, *Journal of the Electrochemical Society*. 166 (2019) C3341–C3354. <https://doi.org/10.1149/2.0431911jes>.

51. N.J. Laycock, M.H. Moayed, R.C. Newman, Metastable Pitting and the Critical Pitting Temperature, *Journal of the Electrochemical Society*. 145 (1998) 2622–2628. <https://doi.org/10.1149/1.1838691>.
52. Y. Ge, X. Xie, J. Roscher, R. Holze, Q. Qu, How to measure and report the capacity of electrochemical double layers, supercapacitors, and their electrode materials, *Journal of Solid State Electrochemistry*. 24 (2020) 3215–3230. <https://doi.org/10.1007/s10008-020-04804-x>.
53. A. J. Bard, L. R. Faulkner. *Electrochemical Methods: Fundamentals And Applications* (New York: Wiley). 2001.
54. A.S. Gruia, C.N. Avram, N.M. Avram, M.G. Brik, Ab initio calculations of the structural, electronic and elastic properties of K₃CrF₆, *Physica Scripta*. T149 (2012) 014065–014065. <https://doi.org/10.1088/0031-8949/2012/t149/014065>.
55. R. G. Compton, C. E. Banks. *Understanding Voltammetry* (Covent Garden, London, UK: Imperial College Press). 2011.
56. G. Zheng, K. Sridharan, Corrosion of Structural Alloys in High-Temperature Molten Fluoride Salts for Applications in Molten Salt Reactors, *JOM*. 70 (2018) 1535–1541. <https://doi.org/10.1007/s11837-018-2981-2>.
57. Y. Liu, Y. Song, H. Ai, M. Shen, H. Liu, S. Zhao, Y. Liu, Z. Fei, X. Fu, J. Cheng, Corrosion of Cr in molten salts with different fluoroacidity in the presence of CrF₃, *Corrosion Science*. 169 (2020) 108636–108636. <https://doi.org/10.1016/j.corsci.2020.108636>.
58. V. Pavlík, V. Trembošová, M. Boča. Influence of chromium salts on corrosion of incoloy 800 h/ht alloy in fluoride eutectic melt flinak. 2020. https://www.ipm.lviv.ua/corrosion2020/Chapter_01/I_5_PAVLIK.pdf
59. H. Yin, J. Qiu, H. Liu, W. Liu, Y. Wang, Z. Fei, S. Zhao, X. An, J. Cheng, T. Chen, P. Zhang, G. Yu, L. Xie, Effect of CrF₃ on the corrosion behaviour of Hastelloy-N and 316L stainless steel alloys in FLiNaK molten salt, *Corrosion Science*. 131 (2018) 355–364. <https://doi.org/10.1016/j.corsci.2017.12.008>.
60. V. Pavlík, M. Kontrík, M. Boča, Corrosion behavior of Incoloy 800H/HT in the fluoride molten salt FLiNaK + MF_x (MF_x = CrF₃, FeF₂, FeF₃ and NiF₂), *New Journal of Chemistry*. 39 (2015) 9841–9847. <https://doi.org/10.1039/c5nj01839k>.
61. X. Li, T. Xu, M. Liu, Y. Zuo, Diffusion behaviors of HF in molten LiF-BeF₂ and LiF-NaF-KF eutectics studied by FPMD simulations and electrochemical techniques, *Journal of Nuclear Materials*. 572 (2022) 154031–154031. <https://doi.org/10.1016/j.jnucmat.2022.154031>.
62. G. Yamazaki, Takuya Nagasaka, T. Tanaka, T. Goto, J. Shen, K. Saito, M.I. Kobayashi, Corrosion of pure Cr and W in molten FLiNaK with hydrogen fluoride solution, *Fusion Engineering and Design*. 172 (2021) 112741–112741. <https://doi.org/10.1016/j.fusengdes.2021.112741>.
63. F. Lantelme and H. Groult. *Molten Salts Chemistry From Lab to Application* (ed 1). “Chapter 12: Corrosion in molten salts by K. Sridharan, T. R. Allen”. (Amsterdam: Elsevier). 2013.
64. Kateryna Gusieva, Katie Lutton Cwalina, William H. Blades, Gopalakrishnan Ramalingam, John H. Perepezko, Petra Reinke, and John R. Scully *The Journal of Physical Chemistry C* 2018 122 (34), 19499-19513 DOI: 10.1021/acs.jpcc.8b04306
65. S. Raiman, S. Lee. Aggregation and data analysis of corrosion studies in molten chloride and fluoride salts, *Journal of Nuclear Materials*. 511 (2018) 523–535. <https://doi.org/10.1016/j.jnucmat.2018.07.036>.
66. F.Y. Ouyang, C.H. Chang, B.C. You, T.K. Yeh, J.J. Kai. Effect of moisture on corrosion of Ni-based alloys in molten alkali fluoride FLiNaK salt environments, *Journal of Nuclear Materials*. 437 (2013) 201–207. <https://doi.org/10.1016/j.jnucmat.2013.02.021>.
67. Holcomb D. E. and Cetiner S. M. 2010 An overview of liquid fluoride salt heat transport systems (<https://osti.gov/biblio/990239-overview-liquid-fluoride-salt-heat-transport-systems>)
68. T. Li, J. Wu, G.S. Frankel. Localized corrosion: Passive film breakdown vs. Pit growth stability, Part VI: Pit dissolution kinetics of different alloys and a model for pitting and repassivation potentials, *Corrosion Science*. 182 (2021) 109277. <https://doi.org/10.1016/j.corsci.2021.109277>.
69. R.N. Wright, T. L. Sham. Status of metallic structural materials for molten salt reactors. Technical Report # INL/EXT-18-45171-Rev000; TRN: US1902748. Idaho National Lab. (INL), Idaho Falls, ID (United States); Argonne National Lab. (ANL), Argonne, IL (United States). 2018. <https://doi.org/10.2172/1467482>

70. J. H. DeVan, R. B. Evans, III. Corrosion behavior of reactor materials in fluoride salt mixtures. Technical Report # ORNL-TM-328. Oak Ridge National Lab. (ORNL), Oak Ridge, TN (United States). 1962.
<https://doi.org/10.2172/4774669>
71. van Ede, U. Angst, Analysis of Polarization Curves Under Mixed Activation-Diffusion Control: An Algorithm to Minimize Human Factors, *Corrosion*. 78 (2022) 1087–1099. <https://doi.org/10.5006/4171>.
72. E. Romanovskaia, H. L. Chan, V. Romanovski, F. Garfias, M. S. Hong, S. Mastromarino, P. Hosemann, R. Scarlet, J. R. Scully. An In Situ, multi-electrode electrochemical method to assess the open circuit potential corrosion of Cr in unpurified molten FLiNaK, *Corrosion Science*. 222 (2023) 111389.
<https://doi.org/10.1016/j.corsci.2023.111389>.
73. M.S. Hong, H.L. Chan, J. R. Scully, P. Hosemann. Corrosion property of Alloy 625 in Molten FLiNaK salt according to the Tellurium Concentrations, *Journal of Nuclear Materials*. 584 (2023) 154548.
<https://doi.org/10.1016/j.jnucmat.2023.154548>.
74. M.S. Hong, H.L. Chan, Y. Xie, E. Romanovskaia, J. R. Scully, P. Hosemann. Effect of tellurium concentration on the corrosion and mechanical properties of 304 stainless steel in molten FLiNaK salt, *Corrosion Science*. 212 (2023) 110913. <https://doi.org/10.1016/j.corsci.2022.110913>.

Chapter 4 Task 3: An *In Situ*, Multi-Electrode Electrochemical Method to Assess the Open Circuit Potential Corrosion of Cr in Unpurified Molten FLiNaK

Ho Lun Chan^{1,2}, Elena Romanovskaia^{1,2}, Valentin Romanovski^{1,2}, Francisco Garfias^{1,2}, Minsung Hong³, Sara Mastromarino³, Peter Hosemann^{3,5}, Raluca Scarlat³, John R. Scully^{1,2}

¹Department of Materials Science and Engineering, University of Virginia, Charlottesville, VA, 22904

²Center for Electrochemical Science and Engineering, University of Virginia, Charlottesville, VA, 22904

³Department of Nuclear Engineering, University of California, Berkeley, CA, 94150

⁴Department of Materials Science and Engineering, University of California, Berkeley, CA, 94720

⁵Materials Science Division, Lawrence Berkeley National Laboratory, Berkeley, CA, 94720, USA

Abstract

An *in situ* electrochemical method to investigate the time-dependent spontaneous corrosion of pure Cr in an unpurified LiF-NaF-KF eutectic salt at 600 °C was developed. A multi-electrode electrochemical cell and a dual-electrode method were utilized to detect Cr(II) and Cr(III) ions on a platinum working electrode using cyclic voltammetry as a function of exposure time and compensating for the distance from the Cr electrode. XRD was performed to characterize the crystalline composition of the exposed FLiNaK and the salt films formed on the working electrodes. The fate of all electro-oxidized Cr must be accounted for to quantify corrosion rates. The concentrations of Cr(II) and Cr(III) species obtained from this work shows reasonable agreement with the gravimetric mass change and ICPOES analysis of the residual salt.

Introduction

Structural materials are required for service in high-temperature Gen IV molten salt reactors (MSR) where environmental degradation by corrosion and other processes is critical. Understanding and illuminating features or attributes essential to describing the corrosion process, such as the effect of microstructure, crystal orientation, environment, and physical characteristics are crucial. The oxidation state and solubilization of the reacting metal species as well as the various rate-controlling factors as a function of electrode potential and impurity concentrations are of interest. Some of these factors can become better understood through the utilization of coupled electrochemical thermodynamic and kinetic analyses and supporting measurements. Cr is a key element component of many commercial alloys. The time-dependent concentrations of all Cr(II) and Cr(III) corrosion products when Cr-containing alloys corrode must be assessed. Moreover, in a closed system such as a reactor they will alter the thermodynamic driving

force of the Cr(II)/Cr or Cr(III)/Cr(II) half-cell reduction reactions¹ and may enable salt film formation. A corrosion system is dynamic and a fundamental understanding requires real-time assessments.

In recent years, some *in situ* spectroscopy methods to detect corrosion products in molten salts have been proposed²⁻⁶, such as Raman and high-temperature UV-Vis absorption spectroscopy² and X-ray absorption spectroscopy (XAS)³. These methods are not quantitative with respect to corrosion rate but shed light on the molecular species participating. Both methods require complex input beam focus and sensing. Furthermore, the Raman database is lacking with respect to many pertinent molten salts (MS) products, and Cr(II) and Cr(III) assignments are often assumed to be CrF₂ and CrF₃ while the actual composition of corrosion products may be much more complex^{4,5}. In addition to these complexities, such studies using molecular spectroscopies while insightful do not provide instantaneous, time-dependent information about a constantly-evolving corrosion system, which motivates the desire to track the electrochemical behavior of both the corroding metal and via its corrosion products in molten salts. In essence, multimodal *in situ* methods are desired in molten salt electrochemical system.

One approach to corrosion analysis often includes long periods of static immersion, exposure to a flow loop, and electrochemical experiments with 3 electrodes in molten fluoride salts followed by post-mortem analysis⁷. The real, practical challenge remains in providing a time-based description of the corrosion phenomenon that informs not only possible morphological evolution but also the physical/electrochemical properties over a range of potential coupled with electrolyte analysis. For instance, immersion or flow-loop experiments at different exposure times provide information at single or a few select times. Only a limited exposure time range has been explored⁷. Regarding the use of electrochemistry, there is an increasing number of scientific works that propose electrochemical methods in molten salts to attain the goal of *in situ* real-time measurements⁶. Some previous studies involved (i) performing open-circuit gravimetric and instrumented electrochemical impedance spectroscopy (EIS) measurements at different exposure periods^{7,8}, and (ii) characterizing the electrochemical properties of their possible corrosion products in molten fluoride salts⁹⁻¹². The former method allows the relative corrosion rates of materials to be compared^{10,13,14} and the later enables the diffusivity, concentration, and composition of corrosion products to be estimated^{9,11,12,15}. Corrosion rates are indirectly inferred. Approaches to estimate corrosion rate, such as mass change measurement^{7,16-19}, EIS^{14,20-22}, and Tafel extrapolation from linear sweep voltammetry (LSV) scans^{10,23,24} have been reported. Often a single method is favored in each report. The corrosion rate can be estimated from these tests, but the published data has shown standard deviations up to 50%⁷.

One combination of these approaches focused on developing a simple *in situ* method to determine corrosion in a high-temperature molten salt process⁶. An electrode-array mini-sensor consisting of a tungsten (W) working electrode (WE), platinum counter electrode (CE), and platinum reference electrode (RE) was developed to measure impurity-driven corrosion of T91 alloy by a fission product, europium, in

the LiCl– KCl eutectic molten salt. The mini-sensor was confirmed to be an appropriate probe for *in situ* corrosion monitoring in high-temperature chloride molten salt. Concentrations of the dissolved solubilized corrosion products were detected by the developed mini-sensor, determined from cyclic voltammetry (CV) reduction peaks (soluble/insoluble) and were compared with inductively coupled plasma mass spectroscopy (ICP-MS) data at the end of the corrosion process. Another study, in which the multifunctional voltammetry sensor consisted of inert in MgCl₂-KCl-NaCl salt tungsten electrodes (an array of four 0.1 cm diameter tungsten WEs with fixed height differences, a 0.3 cm diameter W CE and a 0.1 cm diameter W quasi-RE) was developed to measure the concentration of key corrosion products and corrosive impurities in the heat transfer fluid using CV method²⁵. This study showed a good correlation with errors in not more than 4% for the model corrosion systems containing known concentrations of Fe(II) and Cr(II) cations. Unfortunately, the W electrode was not stable when polarized at highly anodic potential regime[26]. To address this gap and opportunity, a technique that is currently not available commercially, was developed herein to simultaneously track the fate of the Cr(II) and Cr(III) species and determine the concentration of both soluble and insoluble corrosion products as well as relate these quantities to the electrochemical corrosion behavior of metal or alloys in molten fluoride salts.

The objective of this work was to develop an *in situ*, multi-electrode technique to provide temporal information regarding the corrosion processes and rates of metals and alloys in molten FLiNaK salts using corroborating simultaneous application of several methods. The exposure of Cr metal in FLiNaK salts at 600 °C was selected as a model system for investigation since an understanding of Cr corrosion chemistry, thermodynamics, and electrochemical kinetics are pertinent to a number of structural alloys^{4,27}. This work considers the fate of the corrosion products Cr(II) and Cr(III) both in the dissolved state as well as when present in any precipitated corrosion products, such as salt films. The viability of using an auxiliary electrode to determine the concentration of corrosion products at the Cr surface via redox process and diffusional concentration field analysis was examined. This analysis enabled tracking of both the oxidation potential relative to the corrosion potential and to determine the corrosion rate or mass loss during the process of open-circuit potential (OCP) corrosion of Cr in FLiNaK. This work reports the possibility of using the electrochemical techniques to determine Cr mass loss instantaneously when Cr is exposed to 600 °C FLiNaK salts for 50 h. The results of half-cell redox potentials and peak currents pertaining to oxidation/reduction of Cr corrosion products were both correlated with the concentrations of particular Cr species, and compared with the long-term OCP for insights on mixed potential theory of spontaneous corrosion in an unpurified MS. The findings were compared with the results of mass loss experiment, XRD salt film analysis and *ex situ* ICP-OES of post-exposed FLiNaK. The viability of this *in situ* method is discussed. Additionally, Appendix #1 consists of an extended study that investigates and optimizes the use of EIS to accurately determine the charge-transfer resistance (R_p) in molten FLiNaK salts.

Materials and Methods

Metal and salts preparation

High purity Cr (99.995% of Cr, with trace amount of Na 0.2 ppm and Li 0.5 ppm) was purchased from Alfa Aesar. The rectangular Cr sample with the dimensions $20 \pm 2 \text{ mm} \times 13 \pm 1 \text{ mm} \times 1.5 \pm 0.5 \text{ mm}$ was cut and gradually ground on all faces using SiC paper up to 1200 grit. The LiF-NaF-KF eutectic salt (FLiNaK) was used as an electrolyte in this study prepared by mixing 46.5 mol% LiF (99.85% purity, Fisher Scientific), 11.5 mol% NaF (99.9% purity, Fisher Scientific), and 42 mol% KF (>99% purity, Fisher Scientific) salts. All salts were dried in a vacuum oven (Napco, USA) at $100 \text{ }^\circ\text{C}$ for 48 h and immediately transferred to a nitrogen-filled (with oxygen and H₂O controlled below $< 0.1 \text{ ppm}$) glove box (UNILab MBraun, USA). Weighting and mixing of the salts were done inside the glove box. The salt mixture was heated to $600 \text{ }^\circ\text{C}$ and held there for 3 h under ultra-high purity N₂ gas (99.999%) before each test. In a recent work²⁷, the authors utilized CV, square wave voltammetry, and cell-voltage measurements on a Pt WE electrode to identify and elaborate the role of impurities during electrochemical measurements. Our prior measurement shows an estimate of approximately 79.4 ppm of O²⁻ and at least 20 ppm of HF were present in our salts. Further discussion is directed to our prior work²⁷.

Multi-electrodes molten salt electrochemical cell

Figure 1 shows the apparatus developed to perform the *in situ* electrochemical measurement. The experiment was performed in a glove box.

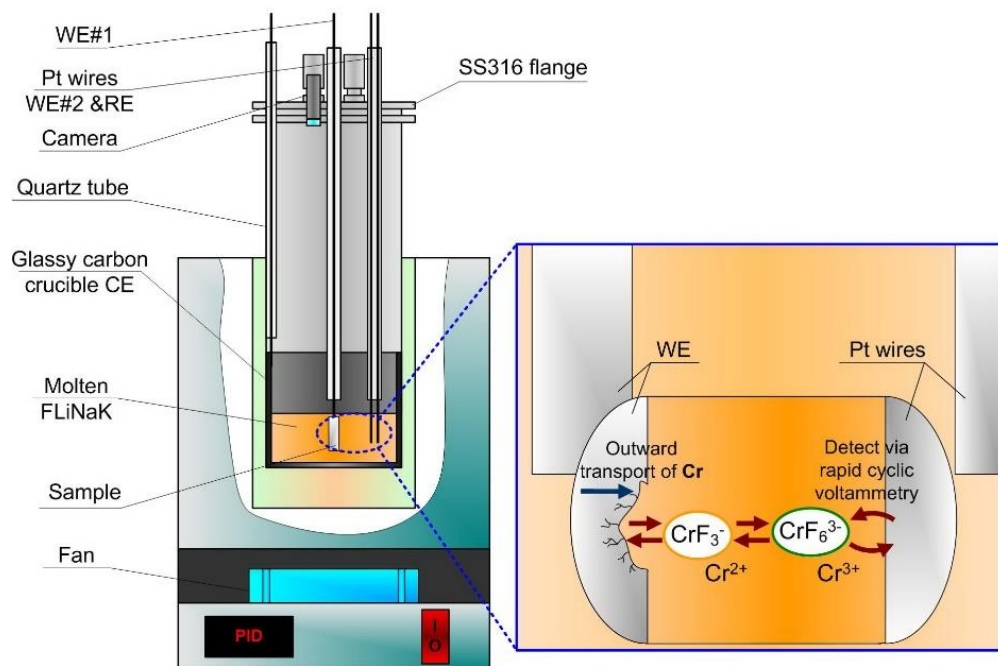


Figure 1. Schematics of the multi-electrode molten salt electrochemical cell.

A glassy carbon crucible (99.999%, Fisher Scientific) was used as both the salt container and counter electrode. A 5 mm Pt wire (99.997%, Alfa Aesar™) was used as a Pt/PtO/O²⁻ quasi-reference electrode (RE). Two working electrodes were inserted into the salt. The first WE (WE#1) comprised the Cr test coupon spot welded to a Ni600 wire (TLP Science Inc.). The welded location was coated with boron nitride paste to avoid any possible contact with the molten salt. The second WE (WE#2) was a Pt wire placed approximately 8 mm away from WE#1. A glassy carbon crucible was employed as the counter electrode (CE) and salt container. This electrode configuration setup enables diffusion analysis to estimate the Cr(II) and Cr(III) concentrations released into the cell. In one of the experiments, Pt wire (WE#2) was substituted with Pt foil with dimensions 20 mm × 10 mm × 0.025 mm to obtain a Cr-containing salt film appropriate for further X-Ray Diffraction analysis. The immersion depth of both WE#1 and WE#2 was measured after the experiment to determine the respective areas exposed. A digital camera was used to ensure that electrodes were not in contact during insertion or subsequent testing. All the electrodes were fed through an alumina tube and placed in a quartz tube to ensure sturdy connections.

Electrochemical methods with dual working electrodes

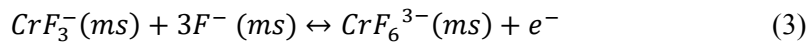
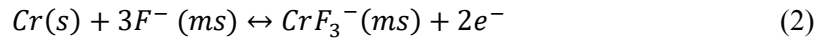
Two potentiostats (Gamry Interface 1000) were synchronized for dual-electrodes electrochemical measurements. Prior to the electrochemical experiment, a CV scan at a rate of 100 mV/s was performed to detect possible reducing or oxidizing species in the molten FLiNaK salts as shown in Figure 2a. Toward the negative/cathodic terminal of the potential scan, a rapid rise in cathodic current densities was observed possibly attributing to the reduction of potassium cation (K⁺)⁸ on the Pt wire (WE#2) via reaction (1). The equilibrium potential for reaction (1), marked in Figure 2a, was used as a pseudo reference potential (V_{K+/K}). Other methods, such as galvanostatic hold^{11, 12, 28, 29–31}, may also obtain this potential value.



The Cr coupon (WE#1) was exposed to the FLiNaK salts for 50 h and corroding spontaneously by the presence of impurities in the salts. The OCP of WE#1 was measured during the static exposure vs. V_{Pseudo K+/K}. It was noted that the Cr coupon was approximately 8 mm away from the Pt wire and less than 5 mm away from the crucible wall. On the Pt wire (WE#2), CV at scan rates of 1000, 500, 250, and 100 mV/s with a step size of 5 mV/s were collected every hour. Each CV series required about 2 min. Fast scan rates were selected to minimize the possible impact caused by a short-duration, local changes in dissolved Cr concentration arising from instantaneous corrosion from the Cr coupon (WE#1).

Estimation of dissolved corrosion product concentration

Based on literature research, the dissolved Cr species in FLiNaK salts may exist in the forms of CrF_3^- and CrF_6^{3-} species^{11,12,28,29-31}. WE#2 was subjected to CV scans periodically from 1.6 $V_{\text{Pseudo K+/K}}$ to 2.0 $V_{\text{Pseudo K+/K}}$ upward and 0.6 $V_{\text{K+/K}}$ downward scan for 2 cycles with 4 scan rates (1000 mV/s; 500 mV/s; 250 mV/s; 100 mV/s) acquired in succession with each period taking 2 min. The second cycle was used for the analysis. During the periodic WE#2 CV scan, two redox reactions: Cr/CrF_3^- (reaction 2) and $\text{CrF}_3^-/\text{CrF}_6^{3-}$ (reaction 3) were detected, which have been shown to be quasi-reversible^{11,12,28,29-31}.



Quasi- or fully reversible means that their peak current densities were found to display a linear relationship with the square root of the scan rate utilized and are applicable to both reaction (2) and reaction (3)^{11,12,29,30-32}. Massot et al.¹² and Wang et al.¹¹ demonstrated that this linearity relationship suffices up to a scan rate of 600 mV/s. In this work, fast scan rates between 100 and 1000 mV/s were selected to avoid significant changes in the bulk concentration of corrosion products due to ongoing corrosion during CV scans.² Nevertheless, this foundation permits the use of established analytical models, such as the Randles-Sevcik and Berzins-Delahay relations, to extract the concentrations of CrF_3^- and CrF_6^{3-} species from the slope of the i_p versus $v^{1/2}$ plot over the range of scan rates utilized in this work. For the Cr/CrF_3^- peak, the Berzins-Delahay relation, or Eq. (4), was used since the Cr(II) or Cr(III) when reduced on the Pt wire surface are considered to be soluble in the FLiNaK salt^{12,33,34}. For the $\text{CrF}_3^-/\text{CrF}_6^{3-}$ peak, the Randles-Sevcik relation, or Eq. (5), was applied to obtain the concentration of CrF_6^{3-} :^{11,12,33,35}

$$i_p = 0.61zFC_b \left(\frac{zFD}{RT} \right)^{1/2} v^{1/2} \quad (4)$$

$$i_p = 0.446zFC_b \left(\frac{zFD}{RT} \right)^{1/2} v^{1/2} \quad (5)$$

where D is the diffusion coefficient in molten salts for the oxidizing or reducing species in cm^2/s ; z is the number of electrons exchanged to complete the half-cell reaction a single time; F is the Faraday's constant 96485 C/mol e^- ; C_b is the bulk concentration in mol/cm^3 ; D is diffusivity in cm^2/s ; v is the scan rate in V/s; T is the temperature in Kelvin; and R is the universal gas constant 8.314 J/mol·K. The diffusivities of CrF_3^- and CrF_6^{3-} at 600°C in FLiNaK salts were reported to be $2.55 \cdot 10^{-5} \text{ cm}^2/\text{s}$ and $7.74 \cdot 10^{-6} \text{ cm}^2/\text{s}$, respectively¹¹.

Corrected half-cell oxidation and reduction potential

The peak potential values measured from the CV are defined by the concentration of CrF_3^- and CrF_6^{3-} species at the location of the Pt electrode (WE#2) measured along the semi-infinite diffusion profile (will be discussed in the Results section). However, the Cr(II) and Cr(III) activities will be greater at the actual Cr surface due to the concentration gradient assuming no stirring to mix uniformly. Therefore, a slight adjustment can be applied to determine the actual oxidation and reduction peak potentials based on the slightly greater Cr surface concentration using the half-cell reactions. Nernst Eq. (6) applied to reactions (2) and (3) to correct the measured peak potential. In the case of (2):

$$E_{1/2} = E^0 + \frac{2.303RT}{zF} \log \left(\frac{a_{\text{CrF}_3^-}}{a_{\text{P}^-}^3} \right) \quad (6)$$

The correction factor potential that results from the difference in dissolved species activities between the Cr surface (WE#1) and Pt wire surface (WE#2) can be obtained by their respective forms of Nernst Equation, resulting in Eq. (7):

$$\Delta E_{\text{correction factor}} \sim \log \left(\frac{C_{\text{CrF}_3^- \text{ Pt location}}}{C_{\text{CrF}_3^- \text{ surface}}} \right) \quad (7)$$

A corrected CV peak potential value can be found using Eq. (8).

$$E_{\text{near surface}} = E_{\text{measured}} + \Delta E_{\text{correction factor}} \quad (8)$$

Static or open-circuit immersion tests

To evaluate the validity of the calculated concentration via the coupled CV and diffusion analysis, the mass loss of a Cr coupon was separately obtained. A Cr coupon (10 mm × 1.5 mm × 3 mm) was exposed in a boron nitride crucible for 10, 20, 30, 40 and 50 h. The salt-to-coupon weight ratio of the immersion experiments was identical as in the case of electrochemical experiments. The mass of each sample was measured before and after immersion tests. Post-exposure samples were sonicated in 1 M $\text{Al}(\text{NO}_3)_3$ and DI water until visible salt products were removed¹⁷.

ICP-OES analysis

Additionally, to ensure the accuracy of calculated concentration values, inductively coupled plasma-optical emission spectrometry (ICPOES) analysis was performed on the pre- and post-experiments, solidified FLiNaK salts to measure the concentration of dissolved Cr(II) or Cr (III) and check for other cation impurities. Salts were ground to obtain a well-mixed powder. Three portions of salts were weighted and transferred into a quartz vessel. 10 mL of concentrated nitric acid (HNO_3), 1 g of boric acid (H_3BO_3 ,

measured by the scale in the glove box), and 5 mL of deionized (DI) water (produced by a Milli-Q system with a resistivity of 18.2 MΩ-cm) were added to the vessel and stirred. The vessel was assembled by applying a fresh silicone cap and placing inside a microwave digestion system. Result of the as-prepared FLiNaK salts is shown in Table 1.

Table 1. Chemical composition of as-solidified FLiNaK salts before and after 50 h of Cr immersion, mg/kg

Element	K	Li	Na	Cr	Ca	Ge	Rh	Zr	Pt	Ce	Sr	Te	Gd
FLiNaK as-prepared	251291 ±835	47618 ±67	23810 ±43	125 ±3	628 ±61	370 ±35	125 ±8	54 ±2	36 ±5	54 ±8	–	104 ±15	–
FLiNaK after 50 h of Cr exposure at OCP	329133 ±5269	79154 ±876	27633 ±280	1038 ±12	301 ±13	500 ±42	84 ±16	17 ±1	–	–	4	–	12 ±1

X-ray diffraction analysis

The compositions of FLiNaK as-prepared FLiNaK and after Cr corrosion tests, and regions of solidified FLiNaK salts on Cr and Pt, were analyzed by *ex situ* using the Malvern-Panalytical Empyrean diffractometer. Salts were ground to a powder and well-mixed using a mortar and pestle. XRD scans were collected using a detector with Cu-Kα radiation [$\lambda_{\text{Cu K}\alpha}$ (1.5405 Å)] at the region from 10 to 95 2θ degrees with 0.1° step size. Diffraction peaks were analyzed using the PDF₄⁺ database in the HighScore Plus software. Rietveld refinements were employed. The peak profile was refined by the pseudo-Voigt function.

Estimation of total Cr Mass Loss

To estimate the total Cr dissolved during the OCP corrosion process, Eq. (9) can be used:

$$\Delta m(\text{Cr}_{\text{lost}}) = \Delta m(\text{Cr}_{\text{film}}) + (\Delta m \text{ Cr}_{\text{MS}}) \quad (9)$$

where $\Delta m(\text{Cr}_{\text{lost}})$ is the total amount of Cr corroded in mg/cm² present in the MS and salt film normalized to test area where $\Delta m(\text{Cr}_{\text{film}})$ is the amount of Cr precipitated per unit area of the sample surface, calculated from the XRD Rietveld refinement in mg/cm²; $\Delta m(\text{Cr}_{\text{MS}})$ is the mass per unit area of Cr(II) and Cr(III) dissolved in the molten salts, determined by the CV method in mg/cm².

Results

In-situ corrosion product detection

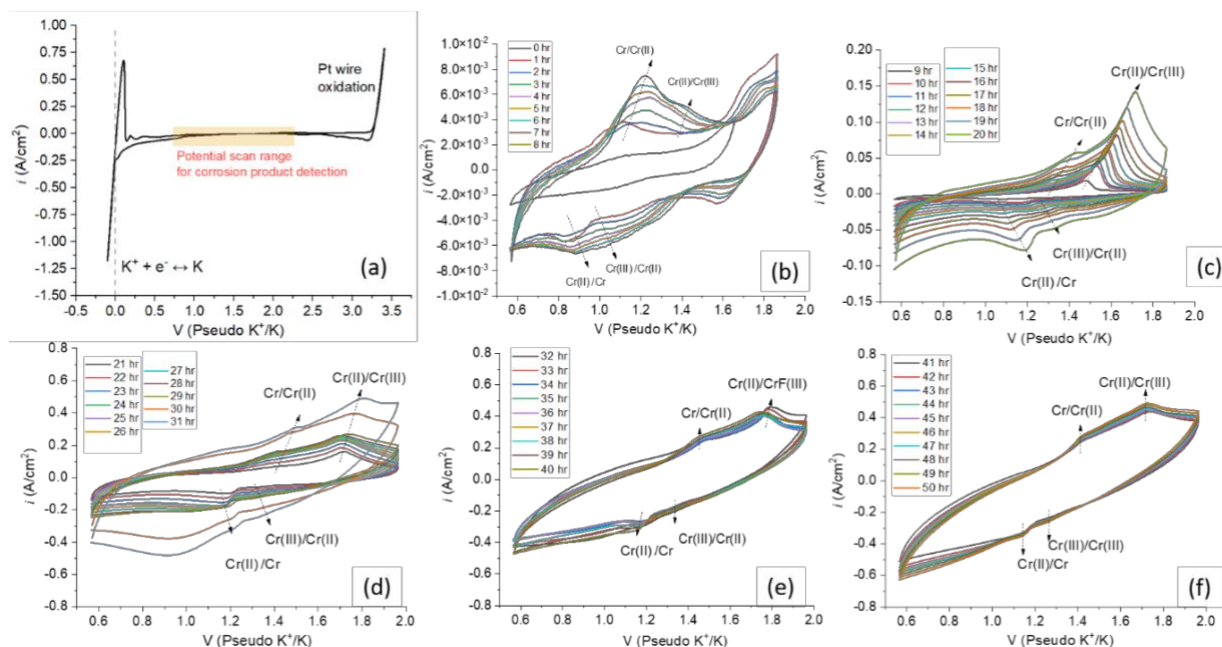


Figure 2. Cyclic voltammogram of Pt in unpurified FLiNaK salts at 600 °C 8 mm away from the Cr metal at 100 mV/s. (a) shows the baseline CV curve before Cr immersion. The orange box highlighted the CV potential scan range for (b) through (f) shows the Pt-CV curve from 0 to 50 h of Cr exposure. The current peaks pertaining to the half-cell redox reactions of Cr/Cr(II), Cr(II)/Cr(III), Cr(III)/Cr(II), and Cr(II)/Cr were marked on the CV curves with the black arrows.

The X-Ray diffractogram of the residual salt after 50 h of Cr exposure is shown in Figure 3. Compounds pertaining to the CrF_3^- and CrF_6^{3-} species were identified from the fitting of diffraction peaks. The CrF_3^- species has a Cr oxidation state of + 2 and was also found as the KCrF_3 (peak 9). The CrF_6^{3-} specie has a Cr oxidation state of + 3 and was manifested in the form of K_3CrF_6 (peak 8). There are other CrF_3^- and CrF_6^{3-} containing compounds as identified by XRD such as K_2NaCrF_6 (peak 7) and NaCrF_3 (peak 6). These two species (CrF_3^- and CrF_6^{3-}) validate the choice of Cr half-cell reactions (2) and (3) to describe the corrosion process. Figure 2 depicts the CV curves on a Pt wire in FLiNaK during each hour of Cr exposure in FLiNaK salts at 600 °C. The 0 h curve shows no presence of any redox couples indicated by absence of reduction/oxidation current peak maximums.^a Between 1 and 8 h, a noticeable development of the two redox couples described by reactions (2) and (3) were observed by their increasing peak current densities, corresponding to the characteristic Cr/Cr(II) (2) and Cr(II)/Cr(III) (3) reactions^{11,12,28,31,36}. Both peak

^a A small amount of Cr(III) could be dissolved from the native air oxide film formed on the surface of the Cr sample. Assuming that film is Cr_2O_3 [38,39] of 5 nm thick the concentration of Cr(III) released into FLiNaK is about 10 $\mu\text{mol/L}$.

potentials gradually shifted to a more positive magnitude (shown by the arrow in Figure 2) over time due to the increasing activities of the oxidized Cr species as predicted by the Nernst theory³⁷. This also indicates that the Pt wire (WE#2) detected the oxidized species released from the corrosion of Cr (WE#1). The reduction peak for Cr(III)/Cr(II) was observed; however, the peak was shallow. This may be because CrF_6^{3-} has a diffusivity in FLiNaK that is about one order of magnitude slower than that of CrF_3^- at 600 °C. The oxidation and reduction peaks at above + 1.7 V_{Pseudo K+/K} are attributed to reactions involving impurities (e.g. O^{2-} because of moisture). These redox peaks were expected to decrease with time as they were depleted and new corrosion products with Cr(II) and Cr (III) were formed.

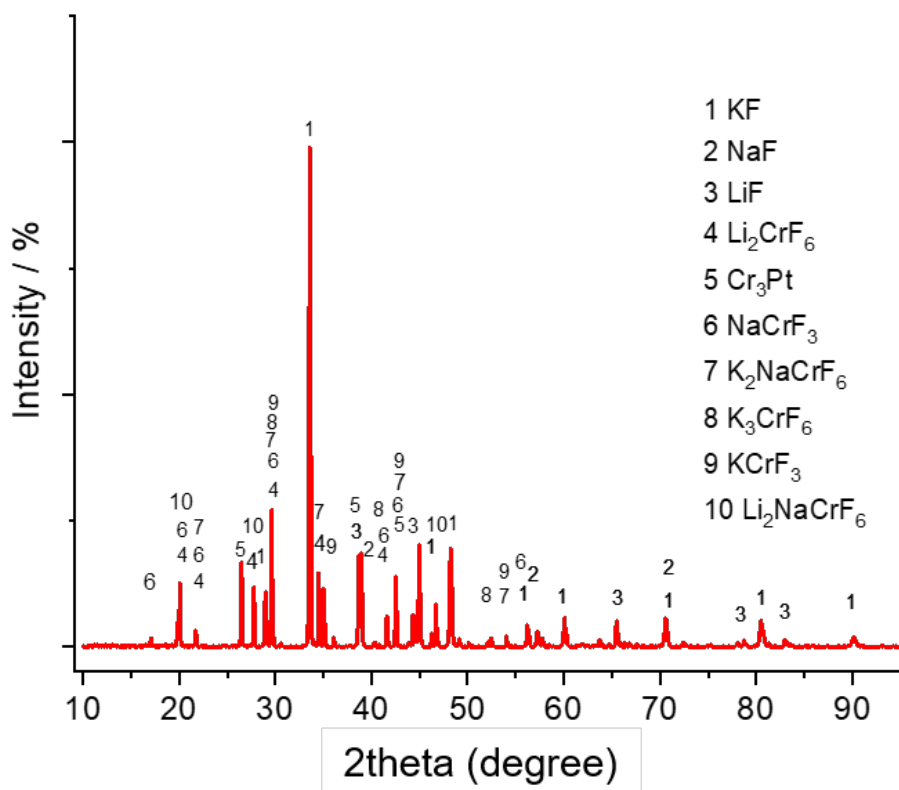


Figure 3. X-Ray diffractogram of residual unpurified FLiNaK salts after 50 h of Cr corrosion at 600 °C (cooling rate ~20 °C/min).

Starting from the 9 h to until the 20 h (Figure 2c), WE#2 current density returned to a steady, non-faradaic region at potentials significantly different from the oxidation and reduction peaks. The non-faradaic current may correspond to double-layer charging [40]. This can be seen in Figure 2b in the 2 to the 8 h scans. However, at the onset of 30 h (Figure 2d through f), the Pt wire (WE#2) did not return to the flat non-faradic region seen in the beginning cycles. This may suggest the formation of an electrochemically reactive, electrically conductive, surface film with a finite resistance deposited on the electrode substrate²⁸. It should be noted that the non-faradaic current (where $C_{dl} \cdot \text{scan rate} = i_{\text{non-faradaic}}$) will increase with scan rate and an ohmic voltage ($E_{IR} = i_{\text{non-faradaic}} R_{\text{film}}$) is now present giving rise to voltage changes with $E + E_{IR}$

and $E-E_{IR}$ depending on scan direction. While Cr was corroding (i.e., adding Cr(II) and Cr(III) to the salts in the form of their fluorides), the CV on the Pt wire was continuously performed in the range between 2.25 and 0.85 $V_{Pseudo\ K+/K}$ (marked by yellow rectangle in Figure 2a) and terminated at 2.25 $V_{Pseudo\ K+/K}$ after each scan. Recall that the oxidation peak for Cr(II)/Cr(III) (3) stabilized near 2.0 $V_{Pseudo\ K+/K}$. Here it is possible that an excess concentration of Cr(III) species remains near the Pt surface that resulted in the formation of the salt film, and such effect became more favorable as more Cr was added to the salt by corrosion. This experiment was replicated with a clean Pt foil as the second WE#2 to identify the presence of any surface film. Upon removal from the molten salt, the existing surface of the Pt foil was analyzed with the XRD method as shown in Figure 4.

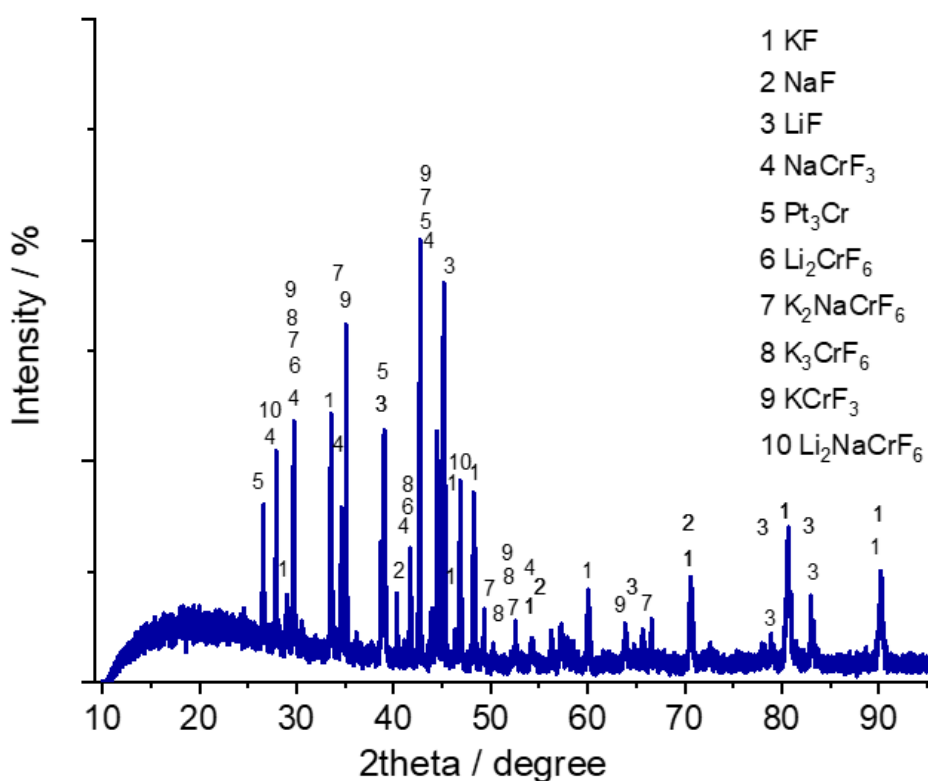


Figure 4. X-Ray diffractogram of the salt film formed on the Pt foil after 50 h of Cr exposure in unpurified FLiNaK salts.

The diffraction patterns in Figure 4 show the presence of metal fluoride compounds, including Li_2CrF_6 (peak 6), K_2NaCrF_6 (peak 7), K_3CrF_6 (peak 8), $KCrF_3$ (peak 9), and Li_2NaCrF_6 (peak 10), that confirm the presence of a salt film. As a proof-of-concept, an identical CV experiment was replicated with only the modification that the Pt wire (WE#2) was inserted into the molten salt at the end of the 50 h Cr exposure instead. The comparison between the cyclic voltammogram measured with a Pt wire (WE#2) continuously exposed and freshly inserted (scan rates between 100 and 1000 mV/s) is displayed in Figure 5. It can be

seen in Figure 5b that when the freshly inserted Pt wire (WE#2) yields a cyclic voltammogram with enhanced clarity of the Cr/Cr(II) and Cr(II)/Cr(III) redox peaks and an absence of surface-film related background E-i behavior. Despite the shape disparity of the cyclic voltammograms, identical peak current densities for the Cr(II)/Cr reduction reaction (black dot in Figure 5c) and Cr(II)/Cr(III) oxidation reaction (red dot in Figure 5c) can be obtained from the graphical analysis³³. However, it is obvious that the resistive non-faradaic salt film presence gives rise to E-i response creates a background E-i profile that could obscure accurate extraction of peak potential and current densities for further quantitative analysis.

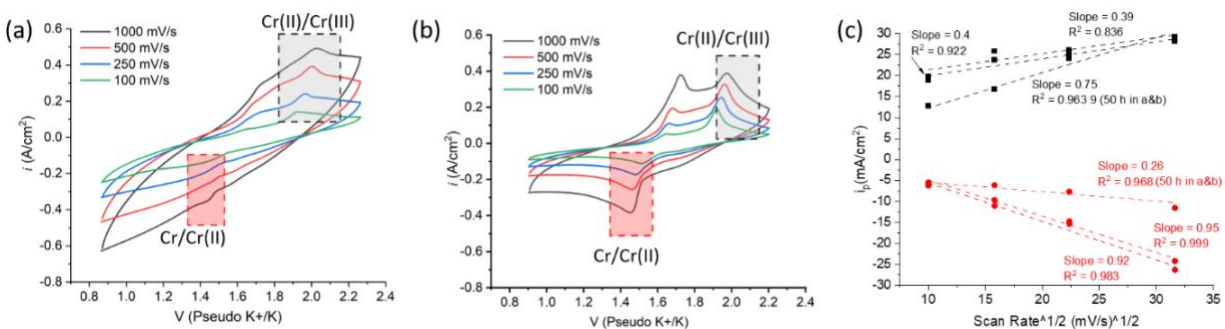


Figure 5. Cyclic voltammograms of a platinum wire (a) that was continuously exposed to or (b) separately inserted into the FLiNaK salts at 50 h at various scan rates. (c) shows the peak current densities plotted versus the square root of scan rates.

Assessment of total Cr(II) and Cr(III) supplied by electrodisolution

The calculated concentration of Cr(II), Cr(III), and their combined value during the 50 h of Cr exposure in FLiNaK are presented in Figure 6. From 5 to 20 h, the concentration of Cr species increased linearly with time, which marks the initial, rapid Cr corrosion. Onward to the end of exposure at 50 h, the detected Cr species began to approach a plateau of 0.035 M, which is close to the CrF₃ saturation value of 0.055 M, as indicated by the dashed line in Figure 6a. It was reported that the CrF₆³⁻ species is more thermodynamically stable than CrF₃⁻,⁴¹ and yet still exhibits an equilibrium relationship with the CrF₃⁻ species¹¹. This is consistent with Figure 6a in that the CrF₆³⁻ concentration is larger than that of CrF₃⁻. (Table 1).

Table 2. Concentration (mol/L) of dissolved Cr in FLiNaK salts determined through CV and ICP-OES methods

Method	Pt Wire CV – Method	ICP-OES Analysis
Cr	0.0355	0.0399
CrF ₃ ⁻	0.00309	-
CrF ₆ ³⁻	0.0324	-

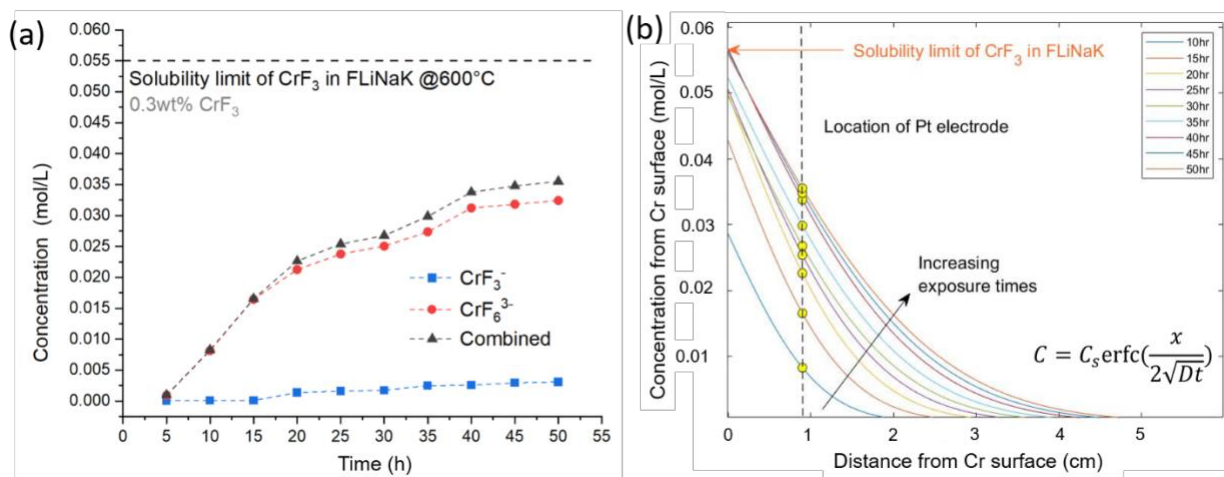


Figure 6. (a) Calculated concentrations of CrF_3^- , CrF_6^{3-} species and their combined value from cyclic voltammetry results are shown in Figure 2. (b) shows the semi-infinite diffusion profile for Cr species reconstructed using results from (a) between 10 and 50 h.

The concentration determined by the Pt-CV method was compared with that measured using ICP-OES analysis as shown in Table 2. The post 50 h Cr exposure FLiNaK salt was found to exhibit 0.0399 M of Cr, which exhibited only a 12.4% difference from the concentration of Cr obtained by the Pt-CV method. In order to fully explore the electrodisolution of Cr and the accumulation of Cr(II) and Cr(III), the fate of all oxidized Cr must be ascertained. The optical photograph of Cr sample after 50 h of corrosion in FLiNaK (Figure 7a) shows the solidified salt layer on the Cr surface, much darker than the usual color of post-exposed FLiNaK (white with a slight green color shade). It could be seen that the layer contained two different bilayers – Region (a) – the inner one of green color, and Region (b) – the outer one of dark green color. These layers were carefully fractured to reveal different regions that are not visually and chemically homogenous, and examined by XRD.

The X-Ray diffractograms presented in Figure 7c show the composition of solidified pure FLiNaK as a baseline and compositions of the salt bilayer at Regions (a) and (b) from Figure 7a. The analysis of the XRD patterns revealed the chemical differences in layers. Both the inner green layer at the Region (a) and the outer dark green layer at the Region (b) contained the initial FLiNaK salt components (KF, NaF, LiF) and Cr(II) and Cr(III) species in the forms of KCrF_3 (peak 5) and K_2NaCrF_6 (peak 4), respectively. The salt layer from the Region (a) was 2.5 times richer in K_2NaCrF_6 than the salt layer from the Region (b) ($36.7\text{ wt}\%$ vs. $14.3\text{ wt}\%$) while the content of KCrF_3 was found less than $0.1\text{ wt}\%$ for Regions (a) and (b) according to the Rietveld refinement calculation. The growth of the salt film layer thickness on the Cr surface was obtained microscopically²⁷, gravimetrically, and by XRD for 50 h of OCP corrosion with a step of 10 h, and the determined Cr mass is presented in Table 3.

Table 3. Salt film layer thickness and Cr mass in the film determined microscopically, gravimetrically and by XRD

Time (h)	Salt film layer thickness, mm	Cr mass in the film, mg
10	0.30±0.04	5.0±0.67
20	0.39±0.04	6.5±0.66
30	0.72±0.13	12.1±1.31
40	0.97±0.19	16.2±3.17
50	1.24±0.17	17.9±2.39

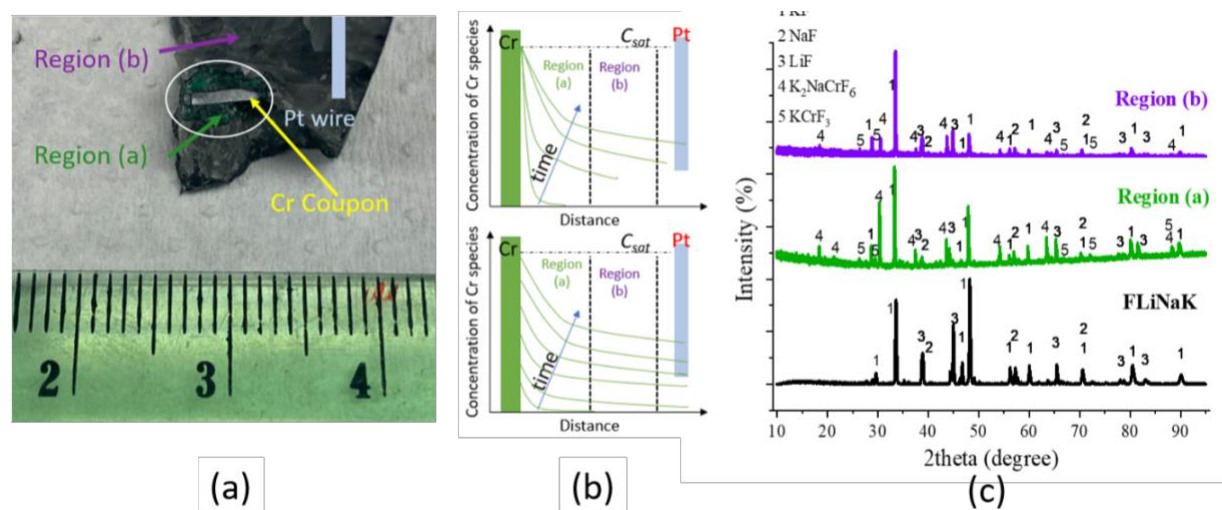


Figure 7. (a) Photograph of post-exposure FLiNaK salts fractured to reveal the location of Cr metal, bulk salt “Region (a)”, salt film “Region (b)”, and the location of a Pt electrode; (b) shows the schematics illustrating the development of a corrosion product concentration profile; (c) shows the X-Ray diffractogram of the different regions highlighted in (a) and unpurified FLiNaK before corrosion (black line) for comparison.

The distribution of Cr in the salt are proposed in Figure 7b. In the first case, the distribution and salt film formation begin after reaching the saturation limit of Cr(III) in FLiNaK. In the second case it starts from the very beginning of Cr corrosion. Each case shows that Cr species distribution into FLiNaK as well as the formation of salt films on Cr and Pt increases with the time of corrosion. This became the basis for the development of a diffusion model that could help to explain the concentration profile and to reconcile the Pt-CV measured Cr concentrations with those determined by ICP-OES and mass loss.

Cr(II) and Cr(III) species could be detected throughout the entire volume of the salt on both working electrodes. However, as the Cr metal was statically exposed to FLiNaK, the highest concentration of Cr corrosion products was found near the surface of the Cr working electrode (see Figure 7a). A concentration profile develops for both Cr(II) and Cr(III) in an unstirred cell, suggesting that the Pt wire of radius r was

only sampling dissolved Cr(II) and Cr(III) at one point along the concentration field of the chromium fluorides diffusing out into the molten salt. Therefore, Eq. (10) was utilized as the most straight forward approach to describe the time-dependent concentration profile of corrosion products. In this case, diffusion is assumed to occur under semi-infinite planar diffusion for Cr planar electrode:

$$C(x, t) = C_s(t) \operatorname{erfc}\left(\frac{x}{2\sqrt{Dt}}\right) \quad (10)$$

Boundary conditions applicable to Eq. (10) are listed from (11) to (13):

$$C_s(x = 0) = 0 @ t = 0 \quad (11)$$

$$C_s(x = 0) = C_{sat} @ t = \infty \quad (12)$$

$$C(x = \infty) = 0 \text{ at all } t \quad (13)$$

where x is the distance from the Cr metal surface (WE#1), $C(x,t)$ is the concentration at x for time t , D is the diffusivity of the chromium fluoride species (assumed to be $10^{-5} \text{ cm}^2/\text{s}$ for calculation), C_s is the surface concentration, and C_{sat} is the 0.055 M solubility limit of CrF_3 in FLiNaK at 600°C . Since the surface concentration C_s was expected to change during Cr corrosion until saturation is reached, C_s was recalculated over time using Eq. (10) with a known Cr-F species concentration (Figs. 6a) and 8 mm distance between the Cr metal (WE#1) and Pt wire (WE#2). The Cr electrode is treated as a flat sheet, and diffusion may be approximated using a one-dimensional expression assuming infinite diffusion perpendicular to a planar electrode. Using the solution to Eq. (10) when $C(x,t) = 1/2$, C_s yields Eq. (14) as an initial estimate, diffusion of chromium fluoride corrosion products will require 9 h to reach the near side of the crucible wall and 322 h for the most distant cell wall. Therefore, the calculation of the first 9 h may be slightly underestimated since the ionic diffusion of corrosion products may obey a finite diffusion model. However, such an effect does not constitute major differences in the calculation of the concentration field.

$$x = \sqrt{Dt} \quad (14)$$

Figure 6b displays the calculated concentration profile of CrF_6^{3-} species in FLiNaK, 600°C relative to the position of Cr surface. Only the diffusion profiles between 10 and 50 h were plotted since the semi-infinite diffusion model likely is a fair approximation for this period. The yellow dots highlight the experimentally measured CrF_6^{3-} concentration and the vertical dotted line shows the location of the Pt wire. The total amount of dissolved corrosion products (M) and the salt film oxidized Cr content is equivalent to the total mass loss from the Cr coupon which can be determined at any time t . The Pt-CV-diffusion measurement and concentration analysis can be utilized to calculate the total dissolved mass loss due to the

Cr corrosion process. This can be approximated by spatially integrating the semi-infinite concentration profile (Eq. (15)), which results in an expression that depends only on the surface concentration, time, and corrosion products diffusivity, and were further elaborated in Figure 5c. The mass loss of Cr (Δm) is proportional to the integration of the Cr(II)/Cr(III) concentration over the salt volume as well as considering the surface area of the Cr working electrode (A_{Cr}) and the width of the Cr working electrode ($w \sim 12$ mm).^b

$$M \left(\frac{mmol}{cm^2} \right) = 1/2 C_s \int_{x=0}^{x=\infty} \operatorname{erfc} \left(\frac{x}{2\sqrt{Dt}} \right) dx \quad (15)$$

$$M'' \left(\frac{mmol}{cm^3} \right) = \frac{2C_s}{w} \left(\frac{Dt}{\pi} \right)^{1/2} \quad (16)$$

$$\Delta m \left(\frac{g}{cm^2} \right) = \frac{M'' V_{cell} A.W.}{A_{Cr}} \quad (17)$$

Figure 8 shows the calculated mass loss of Cr before (green triangle) and after (red circles) the diffusion profile adjustment using Eq. (17) to factor in the bulk concentration.

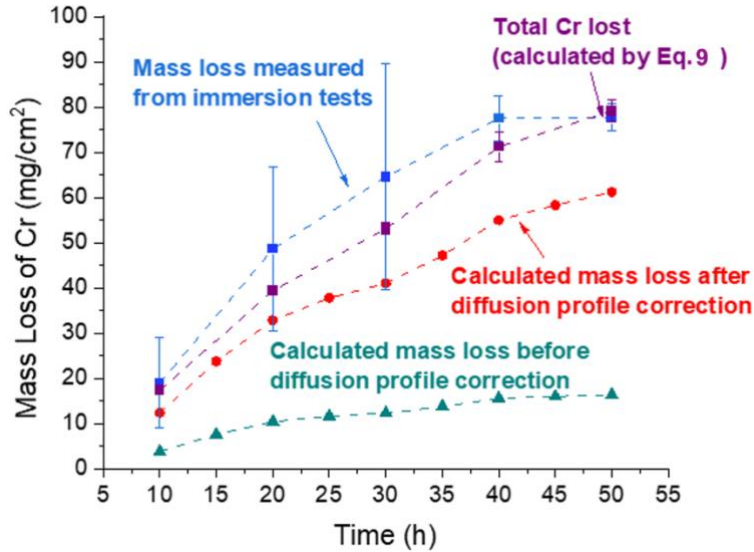


Figure 8. Mass loss measured by the static immersion method and calculated from the electrochemical CV method (with and without diffusion profile correction).

It should be noted that the calculated mass loss after correction is a sum of the amounts of Cr(II) and Cr(III) species dissolved. After the diffusion profile correction, the corrected mass loss from the CV method has a 4–5-fold increase. To verify the calculated, corrected mass loss results, a separate series of immersion experiments were performed on Cr metals over a 10–50 h period in which the weight change was gravimetrically measured. Triplicate tests were carried out to obtain a standard deviation bar for gravimetric

^b This analysis is correct for a prismatic cell of A_{Cr} multiplied by w length of the cell volume. Noted that the glassy carbon cell and geometry and volume are slightly different.

mass loss. As shown in Figure 8, results demonstrate that the Pt-CV calculated, diffusion profile corrected mass shows a reasonable agreement and is within the standard deviation of the gravimetric measurements. The rate of mass loss can be converted to penetration rate utilizing the density of Cr. The Cr dissolution rate was maximum (up to 36 mm/ yr) between 15 and 20 h as can be seen from both CV and mass loss experiments (Figure 8). Table 4 shows that mass loss reached $70 \pm 5 \text{ mg/cm}^2$ in 40 h (both CV calculated and gravimetrically measured mass loss) of the OCP corrosion experiment and plateaued in the last 10 h of the corrosion test.

Table 4. Mass loss measured by gravimetric method and calculated from electrochemical CV method (with and without diffusion profile correction)

Time (h)	Mass Loss, Δm (mg/cm ²)				
	Calculated from CV (Before Correction) <u>Cr(II)/Cr(III)</u> Dissolved in MS $\Delta m(\text{Cr}_{MS})$ in (9)	Calculated from CV (After Diffusion Profile Correction)	Calculated from the salt film $\Delta m(\text{Cr}_{film})$ in (9)	Total Cr lost $\Delta m(\text{Cr}_{lost})$ in (9)	Gravimetric measurements
10	3.8	12.4	5.0±0.67	17.4±0.67	19.0 ± 10
15	7.6	23.8			-
20	10.4	32.9	6.5±0.66	39.4±0.66	48.6 ± 18
25	11.7	37.8			-
30	12.3	41.0	12.1±1.31	53.1±1.31	64.6 ± 25
35	13.8	47.2			-
40	15.6	55.0	16.2±3.17	71.2±3.17	77.5 ± 5
45	16.0	58.3			-
50	16.4	61.2	17.9±2.39	79.1±2.39	77.6 ± 3

Figure 9 shows the Cr-OCP (black line) during the static exposure of Cr in molten FLiNaK at 600 °C. The OCP is the coupled potential between at least one cathodic reaction and one anodic reaction, thermodynamically and kinetically determined. The OCP gradually shifted towards more positive electrode potentials between 0 and 12 h, experienced a sharp increase in potential between 12 and 17 h, and stayed steady between $+ 1.4 V_{\text{Pseudo K+/K}}$ and $+ 1.5 V_{\text{Pseudo K+/K}}$ for the remaining period of exposure. The potential spikes occurring at each hour show the small potential excursion of the Pt-CV measurements. The rises in OCP are likely attributable to the accumulation of Cr corrosion products (CrF_3^- , CrF_6^{3-} or CrF_3) which shifts the anodic half-cell oxidation potential in the positive direction²⁷. The behavior observed is due to spontaneous corrosion of Cr by its electro-dissolution with impurities present as cathodic reactants. However, this analysis for half-cell Cr(II)/Cr(III) reaction peaks does not rely on exact knowledge of the impurities controlling the cathodic reaction rate.

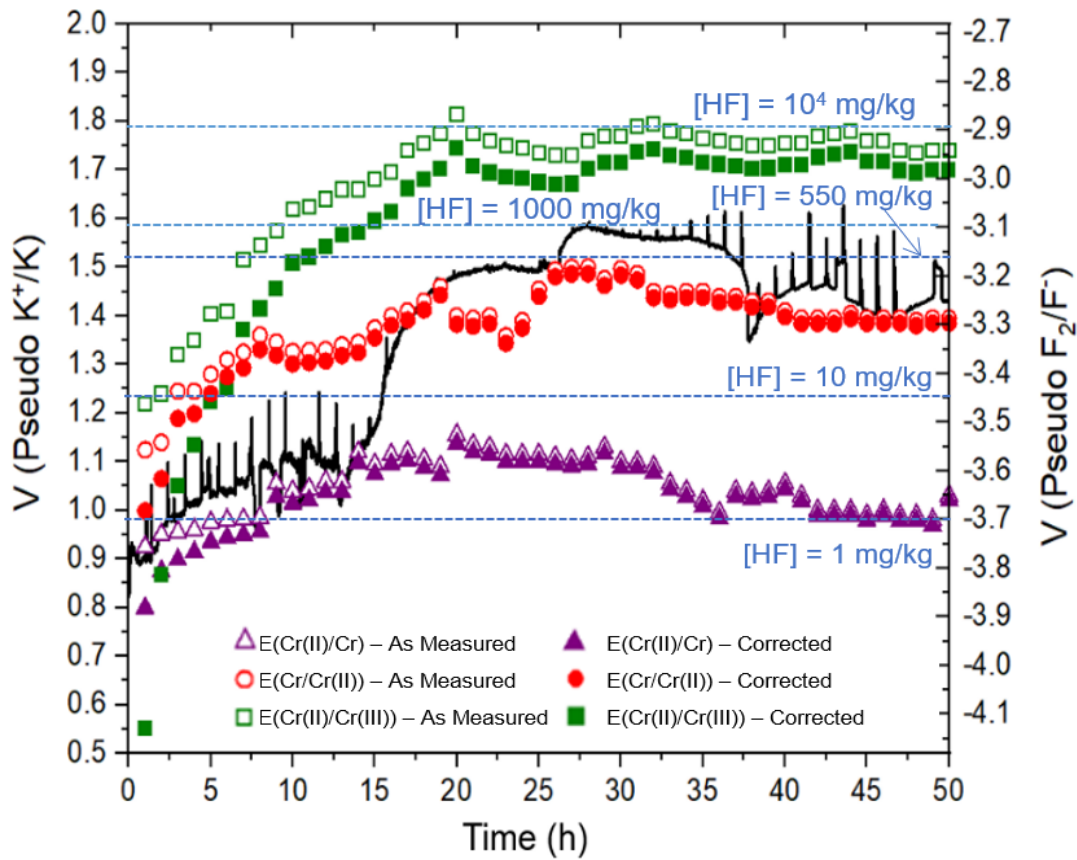


Figure 9. The open-circuit potential of Cr in FLiNaK for 50 h overlaid with square, circular, and triangular symbols representing the half-cell redox potentials of Cr/Cr(II), Cr(II)/Cr(III) and Cr(II)/Cr couples, respectively. The filled symbols represent surface concentration corrected potential values.

Discussion

The multi-electrodes molten salt electrochemical cell utilizes CV on Pt WE#2 to assess Cr/Cr(II) and Cr(II)/Cr(III) redox reactions during the instantaneous dissolution of Cr WE#1, and subsequently determining the concentrations of Cr(II) and Cr(III) species. However, the behavior of CV curves after 30 h of the corrosion experiment was different from the ideal case when the WE#2 current density returns to a steady, non-faradaic region at potentials significantly different from the oxidation and reduction peaks³³. The E-i relationship in Figs. 2d through 2f displayed a roughly linear E-i or ohmic behavior and the extent of distortion (relative to a flat, non-faradaic region) when an E-i slope increased with scan rates. This behavior has been observed in battery electrode studies and is attributed to the formation of an electrochemically reactive, electrically conductive, surface film deposited on an electrode substrate⁴², which provides an additional surface/film resistance that obscured the non-faradaic E-i response.

The experimental result with freshly inserted Pt WE# 2 after 50 h of freely Cr corrosion (Figure 5b) did not reveal any significant difference in the detected peak current values compared to 50 h of instantaneous

measured spontaneous corrosion. This suggests that film on the Pt WE#2 does not strongly influence the measured current response and the Cr(II) and Cr(III) species concentrations determined. However, the difference in the calculated concentration of Cr species obtained by Pt-CV and ICP-OES (Table 2) and in the calculated mass loss from gravimetric measurements (Table 4, Figure 8) was found significant.

Furthermore, the dark green two-layered salt film formed on the surface of Cr WE#1 suggests the presence of the concentration gradient (Figure 7). As introduced in our prior work⁴, FLiNaK salts may become saturated upon achieving 0.3 wt%⁵ of CrF₃ at 600 °C.⁴³ Upon saturation, compounds such as K₃CrF₆ may form on the Cr metal surface and this is currently being investigated by the authors. The diffusion model utilized explained this concentration profile and enabled correlation of the diffusion compensated Pt-CV measured Cr concentrations with those measured by ICP-OES and mass loss. After the diffusion profile adjustment, the corrected mass loss from the Pt-CV method had a 4–5-fold increase and showed reasonable agreement with the gravimetric mass loss, however, it was still lower because of the Cr precipitated in the salt film layer on the surface of the sample. The further correction with Cr precipitated in the salt film ($\Delta m(\text{Cr}_{\text{film}})$ in Table 4) enabled the possibility to determine the total amount of Cr lost ($\Delta m(\text{Cr}_{\text{lost}})$) during the OCP corrosion process. The total Cr lost $\Delta m(\text{Cr}_{\text{lost}})$ calculated by Eq. (9) (Figure 8, Table 4) showed a good correlation with mass loss data at all tested time frames.

The mass loss data of 70 ± 5 mg/cm² obtained in 40 h (remained the same until the end of the experiment) from both Pt-CV and gravimetric methods - are higher than those suggested in literature – 57 mg/cm² at 700 °C after 100 h of exposure in FLiNaK⁴⁵. However, it should be mentioned, that Cr corrosion was driven by impurities (in FLiNaK, oxide, etc.⁴⁴), the amount of which is likely different in our and cited studies. This work aims to evaluate, as a proof-of-concept, the *in-situ* CV method of corrosion products, and thus the FLiNaK salt was not subjected to rigorous purification, and the mass loss for Cr was expected to be high. In fact, an impure salt was useful for this analysis. Moreover, after the diffusion profile correction, a very good correlation was found between the concentration plateau and the solubility limit of CrF₃ 0.3 wt% in FLiNaK at 600 °C. With different impurities, different spontaneous corrosion rates are expected.

To understand the predominant anodic reactions that dictate the OCP of Cr rise and Cr dissolution, the peak potential values may be plotted along with the experimental OCP, which is shown in Figure 9. The OCP is the coupled potential between at least one cathodic reaction and one anodic reaction. It is determined by thermodynamics and kinetic factors. The identity of the most likely anodic and cathodic reactions can now be considered. The cathodic reaction must have a half-cell potential more positive than the OCP while the operative anodic reaction is more negative than the OCP. Figure 9 reports dotted lines reporting half-cell potentials for HF reduction. Recall that the reduction peak potential for Cr(II)/Cr (purple triangles), and oxidation peak potentials for Cr/Cr (II) (red dots) and Cr(II)/Cr(III) reactions (green squares). The correction factor's potentials ($\Delta E_{\text{correction factor}}$) were obtained by Eq. (6) and Eq. (7). The corrected peak

potential values were found using Eq. (8). The driving force for electrodisolution is the difference in half-cell potentials between the anodic and cathodic reactions. The OCP-50 h plot shows as-measured and corrected Cr redox potentials along with OCP, which are plotted in Figure 9 as symbols of identical colors and shapes without and with fill-in respectively. It could be observed that the oxidation peak potentials for Cr/Cr(II) and Cr(II)/Cr(III) reactions are similar in magnitude and very close to the OCP potential within the first ~7 h, and the rate is linear with time suggesting charge transfer control. HF reduction and Cr(III)reduction exhibit a driving force to oxidize the Cr metal⁴. Cr(III) reduction and HF reduction are both eligible cathodic reactions along with O₂ reduction.

After 7 h, the Cr/CrF₃⁻ oxidation potentials remained relatively steady but were within the statistical range in magnitude of the OCP starting at ~20 h. This possibly marks the point at which Cr/Cr(II) may no longer be the predominant anodic reaction for Cr dissolution. At the same time scale, the Cr(II)/Cr(III) potentials began to rise above the Cr/ Cr(II) potentials and OCP to a steady value near 1.73 V_{pseudo K+/K} (after correction) until the end of the measurement. These observations point to a possibility that Cr corrosion was significantly slowed down and eventually stopped starting at ~20 h when the Cr/Cr(II) oxidation potential rises sufficiently to minimize the driving force supplied by HF reduction. It can also be speculated that O₂ and HF reduction potentials become less positive as both species are depleted. Noted that the half-cell reduction potential for HF/H₂ is more positive than that of Cr(II)/Cr(III) over a wide range of realistic ion activities⁴). The OCP trend follows the same trend as that of the gravimetric mass loss (Figure 8) in which the mass loss of Cr plateaued beginning 30 h indicating decay to a very slow rate. It is not possible to conclusively report whether the pause of corrosion is due to the corrosion system reaching a thermodynamic equilibrium where there is little remaining thermodynamic driving force because half-cell potentials are similar ($E_{\text{anodic}} = E_{\text{cathodic}}$) or because of the depletion of oxidizers, e.g. Cr(III) or HF, to the point where the driving force just exists but is low and the reaction is limited.

In any case, this procedure can be followed at various impurity levels and on different alloys to shed light on the open-circuit corrosion rate. The impurity level chosen here is not selected to be representative technologically but to help elucidate the utility of the methodology and possible analysis of open-circuit corrosion. Ultimately, there is a need to improve the concentration field solutions for complex geometries of metal working electrodes for molten salt electrochemistry as most published studies utilize a “partially immersed metal sample”⁴⁶, which provides a complication for such mass transport analysis. Moreover, at the surface, there is a precipitated salt layer that also contains Cr (II) and Cr(III). Additionally, a parallel effort centers on utilizing EIS analysis to estimate the corrosion rate of metal or alloys in molten salts *in-situ* and real-time. This is further detailed in Appendix 1, which explores the use of pure Cr flush-mounted disks as the working electrode geometries to enable the accurate measurement of polarization resistance in conventionally tested frequency regime (10⁻² Hz to 10⁴ Hz) in molten FLiNaK, 600°C environment.

Conclusion

In this work, a high-temperature, multi-electrode corrosion cell was developed to measure the open-circuit potential (OCP) of a primary working electrode (pure Cr) statically submerged in FLiNaK salts at 600 °C while a secondary working electrode (Pt wire) simultaneously performed cyclic voltammetry to capture the dissolved corrosion products in real-time. The viability of using the external auxiliary electrode to measure the concentration of corrosion products and half-cell redox potentials pertaining to oxidation/reduction reactions of these products was shown by the correlation of these measurements to the corrosion regimes and behavior of alloys.

It was found that the concentration of dissolved corrosion products, in the more likely possible forms of CrF_3^- and CrF_6^{3-} , might be calculated by established analytical models, such as Berzins-Delahay (soluble/insoluble) and Randles-Sevcik (soluble/soluble) equations. The calculated values showed the definite concentration of Cr corrosion products as the function of the distance of the external working electrode (due to the static corrosion conditions). A semi-infinite diffusion model was employed in this study to correct the calculated concentrations according to a concentration diffusion profile. It was shown that the semi-infinite diffusion model helps correctly describe this profile between 10 and 50 h, based on the geometry of the working electrode and corrosion cell.

It was found that a salt film containing CrF_3^- and CrF_6^{3-} (of K^+ , Na^+ , Li^+) compounds could be formed on the surface of both Cr (working electrode) and Pt wire (detection electrode) due to the low solubility of CrF_3 in FLiNaK salts. This surface film can obscure the current signals during CV measurements by providing an additional layer possessing uncompensated resistive and capacitive responses.

The mass loss of the Cr metal was approximated by spatially integrating the concentration profiles. This can be useful for quantifying corrosion of select metals and alloys if the molten salt is unmixed. The result of Cr mass loss separately obtained from gravimetric measurements showed a reasonable agreement. Furthermore, the concentration of Cr ions in the residual FLiNaK salt after 50 h of exposure determined by ICP-OES correlated with the electrochemically and gravimetrically obtained mass loss data. In addition to this, the oxidation and reduction peak potentials pertaining to Cr/Cr(II) and Cr(II)/Cr(III) redox reactions (measured on Pt wire) were comprehensively compared with the OCP (measured on Cr) to provide insights on the predominant anodic reactions.

References

1. H. Yin, J. Qiu, H. Liu, W. Liu, Y. Wang, Z. Fei, S. Zhao, X. An, J. Cheng, T. Chen, P. Zhang, G. Yu, L. Xie, Effect of CrF_3 on the corrosion behaviour of Hastelloy-N and 316L stainless steel alloys in FLiNaK molten salt, *Corrosion Science*. 131 (2018) 355–364, <https://doi.org/10.1016/j.corsci.2017.12.008>.

2. Y. Liu, Y. Song, H. Ai, M. Shen, H. Liu, S. Zhao, Y. Liu, Z. Fei, X. Fu, J. Cheng, Corrosion of Cr in molten salts with different fluoroacidity in the presence of CrF₃, *Corrosion Science*. 169 (2020) 108636. <https://doi.org/10.1016/j.corsci.2020.108636>.
3. S. Fayfar, G. Zheng, D. Sprouster, M. Marshall, E. Stavitski, D. Leshchev, B. Khaykovich, In-situ analysis of corrosion products in molten salt: concurrent X-ray absorption and electrochemistry reveal both ionic and metallic species, (2022). <https://doi.org/10.26434/chemrxiv-2022-3nspm>.
4. H.L. Chan, E. Romanovskaia, J. Qiu, P. Hosemann, J.R. Scully, Insights on the corrosion thermodynamics of chromium in molten LiF-NaF-KF eutectic salts, *Npj Mater Degrad*. 6 (2022) 46. <https://doi.org/10.1038/s41529-022-00251-3>.
5. N. Winner, H. Williams, R.O. Scarlat, M. Asta, Ab-initio simulation studies of chromium solvation in molten fluoride salts, *Journal of Molecular Liquids*. 335 (2021) 116351. <https://doi.org/10.1016/j.molliq.2021.116351>.
6. Y. Wang, B. Goh, K. Sridharan, A. Couet, In Situ Corrosion Monitoring of the T91 Alloy in a Molten Chloride Salt Using a Miniaturized Electrochemical Probe for High-Throughput Applications, *Anal. Chem*. 94 (2022) 4012–4020. <https://doi.org/10.1021/acs.analchem.1c05196>.
7. S.S. Raiman, S. Lee, Aggregation and data analysis of corrosion studies in molten chloride and fluoride salts, *Journal of Nuclear Materials*. 511 (2018) 523–535. <https://doi.org/10.1016/j.jnucmat.2018.07.036>.
8. S. Guo, J. Zhang, W. Wu, W. Zhou, Corrosion in the molten fluoride and chloride salts and materials development for nuclear applications, *Progress in Materials Science*. 97 (2018) 448–487. <https://doi.org/10.1016/j.pmatsci.2018.05.003>.
9. W.H. Doniger, K. Sridharan, Application of voltammetry for quantitative analysis of chromium in molten 2LiF-BeF₂ (FLiBe) salt, *Journal of Electroanalytical Chemistry*. 838 (2019) 73–81. <https://doi.org/10.1016/j.jelechem.2019.02.048>.
10. S. Fabre, C. Cabet, L. Cassayre, P. Chamelot, S. Delepech, J. Finne, L. Massot, D. Noel, Use of electrochemical techniques to study the corrosion of metals in model fluoride melts, *Journal of Nuclear Materials*. 441 (2013) 583–591. <https://doi.org/10.1016/j.jnucmat.2013.03.055>.
11. Y. Wang, J. Zhang, Electrochemical Properties of CrF₂ in FLiNaK Molten Salt and the New Analytical Methods for their Determination, *J. Electrochem. Soc*. 167 (2020) 086503. <https://doi.org/10.1149/1945-7111/ab8923>.
12. L. Massot, M. Gibilaro, D. Quaranta, P. Chamelot, Corrosion Products Electrochemical Behaviour into Molten LiF-NaF: Investigation of Cr(II) System, *J. Electrochem. Soc*. 168 (2021) 026510. <https://doi.org/10.1149/1945-7111/abe088>.
13. W.H. Doniger, C. Falconer, M. Elbakhshwan, K. Britsch, A. Couet, K. Sridharan, Investigation of impurity driven corrosion behavior in molten 2LiF-BeF₂ salt, *Corrosion Science*. 174 (2020) 108823. <https://doi.org/10.1016/j.corsci.2020.108823>.
14. Y.L. Wang, Q. Wang, H.J. Liu, C.L. Zeng, Effects of the oxidants H₂O and CrF₃ on the corrosion of pure metals in molten (Li,Na,K)F, *Corrosion Science*. 103 (2016) 268–282. <https://doi.org/10.1016/j.corsci.2015.11.032>.
15. P. Zhu, Y. Zhao, Cyclic voltammetry measurements of electroactive surface area of porous nickel: Peak current and peak charge methods and diffusion layer effect, *Materials Chemistry and Physics*. 233 (2019) 60–67. <https://doi.org/10.1016/j.matchemphys.2019.05.034>.
16. Shay, Nikolas, Guo, Shaoqiang, and Zhang, Jinsuo. *Electrochemical Sensor Development for Fluoride Molten Salt Redox Control*. United States: N. p., 2017. Web.

17. F.-Y. Ouyang, C.-H. Chang, J.-J. Kai, Long-term corrosion behaviors of Hastelloy-N and Hastelloy-B3 in moisture-containing molten FLiNaK salt environments, *Journal of Nuclear Materials*. 446 (2014) 81–89. <https://doi.org/10.1016/j.jnucmat.2013.11.045>
18. F.-Y. Ouyang, C.-H. Chang, B.-C. You, T.-K. Yeh, J.-J. Kai, Effect of moisture on corrosion of Ni-based alloys in molten alkali fluoride FLiNaK salt environments, *Journal of Nuclear Materials*. 437 (2013) 201–207. <https://doi.org/10.1016/j.jnucmat.2013.02.021>.
19. K. Sridharan, T.R. Allen, 12 - Corrosion in Molten Salts, in: F. Lantelme, H. Groult (Eds.), *Molten Salts Chemistry*, Elsevier, Oxford, 2013: pp. 241–267. <https://doi.org/10.1016/B978-0-12-398538-5.00012-3>.
20. Q. Liu, H. Sun, H. Yin, L. Guo, J. Qiu, J. Lin, Z. Tang, Corrosion behaviour of 316H stainless steel in molten FLiNaK eutectic salt containing graphite particles, *Corrosion Science*. 160 (2019) 108174. <https://doi.org/10.1016/j.corsci.2019.108174>.
21. F. Carotti, E. Liu, D.D. Macdonald, R.O. Scarlat, An Electrochemical Study of Hydrogen in Molten 2LiF-BeF₂ (FLiBe) with Addition of LiH, *Electrochimica Acta*. (2020) 137114. <https://doi.org/10.1016/j.electacta.2020.137114>.
22. H. Ai, M. Shen, H. Sun, K.P. Dolan, C. Wang, M. Ge, H. Yin, X. Li, H. Peng, N. Li, L. Xie, Effects of O₂⁻ additive on corrosion behavior of Fe–Cr–Ni alloy in molten fluoride salts, *Corrosion Science*. 150 (2019) 175–182. <https://doi.org/10.1016/j.corsci.2019.01.040>.
23. W.H. Doniger, A. Couet, K. Sridharan, Potentiodynamic Polarization of Pure Metals and Alloys in Molten LiF-NaF-KF (FLiNaK) Using the K/K⁺ Dynamic Reference Electrode, *J. Electrochem. Soc.* 169 (2022) 071502. <https://doi.org/10.1149/1945-7111/ac7a66>.
24. Y. Wang, H. Liu, G. Yu, J. Hou, C. Zeng, Electrochemical study of the corrosion of a Ni-based alloy GH3535 in molten (Li,Na,K)F at 700°C, *Journal of Fluorine Chemistry*. 178 (2015) 14–22. <https://doi.org/10.1016/j.jfluchem.2015.06.014>.
25. J. Guo, N. Hoyt, M. Williamson, Multielectrode array sensors to enable long-duration corrosion monitoring and control of concentrating solar power systems, *Journal of Electroanalytical Chemistry*. 884 (2021) 115064. <https://doi.org/10.1016/j.jelechem.2021.115064>.
26. M. Ambrová, V. Danielik, Corrosion resistance of tungsten and nickel in molten eutectic mixture LiF-NaF-KF, *Acta Chimica Slovaca*. 5 (2012) 121–125. <https://doi.org/10.2478/v10188-012-0018-y>.
27. H.L. Chan, E. Romanovskaia, M. Hong, V. Romanovski, D. Sur, P. Hosemann, J. R. Scully, Corrosion Electrochemistry of Chromium in Molten FLiNaK Salt at 600°C, *J. Electrochem. Soc.* (2023), <https://doi.org/10.1149/1945-7111/ace8c0>.
28. V.V. Zakharova, A.A. Ryzhov, V.A. Volkovich, Electrochemistry of iron, nickel and chromium in LiF–NaF–KF (FLiNaK) eutectic melt: A cyclic voltammetry study, *AIP Conference Proceedings*. 2313 (2020) 050039. <https://doi.org/10.1063/5.0032424>.
29. H. Peng, M. Shen, C. Wang, T. Su, Y. Zuo, L. Xie, Electrochemical investigation of the stable chromium species in molten FLiNaK, *RSC Adv.* 5 (2015) 76689–76695. <https://doi.org/10.1039/C5RA09919F>.
30. W. Wu, Electrochemical Behaviors of Cr(III) in Molten LiF-NaF-KF Eutectic, *Int. J. Electrochem. Sci.* (2018) 225–234. <https://doi.org/10.20964/2018.01.21>.
31. D. Ludwig, L. Olson, K. Sridharan, M. Anderson, T. Allen, High temperature electrochemistry of molten fluoride salt for measurement of dissolved chromium, *Corrosion Engineering, Science and Technology*. 46 (2011) 360–364. <https://doi.org/10.1179/147842209X12579401586645>.

32. R.G. Compton, C.E. Banks. Understanding Voltammetry, Second ed., Imperial College Press, 2010, <https://doi.org/10.1142/p726>.
33. Carl H. Hamann, Andrew Hamnett, Wolf Vielstich, Electrochemistry, 2nd, Completely Revised and Updated Edition, John Wiley & Sons, Inc, 2007.
34. P. Delahay, Theory of Irreversible Waves in Oscillographic Polarography, J. Am. Chem. Soc. 75 (1953) 1190–1196. <https://doi.org/10.1021/ja01101a054>.
35. N. Elgrishi, K.J. Rountree, B.D. McCarthy, E.S. Rountree, T.T. Eisenhart, J.L. Dempsey, A Practical Beginner's Guide to Cyclic Voltammetry, J. Chem. Educ. 95 (2018) 197–206. <https://doi.org/10.1021/acs.jchemed.7b00361>.
36. T. Yoko, R.A. Bailey, Electrochemical Studies of Chromium in Molten LiF - NaF - KF (FLINAK), J. Electrochem. Soc. 131 (1984) 2590–2595. <https://doi.org/10.1149/1.2115363>.
37. D.A. Jones, Principles and Prevention of Corrosion, Prentice Hall, 1996.
38. K. Lutton, J. Han, H.M. Ha, D. Sur, E. Romanovskaia, J.R. Scully, Passivation of Ni-Cr and Ni-Cr-Mo Alloys in Low and High pH Sulfate Solutions, J. Electrochem. Soc. 170 (2023) 021507. <https://doi.org/10.1149/1945-7111/acb9c3>.
39. R. Auguste, H.L. Chan, E. Romanovskaia, J. Qiu, R. Schoell, M.O. Liedke, M. Butterling, E. Hirschmann, A.G. Attallah, A. Wagner, F.A. Selim, D. Kaoumi, B.P. Uberuaga, P. Hosemann, J.R. Scully, A multimodal approach to revisiting oxidation defects in Cr₂O₃, Npj Mater Degrad. 6 (2022) 1–13. <https://doi.org/10.1038/s41529-022-00269-7>.
40. J.R. Scully, Polarization Resistance Method for Determination of Instantaneous Corrosion Rates, Corrosion. 56 (2000) 199–218. <https://doi.org/10.5006/1.3280536>.
41. A. Kumar, C.S. Prajapati, P.P. Sahay, Modification in the microstructural and electrochromic properties of spray-pyrolysed WO₃ thin films upon Mo doping, J Sol-Gel Sci Technol. 90 (2019) 281–295. <https://doi.org/10.1007/s10971-019-04960-1>.
42. K.J. Chan, R.J. Ambrecht, J.M. Luong, W.T. Choi, P.M. Singh, Carburization effects on the corrosion of Cr, Fe, Ni, W, and Mo in fluoride-salt cooled high temperature reactor (FHR) coolant, Annals of Nuclear Energy. 120 (2018) 279–285. <https://doi.org/10.1016/j.anucene.2018.05.013>.
43. Y. Liu, Y. Song, H. Ai, M. Shen, H. Liu, S. Zhao, Y. Liu, Z. Fei, X. Fu, J. Cheng, Corrosion of Cr in molten salts with different fluoroacidity in the presence of CrF₃, Corrosion Science. 169 (2020) 108636. <https://doi.org/10.1016/j.corsci.2020.108636>.
44. J. Busby, L. Garrison, L. Lin, S. Raiman, S. Sham, C. Silva, H. Wang, R. Iyengar, G. Tartal, Technical Gap Assessment for Materials and Component Integrity Issues for Molten Salt Reactors, 2019. <https://doi.org/10.2172/1763501>.
45. S. Delpech, Céline Cabet, C. Slim, G.S. Picard, Molten fluorides for nuclear applications, Materials Today. 13 (2010) 34–41. [https://doi.org/10.1016/s1369-7021\(10\)70222-4](https://doi.org/10.1016/s1369-7021(10)70222-4).
46. G.L. Fredrickson, G. Cao, P.K. Tripathy, M.R. Shaltry, S.D. Herrmann, T.-S. Yoo, T.Y. Karlsson, D.C. Horvath, R. Gakhar, A.N. Williams, R.O. Hoover, W.C. Phillips, K.C. Marsden, Review— Electrochemical Measurements in Molten Salt Systems: A Guide and Perspective, J. Electrochem. Soc. 166 (2019) D645. <https://doi.org/10.1149/2.0991913jes>.

Chapter 5 Task 4: Morphological Evolution and Dealloying During Corrosion of Ni20Cr (wt.%) in Molten LiF-NaF-KF Salts, 600°C

Ho Lun Chan^{1,2}, Elena Romanovskaia^{1,2}, Sean H. Mills^{3,4}, Minsung Hong^{5,6}, Valentin Romanovski^{1,2}, Nathan Bieberdorf³, Chaitanya Peddeti³, Andrew M. Minor^{3,4}, Peter Hosemann^{5,7}, Mark Asta³, John R. Scully^{1,2}

¹Department of Materials Science and Engineering, University of Virginia, Charlottesville, VA, 22904

²Center for Electrochemical Science and Engineering, University of Virginia, Charlottesville, VA, 22904

³Department of Materials Science and Engineering, University of California, Berkeley, CA, 94720

⁴National Center for Electron Microscopy, Molecular Foundry, Lawrence Livermore National Laboratory, Berkeley, CA, 94720

⁵Department of Nuclear Engineering, University of California, Berkeley, CA, 94150

⁶Materials Science Division, Lawrence Berkeley National Laboratory, Berkeley, CA, 94720, USA

Abstract

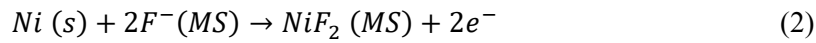
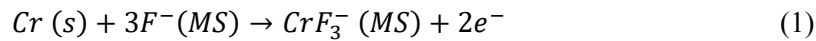
The dealloying corrosion behavior of the FCC Ni20Cr (wt%) in molten LiF-NaF-KF (FLiNaK) salts at 600 °C under varying applied potentials was investigated. Using in-operando electrochemical techniques and a multi-modal suite of characterization methods, we connect electrochemical potential, thermodynamic stability, and electro-dissolution kinetics to the corrosion morphologies. Notably, under certain potential regimes, a micron-scale bicontinuous structure, characterized by a network of interconnected pores and ligaments riched with the composition of the more noble (MN) element, becomes prominent. At other potentials both MN and less noble (LN) elements dealloy but at different rates. The dealloying process consists of lattice and grain boundary diffusion of Cr to the metal/salt interface, interphase Cr oxidation, accompanied by surface diffusion of Ni to form interconnected ligaments. At higher potentials, the bicontinuous porous structure undergoes further surface coarsening. Concurrently, Cr(II), Cr(III), and Ni(II) begin to dissolve, with the dissolution of Ni occurring at a significantly slower rate. When solid-state transport of Cr is exceeded by the interfacial rates, dealloying depths are limited.

Introduction

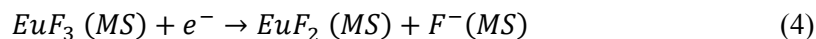
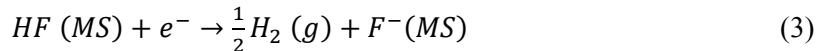
Molten salt reactor (MSR), whether in modular or industrial-scale configuration, is on the cusp of commercial deployment, representing a substantial step forward in the evolution of next-generation nuclear power systems. In essence, MSR employs a molten chloride or fluoride salt blend for nuclear power

generation and energy storage applications.¹ The corrosion protection of structural alloys in these applications necessitates resistance both to molten salt corrosion for salt-facing materials and to air oxidation for external surfaces.²⁻⁵ Ni-based superalloys and stainless steels (304 and 316) are often considered for use in structural applications in hot water reactors and MSR. However, Cr(II)-O and Cr(III)-O species are not as thermodynamically stable as Cr(II)-F and Cr(III)-F species, such as CrF₂, CrF₃, CrF₃⁻ or CrF₆³⁻.^{6,7} The unavoidable presence of oxidizing impurities, such as moisture-induced hydrofluoric acid (HF) and chromium cations (Cr(III)),^{7,8} induce a potential-dependent thermodynamic driving force to dissolve LN from the alloy.

One example is the corrosion of NiCr alloys in molten fluorides.^{6,7,9,10} In this system, the dissolution of Cr and Ni from the alloy can occur via reactions (1) and (2) to their stable fluoride forms. The notation “MS” represents the ionic molten salt phase. In molten fluorides, Cr is the LN and Ni is the MN.² The LN can leach from the alloy preferentially through short-circuit diffusion pathways, such as grain boundaries.^{11,12} The driving force for (1) and (2) is described in terms of their half-cell redox potentials (E_{redox}) and can be manipulated through chemical or electrochemical methods.



To introduce a controlled concentration, or activity, an oxidizer with a higher reduction power than (1) and (2), such as HF/H₂ (reaction 3) and EuF₃/EuF₂ (reaction 4) can be added to the salt.^{13,14} The coupled anodic and cathodic reactions thermodynamically and kinetically establish the corrosion potential (E_{corr}), which is a mixed potential under open-circuit conditions. An earlier work by the authors has tabulated and compared a range of possible half-cell redox reactions suitable for identifying LN and MN elements in an alloy as well as oxidizing species, such as HF and EuF₃, that may drive spontaneous corrosion.⁹ However, controlling the activity of an oxidant *in-situ* during a corrosion experiment is challenging as it is being continuously consumed during exposure⁷ and difficult to maintain in a large and complicated system where several other factors need to be balanced. Some other approaches include changing temperature¹⁵ and applying a precise electrochemical potential relative to the thermodynamic phase stability of the salt system.^{6,9} Through these approaches, electrode potential can be regulated to enable selective dealloying of Cr (i.e., $E_{\text{redox}}^{\text{Cr/LN}} < E_{\text{Corr}}^{\text{Alloy}} < E_{\text{redox}}^{\text{Ni/MN}}$) or simultaneous dissolution both Ni and Cr (i.e., $E_{\text{Corr}}^{\text{Alloy}} > E_{\text{redox}}^{\text{Cr/LN}}$ and $E_{\text{redox}}^{\text{Ni/MN}}$).



The selective dealloying of Cr in NiCr alloys results in Ni enrichment on the surface, which undergoes surface diffusion, collection and coarsening of surface features, leading to the formation of a micron-scale bicontinuous porous structure.^{15–21} The phenomenon of dealloying corrosion is of particular concern as the dealloyed layer can become vulnerable to stress corrosion cracking²² and/or hot spot formation¹³ during heat transfer that endangers the Generation IV reactor application. The phenomenon of dealloying corrosion has garnered considerable interest, particularly due to its prevalence at high homologous temperatures. A high homologous temperature (T_H : 0.3–0.5) is within the practical service temperature range of the MSR between 500 °C and 900 °C²³, where rapid bulk solid-state diffusion of LN element can become the rate-limiting mechanism for corrosion dealloying. The multiple solid-state diffusion processes include LN element outward bulk lattice diffusion, short-circuit diffusion via grain boundaries and dislocation pipes or accelerated by radiation-induced defects,²⁴ MN element surface diffusion which uncovers unreacted Cr in underlying layers, and long-range ionic diffusion of dissolved metal cations or oxidizers, influenced by the solubility and fluid dynamics of the molten salts.^{16,25–27} The bulk diffusion-assisted dealloying is observed to reduce the parting limit of dealloying in binary NiCr and FeCr alloys to approximately 20 at% of the LN in molten salts,^{16,25–27} a sharp contrast to the 50–60 at% typical in RT aqueous solutions.²² In contrast, at lower T_H such as during Ag-Au dealloying at RT, the LN bulk diffusion (Ag in this case) becomes negligible relative to its rate of oxidation. A LN element concentration limit to enable a connected silver path with Ag essentially frozen in place can be defined by a percolation or advanced percolation processes²⁸. The implication of bulk diffusion-assisted dealloying is that the corrosion process is now governed by a myriad of factors at different length scales that introduces further variability to the corrosion morphology,²⁹ including grain size, point defect solute interaction^{30,31} and electrochemical potential.²⁵ For instance, if the grain boundary diffusion of LN element is much faster than bulk lattice diffusion (e.g. due to finer grain size²⁷), severe grain boundary corrosion can be anticipated. Within the grain surface, the surface diffusion of MN element occurs simultaneously with LN oxidation and bulk diffusion, leading to the formation of a three-dimensional, bicontinuous porous morphology.

In a collection of investigations led by Chen-Wiegart et al.,^{16–18,32,33} using *in-situ* synchrotron X-ray nano-tomography, the authors observed the formation of bicontinuous porous structure on Ni20Cr (wt%) microwires and thin foils at both nano and micron scale when statically exposed to molten chlorides (e.g. KCl–MgCl₂) between 500 °C and 800°C. The dealloying process in their cases relied on moisture and other impurities as oxidizers to drive the Cr dealloying process.^{16–18,32,33} The electrode potential of the NiCr was not controlled. More recently, Ghaznavi, Persaud, and Newman^{15,19,20} employed a single potentiostatic hold approach applying a small overpotential of 30 to 100 mV to prompt the dealloying of Cr in molten LiCl–KCl and LiCl–KCl–MgCl₂ from Fe52Ni48 (at%), Fe30Cr22Ni48 (at%), Ni78Cr22 (at%), and other model alloys between 350 °C and 700°C. Specifically, the authors elaborate on the bicontinuous dealloying

process mechanism relative to the effects of temperature,¹⁵ alloy composition,²⁰ and crystallographic orientation. Both authors recognize the role of bulk diffusion at high T_H in dealloying.^{15–20} While both methodologies offer numerous advantages, challenges in controlling corrosion-driving forces persist. This aspect is critical as the process is highly dependent on the condition of $E_{\text{Nernst}}^{\text{Cr/LN}} < E_{\text{Alloy}} < E_{\text{redox}}^{\text{Ni/MN}}$, where it is commonly assumed that only LN dissolves, although in certain instances, both elements may dissolve. In many instances of impurity-driven corrosion, the depletion of impurities and accumulation of dissolved corrosion products can alter the driving force for half-cell cathodic reactions (according to the Nernst equation) as a function of exposure time, though this behavior is difficult to predict.⁷

A fundamental knowledge gap exists in systematically considering tight control of electrode potential that alters the corrosion morphology. This issue is multi-faceted at high T_H , owing to the vast combination of possible influencing factors, including but not limited to temperature,^{15,32} composition,^{20,34,35} time,^{16,36,37} microstructural properties (such as grain size and grain orientation),^{26,27,31,38} and salt impurities.^{14,39} The corrosion potential determines which alloying species are thermodynamically favorable to dissolve as well as their rates during activation-controlled electrolytic dissolution². Critically, the primary mechanism limiting dealloying may shift during this potential-dependent dissolution process. For example, initial fully activation-controlled dissolution of Cr can lead to Ni surface enrichment, which then serves as a barrier to slow down the bulk diffusion of Cr,⁴⁰ and may change the primary rate-limiting mechanism from interfacial reaction-control to Ni surface diffusion or bulk diffusion regulated mass transport-controlled.¹⁵ Another scenario that requires further investigation is whether a bicontinuous structure will still form in a molten salt medium if both Ni and Cr dissolve under sufficient driving force. There is a need for comprehensive studies correlating variations in applied electrochemical potential with the thermodynamic regions for stability of selected soluble metal salt species and the associated alloy dissolution kinetics.^{6,9} Our previous work, which investigated the corrosion behavior of pure Cr in molten FLiNaK,²⁵ demonstrated that Cr can exhibit a diverse range of potential dependent corrosion morphologies—from micro-porosity to surface faceting to salt-film induced smoothing—depending on the applied potential. Extending this approach, the present study explores the morphological evolution of Ni20Cr in FLiNaK under various applied potentials that enable dealloying.

This work aims to study the morphological evolution of Ni20Cr in molten FLiNaK salts at 600 °C due to various applied potentials where preferential dissolution and dealloying occur. By modulating the applied potential, the corrosion behavior of Ni20Cr experiencing various controlled driving forces can be investigated. The objective is to pinpoint the potential effects and mechanisms responsible for morphologies such as bicontinuous dealloying, as well as identify the governing thermodynamic and kinetic regimes.

Materials and Methods

Materials preparation

Ni₂₀Cr alloys (80 wt%Ni-20 wt%Cr) were prepared by mixing high purity Ni (99.98%, Thermo Scientific) and Cr (99.99%, Thermo Scientific) at a desired stoichiometric ratio, then subjecting the alloys to a vacuum arc-melting process (>10⁻⁵ torr). The Ni₂₀Cr alloys were re-melted three times to ensure a homogenous composition. Additionally, the Ni₂₀Cr alloys were also solution homogenized at 1050°C for 6 h in an encapsulated Ar-filled quartz tube and were then quenched in room temperature water. The as-homogenized Ni₂₀Cr alloy was a random solid solution that exhibits an average grain size of 351 ± 154 μm. The Ni₂₀Cr samples were then machined to a rectangular plate with the dimension of 2 ± 0.5 × 1 ± 0.5 × 0.5±0.3 cm, polished to 1200 grit surface finish using silicon carbide paper, and lastly sonicated in deionized water (18.2 Ω·cm²) and isopropanol for 3 min prior to experimentation. Baseline microstructural characterization was carried out on fabricated Ni₂₀Cr samples and can be seen in Figure S1.

Salt preparation

The LiF-NaF-KF (46.5–11.5–42 mol%) eutectic salt (FLiNaK) was selected as the salt electrolyte. Fluoride salt constituents, including LiF (99.99% purity, Fisher Scientific), 11.5 mol% NaF (99.99% purity, Fisher Scientific), and 42 mol% KF (>99.5% purity, Fisher Scientific) salts, were obtained from commercial vendors, dried in a vacuum oven at 100°C for 48 h, transferred to an N₂-filled (with oxygen and H₂O controlled below <0.1 ppm) glove box (UNILab MBraun, USA), and mixed into their targeted stoichiometric ratio. 30 g of FLiNaK salt was used for each test. This study employs a two-step drying process. The salt mixture was first heated to 600 °C under the flow of ultra-high purity (UHP) N₂ gas with 99.999% purity for a minimum of 6 h. This was done to ensure the removal of any trapped oxygen and moisture. After cooling and solidifying, the salt mixture was reheated to the target temperature and maintained for 3 h before the electrochemical experiment.

No additional purification steps (e.g. HF purging³⁹) were performed to enable the removal of all metallic cations, O₂, or moisture. Thus, the salt may be considered as unpurified. Nevertheless, our recent work focusing on the validation of molten salt electrochemistry²⁵ reveals that during anodic polarization on the working electrode, impurities such as metallic cations, moisture, and molten K⁺ ions can be consumed by reduction at the counter electrode to support the ionic current flow. This phenomenon merely suggests that the driving force of Cr/Cr (III) and/or Ni/Ni(II) reactions responsible for Ni₂₀Cr dealloying is supported by the potentiostat instead of relying on the oxidizing impurities (e.g. HF/H₂). While the effect of impurities may still be present during an anodic polarization scan, this has not been investigated in the current study and will be addressed in future work.

Molten salt electrochemistry experiments

The electrochemical experiments were conducted in a 4-electrodes cell in a glove box environment. Schematics and additional details on the electrochemical cell configuration as well as electrode design are outlined in our earlier work.⁷ A high purity boron nitride crucible (>99.6%, MSE Supplies) was utilized as the salt container. A graphite rod (0.25 inch in diameter) was used as the counter electrode (CE) and a high purity 5 mm diameter Pt wire (99.95%, Fisher Scientific) as the pseudo-reference electrode. Two working electrodes (WE) were employed in this work. The primary WE was the Ni20Cr sample, on the end of which a Ni20Cr wire (99.99%, Fisher Scientific) was spot-welded. This wire was threaded through an alumina tube, and the welded spot was covered with boron nitride paste. The secondary WE was another high purity Pt wire (99.95%, Fisher Scientific). It is noted that no gas flow was maintained during the electrochemistry experiments. Prior to testing the Ni20Cr samples, cyclic voltammetry (CV) experiment was performed at 100 mV s^{-1} in the potential range from 0 V_{Pt} to $-2.0 \pm 0.3 \text{ V}_{\text{Pt}}$ to identify the equilibrium K^+/K potential as well as any redox reactions that may suggest the presence of metallic cation impurities within the potential range (Figure S2).^{6,7,25,41,42} It is noted, however, that the K^+/K electron transfer kinetics are significantly faster than the typical range of scan rates utilized in CV experiments (up to 500 mV s^{-1}),⁶ and therefore the effect of scan rate on the equilibrium K^+/K potential value is minimal (see Figure S2). It is noted that the K^+/K potential can also be obtained by a dynamic reference electrode (DRE) method in which the pseudo reference electrode is cathodically polarized;^{19,25,41} however, F_2 bubble evolution may occur from F^- oxidation that adds infinite resistance to disrupt the polarization experiments.²⁵ In this work, the K^+/K potential was determined immediately prior to the electrochemical scan on a Pt wire. The K^+/K potential measurement was performed during the experiment to ensure the continuous verification and/or calibration of the applied potential in relation to the established K^+/K potential.

In this study, three sets of electrochemical experiments were conducted. Each experiment was performed in triplicate to ensure replicability:

Experiment #1: Ni20Cr alloys were subjected to a 60 s open-circuit potential (E_{oc}) measurement coupled with linear sweep voltammetry (LSV) (or potentiodynamic polarization) at 1 mV/s from -0.4 V to $+1.5 \text{ V}$ vs. E_{oc} . The 60 s period was deemed enough time to dissolve oxides based on previous work.⁴³ The fast scan rate precludes significant dissolution. The same scan was also conducted on pure Ni and Cr for baseline comparison. Electrochemical thermodynamic calculations were performed following previously established methods^{2,6,9,42} to relate the potential regimes to the phase stability of Cr, Ni, Ni(II), Cr(II), and Cr (III) species in molten FLiNaK. Additionally, the anodic polarization portion of the $E\text{-log}(i)$ result was also corrected with iR drop and for the presence of cathodic current densities.^{25,44}

Experiment #2: Potentiostatic polarization was carried out on Ni20Cr samples at applied potentials (E_{applied}) over a 1 V range from $+1.75$, $+1.90$, $+2.10$, $+2.30$, $+2.50$, to $+2.75 \text{ V}_{\text{K}^+/\text{K}}$ for 10 ks. During each 1

ks interval, electrochemical impedance spectroscopy (EIS) was performed on the samples at the specified E_{applied} , spanning a frequency domain from 10 kHz to 10 mHz, with an AC perturbation of 20 mV. An electrical equivalent circuit (EEC) model was used to calculate the interfacial charge-transfer resistance (Rct). Simultaneously, CV scans were also performed on the secondary WE Pt wire at each 1 ks interval with a scan rate of 100 mV s⁻¹ to identify the presence of dissolved Cr(II), Cr(III), and Ni(II) species remote from the Ni20Cr electrode. Additionally, to estimate the dissolved NiCr depth of attack ($h_{\text{dissolved}}$) neglecting porosity during the potentiostatic hold, Faraday's Law of mass and charge conversion was utilized, as outlined in Eq. 5:^{7,25}

$$h_{\text{dissolved}} = \frac{EW \cdot i_{\text{electric}} \cdot t}{F \cdot \rho} \quad (5)$$

where i_{electric} is measured current density in A cm⁻², t is time in seconds, F is the Faraday constant of 96500 C mol⁻¹, ρ is the density in g cm⁻³, and EW is the equivalent weight (EW). The method of determining EW can be found in the ASTM G102-89 standard via Eq. 6:⁴⁵

$$EW = \sum \frac{W_i}{n_i f_i} \quad (6)$$

where W_i represents the atomic weight, n_i is the oxidation state, and f_i is the weight fraction of the i^{th} alloying elements. Noted the dissolution flux (J_e) was also calculated in terms of i_e via $J_e = i_e/nF$.

Experiment #3: *Experiment #2* was replicated on Ni20Cr alloys in FLiNaK with 1 wt% NiF₂ addition (97 wt%, Alfa Aesar) at the E_{applied} of +1.90 and +2.10 V_{K+/K} for 10 ks. A series of CV diagnostics was performed on a Pt wire in FLiNaK with the addition of 0.05 wt% to 1.00 wt% NiF₂ to approximate the half-cell redox potential of the Ni/Ni(II) reaction in molten FLiNaK at 600 °C as shown in Figure S3.

Scanning electron microscopy (SEM) and energy dispersive spectroscopy (EDS)

Both the surface and cross-section of the corroded Ni20Cr samples were examined using a FEI Quanta 3D FEG scanning electron microscopy (SEM) equipped with an Oxford Energy Dispersive Spectroscopy (EDS). Upon experiments, the electrodes were removed immediately from the salt bath and N₂ cooled in the glove box. The samples were then sonicated in deionized H₂O until visible residual salts on the surface were removed. Upon surface SEM analysis, the corroded Ni20Cr coupons were sectioned and mechanically polished sequentially from 400 to 1200 grit using SiC metallography pads, and finally polished via a vibratory polisher in a 0.5 μm colloidal SiO₂ polishing suspension. This paper focused on the planar dealloying front.

Electron backscattered diffraction (EBSD)

Electron Backscatter Diffraction (EBSD) (Thermo Fisher Scientific, Scios 2, field emission gun SEM) was performed to observe the selective dissolution along the grain boundaries. The specimen was polished to 0.05 μm using an alumina suspension and at sonicated for 10 min in ethanol. For EBSD, the sample was mounted on 45 degrees using a pre-tilted polarizer and totally tilted to 70 degrees. An acceleration voltage of 20 kV was set for the EBSD analysis, and the vacuum pressure was maintained below $1 \cdot 10^{-5}$ Torr. EBSD analysis with a step size of 0.5 μm was conducted in the $50 \times 80 \mu\text{m}^2$ analyzed area. EDS and EBSD maps were processed and rendered using Oxford AZtec and AZtecCrystal (Aztec, Oxford Instruments, High Wycombe, UK) analysis software packages.

X-ray diffraction analysis

The chemical and phase composition of the residual salt was examined using the Malvern-Panalytical Empyrean diffractometer [wavelength Cu $K\alpha$ (1.5405 Å)]. The PDF4+ database was employed as the reference data. For Rietveld refinement, the software HighScore Plus was utilized where the pseudo-Voigt function was used to refine the peak profile. It is important to recognize that XRD data from residual salts may not accurately reflect the molecular structure of species in their molten state, given that cooling could induce phase transitions upon solidification. However, analyzing these data enables the detection of the presence of Ni and Cr species, which is one primary focus of this work.

Inductively coupled plasma-mass spectrometry (ICP-MS) analysis

To quantify Cr and Ni contents in FLiNaK salts using the ICP-MS method, approximately 0.22 g of the FLiNaK samples were dissolved into 100 ml of deionized (DI) water. This solution was subsequently analyzed using the mass spectrometer. To ensure accuracy and calibration, standard solutions of Ni (MSNI100PPM-125 ml, Inorganic Ventures) and Cr (MSCR(3) –100PPM-125 ml, Inorganic Ventures) consisting of 2vol.% of nitric acid were used as baselines. Multiple standard solutions were then fabricated by dilution in DI water and subsequently sonicated for 15 min to achieve homogeneity. Concentrations for these standards were set at 100, 50, 25, 10, and 1 ppb for both Ni and Cr. DI water was employed as a blank so that any background readings emanating from the instrument can be subtracted. The result is shown in Table S1. Additionally, the ICP-MS result of the as-prepared FLiNaK salts was also consistent with the Ni and Cr composition specified in the certificate of analysis provided by the commercial supplier shown in Table S2, showing approximately 0.67 ppm of Cr and 2.42 ppm of Ni.

Results

Thermodynamics and kinetics for Ni20Cr dissolution

The possibility of bicontinuous dealloying in Ni20Cr alloys within molten FLiNaK was initially explored through the identification of electrochemical potential ranges where only Cr is dissolved as Cr(II) or Cr(III) and Ni remains stable in its zero-valence state. To guide choice of the relevant potential ranges, a one-dimensional phase stability diagram for Ni20Cr was calculated at 600 °C for Ni, Ni(II), Cr, Cr(II), and Cr(III) in FLiNaK relative to the K^+/K potential, presented in Figure 1a.^{6,9}

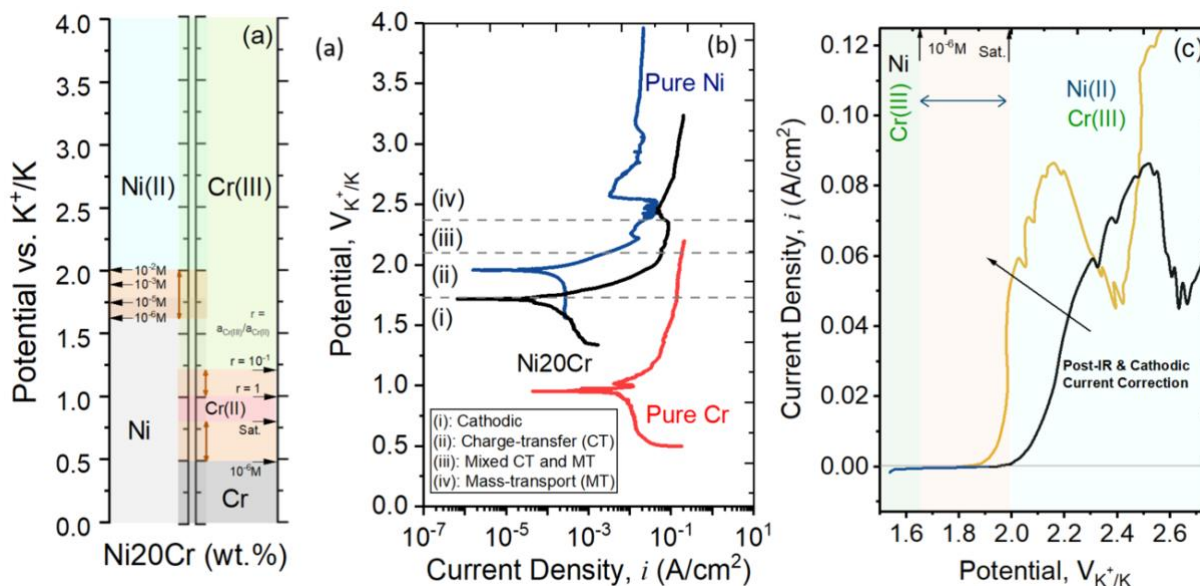


Figure 1. (a) The one-dimensional phase stability diagram for Cr, Ni, Cr(II), Cr(III), and Ni(II) species calculated assuming a F^- ion activity (a_{F^-}) of 49.3 M at 600 °C and using the activity of Cr and Ni in Ni20Cr (wt%). Horizontal black arrows on the diagram represent phase boundaries based on an assumed species concentration, while the double-headed vertical arrow highlights the range of phase boundary conditions, extending from 10^{-6} M to bulk saturation. (b) and (c) display the experimental polarization curves for pure Ni, Cr, and the Ni20Cr alloy in the form of linear sweep voltammograms at 1 mV s^{-1} . (c) illustrate the polarization curve for the Ni20Cr alloy, both in its as-measured state and after corrections for iR and cathodic current density

It is noted that all thermodynamic calculation are first calculated relative to the E_{redox} of F_2/F^- assuming a zero E° redox at 600 °C, then the E_{redox} of all half-cell redox reactions are calculated also considering the activity of Cr and Ni in Ni20Cr alloy at 600 °C in terms of V_{F_2/F^-} , which is then calibrated with the calculated E_{redox} of K^+/K reaction of $-4.63 V_{F_2/F^-}$.⁹ The E_{redox} of Cr/ Cr(II), which Cr(II) and Cr(III) are considered as CrF_3^- or CrF_6^{3-} ,⁶ is found to be highly favorable above $+0.27 V_{K^+/K}$. The E_{redox} of Cr (II)/Cr(III) is favorable above $+0.67 V_{K^+/K}$.^{6,46} In scenarios where Ni(II) is absent or an impurity (assumed to be 10^{-3} M), the E_{redox} of Ni/Ni(II) is calculated to be $+1.75 V_{K^+/K}$. The calculated E_{redox} of Ni/Ni(II) redox reaction was verified experimentally via a series of diagnostic CV on a Pt wire electrode with incremental addition of NiF_2 from 0.05 to 1 wt% in FLiNaK salts. The results, as shown in Figure S3, reveal a bulk saturation limit of

approximately ~ 0.1 wt% NiF_2 with an E_{redox} of $\sim 2 V_{\text{K+K}}$ marked in Figure 1a. For a more in-depth elaboration on the kinetic properties of NiF_2 or Ni(II) in FLiNaK, readers are referred to a recent study by Smith et al.⁴⁷ These thermodynamic redox potentials can guide understanding of E-log(i) corrosion behavior.

Figure 1b depicts the E-log(i) curve of Ni, Ni20Cr, and Cr in molten FLiNaK at 600 °C. The LSV of Cr in molten FLiNaK was investigated previously.²⁵ High purity Ni displays a very similar qualitative E-log(i) behavior when compared to Cr except shifted to more positive potentials, characterized by the presence of both charge-transfer (CT) and mass-transport (MT) E-log(i) regimes,^{13,48} The latter may be attributed to the formation of K-Ni-F salt film due to the low solubility of NiF_2 (< 0.1 wt.%)⁴⁹. The E_{oc} values for Ni and Cr differ by approximately 1.3 V due to their significant difference in thermodynamic stability.^{2,9} The anodic polarization regime of Ni20Cr (wt%) is CT-controlled over a ~ 300 mV range between $+1.72 V_{\text{K+K}}$ and $+2.05 V_{\text{K+K}}$, followed by a mixed CT and MT-controlled regime to $+2.32 V_{\text{K+K}}$, and eventually reaches a limiting current density. Each kinetic regime pertaining to the electrodisolution step is separated by a dashed horizontal line and labeled accordingly: (i) cathodic, (ii) CT, (iii) mixed CT and MT, and (iv) MT. The potential domain for cathodic regimes is dependent upon factors, including the oxidizers present, temperature, and convection effects.^{25,50} Figure 1c shows the i-E curve of Ni20Cr before (dark) and after (yellow) iR and cathodic current density correction, overlaid with color maps to indicate potential ranges where Cr(III) and Ni(II) are stable. As predicted in Figure 1a, the potential up to $+1.75 V_{\text{K+K}}$ is the region in which only Cr dissolves. The boundary gradually increases up to $+2.134 V_{\text{K+K}}$ as Ni begins to dissolve, saturating in FLiNaK and shifting E_{redox} . Above $+2.134 V_{\text{K+K}}$, both Cr and Ni may dissolve.

Figure 1 indicates that dealloying can occur solely through Cr dissolution, and at a more positive potential with Cr exhibiting high rates and Ni showing lower rates, differing by three orders of magnitude. The implications align with classical interpretations derived from aqueous studies. Specifically, the greater the difference in equilibrium oxidation reactions between Cr and Ni, the easier it is to dealloy, especially when there is thermodynamic immunity of Ni. In this scenario, the ratio of dealloying front velocity to uniform corrosion front velocity approaches infinity.

Morphological evolution with applied potential

Ni20Cr (wt %) alloys are potentiostatically held in FLiNaK at 600 °C over a 1 V potential range at $+1.75$, $+1.90$, $+2.10$, $+2.30$, $+2.50$, and $+2.75 V_{\text{K+K}}$ for 10 ks. The post-corrosion surface morphologies in plan view are examined using SEM as shown in Figure 2. In Figs. 2a–2c, which correspond to Ni20Cr alloys polarized at $+1.75$, $+1.90$, and $+2.10 V_{\text{K+K}}$, respectively, the plan view surface exhibits microporosity coupled with interconnected discrete ligaments. This potential regime falls within the CT-controlled in which the oxidation step produces rapid dissolution where $i_{\text{anodic}} \sim \exp(E_{\text{app}})$ and Ni remains thermodynamically stable (Figure 1a), or dissolves at a significantly slower rate relative to Cr (Figure 1b).

The presence of an interconnected pores-ligaments network indicates that bicontinuous dealloying can occur in the Ni20Cr alloy in FLiNaK at 600 °C. One point of note is that the ligament features are similar to the case of molten chloride dealloying^{15–20,32,33} and liquid metal dealloying,⁵¹ but are significantly coarser relative to the features observed upon dealloying of Cu-Zn, Ag-Au, and Pt-Ni alloys in aqueous solution such as HClO₄,²² H₂NO₃,⁵² and others,^{53,54} surmised to be due to the high homologous temperature in the case of molten salts. Given that the potentials of +1.75, +1.90, and +2.10 V_{K+/K} indicate bicontinuous dealloying, additional electrochemical and morphological characterization was performed, as presented in Figure 3–8.

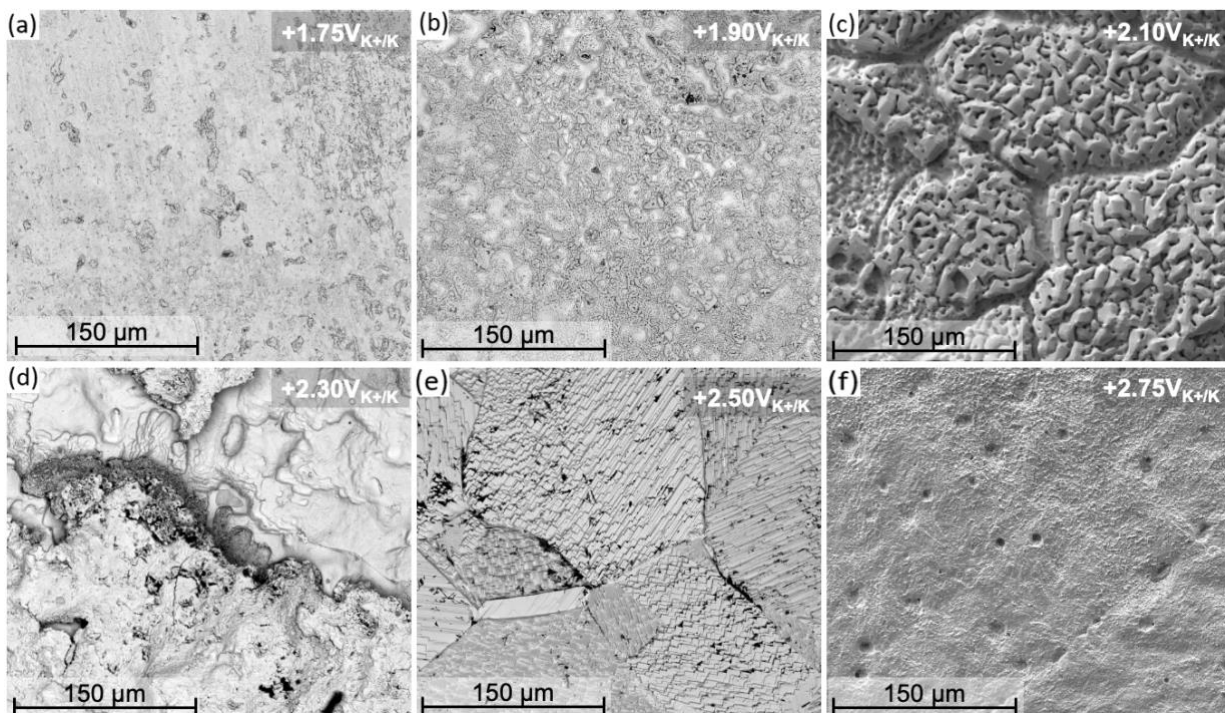


Figure 2. Representative backscattered electron micrographs depicting the top-view surfaces of Ni20Cr (wt.%) subjected to potentiostatic polarization conditions: (a) at +1.75 V_{K+/K}, (b) at +1.90 V_{K+/K}, (c) at +2.1 V_{K+/K}, (d) at +2.3 V_{K+/K}, (d) at +2.5 V_{K+/K}, and (e) at +2.7 V_{K+/K}. The alloys were exposed to molten FLiNaK salts at a temperature of 600 °C for a duration of 10 ks

As the applied potential increases, a gradual diminishment of the microporous morphology is observed, transitioning into different corrosion morphologies as evidenced in Figs. 2d through 2f. When polarized at +2.30 V_{K+/K} and +2.50 V_{K+/K} for 10 ks, Ni20Cr alloys are found to exhibit grain surfaces that are relatively sharp, rough and appeared crystallographically jagged. Some interconnected ligaments are observed in the +2.30 V_{K+/K} sample, as shown in Figure S4. Conversely, no porous structure is detected in the +2.50 V_{K+/K} sample; instead, grains with sharply visualized facets were seen. These facets are interpreted as manifestations of direct and rapid dissolution of both Cr forming Cr(III) and Ni(II), revealing facets formed by different crystallographic orientations.²⁵ Between +2.30 V_{K+/K} and +2.50 V_{K+/K}, both Ni and Cr dissolve

governed by a mixed CT- and MT- controlled dissolution. Lastly, at $2.75 V_{K+/K}$, the dissolution of Ni20Cr is controlled by MT at the limiting current density (i.e. maximum dissolution rate), yielding a relatively smooth surface containing surface-level micropores.^{25,55} The smooth surface implies that the Ni20Cr substrate could be dissolving underneath a salt film, formed in situ by the saturation of Cr(III)-F and Ni(II)-F compounds on the surface, whereby the microstructural effect on alloy dissolution is believed to be negligible at the MT limit. It is noted that grain boundary (GB) dissolution is observed at the potentiostatic polarization potentials between $+1.90 V_{K+/K}$ and $+2.50 V_{K+/K}$; A follow-on work will be conducted to investigate the behavior of grain boundary dissolution during potentiostatic dealloying.

Dealloying at $+1.75 V_{K+/K}$

At $+1.75 V_{K+/K}$ (Figure 3a), Cr dissolution to Cr(III) dominates while Ni dissolution is negligible. In Figure 3a, a constant anodic i_{electric} is observed and sustained at $\sim 10^{-5} A cm^{-2}$ until reaching ~ 4 ks, at which point the i_{electric} decreases and fluctuates between $10^{-6} A cm^{-2}$ and $10^{-8} A cm^{-2}$.

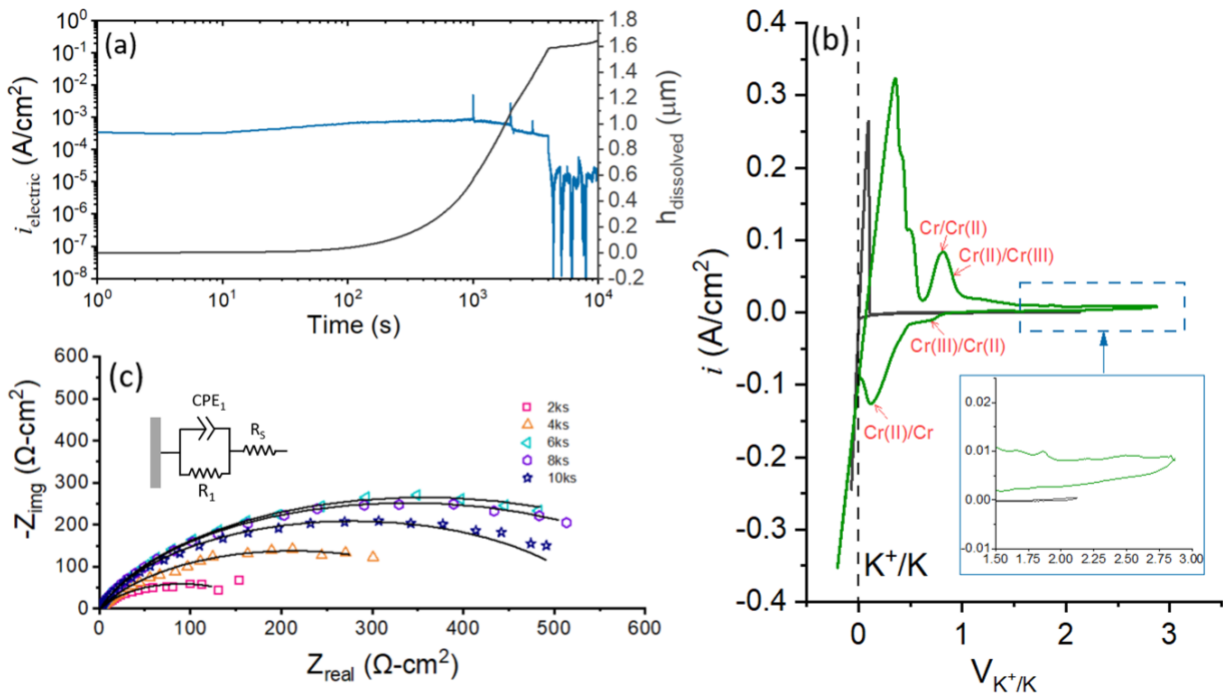


Figure 3. Ni20Cr (wt%) subjected to potentiostatic hold in molten FLiNaK at 600 °C at $+1.75 V_{K+/K}$. (a) display the current-time relationship, (b) shows the cyclic voltammogram measured the secondary Pt WE before (black) and after 10 ks of potentiostatic hold of Ni20Cr. The redox peaks of possible Cr/Cr(II) and Cr(II)/Cr(III) reactions are labeled. The inset in (b) highlights the potential range in which the Ni/Ni(II) half-cell redox reactions are possible (c) shows the Nyquist plots measured at each 2 ks time increment containing the EEC used for fitting analysis and fitting results (black lines)

Up until this point, $0.33 \mu m$ of Cr may have dissolved according to Eq. 5 assuming 0% remaining Cr in ligaments neglecting porosity. Due to the close proximity of E_{oc} ($\sim 1.7 V_{K+/K}$) to this applied potential,

the drop in i_{electric} is likely associated with the cathodic reduction of Cr(III)/Cr(II) becoming kinetically dominant (i.e. more Cr(III) available to be electrochemically reduced), resulting in a decrease in net i_{electric} ^{13,25,41,56,57}. This behavior is further validated in Figure S5. Confirmation of this thermodynamic prediction is provided by *in situ* CV measurements on the secondary Pt WE, as shown in Figure 3b. Redox reactions associated with Cr/Cr(II) and Cr(II)/Cr(III) are possible in the potential range of +0.1 to +1.2 $V_{\text{K+/K}}$ (shaded red region), while reactions for Ni/Ni(II) in the potential window from +1.50 to +2.25 $V_{\text{K+/K}}$ (shaded blue region) are absent. For clarity, only the CV scan conducted before and after 10ks of pstat dealloying is shown in Figure 3b to identify the presence of Cr and/or Ni species in salt. All CV plots between 1ks and 10ks at 1.75, 1.90, and 2.10 $V_{\text{K+/K}}$ are shown in Figure S6.1.

Regarding Figure 3c, the impedance spectra of the test sample can be fitted with an EEC, containing R_s as the solution resistance, R_1 as the charge-transfer resistance (R_{ct}), and the constant phase element CPE_1 as the double-layer capacitance (C_{dl}). As the duration of potentiostatic hold progressed, an increase in the semicircles on the Nyquist plot was observed, indicating a rise in R_{ct} as detailed in Table S3. This change in impedance behavior points to the surface becoming more electrochemically resistive, potentially as a result of the depletion or encapsulation of Cr within the Ni ligaments spreading by surface diffusion.¹⁹ This phenomenon is marked by Ni exhibiting low dissolution rates and/or remaining stable at these potentials. It is noted that, for simplicity, only impedance results for intervals from 2 ks to 10 ks (in increments of 2 ks) are shown here. However, all of these data, along with the fitted Bode plots, can be accessed in Figure S6.2 and Tables S4 through Table S5.

Figure 4a shows that the Ni20Cr surface, potentiostatically polarized at +1.75 $V_{\text{K+/K}}$ for 10 ks, revealing two distinct grains. One grain exhibits a dealloyed bicontinuous porous structure, while the other appears to be partially dealloyed. The dealloyed grain exhibits an interconnected network of nano-pores and sub-micron sized ligaments, with a measured width of $0.29 \pm 0.08 \mu\text{m}$. Three distinct locations were analyzed with EDS point analysis as shown in Figure 4b and Table I. Point #1, located on a ligament, contained 3.7 wt % Cr above a Ni-rich substrate (Point #2) with 16.2 wt% Cr, while the partially dealloyed grain at Point #3 possessed 7.5 wt% Cr. It is noted that the EDS point analysis serves to qualitatively correlate select surface features and approximate composition. Due to the size of the interaction volume relative to the submicron dealloying features, the results in Table I are averaged and estimated values.

The cross-section of the ligament is further examined in Figs. 4c and 4f. The sample exhibits a top dealloyed layer with a measured depth of $0.81 \pm 0.18 \mu\text{m}$, which is higher than the calculated $h_{\text{dissolved}}$ presented in Figure 3a. The discrepancy, where $h_{\text{dissolved}}$ is underestimated, can be attributed to the net i_{electric} at this potential being close to zero due to the progressive dominance of cathodic current densities. This top layer reveals nanoporosity that is Ni-enriched (Figure 4d). Notably, the interface between this top layer and the bulk Ni20Cr substrate was characterized by interconnected micro-voids, suggesting poor adhesion of

the Ni enrichment layer to the underlying substrate.^{15,58,59} Line scan data delineate the concentration profiles of Ni and Cr at the near-surface region, revealing the depletion of Cr with a residual presence of about 5 wt. % within the layer and a concentration profile that is 0.57 μm wide. A critical observation from this study is that the bicontinuous morphological evolution is restricted to the top layer, with no significant penetration into the deeper alloy substrate at this dealloying potential and time. The role of grain boundaries is to be addressed elsewhere.

Figure 4g shows the inverse pole figure (IPF) map from a different cross-sectional area of the sample. Two adjacent grains both nearly aligned with the (001)FCC are shown in Figure 4g. Submicron sized segments that take on various crystal orientations are displayed within the top enrichment layer. It is noted that Ni deposition (i.e. the reduction reaction from Ni(II) to Ni) is negligible at this potential. Therefore, the shift of crystallographic orientation of grain cross-section near the top surface may be triggered by the combination of surface rearrangement and grain boundary reorientation for the minimization of internal energy once Cr is depleted; a similar behavior was observed by Ghaznavi, Persaud, and Newman.^{15,19,20}

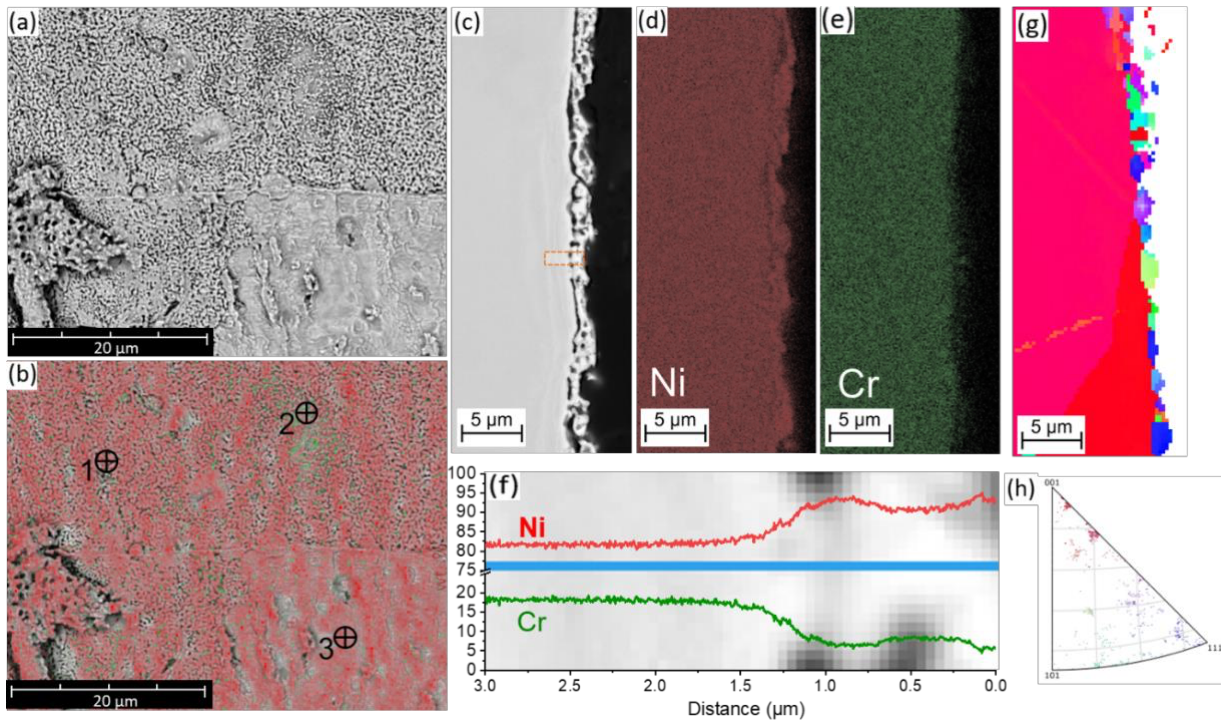


Figure 4. Ni20Cr (wt.%) potentiostatically polarized at +1.75 $V_{K+/K}$ for 10 ks. (a) Plan-view SEM image showing surface morphology. (b) Composite EDS elemental maps overlaid on SEM image, highlighting Ni (red) and Cr (green) distribution. Specific locations were marked for point analysis. (c) Cross-sectional SEM image of the sample. (d) and (e) EDS maps for Ni (red) and Cr (green), respectively. The semi-transparent rectangle in (c) indicates the area subjected to EDS line scan analysis, with corresponding elemental profiles for Ni and Cr presented in (f). EBSD analysis is shown via the inverse pole figure (IPF) plot of a separate cross-sectional surface in (g). The stereographic triangle in (h) marks the orientation of the grains present in (g)

Dealloying at +1.90V_{K+/K}

At +1.90 V_{K+/K} (Figure 5d), the anodic i_{electric} remains relatively constant at $\sim 10^{-2}$ A cm⁻² throughout the 10 ks polarization duration, estimating an $h_{\text{dissolved}}$ of 11 μm based on Eq. 5. At this potential, both Ni and Cr are thermodynamically favorable to dissolve, though Ni dissolves at least three orders of magnitude slower than Cr, as evidenced in Figure 1b at the potential of +1.90 V_{K+/K}. Figure 5b illustrates the occurrence of Cr/Cr(II)/Cr(III) redox reactions within the potential window of +0.1 V to +1.0 V_{K+/K}, and Ni/Ni(II) redox reactions in the range of +1.50 to +3.00 V_{K+/K}.^{47,56} Several oxidation peaks are visible observed in vicinity to the Ni/Ni(II) peaks. This may be attributed to the polycrystalline nature of the Pt wire and the possible formation of Ni-Cr-F complex species, which has yet to be investigated in this salt environment.

The Nyquist impedance spectra (Figure 5f) can also be fitted with an EEC comprising of Rs connected in series with two-time constants (CPE₁/R₁ & CPE₂/R₂). The first time constant (CPE₁/R₁) is used to describes the slightly depressed semicircle at the high frequency region, possibly attributed to the dispersion or nanoporosity, whereas the second time constant (CPE₂/R₂) described the low frequency semicircle that exhibits a very similar impedance magnitude as seen at +1.75 V_{K+/K}. The origin of the second time constant is still being investigated, but another possible origin is the formation of localized salt film in FLiNaK.^{7,16,25} Due to this uncertainty, the R_{ct} was estimated by the summation of R₁ and R₂.

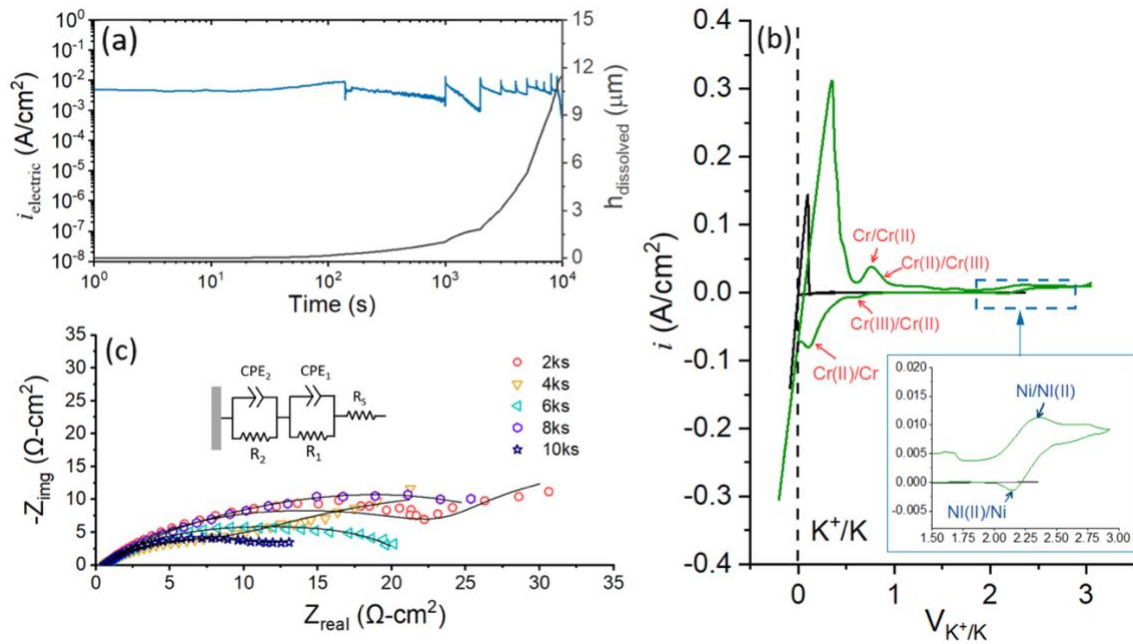


Figure 5. Ni₂₀Cr (wt%) subjected to potentiostatic hold in molten FLiNaK at 600 °C at +1.90V_{K+/K}. (a) display the current time relationship, (b) shows the cyclic voltammogram measured the secondary Pt WE before (black) and after 10 ks of potentiostatic hold of Ni₂₀Cr. The redox peaks of possible Cr/Cr(II), Cr (II)/Cr(III), Ni/Ni(II) reactions are labeled. The inset in (b) highlights the potential range in which the Ni/Ni(II) half-cell redox reactions are possible (c) shows the Nyquist plots measured at each 2 ks time increment containing the EEC used for fitting analysis and fitting results (black lines)

As illustrated in Figure 6a, the post-dealloying surface of Ni20Cr at +1.90 V_{K+/K} for 10 ks presents a coarser interconnected ligament structure with a width of $0.95 \pm 0.15 \mu\text{m}$. Beneath these coarser features, finer submicron ligaments are visible. According to the EDS point analysis detailed in Table 1, the ligament consists entirely of pure Ni (Point #1), an undealloyed bare surface with 11.9 wt% Cr (Point #2), and the grain boundary, which contains 2.3 wt% Cr (Point #3). It is important to note that, in contrast to Figure 4a, the ligaments appear somewhat directional, indicating a possible influence of crystallographic orientation^{19,21}, which will be discussed later.

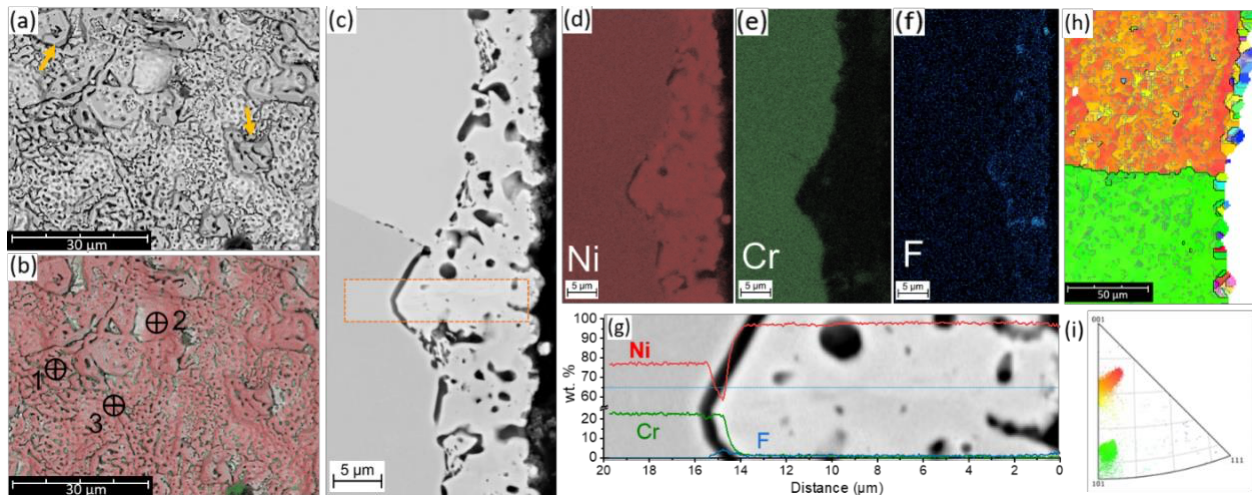


Figure 6. Ni20Cr (wt.%) potentiostatically polarized at +1.90 VK+/K for 10 ks. (a) Plan-view SEM image showing surface morphology. (b) Composite EDS elemental maps overlaid on (a), highlighting Ni (red) and Cr (green) distribution. Specific locations were marked for point analysis. (c) Cross-sectional SEM image of the sample. (d), (e), (f) are EDS maps for Ni (red), Cr (green), and F (blue) respectively. The semi-transparent rectangle in (c) indicates the area subjected to EDS line scan analysis, with corresponding elemental profiles for Ni and Cr presented in (g). EBSD analysis is shown via the inverse pole figure (IPF) plot of a separate cross-sectional surface in (h). The stereographic triangle in (i) marks the orientation of the grains present in (h).

The cross-sectional characterizations from Figs. 6c–6e unveils a distinct top layer enriched with Ni and infiltrated with residual fluoride salts. This layer, with a measured thickness of $10.9 \pm 3.45 \mu\text{m}$, displays notable micro-porosities and curvature, which may correlate with the coarser ligament structure identified, and a non-uniform interface between the top Ni layer and the substrate. Additionally, the cross-section thickness also closely matches the $h_{\text{dissolved}}$ calculated in Figure 5b. Figure 6c also captures a grain boundary that exhibits some level of dissolution. Grain boundary dissolution was deeper at this potential, however it does not seem to significantly influence the intragranular dealloying process located $\sim 100 \mu\text{m}$ laterally away from grain boundaries. Furthermore, EDS line scan analysis reveal a complete depletion of Cr in the ligaments, with a concentration profile extending $1 \mu\text{m}$ in width. Figure 6h shows the IPF from another cross-section location that contains two adjacent grains with orientations close to (103)FCC and within 5

degrees of (101)FCC. Localized segments sized between 0.5 and 2 μm at the alloy surface display different crystallographic orientations than their parent grains. For instance, on the (103)FCC grain, small regions with directions closer to (110)FCC and (111)FCC are seen. A similar argument can be made regard to the minimization of internal and surface energy via Ni coarsening (due to surface diffusion) and CSL grain boundary formation.¹⁵ Although the possibility of Ni plating onto Ni20Cr at 1.9 $V_{K+/K}$ in FLiNaK was initially considered, subsequent findings (Figure S7) refute this assumption therefore attributing the surface near orientation to grain restructuring rather than surface plating.

On the effect of time, Figure 7 displays the plan view morphology of a Ni20Cr sample sequentially held at +1.90 $V_{K+/K}$ for 1, 3, 5, and 10 ks in FLiNaK at 600 °C, utilizing the same sample to guarantee consistency in observing time-dependent changes. The initial state at 1 ks (Figure 7a) shows minimal corrosion, yet a closer inspection at 10,000x magnification (Figure 7b) reveals the formation of granulated surface texture, signaling initial material dissolution with an estimated depth of 1.18 μm as determined from Figure 5a. After 3 ks, both grains and grain boundaries become visually distinguishable (Figure 9c), suggesting some etching effect, although the sample preparation scratches remain. Figure 9d, at 10,000x magnification, shows surface features resembling those observed at 1 ks but with a coarser appearance. By 5 ks, bicontinuous dealloying morphologies emerge, with up to 5.36 μm of total dissolved materials, and the grain surfaces exhibit either micron-scale rectangular pits—similar to features noted in pure Cr samples affected by salt attacks—or micro-porosities (Figure 7f), with darker spots among the ligaments indicating residual salt presence. Lastly, after 10 ks of ligament coarsening, the ligament features became distinct.

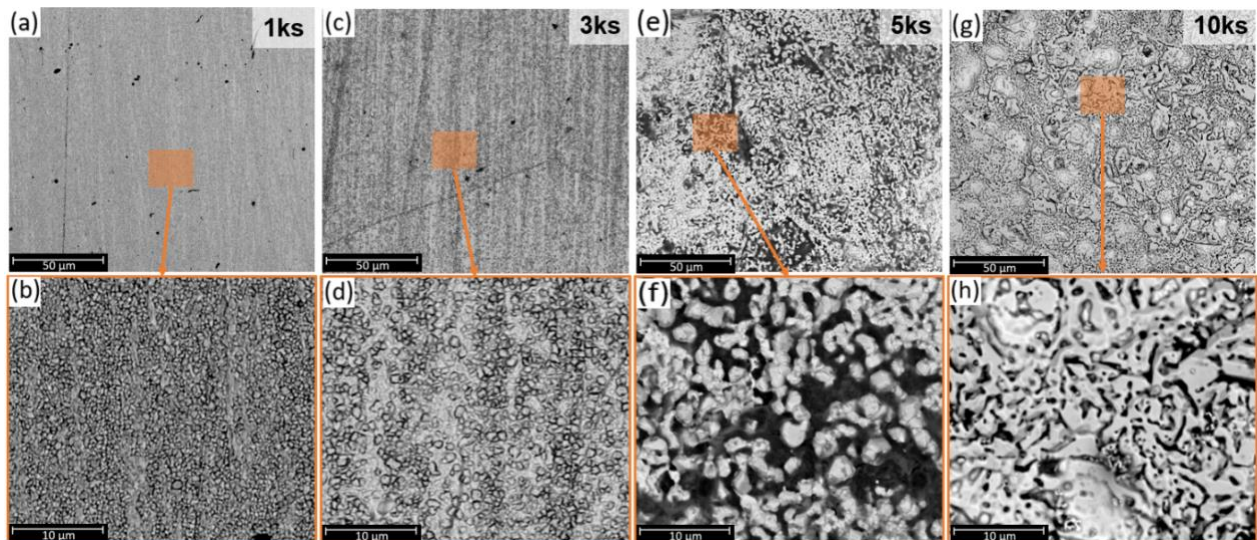


Figure 7. Backscattered electron micrographs of Ni20Cr potentiostatically held at +1.90 $V_{K+/K}$ for (a) 1ks, (b) 3ks, (c) 5ks, and (d) 10ks in molten FLiNaK salts, 600 °C taken at 2,000x magnification. (e), (f), (g), and (h) display the 10,000x magnified region of (a), (b), (c), and (d), respectively

Dealloying at $+2.10V_{K+/K}$

At $+2.10 V_{K+/K}$ (Figure 8a), both Ni and Cr rapidly dissolve at a significant rate, resulting in a $h_{\text{dissolved}}$ of $44.5 \mu\text{m}$. Both Ni and Cr corrosion products were detected by the *in situ* CV measurements as shown in Figure 8b, consistent with thermodynamic predictions. The i_{electric} starts near $10^{-1} \text{ A cm}^{-2}$, gradually reduces an order of magnitude to $10^{-2} \text{ A cm}^{-2}$ starting at 1 ks, but remains overall anodic. In Figure 8c, the Nyquist impedance spectra behave as a highly depressed semicircle, in both low and high frequency domains, dominated by the CT process due to the accelerated dissolution of both Ni and Cr. It is worth noting that the Nyquist plot gradually shifts upward (i.e. larger imaginary and real impedance) as time elapsed. The impedance spectra can be fitted with the EEC used for the $+1.90 V_{K+/K}$ sample with possibly identical attributes for the first time constant. However, the second time constant is found to exhibit an α value of 0.45 (see Table S4), suggesting that the low frequency domain (or depressed semicircle) may be attributed to the diffusional impedance mediated by the salt film^{60,61} which imposes mass-transport controlled behavior the authors previously observed.^{25,57}

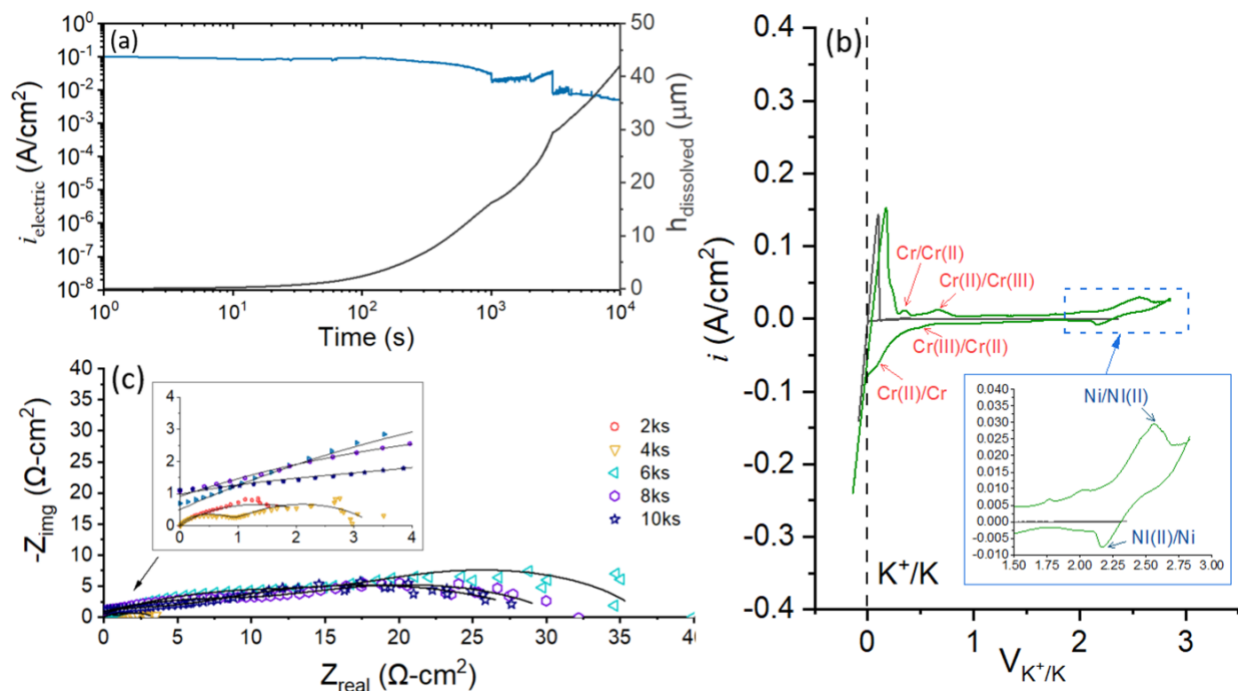


Figure 8. Ni₂₀Cr (wt%) subjected to potentiostatic hold in molten FLiNaK at 600 °C at $+2.10 V_{K+/K}$. (a) display the current time relationship, (b) shows the cyclic voltammogram measured the secondary Pt WE before (black) and after 10 ks of potentiostatic hold of Ni₂₀Cr. The redox peaks of possible Cr/Cr(II) and Cr(II)/Cr(III) reactions are labeled. The inset in (b) highlights the potential range in which the Ni/Ni(II) half-cell redox reactions are possible (c) shows the Nyquist plots measured at each 2 ks time increment containing the EEC used for fitting analysis and fitting results (black lines).

Figure 9a and 9b display bicontinuous dealloying features similar to Figure 6 where the polarization was at $+1.90 V_{K+/K}$. The coarsening and faceting of surface Ni ligaments are more pronounced and, to an extent, densified as the microporosities become less distinct. The faceted ligaments are $8.99 \pm 1.37 \mu\text{m}$ in width. Grain boundaries show the appearance of trenches comprised of 15.4 wt% of Cr, hinting at preferential dissolution from these regions and possible re-supply by fast-path dissolution. Some ligaments appear detached from the substrate, resulting in the exposure of the bare Ni₂₀Cr (wt%) substrate as verified by the EDS map and the analysis of Point #2 in Figure 9b.

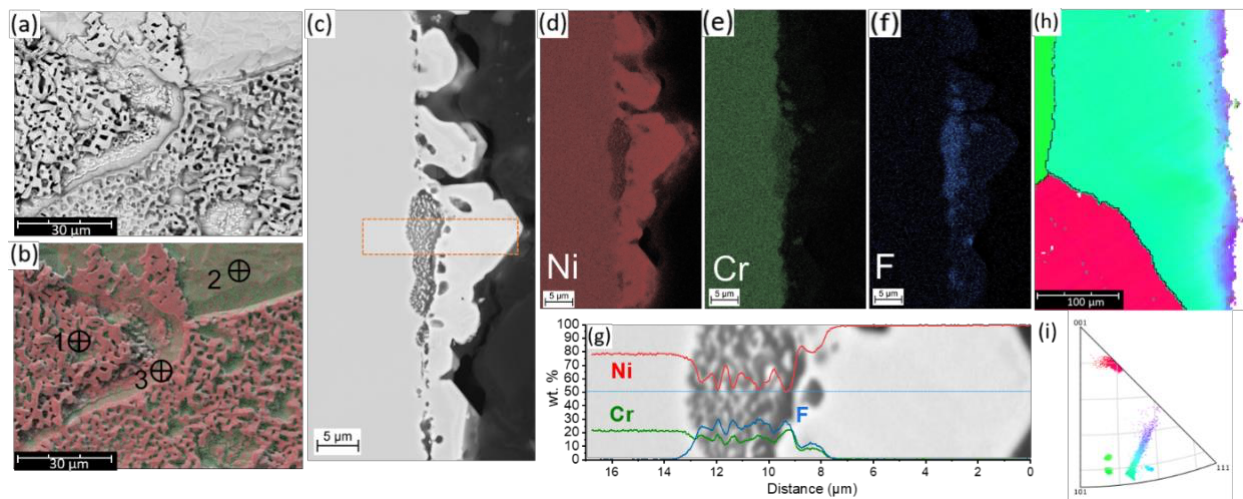


Figure 9. Ni₂₀Cr (wt.%) potentiostatically polarized at $+2.10 V_{K+/K}$ for 10 ks. (a) Plan-view SEM image showing surface morphology. (b) Composite EDS elemental maps overlaid on (a), highlighting Ni (red) and Cr (green) distribution. Specific locations were marked for point analysis. (c) Cross-sectional SEM image of the sample. (d), (e), (f) are EDS maps for Ni (red), Cr (green), and F (blue) respectively. The semi-transparent rectangle in (c) indicates the area subjected to EDS line scan analysis, with corresponding elemental profiles for Ni and Cr presented in (g). EBSD analysis is shown via the inverse pole figure (IPF) of a separate cross-sectional surface in (h). The stereographic triangle in (i) marks the orientation of the grains present in (h)

The cross-sectional analysis in Figure 9c reveals a significantly coarsened ligament structure on the top surface, which is enriched with Ni (Figure 9d). The thickness of the dealloyed layer is measured at $12.0 \pm 2.83 \mu\text{m}$, and the presence of underlying microvoids likely contributed to the poor adherence and detachment of ligaments seen in Figure 9a. The EDS line scan in Figure 9g indicated that the top layer is completely depleted of Cr. An EDS line scan was also conducted in a region without salt filtration to obtain the concentration profile of Cr depletion, with the results further detailed in Figure S9. Underneath the coarser ligaments, a region about $3 \mu\text{m}$ in width shows residual fluoride infiltration. In this region, the presence of Ni, Cr, and F suggests the possibility of metal fluoride salt film formation due to salt infiltration and Cr and/or Ni saturation (Figure S8).^{7,49,62} Lastly, at $+2.10 V_{K+/K}$, the IPF in Figure 9h reveals two grain orientations close to the (001)FCC and (101)FCC planes on the top surface. Intriguingly, the dealloyed

layer appears to align with the (111)FCC directions within the upper 5 μm and displays a color gradient beneath it, suggesting the presence of strain accumulation and the possibly of grain rotation. Given that the original grain size exceeds 100 μm , this change in direction is attributable to the dealloying process rather than the remnants of another grain. The formation and coarsening of the ligaments may also be affected by the crystallographic orientation of the parent grain,^{15,19,53} though this relationship is not clear in this work. It was shown that these features are not a result of possible Ni(II) to Ni plating detailed in Figure S7.

XRD of as-solidified salts

The X-ray diffractogram in Figure 10 shows that the residual salt after the potentiostatic polarization at +1.75 $V_{\text{K}^+/\text{K}}$ contains oxidized Cr species such as KCrF_3 , Li_2CrF_6 , and K_3CrF_6 ,⁶² though no Ni species are found. This correlates with the results of ICP-MS detection of Cr and Ni (Table S1) and the *in situ* CV presented in Figure 3b, where current peaks corresponding to Cr/Cr(II) and Cr(II)/Cr(III) are detected while Ni oxidation and/or reduction peaks are absent. It is noted that the ICP-MS data is collected after the experiment and after the salt is frozen, and therefore it is unclear what the isotope/ element concentration was during the liquid salt *in-operando*. With E_{applied} of +1.9 $V_{\text{K}^+/\text{K}}$ and +2.1 $V_{\text{K}^+/\text{K}}$ (Figure 10), the presence of NiF_2 compounds is detected in the salt together with K_3CrF_6 . The obtained results are also in agreement with the CV data for +1.9 $V_{\text{K}^+/\text{K}}$ and +2.1 $V_{\text{K}^+/\text{K}}$ where current peaks for Cr/Cr(II) and Cr(II)/Cr(III) and Ni/Ni(II) were found.

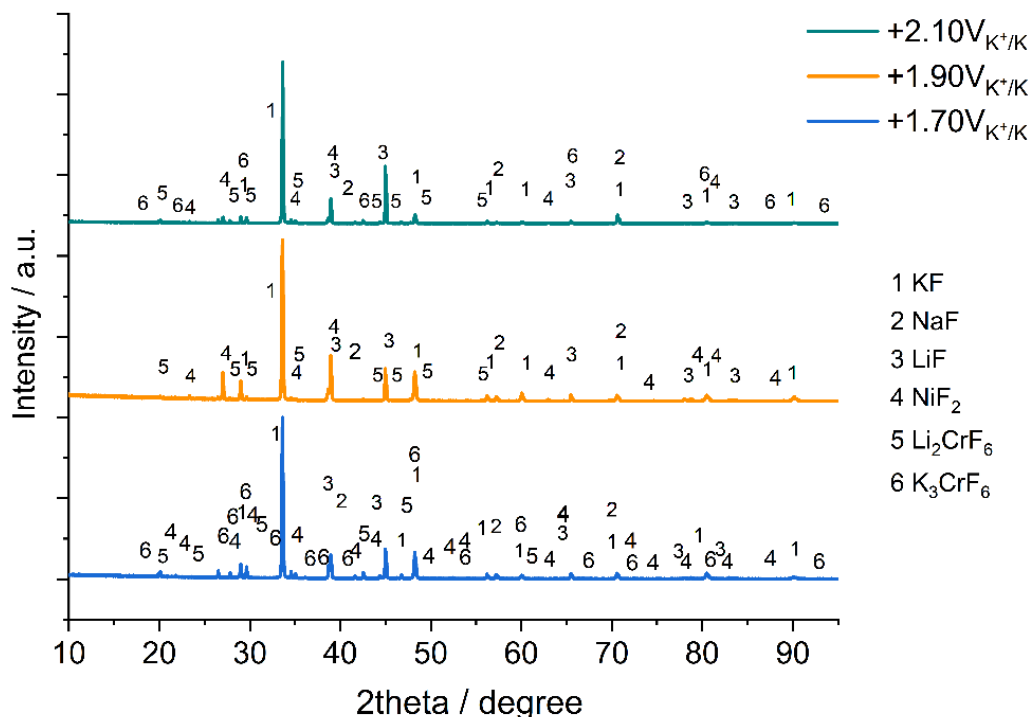


Figure 10. X-ray diffractogram of as-solidified salt mixture subjected to Ni20Cr potentiostatic hold at (a) +1.75 $V_{\text{K}^+/\text{K}}$, (b) +1.90 $V_{\text{K}^+/\text{K}}$, and (c) +2.10 $V_{\text{K}^+/\text{K}}$ in FLiNaK, 600 °C for 10 ks

The increase in the E_{applied} to $+2.3 V_{\text{K+K}}$ and $+2.5 V_{\text{K+K}}$ do not influence the salt phase composition (Figure S9); the salt phase contains Li_2CrF_6 , K_3CrF_6 , NiF_2 , and NaNiF_3 compounds, similar to the salt composition after potentiostatic polarization at $+1.9 V_{\text{K+K}}$ and $+2.1 V_{\text{K+K}}$ (Figure 10). However, when the potential is held at $+2.75 V_{\text{K+K}}$, diffraction peaks corresponding to Ni(III) compounds such as Na_3NiF_6 are also detected (dark blue line in Figure S9).

Table 1. Plan-view EDS point analysis on Ni20Cr (wt.%) upon potentiostatic hold at $+1.75 V_{\text{K+K}}$, $+1.90 V_{\text{K+K}}$, and $+2.10 V_{\text{K+K}}$ for 10 ks in molten FLiNaK, 600 °C.

Point #	1.75 $V_{\text{K+K}}$		1.90 $V_{\text{K+K}}$		2.10 $V_{\text{K+K}}$	
	Ni (wt.%)	Cr (wt.%)	Ni (wt.%)	Cr (wt.%)	Ni (wt.%)	Cr (wt.%)
1	96.3	3.7	100	0	98.0	2.0
2	83.8	16.2	88.1	11.9	79.8	20.2
3	92.5	7.5	97.7	2.3	84.6	15.4

Discussion

Dealloying encompasses the outward diffusion of Cr over 10ks from the bulk substrate, across the metal/salt interface to the salt through various transport mechanisms. At room temperature Cr mobility is limited but Cr can more readily diffuse at 600 °C. This process involves a series of sequential and concurrent transport phenomena that elucidate the control mechanisms behind the release of Cr(II) and Cr(III). Transport through the bulk and along grain boundaries facilitates the movement of Cr to areas where Cr is depleted. Furthermore, the interface between the metal and salt, along with the electrochemical double layer, plays a critical role in mediating electrochemical oxidation processes, which are influenced by the CT, MT, or mixed controlled polarization behavior. As the applied potential changes, the rate-determining process that controls the mechanism of Cr transport and subsequent release is altered. While this process is interconnected with the morphology, the i_{electric} alone is inadequate to account for all the controlling factors. The molten fluoride dealloying process supports features characteristic of bicontinuous morphology, notably the formation of an interconnected network of micro-pores and ligaments enriched with the MN element Ni. Interestingly, the ligaments coarsen with increasing applied potential, from 0.29 μm ($+1.75 V_{\text{K+K}}$, 10 ks) and 0.95 μm ($+1.90 V_{\text{K+K}}$, 10 ks) to 8.99 μm ($+2.10 V_{\text{K+K}}$, 10 ks), as shown in Table 2. Such potential dependent coarsening has been observed elsewhere^{63–66} and will be discussed.

Table 2. Correlation between applied potential, total charge consumed, and select morphological properties in Ni20Cr (wt.%) alloys post 10ks of potentiostatic dealloying in FLiNaK at 600 °C.

E (vs. K^+/K)	$h_{\text{dissolved}}$ (μm)	w (μm)	λ (μm)
1.75	1.09	0.81±0.18	0.29±0.08
1.90	12.2	10.9±3.45	0.95±0.15
2.10	44.9	12.0±2.83	8.99±1.37

Applied potential effect on surface diffusions

The dealloying process leaves unoxidized Ni-rich material on the sample surface. However, the remaining material forms ligament features that do not exhibit nanometer porosity but instead coarsen and densify during the dealloying process. To understand whether the coarsening mechanism is solely governed by surface diffusion or concurrently assisted by bulk diffusion, Eq. 7 can be utilized to study the relationship between morphology and time:

$$\frac{d\lambda^n}{dt} = \text{constant} \quad (7)$$

where n is a coarsening exponent, and t is time. In this work, we chose the feature size to be the ligament width measured in plan view based on Figure 7, since these ligaments will have already undergone dealloying and their evolution is only governed by coarsening and capillary effects. It is noted that a n value of 4 corresponds to a coarsening process that is a surface diffusion mediated process, whereas a value of 3 indicates bulk diffusion mediated.⁶⁶⁻⁶⁹

As shown in Figure 11 and Table 3, the ligament width and time display a slope of $0.41 \pm 0.14 \mu\text{m}$, which corresponds to a n value of 2.43 ± 1.26 . Therefore, the current data cannot conclusively determine whether coarsening behavior is dominated solely by surface or bulk diffusion. Nevertheless, the measurement is carried out on the plan view of a limited size of dealloying times while the ligament size may vary with the dealloying depth,¹⁶ suggesting the need for further study to confirm these findings.

Table 3. Plan view measurements of ligament Width for Ni20Cr potentiostatically polarized at +1.90 V_{K+/K} for 1, 3, 5 and 10 ks in molten FLiNaK at 600 °C

Time (ks)	λ (μm)
1	0.43±0.11
3	0.65±0.12
5	0.84±0.14
10	1.08±0.26

When ligament coarsening is primarily controlled by Ni surface diffusion and capillary forces for the minimization of surface free energy, the surface diffusivity of Ni (D_s^{Ni}) may be estimated via Eq. 8:⁷⁰⁻⁷²

$$D_s^{\text{Ni}} = \frac{\lambda^4 kT}{32\gamma t a^4} \quad (8)$$

where k is the Boltzmann constant ($1.38 \cdot 10^{-23} \text{ J K}^{-1}$), γ is surface energy of Ni in molten salts (an assumed value of 200 mJ m^{-2} due to the lack of experimental and computational data related to the interface between metal and molten salt),⁷⁰ t is the potentiostatic polarization hold time, T is temperature, and a is the lattice parameter of pure Ni at 600 °C (0.356 nm was used).⁷³ The surface energy is estimated based on Marcus et al.⁷⁴ Eq. 8 is only used for the condition of +1.75 V_{K+/K} and +1.90 V_{K+/K} since significant Ni

dissolution is seen at $+2.10 V_{K+/K}$ and this effect cannot be ignored. This yields D_S^{Ni} values of $8.02 \cdot 10^{-10}$ and $9.93 \cdot 10^{-8} \text{ cm}^2 \text{ s}^{-1}$, which are at least three orders of magnitude higher than the typical range of D_S^{Ni} values reported in room temperature aqueous solution between 10^{-13} and $10^{-16} \text{ cm}^2 \text{ s}^{-1}$.^{66,75} This increase is expected at the elevated temperatures for FLiNaK and is thermally activated. Furthermore, the curvature induced by the ligaments (i.e., convex ligaments and concave pores) also drives the further coarsening and densification behavior as reported by Henkelmen et al.⁷⁶ Their experimental observations and kMC simulations bear a striking resemblance to those depicted in Figs. 4, 6, and 9.

Using the nominal diffusion equation ($x = \sqrt{Dt}$), the calculation shows that in 10 ks at 600 °C and $T_H = 0.522$, surface diffusion of unoxidized Ni can readily occur across distances exceeding 1 μm (1000 nm). This contributes to the reorganization of Ni into new FCC ligament structures, potentially realigning their orientations to alleviate stress and forming new grain boundaries. Another possibility to explain the formation of new grain boundaries in the dealloyed layer is the generation and reorganization of dislocations. During Cr dealloying, a new semicoherent, void-rich interface is created between the Ni-rich dealloyed layer and the parent substrate as evident in Figures 4, 6 and 9, which creates dislocations. This interface accumulates strains consisting of the lattice parameter differential between the parent grain (Ni-20Cr, wt%) and pure Ni, an increasing length of pure Ni (analogous to the presence of shear strain imposed by a thin film on a substrate)⁹¹, the presence of thermal and non-equilibrium vacancies etc. The formation of a core-shell structure within a MN ligament will further escalate this effect^{15,19}. It is an ongoing work to quantify the percent strains and the density of dislocation formed during dealloying. Nevertheless, as dealloying proceeds, a new interface is created, leaving behind dislocations within the Ni dealloyed layer or ligaments, which may possibly reorganize into new grain boundaries, contributing to the phenomenon observed in Figures 4, 6 and 9. Lastly, it is also acknowledged that the rapid Ni surface diffusion may potentially decelerate both interfacial Cr dissolution (J_{electric}) and bulk transport of Cr ($J_{\text{Bulk}}^{\text{Cr}}$) as it alters the alloy surface chemistry and microstructure. However, determining the extent of this effect necessitates more sensitivity analysis in our future study.

The following presents a hypothesis to explain the apparent Ni ligament coarsening behavior with applied potential. Based on the Terrace-Ledge-Kink model (TLK)⁷⁷ and the Gibbs-Thomson effect, as dealloying occurs Ni adatoms can surface-diffuse to passivate receding sites created by Cr dissolution, which include step edges, terrace, and kink sites.^{52,78-80} As the electrode potential approaches the Ni dissolution potential, the diffusion rates of kink sites can increase drastically—an observation made by Kolb et al. using scanning tunneling microscope during potentiostatic dealloying of Ag-Au.⁶³ This behavior was attributed to the interaction between possible physi-/chemi-absorbed species and the double layer.⁶³⁻⁶⁵ When the dissolution of Ni becomes favorable, two phenomena may occur: (1) structures formed by surface reconstruction may be annihilated and lowering the energy barriers for surface diffusion;^{63-65,81} (2) Ni

adatoms preferentially dissolve due to their low-coordination nature,⁷⁸ leaving Ni atoms situated in the more coordinated step edges or terrace sites to passivate vacancies created by Cr dissolution. Either mechanism is a function of crystallographic orientation. Higher index, more irrational planes exhibit a different or lower γ (thus a higher D_s from Eq. 8), shorter hopping distance, higher number of low-coordination sites,⁷⁸ and possibly leads to faster ligament coarsening. Consequently, despite all three applied potentials having identical potentiostatic polarization periods, the Ni ligaments are coarser at high potentials possibly due to an enhanced MN surface mobility.

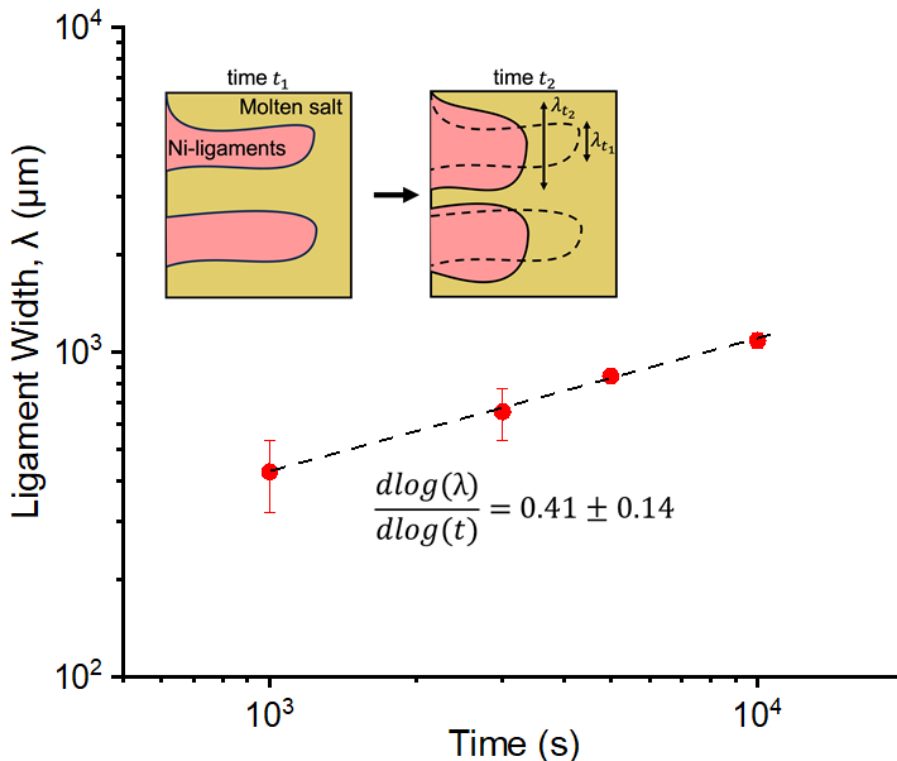


Figure 11. Plan view measurements of ligament width between 1 and 10 ks for Ni20Cr (wt.%) for Ni20Cr potentiostatically polarized in Molten FLiNaK at 600 °C. The inset displays a simplified schematic of Ni-rich ligament coarsening process.

Applied potential effect on electrolytic dissolution

In aqueous dealloying, the potentiostatic polarization (also known as chronoamperometry) is a popular approach for fabricating bicontinuous dealloying porous structures, particularly in Ag-Au systems.^{28,34,75,82} The trend of current decay over time, i.e. $i \propto t^{-n}$, can also shed light on possible rate-controlling surface diffusion mechanisms, as further elucidated by Sieradzki et al.^{53,82} However, these relationships are not as apparent in molten salt systems. Depending on the applied potentials (such as +1.90 V_{K+/K}), the anodic current behavior could remain at a relatively constant magnitude over time. Such behavior has also been noted in molten chlorides¹⁹ and fluorides²⁵ systems. This may be explained by the recent kMC modeling by

Henkelmann et al.,⁷⁶ who simulated the *i-t* behavior for surface-mediated primary and secondary dealloying behavior on a nanoporous gold alloy.

Figure 12 illustrates that $Q_{\text{consumed}} (= \int_0^t i dt)$ increases linearly with increasing time at fixed *i*, exhibiting a unity slope and suggesting CT controlled behavior. For the +1.75 $V_{\text{K+K}}$ condition, the plateau of the curve can be attributed to the net current density dropping to near zero as i_{electric} switches to cathodic. A unity slope suggests that the reaction proceeds at a consistent rate, with both the dissolution rate and the outward diffusing supply of receding Cr and/ or Ni remaining steady. Intriguingly, at +2.10 $V_{\text{K+K}}$, the slope shifts to 0.5 starting at 409 s, as highlighted by the black arrow. A slope of 0.5 points to potential mass transport limitations.⁸³ These could arise from bulk Cr lattice diffusion and/ or possibly from limitations in the longer range, ionic phase mass transport initiated by the formation of fluoride salt film on the metal/salt interface.¹⁷ It is noted that the dissolution of Ni may also contribute to the unity slope seen at the +1.90 and +2.10 $V_{\text{K+K}}$. Nevertheless, this observation is consistent with the R_{ct} trend (which is inversely proportional to the interfacial dissolution rate⁸⁴) with time extracted from EEC fittings of EIS spectra as displayed in Figure 13 and Table S6. Both the +1.75 $V_{\text{K+K}}$ and +1.90 $V_{\text{K+K}}$ conditions exhibit relatively constant R_{ct} values. However, the +2.10 $V_{\text{K+K}}$ condition reveals an order of magnitude decrease in R_{ct} , coinciding where the rate of dissolution is MT-limited through the salt film.

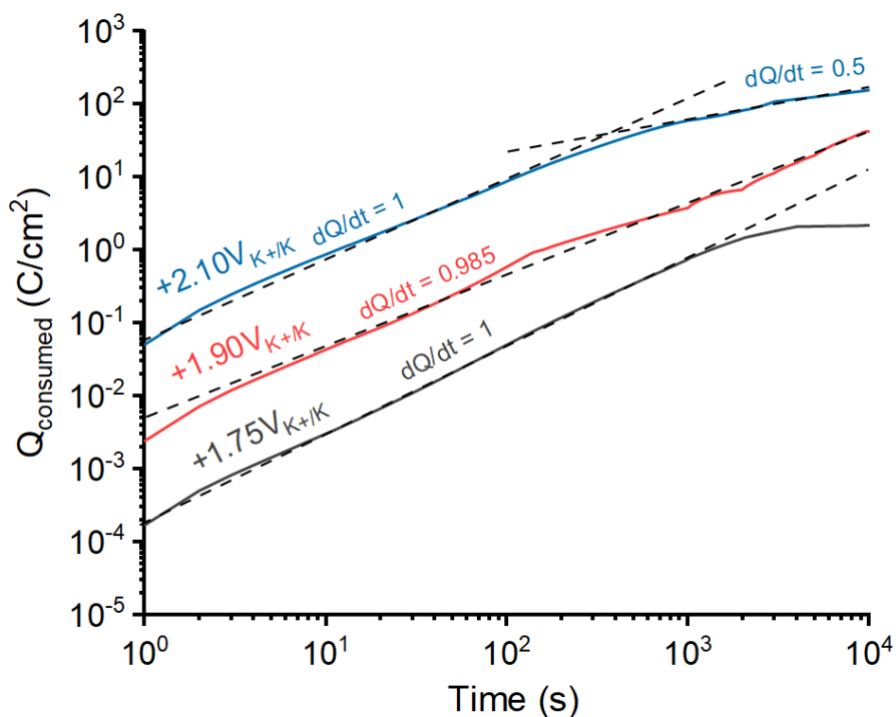


Figure 12. Cumulative charge consumed (Q_{consumed}) during the potentiostatic hold of Ni20Cr in molten FLiNaK salts, 600 °C at +1.75 $V_{\text{K+K}}$, +1.90 $V_{\text{K+K}}$, and +2.10 $V_{\text{K+K}}$ for 10 ks

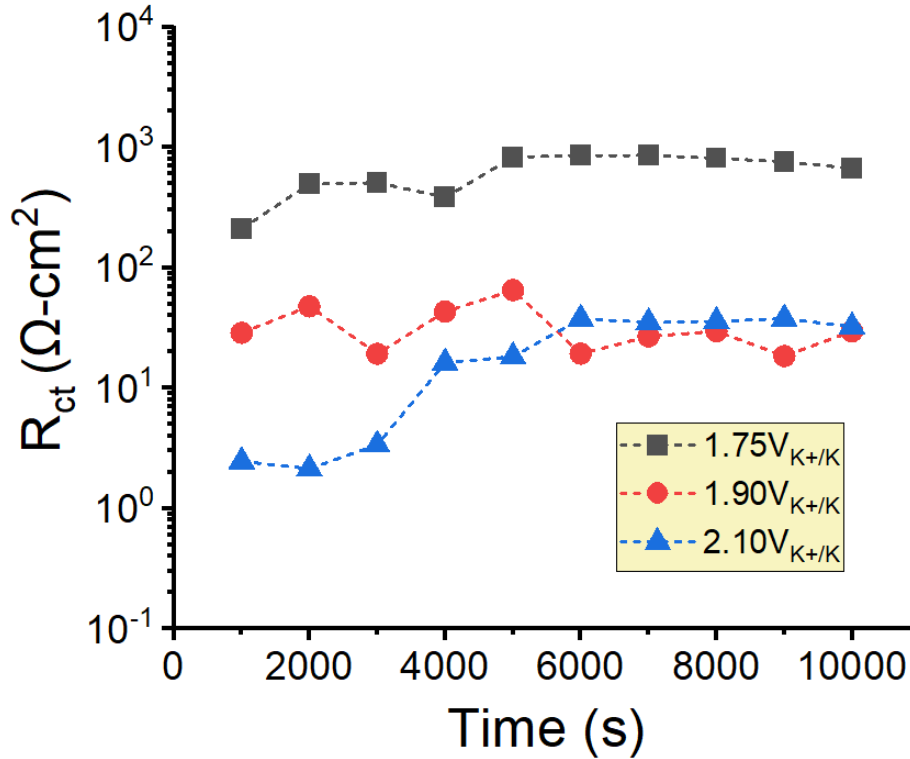


Figure 13. Charge transfer resistance (R_{ct}) of Ni20Cr in molten FLiNaK salts, 600 °C potentiostatically held at +1.75 $V_{K+/K}$, +1.90 $V_{K+/K}$, and +2.10 $V_{K+/K}$ from 1 ks to 10 ks

Effect of bulk diffusion on dealloying

We now shift our focus to the transport of Cr in the Ni20Cr alloy. EDS line scans reveal that Cr, being the LN element, is retained at the ~5 wt. % level within the surface ligaments at +1.75 $V_{K+/K}$. However, at higher potentials of +1.90 $V_{K+/K}$ and +2.10 $V_{K+/K}$, Cr is completely depleted from both the ligaments and the dealloyed zone (Figs. 6 and 9). This partial depletion raises questions about the necessity of Ni reorganizing into new grains with various crystallographic orientations. At higher TH, the bulk diffusion of Cr, via lattice and short-circuit pathways, can become predominant.^{15,32} A standing question is whether the bulk diffusion of Cr can sufficiently maintain the $J_{electric}$ —the interfacial dissolution rate measured. The following consideration assumes only Cr oxidation is the source of anodic charge that is solely responsible for $J_{electric}$. By equating the necessary $J_{electric}$ to a hypothetical Cr bulk diffusion flux, represented as J_{Bulk}^{Cr} , Bulk Cr the required J_{Bulk}^{Cr} to match $D_{i_{electric}}$ can be described as a function of $i_{electric}$ using Eq. 9:

$$J_{electric} = J_{Bulk}^{Cr} = \frac{i_{electric}}{zF} \quad (9)$$

where z represents the oxidation state of the dissolved species (assumed to be 3). The i_{electric} values were measured at each dealloying potential (Figs. 3, 5, 8). At constant J_{electric} , the $J_{\text{Bulk}}^{\text{Cr}}$ can be estimated with Fick's 1st Law assuming a pseudo-steady state diffusion condition, starting with Eq. (10):

$$J_{\text{Bulk}}^{\text{Cr}} = -D_{\text{eff}}^{\text{Cr}} \frac{\Delta C^{\text{Cr}}}{\Delta x} \quad (10)$$

where Δx is the diffusion distance and ΔC^{Cr} is the difference in bulk and depleted concentrations of Cr consumed during selective leaching of Cr from Ni20Cr alloy. This value is taken to be 0.0340 mol/cm³ (equivalent to complete Cr depletion). Accordingly, the effective solid-state diffusion coefficient ($D_{\text{eff}}^{\text{Cr}}$) for Cr in FCC Ni20Cr including grain boundaries can be quantitatively assessed using Eq. 11:

$$D_{\text{eff}}^{\text{Cr}} = \left(\frac{2\delta}{L}\right)D_{\text{gb}}^{\text{Cr}} + \left(1 - \frac{2\delta}{L}\right)D_1^{\text{Cr}} \quad (11)$$

where D_{gb} and D_1 are the grain boundary and bulk diffusivities of Cr in Ni20Cr in cm²/s, δ is the grain boundary thickness ($\sim 10^{-7}$ cm⁸⁵), and L is the grain size. Based on published literature, the D_{gb} and D_1 of Cr in Ni20Cr are on the order of $9.55 \cdot 10^{-11}$ cm²/s and $8.71 \cdot 10^{-15}$ cm³/s,⁸⁶⁻⁸⁹ respectively. With an average L of 351 μm (Figure S1), the D_{eff} for Cr diffusion is taken as $9.25 \cdot 10^{-15}$ cm²/s. Eq. 11 does not consider the effects of non-equilibrium vacancies nor dislocations that may accelerate solid-state diffusion. It is important to note that $J_{\text{Bulk}}^{\text{Cr}}$ is also time-dependent. To connect $J_{\text{Bulk}}^{\text{Cr}}$ with time (Δt), Δx was estimated using the nominal diffusion distance via Eq.12:

$$\Delta x = \sqrt{D_{\text{eff}}^{\text{Cr}} \Delta t} \quad (12)$$

Rearranging Eqs. 10 and 12 results in Eq. 13, which is the time dependent current density ($i_{\text{electric}}^{\text{required}}$) corresponding to a condition where Cr bulk diffusion becomes the rate-limiting mechanism in a series of diffusion processes (see Figure 14).

$$J_{\text{Bulk}}^{\text{Cr}} = - \frac{\Delta C^{\text{Cr}} \sqrt{D_{\text{eff}}^{\text{Cr}}}}{\sqrt{\Delta t}} \quad (13)$$

Moreover, to compare with the possible mass-transport effect in the ionic phase, the diffusion flux of Cr (III) ions in FLiNaK can also be estimated using Eq. 14:

$$J_{\text{FLiNaK}}^{\text{Cr(III)}} = \frac{D_{\text{Cr}} C_{\text{Cr(III)}}}{\delta_b} \quad (14)$$

where $D_{\text{FLiNaK}}^{\text{Cr(III)}}$ is the diffusivity of Cr (III) ions in FLiNaK at 600 °C (assumed to be $10^{-5} \text{ cm}^2 / \text{s}^{10,25}$), δ_b is the boundary layer thickness (estimated to be $10 \text{ } \mu\text{m}^{25}$), and $C_{\text{Cr(III)}}$ is the concentration of dissolved Cr in mol/cm^3 . Eq. 15 can also be expressed as a function of time:

$$J_{\text{FLiNaK}}^{\text{Cr(III)}} = \frac{C_{\text{Cr(III)}} \sqrt{D_{\text{FLiNaK}}^{\text{Cr(III)}}}}{\sqrt{\Delta t}} \quad (15)$$

The Faraday's law of mass and charge conversion, akin to Eq. 5, can be used to calculate $C_{\text{Cr(III)}}$, resulting in Eq. 16:

$$J_{\text{FLiNaK}}^{\text{Cr(III)}} = \frac{EW * Q_{\text{consumed}} * \sqrt{D_{\text{FLiNaK}}^{\text{Cr(III)}}}}{V_{\text{FLiNaK}} \sqrt{\Delta t}} \quad (16)$$

where V_{FLiNaK} is 15 cm^3 representing the volume of FLiNaK salt used in this study. $J_{\text{FLiNaK}}^{\text{Cr}}$ was calculated for each dealloying potential condition. Figure 14 presents a simplified schematic of the multiple diffusion processes that occur concurrently during molten salt dealloying.

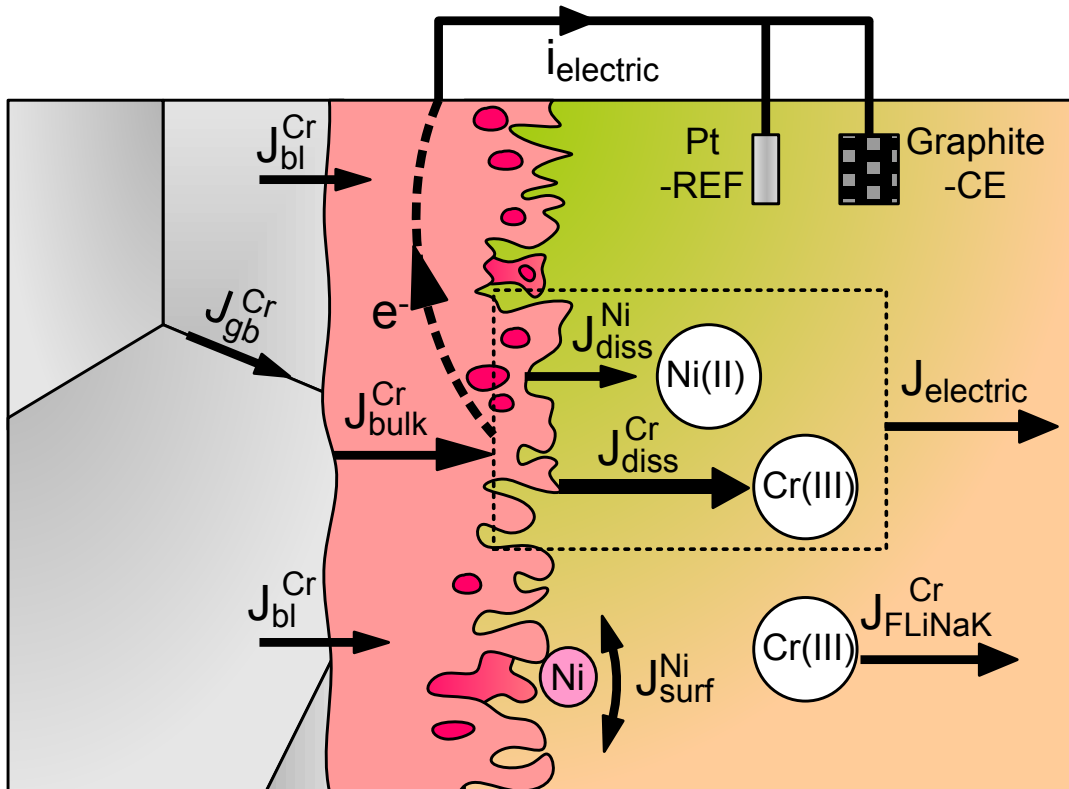


Figure 14. Schematics displaying a simplified mechanism of molten fluoride dealloying

Figure 15 presents a comparative analysis of J_{electric} , $J_{\text{Bulk}}^{\text{Cr}}$, and $J_{\text{FLiNaK}}^{\text{Cr(III)}}$ over time. At +1.75 $V_{\text{K+/K}}$, $J_{\text{Bulk}}^{\text{Cr}}$ at first exceeds J_{electric} for the initial ~200 s of the potentiostatic hold period, suggesting that the bulk diffusion of Cr is sufficiently fast to support the Cr dissolution reaction, but not for extended periods of time. This can lead to significant salt penetration by dealloying to develop the observed corrosion pores. As time progresses, J_{electric} decreases slightly and diminishes to nearly zero as Cr is only supplied when Ni surface diffusion uncovers unexposed FCC Ni-Cr. Moreover, for the entire 10 ks hold period, $J_{\text{FLiNaK}}^{\text{Cr(III)}}$ is at least three orders of magnitude larger than J_{electric} and $J_{\text{Bulk}}^{\text{Cr}}$ and thus ionic diffusion of Cr(III) is unlikely to act as a rate-limiting step in the process at any potential. This observation holds true for the dealloying potentials of +1.75 (Figure 14a), +1.90 $V_{\text{K+/K}}$ (Figure 14b) and +2.10 $V_{\text{K+/K}}$ (Figure 14c).

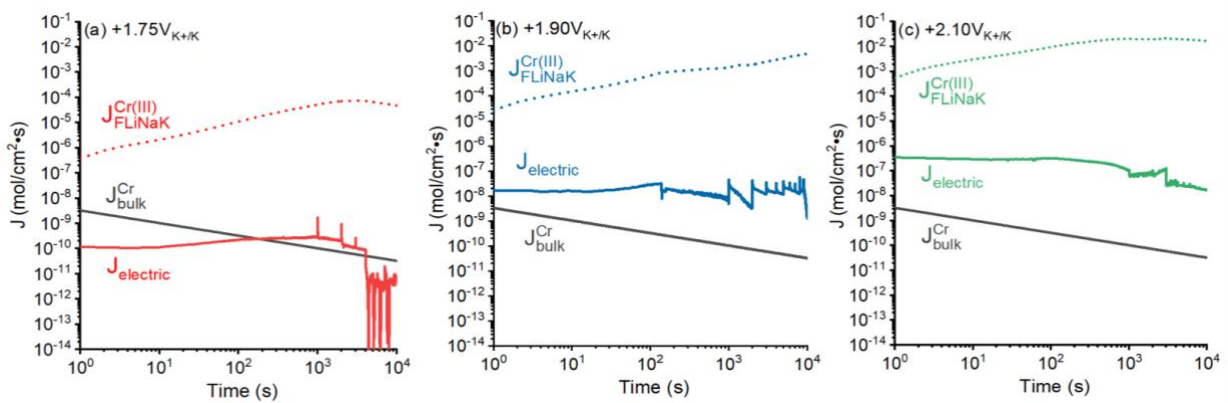


Figure 15. J_{electric} vs.time for Ni20Cr (wt.%) potentiostatically held at (a) +1.75 $V_{\text{K+/K}}$, (b) +1.90 $V_{\text{K+/K}}$, and (c) +2.10 $V_{\text{K+/K}}$ for 10 ks. The solid grey line represents the calculated effective bulk diffusion flux ($J_{\text{Bulk}}^{\text{Cr}}$) and the dashed line shows the ionic diffusion flux of Cr(III), $J_{\text{FLiNaK}}^{\text{Cr}}$, ions in FLiNaK at 600 °C

On the contrary, J_{electric} is higher than $J_{\text{Bulk}}^{\text{Cr}}$ for the entire potentiostatic hold period for +1.90 $V_{\text{K+/K}}$ and +2.10 $V_{\text{K+/K}}$. This suggests that the dealloying process at constant potential can be rate-limited by the insufficient bulk transport of Cr. At potentials higher than +2.10 $V_{\text{K+/K}}$, the dissolution of Cr to Cr(III) and Ni to Ni(II) is relatively fast. The combination of insufficient bulk outward diffusion of Cr and an expected increase in $J_{\text{diss}}^{\text{Ni}}$ causes the uniform dissolution rate to exceed the dealloying rate at these high potentials. At some potential both the rate of LN and MN dissolution results in a smooth surface morphology. Here, the uniform corrosion front moves at a velocity exceeding the dealloying front. It is noted that $J_{\text{Bulk}}^{\text{Cr}}$ can be increased by increasing temperature,²⁰ reducing grain sizes,²⁷ cold working,²⁶ radiating the alloy,³¹ or any other means to introduce defects to the alloys.²

The interaction between the interfacial dealloying process, the underlying microstructure, and how the role of crystallographic orientation to modify the rates and mechanisms by which surface diffusion and bulk-diffusion controlled dealloying are all current subjects of investigation. The findings of this current study provide a foundational methodology and dealloying condition that will allow us to interrogate and

isolate these individual effects. Another open knowledge gap is the speciation effect of metallic cations in molten salts, e.g. CrF_6^{3-} in molten fluorides,^{6,9,90} on the development of dealloying structure. For instance, speciation can modify the driving force of LN dissolution (thus altering J_{electric}),^{6,9} alter the surface mobilities of MN,⁹¹ possibly restrict the refinement of pore size due to the larger ionic radii,^{52,92,93} and/or slow down the long-range diffusion of corrosion products in molten salts.¹⁸ Lastly, independent in-operando elemental measurements (in the liquid salt) have not been conducted and may be the subject of future studies.

Conclusion

This work investigates the morphological evolution of Ni20Cr (wt.%) in FLiNaK at 600 °C at a systematic range of applied potentials between $+1.75 V_{\text{K+/K}}$ and $2.75 V_{\text{K+/K}}$. By employing a framework that couples thermo-kinetic analysis, *in-operando* electrochemistry, and together with a multi-modal materials characterization method, the possible mechanism that regulates the rates of Cr dealloying can be pinpointed at different potential regimes. At an intermediate potential regime between $+1.75 V_{\text{K+/K}}$ and $+2.10 V_{\text{K+/K}}$ for 10ks at high homologous temperature, bicontinuous dealloying is evident through the formation of a micron-scale interconnected pure Ni ligament-pores network. Only Cr dissolved at $+1.75 V_{\text{K+/K}}$. With increasing applied potential, there is a noticeable bulk diffusion-assisted coarsening and densification of the Ni ligaments.

In this regime, the bulk outward diffusion of Cr ($J_{\text{Bulk}}^{\text{Cr}}$) initially exceeds the dissolution flux (J_{electric}) at $+1.75V_{\text{K+/K}}$, but subsequently falls below J_{electric} , suggesting Cr bulk outward diffusion eventually limits the dealloying process. At the metal/salt interface under CT controlled dissolution, Cr is instantly oxidized. At the higher potentials of $+1.90V_{\text{K+/K}}$ and $+2.10V_{\text{K+/K}}$, J_{electric} consistently surpasses $J_{\text{Bulk}}^{\text{Cr}}$ from the outset, signaling that $J_{\text{Bulk}}^{\text{Cr}}$ is not sufficient to sustain the dissolution reactions of Cr and Ni. Under these conditions, the dissolution of Ni also contributes to J_{electric} . The ionic phase Cr(III) ion diffusion in FLiNaK is not rate-limiting at these potentials. Therefore, it is evident that while the impact of the Cr bulk is significant in the context of molten salt dealloying, the rate-limiting step can shift depending on the applied potential and the duration of the process. The applied potential (or driving force) determines the dissolution rates of Cr and Ni, while time reflects the morphological evolution that affects $J_{\text{Bulk}}^{\text{Cr}}$.

At the elevated potential regime between $+2.30 V_{\text{K+/K}}$ and $+2.50 V_{\text{K+/K}}$, mixed CT- and MT-controlled dissolution of both Cr and Ni lead to the formation of a crystallographic faceted structure. At high enough potential, the rate of Ni(II) release is nearly as fast as that of Cr(III) and evidence of dealloying disappears as uniform dissolution occurs at nearly the same rate as dealloying. Hence the dissolution flux of surface Ni ($J_{\text{diss}}^{\text{Ni}}$) also becomes significant. At $+2.75 V_{\text{K+/K}}$, electro-dissolution is completely regulated by MT controlled behavior due to the formation of a potentially K-Cr-Ni-F salt film, leading to the smoothing of

surfaces. At this potential, Ni (II) and Cr(III) are dissolving at nearly the same rate. The presence of the salt film can also be observed on the edges of corrosion pores at the dealloying potential of +2.10 V_{K+/K}. This suggests an additional mass transport constraint arising from the diffusion of corrosion products, such as Cr(III) and Ni(II), through salt-penetrated channels.

These analyses point to the bulk outward diffusion of LN(Cr) as the predominant mechanism driving molten salt dealloying at high homologous temperatures. The occurrence of bicontinuous dealloying necessitates specific combinations of J_{electric} , $J_{\text{Bulk}}^{\text{Cr}}$ (including lattice and grain boundary diffusions), $J_{\text{FLiNaK}}^{\text{Cr(III)}}$, $J_{\text{diss}}^{\text{Ni}}$, and $J_{\text{surf}}^{\text{Ni}}$. Bicontinuous porosity still forms when Ni dissolves at +1.90V_{K+/K} and +2.10V_{K+/K}, likely due to the $J_{\text{diss}}^{\text{Ni}}$ being sufficiently low relative to $J_{\text{diss}}^{\text{Cr}}$ and $J_{\text{diff}}^{\text{Ni}}$. The current findings suggest that the interplay of rapid bulk diffusion, surface diffusion, and interfacial dissolution of Cr and Ni, underlined by a constant current may enable fast dealloying in a specific potential range

References

1. D. Rodrigues, G. Durán-Klie, S. Delpech, Pyrochemical reprocessing of molten salt fast reactor fuel: focus on the reductive extraction step, *Nukleonika* 60 (2015) 907–914. <https://doi.org/10.1515/nuka-2015-0153>.
2. S. Guo, J. Zhang, W. Wu, W. Zhou, Corrosion in the molten fluoride and chloride salts and materials development for nuclear applications, *Progress in Materials Science* 97 (2018) 448–487. <https://doi.org/10.1016/j.pmatsci.2018.05.003>.
3. F. Schmidt, P. Hosemann, R.O. Scarlat, D.K. Schreiber, J.R. Scully, B.P. Uberuaga, Effects of Radiation-Induced Defects on Corrosion, *Annu. Rev. Mater. Res.* 51 (2021) 293–328. <https://doi.org/10.1146/annurev-matsci-080819-123403>.
4. H.E. McCoy, R.E. Gehlbach, Influence of Irradiation Temperature on the Creep-Rupture Properties of Hastelloy-N, *Nuclear Technology* 11 (1971) 45–60. <https://doi.org/10.13182/NT71-A30901>.
5. R. Auguste, H.L. Chan, E. Romanovskaia, J. Qiu, R. Schoell, M.O. Liedke, M. Butterling, E. Hirschmann, A.G. Attallah, A. Wagner, F.A. Selim, D. Kaoumi, B.P. Uberuaga, P. Hosemann, J.R. Scully, A multimodal approach to revisiting oxidation defects in Cr₂O₃, *Npj Mater Degrad* 6 (2022) 1–13. <https://doi.org/10.1038/s41529-022-00269-7>.
6. H.L. Chan, E. Romanovskaia, J. Qiu, P. Hosemann, J.R. Scully, Insights on the corrosion thermodynamics of chromium in molten LiF-NaF-KF eutectic salts, *Npj Mater Degrad* 6 (2022) 46. <https://doi.org/10.1038/s41529-022-00251-3>.
7. E. Romanovskaia, H.L. Chan, V. Romanovski, F. Garfias, M. Hong, S. Mastromarino, P. Hosemann, R. Scarlat, J.R. Scully, An In Situ, multi-electrode electrochemical method to assess the open circuit potential corrosion of Cr in unpurified molten FLiNaK, *Corrosion Science* 222 (2023) 111389. <https://doi.org/10.1016/j.corsci.2023.111389>.
8. S.S. Raiman, S. Lee, Aggregation and data analysis of corrosion studies in molten chloride and fluoride salts, *Journal of Nuclear Materials* 511 (2018) 523–535. <https://doi.org/10.1016/j.jnucmat.2018.07.036>.
9. H.L. Chan, J.R. Scully, Deciphering when Metal Corrosion is Spontaneous in Molten Fluorides Using Potential-Activity Diagrams, *Corrosion* (2023). <https://doi.org/10.5006/4401>.
10. Y. Wang, J. Zhang, Electrochemical Properties of CrF₂ in FLiNaK Molten Salt and the New Analytical Methods for their Determination, *J. Electrochem. Soc.* 167 (2020) 086503. <https://doi.org/10.1149/1945-7111/ab8923>.

11. Ketan Kumar Sandhi, J. Szpunar, Analysis of Corrosion of Hastelloy-N, Alloy X750, SS316 and SS304 in Molten Salt High-Temperature Environment, *Energies*. 14 (2021) 543–543. <https://doi.org/10.3390/en14030543>.
12. L.C. Olson, J.W. Ambrosek, K. Sridharan, M.H. Anderson, T.R. Allen, Materials corrosion in molten LiF–NaF–KF salt, *Journal of Fluorine Chemistry* 130 (2009) 67–73. <https://doi.org/10.1016/j.jfluchem.2008.05.008>.
13. Y.L. Wang, Q. Wang, H.J. Liu, C.L. Zeng, Effect of grain refinement on the corrosion of Ni-Cr alloys in molten (Li,Na,K)F, *Corrosion Science* 109 (2016) 43–49. <https://doi.org/10.1016/j.corsci.2016.03.027>.
14. F.-Y. Ouyang, C.-H. Chang, B.-C. You, T.-K. Yeh, J.-J. Kai, Effect of moisture on corrosion of Ni-based alloys in molten alkali fluoride FLiNaK salt environments, *Journal of Nuclear Materials* 437 (2013) 201–207. <https://doi.org/10.1016/j.jnucmat.2013.02.021>.
15. T. Ghaznavi, S.Y. Persaud, R.C. Newman, Electrochemical Corrosion Studies in Molten Chloride Salts, *J. Electrochem. Soc.* 169 (2022) 061502. <https://doi.org/10.1149/1945-7111/ac735b>.
16. K. Bawane, X. Liu, R. Gakhar, M. Woods, M. Ge, X. Xiao, W.-K. Lee, P. Halstenberg, S. Dai, S. Mahurin, S.M. Pimblott, J.F. Wishart, Y.K. Chen-Wiegart, L. He, Visualizing time-dependent microstructural and chemical evolution during molten salt corrosion of Ni-20Cr model alloy using correlative quasi in situ TEM and in situ synchrotron X-ray nano-tomography, *Corrosion Science* 195 (2022) 109962. <https://doi.org/10.1016/j.corsci.2021.109962>.
17. X. Liu, A. Ronne, L.-C. Yu, Y. Liu, M. Ge, C.-H. Lin, B. Layne, P. Halstenberg, D.S. Maltsev, A.S. Ivanov, S. Antonelli, S. Dai, W.-K. Lee, S.M. Mahurin, A.I. Frenkel, J.F. Wishart, X. Xiao, Y.K. Chen-Wiegart, Formation of three-dimensional bicontinuous structures via molten salt dealloying studied in real-time by in situ synchrotron X-ray nano-tomography, *Nat Commun* 12 (2021) 3441. <https://doi.org/10.1038/s41467-021-23598-8>.
18. L.-C. Yu, C. Clark, X. Liu, A. Ronne, B. Layne, P. Halstenberg, F. Camino, D. Nykypanchuk, H. Zhong, M. Ge, W.-K. Lee, S. Ghose, S. Dai, X. Xiao, J.F. Wishart, Y.K. Chen-Wiegart, Evolution of micro-pores in Ni–Cr alloys via molten salt dealloying, *Sci Rep* 12 (2022) 20785. <https://doi.org/10.1038/s41598-022-20286-5>.
19. T. Ghaznavi, S.Y. Persaud, R.C. Newman, The Effect of Temperature on Dealloying Mechanisms in Molten Salt Corrosion, *J. Electrochem. Soc.* 169 (2022) 111506. <https://doi.org/10.1149/1945-7111/aca07e>.
20. T. Ghaznavi, M.A. Bryk, S.Y. Persaud, R.C. Newman, Alloying effects in high temperature molten salt corrosion, *Corrosion Science* 197 (2022) 110003. <https://doi.org/10.1016/j.corsci.2021.110003>.
21. H. Gholamzadeh, M. Topping, K. Daub, S.Y. Persaud, Characterization of dealloying and associated stress corrosion cracking: The effect of crystallographic orientation, *Acta Materialia*. 260 (2023) 119278–119278. <https://doi.org/10.1016/j.actamat.2023.119278>.
22. *Electrochemical Impedance: Analysis and Interpretation*. J. R. Scully, D. C. Silverman, and M. W. Kendig et al. (ed.), (ASTM STP 1188, Philadelphia) 94 (1993).
23. R. N. Wright and T.-L. Sham, Status of Metallic Structural Materials for Molten Salt Reactors INL/EXT-18-45171, Idaho National Laboratory, (2018).
24. N. Bieberdorf, M. Asta, Laurent Capolungo, Grain boundary effects in high-temperature liquid-metal dealloying: a multi-phase field study, *Npj Computational Materials*. 9 (2023). <https://doi.org/10.1038/s41524-023-01076-7>.
25. Ho Lun Chan, E. Romanovskaia, V. Romanovski, D. Sur, M. Hong, P. Hosemann, J.R. Scully, Corrosion Electrochemistry of Chromium in Molten FLiNaK Salt at 600 °C, *Journal of the Electrochemical Society*. 170 (2023) 081502–081502. <https://doi.org/10.1149/1945-7111/ace8c0>.
26. M. Maric, O. Muránsky, I. Karatchevtseva, T. Ungár, J. Hester, A. Studer, N. Scales, G. Ribárik, S. Primig, M.R. Hill, The effect of cold-rolling on the microstructure and corrosion behaviour of 316L alloy in FLiNaK molten salt, *Corrosion Science* 142 (2018) 133–144. <https://doi.org/10.1016/j.corsci.2018.07.006>.

27. Yan Li Wang, Q. Wang, Hui Jun Liu, Chao Liu Zeng, Effect of grain refinement on the corrosion of Ni-Cr alloys in molten (Li,Na,K)F, *Corrosion Science*. 109 (2016) 43–49. <https://doi.org/10.1016/j.corsci.2016.03.027>.
28. D.M. Artymowicz, J. Erlebacher, R.C. Newman, Relationship between the parting limit for dealloying and a particular geometric high-density site percolation threshold, *Philosophical Magazine* 89 (2009) 1663–1693. <https://doi.org/10.1080/14786430903025708>.
29. H.L. Chan, R. Auguste, E. Romanovskaia, A.L. Morales, F. Schmidt, V. Romanovski, C. Winkler, J. Qiu, Y. Wang, D. Kaoumi, F.A. Selim, B.P. Uberuaga, P. Hosemann, J.R. Scully, Multi-length scale characterization of point defects in thermally oxidized, proton irradiated iron oxides, *Materialia* 28 (2023) 101762. <https://doi.org/10.1016/j.mtla.2023.101762>.
30. Y.Q. Yang, Y.C. Zhao, Z.X. Wen, G.X. Lu, H.Q. Pei, Z.F. Yue, Synergistic effect of multiple molten salts on hot corrosion behaviour of Ni-based single crystal superalloy, *Corrosion Science*. 204 (2022) 110381–110381. <https://doi.org/10.1016/j.corsci.2022.110381>.
31. W. Zhou, Y. Yang, G. Zheng, K.B. Woller, P.W. Stahle, A.M. Minor, M.P. Short, Proton irradiation-decelerated intergranular corrosion of Ni-Cr alloys in molten salt, *Nature Communications* 11 (2020) 3430. <https://doi.org/10.1038/s41467-020-17244-y>.
32. Xiaoyang Liu, Kaustubh Bawane, Xiaoyin Zheng, Mingyuan Ge, Phillip Halstenberg, Dmitry S. Maltsev, Alexander S. Ivanov, Sheng Dai, Xianghui Xiao, Wah-Keat Lee, Lingfeng He, and Yu-chen Karen Chen-Wiegart. Temperature-Dependent Morphological Evolution during Corrosion of the Ni-20Cr Alloy in Molten Salt Revealed by Multiscale Imaging. *ACS Applied Materials & Interfaces* 2023 15 (10), 13772-13782. <https://doi.org/10.1021/acsami.2c2320>.
33. A. Ronne, L. He, D. Dolzhanov, Y. Xie, M. Ge, P. Halstenberg, Y. Wang, B.T. Manard, X. Xiao, W.-K. Lee, K. Sasaki, S. Dai, S.M. Mahurin, Y.K. Chen-Wiegart, Revealing 3D Morphological and Chemical Evolution Mechanisms of Metals in Molten Salt by Multimodal Microscopy, *ACS Appl. Mater. Interfaces* 12 (2020) 17321–17333. <https://doi.org/10.1021/acsami.9b19099>.
34. D. Artymowicz, R. Newman, J. Erlebacher, Insights into the Parting Limit for De-Alloying from Reconsideration of Atomistic Considerations, *ECS Trans.* 3 (2007) 499–506. <https://doi.org/10.1149/1.2789252>.
35. R.H. Banerjee, V. Singh, P. Chakraborty, V. Karki, G. Abraham, R. Tewari, Investigating Cr dealloying and Li ingress in Ni-Mo-Cr alloys with different Mo/Cr ratio exposed to FLiNaK salt, *Corrosion Science*. 212 (2023) 110929–110929. <https://doi.org/10.1016/j.corsci.2022.110929>.
36. J. Erlebacher, M.J. Aziz, A. Karma, N. Dimitrov, K. Sieradzki, Evolution of nanoporosity in dealloying, *Nature* 410 (2001) 450–453. <https://doi.org/10.1038/35068529>.
37. Y. Li, B.-N. Ngo-Dinh, J. Markmann, J. Weissmüller, Evolution of length scales and of chemical heterogeneity during primary and secondary dealloying, *Acta Materialia* 222 (2022) 117424. <https://doi.org/10.1016/j.actamat.2021.117424>.
38. G. Zheng, K. Sridharan, Corrosion of Structural Alloys in High-Temperature Molten Fluoride Salts for Applications in Molten Salt Reactors, *JOM* 70 (2018) 1535–1541. <https://doi.org/10.1007/s11837-018-2981-2>.
39. D. Sulejmanovic, J.M. Kurley, K. Robb, S. Raiman, Validating modern methods for impurity analysis in fluoride salts, *Journal of Nuclear Materials* 553 (2021) 152972. <https://doi.org/10.1016/j.jnucmat.2021.152972>.
40. L. Olson, K. Sridharan, M. Anderson, T. Allen, Nickel-plating for active metal dissolution resistance in molten fluoride salts, *Journal of Nuclear Materials* 411 (2011) 51–59. <https://doi.org/10.1016/j.jnucmat.2011.01.032>.
41. W.H. Doniger, A. Couet, K. Sridharan, Potentiodynamic Polarization of Pure Metals and Alloys in Molten LiF-NaF-KF (FLiNaK) Using the K/K⁺ Dynamic Reference Electrode, *J. Electrochem. Soc.* 169 (2022) 071502. <https://doi.org/10.1149/1945-7111/ac7a66>.

42. L. Massot, M. Gibilaro, D. Quaranta, P. Chamelot, Corrosion Products Electrochemical Behaviour into Molten LiF-NaF: Investigation of Cr(II) System, *J. Electrochem. Soc.* 168 (2021) 026510. <https://doi.org/10.1149/1945-7111/abe088>.
43. J. Qiu, D.D. Macdonald, R. Schoell, J. Han, S. Mastromarino, J.R. Scully, D. Kaoumi, P. Hosemann, Electrochemical study of the dissolution of oxide films grown on type 316L stainless steel in molten fluoride salt, *Corrosion Science* 186 (2021) 109457. <https://doi.org/10.1016/j.corsci.2021.109457>.
44. R. Kelly, J. Scully, D. Shoesmith, and R. Buchheit, *Electrochemical Techniques in Corrosion Science and Engineering* (CRC Press, Boca Raton, FL) (2002), (<https://taylorfrancis.com/books/9780203909133>).
45. ASTM International, Standard Practice for Calculation of Corrosion Rates and Related Information from Electrochemical Measurements ASTM G102-89, ASTM International (2015), 03.
46. H. Yin, P. Zhang, X. An, J. Cheng, X. Li, S. Wu, X. Wu, W. Liu, L. Xie, Thermodynamic modeling of LiF-NaF-KF-CrF₃ system, *Journal of Fluorine Chemistry* 209 (2018) 6–13. <https://doi.org/10.1016/j.jfluchem.2018.02.005>.
47. N.D. Smith, S. Lombardo, S.-L. Shang, Z.-K. Liu, H. Kim, Determination of Kinetic Properties of Ni(II) Ions in Molten LiF-NaF-KF via Voltammetry, *J. Electrochem. Soc.* 170 (2023) 066505. <https://doi.org/10.1149/1945-7111/acd6c1>.
48. S. Fabre, C. Cabet, L. Cassayre, P. Chamelot, S. Delepech, J. Finne, L. Massot, D. Noel, Use of electrochemical techniques to study the corrosion of metals in model fluoride melts, *Journal of Nuclear Materials* 441 (2013) 583–591. <https://doi.org/10.1016/j.jnucmat.2013.03.055>.
49. J.A. Ocadiz-Flores, E. Capelli, P.E. Raison, R.J.M. Konings, A.L. Smith, Thermodynamic assessment of the LiF-NiF₂, NaF-NiF₂ and KF-NiF₂ systems, *The Journal of Chemical Thermodynamics* 121 (2018) 17–26. <https://doi.org/10.1016/j.jct.2018.01.023>.
50. J. Ge, B. Cai, F. Zhu, Y. Gao, X. Wang, Q. Chen, M. Wang, S. Jiao, Natural Convection in Molten Salt Electrochemistry, *J. Phys. Chem. B* 127 (2023) 8669–8680. <https://doi.org/10.1021/acs.jpcc.3c03938>.
51. I. McCue, B. Gaskey, P.-A. Geslin, A. Karma, J. Erlebacher, Kinetics and morphological evolution of liquid metal dealloying, *Acta Materialia* 115 (2016) 10–23. <https://doi.org/10.1016/j.actamat.2016.05.032>.
52. I. Mccue, E. Benn, B. Gaskey, J. Erlebacher, Dealloying and Dealloyed Materials, *Annual Review of Materials Research* 46 (2016). <https://doi.org/10.1146/annurev-matsci-070115-031739>.
53. K. Sieradzki, J.S. Kim, A.T. Cole, R.C. Newman, The Relationship Between Dealloying and Transgranular Stress-Corrosion Cracking of Cu-Zn and Cu-Al Alloys, *J. Electrochem. Soc.* 134 (1987) 1635. <https://doi.org/10.1149/1.2100726>.
54. H.W. Pickering, Characteristic features of alloy polarization curves, *Corrosion Science* 23 (1983) 1107–1120. [https://doi.org/10.1016/0010-938X\(83\)90092-6](https://doi.org/10.1016/0010-938X(83)90092-6).
55. R.-D. Grimm, D. Landolt, Salt films formed during mass transport controlled dissolution of iron-chromium alloys in concentrated chloride media, *Corrosion Science* 36 (1994) 1847–1868. [https://doi.org/10.1016/0010-938X\(94\)90023-X](https://doi.org/10.1016/0010-938X(94)90023-X).
56. V. Pavlík, M. Kontrík, M. Boča, Corrosion behavior of Incoloy 800H/HT in the fluoride molten salt FLiNaK + MF_x (MF_x = CrF₃, FeF₂, FeF₃ and NiF₂), *New J. Chem.* 39 (2015) 9841–9847. <https://doi.org/10.1039/C5NJ01839K>.
57. H. Yin, J. Qiu, H. Liu, W. Liu, Y. Wang, Z. Fei, S. Zhao, X. An, J. Cheng, T. Chen, P. Zhang, G. Yu, L. Xie, Effect of CrF₃ on the corrosion behaviour of Hastelloy-N and 316L stainless steel alloys in FLiNaK molten salt, *Corrosion Science* 131 (2018) 355–364. <https://doi.org/10.1016/j.corsci.2017.12.008>.
58. M. Hong, H.L. Chan, Y. Xie, E. Romanovskaia, J.R. Scully, P. Hosemann, Effect of tellurium concentration on the corrosion and mechanical properties of 304 stainless steel in molten FLiNaK salt, *Corrosion Science* 212 (2023) 110913. <https://doi.org/10.1016/j.corsci.2022.110913>.

59. R. B. Evans III, J. H. Devan, and G. M. Watson, Self-Diffusion of Chromium In Nickel-Base Alloys. ORNL-2982, Oak Ridge National Laboratory (1961).
60. M.C. van Ede, U. Angst, Analysis of Polarization Curves Under Mixed Activation-Diffusion Control: An Algorithm to Minimize Human Factors, *Corrosion* 78 (2022) 1087–1099. <https://doi.org/10.5006/4171>.
61. P. Jakupi, D. Zagidulin, J.J. Noël, D.W. Shoesmith, The impedance properties of the oxide film on the Ni–Cr–Mo Alloy-22 in neutral concentrated sodium chloride solution, *Electrochimica Acta* 56 (2011) 6251–6259. <https://doi.org/10.1016/j.electacta.2010.07.064>.
62. T. Dumaire, R.J.M. Konings, A.L. Smith, Thermodynamic Assessment of the AF–CrF₃ (A = Li, Na, K) and CrF₂–CrF₃ Systems, *Thermo* 1 (2021) 205–219. <https://doi.org/10.3390/thermo1020014>.
63. M.S. Zei, G. Lehmpfuhl, D.M. Kolb, On the stability of reconstructed gold surfaces in an electrochemical cell, *Surface Science*. 221 (1989) 23–34. [https://doi.org/10.1016/0039-6028\(89\)90563-3](https://doi.org/10.1016/0039-6028(89)90563-3).
64. D. Kolb, Reconstruction phenomena at metal-electrolyte interfaces, *Progress in Surface Science*. 51 (1996) 109–173. [https://doi.org/10.1016/0079-6816\(96\)00002-0](https://doi.org/10.1016/0079-6816(96)00002-0).
65. D.M. Kolb, J. Schneider, Surface reconstruction in electrochemistry: Au(100)-(5 × 20), Au(111)-(1 × 23) and Au(110)-(1 × 2), *Electrochimica Acta*. 31 (1986) 929–936. [https://doi.org/10.1016/0013-4686\(86\)80005-6](https://doi.org/10.1016/0013-4686(86)80005-6).
66. S.A. Policastro, J.C. Carnahan, G. Zangari, H. Bart-Smith, E. Seker, M.R. Begley, M.L. Reed, P.F. Reynolds, R.G. Kelly, Surface Diffusion and Dissolution Kinetics in the Electrolyte–Metal Interface, *J. Electrochem. Soc.* 157 (2010) C328. <https://doi.org/10.1149/1.3478572>.
67. W.W. Mullins, Flattening of a Nearly Plane Solid Surface due to Capillarity, *Journal of Applied Physics*. 30 (1959) 77–83. <https://doi.org/10.1063/1.1734979>.
68. Yu-chen Karen Chen-Wiegart, S. Wang, Y.S. Chu, W. Liu, I. McNulty, P.W. Voorhees, D.C. Dunand, Structural evolution of nanoporous gold during thermal coarsening, *Acta Materialia*. 60 (2012) 4972–4981. <https://doi.org/10.1016/j.actamat.2012.05.012>.
69. J. Erlebacher, Mechanism of Coarsening and Bubble Formation in High-Genus Nanoporous Metals, *Physical Review Letters*. 106 (2011). <https://doi.org/10.1103/physrevlett.106.225504>.
70. C. Alonso, R.C. Salvarezza, J.M. Vara, A.J. Arvia, L. Vazquez, A. Bartolome, A.M. Baro, The Evaluation of Surface Diffusion Coefficients of Gold and Platinum Atoms at Electrochemical Interfaces from Combined STM-SEM Imaging and Electrochemical Techniques, *Journal of the Electrochemical Society*. 137 (1990) 2161–2166. <https://doi.org/10.1149/1.2086904>.
71. L.H. Qian, M.W. Chen, Ultrafine nanoporous gold by low-temperature dealloying and kinetics of nanopore formation, *Applied Physics Letters*. 91 (2007). <https://doi.org/10.1063/1.2773757>.
72. R. Song, J. Han, Masayuki Okugawa, Rodion Belosludov, T. Wada, J. Jiang, D. Wei, A. Kudo, Y. Tian, M. Chen, H. Kato, Ultrafine nanoporous intermetallic catalysts by high-temperature liquid metal dealloying for electrochemical hydrogen production, *Nature Communications*. 13 (2022). <https://doi.org/10.1038/s41467-022-32768-1>.
73. J. Zhang, P.A. Korzhavyi, First Principles Investigation on Thermodynamic Properties and Stacking Fault Energy of Paramagnetic Nickel at High Temperatures, *Metals*. 10 (2020) 319–319. <https://doi.org/10.3390/met10030319>.
74. Y. Marcus, Surface tension and cohesive energy density of molten salts, *Thermochimica Acta*. 571 (2013) 77–81. <https://doi.org/10.1016/j.tca.2013.08.018>.
75. A. Dursun, D.V. Pugh, S.G. Corcoran, Dealloying of Ag-Au Alloys in Halide-Containing Electrolytes : Affect on Critical Potential and Pore Size, *J. Electrochem. Soc.* 150 (2003) B355. <https://doi.org/10.1149/1.1580824>.
76. Gideon Henkelmann, D. Waldow, M. Liu, Lukas Lühns, Y. Li, Jörg Weissmüller, Self-Detachment and Subsurface Densification of Dealloyed Nanoporous Thin Films, *Nano Letters*. 22 (2022) 6787–6793. <https://doi.org/10.1021/acs.nanolett.2c02666>.

77. B. E. Douglas and S.-M. Ho, Structure and Chemistry of Crystalline Solids. Structure and Chemistry of Crystalline Solids (Springer, New York) (2006).
78. J. Erlebacher, An Atomistic Description of Dealloying, Journal of the Electrochemical Society. 151 (2004) C614. <https://doi.org/10.1149/1.1784820>.
79. J. Erlebacher, R. Seshadri, Hard Materials with Tunable Porosity, MRS Bulletin. 34 (2009) 561–568. <https://doi.org/10.1557/mrs2009.155>.
80. J. Erlebacher, K. Sieradzki, Pattern formation during dealloying, Scripta Materialia 49 (2003) 991–996. [https://doi.org/10.1016/S1359-6462\(03\)00471-8](https://doi.org/10.1016/S1359-6462(03)00471-8).
81. Junling Xu, Yan Wang, and Zhonghua Zhang. Potential and Concentration Dependent Electrochemical Dealloying of Al₂Au in Sodium Chloride Solutions. The Journal of Physical Chemistry C 2012 116 (9), 5689–5699 <https://doi.org/10.1021/jp210488t>.
82. K. Wagner, S.R. Brankovic, N. Dimitrov, K. Sieradzki, Dealloying below the Critical Potential, Journal of the Electrochemical Society. 144 (1997) 3545–3555. <https://doi.org/10.1149/1.1838046>.
83. D.M. Rishel, F.S. Pettit, N. Birks, Some principal mechanisms in the simultaneous erosion and corrosion attack of metals at high temperatures, Materials Science and Engineering A. 143 (1991) 197–211. [https://doi.org/10.1016/0921-5093\(91\)90739-a](https://doi.org/10.1016/0921-5093(91)90739-a).
84. J.R. Scully, Polarization Resistance Method for Determination of Instantaneous Corrosion Rates, Corrosion 56 (2000) 199–218. <https://doi.org/10.5006/1.3280536>.
85. J. Ding, D. Neffati, Q. Li, R. Su, J. Li, S. Xue, Z. Shang, Y. Zhang, H. Wang, Y. Kulkarni, X. Zhang, Thick grain boundary induced strengthening in nanocrystalline Ni alloy, Nanoscale. 11 (2019) 23449–23458. <https://doi.org/10.1039/c9nr06843k>.
86. T.-F. Chen, G. Tiwari, Y. Iijima, K. Yamauchi, Volume and Grain Boundary Diffusion of Chromium in Ni-Base Ni-Cr-Fe Alloys, Materials Transactions. 44 (2003) 40–46. <https://doi.org/10.2320/matertrans.44.40>.
87. S.P. Murarka, M.S. Anand, R.P. Agarwala, Diffusion of Chromium in Nickel, Journal of Applied Physics. 35 (1964) 1339–1341. <https://doi.org/10.1063/1.1713615>.
88. T. Gheno, F. Jomard, C. Desgranges, L. Martinelli, Tracer diffusion of Cr in Ni and Ni₂₂Cr studied by SIMS, Materialia. 3 (2018) 145–152. <https://doi.org/10.1016/j.mtla.2018.08.004>.
89. T.-F. Chen, Y. Iijima, K. Hirano, K. Yamauchi, Diffusion of chromium in Nickel-Base Ni-Cr-Fe Alloys, Journal of Nuclear Materials. 169 (1989) 285–290. [https://doi.org/10.1016/0022-3115\(89\)90546-1](https://doi.org/10.1016/0022-3115(89)90546-1).
90. N. Winner, H. Williams, R.O. Scarlat, M. Asta, Ab-initio simulation studies of chromium solvation in molten fluoride salts, Journal of Molecular Liquids. 335 (2021) 116351–116351. <https://doi.org/10.1016/j.molliq.2021.116351>.
91. R. O'Hare, Materials Kinetics Fundamentals (Wiley, New Jersey) (2015).
92. C. Bessada et al., in Molten Salts Chemistry and Technology (John Wiley & Sons, Ltd.) 219 (2014).
93. Qiu Jie, Zou Yang, Yu Guojun, He Shangming, Liu Wenguan, Jia Yanyan, Li Zhijun, & Xu Hongjie (2015). Speciation study of chromium corrosion product in molten LiF-NaF-KF salt. Nuclear Science and Techniques, 26(6), 4.

Supplemental Tables, Chapter 5 Task 4

Table S1. Elemental composition of bulk FLiNaK salts measured using ICP-MS technique: as-prepared vs. subjected potentiostatic hold of Ni20Cr alloy at 600 °C

Conditions	Elemental Composition (ppm)	
	Cr	Ni
As-Prepared	0.67	2.42
1.75 V _{K+/K}	1.36	2.59
1.90 V _{K+/K}	2.06	40.8
2.10 V _{K+/K}	21.1	104

Table S2. Weighted fractional elemental composition (in ppm) of LiF, NaF, and KF salts according to supplier's certificates of analysis

Ag	Al	As	B	Ba	Bi	Ca	Cd	Co	Cr	W
0.0292	0.0584	0.0876	0.146	0.146	0.146	0.292	0.292	0.292	0.292	4.3
Ni	Pb	Re	Sb	Si	Sn	Te	Ti	Tl	V	Zr
3.25	3.25	3.25	3.25	3.26	3.36	3.54	3.54	3.80	4.12	6.32
Cs	Cu	Fe	Ga	Ge	In	Mg	Sr	Mo	Mn	Zn
0.292	0.292	0.292	0.526	0.584	0.818	0.993	6.757	2.955	1.86	5.00

Table S3. The EEC fitting parameters for impedance spectra of Ni20Cr potentiostatically held at +1.75 V_{K+/K} for 10 ks in molten FLiNaK salts at 600°C

Time	R _e (Ω·cm ²)	CPE ₁ , Q (S·s ^α /cm ²)	CPE ₁ , α	R ₁ (Ω·cm ²)	R _{ct} (Ω·cm ²)	χ ² *10 ⁻³
1000	0.879	0.022	0.759	210	210	3.23
2000	0.843	0.028	0.688	494	494	4.34
3000	0.875	0.010	0.736	508	508	2.55
4000	0.892	0.005	0.825	384	384	3.32
5000	0.855	0.007	0.811	829	829	1.14
6000	0.878	0.007	0.816	853	853	2.63
7000	0.877	0.006	0.816	854	854	2.69
8000	0.892	0.006	0.815	812	812	2.73
9000	0.890	0.004	0.821	758	758	1.88
10000	0.891	0.004	0.821	667	667	2.09

*Noted that χ² represents the goodness of fits.

Table S4. The EEC fitting parameters for impedance spectra of Ni20Cr potentiostatically held at +1.90 $V_{K+/K}$ for 10 ks in molten FLiNaK salts at 600°C.

Time	R_e ($\Omega \cdot \text{cm}^2$)	CPE_1, Q ($S \cdot s^\alpha / \text{cm}^2$)	CPE_1, α	R_1 ($\Omega \cdot \text{cm}^2$)	CPE_2, Q ($S \cdot s^\alpha / \text{cm}^2$)	CPE_2, α	R_2 ($\Omega \cdot \text{cm}^2$)	R_{ct} ($\Omega \cdot \text{cm}^2$)	χ^{2*} 10^{-3}
1000	0.507	0.242	0.689	18.5	0.023	0.712	10.2	28.7	3.55
2000	0.533	1.284	1.000	24.7	0.025	0.720	22.9	47.7	2.98
3000	0.495	0.024	0.710	19.2				19.2	3.09
4000	0.504	0.274	0.630	35.9	0.048	0.688	7.2	43.1	2.91
5000	0.519	9.776	1.000	44.5	0.041	0.668	20.6	65.1	2.07
6000	0.526	0.055	0.702	13.9	0.736	0.895	5.4	19.3	2.05
7000	0.526	0.251	0.726	20.4	0.161	0.706	6.4	26.7	1.89
8000	0.537	0.610	0.923	13.9	0.127	0.658	15.7	29.6	1.80
9000	0.535	0.224	0.905	9.5	0.121	0.619	8.9	18.4	2.29
10000	0.509	1.753	0.627	19.3	0.096	0.707	10.2	29.6	1.61

*Noted that χ^2 represents the goodness of fits.

Table S5. The EEC fitting parameters for impedance spectra of Ni20Cr potentiostatically held at +2.10 $V_{K+/K}$ for 10 ks in molten FLiNaK salts at 600 °C

Time	R_e ($\Omega \cdot \text{cm}^2$)	CPE_1, Q ($S \cdot s^\alpha / \text{cm}^2$)	CPE_1, α	R_1 ($\Omega \cdot \text{cm}^2$)	CPE_2, Q ($S \cdot s^\alpha / \text{cm}^2$)	CPE_2, α	R_2 ($\Omega \cdot \text{cm}^2$)	R_{ct} ($\Omega \cdot \text{cm}^2$)	χ^{2*} 10^{-3}
1000	0.806	0.658	0.603	0.894	5.207	1.000	1.57	2.46	2.98
2000	0.813	0.875	0.631	2.137				2.14	2.28
3000	1.399	0.347	0.624	2.489	0.006	0.799	0.885	3.37	8.53
4000	2.980	0.244	1.000	5.988	0.032	0.368	10.3	16.24	1.14
5000	31.020	0.053	0.005	0.425	14.780	0.601	17.8	18.21	0.644
6000	14.990	0.008	0.470	20.7	0.144	0.830	15.1	35.79	0.053
7000	21.000	0.007	0.464	21.2	0.086	0.814	16.3	37.53	0.091
8000	23.250	0.006	0.479	20.7	0.060	0.745	14.4	35.08	0.292
9000	32.450	0.016	0.235	28.7	0.067	0.829	9.07	37.73	0.266
10000	39.840	0.036	0.493	24.2	0.006	0.368	8.15	32.37	0.587

*Noted that χ^2 represents the goodness of fits.

Table S6. Charge-transfer resistance (R_{ct}) calculated from eec fitting of impedance spectra for Ni20Cr potentiostatically held at +1.75 $V_{K+/K}$, +1.90 $V_{K+/K}$, and +2.10 $V_{K+/K}$ from 1 to 10 ks

Time (s)	1000	2000	3000	4000	5000	6000	7000	8000	9000	10000	
R_{ct} ($\Omega \cdot \text{cm}^2$)	1.75 $V_{K+/K}$	210	494	508	384	829	853	854	812	758	667
	1.90 $V_{K+/K}$	28.7	47.7	19.2	43.1	65.1	19.3	26.7	29.6	18.4	29.6
	2.10 $V_{K+/K}$	2.5	2.1	3.4	16.2	18.2	37.5	35.1	35.8	37.7	32.4

Supplemental Figures, Chapter 5 Task 4

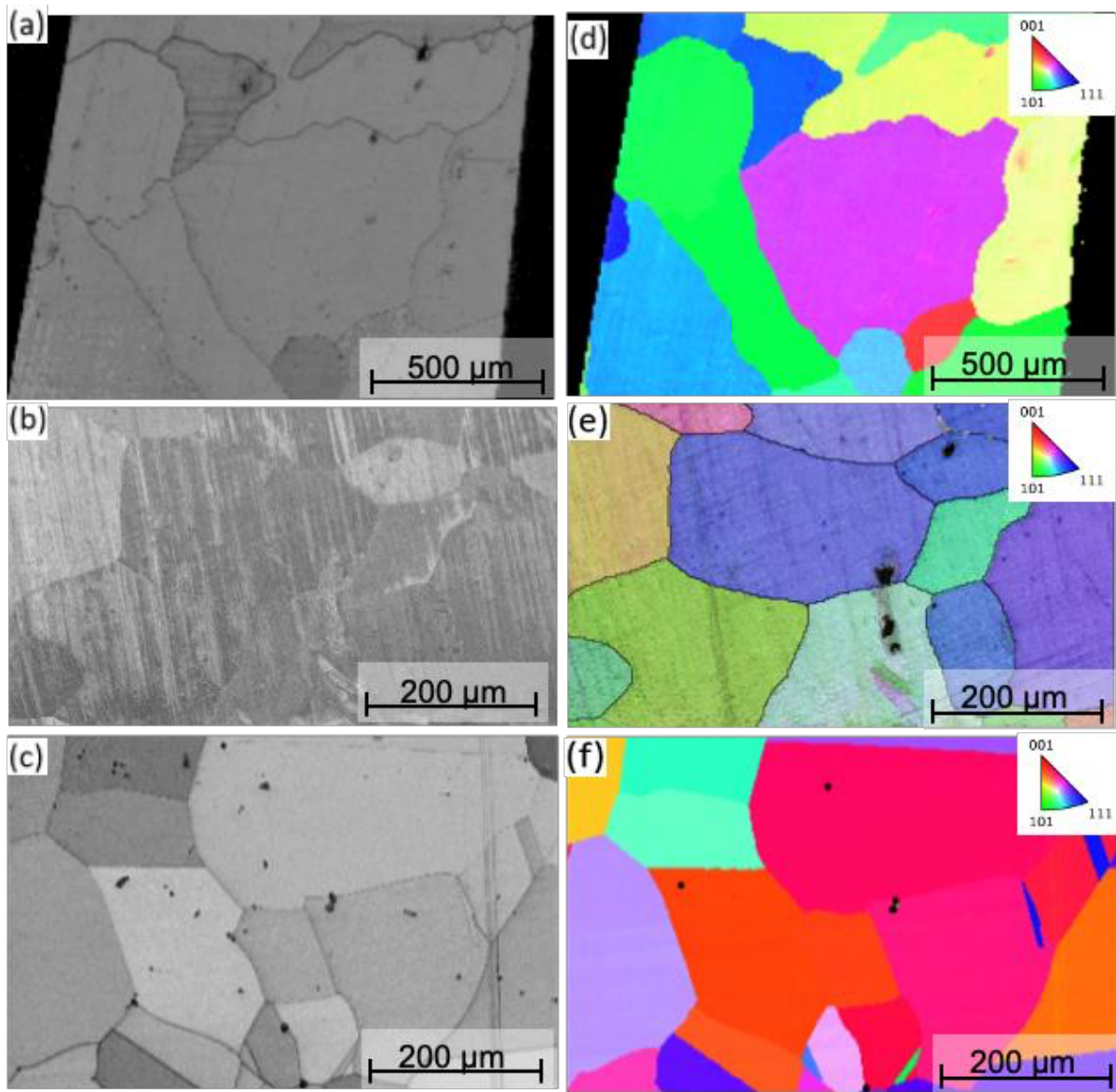


Figure S1. Characterization of as-homogenized Ni20Cr alloys. (a,b,c) shows the backscattered electron micrographs and (d,e,f) shows the respective inverse pole figures.

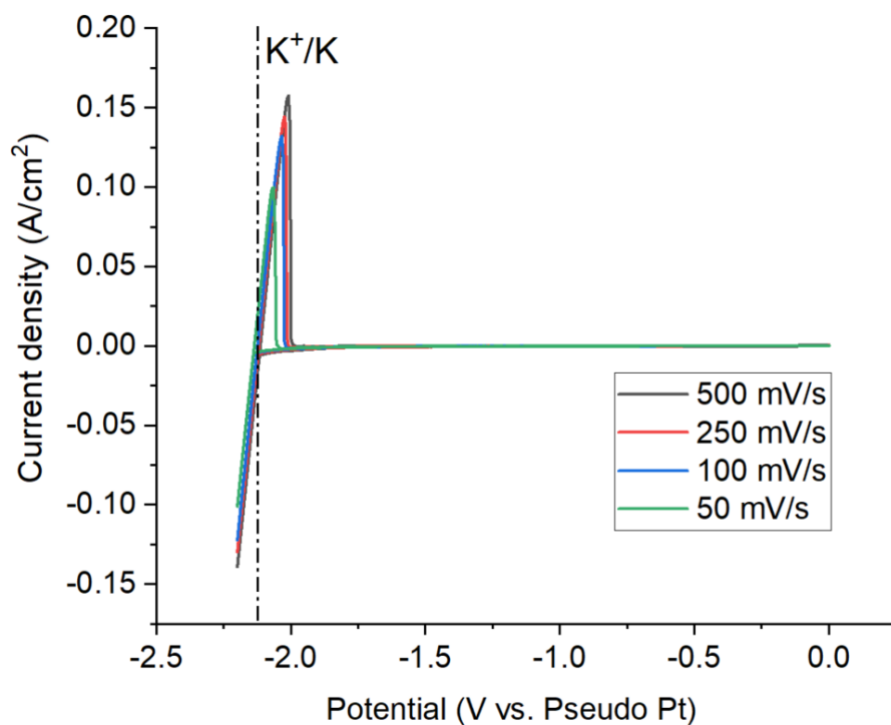


Figure S2. Cyclic voltammograms of Pt wire in molten FLiNaK salts, 600 °C with scan rates between 50 mV/s and 500 mV/s.

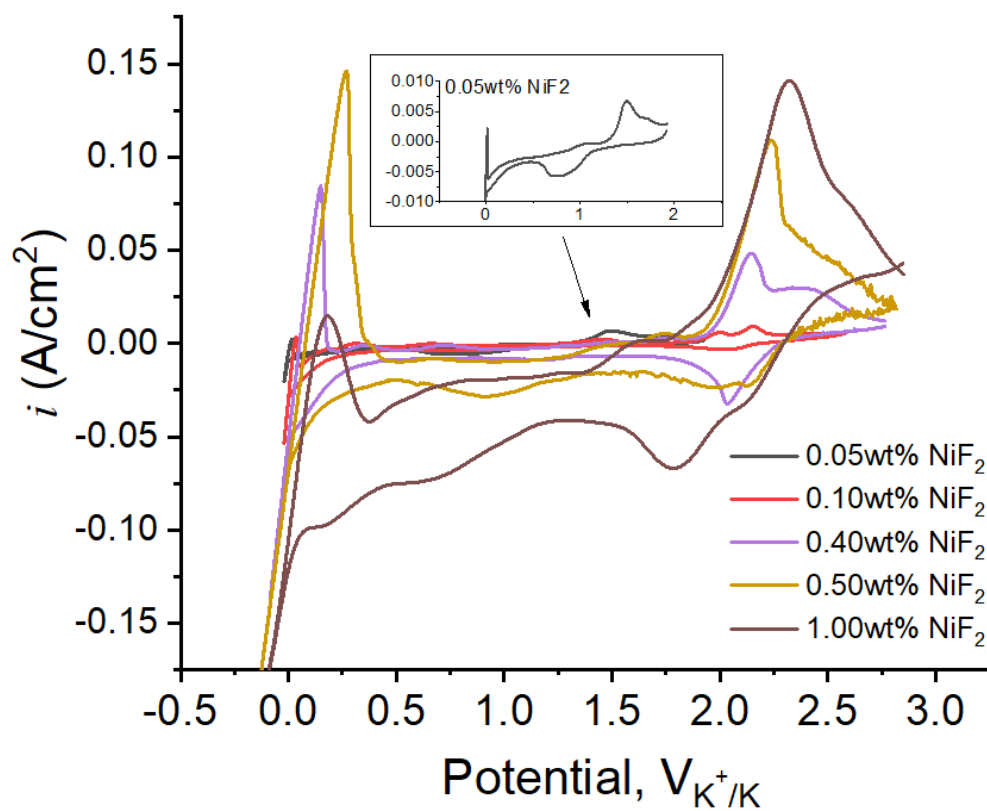


Figure S3. Cyclic voltammograms of Pt wire in molten FLiNaK salts with the addition of NiF₂ salts between 0.05 wt.% and 1.00 wt.%.

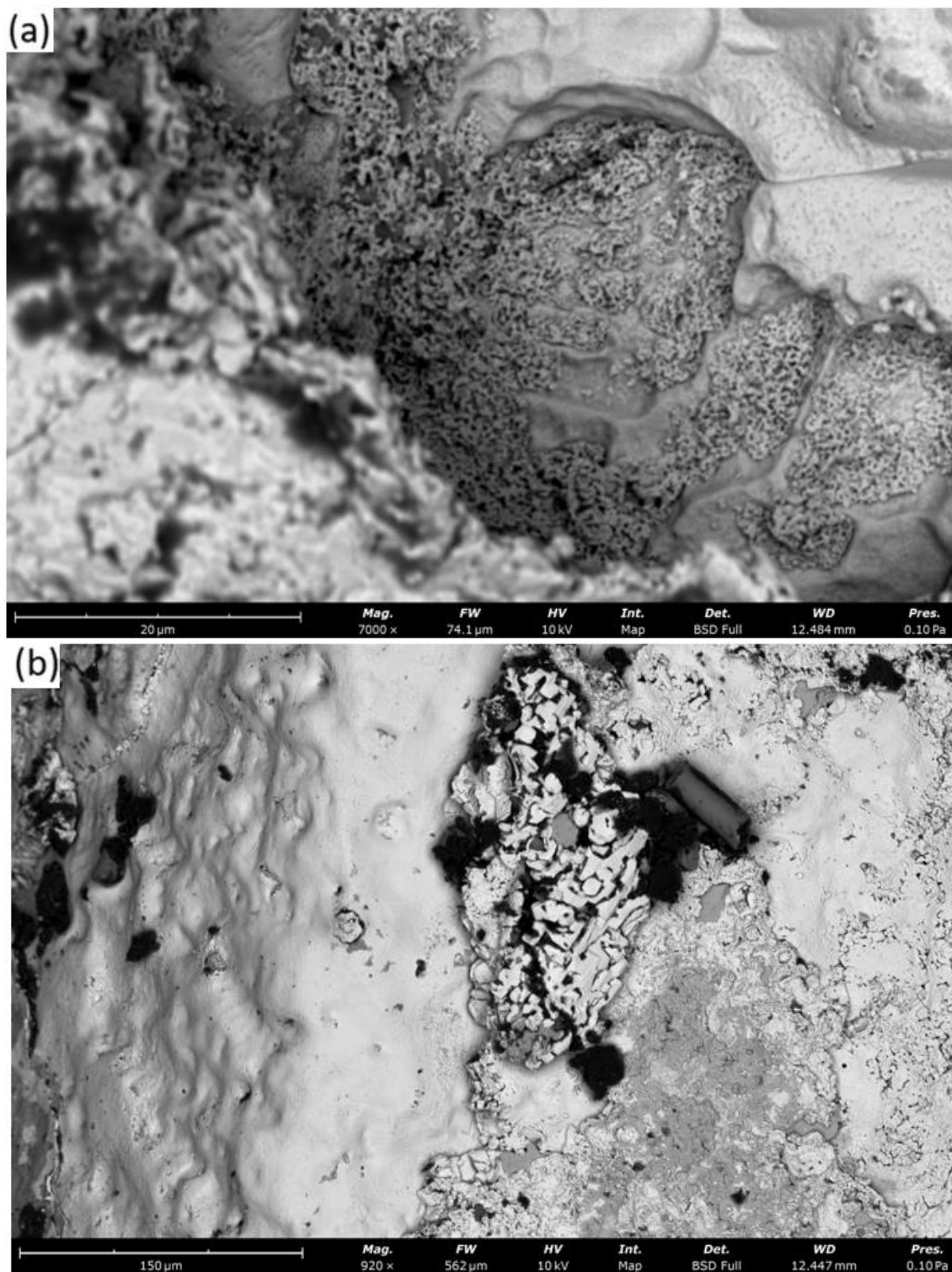


Figure S4. Backscattered electron micrographs depicting the top-view surfaces of Ni20Cr alloys potentiostatically held at +2.30 $V_{K+/K}$ for 10 ks

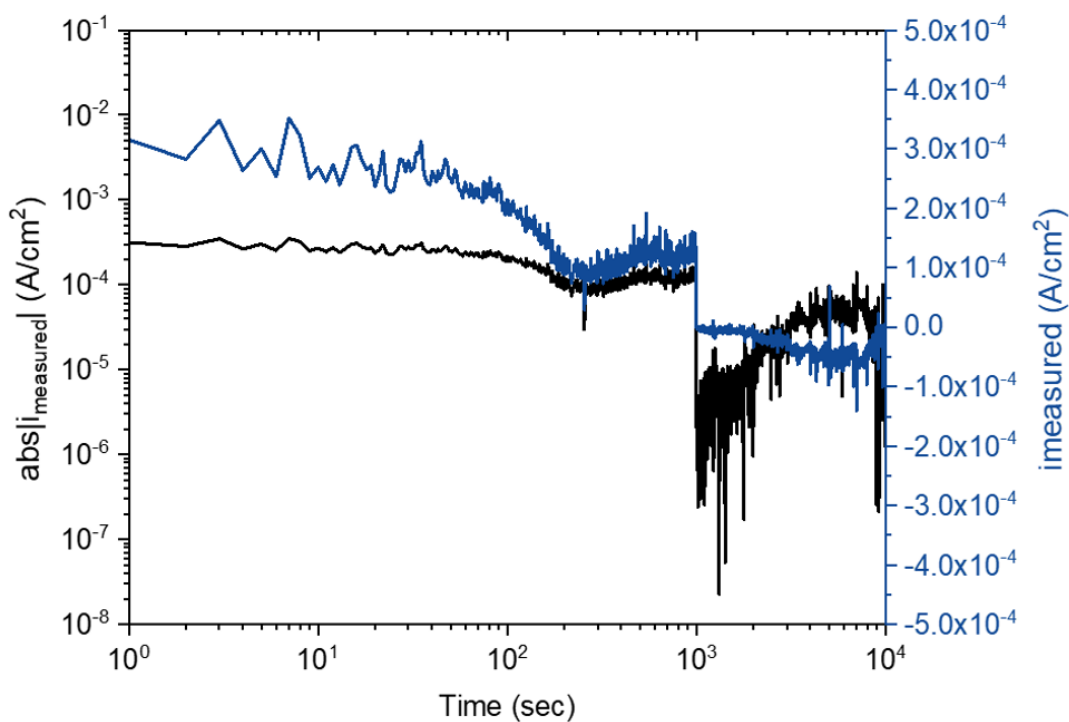


Figure S5. Current-time relationship of Ni20Cr (wt.%) potentiostatically polarized at +1.75V_{K+/K} in molten FLiNaK at 600°C.

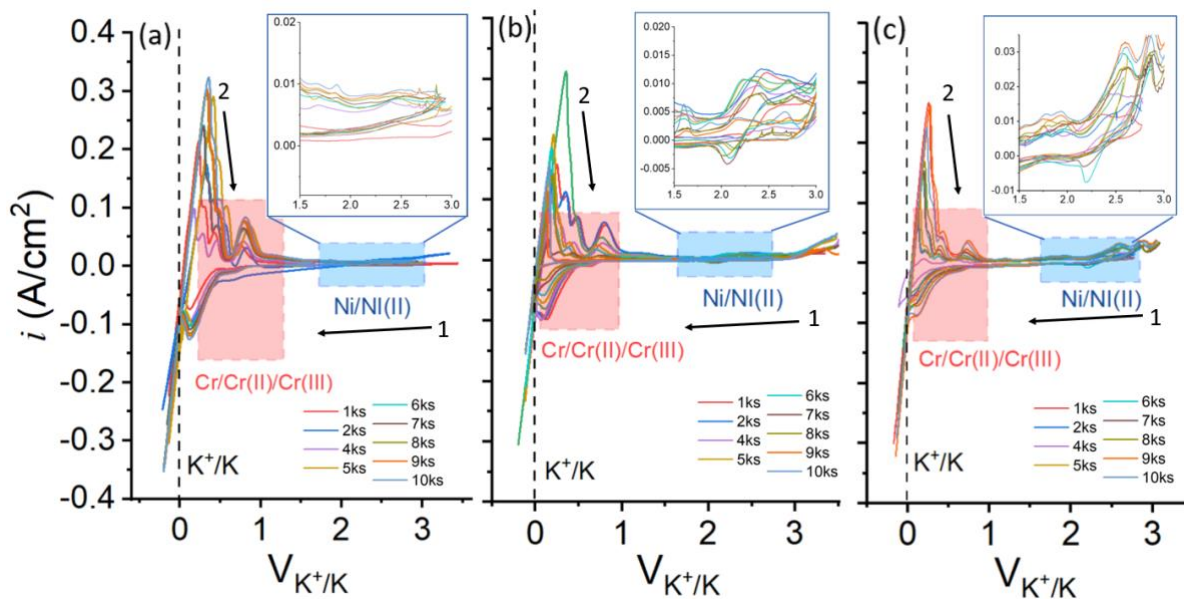


Figure S6.1. Cyclic voltammograms of Pt wire measured at a scan rate of 100 mV/s before and after 10ks of potentiostatic dealloying of Ni20Cr in molten FLiNaK, 600°C with the applied potential of (a) +1.75, (b) +1.90, and (c) 2.10V_{K+/K}.

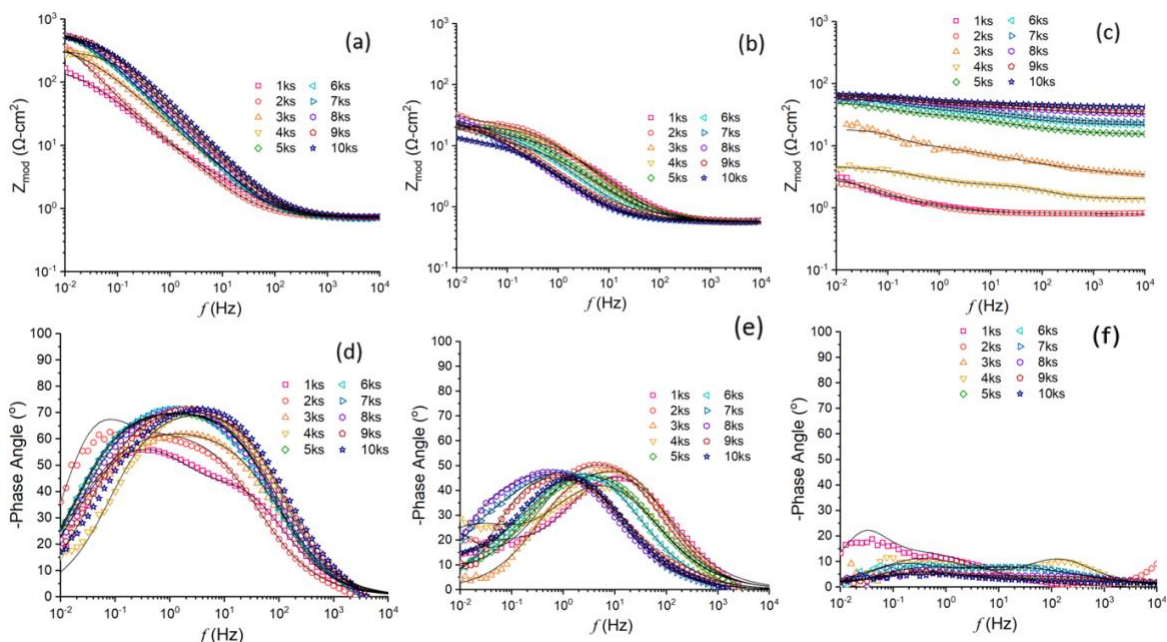


Figure S6.2. (a,b,c) Bode Impedance and (d,e,f) phase angle plots for Ni20Cr potentiostatically held at (a,d) $+1.75 V_{K+/K}$, (b,e) $+1.90 V_{K+/K}$, and (c,f) $+2.10 V_{K+/K}$, respectively.

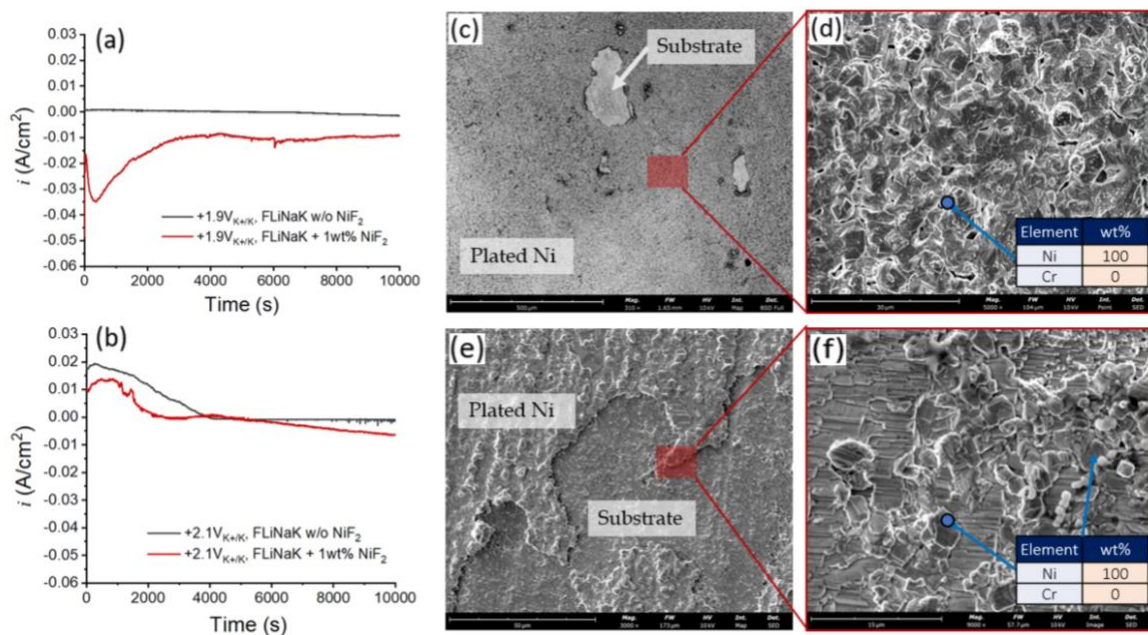


Figure S7. Ni20Cr potentiostatically polarized at (a,b,c) $+1.90 V_{K+/K}$ and (d,e,f) $+2.10 V_{K+/K}$ for 10 ks with the addition of 1 wt.% of NiF₂. The current-time relationship is shown in (a) and (d). The top view surface morphologies of the Ni20Cr are shown in (b,c) for the hold potential of $+1.90 V_{K+/K}$ and in (e,f) of $+2.10 V_{K+/K}$. EDS point analysis of these surfaces are provided in the supplemental sections.

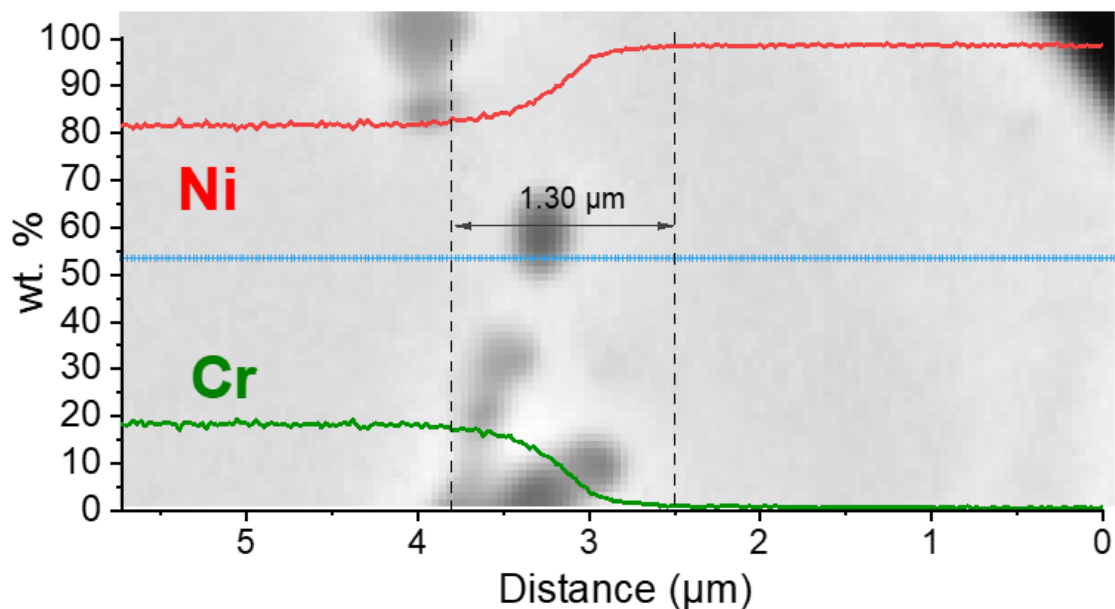


Figure S8. Cross-sectional backscattered electron micrographs and overlaid EDS line profile of Ni20Cr subjected to 10 ks of potentiostatic hold at +2.10 V_{K+/K}.

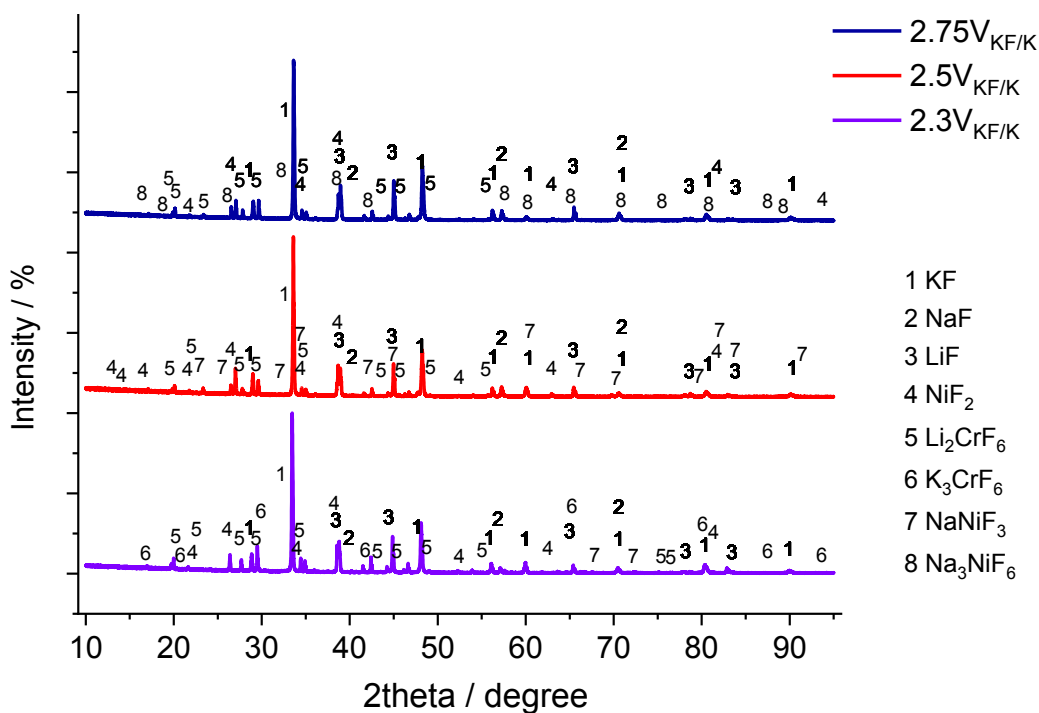


Figure S9. X-Ray Diffractogram of FLiNaK salts subjected to Ni20Cr potentiostatically held at +2.30 V_{K+/K}, +2.50 V_{K+/K}, and +2.75 V_{K+/K} for 10 ks.

Chapter 6 Task 5: Dealloying of Cold-Worked Ni-20Cr (wt.%) Alloy in Molten LiF-NaF-KF Salts, 600°C

Ho Lun Chan^{1,2}, Elena Romanovskaia^{1,2}, Sean H. Mills^{3,4}, Valentin Romanovski^{1,2}, Xikai Wang^{1,2}, Iliana Marrujo³, Harjot Singh^{1,2}, Andrew M. Minor^{3,4}, Peter Hosemann^{5,6} John R. Scully^{1,2}

¹Department of Materials Science and Engineering, University of Virginia, Charlottesville, VA, 22904

²Center for Electrochemical Science and Engineering, University of Virginia, Charlottesville, VA, 22904

³Department of Materials Science and Engineering, University of California, Berkeley, CA, 94720

⁴National Center for Electron Microscopy, Molecular Foundry, Lawrence Livermore National Laboratory, Berkeley, CA, 94720

⁵Department of Nuclear Engineering, University of California, Berkeley, CA, 94150

⁶Materials Science Division, Lawrence Berkeley National Laboratory, Berkeley, CA, 94720, USA

Abstract

The corrosion dealloying behavior of cold-worked (CW) Ni20Cr alloy (wt.%) was studied in molten LiF-NaF-KF (or FLiNaK) salts at 600 °C equal to a homologous temperature (T_H) of 0.522. Alloys were cold-rolled to achieve reductions of thickness of 10%, 30%, and 50% introducing a high density of dislocations. Potentiostatic holds (E_{applied}) were applied in two different electrode potential regimes. At 1.75 $V_{K+/K}$, Cr dealloying to Cr(II) and Cr(III) dominates, while at 1.90 $V_{K+/K}$ both Ni and Cr are oxidized in molten FLiNaK at 600 °C. Dealloyed NiCr displayed the formation of bicontinuous porosity within the grain interior and grain boundaries driven to rapid Ni surface diffusion and Cr dissolution and bulk diffusion. Moreover, the depths of dealloying increased up until 30%CW. Such corrosion behavior was attributed to the different dislocation substructures present at varying CW%. These linear defects are argued to serve as fast paths to guide Cr dissolution by pipeline transport for corrosion dealloying given a high T_H . Dealloying occurred under charge transfer control at +1.75 $V_{K+/K}$ when the bulk outward diffusion flux of Cr ($J_{\text{Bulk}}^{\text{Cr}}$) exceeded the interfacial rate of Cr dissolution regulated by electrode potential ($J_{\text{electric}}^{\text{Cr}}$). When $J_{\text{Bulk}}^{\text{Cr}}$ is lower than $J_{\text{electric}}^{\text{Cr}}$, dealloying is limited by Cr bulk diffusion. CW ameliorates this effect by providing enhanced Cr bulk diffusion to the metal-salt interface. At 1.90 $V_{K+/K}$, dealloying was easier to achieve enabled by simultaneous Cr/Cr(II)/Cr(III) and Ni/Ni(II) dissolutions, albeit at different rates, which further coarsened and densified the Ni-rich ligaments. Of all the CW conditions, the dealloying of 50%CW was limited by Cr bulk diffusion at 1.90 $V_{K+/K}$.

Introduction

A critical milestone toward the deployment of molten salt reactor (MSR) technology is to ensure the durability of structural alloys used for reactor vessels and heat-exchanging loops¹⁻⁵. Alloys considered to be used in MSR and other salt systems are exposed to an array of harsh environments, such as high-temperature molten salts, corrosion due to thermal gradients coupled with impurities functioning as oxidants, radiation, and stress, posing critical challenges even to nuclear reactor alloys specified in the ASME Section III division 5, such as Alloy 800H, Alloy 617, and stainless steel 316H⁶. Among these challenges, the understanding of corrosion and its associated degradation mechanism is crucial for predicting the operational lifespan and thus has been the subject of intensified laboratory research in recent years⁷⁻¹².

It is widely reported that intergranular corrosion (IGC) is a predominant form of corrosion attack observed across a number of alloy systems in molten chlorides and fluorides⁷. While the usually protective oxides of structural alloys is unstable in these conditions¹³, alloying elements that are thermodynamically less noble (LN), e.g., Cr and Fe in Ni-containing alloys, will be selectively “dealloyed” owing to their high thermodynamic driving force for spontaneous dissolution at commonly observed corrosion potentials with an oxidant and easy solubilization of their metal cations. Dealloying also is aided by Cr availability from the bulk via short-circuit diffusion pathways, e.g. grain boundaries (GBs)^{14,15} and dislocation networks. Which of these elements will be selectively removed depends on the precise electrode potential sensed by the alloy relative to the thermodynamic equilibrium of their oxidized species, e.g. Cr(III), Ni(II) relative to elemental state (i.e., Cr), unique to each salt chemistry^{16,17}. Apart from IGC attack, the process of dealloying also brings about morphological instability due to the coupled effect of LN dissolution and more noble (MN) element surface diffusion^{18,19}, leading to the formation of bicontinuous porous structures, termed “bicontinuous dealloying”, at both the grain interiors²⁰⁻²⁴ and at grain boundaries (GBs)^{19,25}. Although this phenomena is not well investigated for molten salt systems, it has recently been observed on Ni20Cr (wt.%), Fe-Cr-Ni, and Fe-Ni alloys in molten chloride salts between 500 °C and 800 °C^{20-24,26}, and may increase the susceptibility to stress corrosion cracking (SCC)²⁷⁻³⁰ or transition to creep induced cracking^{31,32}.

In our recent work, model Ni20Cr (wt%) alloys were subjected to applied potentials in molten LiF-NaF-KF (FLiNaK) at 600 °C between 1.75 and 2.75 $V_{K+/K}$ ³³. Bicontinuous porosity with remaining μm -scale surface MN ligaments and dealloying depth was observed at the dealloying potential of +1.75, +1.90, and +2.10 $V_{K+/K}$. These features are attributed to MN element surface diffusion, metal/salt interfacial LN dissolution, and LN element bulk outward diffusion, which all occur simultaneously^{25-27,33,34}. At high homologous temperatures ($T_H = 0.4-0.6$), the effect of LN element bulk diffusion is particularly notable during molten salt corrosion ($T_H = 0.4-0.6$)^{25-27,33,34}; the rate of MN element surface diffusion dictates the interfacial morphological evolution and has shown to form μm -scale ligaments similar to the case of liquid

metal dealloying.^{35–37} This situation raises a new question: when the rate and mechanism of LN outward bulk diffusion are altered, e.g. introducing new short-circuit diffusion pathways such as GB and dislocation, how would the rate and morphology of dealloying be affected?

Answering this question is especially crucial for MSR alloy development since factors including irradiation³⁸, stress induced by thermal gradients³⁹, thermomechanical processing^{40–44}, and its residual stress^{8,45}, are known to form non-equilibrium point and line defects and dislocation substructures, such as low angle grain boundaries, deformation twins, non-equilibrium vacancies, and even new phases, that operate in parallel with bulk diffusion in a perfect lattice with only near-equilibrium vacancies. It is well established that plastic deformation in face center cubic (FCC) structured metal alloys is controlled by their stacking fault energy (SFE)⁴⁶. Ni-based alloys have a relatively high SFE⁴⁶ and reduced SF widths, which influences their mechanical properties, such as promoting easy cross-slip and reducing the likelihood of deformation twinning. The resultant deformation structures typically exhibit dislocation walls or microbands^{47,48}. For instance, transmission electron microscopy (TEM) studies^{47,48} show that cold-worked (CW) Ni-Cr alloy may exhibit planar dislocation pileup and densification into low angle grain boundaries (LAGBs) on stacking faults at a low degree of CW (5%). Interconnected dislocation cell (DC) structures were observed at a moderate degree of CW (10–30%), eventually forming microbands at high degree of CW (>50%)^{44,49}. These characteristics of severe plastic deformation are also observed by Dudova et al.⁴⁹ and Koukolikova et al.⁴⁴.

In prior studies, CW has been shown to increase the susceptibility of austenitic stainless steels⁵⁰, 316L^{43,51}, and alloy 690^{52–54} to SCC in simulated pressurized water reactor environments. In molten $\text{Li}_2\text{CO}_3\text{-K}_2\text{CO}_3\text{-Na}_2\text{CO}_3$ at 450 °C, cold working impedes the ability of Inconel 601 to form a uniform protective oxide film which appears to demonstrate more adherence to highly strained lattice areas and dislocation end points⁵⁵. According to⁴³, a high degree of CW (50%) on 316SS has led to grain fragmentations and subgrains characterized by the densification of high geometrically necessary dislocations (GNDs) and high-angle grain boundaries (HAGBs). These observations correlate with significant intergranular dealloying and possible bicontinuous dealloying within the grain interior in molten FLiNaK, 700 °C. A similar observation was made on 316LSS alloys in molten FLiNaK, 600 °C⁵⁶.

Therefore, there is a notional observation that the susceptibility to bicontinuous dealloying in molten salts may be increased by CW. In our prior work³³, the possible diffusion mechanism that controls the molten salt dealloying process was identified by calculating and comparing the flux for Cr interfacial oxidation to Cr(III) (i.e., J_{electric}) to the Cr bulk outward diffusion of Cr (J_{bulk}) and the ionic diffusion of Cr(III) using established kinetic diffusion models. This comparison help to inform whether Cr bulk diffusion is sufficiently rapid to support Cr oxidation at an applied potential. In the case of Ni20Cr(wt.%) alloy with minimal CW, J_{bulk} was found rate-controlling in molten FLiNaK, 600 °C³³. A similar and

improved approach was also employed in this work to elucidate the role of CW to dealloying, particularly confirmation of the hypothesis that CW can increase J_{bulk} due to the introduction of dislocation densities⁴⁹.

In this work, the potentiostatic dealloying behavior of 10%, 30%, and 50% CW Ni20Cr (wt%) alloy was studied in molten FLiNaK salts at 600 °C. The method for potentiostatic dealloying is based on our prior work³³ in which +1.75 $V_{\text{K}^+/\text{K}}$ and +1.90 $V_{\text{K}^+/\text{K}}$ were applied to the test alloys for the duration of 10 ks. A multi-modal suite of characterization methods, including electrochemical impedance spectroscopy (EIS), X-ray diffraction (XRD), scanning electron microscopy (SEM), energy dispersive X-ray spectroscopy (EDS), electron backscatter diffraction (EBSD), and S/TEM techniques, were leveraged to understand how the material's grain orientation, microstructure, dislocation substructure and phase composition after cold working affected dealloying. The goal is to understand how CW alters the rate-determining step or steps of dealloying as a function of CW.

Materials and Methods

Materials Preparation

Ni20Cr alloys (80wt.%Ni-20wt.%Cr) were fabricated by a vacuum arc-melting process in this study. Ni slug (99.98%, Thermo Scientific) and Cr pieces (99.99%, Thermo Scientific) were first mixed at the targeted weight ratio, melted, and remelted at least three times under a high vacuum environment of $>10^{-5}$ torr. The as-cast alloys were then encapsulated in an Ar-filled quartz tube and solutionized at 1050 °C for 6 h followed by water quenching at room temperature. Using this process, the as-homogenized alloys demonstrated a uniform composition, characterized by a single FCC phase and a grain size of 351 ± 154 μm .⁵⁷ The alloys were then machined into rectangular plates with the dimension of $20 \pm 0.5 \times 1 \pm 0.5 \times 1 \pm 0.5$ mm, polished to a 1200 grit surface finish using silicon carbide paper. Ni20Cr alloys were cold-worked (CW) by cold rolling to achieve a reduction in cross-sectional area by 10%, 30%, and 50%, quantified using the change in cross-sectional area ($(A_0 - A_f)/A_0 \cdot 100\%$). The tests were conducted in the as-rolled conditions without further heat treatment. Lastly, the as-homogenized alloys are referred as "0% CW".

Salt preparation

The LiF-NaF-KF (46.5–11.5–42 mol%) eutectic salt (FLiNaK) was selected as the electrolyte. The salt constituents including LiF (99.99% purity, Fisher Scientific), 11.5 mol% NaF (99.99% purity, Fisher Scientific), and 42 mol% KF (>99.5% purity, Fisher Scientific) salts, were used. **Table S1** displays a list of metallic cation impurities reported from the certificate of analysis from commercial vendors. Salts were dried in a vacuum oven at 100 °C for 48 h, and were then transferred to an N₂-filled (with O₂ and H₂O controlled below <0.1 ppm) glove box (UNIlab MBraun, USA). 30 g of FLiNaK salt mixture was used for each electrochemistry experiment and was prepared by mixing individual salt constituents into their desired

stoichiometric ratio. To minimize residual O₂ and H₂O impurities, the salt mixture was heated in a high-purity boron nitride crucible (>99.6% purity, MSE supplies) for at least 6 h under the flow of 99.999% ultra-high purity (UHP) N₂ gas and allowed to solidify. The salt was then reheated to 600 °C before each electrochemical experiment. Concerns regarding the possible influence of salt impurities on electrochemical polarization measurements have been addressed in prior work^{17,58–60}.

X-ray diffraction analysis

X-ray diffraction was performed on as-CW, pre-dealloying and post-dealloyed Ni20Cr alloys utilizing a Malvern-Panalytical Empyrean diffractometer [wavelength Cu K (1.5405 Å)]. The analysis was done in order to obtain the chemical and phase composition of the residual salt, extract the lattice parameters, and calculate the dislocation density in these samples. The PDF4+ database was employed as the reference data. For Rietveld refinement, the software HighScore Plus was utilized where the pseudo-Voigt function was used to refine the peak profile. To estimate the dislocation densities (ρ) imparted by cold-rolling, the following analytical approach is adopted^{61–63}. Firstly, crystallite size was determined by Eq. 1^{61–63}:

$$D = \frac{K\lambda}{\beta \cos \theta} \quad (1)$$

where D is the average crystallite/grain size in nm, K is dimensionless shape factor = 0.94 for spherical crystallites with cubic symmetry, λ is X-ray wavelength = 0.15405 nm (1.5405 Å), θ (is Bragg's angle in degrees, half 2θ , taken from XRD plot, ϵ_m is the microstrain, β is line broadening at FWHM in radians. Θ , β and ϵ_m were obtained by fitting the XRD diffraction patterns using OriginPro 2023 software. ρ were calculated in nm⁻² based on obtaining D by Eq. 2:

$$\rho = \frac{2\sqrt{3}\epsilon_m}{Db} \quad (\text{Eq. 2})$$

Moreover, the FCC lattice parameter, a , and interplanar spacing, d , were determined with Bragg's law using Eq. 3 and Eq. 4:

$$a = d \cdot \sqrt{h^2 + k^2 + l^2} \quad (3)$$

$$d = \frac{\lambda}{2 \sin(\frac{\theta}{2})} \quad (4)$$

where d is the perpendicular distance between designated crystal plane (hkl) or the distance between planes of atoms that give rise to diffraction peaks found by fitting the XRD diffraction patterns using Origin 2021 software,. h, k, l are miller indices obtained from the HighScore Plus database. The results are shown in *Supplemental Section A Figure S1* and **Table 1**.

Table 1. The calculated dislocation densities and lattice parameters from the X-ray diffractogram of Ni20Cr 10%, 30% and 50% CW samples

%CW	ρ (cm ⁻²)	a _{Ni20Cr} (nm)
10% CW	$4.54 \cdot 10^{11} \pm 2.75 \cdot 10^{11}$	0.3543
30% CW	$4.95 \cdot 10^{11} \pm 2.57 \cdot 10^{11}$	0.3554
50% CW	$7.49 \cdot 10^{11} \pm 5.98 \cdot 10^{11}$	0.3555

Molten Salt Electrochemistry

Electrochemical experiments were conducted in a custom four-electrode cell, utilizing the same configuration and electrode preparation steps as described in our previous work⁶⁰. In brief, the setup consists of a BN crucible (>99.6%, MSE Supplies), a graphite rod used as the counter electrode (CE), a Pt wire (99.95%, Fisher Scientific) as the pseudo-reference electrode, a NiCr sample as the primary working electrode (WE), and another Pt wire as the secondary WE. The purpose of implementing a secondary WE blocking electrode is to detect the release of Ni(II) and Cr(III) corrosion products *in-situ*⁶⁰ while measuring the equilibrium K⁺/K potential using Cyclic Voltammetry (CV). The equilibrium K⁺/K potential was utilized as the dynamic reference potential and determined immediately prior to the electrochemical scan and over each period of potentiostatic dealloying. The validation of the CV method for K⁺/K potential determination, e.g. assessing sensitivity to scan rate, identifying optimal scan range, and supporting reaction(s) on CE, are detailed elsewhere.¹⁷ The result is further discussed in **Figure S2**.

Potentiostatic (pstat) polarization was applied in potential range where, according to thermodynamic stability diagrams^{16,57} to selectively dealloy Cr from the Ni20Cr (wt.%) alloys in molten FLiNaK, 600 °C occurred. Both as-homogenized and CW Ni20Cr (wt.%) alloys were subjected to applied potentials of +1.75 and +1.90 V_{K⁺/K} for up to 10 ks for 1 ks. CV scans on the secondary Pt WE were performed at a scan rate of 100 mV/s every 1 ks to detect the release of Ni(II) and Cr(III) and calibrate the applied potential with respect to the measured K⁺/K dynamic reference potential. It is noted that the selection of pstat hold potential and time was based on our recent work⁵⁷, which investigated the electrochemical thermodynamic, kinetic, and morphological dependence of the as-homogenized Ni20Cr alloy from +1.75 to +2.75 V_{K⁺/K}.

In this work⁵⁷, dealloying was conducted by pstat polarization at +1.75 V_{K⁺/K} and +1.90 V_{K⁺/K} for 10 ks. Upon pstat-dealloying, an electrochemical impedance spectroscopy (EIS) scan was performed on the samples at the applied potential from 10 kHz to 10 mHz, with an AC perturbation of 20 mV. As-measured EIS spectra were fitted and described by an electrical equivalent circuit (ECM) model shown in **Figure S3**, **Figure S4**, **Table S2** and **Table S3**. Additionally, linear sweep voltammetry (LSV) measurements were separately employed to investigate the potential-dependent rate-controlling regimes of Ni20Cr alloy as a function of CW. LSV results are further elaborated in **Figure S5** and **Figure S6**. It is noted that upon pstat

dealloying, the electrodes were removed immediately from the salt bath and rapidly cooled with N₂ gas. The sample surface was then sonicated in deionized H₂O until visible residual salts were removed.

Scanning Electron Microscopy (SEM) and Energy Dispersive Spectroscopy (EDS)

Both the plan view and cross-sections of the post-dealloyed samples were analyzed. Scanning electron microscopy (SEM) coupled with elemental analysis via energy dispersive X-ray spectroscopy (EDS) (Thermo Phenom XLG2 SEM) was utilized. The input of electron energy used are 10–20 kV for surface topographic analysis and >20 kV for EDS analysis. Both sets of samples were initially mounted in conductive bakelite mounting pucks. Samples were then polished to a 1200 grit finish using SiC paper, followed by 6 μm and 3 μm diamond polishing steps, and a final vibratory polishing step in 0.05 μm colloidal Al₂O₃/SiO₂ to produce smooth scratch-free surfaces for high-quality SEM imaging. Between steps, the samples were cleaned in deionized water and isopropanol. Finally, samples were cross-sectionally polished using a Fischione Fischione model 1061 SEM mill (broad-beam Ar-ion milling) prior to EBSD characterization to remove any remnant mechanical deformation produced by the polishing steps.

Electron Backscattered Diffraction (EBSD)

Electron Backscatter Diffraction (EBSD) (Thermofisher Scientific Scios 2 DualBeam) was performed on the post-CW (**Figure S7**) as well as the post-dealloyed samples, where the analysis focused on the microstructural orientation and geometrically necessary dislocation (GND) mapping of the dealloyed layer and interfacial region between uncorroded grains and dealloyed regions. Grain orientation of cross-sections was conducted by mapping inverse pole figure (IPF) plots relative to documented crystallographic orientations. The sample surface was inspected using secondary electron imaging (SEI) at 5 keV and 0.1 nA. EDS maps were processed and rendered using the Oxford AZtec EDS software package⁶⁴. Images were then analyzed using the Fiji image analysis software [30]. EBSD scans were acquired at 20 keV and 1.6 nA at a pre-tilt of 70° and a working distance of ~13 μm. All EBSD data was acquired using Oxford AZtec software and analysis was performed using the AZtecCrystal software package⁶⁴.

Optical Microscopy & Electrolytic Etching

The thermally activated recrystallization behavior of as-CW Ni20Cr(wt.%) was investigated in isolation without molten salt exposure when exposed to the same test temperature of 600°C. The samples investigated include those subjected to the cold-rolling process (10%CW, 30%CW, 50%CW), and those that were cold-rolled and then thermally annealed in an Ar-encapsulated tube at 600°C for up to 10,000 s. Firstly, the samples were metallographically prepared to a 1 μm surface finish. Secondly, an electrolytic etching process was performed in a custom-built setup consisting of a DC power supply, a glassy carbon crucible as both the cathode and etchant container and an etchant solution of 1 M H₂SO₄ solution[65,66].

+6 V was applied to the samples at an increment of 5 s until the underlying grain structure was visible [65,66]. Lastly, optical micrographs (Hirox RH-8800) of the plan-view surface of etched samples were then taken at various magnifications. Results are further illustrated in **Figure S8** through **Fig S10**.

Kinetic Analysis of Potentiostatic Dealloying

The pstat polarization results were analyzed based on ref⁵⁷. The as-measured current density (i_{electric}) was first corrected from the contribution of cathodic current densities due to impurities (e.g. HF) at +1.75 and +1.90 V_{K+/K} performed in **Figure S6**⁵⁸. Thus, the corrected current density ($i_{\text{electric}}^{\text{anodic}}$) will primarily represent that due to Cr and/or Ni dissolution. Then, $i_{\text{electric}}^{\text{anodic}}$ was used to calculate the electric dissolution flux (J_{electric}^m) via **Eq.5**:

$$J_{\text{electric}}^m = \frac{i_{\text{electric}}^{\text{anodic},m}}{zF} \quad (5)$$

where the superscript “m” represents either Cr or Cr and Ni to represent the dissolving elements, z was assumed to be 3 moles of electrons removed per each mole of Cr atom oxidized to Cr(III) oxidized (i.e., 3 equiv/mol) since the dissolution of Ni-Cr to Cr(III) is predominant at the potentials studied^{16,66}, and F is the Faraday’s constant taken as 96,485 coulombs/equivalent of electrons. Expressing $i_{\text{electric}}^{\text{anodic}}$ as a flux density of J_{electric}^m allows for a comparison between the observed interfacial oxidation rate of Cr in moles/cm²-sec, with the effective bulk outward diffusion flux of Cr ($J_{\text{bulk}}^{\text{Cr}}$) or ionic diffusion flux of Cr(III) ($J_{\text{FLiNaK}}^{\text{Cr(III)}}$) across the Cr(III) concentration gradient in the molten salt away from the initially planar interface. These distinctions enable a comparison and identification of the rate-determining diffusion steps (rds).

In this chapter, in contrary to using Fick’s First Law⁵⁷, a more rigorous approach is adopted to obtaining $J_{\text{bulk}}^{\text{Cr}}$ based on the corrosion kinetic modeling works by Pillai and Pint^{67,68}, as well as Larrison et al.^{69,70}, who utilized a flux equation (**Eq. 6**) derived based on Eyring’s absolute reaction rate theory in the lattice-fixed frame of reference⁷¹:

$$J_{\text{bulk}}^{\text{Cr}} = -\frac{M_{\text{Cr}}RT}{\Omega dx} \sqrt{x_{\text{Cr}}^{\text{bulk}} x_{\text{Cr}}^{\text{di}}} \sinh\left(\frac{d\mu_{\text{Cr}}}{2RT}\right) \quad (6)$$

where M_{Cr} is the mobility of Cr in Ni-Cr alloys, Ω is the molar volume of Cr in cm³/mol, x_{Cr} is the mole fraction of Cr in the bulk alloy and on the surface, and $d\mu_{\text{Cr}}$ is the corresponding difference in chemical potential. **Eq. 6** can be further simplified to **Eq. 7** by considering the Nernst-Einstein relation ($D_{\text{eff}}^{\text{Cr}} = M_{\text{Cr}}RT$), the relation of chemical potential to activity ($\mu_{\text{Cr}} = \mu_{\text{Cr}}^0 + RT \ln a_{\text{Cr}}$), while considering nominal diffusion to estimate the Cr depletion depth (ie., $dx = \sqrt{D_{\text{eff}}^{\text{Cr}} t}$):

$$J_{\text{bulk}}^{\text{Cr}} = -\frac{1}{\Omega} \sqrt{\frac{D_{\text{eff}}^{\text{Cr}} x_{\text{Cr}}^{\text{bulk}} x_{\text{Cr}}^{\text{di}}}{t}} \sinh \left(\ln \left(\frac{a_{\text{Cr}}^{\text{di}}}{a_{\text{Cr}}^{\text{bulk}}} \right) \right) \quad (7)$$

where $D_{\text{Cr}}^{\text{eff}}$, in the unit of cm^2/s , is the effective Cr diffusivity accounting for vacancy-mediated self-diffusion, interface, and t represents the potentiostatic dealloying time in s, $a_{\text{Cr}}^{\text{di}}$ and $a_{\text{Cr}}^{\text{bulk}}$ are the activities of Cr at the dealloying interface and in the bulk alloys, respectively, determined from the ThermoCal TCNI9: Ni Alloys v9.1 database⁷². As an initial estimate, $a_{\text{Cr}}^{\text{di}}$ and $a_{\text{Cr}}^{\text{bulk}}$ are set to be $2.80 \cdot 10^{-4} \text{ mol/cm}^3$ and $6.33 \cdot 10^{-3} \text{ mol/cm}^3$, respectively, corresponding to a Cr depleted interface with 5 wt.% remaining Cr. This assumption provides a reasonable basis for $J_{\text{bulk}}^{\text{Cr}}$ analysis, with further validation presented in the results section. For instances, Cr solute may preferentially segregate to dislocation cores⁷³, increasing the local concentration. These effects are acknowledged but not incorporated in **Eq. 7** to enable a straight forward comparison between $J_{\text{electric}}^{\text{Cr}}$, $J_{\text{bulk}}^{\text{Cr}}$, and $J_{\text{FLiNaK}}^{\text{Cr(III)}}$.

Previously, D_{eff} was calculated based the composite rule of mixture (i.e., $D_{\text{eff}}^{\text{Cr}} = \left(\frac{2\delta}{L}\right) D_{\text{gb}}^{\text{Cr}} + \left(1 - \frac{2\delta}{L}\right) D_{\text{l}}^{\text{Cr}}$) derived based on a square grain embedded in an isotropic FCC polycrystal [57]. Here, following the work by Chen and Schuh et al.⁷⁴, $D_{\text{eff}}^{\text{Cr}}$ was more accurately calculated by considering the simultaneous grain boundary, triple point, and dislocation core pipe transport in a realistic FCC polycrystal with a more realistic Voronoi polyhedral grain geometry via **Eq.8**:

$$D_{\text{eff}}^{\text{Cr}} = f_{\text{tj}} D_{\text{tj}}^{\text{Cr}} + f_{\text{gb}} D_{\text{gb}}^{\text{Cr}} + f_{\text{l}} D_{\text{l}}^{\text{Cr}} + \frac{f_{\text{dis}}^{\xi}}{(f_{\text{l}} + f_{\text{dis}})^{\xi-1}} D_{\text{dis}}^{\text{Cr}} + E_{\text{r}_1} + E_{\text{r}_2} \quad (8)$$

where f_{tj} , f_{gb} , f_{l} , and f_{dis} are the fractions of triple point, grain boundary, lattice and dislocation sites, respectively (further defined from **Eq. 9** to **Eq. 12**); the power-law scaling term adjacent to $D_{\text{dis}}^{\text{Cr}}$ models dislocations as a Frank network a zero percolation threshold, where ξ is the scaling factor estimated to be 1.4 in three dimensions⁷⁵:

$$f_{\text{gb}} = H_{\text{gb}} \frac{\delta}{L} \quad (9)$$

$$f_{\text{tj}} = H_{\text{tj}} \left(\frac{\delta}{L}\right)^2 \quad (10)$$

$$f_{\text{dis}} = \rho b^2 \quad (11)$$

$$f_{\text{l}} = 1 - f_{\text{gb}} - f_{\text{tj}} - f_{\text{dis}} \quad (12)$$

where H_{gb} and H_{tj} are grain shape factors taken to be 2.91 and 2.52, respectively, to resemble a Voronoi polyhedral ⁷⁴, δ is the assumed grain boundary thickness ($\sim 5 \cdot 10^{-8}$ cm ⁷⁶), L is the grain size (diameter) in cm, ρ is the dislocation density in cm⁻², and b is the burgers vector calculated from the lattice parameter ($=a/\sqrt{2}$) for FCC Ni20Cr (wt.%) at 600 °C ⁷⁷. From **Eq. 8**, Er_1 and Er_2 are error factors which capture the distribution of polyhedra geometric features for the intragrandular (ia) and intergrandular (ie) regions defined in **Eq. 13** and **Eq. 14**, respectively;

$$Er_1 = \frac{f_{tj}f_{gb}(D_{tj}^{Cr}-D_{gb}^{Cr})^2}{f_{tj}(D_{tj}^{Cr}-D_{gb}^{Cr})-2(f_{gb}+f_{tj})D_{tj}} \quad (13)$$

$$Er_2 = \frac{f_{ig}f_v(D_{ig}^{Cr}-D_v^{Cr})^2}{f_{ig}(D_{ig}^{Cr}-D_v^{Cr})-3D_{ig}^{Cr}} \quad (14)$$

where f_{ig} and f_v are the fractions of intergranular ($=f_{gb}+f_{tj}$) and intragranular ($=f_l+f_{dis}$) regions, respectively. The intergrandular(D_{ig}^{Cr}) and intragranular (D_v^{Cr}) diffusivities are defined in **Eq. 15** and **Eq. 16**, respectively ⁷⁵:

$$D_{ig}^{Cr} = \frac{1}{f_{ig}}(f_{gb}D_{gb} + f_{tj}D_{tj} + \frac{f_{tj}f_{gb}(D_{tj}-D_{gb})^2}{f_{tj}(D_{tj}-D_{gb})-2f_{ig}D_{tj}}) \quad (15)$$

$$D_v^{Cr} = \left(1 - \frac{f_{dis}}{f_v}\right) D_l^{Cr} + \left(\frac{f_{dis}}{f_v}\right)^\xi D_{dis}^{Cr} \quad (16)$$

Based on literature that experimentally measure the intrinsic Cr diffusivities in Ni-Cr alloys or in a similar system, D_{gb}^{Cr} may be estimated on the order of 10^{-11} cm²/s ⁷⁸⁻⁸¹, D_l^{Cr} of 10^{-15} cm³/s ⁷⁸⁻⁸¹, and D_{dis} of 10^{-8} cm²/s^{82,83} at 600 °C. There is a lack of reported D_{tj}^{Cr} values and thus D_{tj}^{Cr} is assumed to be 10^3 larger than D_{gb}^{Cr} ^{74,84,85}. Moreover, the ρ values for the 10%, 30%, and 50% CW samples are estimated using an XRD method before and after dealloying.

$J_{FLiNaK}^{Cr(III)}$ was calculated based on method presented in chapter 4 and ref ^{59,86}, which utilizes the Fick's 1st law incorporating the diffusivity of Cr(III), $D_{FLiNaK}^{Cr(III)}$, in FLiNaK at 600°C ($\sim 10^{-5}$ cm²/s ⁸⁷), and the nominal diffusion equation to estimate boundary layer thickness (ie., $\delta = \sqrt{D_{FLiNaK}^{Cr(III)} t}$). Additionally, the mass of Cr dissolved ($m_{dissolved}^{Cr}$) can be calculated via the Faraday's Law of electrolysis (**Eq. 17**):

$$m_{dissolved}^{Cr} = \frac{EW \cdot Q(t)}{F} \quad (17)$$

Where $Q(t)$ represents the cumulative anodic charge released and EW as the equivalent weight (EW). ASTM G102-89 standard guides to obtain a solid solution alloy EW via **Eq. 18**⁸⁸:

$$EW = \sum \frac{W_i}{n_i f_i} \quad (18)$$

where W_i represents the atomic mass of each element participating, n_i is the number of electrons transferred when the oxidizing half cell reaction occurs a single time, and f_i is the weight fraction of the i^{th} alloying elements. An EW of 52 is used for the E_{applied} of 1.75V_{K+/K} (where only Cr(II) and Cr(III) dissolution are considered). However the EW is 21.5 at 1.90 V_{K+/K} where Ni(II) dissolution is also considered. The $m_{\text{dissolved}}^{\text{Cr}}$ can be represented by both $C_{\text{Cr(III)}}$ using **Eq. 19** and the depth of Cr dealloying perpendicular to the plane of the surface ($h_{\text{dissolved}}$) using **Eq. 20**:

$$C_{\text{Cr(III)}} = \frac{EW \cdot \int i_{\text{electric}}^{\text{anodic}} dt}{F \cdot V_{\text{FLiNaK}} M_{\text{Cr(III)}}} \quad (19)$$

$$h_{\text{dissolved}} = \frac{EW \cdot \int i_{\text{electric}}^{\text{anodic}} dt}{F \cdot d_{\text{Ni20Cr}} \cdot p(t)} \quad (20)$$

where V_{FLiNaK} is the volume of FLiNaK salts, $M_{\text{Cr(III)}}$ is the molar mass of Cr(III) (calculated based on the molecular species of CrF_6^{3-})¹⁷, d_{Ni20Cr} is the Ni20Cr density in g/cm³, and $p(t)$ is the time-dependent porosity of the dealloyed layer estimated using the area fraction of void space. A p for each E_{applied} and CW conditions was approximated at 10 ks. The steps for obtaining p are outlined in the supplemental sections **Table S4**. Lastly, the surface diffusion flux of Ni ($J_{\text{surf}}^{\text{Ni}}$) was estimated based on the Ni adatom capillary diffusion driven by surface curvature K described by the Gibbs-Thomson effect⁸⁹, and is derived to **Eq. 21** by Mullins^{90,91}, Herring⁹², and validated by Erlebacher and Sieradzki et al.⁹³⁻⁹⁵:

$$J_{\text{surf}}^{\text{Ni}} = \nabla J_{\text{cap}}^{\text{Ni}} = -M \nabla^2 (\Delta \mu_o + \gamma \Omega K) = \frac{-\gamma \Omega D_{\text{surf}}^{\text{Ni}}}{k_B T} \nabla^2 K \quad (21)$$

where M and $D_{\text{surf}}^{\text{Ni}}$ represent the mobility and surface diffusivity of Ni, $C_{\text{surf}}^{\text{Ni}}$ as the surface concentration of Ni in mol/cm², k_B is the Boltzman constant of $1.38 \cdot 10^{-23}$ J/K, Ω is the atomic volume in cm³/mol, γ is the surface energy in J/cm², ∇K is the curvature gradient in 1/cm². A range of reported $D_{\text{surf}}^{\text{Ni}}$ in literature was stated in **Table S5**, averaging an Ni adatom diffusivity of 10^{-9} cm²/s at 600 °C. *Supplemental section* outlines the detailed steps to simplify **Eq. 21**, leading to the derivation of **Eq. 22** estimating an averaged $J_{\text{surf}}^{\text{Ni}}$ using ligament width, $\lambda_{\text{lig}}(t)$:

$$\bar{J}_{\text{surf}}^{\text{Ni}} = \frac{\gamma \Omega D_{\text{surf}}^{\text{Ni}}}{k_B T} \left(\frac{16 \pi^4 A_o}{\int_0^t \lambda_{\text{lig}}^4(t) dt} \right) \quad (22)$$

where A_0 is the initial amplitude assumed to be 10nm and $\lambda_{lig}(t)$ was estimated from experimental results. It is noted that Ni adatom diffusion at the early stage of dealloying drives surface coalescence and porosity formation, which is related the Cahn-Hilliard (CH) effect^{18,94}, dominating J_{surf}^{Ni} . However, capturing this diffusion rate requires solving $\Delta\mu_{ch}$ coupled with specific assumptions about the initial geometric and compositional distribution of surface Ni^{93} . These complexities are beyond the scope of the current study.

Results

Microstructural Characterization of As-Cold Worked Ni20Cr Alloys

EBSD analyses for the as cold-rolled 0% (**Figure 1a**), 10% (**Figure 1b**), 30% (**Figure 1c**), and 50% (**Figure 1d**) CW sample conditions prior to the corrosion experiment are summarized in **Figure 1**. The scan was also performed at low magnification over the entire sample surface and is further illustrated in **Figure S7**. The inverse pole figure (IPF), geometrically necessary dislocation (GND) density, and local average misorientation (LAM) maps were provided for each condition. GND maps were used to highlight the overall lattice curvature across a larger length scale and indicate regions of higher dislocation density and (i.e. prior GBs, microbands (MBs), etc.). Similarly, the LAM maps were used to indicate regions where local lattice distortions, such (i.e. DDWs and subgrain boundaries) and to highlight the local lattice distortions over a shorter length scale. XRD was also performed as shown in **Figure S1**, revealing that cold-rolling induced a (220) and (220) texture on all samples.

The 0% CW (**Figure 1a**) sample contained an equiaxed grain structure. The GND density map indicated that the dislocation density is low in grain interiors with a sharp transition to high density at grain boundaries. The 10% CW (**Figure 1b**) sample displayed large grains with increased texture where the in-grain orientation gradient within the grain, indicating the accumulation of GND throughout the grain interior, connected to increased slip activity.⁴⁶ The misorientation in the grain interiors at low % CW condition indicated dense dislocation walls (DDWs) and the onset of low angle ($< 5^\circ$) grain boundaries (LAGB) within the grain. These slip traces appeared to terminate at higher angle ($> 15^\circ$) GBs. The 30% CW sample (**Figure 1b**) contains grains that exhibited a strong texture with elongated grains oriented in the cold rolling direction. Much of the same type of dislocation networks (as observed in the 10% CW sample) were visible within the grain interior. The severe work hardening conditions correspond to an increase in dislocation density within the grains and at sub-GBs as shown in the GND map (**Figure 1b, Figure 1c**). At 30% CW, sub μm -sized networks of dislocation cell blocks (CBs), possibly formed by tangled dislocations,^{47,48} were observed. At 50% CW, dislocation CBs were arranged into a microband (MB) typically following pre-existing GB pathways and were common features in FCC materials undergoing moderate to severe plastic⁴⁶. Upon closer inspection of the 50% CW sample (highest plastic deformation), the size of the MBs has

increased, and was not restricted to GBs but rather also forms in the grain interiors. The MB interior exhibited a dense μm -sized recrystallized grain structure containing high angle GBs ($> 10^\circ$) and CBs with a low misorientation ($1\text{--}5^\circ$). There was a high fraction of LABGs within the dislocation CB structure. Moreover, there is a sparse distribution of twin boundaries (60°) within the highly deformed microstructure. All these observations align with previous findings for cold-rolled Ni20Cr (wt.%) alloy.^{47,48}

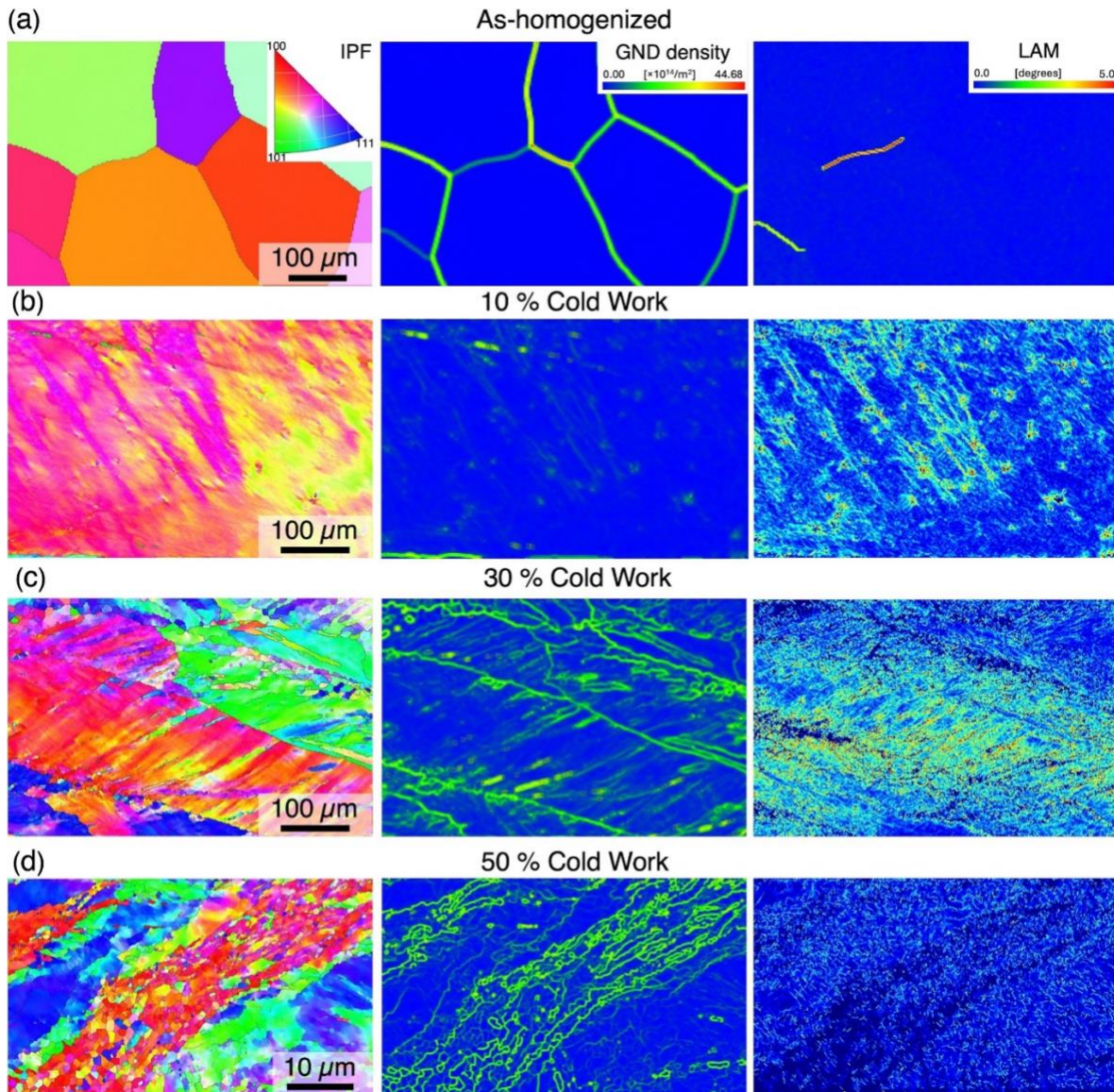


Figure 1. EBSD analysis on as cold-rolled Ni20Cr (wt.%) at (a) 0%CW, (b) 10% CW, (c) 30% CW, and (d) 50% CW conditions before molten salt dealloying. (left) Inverse pole figure (IPF) maps, (middle) geometrically necessary dislocation density (GND) maps with the maximum misorientation angle between neighboring pixels was set to 60 degrees, (right) local average misorientation (LAM) map angle was set to 0–5 degrees.

These results presented here are consistent with prior knowledge that plastic deformation leads to the initiation of dislocation slip to form sub-grains within the grain interiors and CBs at pre-existing GBs. Upon further plastic deformation, MBs emerged at prior GBs and expanded to full pathways within grain interiors. These dislocation substructures are postulated in this study as the predominant short-circuit diffusion pathway within the bulk alloy, especially when rapid thermally activated processes such as corrosion dealloying are involved⁵⁷. Connections between these deformation pathways containing high-density dislocations and corrosion de-alloying are discussed in later sections of this study.

Effect of Cold Work on Dealloying at +1.75 V_{K+K}

Morphological Evolution vs. Degree of Cold Work at +1.75 V_{K+K}

Figure 2 displays the plan view of Ni20Cr (wt.%) dealloyed at +1.75 V_{K+K} in FLiNaK, 600 °C for 10 ks as a function of CW at 2,500× magnification (**Figure 2a - d**) and 10,000× magnification (**Figure 2e - h**). At this condition, only Cr was dealloyed irrespective of the CW levels^{16,96}, which was also verified by *in-operando* CV measurements as shown in **Figure S2** where only Cr(III)/Cr(II) peaks were detected. At the baseline (w/o CW) condition, dealloying produced a bicontinuous porosity with a “fissure-like” ligament width ($\lambda_{\text{ligament}}$) of $0.55 \pm 0.05 \mu\text{m}$ ⁶⁶. Such morphology was modified in the presence of CW. **Figure 2b** and **Figure 2f** show the distinct formation of an interconnected pores-ligament structure with a $\lambda_{\text{ligament}}$ of $0.63 \pm 0.15 \mu\text{m}$, and residual salts were found to trap within the pores (notably in **Figure S12**). The ligaments at 30% CW appeared to coarsen to $1.03 \pm 0.35 \mu\text{m}$ (**Table 2**), while reaching $1.13 \pm 0.45 \mu\text{m}$ at 50% CW. It is noteworthy that intragranular dealloying does not occur evenly across all surfaces on the 10% CW and 30% CW samples. Moreover, the pore geometry also differed across CW levels as those on the 50% CW display elongated, stratified pores and ligaments compared to those of other conditions.

Table 2. Plan view measurements of pore width (l_{pore}) and ligament ($\lambda_{\text{ligament}}$), and cross-sectional measurements of dealloying depth ($h_{\text{dissolved}}$) for CW and dealloyed Ni20Cr (wt.%)

%CW	+1.75 V_{K+K}			+1.90 V_{K+K}		
	$l_{\text{pore}} (\mu\text{m})$	$\lambda_{\text{ligament}}(\mu\text{m})$	$h_{\text{dissolved}}(\mu\text{m})^*$	$l_{\text{pore}} (\mu\text{m})$	$\lambda_{\text{ligament}}(\mu\text{m})$	$h_{\text{dissolved}}(\mu\text{m})^*$
0% CW	0.46 ± 0.15	0.55 ± 0.06	1.60 ± 0.25	0.65 ± 0.20	1.08 ± 0.20	8.47 ± 2.36
10% CW	0.46 ± 0.06	0.63 ± 0.15	2.71 ± 0.61	1.09 ± 0.29	1.04 ± 0.21	12.0 ± 3.04
30% CW	0.67 ± 0.18	1.03 ± 0.35	13.2 ± 1.95	1.66 ± 0.61	1.69 ± 0.39	28.0 ± 4.97
50% CW	0.65 ± 0.07	1.13 ± 0.45	9.29 ± 1.16	0.23 ± 0.22	2.47 ± 0.30	30.2 ± 3.90

*It is noted that the $h_{\text{dissolved}}$ here represents the depth of Cr depletion measured in Fig. 3 and Fig. 6

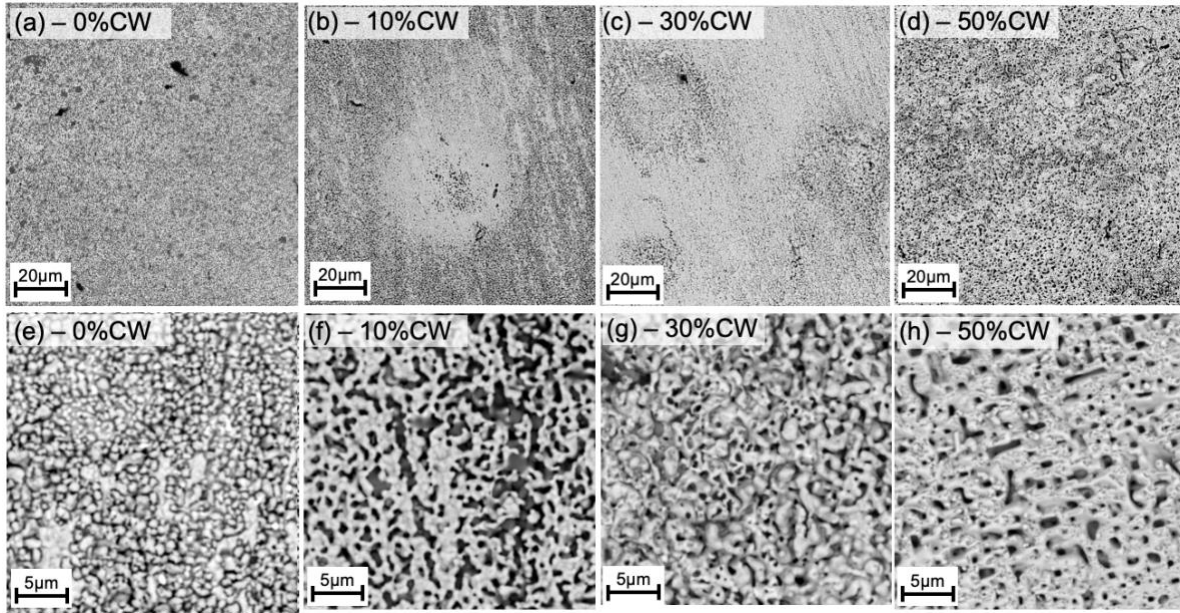


Figure 2. Plan view backscattered scanning electron (BSE) micrographs of Ni20Cr alloys subjected to an E_{applied} at $+1.90 V_{K/K^+}$ for 10 ks in molten FLiNaK at $600\text{ }^{\circ}\text{C}$. Panels (a) through (d) depict the samples after 0%, 10%, 30%, and 50% CW, respectively, all captured at $2,500\times$ magnification. Panels (e) through (h) present the corresponding micrographs at $10,000\times$ magnification.

Figure 3 shows the corresponding cross-section with the EDS maps of Cr, Ni, K, and F elements shown in **Figure S11** to **Figure S14**. Without CW, a $h_{\text{dissolved}}$ of $1.60\pm 0.25\text{ }\mu\text{m}$ exhibits a 'fissure-like' morphology as shown in **Figure 3a**. This morphology shows a gradual decrease in Cr through the EDS line profile, retaining approximately 4 wt.% of Cr in the dealloyed layer. It is possible that Cr is retained in the inner core of the ligament surrounded by Ni as a shell.^{97,98} As shown in **Figure 3b**, the 10% CW sample exhibited a h_{dissolve} of $2.71\pm 0.61\text{ }\mu\text{m}$ and a coarser pore-ligament feature, while retaining similar morphological features as the 0% CW sample. For the 30% CW sample, the $h_{\text{dissolved}}$ increased ~ 4 fold to $13.2\pm 1.95\text{ }\mu\text{m}$ (**Figure 3c**). In contrast to the 10% CW condition, this sample exhibited a finer porosities and ligament width throughout the dealloyed layer. The EDS line scan revealed a gradual reduction of Cr to ~ 1.8 wt.% near the outer layer, with numerous spikes of Cr concentration suggesting that the Cr-F salt accumulated at the pores. Lastly, the 50% CW sample exhibited a slightly lower $h_{\text{dissolved}}$ of $9.29\pm 1.16\text{ }\mu\text{m}$ and demonstrated different morphological features (**Figure 3d**). The outer layer displayed coarsened and stratified pore-ligament structures that were entirely depleted of Cr, while the inner layer contained fine, sponge-like, bicontinuous porosity with ~ 1.2 wt.% of Cr remaining.

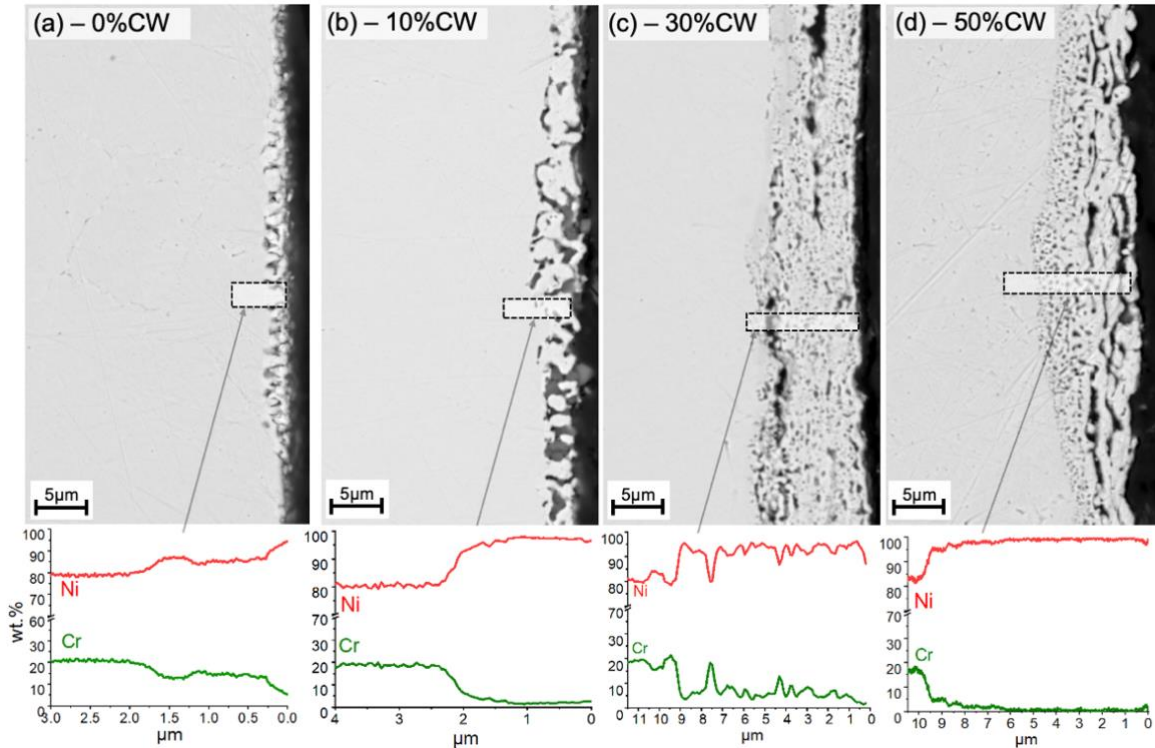


Figure 3. BSE micrographs displaying cross sectional view of Ni20Cr alloys subjected to (a) 0% CW, (b) 10% CW, (c) 30% CW, and (d) 50% CW dealloyed at +1.75 V_{K/K} for 10 ks in molten FLiNaK at 600 °C. The insets display regions analyzed with EDS line scan

Electrochemistry of Dealloying: Potential hold at +1.75 V_{K/K}

Figure 4 displays the i_{electric} vs. t curve under the E_{applied} of +1.75 V_{K/K} for (a) 10% CW, (b) 30% CW, and (c) 50% CW Ni20Cr alloys in molten FLiNaK, 600°C. At this potential, Cr dissolution dominates and Ni dissolution is negligible (validated in **Figure S2**)^{58,99}. Three features are observed: (1) there is a modest effect of CW on i_{electric} ; (2) a time dependent drop in i_{electric} ; (3) and later rapid fluctuations in i_{electric} . In **Figure 4a**, the i_{electric} of the 10% CW sample gradually dropped an order of magnitude over the first 1 ks. Between 1 ks and 10 ks, i_{electric} fluctuated between 10^{-3} and 10^{-7} A/cm². This variation can be attributed to two effects. The first effect is the rise of open-circuit potential (E_{oc}) as it approaches E_{applied} and the second effect is the depletion of Cr near the dealloyed zone-electrolyte interface. E_{oc} rises as the half-cell redox potential of cathodic reactions increases. In this case, as Cr dealloys, Cr(II) and Cr(III) ions are released, raising the surface concentration and thereby increasing the Cr(III)/Cr(II) redox potential⁶⁰. This in turn affects the corrosion potential (E_{corr}) and thus E_{oc} . When $E_{\text{applied}} \sim E_{\text{oc}}$, the net $i_{\text{electric}} (= i_{\text{anodic}} - i_{\text{cathodic}})$ approached zero. Compared to the 10% CW sample, the 30% CW sample (**Figure 4b**) displays a very similar $i_{\text{electric}}-t$ relationship. The 50% CW sample exhibited a greater amount of $i_{\text{electric}}-t$ variation. Between ~30 and ~300 s, the i_{electric} dropped two orders of magnitude then fluctuated near 10^{-3} A/cm² after 500 s.

The non-linear $i_{\text{electric}}-t$ behavior implies a disturbance to the charge-transfer (CT) controlled Cr dissolution process. All three $i_{\text{electric}}-t$ curves are similar in magnitude (**Figure S5**) with slight increase in initial i_{electric} with CW and are consistent with their E-log(i) behavior (**Figure S5a**). Linear behavior between i_{electric} and t in log-log scale with a slope close to zero confirms that the Cr dealloying process is CT controlled.

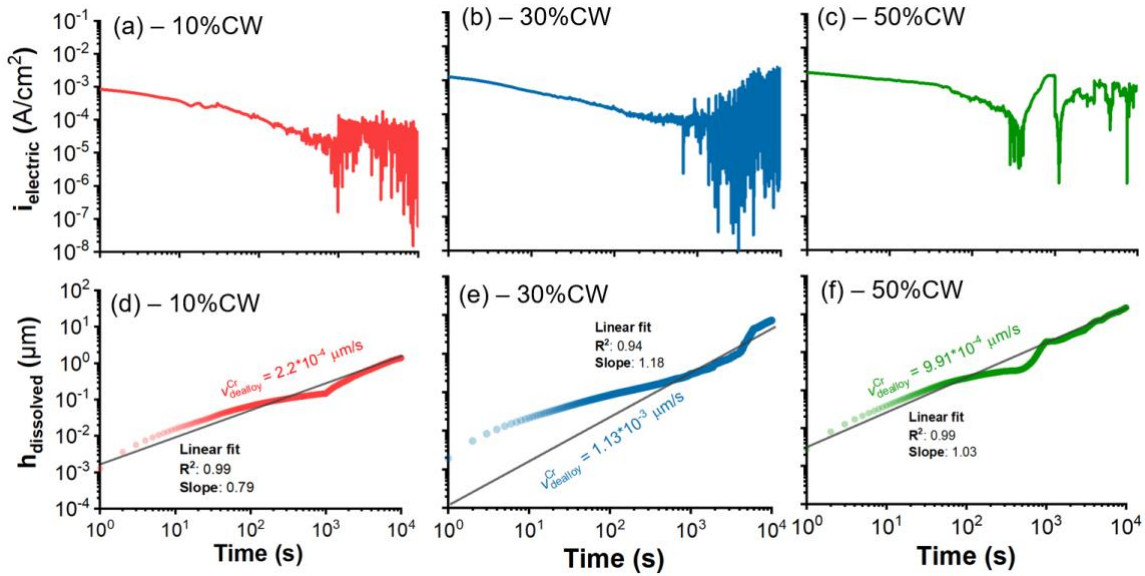


Figure 4. The relationship between current density (i_{electric}) and time (t) during potentiostatic dealloying of (a) 10%CW, (b) 30%CW, and (c) 50%CW Ni20Cr (wt.%) alloys in molten FLiNaK at 600 °C under the E_{applied} of $1.75V_{K+/K}$, 10ks. Corresponding plots of calculated dealloyed thickness ($h_{\text{dissolved}}$) with best linear fits are shown in (d), (e), and (f).

Using Eq. (20), the $h_{\text{dissolved}}$ was calculated versus time and displayed as lot-plot plots shown in **Figure 4e** (10% CW), **Figure 4e** (30% CW), and **Figure 4f** (50% CW). At $+1.75 V_{K+/K}$, Ni is negligible and thus the ligament formed remained Ni rich.^{58,99} The $h_{\text{dissolved}}$ calculated for the 10%CW, 30%CW, and 50%CW samples are 2.12 µm, 9.85 µm, and 9.84 µm, respectively, matching closely with the dealloyed depth measured in **Figure 3**. Slightly declining slopes yield the velocities of the dealloying front ($v^{\text{Cr}}_{\text{dealloy}}$) of $2.2 \cdot 10^{-4}$ µm/s, $1.1 \cdot 10^{-3}$ µm/s, and $9.9 \cdot 10^{-4}$ µm/s for the 10% CW, 30% CW, and 50% CW samples, respectively. It is important to emphasize that the porosity factor, $p(t)$, must be considered when using Eq. (20). **Figure S15** shows the $h_{\text{dissolved}}$ vs. t curves, one calibrated with the porosity factor (solid lines) and one assuming only uniform dissolution (short dashed lines). The uncalibrated curves show about an order of magnitude underestimation of $h_{\text{dissolved}}$.

Cold Work Effect on Dealloying at $+1.90 V_{K+/K}$

Morphological Evolution vs. Degree of Cold Work at $+1.90 V_{K+/K}$

Figure 5 shows the plan view of Ni20Cr dealloyed at $+1.90 V_{K+/K}$ in molten FLiNaK at 600 °C, which was the potential in which both Cr and Ni were both thermodynamically eligible to electro-dissolve to

Cr(III) and Ni(II), respectively (validated in **Figure S2**), with Ni dissolution occurring at a significantly slower rate than Cr⁶⁶. Compared to the E_{applied} at $+1.75 V_{\text{K}/\text{K}}$, the bicontinuous porous structure at $+1.90 V_{\text{K}/\text{K}}$ underwent further coarsening with E_{applied} ⁶⁶.

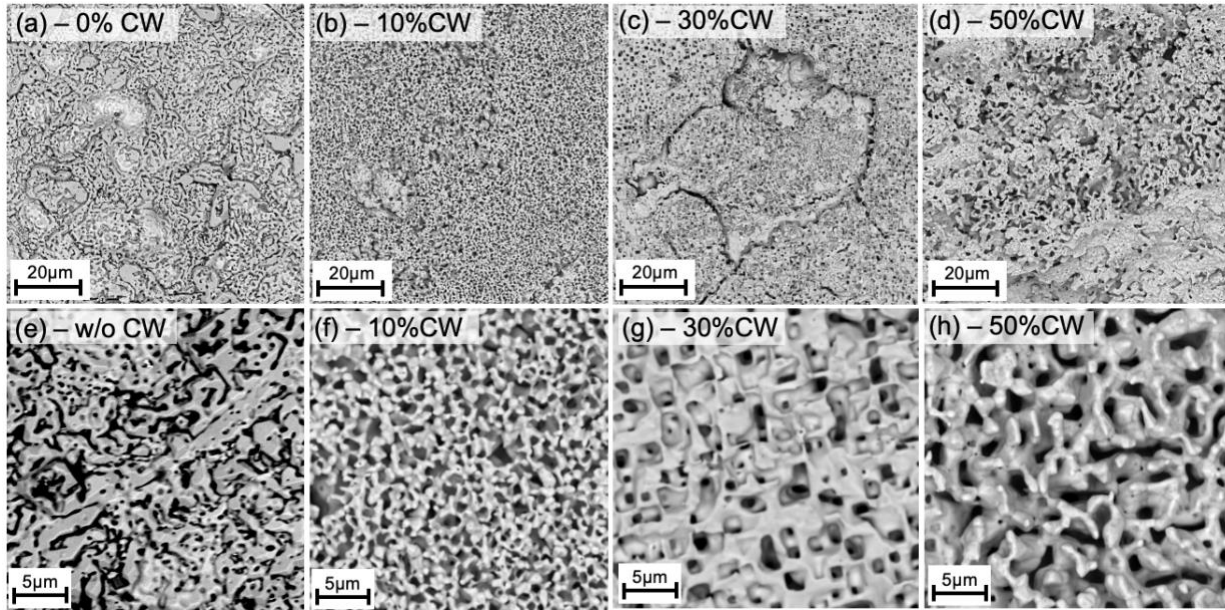


Figure 5. Plan view BSE micrographs of Ni20Cr alloys subjected to an E_{applied} at $+1.75 V_{\text{K}/\text{K}}$ for 10 ks in molten FLiNaK at 600 °C. Panels (a) through (d) depict the samples after 0%, 10%, 30%, and 50% CW, respectively, all captured at 2,500× magnification. Panels (e) through (h) present the corresponding micrographs at 10,000× magnification

Introducing 10% CW resulted in a slight reduction in the $\lambda_{\text{ligament}}$ and produced a similar, uniform porous morphology across the exposed intragranular surface as seen in **Figure 5b** and **5f**. As the degree of CW increased, the ligaments coarsen from $1.04 \pm 0.21 \mu\text{m}$ (10% CW) to $1.69 \pm 0.39 \mu\text{m}$ (30% CW) to $2.47 \pm 0.3 \mu\text{m}$ (50% CW). The ligament is Ni rich even though some Ni dissolved at $1.90 V_{\text{K}/\text{K}}$. The plan view ligament morphology also differed among the different %CW. The 30% CW sample exhibited more distinct dissolution at the GBs (**Figure 5c**). At higher magnification, **Figure 5g** revealed a relatively faceted, porous surface, similar to findings in³⁴ on the same material dealloyed in LiCl-KCl-MgCl₂ salts at 700°C. Lastly, **Figure 5d** shows that the 50% CW sample exhibited a non-uniform, porous surface. Some regions were severely coarsened as displayed in **Figure 5h**.

Figure 6 shows the corresponding cross-section views. In **Figure 6a**, the 0% CW sample exhibited a $8.47 \pm 2.36 \mu\text{m}$ deep dealloyed layer comprised entirely of high purity Ni. It can be inferred that the interface between the Ni-rich layer/ligaments and the bulk alloy substrate is semicoherent with poor adhesion.

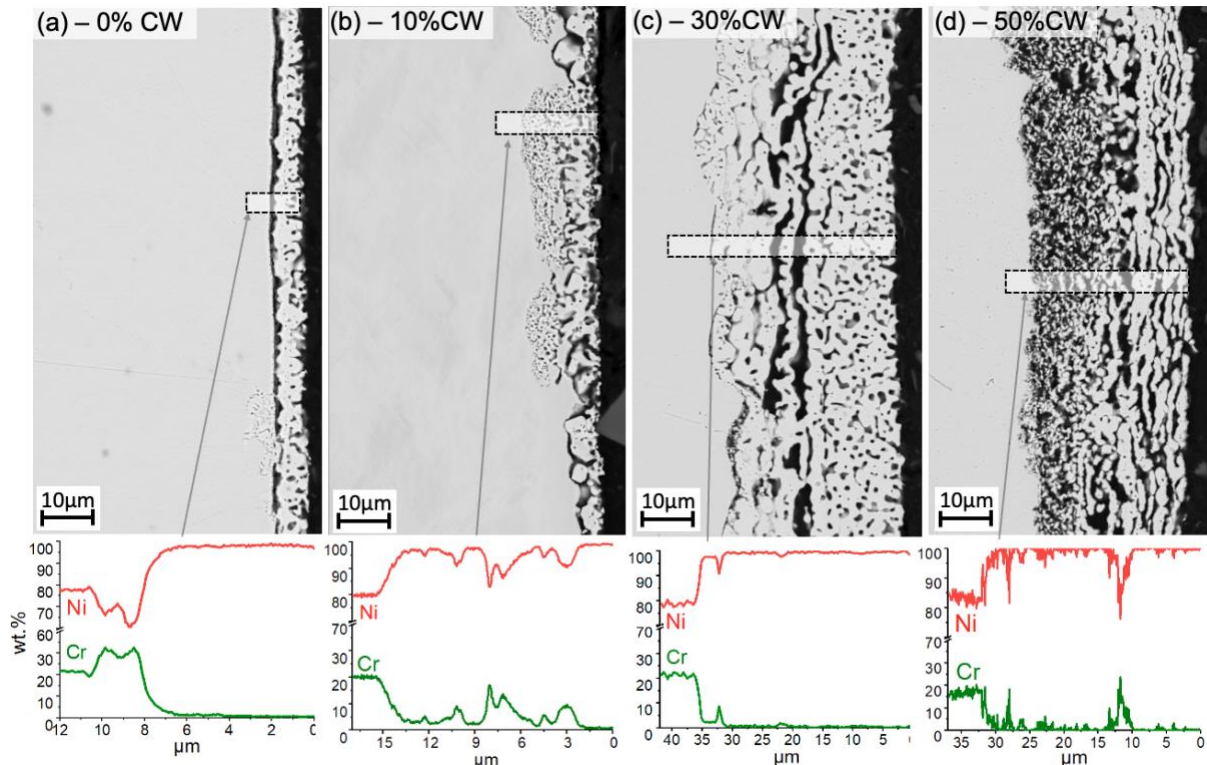


Figure 6. BSE micrographs displaying cross sectional view of Ni20Cr alloys subjected to (a) 0% CW, (b) 10% CW, (c) 30% CW, and (d) 50% CW dealloyed at +1.90 V_{K/K+} for 10 ks in molten FLiNaK at 600 °C. The insets display regions analyzed with EDS line scan

The red arrow in **Figure 6a** shows a microporous region which possibly indicated the onset of bicontinuous dealloying. At 10%CW, multiple microporous regions appeared beneath the Ni-rich top coarsened layer, achieving a dealloyed thickness of $12 \pm 3.04 \mu\text{m}$, while retaining about 5 wt% Cr, as confirmed by the EDS line scan shown in **Figure 6b**. The corresponding EDS maps are shown in **Figure S16** through **Figure S19**. As shown in **Figure 6c**, the 30% CW sample exhibited a dealloyed layer $28 \pm 4.97 \mu\text{m}$ thick almost entirely depleted in Cr, characterized by pores and ligaments that were uniformly sized and spaced within the top $\sim 20 \mu\text{m}$. Deeper within the layer, the pores appeared interconnected, wider, and extended laterally. Adjacent to the alloy substrate, the dealloyed region appeared coarser, in contrast to the fine microporous regions observed in **Figure 6b**, retaining roughly 2 wt.% of Cr. Moreover, non-uniform corrosion dealloying was observed in some instances that penetrates much farther into the sample than the surface-level pore-ligament structure. One particular example of this non-uniform dealloying behavior is provided in the *Supplemental Section A Figure S20* where dealloying along GBs converges at a triple point $\sim 100 \mu\text{m}$ from the salt-facing sample surface. This non-uniform dealloyed zone at GBs is also connected to recrystallized sub-grain structure observed at the triple point and is a current focus of a follow-on study.

For the 50% CW sample, the dealloyed layer remained near $30 \pm 3.90 \mu\text{m}$ thick yet the dealloyed morphology showed sharp contrast relative to the other samples. Along the top $\sim 20 \mu\text{m}$, the ligaments were

coarsened, stratified, and completely depleted of Cr while extending laterally. In contrast, at the 20 μm depth, the structure exhibited bicontinuous porosity exhibiting ligaments that were sub- μm in width. Some Cr possibly remained in these ligaments, as suggested by the spike observed in the Cr EDS profile in **Figure 7d**. However, quantifying this was challenging due to the small size of the ligaments. Nevertheless, dealloying the different %CW samples at $+1.75 V_{K+/K}$ (**Figure 3d**) and $+1.90 V_{K+/K}$ (**Figure 7d**) resulted in a similar dealloying morphology, with the higher E_{applied} produced a more coarsened and deeper bicontinuous porous structure after 10 ks tests. Moreover, based on a reasonable assumption that Ni dissolves at a constant rate, i.e. under CT controlled, the depth of Ni thickness dissolved versus time was calculated using **Eq. (22)**, applying the i_{electric} of pure Ni at $1.19 \cdot 10^{-4} \text{ A/cm}^2$ (**Table 3**). The results are shown as dashed lines in **Figure 7d** through **Figure 7f**. Here, the dissolution velocity ($v_{\text{diss}}^{\text{Ni}}$) of Ni is also $4.06 \cdot 10^{-5} \mu\text{m/s}$, which is two orders of magnitude lower than the $v_{\text{dealloy}}^{\text{Cr}}$ for Cr dealloying. Thus a dealloyed layer develops proportional to the difference between $v_{\text{dealloy}}^{\text{Cr}}$ and $v_{\text{diss}}^{\text{Ni}}$.

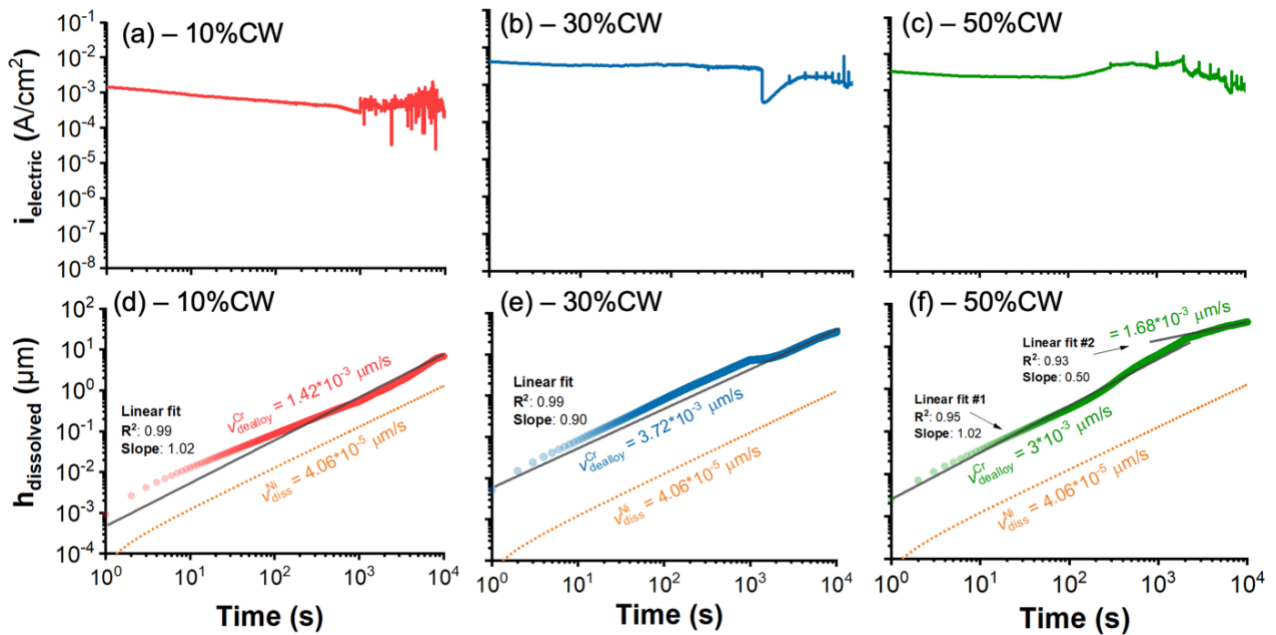


Figure 7. The relationship between current density (i_{electric}) and time (t) during potentiostatic dealloying of (a) 10%CW, (b) 30%CW, and (c) 50%CW Ni20Cr (wt.%) alloys in molten FLiNaK at 600°C under the E_{applied} of $1.90 V_{K+/K}$, 10ks. Corresponding plots of calculated dealloyed thickness ($h_{\text{dissolved}}$) with best linear fits are shown in (d), (e), and (f).

Electrochemistry of Corrosion Dealloying: Potentiostatic at $+1.90 V_{K+/K}$

At $+1.90 V_{K+/K}$, both Cr and Ni are favorable to dissolve⁶⁶. To quantify the effect of Ni dissolution, the i_{electric} of pure Ni, pure Cr, Ni20Cr with 0–50% CW samples are presented in **Table 3**. At $+1.90 V_{K+/K}$, the i_{electric} of pure Ni is lower than those of the Ni20Cr alloys by an order of magnitude, regardless of their

degree of CW. While the contribution of Ni dissolution to i_{electric} is not substantial enough to alter the overall order of magnitude, it warrants recognition due to its measurable contribution and effect of morphology.

Figures 7a to 7c display the i_{electric} vs. t behavior under the E_{applied} of +1.90 V_{K+/K} for 10%, 30%, and 50% CW Ni20Cr alloys in molten FLiNaK, 600°C. All three CW conditions show a nearly constant i_{electric} with time over the 10ks pstat hold, except for the 50% CW after 1ks in which a gradual drop in i_{electric} is observed. Increasing %CW also slightly increases i_{electric} in the same order (**Figure S5c**). Using **Eq. (20)**, the corresponding $h_{\text{dissolved}}$ was calculated versus time as shown in **Figure 7d, 7e, and 7f**. The $h_{\text{dissolved}}$ at 10 ks was calculated to be 13.1 μm for 10% CW, 38.3 μm for 30% CW, and 31.5 μm for 50% CW samples, overestimating their Cr depletion profiles measured in **Fig 6** on the order of 10%, that is attributed to the effect of Ni dissolution. For both the 10% and 30% CW samples, the logarithmic slopes of $h_{\text{dissolved}}$ vs. t are close to unity, suggesting that their dealloying process is CT controlled as this implies that i_{electric} is constant with time. The v^{Cr}_{dealloy} for all three CW samples is on the order of 10^{-3} $\mu\text{m/s}$ with a 2 fold increase from 10% to 30% CW then slightly reduced at 50% CW. However, for the 50% CW sample, a logarithmic slope of 0.5 was measured after ~1ks of dealloying, suggesting that the subsequent dealloying may become MT or bulk diffusion controlled, reducing v^{Cr}_{dealloy} by a factor of 2.

Table 3. Comparison of i_{electric} measured on pure Ni, pure Cr, and Ni20Cr alloys between 0 and 50% CW at 1.90V_{K+/K} in molten FLiNaK, 600°C

Sample	Pure Ni	Pure Cr	Ni20Cr (0% CW)	Ni20Cr (10% CW)	Ni20Cr (30% CW)	Ni20Cr (50% CW)
i_{electric} (A/cm ²)	$1.19 \cdot 10^{-4}$ [57]	$2.50 \cdot 10^{-2}$ [58]	$1.44 \cdot 10^{-3}$ [57]	$1.48 \cdot 10^{-3}$	$4.15 \cdot 10^{-3}$	$3.24 \cdot 10^{-3}$
$\frac{i_{\text{electric}}}{i_{\text{electric}}^{\text{Ni}}}$	1	$2.10 \cdot 10^2$	$1.21 \cdot 10^1$	$1.24 \cdot 10^1$	$3.49 \cdot 10^1$	$2.72 \cdot 10^1$

Dealloying at +1.90 V_{K+/K} on Morphology and Composition over time

Despite the 30% CW and 50% CW samples display a similar dealloying thickness, they exhibit a very different dealloying morphology at both E_{applied} . This necessitated further study into the morphological evolution of this sample as a function of time. **Figure8** shows the surface and cross-sectional morphologies of 50% CW Ni20Cr (wt.%) dealloyed at +1.90 V_{K+/K} between 0.5 ks and 10 ks coupled with qualitative EDS analysis. The cross-sections were also subjected to EBSD analysis (**Figure9**) to track changes in near-surface crystallographic orientation during dealloying. At all dealloying times, the plan view surface displayed μm -sized pores and ligaments as tabulated in **Table 4**. The ligament width coarsened at a rate of 0.43 ± 0.12 , suggesting ligament coarsening is possibly controlled by surface diffusion^{100–103}.

Table 4. Time-dependent changes in l_{pore} , $\lambda_{\text{ligament}}$, and $h_{\text{dealloyed}}$ of 50% CW Ni20Cr alloy dealloyed in FLiNaK, 600 °C at +1.90 V_{K+/K}

Time (ks)	l_{pore} (μm)	$\lambda_{\text{ligament}}$ (μm)	$h_{\text{dealloyed}}$ (μm)
0.5	0.39±0.08	0.66±0.05	3.77±0.48
1.0	0.39±0.19	0.67±0.27	5.99±0.85
5.0	0.49±0.12	1.19±0.09	25.3±4.84
10	0.23±0.23	2.47±0.30	30.2±3.90
Slope	-	0.43±0.12	-

Conversely, the cross-sections display markedly evolving dealloying morphologies over time. After 0.5 ks, a 3.77±0.48 μm Ni-rich, salt-infiltrated, micro-porous layer (**Figure 8e**) can be observed. These dealloying features are exacerbated at 1 ks showing a 5.99±0.85 μm layer that is even at the top, yet consists of salt-infiltrated regions and dissolved fine ligaments deeper into the sample. The grain orientation of this micro-porous layer is displayed by the IPF maps acquired by EBSD at 0.5 ks (**Figure 9a**) and 1 ks (**Figure 9c**). Both of these sample conditions exhibit sub-micrometer sized facets that constitute different orientations from their parent grains. Moreover, these recrystallized regions also contain a high density of GNDs, indicating relatively high strain localization. As hypothesized in our earlier work [15], there are multiple sources of strains during Cr dealloying. This includes strain created due to a difference in lattice parameter between Ni and Ni20Cr alloy, shear strain exerted by the growing thickness of pure Ni, the presence of a core-shell structure which creates another semicoherent interface, and the presence of non-equilibrium defects including vacancies and dislocations [15]. These phenomena contribute to the formation of dislocations, which will reorganize themselves into grain boundaries or other low energy substructures. Additionally, grain boundaries may also be created by Ni surface diffusion and reorganization, yet it is unclear whether this formation mechanism will result in a high angle grain boundaries seen in Figure 9. This phenomenon of new GB formation in dealloyed layer will be investigated in our future work.

At 5 ks, a gradient dealloying morphology emerged with the top ~5 μm layer exhibiting fine ligament-pore features followed by ~7 μm of coarse middle layer and ~10 μm of salt-infiltrated inner layer. Within the grain interior, grains sized between 5 and 10 μm could nucleate from the recrystallization of severely plastically deformed grains to relieve the high dislocation density, seen at both 5ks and 10ks. It is noted that all three %CW samples display grains possibly nucleated from recrystallization were exposed to Ar gas at 600 °C for 10 ks instead, with the largest reduction seen for the 50% CW sample (**Figure S8-S10**). At 10 ks of dealloying, Ni pore-ligament networks stratified, only leaving behind a fine porous region in the inner layer. The dense and highly curved nature of the porous ligament structures present in the dealloyed layer made it difficult to obtain clear Kikuchi diffraction patterns at each scan position for uniform EBSD mapping, however the sub-grain structure identified initially via channeling contrast is consistent with the sharp changes in orientation and higher angle GBs in the EBSD-IPF maps (**Figures 9e and 9f**).

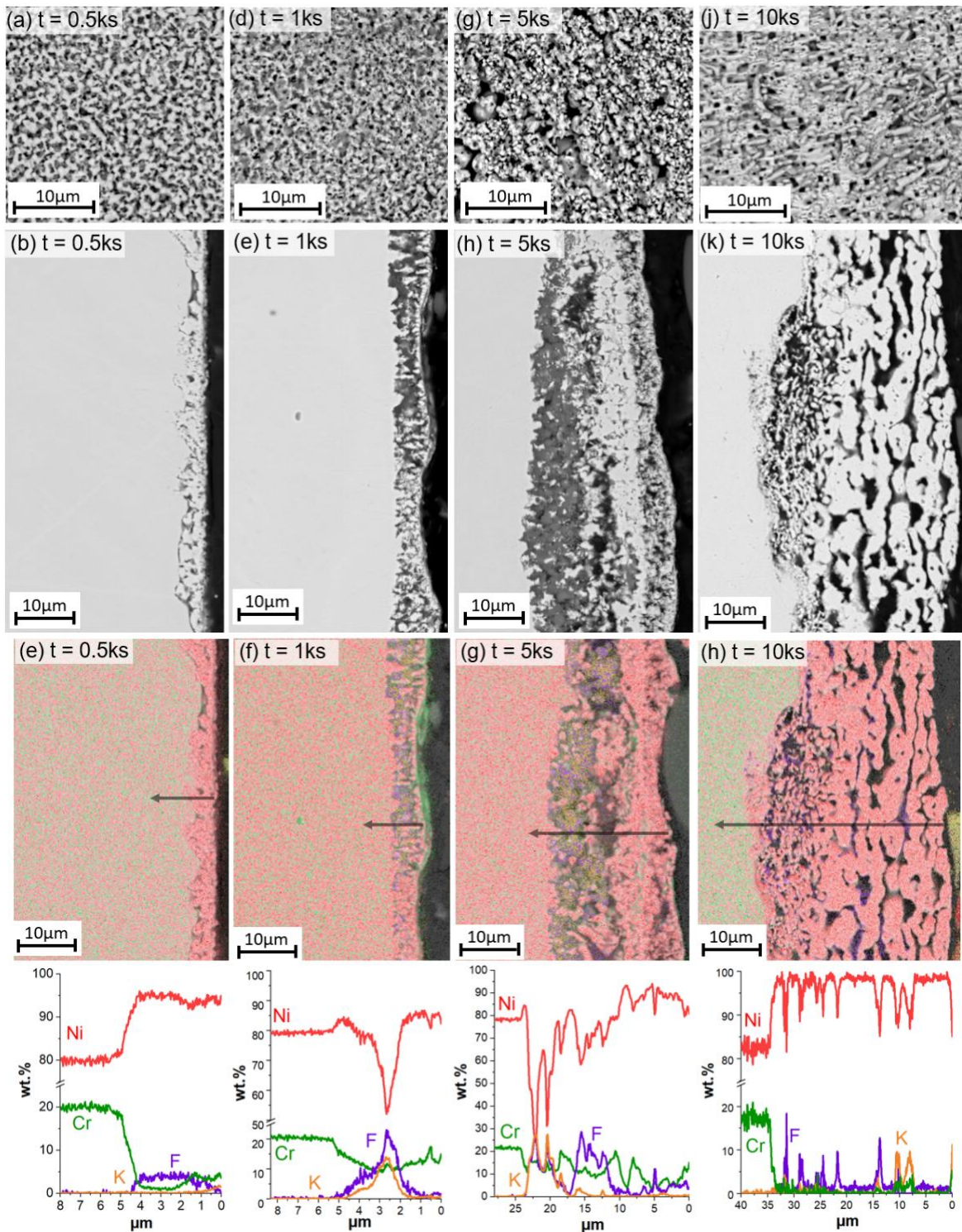


Figure 8. Cross sectional morphology of 50% CW Ni₂₀Cr subjected to an E_{applied} at +1.90 in molten FLiNaK salts, 600 °C for (a,e) 0.5 ks, (b,d) 1 ks, (c,g) 5 ks, and (d,h) 10 ks. Panels (e-h) show overlaid EDS elemental maps with Ni in red, Cr in green, F in blue, and K in purple, corresponding to panels (a-d), respectively. Panels (e-h) also a semi-transparent grey arrow representing the region analyzed with compositional line profile (wt.%)

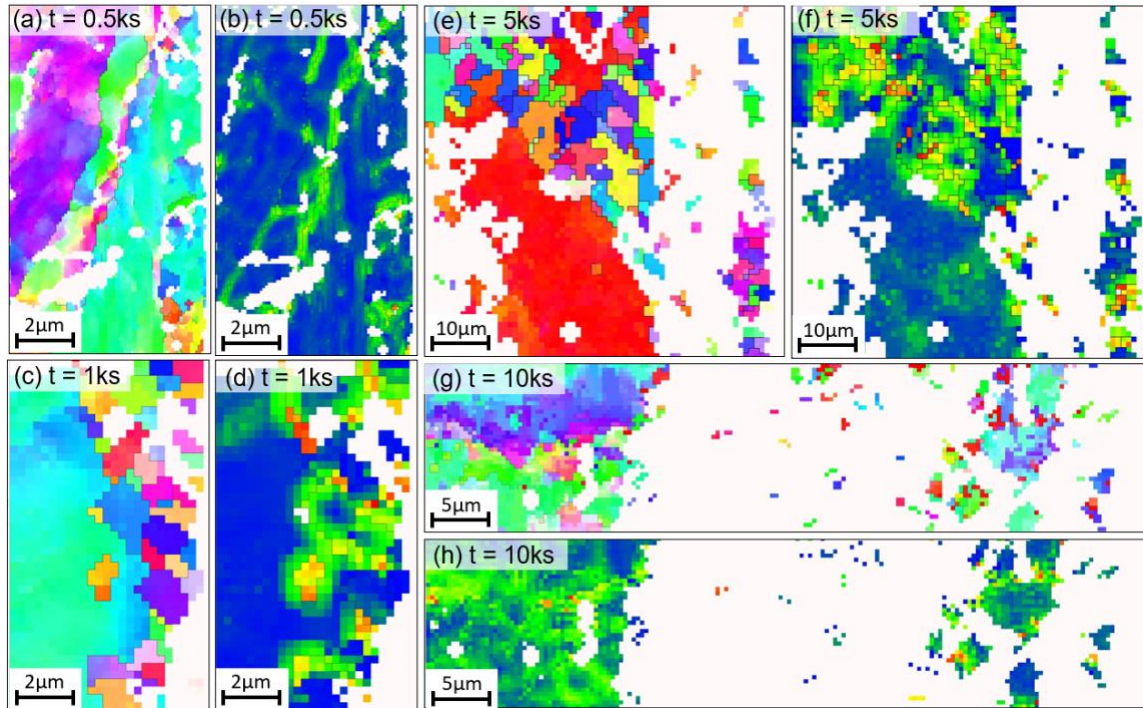


Figure 9. EBSD analysis on 50% CW Ni20Cr sample potentiostatically polarized in molten FLiNaK salts, 600 °C at +1.90 V_{K+/K} for (a,b) 0.5 ks, (c,d) 1 ks, and (e,f) 5 ks, (g,h) 10 ks. (left) IPF maps and (right) GND maps

Discussion

Results indicate that the dealloying morphology of Ni20Cr in molten FLiNaK is strongly influenced by the degree of CW, E_{applied} and time. In other words, bulk diffusion is central to the mechanism of molten salt dealloying. Fundamentally, the evolution of bicontinuous porosity at high T_H is governed by various competing mass transport processes that regulate Cr electro-dissolution and thus morphological evolution.

As simplified in Figure 10, during Cr dealloying, an electrochemical driving force for Cr/Cr(II)/Cr(III) oxidation, $J_{\text{electric}}^{\text{Cr}}$ (gray solid lines), is present due to an E_{applied} (or in practical cases by a chemical oxidizer), leading to a Cr dealloying front highlighted as $v_{\text{dealloy}}^{\text{Cr}}$ (red dashed lines). $J_{\text{electric}}^{\text{Cr}}$ may be predicted by the Butler-Volmer equation¹⁰⁴. Depending on the E_{applied} , Ni dissolution may occur ($J_{\text{diss}}^{\text{Ni}}$), causing a velocity of Ni dissolution ($v_{\text{diss}}^{\text{Ni}}$). When E_{applied} is sufficiently high, such as when $v_{\text{diss}}^{\text{Ni}}$ equals or larger than $v_{\text{dealloy}}^{\text{Cr}}$, the plan-view corrosion morphology will manifest as uniform corrosion without dealloying characterized by granular facets. This was demonstrated in our prior work at the E_{applied} of +2.50V_{K+/K} for the same test conditions⁵⁷. The Cr electro-dissolution occurring at a high enough $J_{\text{electric}}^{\text{Cr}}$ creates a concentration gradient in the solid, thereby driving the bulk outward diffusion of Cr ($J_{\text{bulk}}^{\text{Cr}}$), which is a dissolution flux that is primarily controlled by microstructural features. CW introduces a high degree of lattice strain and dislocation substructures within the grain interior as well as likely entanglements at the prior GBs, providing

more rapid diffusion pathways for Cr bulk diffusion. However, the effect of CW may also be constrained by alloy grain size (L). **Figure 11** displays the relationship between L and $D_{\text{eff}}^{\text{Cr}}$ analogous to the diffusion mechanism maps developed by Chen and Schuh et al.⁷⁴. The curves are constructed w/ and w/o considering the effect of CW and overlaid with a range of $D_{\text{surf}}^{\text{Ni}}$ values at 600 °C based on **Table S6**. A notable observation is that when $L > 1\mu\text{m}$, $D_{\text{eff}}^{\text{Cr}}$ begins to be dominated by intragrandular features, notably volume and dislocation diffusions. In contrast, when $L < 1\mu\text{m}$, the effect of $D_{\text{dis}}^{\text{Cr}}$ is negligible as two curves overlap, suggesting that diffusion is primarily dominated by intergranular features (e.g. GBs, TPs). A similar $D_{\text{eff}}^{\text{Cr}}$ does not equate to an identical corrosion mechanism; however, this may change the relative severity of intergranular corrosion and intragrandular bicontinuous dealloying. This analysis implies that when micrometer-sized recrystallized grains form, the influence of dislocation density on Cr bulk diffusion—and consequently on the conditions for MT controlled dealloying – may be reduced compared to samples with larger grains. $D_{\text{surf}}^{\text{Ni}}$ remain high all most practical grain sizes (0.1–100 μm).

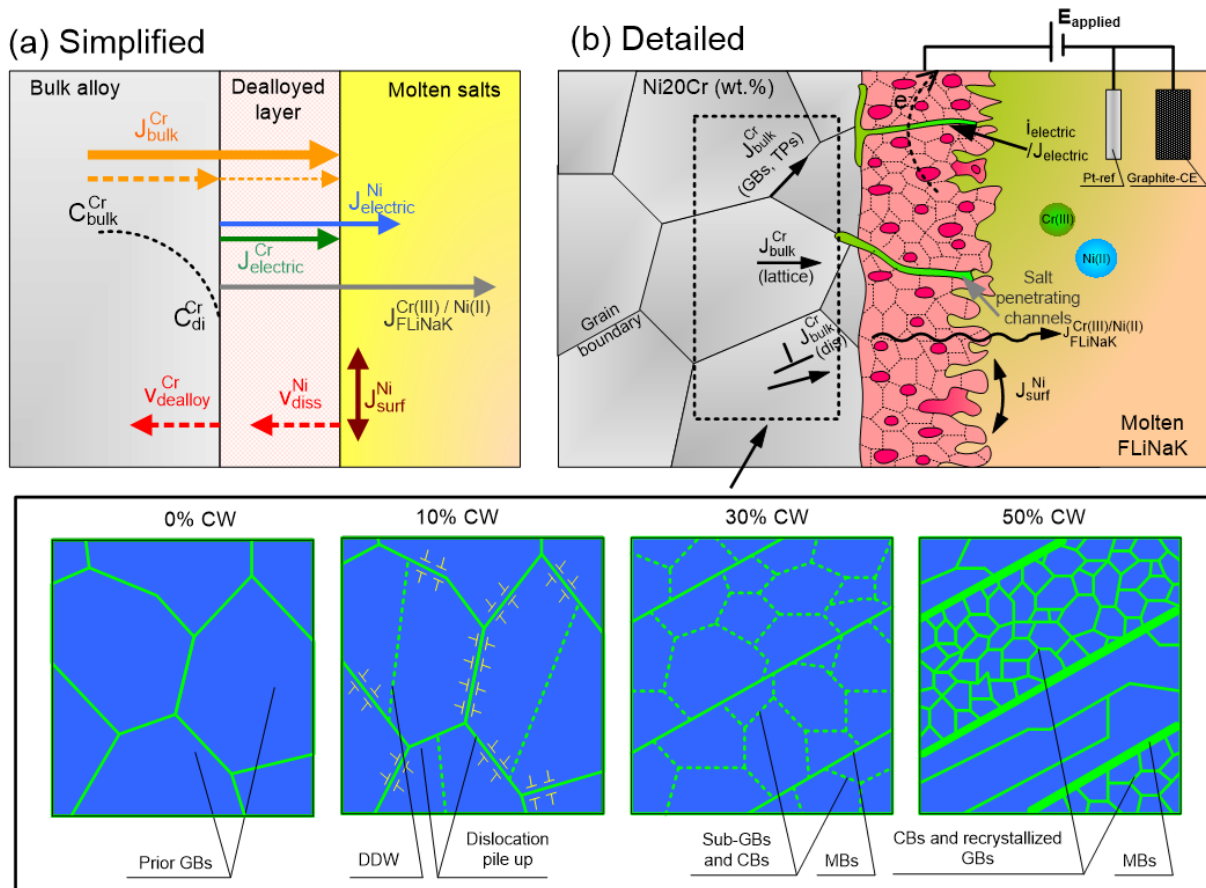


Figure 10. (a) displays a simplified diagram illustrating the presence of diffusion fluxes through the bulk alloy, dealloyed layer and the bulk molten salt; (b) shows a schematic highlighting the role of various microstructural features, including grain boundaries, dislocation substructures due to CW, lattice, recrystallized grains, critical to the molten salt dealloying process.

Over time, the $J_{\text{bulk}}^{\text{Cr}}$ can reduce as the Cr depletion profile widens and the surface is completely depleted of Cr, ultimately leading to bulk diffusion limiting the rate of the Cr dealloying (termed $J_{\text{diss}}^{\text{Cr}}$ in Eq. 23).

$$\frac{1}{J_{\text{diss}}^{\text{Cr}}} = \frac{1}{J_{\text{electric}}^{\text{Cr}}} + \frac{1}{J_{\text{bulk}}^{\text{Cr}}} \quad (23)$$

This is the case without CW⁵⁷. It is noted that $J_{\text{electric}}^{\text{Cr}}$ and $J_{\text{bulk}}^{\text{Cr}}$ are processes which occur in series because an insufficient $J_{\text{bulk}}^{\text{Cr}}$ can cause $J_{\text{electric}}^{\text{Cr}}$ to decrease over time. Additionally, the Cr dissolution drives Ni adatoms diffusion to passivate those sites in principle based on the Cahn–Hilliard effect^{18,94}. At a later stage, as Ni ligaments coarsen due to the Gibbs–Thomson effect⁸⁹. Subsequently, Ni surface diffusion ($J_{\text{surf}}^{\text{Ni}}$) competes with Cr dissolution at uncovered sites. Lastly, as Cr(III) and Ni(II) products will diffuse from the metal surface to the bulk salts at a rate of $J_{\text{FLiNaK}}^{\text{Cr(III)/Ni(II)}}$.

This mechanistic description provides a basis to answer two key questions critical to molten salt dealloying: (1) Is Cr bulk diffusion sufficiently rapid to support Cr oxidation once it arrives at the alloy surface? (2) Can the rds be modified by CW? **Figure 12** compares the calculated $J_{\text{Bulk}}^{\text{Cr}}$, $J_{\text{electric}}^{\text{Cr}}$, $J_{\text{FLiNaK}}^{\text{Cr(III)}}$, and $J_{\text{Surf}}^{\text{Ni}}$ versus time for all the CW conditions at the E_{applied} of +1.75V_{K+K} (**Figures 12a-c**) and +1.90V_{K+K} (**Figures 12b-d**). The $D_{\text{eff}}^{\text{Cr}}$ values used to calculate $J_{\text{Bulk}}^{\text{Cr}}$ are listed in **Table 5 based on Eq. 8**. The $\bar{J}_{\text{Surf}}^{\text{Ni}}$ was estimated using **Eq. 22** with an Ni adatom surface diffusivity of 10⁻⁹ cm²/s (See **Table S6**)¹ and the linear intrapolation between λ_{lig} and time in **Table 4**.

To simplify the complexity presented in **Figure 12**, a key observation to note is that across all %CW and E_{applied} , $J_{\text{FLiNaK}}^{\text{Cr(III)}}$ and then $\bar{J}_{\text{Surf}}^{\text{Ni}}$ are the fastest diffusion fluxes, suggesting they are likely not rate-controlling. The attention is thus drawn to the comparison between $J_{\text{Bulk}}^{\text{Cr}}(w/CW)$ and $J_{\text{electric}}^{\text{Cr}}$. Here, recall that $J_{\text{electric}}^{\text{Cr}}$ is measured and other fluxes are estimates. At +1.75V_{K+K}, if no dislocations are considered, $J_{\text{Bulk}}^{\text{Cr}}$ w/o CW (yellow dashed lines) may fall below $J_{\text{electric}}^{\text{Cr}}$ and may be rate-limiting. This has been observed in our prior work⁵⁷. When CW is considered, $J_{\text{Bulk}}^{\text{Cr}}(w/CW)$ exceeds $J_{\text{electric}}^{\text{Cr}}$ at all %CW levels, confirming the dealloying is interfacial CT controlled as demonstrated in **Figure 4**. It is noted that Cr dealloying can proceed no faster than $J_{\text{electric}}^{\text{Cr}}$ regardless of the $J_{\text{Bulk}}^{\text{Cr}}$ values under CT controlled regime.

¹ It is challenging to calculate $J_{\text{surf}}^{\text{Ni}}$ owing to its dependence on the surface curvature, salt/alloy surface energy, and surface diffusivities ($D_{\text{diff}}^{\text{Ni}}$), which is also a function of crystallographic orientation⁸⁹. Our future work seeks to provide a more accurate representation of $J_{\text{surface}}^{\text{Ni}}$ values.

Table 5. Summary of diffusivities used for the calculation of J_{Bulk}^{Cr} , $J_{electric}^{Cr}$, $J_{FLiNaK}^{Cr(III)}$, and J_{Surf}^{Ni} .

%CW	$f_{tj}D_{tj}^{Cr}$	$f_{gb}D_{gb}^{Cr}$	$f_lD_l^{Cr}$	$\frac{f_{dis}^\epsilon}{(f_l + f_{dis})^{\epsilon-1}} D_{dis}^{Cr}$	$\Sigma E (Er_1+Er_2)$	D_{eff}^{Cr}	D_{surf}^{Ni}
0%				-	$-2.43 \cdot 10^{-16}$	$1.49 \cdot 10^{-15}$	
10%				$1.10 \cdot 10^{-13}$	$-2.42 \cdot 10^{-16}$	$2.86 \cdot 10^{-12}$	
30%	$1.58 \cdot 10^{-18}$	$7.28 \cdot 10^{-16}$	10^{-15}	$1.24 \cdot 10^{-13}$	$-2.42 \cdot 10^{-16}$	$3.13 \cdot 10^{-12}$	10^{-9}
50%				$2.20 \cdot 10^{-13}$	$-2.42 \cdot 10^{-16}$	$4.72 \cdot 10^{-12}$	

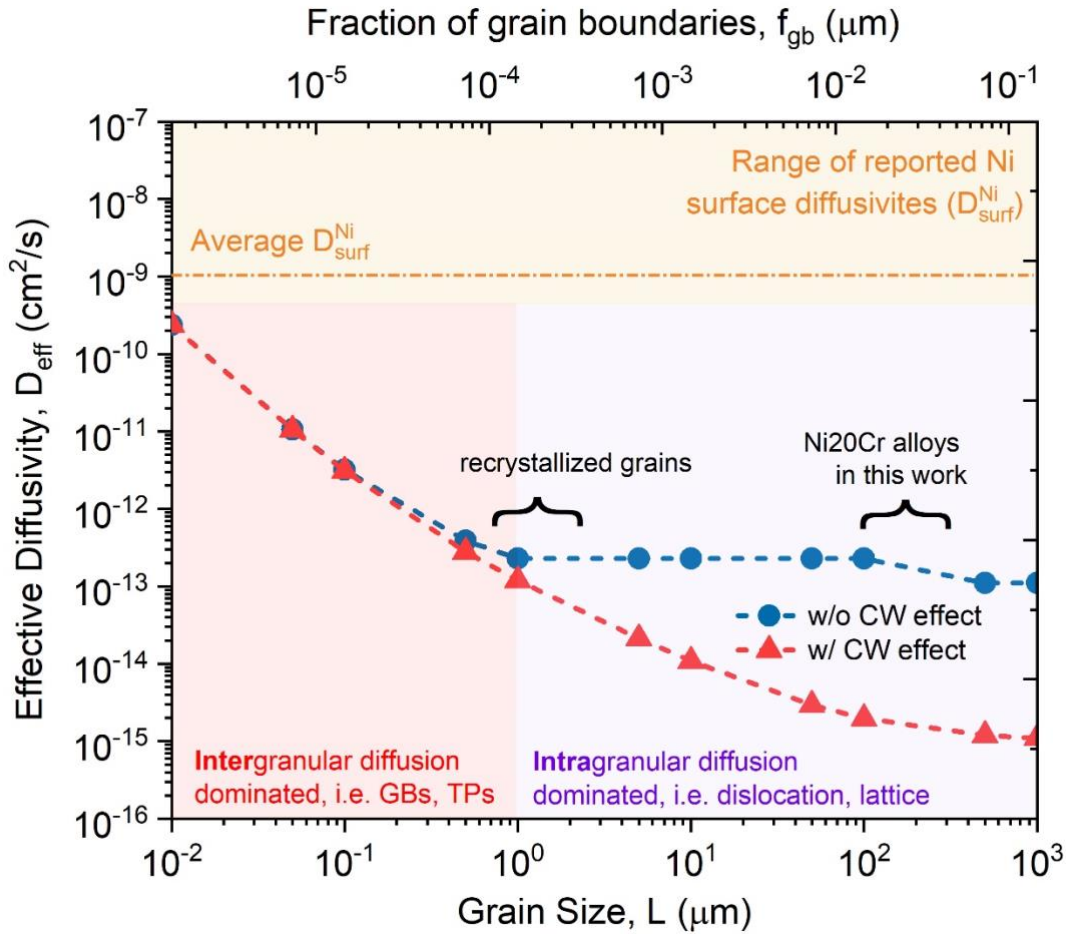


Figure 11. Effective diffusion coefficients (D_{eff}^{Cr}) as a function of grain size (L) and grain boundary fraction (f_{gb}) calculated using Eq.9 w/ and w/o considering CW effect. Kinetic parameters used are $D_l=10^{-15}$ cm²/s, $D_{gb}^{Cr}=10^{-10}$ cm²/s, $D_{tj}^{Cr}=10^{-10}$ cm²/s, $D_{dis}^{Cr}=10^{-8}$ cm²/s, $\rho = 10^{11}$ cm⁻², $b = 2.51 \cdot 10^{-8}$ cm and $\delta=5 \cdot 10^{-8}$ cm. Red shaded regions indicate where D_{eff}^{Cr} is dominated by intergranular diffusion (i.e. GBs, TPs), while purple regions show dominance by intragranular diffusion in which the dislocation density manifests. The size of recrystallized grains observed and the grain size of the as-homogenized Ni20Cr alloy are also marked by two brackets. A range of D_{surf}^{Ni} from literature (Table S6) is highlighted in orange, with an averaged value of 10^{-9} cm²/s shown by a dashed line.

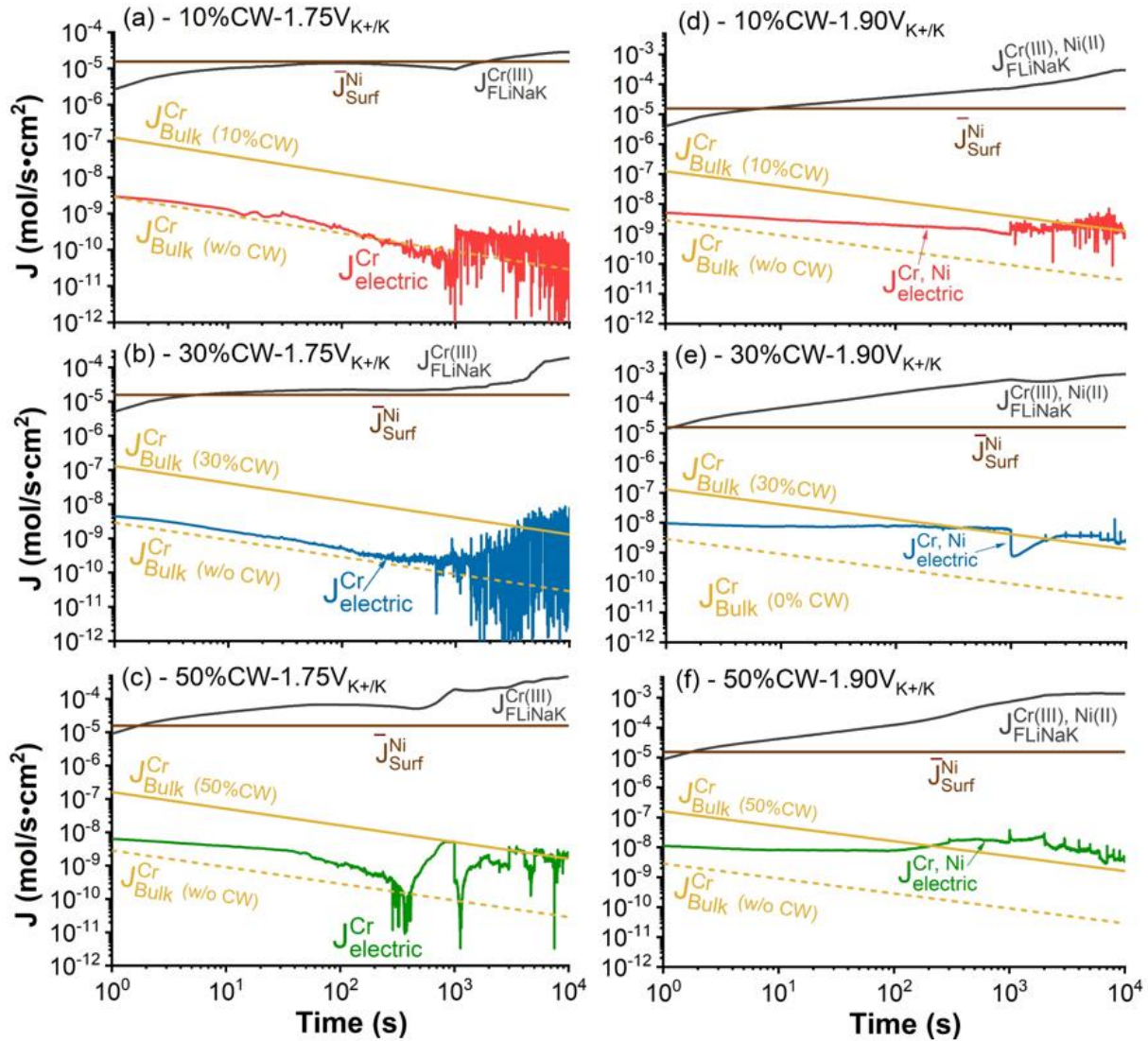


Figure 12. The comparison of $J_{\text{Bulk}}^{\text{Cr}}$, $J_{\text{electric}}^{\text{Cr}}$, $J_{\text{FLiNaK}}^{\text{Cr(III)}}$, and $J_{\text{Surf}}^{\text{Ni}}$ during 10,000 s of potentiostatic dealloying of Ni₂₀Cr (wt.%) in molten FLiNaK, 600 °C. (a), (b), and (c) correspond to the 10%CW, 30%CW, and 50%CW conditions under the E_{applied} of 1.75V_{K+/K}, respectively. (d), (e), and (f) follows the same order of annotation under the E_{applied} of 1.90V_{K+/K}. It is noted that $J_{\text{Bulk}}^{\text{Cr}}$ was calculated with (solid line) and without (dashed line) considering CW effect. For (d), (e), and (f), the labeling of $J_{\text{electric}}^{\text{Cr, Ni}}$ and $J_{\text{FLiNaK}}^{\text{Cr(III), Ni(II)}}$ are used instead to indicate Ni dissolution.

The $J_{\text{Bulk}}^{\text{Cr}}$ value is changing during the dealloying process bounded by the conditions w/ and w/o CW. The CW alloys exhibited high dislocation densities, which enhance $D_{\text{eff}}^{\text{Cr}}$ according to Eq. 9; however, some of these defects would be thermally annihilated at the T_{H} of 0.52 at 600 °C for 10ks. To clarify this possibility, the dislocation densities (ρ) of post-CW, post-dealloyed samples were analyzed from XRD measurements (Figure S20). As shown in Table S7, ρ was reduced by a factor of 2 after the experiments, and did not tangibly affect the $D_{\text{eff}}^{\text{Cr}}$ values. This is also confirmed by a series of low magnification EBSD analysis on

post-dealloyed Ni20Cr samples, showing that a high density of GND remain in the bulk alloy after dealloying (**FigureS22**).

At +1.90V_{K+K}, starting with the 10% CW (**Figure 12d**) and 30% CW (**Figure 12e**) samples display a similar time-dependent behavior for $J_{\text{electric}}^{\text{Cr \& Ni}}$ and $J_{\text{Bulk}}^{\text{Cr}}$, respectively. The Cr dealloying process for the 10% CW samples remains the interfacial CT controlled. For the 30% CW sample, $J_{\text{Bulk}}^{\text{Cr}}$ (w/ CW) is comparable to $J_{\text{electric}}^{\text{Cr \& Ni}}$, making it inconclusive whether the dealloying process is controlled by CT or solid state Cr MT based on diffusion flux comparisons. However, the analysis presented in Figure 4 suggests it is likely CT-controlled. For the 50%CW samples, $J_{\text{Bulk}}^{\text{Cr}}$ (w/ CW) exceeds $J_{\text{electric}}^{\text{Cr \& Ni}}$ only in the first ~200s. After this period, the $J_{\text{Bulk}}^{\text{Cr}}$ (w/ CW) fell slightly below $J_{\text{electric}}^{\text{Cr \& Ni}}$ indicating that outward diffusion of Cr might not keep up with the the rate of Cr oxidation. This analysis suggested that at relative high degree of CW and E_{applied} , $J_{\text{Bulk}}^{\text{Cr}}$ was likely the primary rds. In all CW conditions, the $J_{\text{FLiNaK}}^{\text{Cr(III),Ni(II)}}$ exceeded $J_{\text{electric}}^{\text{Cr \& Ni}}$ at all times indicating no mass transport limitation in the salt to the overall rate.

As shown in **Figure 1** and **Figure S1**, 10–50% CW introduces $\rho \sim 10^{14} \text{ m}^{-2}$, with similar $D_{\text{eff}}^{\text{Cr}}$ values differing by less than a factor of 2 (**Table 5**). Therefore, it is postulated that the difference in morphological features may be attributed to the initial dislocation substructures as illustrated in **Figure 10b**. The geometries of these dislocation substructures represent short-circuit diffusion paths, and thus preferential direction of Cr dissolution. Dislocation pile-ups at the surface, GBs, or triple points (TPs) can also accelerate Cr dissolution locally. Such behavior has been observed in **Figure S20** and will be presented in a follow-on work. Moreover, the grain reorientation and fragmentation created by CW also lead to a higher number of new grain and/or sub-GBs exposed to the salts, which mean more short-circuit diffusion pathways for Cr transport^{43,56}.

Diffusion along dislocation cores is thought to be predominately driven by the reduction of lattice strain 105. Intrinsic dislocation diffusion is regulated by the nucleation and spreading of jogs, or a pipe of atoms migrating a few Å away from the core 106,107 at a diffusivity that may reach 10-8 cm²/s 82,83. The $D_{\text{dis}}^{\text{Cr}}$ can also vary on the local ρ and dislocation character (e.g., edge vs. screw) 82,108. At high TH, a large population of thermal vacancies are expected, and therefore their interaction with dealloying front and dislocation cores should also be considered. Particularly, these sites of dislocation entanglement in high SFE FCC alloy, such as Lomer-Cottrell locks, are found to exhibit a lower formation energy for vacancies and interstitials 109, which aids the vacancy-mediated Cr diffusion process necessary for dealloying.

This may offer a hypothesis behind the connection between the dislocation substructures and dealloying morphologies. For instance, Cr dissolved via the CB substructures (30% CW) is likely to create a mesh-like interconnected network of salt-penetrating channels. Following this rationale, the minimum width of these corrosion channels is determined by the corresponding cellular wall thickness (at the nanometer scale)

and possibly the size of the Cr-F ion complexes¹¹⁰. For the 50% CW sample, Cr dealloying preferentially proceed through the localized paths of CBs, MBs and GBs, possibly leading to the stratified morphologies observed in **Figure 3d** and **Figure 6d**. Dislocation-guided dealloying is expected to be continue until either the dislocation substructures are annihilated or a change in the bulk microstructure occurred (e.g. nucleation of new grains). A higher $J_{\text{electric}}^{\text{Cr}}$ (i.e. higher E_{applied}) equating to more dissolved Cr and/or Ni sites. This correlates with a greater depth of dissolution, earlier Ni coarsening, and thus sharper dealloyed features.

Conclusion

In this work, model Ni20Cr (wt%) alloys were cold-rolled to achieve 10%, 30% and 50% CW and then dealloyed at the E_{applied} of +1.75 $V_{\text{K+/K}}$ and +1.90 $V_{\text{K+/K}}$ in molten FLiNaK, 600 °C for 10 ks. Under these conditions, dealloying occurs via mixed IGC and bicontinuous porosity, yet the varying degree of CW leads to different morphologies. The morphological evolution is a result of competing diffusion fluxes occurring simultaneously in the solid state, metal/salt interface, and ionic phase media, encompassing $J_{\text{Bulk}}^{\text{Cr}}$, $J_{\text{electric}}^{\text{Cr}}$, $J_{\text{surface}}^{\text{Ni}}$, and $J_{\text{FLiNaK}}^{\text{Cr(III)}}$, all influenced to varying degrees changing by E_{applied} and CW. Specifically, the following conclusions can be drawn:

- A high density of dislocation and its substructures are introduced as a function of CW, notable features are DDW and dislocation pile-up at 10% CW, cellular substructures at 30% CW as well as microbands and recrystallization formation at 50% CW. All degrees of CW also introduce texturing toward the (220) direction and introduction of subgrain boundaries.
- All degree of CW introduces sufficient dislocation densities that enable Cr outward bulk diffusion ($J_{\text{Bulk}}^{\text{Cr}}$) to support Cr dissolution ($J_{\text{electric}}^{\text{Cr}}$) at the two E_{applied} studied. Therefore, at +1.75 $V_{\text{K+/K}}$, the Cr dealloying process for the 10%, 30%, and 50% CW samples is rate-limited by the CT, interfacial dissolution of Cr to Cr(III). This remains true for the 10% and 30% CW samples at the higher E_{applied} of +1.90 $V_{\text{K+/K}}$. Only for the 50% CW sample at +1.90 $V_{\text{K+/K}}$, the mechanism of dealloying was initially limited by CT (or $J_{\text{electric}}^{\text{Cr}}$) during the first ~1 ks, and then controlled by MT in the bulk solid phase (or $J_{\text{Bulk}}^{\text{Cr}}$).
- Each degree of CW produces different dealloying morphology. It is proposed that the morphological evolution is dictated by the dislocation substructures relative to their level of CW, which facilitate and confine Cr diffusion from high-density dislocation regions, creating non-linear corrosion channels for salt penetration that become corrosion sites. Increasing E_{applied} coarsens and densifies the structure further.

- The 50% CW sample exhibited a sharp evolution of dealloying morphology over the 10ks of post hold. At first 1 ks, sub- μm sized, Ni-rich, high GND density grains form on the top layer that take on different crystallographic orientations relative to the parent grains, and are textured in line with a (111) direction. After 5 ks, strain-induced recrystallization was observed in the grain interior. The dealloying morphology consists of stratified Ni-rich coarsened layers in the top layer and fine bicontinuous porosity in the inner layer.

References

1. D. Rodrigues, G. Durán-Klie, S. Delpech, Pyrochemical reprocessing of molten salt fast reactor fuel: focus on the reductive extraction step, *Nukleonika* 60 (2015) 907–914. <https://doi.org/10.1515/nuka-2015-0153>.
2. A Technology Roadmap for Generation IV Nuclear Energy Systems Executive Summary, DOENE (USDOE Office of Nuclear Energy, Science and Technology (NE)), 2003. <https://doi.org/10.2172/859105>.
3. J. Serp, M. Allibert, O. Beneš, S. Delpech, O. Feynberg, V. Ghetta, D. Heuer, D. Holcomb, V. Ignatiev, J.L. Kloosterman, L. Luzzi, E. Merle-Lucotte, J. Uhlíř, R. Yoshioka, D. Zhimin, The molten salt reactor (MSR) in generation IV: Overview and perspectives, *Progress in Nuclear Energy* 77 (2014) 308–319. <https://doi.org/10.1016/j.pnucene.2014.02.014>.
4. Development Status of Molten-Salt Breeder Reactors, Oak Ridge National Lab. (ORNL), Oak Ridge, TN (United States), 1972. <https://doi.org/10.2172/4622532>.
5. M.S. Sohal, M.A. Ebner, P. Sabharwall, P. Sharpe, Engineering Database of Liquid Salt Thermophysical and Thermochemical Properties, Idaho National Lab. (INL), Idaho Falls, ID (United States), 2010. <https://doi.org/10.2172/980801>.
6. BPVC Section III-Div 5 - High Temperature Reactors - ASME, (n.d.). <https://www.asme.org/codes-standards/find-codes-standards/bpvc-iii-5-bpvc-section-iii-rules-construction-nuclear-facility-components-division-5-high-temperature-reactors> (accessed June 9, 2024).
7. S. Guo, J. Zhang, W. Wu, W. Zhou, Corrosion in the molten fluoride and chloride salts and materials development for nuclear applications, *Progress in Materials Science* 97 (2018) 448–487. <https://doi.org/10.1016/j.pmatsci.2018.05.003>.
8. F. Schmidt, P. Hosemann, R.O. Scarlat, D.K. Schreiber, J.R. Scully, B.P. Uberuaga, Effects of Radiation-Induced Defects on Corrosion, *Annual Review of Materials Research* 51 (2021). <https://doi.org/10.1146/annurev-matsci-080819-123403>.
9. H.E. McCoy, R.E. Gehlbach, Influence of Irradiation Temperature on the Creep-Rupture Properties of Hastelloy-N, *Nuclear Technology* 11 (1971) 45–60. <https://doi.org/10.13182/NT71-A30901>.
10. R. Auguste, H.L. Chan, E. Romanovskaia, J. Qiu, R. Schoell, M.O. Liedke, M. Butterling, E. Hirschmann, A.G. Attallah, A. Wagner, F.A. Selim, D. Kaoumi, B.P. Uberuaga, P. Hosemann, J.R. Scully, A multimodal approach to revisiting oxidation defects in Cr₂O₃, *Npj Mater Degrad* 6 (2022) 1–13. <https://doi.org/10.1038/s41529-022-00269-7>.
11. S. Bell, T. Steinberg, G. Will, Corrosion mechanisms in molten salt thermal energy storage for concentrating solar power, *Renew. Sustain. Energy Rev.* 114 (2019) 109328. <https://doi.org/10.1016/j.rser.2019.109328>.
12. S. Fayfar, R. Chahal, H. Williams, D.N. Gardner, G. Zheng, D. Sprouster, J.C. Neuefeind, D. Olds, A. Hwang, J. McFarlane, R.C. Gallagher, M. Asta, S. Lam, R.O. Scarlat, B. Khaykovich, Complex structure of molten FLiBe (2LiF–BeF₂) examined by experimental neutron scattering, X-ray scattering, and deep-neural-network based molecular dynamics, *PRX Energy* 3 (2024) 013001. <https://doi.org/10.1103/PRXEnergy.3.013001>.
13. J. Qiu, D.D. Macdonald, R. Schoell, J. Han, S. Mastromarino, J.R. Scully, D. Kaoumi, P. Hosemann, Electrochemical study of the dissolution of oxide films grown on type 316L stainless steel in molten fluoride salt, *Corrosion Science* 186 (2021) 109457. <https://doi.org/10.1016/j.corsci.2021.109457>.

14. L.C. Olson, J.W. Ambrosek, K. Sridharan, M.H. Anderson, T.R. Allen, Materials corrosion in molten LiF–NaF–KF salt, *Journal of Fluorine Chemistry* 130 (2009) 67–73. <https://doi.org/10.1016/j.jfluchem.2008.05.008>.
15. Y. Yang, W. Zhou, S. Yin. et al. One dimensional wormhole corrosion in metals. *Nat Commun* 14, 988 (2023). <https://doi.org/10.1038/s41467-023-36588-9>
16. H.L. Chan, J.R. Scully, Deciphering when Metal Corrosion is Spontaneous in Molten Fluorides Using Potential-Activity Diagrams, *Corrosion* (2023). <https://doi.org/10.5006/4401>.
17. H.L. Chan, E. Romanovskaia, J. Qiu, P. Hosemann, J.R. Scully, Insights on the corrosion thermodynamics of chromium in molten LiF–NaF–KF eutectic salts, *Npj Mater Degrad* 6 (2022) 46. <https://doi.org/10.1038/s41529-022-00251-3>.
18. I. Mccue, E. Benn, B. Gaskey, J. Erlebacher, Dealloying and Dealloyed Materials, *Annual Review of Materials Research* 46 (2016). <https://doi.org/10.1146/annurev-matsci-070115-031739>.
19. N. Bieberdorf, M.D. Asta, L. Capolungo, Grain Boundary Effects in Dealloying Metals: A Multi-Phase Field Study, *Npj Comput Mater* 9 (2023) 127. <https://doi.org/10.1038/s41524-023-01076-7>.
20. K. Bawane, X. Liu, R. Gakhar, M. Woods, M. Ge, X. Xiao, W.-K. Lee, P. Halstenberg, S. Dai, S. Mahurin, S.M. Pimblott, J.F. Wishart, Y.K. Chen-Wiegart, L. He, Visualizing time-dependent microstructural and chemical evolution during molten salt corrosion of Ni–20Cr model alloy using correlative quasi in situ TEM and in situ synchrotron X-ray nano-tomography, *Corrosion Science* 195 (2022) 109962. <https://doi.org/10.1016/j.corsci.2021.109962>.
21. X. Liu, A. Ronne, L.-C. Yu, Y. Liu, M. Ge, C.-H. Lin, B. Layne, P. Halstenberg, D.S. Maltsev, A.S. Ivanov, S. Antonelli, S. Dai, W.-K. Lee, S.M. Mahurin, A.I. Frenkel, J.F. Wishart, X. Xiao, Y.K. Chen-Wiegart, Formation of three-dimensional bicontinuous structures via molten salt dealloying studied in real-time by in situ synchrotron X-ray nano-tomography, *Nat Commun* 12 (2021) 3441. <https://doi.org/10.1038/s41467-021-23598-8>.
22. L.C. Yu, C. Clark, X. Liu, A. Ronne, B. Layne, P. Halstenberg, F. Camino, D. Nykypanchuk, H. Zhong, M. Ge, W.-K. Lee, S. Ghose, S. Dai, X. Xiao, J.F. Wishart, Y.K. Chen-Wiegart, Evolution of micro-pores in Ni–Cr alloys via molten salt dealloying, *Sci Rep* 12 (2022) 20785. <https://doi.org/10.1038/s41598-022-20286-5>.
23. X. Liu, K. Bawane, X. Zheng, M. Ge, P. Halstenberg, D.S. Maltsev, A.S. Ivanov, S. Dai, X. Xiao, W.K. Lee, L. He, Y.C.K. Chen-Wiegart, Temperature-Dependent Morphological Evolution during Corrosion of the Ni–20Cr Alloy in Molten Salt Revealed by Multiscale Imaging, *ACS Applied Materials and Interfaces* 15 (2023) 13772–13782. <https://doi.org/10.1021/acsami.2c23207>.
24. A. Ronne, L. He, D. Dolzhanikov, Y. Xie, M. Ge, P. Halstenberg, Y. Wang, B.T. Manard, X. Xiao, W.-K. Lee, K. Sasaki, S. Dai, S.M. Mahurin, Y.K. Chen-Wiegart, Revealing 3D Morphological and Chemical Evolution Mechanisms of Metals in Molten Salt by Multimodal Microscopy, *ACS Appl. Mater. Interfaces* 12 (2020) 17321–17333. <https://doi.org/10.1021/acsami.9b19099>.
25. T. Ghaznavi, M.A. Bryk, S.Y. Persaud, R.C. Newman, Alloying effects in high temperature molten salt corrosion, *Corrosion Science* 197 (2022) 110003. <https://doi.org/10.1016/j.corsci.2021.110003>.
26. T. Ghaznavi, S.Y. Persaud, R.C. Newman, Electrochemical Corrosion Studies in Molten Chloride Salts, *J. Electrochem. Soc.* 169 (2022) 061502. <https://doi.org/10.1149/1945-7111/ac735b>.
27. H. Gholamzadeh, Characterization of dealloying and associated stress corrosion cracking: The effect of crystallographic orientation, *Acta Materialia* (2023).
28. K. Sieradzki, R.C. Newman, Stress-corrosion cracking, *Journal of Physics and Chemistry of Solids* 48 (1987) 1101–1113. [https://doi.org/10.1016/0022-3697\(87\)90120-X](https://doi.org/10.1016/0022-3697(87)90120-X).
29. K. Sieradzki, J.S. Kim, A.T. Cole, R.C. Newman, The Relationship Between Dealloying and Transgranular Stress-Corrosion Cracking of Cu–Zn and Cu–Al Alloys, *J. Electrochem. Soc.* 134 (1987) 1635. <https://doi.org/10.1149/1.2100726>.
30. Y. Gu, W. Zhang, Y. Xu, Y. Shi, K. Volodymyr, Stress-assisted corrosion behaviour of Hastelloy N in FLiNaK molten salt environment, *Npj Mater Degrad* 6 (2022) 1–10. <https://doi.org/10.1038/s41529-022-00300-x>.
31. X. Quintana, J. Quincey, S.A. Briggs, Environmentally-assisted cracking of electropolished 316L stainless steel in molten FLiNaK salt, *Journal of Nuclear Materials* 594 (2024) 155010. <https://doi.org/10.1016/j.jnucmat.2024.155010>.

32. Assessing Environmentally Assisted Cracking Of Structural Alloys In Molten Salts, AMPP Store (n.d.). <https://store.ampp.org/assessing-environmentally-assisted-cracking-of-structural-alloys-in-molten-salts> (accessed August 21, 2024).
33. S.H. Mills, R.D. Hayes, N. Bieberdorf, S.E. Zeltmann, A.M. Kennedy, L. Capolungo, M. Asta, R.O. Scarlet, A.M. Minor, Elucidating the role of Cr migration in Ni-Cr exposed to molten FLiNaK via multiscale characterization, *Acta Mater.* 279 (2024) 120206. <https://doi.org/10.1016/j.actamat.2024.120206>.
34. T. Ghaznavi, S.Y. Persaud, R.C. Newman, The Effect of Temperature on Dealloying Mechanisms in Molten Salt Corrosion, *J. Electrochem. Soc.* 169 (2022) 111506. <https://doi.org/10.1149/1945-7111/aca07e>.
35. T. Wada, P.-A. Geslin, D. Wei, H. Kato, Partial liquid metal dealloying to synthesize nickel-containing porous and composite ferrous and high-entropy alloys, *Commun Mater* 4 (2023) 43. <https://doi.org/10.1038/s43246-023-00374-3>.
36. I. McCue, A. Karma, J. Erlebacher, Pattern formation during electrochemical and liquid metal dealloying, *MRS Bull.* 43 (2018) 27–34. <https://doi.org/10.1557/mrs.2017.301>.
37. L. Lesage, T. Suga, T. Wada, H. Kato, C. Le Bourlot, E. Maire, N. Mary, P.-A. Geslin, A diffusion model for liquid metal dealloying. Application to NiCu precursors dealloyed in liquid Ag, *Acta Materialia* 272 (2024) 119908. <https://doi.org/10.1016/j.actamat.2024.119908>.
38. W. Zhou, Y. Yang, G. Zheng, K.B. Woller, P.W. Stahle, A.M. Minor, M.P. Short, Proton irradiation-decelerated intergranular corrosion of Ni-Cr alloys in molten salt, *Nature Communications* 11 (2020) 3430. <https://doi.org/10.1038/s41467-020-17244-y>.
39. Y. Luo, G. Li, T. Lu, R. Wang, Analysis of thermal stress, fatigue life and allowable flux density for the molten salt receiver in solar power tower plants, *International Journal of Low-Carbon Technologies* 17 (2022) 1385–1398. <https://doi.org/10.1093/ijlct/ctac110>.
40. C.-M. Suh, G.-H. Song, M.-S. Suh, Y.-S. Pyoun, Fatigue and mechanical characteristics of nano-structured tool steel by ultrasonic cold forging technology, *Materials Science and Engineering: A* 443 (2007) 101–106. <https://doi.org/10.1016/j.msea.2006.08.066>.
41. S.-H. Nahm, H.-B. Shim, U.-B. Baek, C.-M. Suh, Very High Cycle Fatigue Behaviors and Surface Crack Growth Mechanism of Hydrogen-Embrittled AISI 304 Stainless Steels, *Materials Sciences and Applications* 9 (2018) 393–411. <https://doi.org/10.4236/msa.2018.94027>.
42. M. Milad, N. Zreiba, F. Elhalouani, C. Baradaï, The effect of cold work on structure and properties of AISI 304 stainless steel, *Journal of Materials Processing Technology* 203 (2008) 80–85. <https://doi.org/10.1016/j.jmatprotec.2007.09.080>.
43. M. Hong, S. Samuha, P. Hosemann, Corrosion mechanism of cold forged 316 stainless steel in molten FLiNaK salt, *Corrosion Science* 232 (2024) 111990. <https://doi.org/10.1016/j.corsci.2024.111990>.
44. M. Koukolikova, P. Slama, J. Dlouhy, J. Cerny, M. Marecek, Cold/Hot Deformation Induced Recrystallization of Nickel-Based Superalloys for Molten Salt Reactors, *Metals* 8 (2018) 477. <https://doi.org/10.3390/met8070477>.
45. D.A. Petti, G.R. Smolik, M.F. Simpson, J.P. Sharpe, R.A. Anderl, S. Fukada, Y. Hatano, M. Hara, Y. Oya, T. Terai, D.-K. Sze, S. Tanaka, JUPITER-II molten salt Flibe research: An update on tritium, mobilization and redox chemistry experiments, *Fusion Engineering and Design* 81 (2006) 1439–1449. <https://doi.org/10.1016/j.fusengdes.2005.08.101>.
46. R. Madhavan, R.K. Ray, S. Suwas, Micro-mechanical aspects of texture evolution in nickel and nickel–cobalt alloys: role of stacking fault energy, *Philosophical Magazine* 96 (2016) 3177–3199. <https://doi.org/10.1080/14786435.2016.1229061>.
47. M. Yonemura, K. Inoue, Dislocation Substructure in the Cold-Rolled Ni-20 Mass Pct Cr Alloy Analyzed by X-ray Diffraction, Positron Annihilation Lifetime, and Transmission Electron Microscopy, *Metall Mater Trans A* 47 (2016) 6384–6393. <https://doi.org/10.1007/s11661-016-3717-y>.
48. I. Yamaguchi, M. Yonemura, Recovery and Recrystallization Behaviors of Ni-30 Mass Pct Fe Alloy During Uniaxial Cold and Hot Compression, *Metall Mater Trans A* 52 (2021) 3517–3529. <https://doi.org/10.1007/s11661-021-06323-4>.

49. N.R. Dudova, R.O. Kaibyshev, V.A. Valitov, Short-range ordering and the abnormal mechanical properties of a Ni-20% Cr alloy, *Phys. Metals Metallogr.* 108 (2009) 625–633. <https://doi.org/10.1134/S0031918X0912014X>.
50. F. Meng, Z. Lu, T. Shoji, J. Wang, E. Han, W. Ke, Stress corrosion cracking of uni-directionally cold worked 316NG stainless steel in simulated PWR primary water with various dissolved hydrogen concentrations, *Corrosion Science* 53 (2011) 2558–2565. <https://doi.org/10.1016/j.corsci.2011.04.013>.
51. A. Sáez-Maderuelo, D. Gómez-Briceño, Stress corrosion cracking behavior of annealed and cold worked 316L stainless steel in supercritical water, *Nuclear Engineering and Design* 307 (2016) 30–38. <https://doi.org/10.1016/j.nucengdes.2016.06.022>.
52. K. Chen, J. Wang, Z. Shen, D. Du, X. Guo, B. Gong, J. Liu, L. Zhang, Comparison of the stress corrosion cracking growth behavior of cold worked Alloy 690 in subcritical and supercritical water, *Journal of Nuclear Materials* 520 (2019) 235–244. <https://doi.org/10.1016/j.jnucmat.2019.04.017>.
53. K. Chen, D. Du, W. Gao, X. Guo, L. Zhang, P.L. Andresen, Effect of cold work on the stress corrosion cracking behavior of Alloy 690 in supercritical water environment, *Journal of Nuclear Materials* 498 (2018) 117–128. <https://doi.org/10.1016/j.jnucmat.2017.10.003>.
54. K. Sourabh, J.B. Singh, Creep behaviour of alloy 690 in the temperature range 800–1000 °C, *Journal of Materials Research and Technology* 17 (2022) 1553–1569. <https://doi.org/10.1016/j.jmrt.2022.01.060>.
55. M. Sarvghad, T. Chenu, G. Will, Comparative interaction of cold-worked versus annealed inconel 601 with molten carbonate salt at 450 °C, *Corrosion Science* 116 (2017) 88–97. <https://doi.org/10.1016/j.corsci.2017.01.004>.
56. M. Maric, O. Muránsky, I. Karatchevtseva, T. Ungár, J. Hester, A. Studer, N. Scales, G. Ribárik, S. Primig, M.R. Hill, The effect of cold-rolling on the microstructure and corrosion behaviour of 316L alloy in FLiNaK molten salt, *Corrosion Science* 142 (2018) 133–144. <https://doi.org/10.1016/j.corsci.2018.07.006>.
57. H.L. Chan, E. Romanovskaia, S.H. Mills, M. Hong, V. Romanovski, N. Bieberdorf, C. Peddeti, A.M. Minor, P. Hosemann, M. Asta, J.R. Scully, Morphological Evolution and Dealloying During Corrosion of Ni20Cr in Molten FLiNaK Salt, *J. Electrochem. Soc.* (2024). <https://doi.org/10.1149/1945-7111/ad6037>.
58. H.L. Chan, E. Romanovskaia, V. Romanovski, D. Sur, M. Hong, P. Hosemann, J.R. Scully, Corrosion Electrochemistry of Chromium in Molten FLiNaK Salt at 600 °C, *J. Electrochem. Soc.* 170 (2023) 081502. <https://doi.org/10.1149/1945-7111/ace8c0>.
59. J. Kerr, N. Bieberdorf, L. Capolungo, M. Asta, Morphology selection in dealloying: A phase field study of the coupling among kinetic mechanisms, *Phys. Rev. Mater.* 8 (2024) 103802. <https://doi.org/10.1103/PhysRevMaterials.8.103802>.
60. E. Romanovskaia, H.L. Chan, V. Romanovski, F. Garfias, M. Hong, S. Mastromarino, P. Hosemann, R. Scarlet, J.R. Scully, An In Situ, multi-electrode electrochemical method to assess the open circuit potential corrosion of Cr in unpurified molten FLiNaK, *Corrosion Science* 222 (2023) 111389. <https://doi.org/10.1016/j.corsci.2023.111389>.
61. P. Gay, P.B. Hirsch, A. Kelly, The estimation of dislocation densities in metals from X-ray data, *Acta Metallurgica* 1 (1953) 315–319. [https://doi.org/10.1016/0001-6160\(53\)90106-0](https://doi.org/10.1016/0001-6160(53)90106-0).
62. J.J. Sidor, P. Chakravarty, J.G. Bátorfi, P. Nagy, Q. Xie, J. Gubicza, Assessment of Dislocation Density by Various Techniques in Cold Rolled 1050 Aluminum Alloy, *Metals* 11 (2021) 1571. <https://doi.org/10.3390/met11101571>.
63. S. Shukla, A.P. Patil, V. Tandon, The effect of cold work by rolling on electrochemical behaviour of Cr-Mn austenitic stainless steel in chloride environment, *Mater. Res. Express* 5 (2018) 066535. <https://doi.org/10.1088/2053-1591/aac974>.
64. AZtecCrystal Processing Software, Oxford Instruments (n.d.). <https://www.ebsd.com/ois-ebsd-system/azteccrystal-processing-software> (accessed August 3, 2024).
65. Section 3: Metals Test Methods and Analytical Procedures, (n.d.). <https://www.astm.org/astm-bos-3.html> (accessed August 3, 2024).
66. W.-C. Chen, F.-Y. Teng, C.-C. Hung, Characterization of Ni–Cr alloys using different casting techniques and molds, *Mater. Sci. Eng. C* 36 (2014) 1–9. <https://doi.org/10.1016/j.msec.2013.11.014>.

67. R. Pillai, D. Sulejmanovic, T. Lowe, S.S. Raiman, B.A. Pint, Establishing a Design Strategy for Corrosion Resistant Structural Materials in Molten Salt Technologies, *JOM* 75 (2023) 994–1005. <https://doi.org/10.1007/s11837-022-05647-9>.
68. R. Pillai, S.S. Raiman, B.A. Pint, First steps toward predicting corrosion behavior of structural materials in molten salts, *Journal of Nuclear Materials* 546 (2021) 152755. <https://doi.org/10.1016/j.jnucmat.2020.152755>.
69. H. Larsson, H. Strandlund, M. Hillert, Unified treatment of Kirkendall shift and migration of phase interfaces, *Acta Materialia* 54 (2006) 945–951. <https://doi.org/10.1016/j.actamat.2005.10.022>.
70. H. Larsson, A. Engström, A homogenization approach to diffusion simulations applied to $\alpha+\gamma$ Fe–Cr–Ni diffusion couples, *Acta Materialia* 54 (2006) 2431–2439. <https://doi.org/10.1016/j.actamat.2006.01.020>.
71. S. Glasstone, K.J. Laidler, H. Eyring, *The theory of rate processes: the kinetics of chemical reactions, viscosity, diffusion and electrochemical phenomena*, McGraw-Hill, New York, 1941.
72. D.N. Dupin, Database Revision History, (n.d.).
73. X. Zhou, J.R. Mianroodi, A. Kwiatkowski da Silva, T. Koenig, G.B. Thompson, P. Shanthraj, D. Ponge, B. Gault, B. Svendsen, D. Raabe, The hidden structure dependence of the chemical life of dislocations, *Science Advances* 7 (2021) eabf0563. <https://doi.org/10.1126/sciadv.abf0563>.
74. Y. Chen, C.A. Schuh, Geometric considerations for diffusion in polycrystalline solids, *Journal of Applied Physics* 101 (2007) 063524. <https://doi.org/10.1063/1.2711820>.
75. M.B. Isichenko, Percolation, statistical topography, and transport in random media, *Rev. Mod. Phys.* 64 (1992) 961–1043. <https://doi.org/10.1103/RevModPhys.64.961>.
76. J. Ding, D. Neffati, Q. Li, R. Su, J. Li, S. Xue, Z. Shang, Y. Zhang, H. Wang, Y. Kulkarni, X. Zhang, Thick grain boundary induced strengthening in nanocrystalline Ni alloy, *Nanoscale* 11 (2019) 23449–23458. <https://doi.org/10.1039/C9NR06843K>.
77. T. Gheno, F. Jomard, C. Desgranges, L. Martinelli, Grain boundary diffusion of chromium in polycrystalline nickel studied by SIMS, *Materialia* 6 (2019) 100283. <https://doi.org/10.1016/j.mtla.2019.100283>.
78. T.-F. Chen, G. Tiwari, Y. Iijima, K. Yamachi, Volume and Grain Boundary Diffusion of Chromium in Ni-Base Ni-Cr-Fe Alloys, *Mater. Trans.* 44 (2003) 40–46. <https://doi.org/10.2320/matertrans.44.40>.
79. S.P. Murarka, M.S. Anand, R.P. Agarwala, Diffusion of Chromium in Nickel, *Journal of Applied Physics* 35 (1964) 1339–1341. <https://doi.org/10.1063/1.1713615>.
80. T. Gheno, F. Jomard, C. Desgranges, L. Martinelli, Tracer diffusion of Cr in Ni and Ni-22Cr studied by SIMS, *Materialia* 3 (2018) 145–152. <https://doi.org/10.1016/j.mtla.2018.08.004>.
81. Seltzer, M. S., and B. A. Wilcox. Diffusion of chromium and aluminum in Ni-20Cr and TDNiCr (Ni-20Cr-2ThO 2). *Metallurgical Transactions* 3 (1972): 2357-2362.
82. Ruoff, A. L., and R. W. Balluffi. Strain-enhanced diffusion in metals. II. Dislocation and grain-boundary short-circuiting models. *Journal of Applied Physics* 34.7 (1963): 1848-1853.
83. Legros, M., Dehm, G., Arzt, E., & Balk, T. J. Observation of giant diffusivity along dislocation cores. *Science*, 319 (2008) 1646-1649.
84. G.M. Poletaev, D.V. Novoselova, R.Y. Rakitin, A.S. Semenov, Modeling the formation of free volume at grain boundaries and triple junctions during nickel crystallization, *Lett. Mater.* 10 (2020) 299–302. <https://doi.org/10.22226/2410-3535-2020-3-299-302>.
85. P. Zięba, A. Pawłowski, W. Gust, The Role of Grain Boundary Diffusion in Discontinuous Reactions, *DDF* 194–199 (2001) 1759–1766. <https://doi.org/10.4028/www.scientific.net/DDF.194-199.1759>.
86. A.J. Bard, L.R. Faulkner, *Electrochemical methods: fundamentals and applications*, 2nd ed., Wiley, New York, 2001.
87. Y. Wang, J. Zhang, Electrochemical Properties of CrF₂ in FLiNaK Molten Salt and the New Analytical Methods for their Determination, *J. Electrochem. Soc.* 167 (2020) 086503. <https://doi.org/10.1149/1945-7111/ab8923>.
88. G102-89(2015)e1.pdf, (n.d.).
89. G. Antczak, G. Ehrlich, Jump processes in surface diffusion, *Surface Science Reports* 62 (2007) 39–61. <https://doi.org/10.1016/j.surfrep.2006.12.001>.
90. W.W. Mullins, R.F. Sekerka, Morphological Stability of a Particle Growing by Diffusion or Heat Flow, *Journal of Applied Physics* 34 (1963) 323–329. <https://doi.org/10.1063/1.1702607>.

91. W.W. Mullins, R.F. Sekerka, Stability of a Planar Interface During Solidification of a Dilute Binary Alloy, *Journal of Applied Physics* 35 (1964) 444–451. <https://doi.org/10.1063/1.1713333>.
92. C. Herring, Some Theorems on the Free Energies of Crystal Surfaces, *Phys. Rev.* 82 (1951) 87–93. <https://doi.org/10.1103/PhysRev.82.87>.
93. J. Erlebacher, K. Sieradzki, Pattern formation during dealloying, *Scripta Materialia* 49 (2003) 991–996. [https://doi.org/10.1016/S1359-6462\(03\)00471-8](https://doi.org/10.1016/S1359-6462(03)00471-8).
94. J. Erlebacher, An Atomistic Description of Dealloying: Porosity Evolution, the Critical Potential, and Rate-Limiting Behavior, *J. Electrochem. Soc.* 151 (2004) C614. <https://doi.org/10.1149/1.1784820>.
95. J. Erlebacher, M.J. Aziz, A. Karma, N. Dimitrov, K. Sieradzki, Evolution of nanoporosity in dealloying, *Nature* 410 (2001) 450–453. <https://doi.org/10.1038/35068529>.
96. Corrosion Behavior of Binary Ni-Cr Alloys in Molten FLiNaK Salts at Different Electrochemical Potentials - IOPscience, (n.d.). <https://iopscience.iop.org/article/10.1149/MA2023-02121112mtgabs/meta> (accessed April 18, 2024).
97. T. Ghaznavi, S.Y. Persaud, R.C. Newman, Electrochemical Corrosion Studies in Molten Chloride Salts, *J. Electrochem. Soc.* 169 (2022) 061502. <https://doi.org/10.1149/1945-7111/ac735b>.
98. T. Ghaznavi, M.A. Bryk, S.Y. Persaud, R.C. Newman, Alloying effects in high temperature molten salt corrosion, *Corrosion Science* 197 (2022) 110003. <https://doi.org/10.1016/j.corsci.2021.110003>.
99. J.R. Scully, Polarization Resistance Method for Determination of Instantaneous Corrosion Rates, *CORROSION* 56 (2000) 199–218. <https://doi.org/10.5006/1.3280536>.
100. W.W. Mullins, Flattening of a Nearly Plane Solid Surface due to Capillarity, *Journal of Applied Physics* 30 (2004) 77–83. <https://doi.org/10.1063/1.1734979>.
101. S.A. Policastro, J.C. Carnahan, G. Zangari, H. Bart-Smith, E. Seker, M.R. Begley, M.L. Reed, P.F. Reynolds, R.G. Kelly, Surface Diffusion and Dissolution Kinetics in the Electrolyte–Metal Interface, *J. Electrochem. Soc.* 157 (2010) C328. <https://doi.org/10.1149/1.3478572>.
102. Y.K. Chen-Wiegart, S. Wang, Y.S. Chu, W. Liu, I. McNulty, P.W. Voorhees, D.C. Dunand, Structural evolution of nanoporous gold during thermal coarsening, *Acta Materialia* 60 (2012) 4972–4981. <https://doi.org/10.1016/j.actamat.2012.05.012>.
103. J. Erlebacher, Mechanism of Coarsening and Bubble Formation in High-Genus Nanoporous Metals, *Phys. Rev. Lett.* 106 (2011) 225504. <https://doi.org/10.1103/PhysRevLett.106.225504>.
104. R. Kelly, J. Scully, D. Shoesmith, R. Buchheit, *Electrochemical Techniques in Corrosion Science and Engineering*, CRC Press, 2002. <https://doi.org/10.1201/9780203909133>.
105. M. Garbrecht, B. Saha, J.L. Schroeder, L. Hultman, T.D. Sands, Dislocation-pipe diffusion in nitride superlattices observed in direct atomic resolution, *Sci Rep* 7 (2017) 46092. <https://doi.org/10.1038/srep46092>.
106. G.P. Purja Pun, Y. Mishin, A molecular dynamics study of self-diffusion in the core of a screw dislocation in Al, *Defect and Diffusion Forum* 266 (2007) 49–62. <https://doi.org/10.4028/www.scientific.net/DDF.266.49>.
107. G.P. Purja Pun, Y. Mishin, A molecular dynamics study of self-diffusion in the cores of screw and edge dislocations in aluminum, *Acta Materialia* 57 (2009) 5531–5542. <https://doi.org/10.1016/j.actamat.2009.07.048>.
108. J. Wang, M. Huang, Y. Zhu, S. Liang, Z. Li, Vacancy diffusion coupled discrete dislocation dynamic modeling of compression creep of micro-pillars at elevated temperature, *International Journal of Solids and Structures* 193–194 (2020) 375–392. <https://doi.org/10.1016/j.ijsolstr.2020.02.024>.
109. S. Soltani, N. Abdolrahim, P. Sepehrband, Mechanism of intrinsic diffusion in the core of screw dislocations in FCC metals – A molecular dynamics study, *Computational Materials Science* 144 (2018) 50–55. <https://doi.org/10.1016/j.commat.2017.11.048>.
110. N. Winner, H. Williams, R.O. Scarlat, M. Asta, Ab-initio simulation studies of chromium solvation in molten fluoride salts, *Journal of Molecular Liquids* 335 (2021) 116351. <https://doi.org/10.1016/j.molliq.2021.116351>.

Supplemental Tables, Chapter 6 Task 5

Table S1. Weighted fractional elemental composition (in ppm) of LiF, NaF, and KF salts according to supplier's certificates of analysis

Ag	Al	As	B	Ba	Bi	Ca	Cd	Co	Cr	W
0.029 2	0.058 4	0.087 6	0.146	0.146	0.146	0.292	0.292	0.292	0.292	4.3
Ni	Pb	Re	Sb	Si	Sn	Te	Ti	Tl	V	Zr
3.25	3.25	3.25	3.25	3.26	3.36	3.54	3.54	3.80	4.12	6.32
Cs	Cu	Fe	Ga	Ge	In	Mg	Sr	Mo	Mn	Zn
0.292	0.292	0.292	0.526	0.584	0.818	0.993	6.757	2.955	1.86	5.00

Table S2. The EEC fitting parameters for impedance spectra of 10%, 30% and 50% CW Ni20Cr alloy potentiostatically dealloyed in FLiNaK, 600 °C at +1.75 V_{K+/K} and +1.90 V_{K+/K}

Parameter (unit)	+1.75 V _{K+/K}			+1.90 V _{K+/K}		
	10% CW	30% CW	50% CW	10% CW	30% CW	50% CW
CPE ₁ , Q (S*s ^α /cm ²)	2.41×10 ⁻³ ±3.99×10 ⁻⁵	1.69×10 ⁻² ±1.12×10 ⁻³	2.51×10 ⁻³ ±3.94×10 ⁻⁴	1.53 ±6.51	2.11×10 ⁻² ±9.11×10 ⁻⁴	7.33×10 ⁻² ±1.95×10 ⁻²
CPE ₁ , α	0.676 ±0.00719	0.653 ±0.0089	0.901 ±0.146	0.572 ±0.14	0.673 ±0.0094	0.744 ±0.0141
R ₁ (Ω-cm ²)	449 ±8.19	27.6 ±7.63	5.09 ±6.73	1.61 ±29.2	16.1 ±2.07	8.96 ±4.58
CPE ₂ , Q (S*s ^α /cm ²)	6.06×10 ⁻⁴ ±1.40×10 ⁻⁴	7.04×10 ⁻² ±2.57×10 ⁻²	2.14×10 ⁻³ ±3.02×10 ⁻⁴	1.63×10 ⁻¹ ±2.70×10 ⁻²	1.38×10 ⁻¹ ±2.80×10 ⁻²	2.77×10 ⁻¹ ±1.84×10 ⁻¹
CPE ₂ , α	1 ±0.049	1 ±0.184	0.843 ±0.065	0.814 ±0.055	0.898 ±0.00944	0.945 ±0.364
R ₂ (Ω-cm ²)	8.572 ±1.26	31.7 ±15.7	42.5 ±7.71	20 ±5.04	30 ±6.73	17.38 ±21.82
Warburg Coeff., σ (Ωcm ² s ^{-1/2})	-	-	-	6.49×10 ⁻¹ ±1.60×10 ⁻¹	4.98×10 ⁻¹ ±2.58×10 ⁻¹	2.52×10 ⁻¹ ±7.41×10 ⁻²
R _s (Ω-cm ²)	0.735±0.019	1.076±0.013	0.736±0.012	1.00±0.199	0.952±0.011	1.13±0.0097
χ ²	1.91×10 ⁻²	1.33×10 ⁻³	3.44×10 ⁻³	5.21×10 ⁻⁴	2.64×10 ⁻³	6.55×10 ⁻⁴

Table S3. Ionic diffusivity (D_{Ox}) of corrosion products calculated from the Warburg diffusion coefficient from Table 4 using Eq. 12

E_{applied} (vs. K^+/K)	D_{ox} (cm^2/s)		
	10% CW	30% CW	50% CW
1.75	-	-	-
1.90	3.47×10^{-6}	5.90×10^{-6}	2.30×10^{-5}

Table S5. Results of digital image porosity analysis for Ni20Cr at varying % CW dealloyed in molten FLiNaK at 600 °C for 10 ks at the E_{applied} of 1.75 and 1.90 $V_{K^+/K}$. The porosity of post-test specimen surfaces was estimated using digital image processing techniques applied to the cross-sectional SEM micrographs. First, the region of interest (ROI), which was the porous, dealloyed surface, was manually isolated from the bulk substrate. Open-source image analysis software was then used to binarize the remaining alloy and voids within the ROI via a global thresholding algorithm. The porosity was calculated as the ratio of the void area to the total image area

E_{applied} ($V_{K^+/K}$)	% CW	% Porosity
1.75	0	42.3
1.75	10	29.9
1.75	30	15.6
1.75	50	33.5
1.90	0	27.9
1.90	10	23.0
1.90	30	24.7
1.90	50	46.6

Table S6. Ni adatoms surface diffusivities reported at 600 °C

Citation	Mobile species	Atom type	Plane species	Orientation	Media	Ds (cm ² /s)	Ref
G. Ayrault, et al. 1974	Ni	Adatom	Ni	(110) [110]	Vacuum	3.75×10^{-7}	S1
G. Ayrault, et al. 1974	Ni	Adatom	Ni	(110) [001]	Vacuum	2.56×10^{-9}	S1
Blakely and Mykura. 1961.	Ni	Adatom	Ni	~(111)	Vacuum	5.95×10^{-7}	S2
Blakely and Mykura. 1961.	Ni	Adatom	Ni	~(100)	Vacuum	3.63×10^{-10}	S2
Maiya and Blakely. 1967	Ni	Adatom	Ni	(100) [110]	Vacuum	3.19×10^{-9}	S3
Maiya and Blakely. 1967	Ni	Adatom	Ni	(110) [001]	Vacuum	1.17×10^{-9}	S4
Maiya and Blakely. 1967	Ni	Adatom	Ni	(110) [110]	Vacuum	5.18×10^{-10}	S4
Latta and Bonzel	Ni	Adatom	Ni	(110) [233]	Vacuum	1.66×10^{-7}	S5
Chan et al. 2024	Ni	N/A	Ni	Polycrystalline	Molten FLiNaK	8.02×10^{-10}	S6
Chan et al. 2024	Ni	N/A	Ni	Polycrystalline	Molten FLiNaK	9.93×10^{-8}	S6

[S1]. G. Ayrault, G. Ehrlich, Surface self-diffusion on an fcc crystal: An atomic view, The Journal of Chemical Physics 60 (1974) 281–294. <https://doi.org/10.1063/1.1680781>.

[S2]. J.M. Blakely, Surface physics of materials, Academic Press, New York, 1975.

[S3]. P.S. Maiya, J.M. Blakely, Surface Self-Diffusion and Surface Energy of Nickel, Journal of Applied Physics 38 (1967) 698–704. <https://doi.org/10.1063/1.1709399>.

[S4]. H.P. Bonzel, E.E. Latta, Surface self-diffusion on Ni(110): Temperature dependence and directional anisotropy, Surface Science. 76 (1978) 275–295. [https://doi.org/10.1016/0039-6028\(78\)90098-5](https://doi.org/10.1016/0039-6028(78)90098-5).

[S5]. E.E. Latta, H.P. Bonzel, Anisotropy of Surface Self-Diffusion on Ni(110), Phys. Rev. Lett. 38 (1977) 839–841. <https://doi.org/10.1103/PhysRevLett.38.839>.

[S6]. H.L. Chan, E. Romanovskaia, S.H. Mills, M. Hong, V. Romanovski, N. Bieberdorf, C. Peddeti, A.M. Minor, P. Hosemann, M. Asta, J.R. Scully, Morphological Evolution and Dealloying During Corrosion of Ni20Cr (wt.%) in Molten FLiNaK Salts, J. Electrochem. Soc. 171 (2024) 081501. <https://doi.org/10.1149/1945-7111/ad6037>.

Table S7. The calculated dislocation densities (ρ) in the as cold-rolled conditions and after potentiostatic dealloying

%CW	As cold rolled ρ (cm ⁻²)	After dealloying (1.75V _{K+K} for 10ks) ρ (cm ⁻²)	After dealloying (1.90V _{K+K} for 10ks) ρ (cm ⁻²)
10% CW	$4.54 \times 10^{11} \pm 2.75 \times 10^{11}$	$4.20 \times 10^{11} \pm 4.11 \times 10^{11}$	$4.69 \times 10^{11} \pm 2.19 \times 10^{11}$
30% CW	$4.95 \times 10^{11} \pm 2.57 \times 10^{11}$	$3.79 \times 10^{11} \pm 1.79 \times 10^{11}$	$3.39 \times 10^{11} \pm 2.22 \times 10^{11}$
50% CW	$7.49 \times 10^{11} \pm 5.98 \times 10^{11}$	$5.64 \times 10^{11} \pm 3.99 \times 10^{11}$	$3.66 \times 10^{11} \pm 1.47 \times 10^{11}$

Supplemental Figures, Chapter 6 Task 5

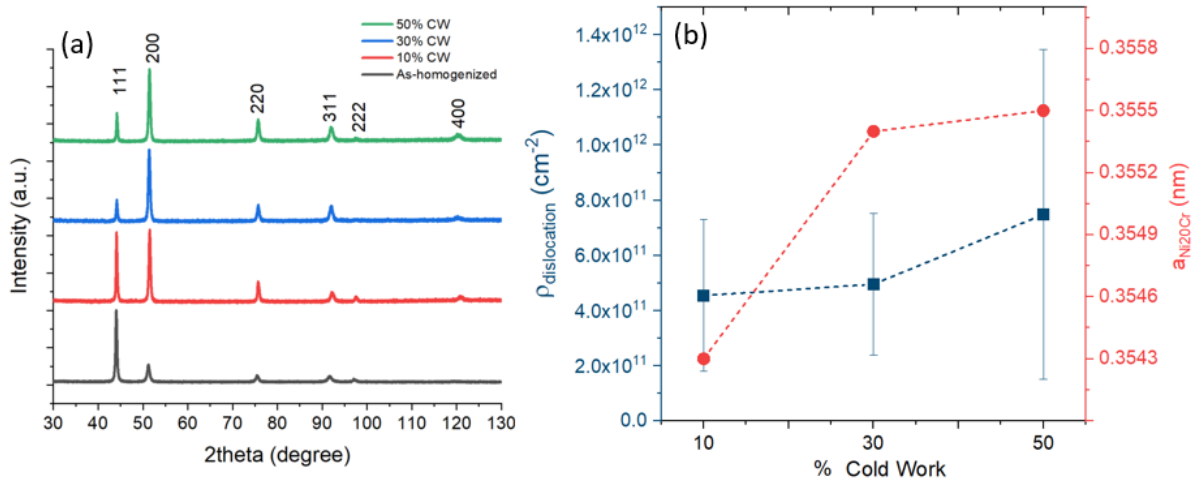


Figure S1. (a) displays the X-ray diffraction patterns for both the as-homogenized and the CW samples at 10%, 30%, and 50%. (b) shows the calculated dislocation density ($\rho_{\text{dislocation}}$) and lattice parameter ($a_{\text{Ni}_2\text{O}_3}$) at different cold work levels.

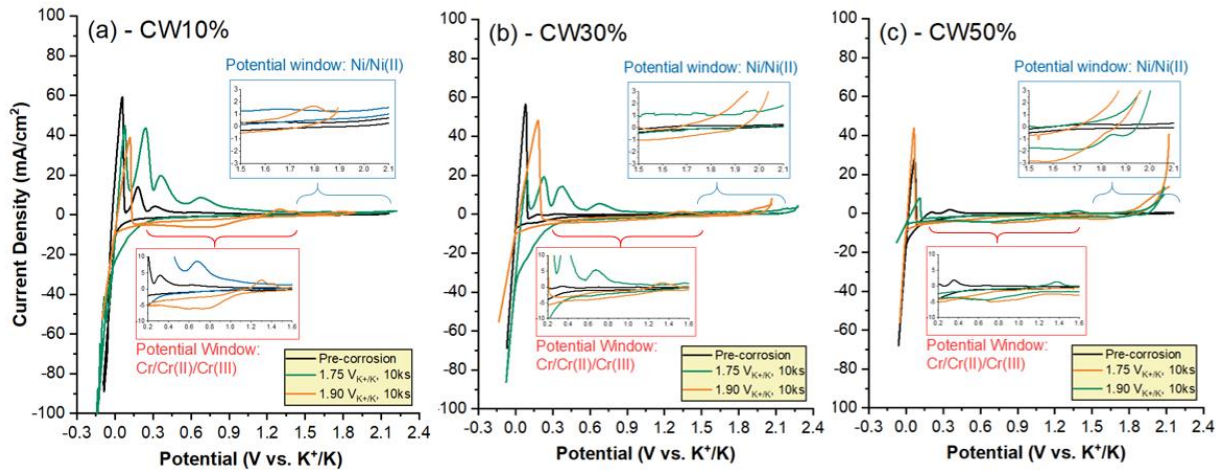


Figure S2. Cyclic voltammogram of a Pt wire measure at a scan rate of 100 mV/s in FLiNaK at 600 °C relative to the K^+/K potential. Scans were recorded prior to the dealloying of Ni_2O_3 (grey), and after potentiostatic hold +1.75 $\text{V}_{\text{K}^+/\text{K}}$ and (green) +1.90 $\text{V}_{\text{K}^+/\text{K}}$ for 10 ks (orange). The red and blue boarder insets show the potential window for $\text{Cr}/\text{Cr(II)}/\text{Cr(III)}$ and $\text{Ni}/\text{(II)}$ redox reactions, respectively. (a), (b), and (c) shows the results measured at 10%, 30%, and 50% CW, respectively

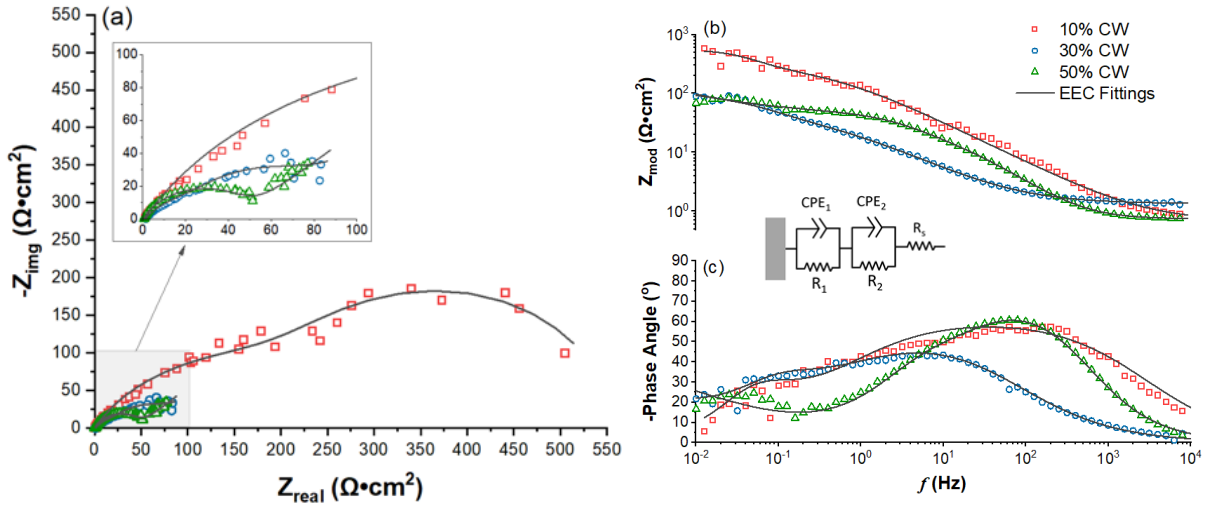


Figure S3. (a) and (b,c) display the Nyquist and Bode plots of Ni20Cr (wt.%) dealloyed at +1.75V_{K+/K} measured at the 10ks mark. The inset in (d) displays the electrical equivalent circuits (EECs) used for fitting analysis

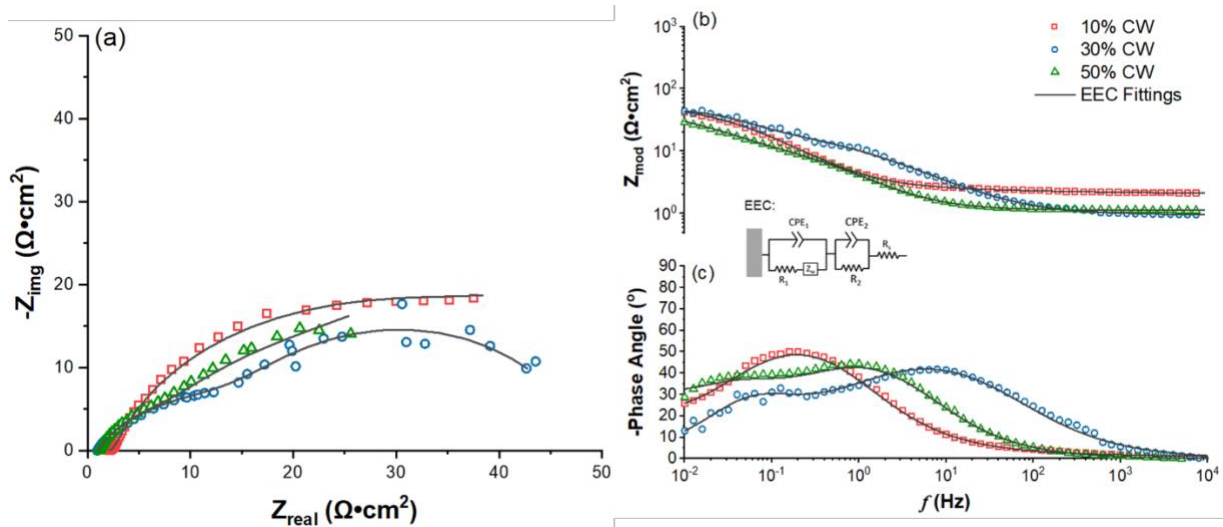


Figure S4. (a) and (b,c) display the Nyquist and Bode plots of Ni20Cr (wt.%) dealloyed at +1.90V_{K+/K} measured at the 10ks mark. The inset in (d) displays the electrical equivalent circuits (EECs) used for fitting analysis

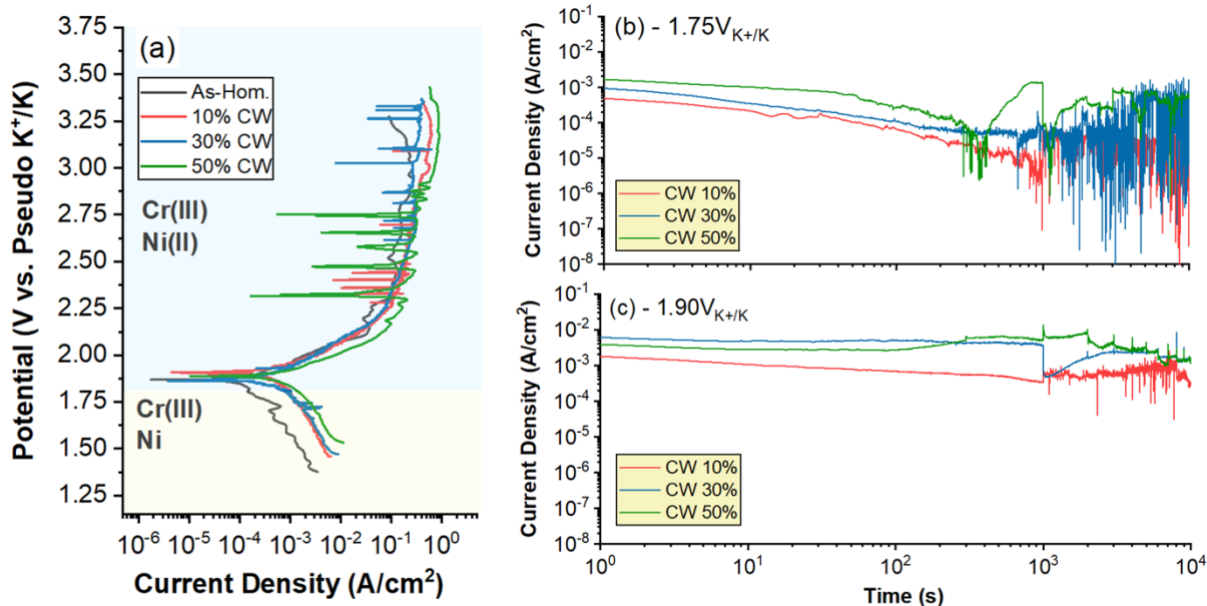


Figure S5. Electrochemical characterization of Ni20Cr in the as-homogenized and 10%, 30%, and 50% CW. (a) displays the linear sweep voltammogram (LSV) measured at a scan rate of 1 mV/s in molten FLiNaK, 600 °C. (b) and (c) display the current-time relationships of the CW samples potentiostatically held at +1.75 V_{K+/K} and +1.90 V_{K+/K} for 10 ks, respectively

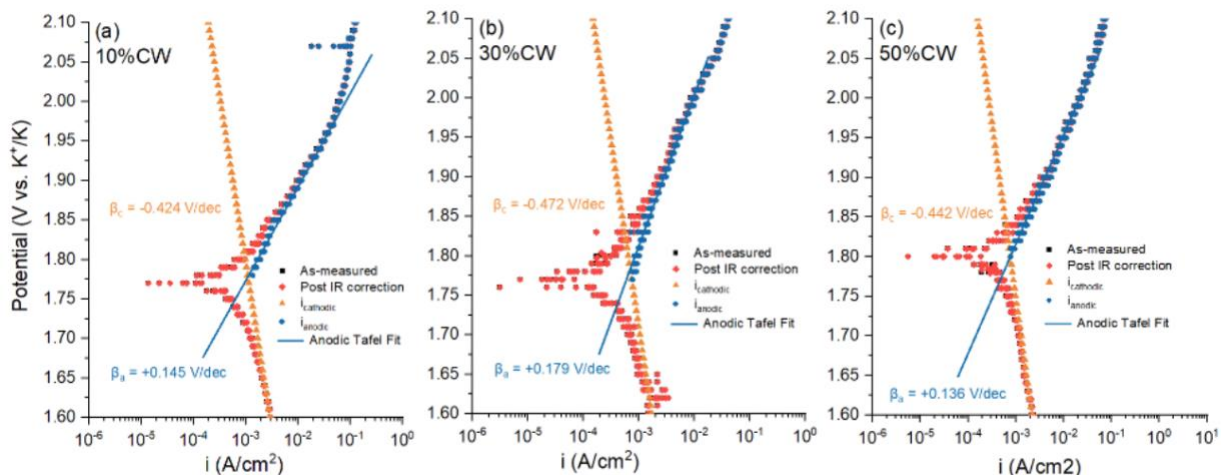


Figure S6. Analysis of LSV results shown in Fig. S3. As-measured LSV plots (black squares) are first IR-corrected (red rhombus). The cathodic Tafel regions are then fitted and plotted as *i*_{cathodic} (orange triangle). The anodic current density (*i*_{anodic}) is then calculated and fitted with a linear line representing the anodic Tafel region (solid blue lines).

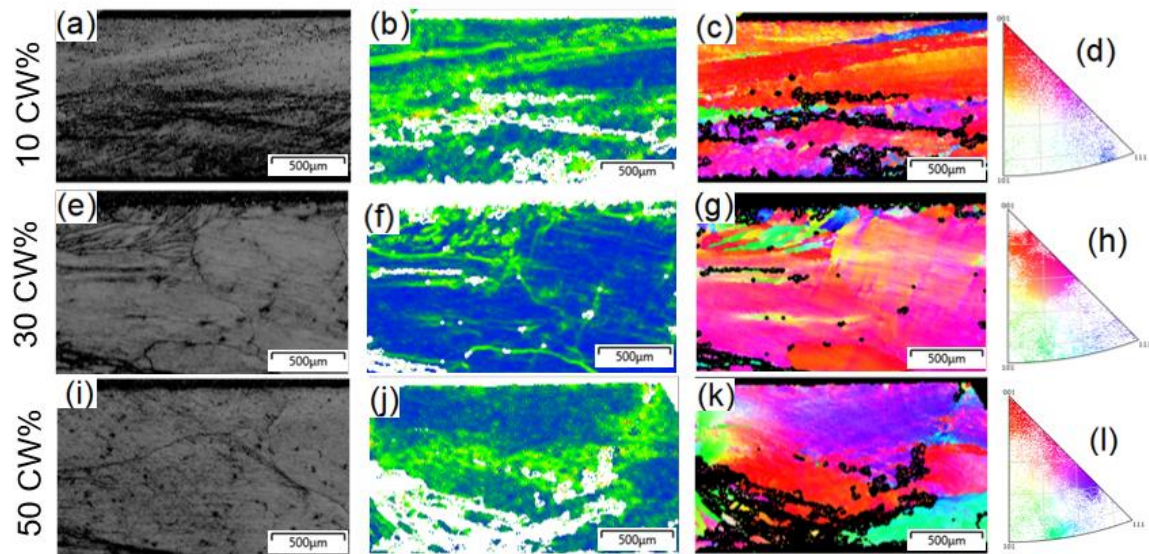


Figure S7. Microstructural characterization of Ni20Cr alloys, subjected to varying degrees of cold work. Panels (a), (b), (c), and (d) show the BSE images, maps of GNDs, IPF and its corresponding stereographic triangle and for the samples with 10% CW, respectively. Similarly, panels (e), (f), (g) as well as panels (i), (j), (k), (l) are organized in the same order for the 30% and 50% CW samples, respectively.

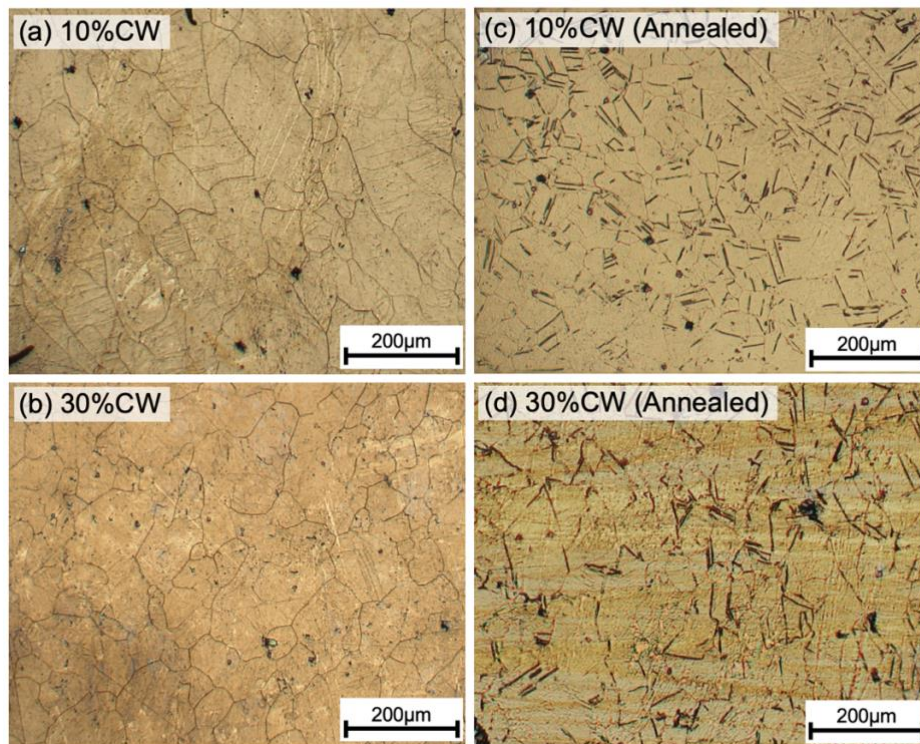


Figure S8. Optical micrographs of (a) 10% CW and (b) 30% CW Ni20Cr samples. The same samples subjected to electrolytic etching in 1M H₂SO₄ at +6 V for ~15 s as displayed in (c) and (d), respectively.

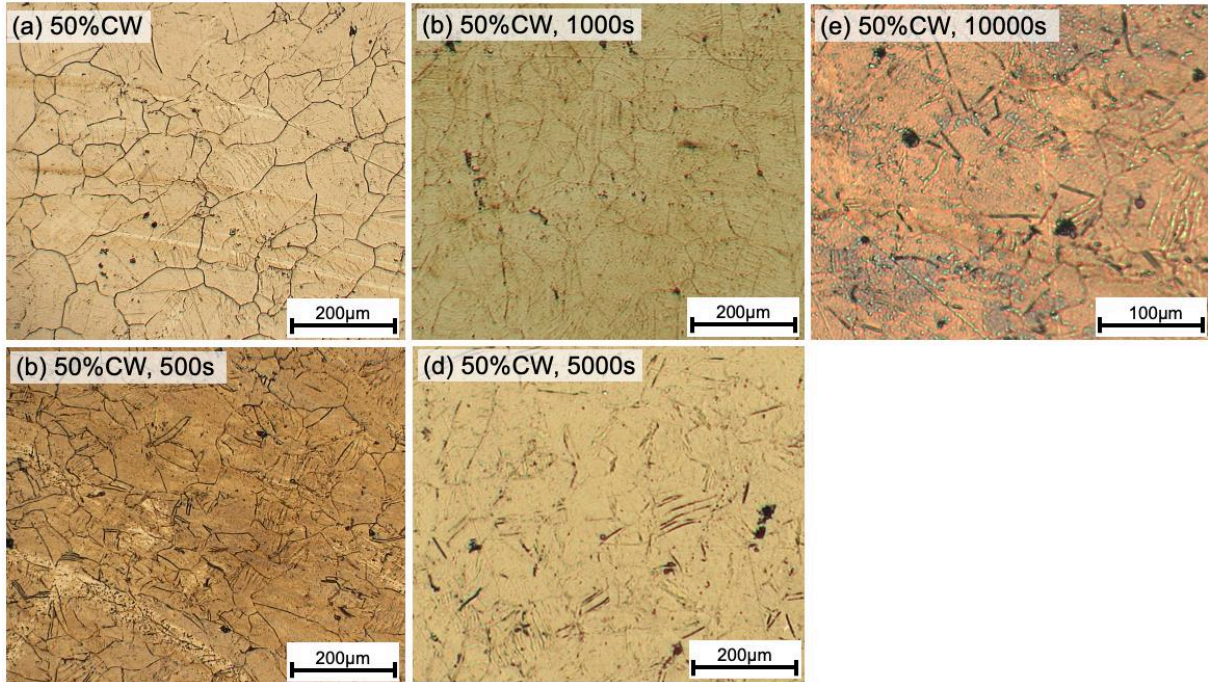


Figure S9. Optical micrographs of (a) 50% CW Ni20Cr sample. (b), (c), (d), and (e) show the electrolytically etched surface (1M H₂SO₄ at +6 V for ~15 s) of a 50% CW sample annealed in Ar gas at 600 °C for 0.5 ks, 1 ks, 5 ks, and 10 ks, respectively.

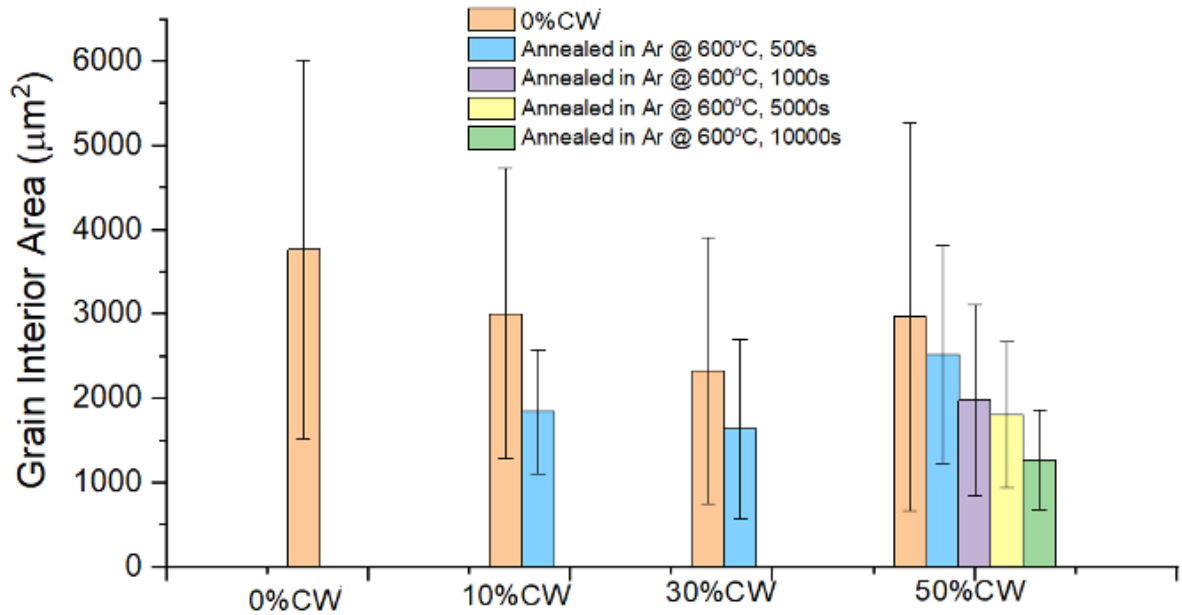


Figure S10. Bar chart comparing the average grain interior area of as-homogenized, 10%, 30%, and 50% CW samples annealed in Ar gas, 600 °C for various duration

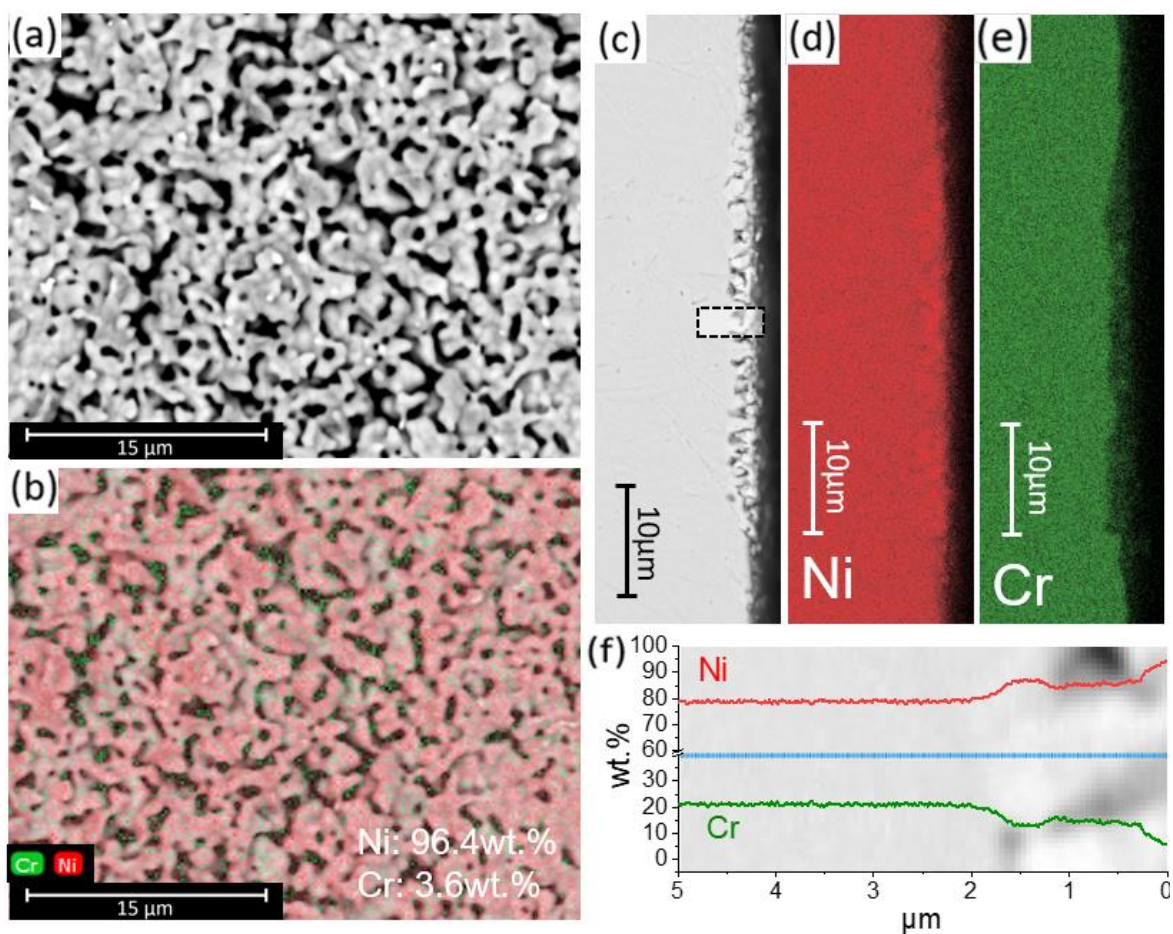


Figure S11. Morphological and compositional analysis of the as-homogenized Ni₂₀Cr alloy subjected to a potentiostatic hold at +1.75 V_{K+/K} for 10 ks: (a) reveals the dealloyed porous surface; (b) shows the corresponding elemental distribution highlighting the predominance of Ni (red) over Cr (green); (c) provides a cross-sectional view; while (d) and (e) present the Ni and Cr elemental maps, respectively. The white semi-transparent rectangle in (c) indicates the region subjected to EDS line scan, the results of which are depicted in (f). **Figures S12 through 19 share this caption format, with additional variations specified for each figure.**

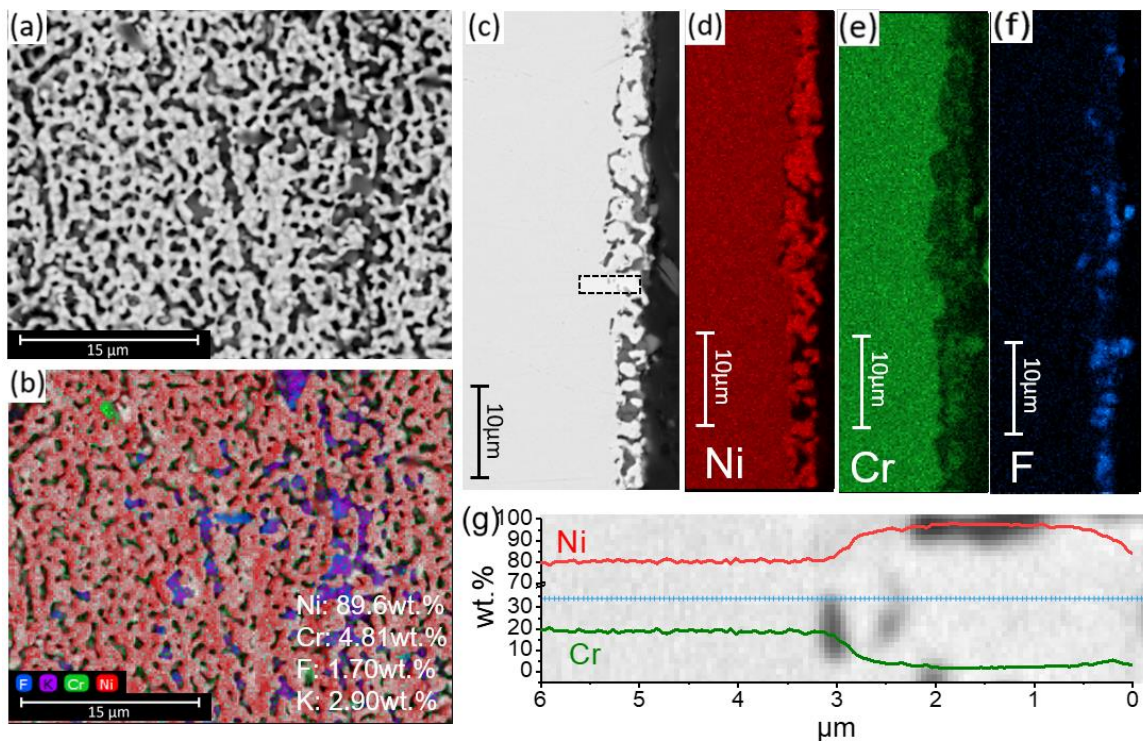


Figure S12. 10% CW Ni₂₀Cr alloy subjected to the potentiostatic hold at +1.75 V_{K+/K} for 10 ks in molten FLiNaK at 600 °C (See Figure 4 for full captions)

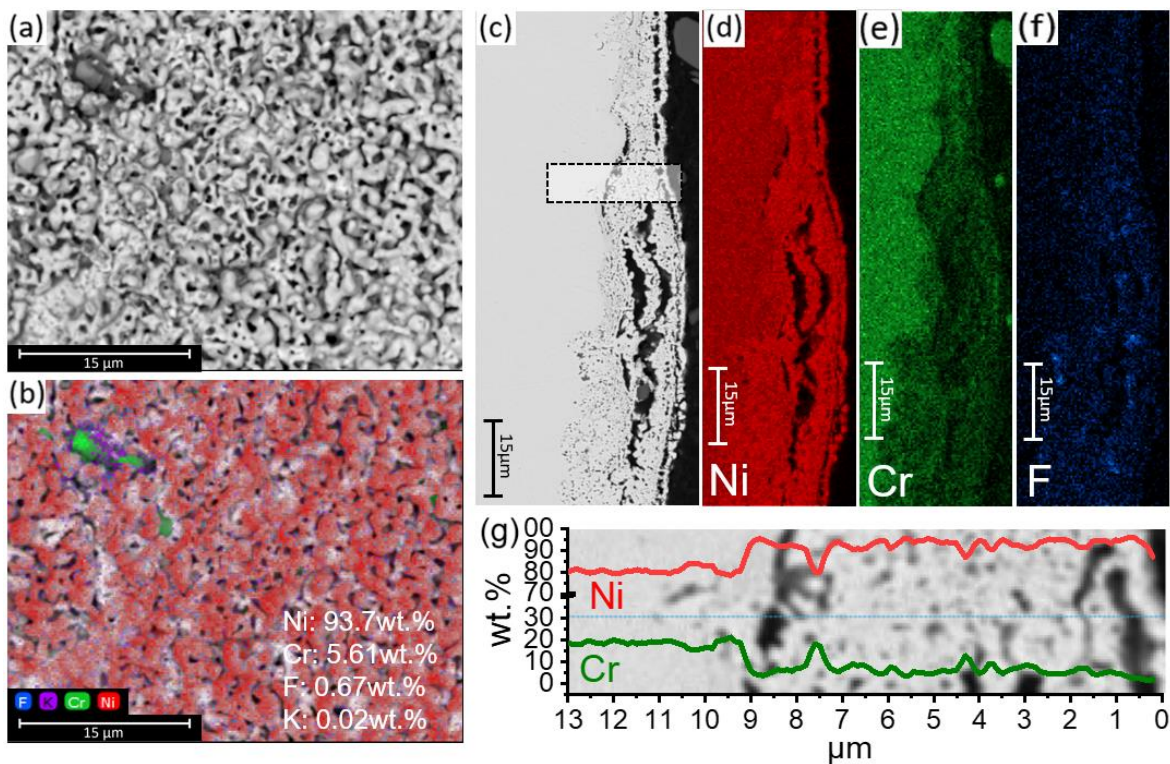


Figure S13. 30% CW Ni₂₀Cr alloy subjected to the potentiostatic hold at +1.75 V_{K+/K} for 10 ks in molten FLiNaK at 600 °C (See Figure 4 for full captions)

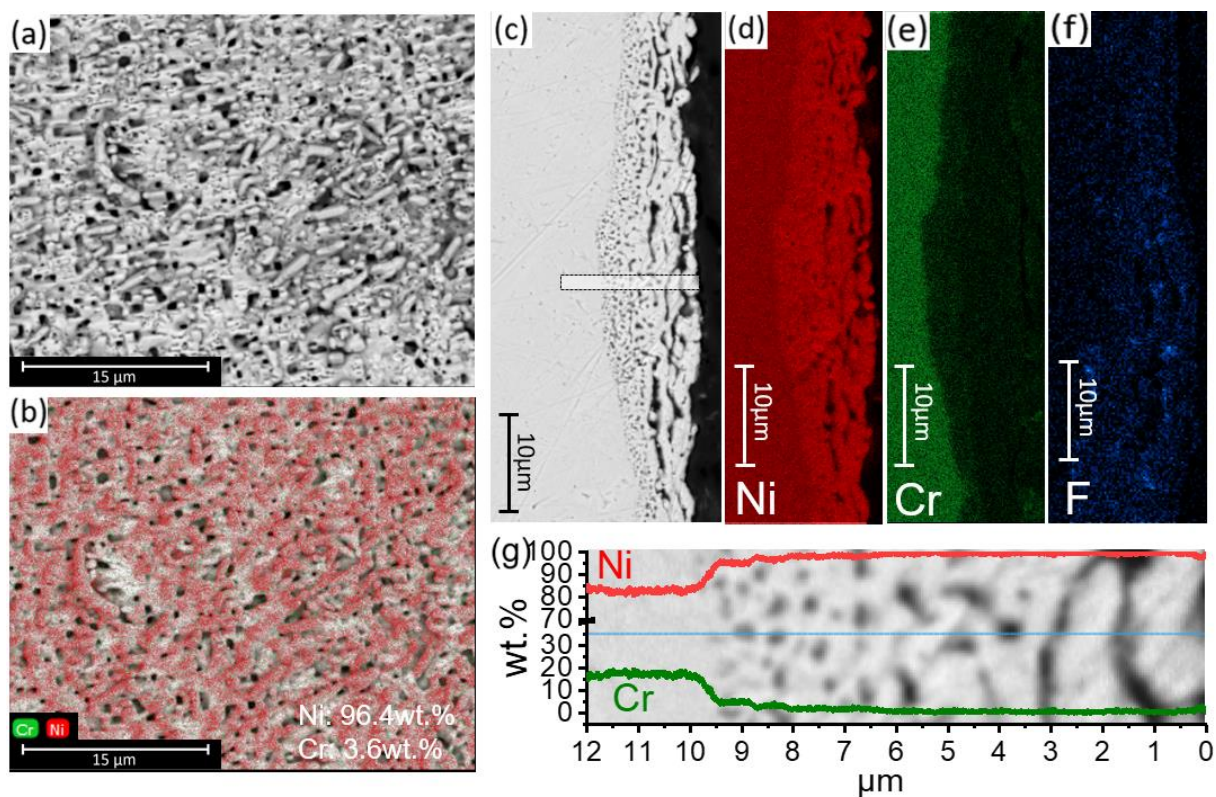


Figure S14. 50% CW Ni₂₀Cr alloy subjected to the potentiostatic hold at +1.90 V_{K+/K} for 10 ks in molten FLiNaK at 600 °C (See Figure 4 for full captions)

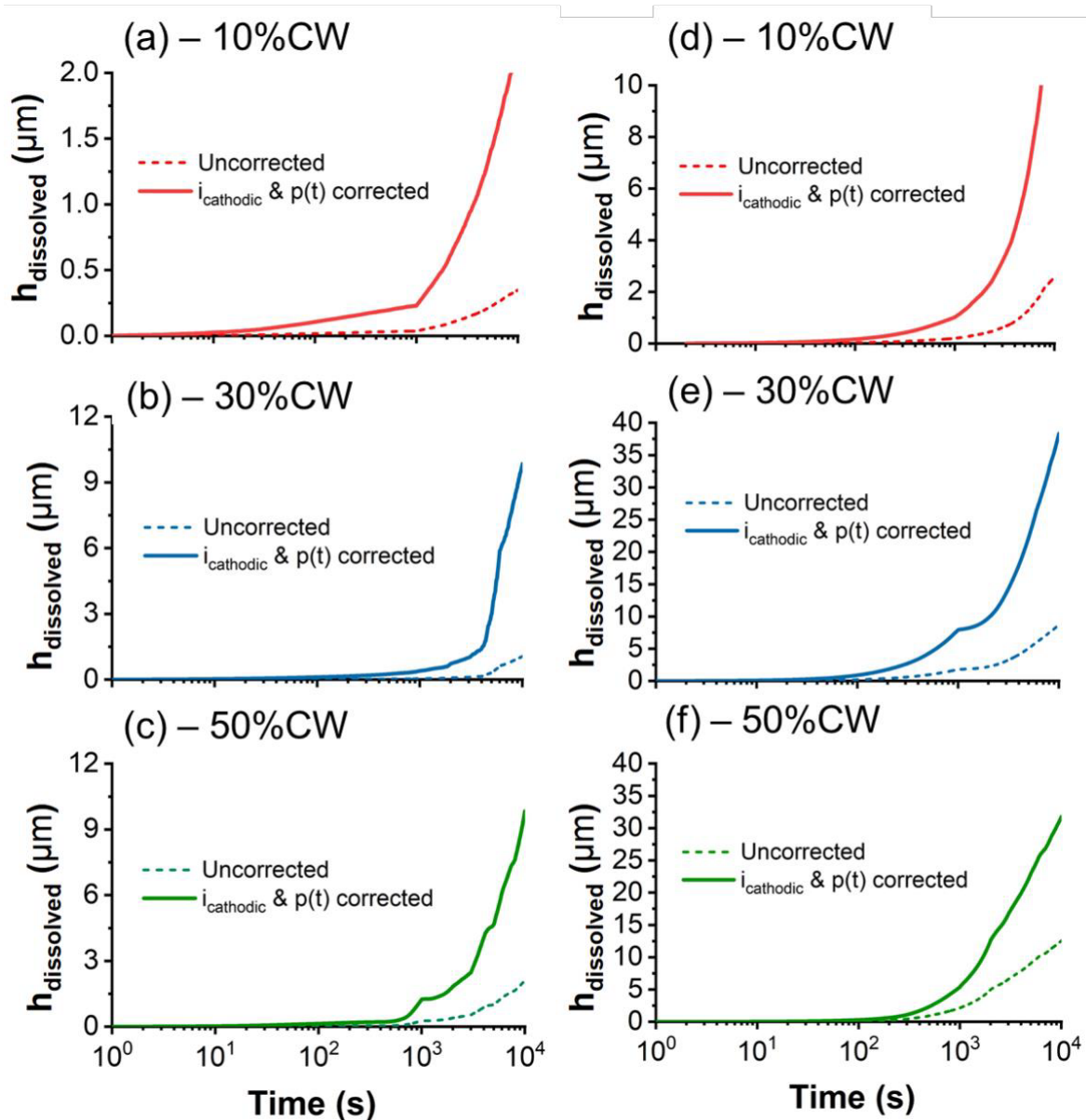


Figure S15. Calculated $h_{\text{dissolved}}$ during 10,000s of potentiostatic dealloying of Ni20Cr (wt.%) in molten FLiNaK, 600°C. (a), (b), and (c) correspond to the 10%CW, 30%CW, and 50%CW conditions under the E_{applied} of 1.75V_{K+/K}, respectively. (d), (e), and (f) follows the same order of annotation under the E_{applied} of 1.90V_{K+/K}. The dashed lines show the uncorrected, as-calculated $h_{\text{dissolved}}$ using Eq. 22, and the solid line shows the curved corrected with the porosity factor and cathodic current density (i_{cathodic}) contribution.

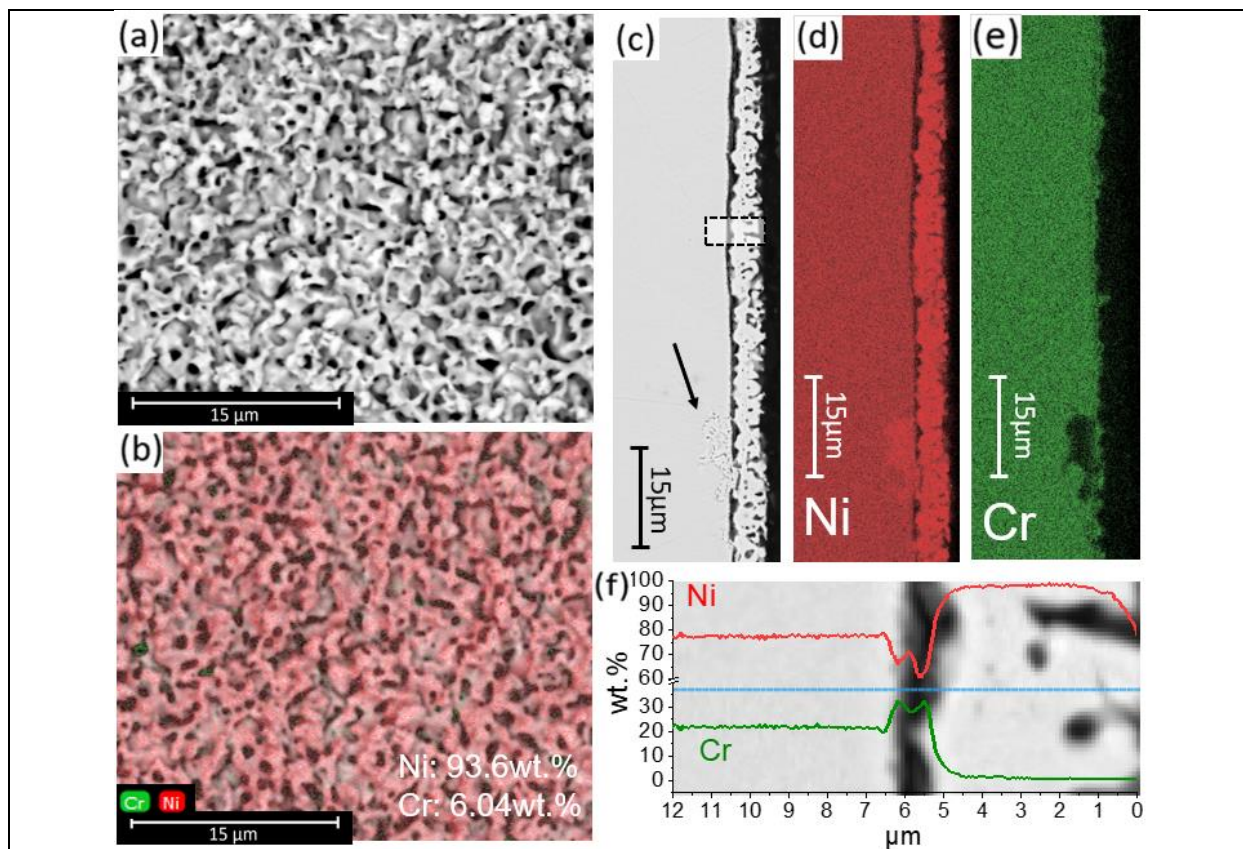


Figure S16. 0% CW Ni20Cr alloy subjected to the potentiostatic hold at +1.9 $V_{K+/K}$ for 10 ks in molten FLiNaK at 600 °C (See Figure 4 for full captions)

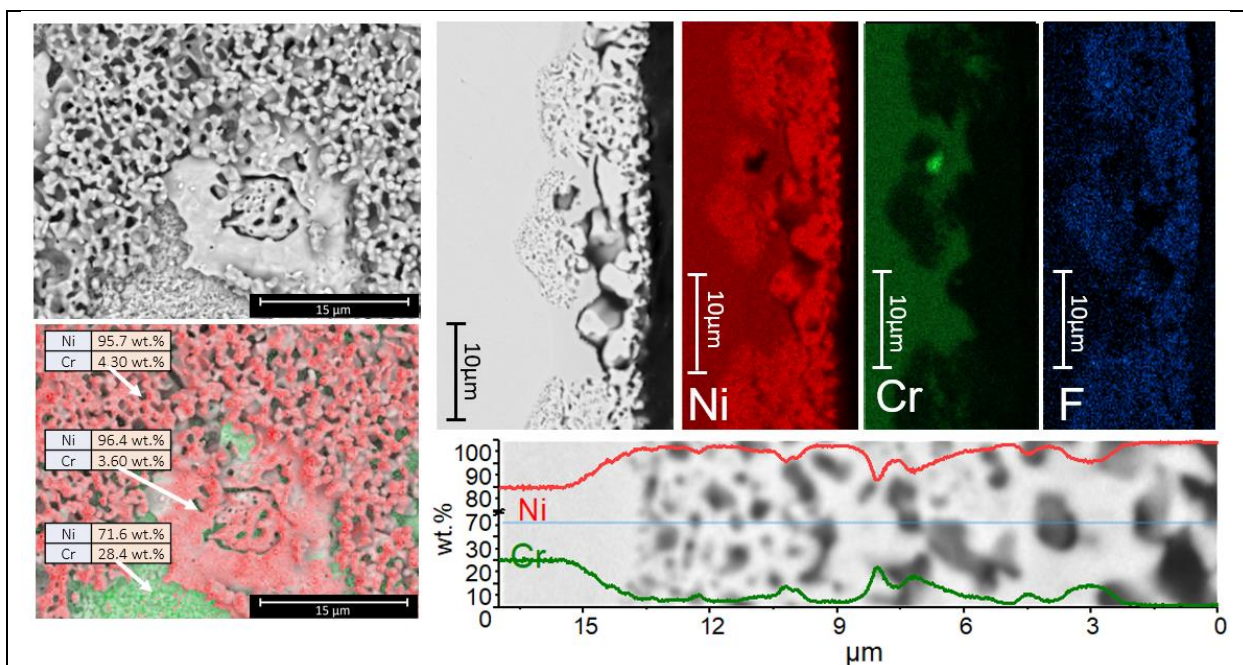


Figure S17. 10% CW Ni20Cr alloy subjected to the potentiostatic hold at +1.90 $V_{K+/K}$ for 10 ks in molten FLiNaK at 600 °C (See Figure 4 for full captions)

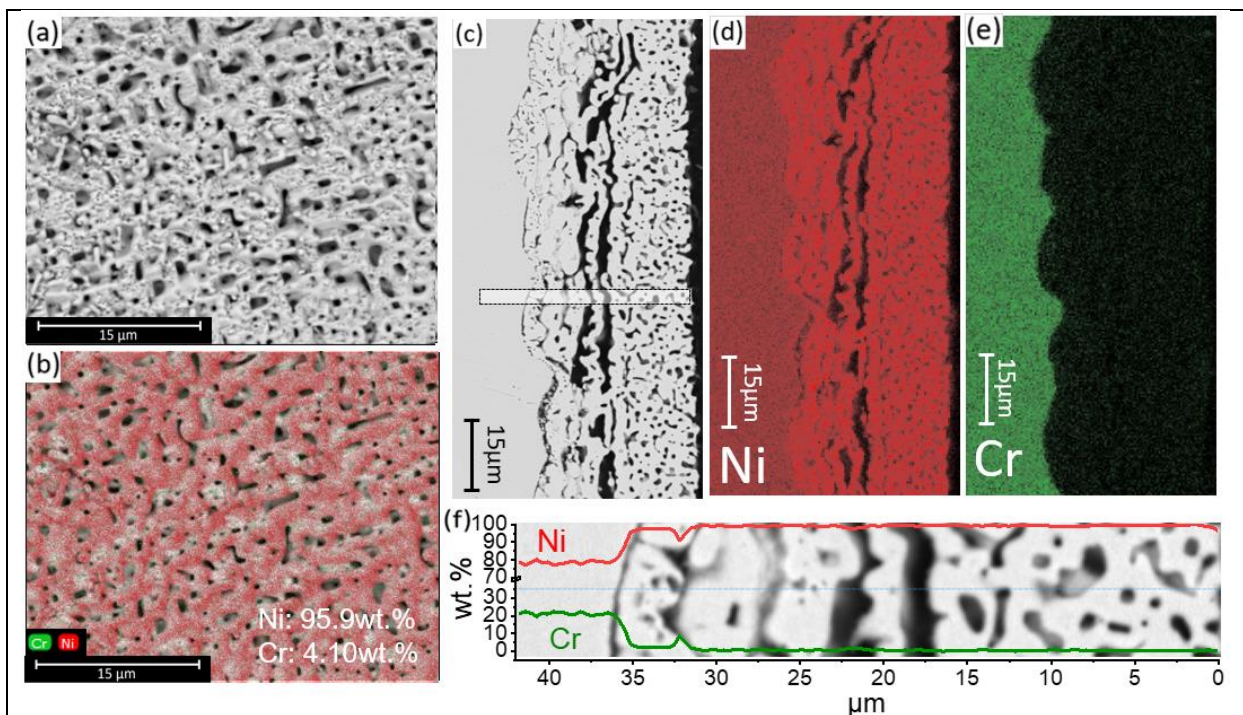


Figure S18. 30% CW Ni20Cr alloy subjected to the potentiostatic hold at +1.90 V_{K+/K} for 10 ks in molten FLiNaK at 600 °C (See Figure 4 for full captions)

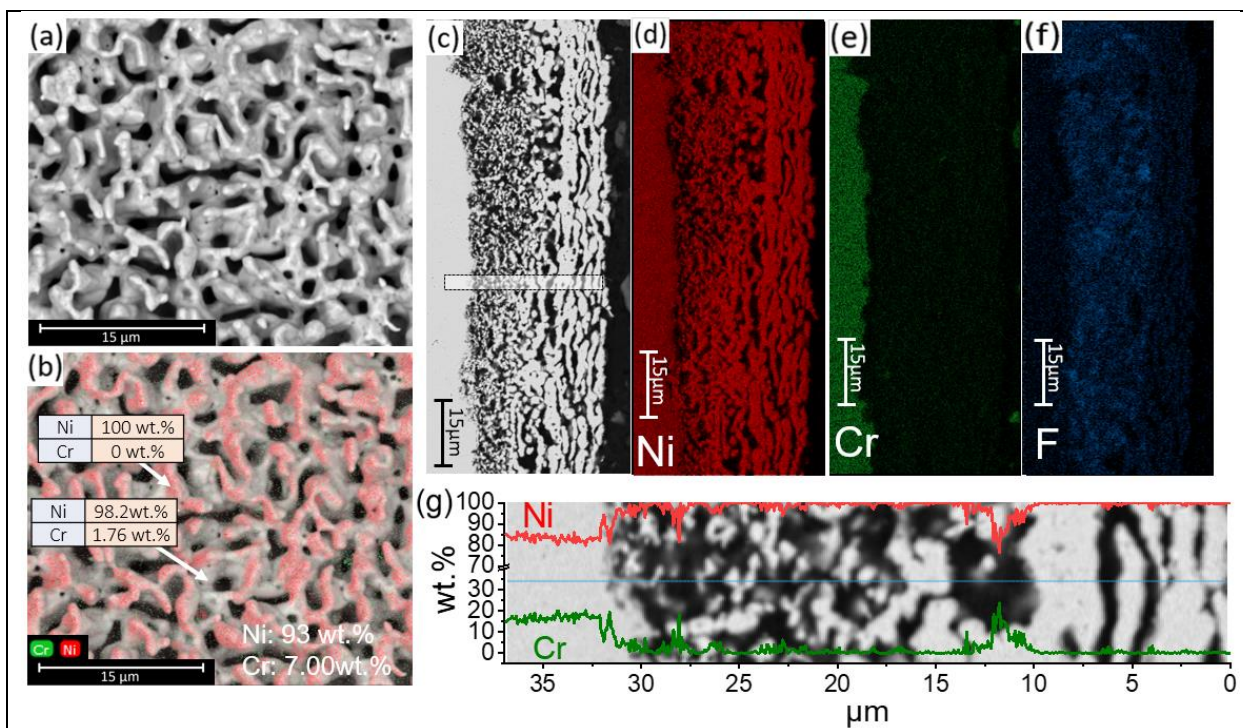


Figure S19. 50% CW Ni20Cr alloy subjected to the potentiostatic hold at +1.90 V_{K+/K} for 10 ks in molten FLiNaK at 600 °C (See Figure 4 for full captions)

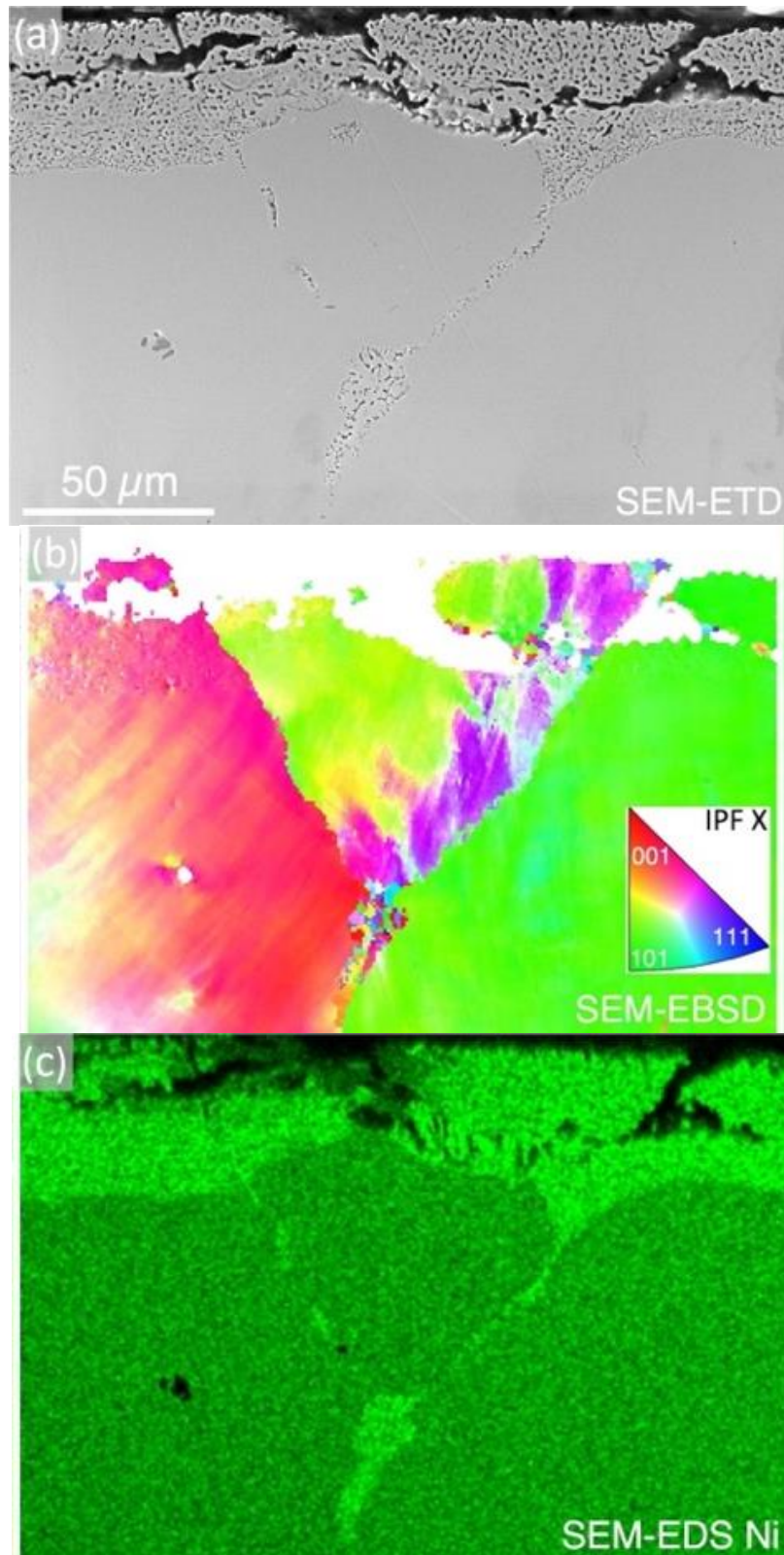


Figure S20. Cross-sectional SEM analysis of 30%CW Ni20Cr alloy dealloyed at $+1.90V_{K+/K}$ in molten FLiNaK at 600°C for 10ks. (a) show the BSE micrograph. (b) and (c) show the corresponding IPF and EDS analysis. Green in (c) indicates the relative fraction of Ni.

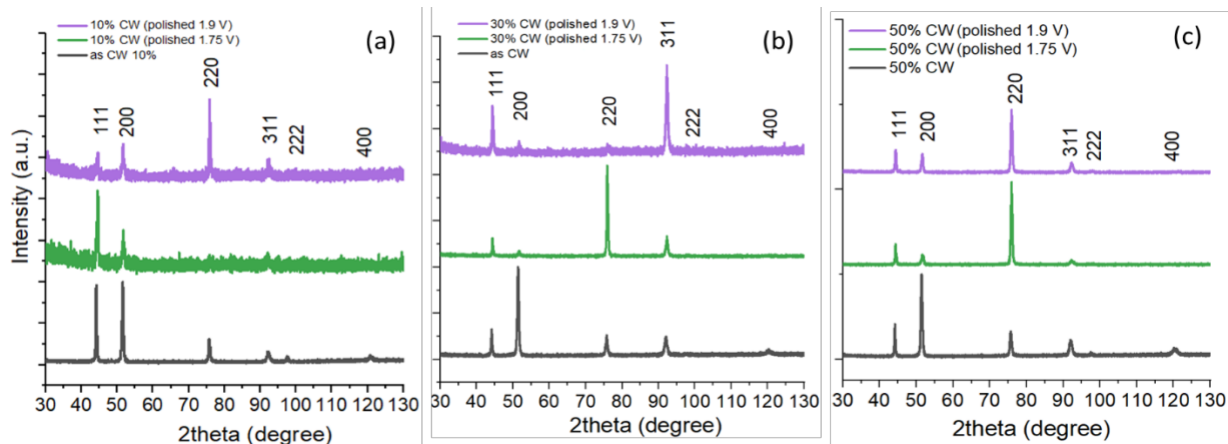


Figure S21. X-Ray diffractogram of Ni20Cr (wt.%) for the (a) 10% CW, (b) 30% CW, (c) 50% CW samples. In each curve, the dark grey line represents the as-cold rolled (“as CW”) conditions. After the dealloying experiments, one side of the sample was polished to 1200 grit surface finish to remove the surface dealloyed layer and residual salts, termed “polished”. The green and purple curves represent the “polished” conditions after potentiostatic dealloying at +1.75V_{K+/K} and +1.90V_{K+/K} in molten FLiNaK at 600°C for 10ks, respectively.

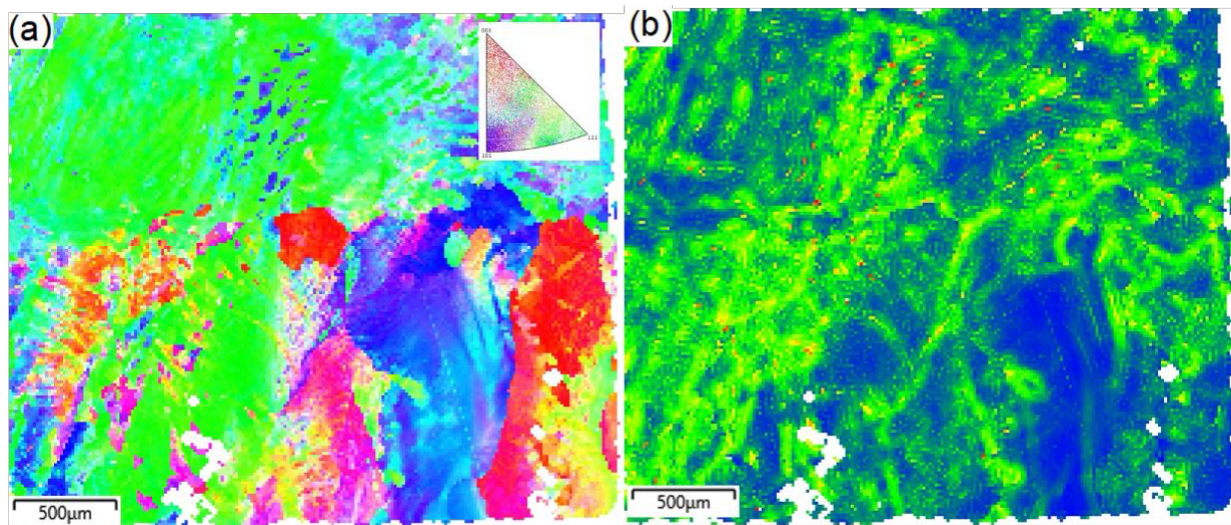


Figure S22. EBSD analysis on 10% CW Ni20Cr sample potentiostatically polarized in molten FLiNaK salts, 600 °C at +1.75 V_{K+/K} 10 ks. (a) shows the IPF and (b) shows the GND map.

Supplemental Section – Derivation of Surface Diffusion Rates

In general, the surface diffusion rates of Ni ($J_{\text{surf}}^{\text{Ni}}$) can be expressed as **Eq. S1** [S7]:

$$J_{\text{surf}}^{\text{Ni}} = -M\nabla \sum \mu_i \quad (\text{Eq. S1})$$

where M represents the mobility of the Ni species and the summation of all driving forces that contribute to Ni surface diffusion. In the case of **Eq. 21**, only the Gibbs-Thomson (GT) effect [S8] is considered. The driving force behind the GT effect, or $\Delta\mu_{\text{cap}}$, leads to the capillary diffusion of Ni (or $J_{\text{cap}}^{\text{Ni}}$), where Ni from a positive curvature, e.g. a bump, diffuses to a negative curvature region, or a pit. $\Delta\mu_{\text{cap}}$ can be expressed as **Eq. S2** [S9,S10]:

$$\Delta\mu_{\text{cap}} = \Delta\mu_o + \gamma\Omega K \quad (\text{Eq. S2})$$

Combining **Eq. S1** and **Eq. S2** yield **Eq. S3**:

$$J_{\text{cap}}^{\text{Ni}} = \frac{-\gamma\Omega D_{\text{surf}}^{\text{Ni}}}{k_B T} \nabla K \quad (\text{Eq. S3})$$

It is noted that $J_{\text{cap}}^{\text{Ni}}$ has a unit of mol/cm*s or atom/cm*s. Thus, to ensure the calculation of $J_{\text{surf}}^{\text{Ni}}$ comparable to other fluxes, a second order gradient must be applied:

$$J_{\text{surf}}^{\text{Ni}} = \nabla J_{\text{cap}}^{\text{Ni}} = \frac{-\gamma\Omega D_{\text{surf}}^{\text{Ni}}}{k_B T} \nabla^2 K = \frac{-\gamma\Omega D_{\text{surf}}^{\text{Ni}}}{k_B T} \frac{\partial^2 K}{\partial x^2} \quad (\text{Eq. S4})$$

Consequently, the geometric profile during dealloying needs to be known. To simplify Eq. S4, only one dimension (along x) is considered. The surface geometric profile during a GT-driven surface coarsening are derived by Mullins[S11] and well-summarized by Blakely [S7] in **Eq. S5**:

$$y(x, t) = A_o \sin(wx) e^{-Bw^4 t} \quad (\text{Eq. S5})$$

where w is the spatial wave length ($2\pi/\lambda$), A_o is the initial peak height when GT-driven coarsening is dominant. It is assumed to be 100nm based on experimental data[S12]. The wave length here, λ , is treated as identical to the ligament width $\lambda_{\text{ligament}}$. The definitions of B is shown in **Eq. S6** [1].

$$B = \frac{D_{\text{surf}}^{\text{Ni}} \gamma \Omega^2 N}{k_B T} \quad (\text{Eq. S6})$$

where N is the number of atoms per unit area on the surface, 10^{19} atoms/cm². A sensitivity analysis using the parameters defined in section 2.8 yields a $-Bw^4$ value between 10^{-4} and 10^{-10} cm⁴/s for a $\lambda_{\text{ligament}}$ between 10 nm and 1 μm . Therefore, the exponential term in **Eq. S5** is treated as 1. Additionally, the mathematical definition of a curvature is shown in **Eq. S7**:

$$K = \frac{y''(x, t)}{(1+y'(x, t))^2} \approx y''(x, t) \quad (\text{Eq. S7})$$

Here, it is assumed that $y'(x, t) \ll 1$, simplifying **Eq. S7**. Thus, $\frac{\partial^2 K}{\partial x^2}$ can be expressed as:

$$J_{\text{surf}}^{\text{Ni}} = \frac{-\gamma\Omega D_{\text{surf}}^{\text{Ni}}}{k_B T} y''''(x, t) \quad (\text{Eq. S8})$$

where $y''''(x, t)$ is the fourth partial derivative of Eq. S5 relative to x (Eq. S9):

$$y''''(x, t) = -A_o w^4 \sin(wx) \quad (\text{Eq. S9})$$

At maxima, $\sin(wx)=1$, leading to Eq. S10.

$$y''''(x, t) \approx -A_o w^4 = \frac{-16\pi^4 A_o}{\lambda_{lig.}^4(t)} \quad (\text{Eq. S10})$$

Combining Eq. S4 and Eq. S11 yield:

$$J_{surf}^{Ni} = \frac{\gamma \Omega D_{surf}^{Ni}}{k_B T} \frac{16\pi^4 A_o}{\lambda_{lig.}^4(t)} \quad (\text{Eq. S11})$$

Here the $\lambda_{lig.}(t)$ is measured from experimental plan view SEM measurement as a function of time (Fig. 9). Due to the complex nature of morphological evolution, it is expected that J_{surf}^{Ni} will vary significantly over a broad range of curvature and depth of dealloying. Therefore, an averaged J_{surf}^{Ni} , or \bar{J}_{surf}^{Ni} , over time period between 1s and 10ks is calculated:

$$\bar{J}_{surf}^{Ni} = \frac{16\pi^4 \lambda_o \gamma \Omega D_{surf}^{Ni}}{k_B T} \left(\frac{A_o}{\tau \int_0^t \lambda^4(t) dt} \right) \quad (\text{Eq. S12})$$

References:

- [S7] P.S. Maiya, J.M. Blakely, Surface Self-Diffusion and Surface Energy of Nickel, Journal of Applied Physics 38 (1967) 698–704. <https://doi.org/10.1063/1.1709399>.
- [S8] M. Perez, Gibbs-Thomson effects in phase transformations, Scripta Materialia 52 (2005) 709–712. <https://doi.org/10.1016/j.scriptamat.2004.12.026>.
- [S9] G. Henkelmann, D. Waldow, M. Liu, L. Lührs, Y. Li, J. Weissmüller, Self-Detachment and Subsurface Densification of Dealloyed Nanoporous Thin Films, Nano Lett. (2022).
- [S10] J. Erlebacher, An Atomistic Description of Dealloying, J. Electrochem. Soc. 151 (2004) C614. <https://doi.org/10.1149/1.1784820>.
- [S11] W.W. Mullins, R.F. Sekerka, Morphological Stability of a Particle Growing by Diffusion or Heat Flow, Journal of Applied Physics 34 (1963) 323–329. <https://doi.org/10.1063/1.1702607>.
- [S12] H.L. Chan, E. Romanovskaia, S.H. Mills, M. Hong, V. Romanovski, N. Bieberdorf, C. Peddeti, A.M. Minor, P. Hosemann, M. Asta, J.R. Scully, Morphological Evolution and Dealloying During Corrosion of Ni20Cr (wt.%) in Molten FLiNaK Salts, J. Electrochem. Soc. 171 (2024) 081501. <https://doi.org/10.1149/1945-7111/ad6037>.

Chapter 7: Conclusions and Future Work

Summary of findings

This thesis investigates the electrochemical thermodynamics and kinetics of molten salt corrosion using the model corrosion systems of Cr, Ni, and Ni-20Cr (wt.%) alloys in molten LiF-NaF-KF salts at 600°C. Result up to date provides critical mechanistic insights that strongly support the initial hypothesis – *there exists a window of corrosion susceptibility where metal or alloy exhibits different forms of morphological damage in molten fluorides*. This window varies with electrode potential and microstructure, as demonstrated in this work, and may also be influenced by factors not examined here, such as composition, temperature and impurity concentration. Throughout this investigation process, a suite of electrochemical techniques was applied, developed and/or optimized for molten salt corrosion studies, including:

- The development of E-log(a_{F^-}) diagrams for molten fluoride salts, akin to Pourbaix diagram in aqueous systems, displayed the effect of applied potential on thermodynamic phase stability of metallic cations, such as Ni(II) and Cr(III), and deciphered the spontaneity of metal and alloy corrosion in FLiNaK at 600°C in the presence of possible oxidizer candidates, e.g. Eu(III), Cr(III), HF (Task 1 & Appendix 1)
- Using linear sweep voltammetry coupled with potentiostatic hold and electrochemical thermodynamic analysis, the dissolution kinetics of Cr, Ni and Ni-20Cr (wt.%) in molten FLiNaK salts was elucidated. Specifically, the rate-regulating dissolution mechanism and corrosion morphological was correlated with electrode potential regimes, where charge-transfer-controlled behavior, mass-transport-controlled behavior (either in the solid bulk alloy phase or ionic phase), or a mixed regime may dominate. (Task 2 & Task 4). Additionally, the cases where “Tafel Extrapolation” is inappropriate to determine the corrosion current density was also studied (Task 2)
- The development, validation and mathematical corrections needed to implement an *in-situ* cyclic voltammetry (CV) method using a secondary blocking electrode (e.g. Pt) to determine instantaneous mass-loss of the corrodent (Task 3). Additionally, the effect of working electrode geometry was also studied and optimized such that electrochemical impedance spectroscopy (EIS) may be used to obtain accurate polarization resistance (R_p) value in molten salts (Appendix 2)

These techniques yielded multiple key fundamental insights into factors that underly the dissolution rate and morphological damages of metal and alloy systems in molten FLiNaK salts. For pure Cr in molten FLiNaK at 600°C, the possibilities were indicated that Cr(II) and Cr(III) cations may form metallic fluoride complexes in the form of CrF_3^- and CrF_6^{3-} , increasing the thermodynamic favorability for Cr oxidation. As shown in Task 1 and Appendix 1, the presence of a sufficient driving force, Cr may spontaneously dissolve to CrF_3^- via a +2 oxidation state, then to a +3 oxidation state solubilizing as a CrF_6^{3-} compound. The electrochemical potential windows of Cr(II) and Cr(III) phase stability were mapped in a E-log(a_{F^-}) potential activity diagram. This prediction was subsequently validated via X-Ray diffraction of residual salts and by corroborating the total charge transferred to total mass loss of Cr metal, which was subjected to potentiostatic holds in electrochemical potential ranges in which Cr(II) and Cr(III) were predicted to be

stable. Subsequently, in Task 2, the relationship between electrode potential and current density for pure Cr in FLiNaK was elucidated by coupling thermodynamic insights from Task 1 and Appendix 1. At low overpotential (~ 100 mV vs. E_{OC}), the oxidation of Cr to Cr(II) was favorable and controlled by charge-transfer as indicated by a linear E-log(i) relationship. At this electrode potential regime, the surface morphology of pure Cr was dominated by facets, implying an role of crystallographic orientation on electro-dissolution. At high overpotential (>200 mV vs. E_{OC}), current density was independent of applied potential coinciding in an electrochemical potential regime in which Cr(III) was favorable. Cr corrosion in this regime resulted in the formation of a stable, millimeter-scale K_3CrF_6 salt film due to surface saturation of Cr(III) on Cr, which possibly regulated the rate of Cr oxidation via a mass-transport-controlled mechanism. Further examinations reveal that the salt film possibly contained multiple constituents, such as K_2NaCrF_6 , $KCrF_3$, and Li_2NaCrF_6 . At high overpotentials, the Cr surface remained relatively smooth, further supporting the mass-transport-controlled nature of the process. Based on experimental results, Evans diagrams were also constructed to simulate the anodic dissolution behavior of Cr and cathodic reduction reactions of prominent salt impurities, including the reductions of HF to H_2 and Cr(III) to Cr(II). This analysis sheds light on possible conditions in which the conventional “Tafel extrapolation” method for the determination of Tafel slopes and other related electrochemical parameters may be inaccurate.

The electrochemical thermodynamic and kinetic foundations developed in Tasks 1 and 2 enable corrosion electrochemical techniques to be further developed. In Task 3, a dual-working electrodes method was designed and implemented, in which Cr (WE#1) was subjected to 50 hrs of open circuit corrosion in molten FLiNaK while a Pt wire blocking electrode (WE#2), in-situ and adjacent to the Cr WE#1, was programmed to perform successive CV measurements at an increment of 1 hour at scan rate between 50 and 1000 mV/s. The E_{OC} -t behavior was interpreted by identifying possible oxidizers and concentrations (e.g. HF) that may drive spontaneous Cr corrosion during this period. Meanwhile, CV results were analyzed via the Randles-Sevcik (soluble/insoluble) and Berzins-Delahay (soluble/soluble) relations, which enables the concentration of Cr(II) and Cr(III) in the bulk salt be identified. By coupling this a time-dependent concentration profile analysis of Cr in the salt (i.e. locating the fate of all oxidized Cr species whether they are in the bulk salt or in the salt film), the instantaneous mass loss of Cr was determined and corroborated with gravimetric mass loss results. Additionally, electrochemical impedance spectroscopy (EIS) was used to determine the instantaneous corrosion rate of Cr corrosion. However, conventional rectangular plate geometry used for molten salt electrochemistry associates with complex current-potential distribution, further amplified by the large double layer capacitance of molten FLiNaK ($\sim mF/cm^2$). This results in a very low frequency ($>10^{-3}$ Hz) required for polarization resistance to manifest in the EIS spectra, and is out of the practical frequency range ($10^{-2} - 10^4$ Hz) used in most molten salt EIS measurements. In Appendix 2,

flush-mounted Cr disk electrodes between 10^0 and 10^{-2} cm² were designed and shown to exhibit reliable polarization resistance at or above 10^{-2} Hz in FLiNaK containing 1 wt% EuF₃ at 600 °C.

Lastly, theories and methods developed in Tasks 1 through 3 were utilized to study the corrosion behavior of as homogenized, large grain (>300 μm), high purity Ni-20Cr (wt.%) binary alloys. In Task 4, the effect of electrode potentials on the corrosion rate and morphology was investigated. Based on the LSV results of Cr and Ni in FLiNaK, the relative rates of Cr/Cr(II)/Cr(III) and Ni/Ni(II) anodic reactions in Ni-20Cr (wt.%) may be compared at different electrode potentials, providing insights on whether the process follows a continuous rate-dependent transition or exhibits an electrode potential dependent threshold ('on/off') for dealloying as a function of LN concentration. Between 1.75V_{K+/K} and 2.10V_{K+/K} (electrode potential regimes in which both Ni and Cr are oxidized at different rates) bicontinuous porosity was observed in Ni-20Cr (wt.%) due to Cr selective dissolution or “dealloying”, with morphological features, e.g. ligament width, depth, were also found to increase with applied potential.

This observation suggests that alloys (e.g. Ni-Cr) may potentially exhibit a parting limit for dealloying significantly lower than the conventional 50-55at.% observed in room temperature (RT) aqueous solutions. It was hypothesized that the high homologous temperature in which molten salt dealloying occurs ($\sim 0.52T_H$) implies that bulk diffusion may be a rate-limiting process, which is typically neglected in RT dealloying studies. Subsequently, an original analysis was performed in which the rate of Cr outward bulk diffusion (J_{bulk}^{Cr}) at a known grain size, the measured rate of Cr oxidation ($J_{electric}^{Cr}$ or $i_{electric}^{Cr}$), and an average rate of Ni surface diffusion (J_{surf}^{Ni}) were compared over time, suggesting that J_{bulk}^{Cr} is likely the rate-controlling process as it slows down the supplies of Cr for oxidation during potentiostatic holds.

To validate this theory, cold working (CW) was proposed to ameliorate this effect by imparting a high density of dislocation to accelerate Cr bulk diffusion. In Task 5, the dealloying morphology of Ni-20Cr (wt.%) cold rolled to 10%, 30%, and 50% were studied at 1.75V_{K+/K} and 1.90V_{K+/K}. Dealloyed NiCr displayed the formation of bicontinuous porosity within the grain interior and at grain boundaries driven by rapid Ni surface diffusion as well as Cr outward diffusion during dealloying. Moreover, the depths of dealloying increased with cold work and plateaued around 30%CW. Such corrosion behavior was attributed to the dislocation substructures present at varying CW%. These linear defects are argued to serve as fast paths which govern Cr dissolution by pipeline transport for corrosion dealloying given a high T_H . The enhanced Cr bulk diffusion to the metal-salt interface controlled dealloying at these potentials.

This thesis, by no means, provides all the answers to molten salt corrosion, nor does it claim that the laboratory experiments conducted perfectly simulate the actual reactor environments. Nevertheless, the techniques and methods developed in this thesis is intended to serve as a foundational framework for corrosion studies. In doing so, MSR developers and the broader molten salt community can systematically study molten salt corrosion of complex alloys, calculate meaningful corrosion rates, and potentially develop

new alloys—avoiding "cook-and-look" approaches and speculative interpretations of corrosion mechanisms. In the long run, the successful development of modular molten salt reactors has the potential to democratize relatively clean, abundant energy, benefiting both affluent and underprivileged nations alike. The following work should be completed and is closely affiliated with this work.

Suggested future work for molten salt electrochemistry fundamental studies

Currently, the construction of potential-activity diagrams relies on using Gibbs free energy of formation (dG_f) and fusion of metal fluoride compounds (e.g. NiF_2 , HF) reported in existing thermodynamic database to calculate the reactions free energy, and thus, the half-cell redox potentials (E_{Nemst}) relative to a standard environmental reference (SER) state. An initial assumption that the dG_f of F^- at 600°C equals to 0 was imposed in our thermodynamic prediction, such that all E_{Nemst} calculated could be represented relative to the fluorine gas evolution (F_2/F^-). To resolve further speculations, future work should seek to design a reference electrode that relies on an actual F_2/F^- salt couple with a flowing F^- gas and a known fluoride salt (analogous to the Standard Hydrogen Electrode in aqueous solutions). This allows a systematic cyclic voltammetry measurement with a controlled concentration of metal fluorides (e.g. NiF_2) to be performed without concerns regarding the stability of a pseudo K^+/K reference potential and thermodynamic assumptions imposed in Task 1 (e.g. $dG_{F^-} = 0$ at 600°C), and thus, enabling an accurate Gibbs free energy of metal fluorides relative to the F_2/F^- reaction to be calculated (analogous to work performed in Task 1). Additionally, techniques such as *in-situ* raman spectroscopy should be considered to incorporate in the molten salt electrochemical cell such as the complexation behavior of metal fluorides may be studied.

Suggested future work for molten salt dealloying

The field of molten salt dealloying (MSD) is an emerging and unique area of study, characterized by fundamentally different chemistry compared to aqueous environments. It operates at a high homologous temperature ($T_H \sim 0.5$ for most alloy systems), where bulk diffusion plays a critical role—unlike aqueous systems where the compositional threshold of dealloying (or parting limit) is described by percolation theory. It is, therefore, necessary to explore whether percolation theory is also applicable in describing the mechanism of molten salt dealloying given that LN solutes are mobile at high homologous temperature. This may be achieved by systematically varying factors that are critical to the fluxes of bulk and surface diffusions, including but not limited to **composition, temperature, grain size, and irradiation effects**. Developing a robust theoretical framework for molten salt dealloying is essential to advance the field. Such a theory could address unanswered questions, such as how dealloying manifests in ternary alloy systems (e.g., NiFeCr) or compositionally complex alloys (e.g., 316SS). For instance, in a ternary alloy system, should Fe + Cr be considered the less noble (LN) composition, or just Cr? Alternatively, is a combination or variation of these elements more appropriate? Another area of interest is the morphology of dealloyed

structures. For example, bicontinuous dealloying has been observed in Ni-20Cr (wt.%), and it would be valuable to investigate whether similar morphologies can develop in alloys like 316SS or Hastelloy N under comparable electrochemical conditions. Such morphologies could be associated with stress corrosion cracking, making their study critical for understanding the structural integrity of these materials in molten salt environments. Additionally, exploring the correlation between impurity concentrations (e.g., HF) and the electrode potentials of metal and alloy systems could provide insights into the relationship between impurity levels and morphological damage. This would help refine predictive models for molten salt corrosion and improve the selection of materials for high-temperature molten salt reactor applications.

Additionally, it is possible that the reduction of dissolved oxygen to oxyanions (i.e. $O_2 + 4e^- \rightarrow 2O^{2-}$) may serve as an oxidizer in the corrosion process. There is yet a comprehensive study that measures or estimates the Nernst potentials of this reaction. Preliminary results suggest this potential can be in the range between 1.75 and 2.20 $V_{K+/K}$ at concentration as shown in Task 2. If this is the case, oxygen may result in a corrosion potential in the dealloying potential range “1.75 - 2.10 $V_{K+/K}$ ” depending on the alloy systems. It is, thus, crucial to perform a systematic investigation on the effect of oxide impurity on dealloying based on the electrochemical corrosion framework developed in this thesis.

Beyond corrosion, the thermodynamic insights and results from molten salt dealloying open new opportunities to create nano- and micro-porous materials that cannot be easily achieved in aqueous environments. For example, Ti, which is highly stable in aqueous environments due to the formation of TiO_2 , reacts readily in molten salts, making it feasible to fabricate porous Ti or Ti-alloy foams. This capability could have significant applications in material design. Molten salt dealloying also holds promise in the field of electrochemical recycling. The high current densities typical of molten salt systems (ranging from tens to hundreds of mA/cm^2) contrast sharply with the $\mu A/cm^2$ scale seen in aqueous systems. This difference highlights the potential of MSD for processing and recycling materials.

Suggested future work for molten salt alloy developments

Building on a foundation in corrosion thermodynamics, kinetics, and mechanisms, the next logical step is to apply these theories toward developing alloys that are either resistant to corrosion in molten salts (under specific potentials) or designed to avoid corrosion morphologies that are prone to stress-corrosion cracking. This effort can leverage recent advancements in high-throughput computational methods for materials discovery. For example, it may be possible to design an alloy where the less noble (LN) component can uniformly passivate across a wide range of operating electrode potentials or impurity concentrations, thereby preventing catastrophic cracking. Additionally, methods for cathodic protection in molten salt environments could be developed, allowing even commercial alloys to be effectively protected in these systems. Such advancements could significantly enhance the durability and reliability of materials in extreme environments, paving the way for innovative solutions in molten salt applications.

Appendix #1: Deciphering when Metal Corrosion is Spontaneous in Molten Fluorides Using Potential-Activity Diagrams

Ho Lun Chan^{1,2}, John R. Scully^{1,2}

¹Department of Materials Science and Engineering, University of Virginia, Charlottesville, VA, 22904

²Center for Electrochemical Science and Engineering, University of Virginia, Charlottesville, VA, 22904

Abstract

The work identifies the conditions for thermodynamically favored spontaneous metal corrosion using potential-activity diagrams tailored for high-temperature molten fluorides. These diagrams provide insights into the thermodynamic phase stability of both solid and dissolved metal species, such as Cr, Cr(II), Cr(III), Ni, Ni(II), Fe, and Fe(II), along with their potential primary oxidizers, including Eu(III), O₂, and HF, over a broad range of theoretical F⁻ anion activities. The work further examines the practical implications, prospects, and challenges associated with the construction of these diagrams. The key objective of this project is to pinpoint crucial thermodynamic variables that substantially affect metal corrosion electrochemistry in the context of molten salt nuclear reactor applications.

Introduction

In the past decade, there has been a notable increase in the publication of corrosion research focused on candidate metals and alloys for Gen-IV molten salt reactor applications.¹ This trend highlights the growing interest in understanding and addressing the corrosion challenges inherent to this technology. Numerous studies have intentionally introduced oxidizers, including HF, CrF₃, and EuF₃, into the salt mixture to explore the impact of oxidizing impurities on the corrosion process, the driving force for corrosion, the rates of corrosion, and the underlying microstructural damage seen in candidate metals and alloys.²⁻³ However, these studies are often conducted phenomenologically⁴ and lack conceptualization of spontaneous corrosion processes explained by foundational thermodynamic and kinetics theories of corrosion.⁵⁻⁷ A step toward improving the thermodynamic foundations involves the construction and partial verification of potential-activity diagrams, similar to Pourbaix diagrams used in aqueous systems. These diagrams can display the stability regions of species such as Cr, Cr(II), and Cr(III) in molten fluorides, as well as indicate the conditions necessary for the reduction of oxidizers and the occurrence of spontaneous corrosion.⁸ However, earlier works were constrained to the discussion of phase stability of Cr species, presuming them to be solvated to F⁻ at 600°C. There is a gap in predicting and comparing oxidizer

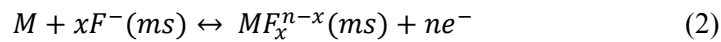
candidates in molten fluorides that can meet the conditions for spontaneous corrosion for a given metal. Specifically, which types of oxidizers, at what concentrations, and for which metals (e.g. Cr, Fe, and Ni) remain unexplored in many previous studies. Hence, the objective is to expand our original approach to define the phase stability of Ni, Fe, and other potential oxidizing elements, such as HF, O₂, Eu(III), and Cr(III) when present in low finite concentrations. When considered together these help to define the conditions for spontaneous corrosion.

Experimental Procedures

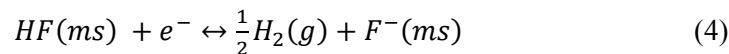
The first assumption of this work is that the corrosion of metallic elements in molten fluorides occurs by electrochemical processes governed by mixed potential theory. Corrosion theory applied to molten fluorides states that the thermodynamic driving force for oxidative corrosion is determined by the difference in the Gibbs free energies of reaction (ΔG_{rxn}^o) present between the cathodic half-cell reduction reactions of the oxidants, coupled with half-cell anodic oxidation reactions associated with transition metals used in structural materials exposed. This difference must be negative for a reaction to occur satisfying the condition $\Delta G < 0$ for a spontaneous process given $\Delta G = -nF\Delta E$. Reaction (1) is the most general approach to describe such a half-cell reaction.⁹



In regards to the anodic reaction, metal dissolution in molten fluorides is often described by the oxidation of pure metals to their metal fluoride species represented in reaction (2)^{2,10-12}:

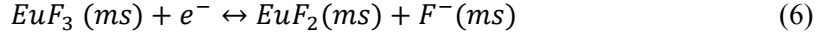


where (ms) indicates dissolved species in the molten salt and M represents the dissolving metallic element, including Ni, Cr, and Fe. The relative tendencies of metal dissolution depend on the of the relevant half-cell redox reactions. In the context of the cathodic reactions, hydrofluoric acid (HF), formed due to H₂O moisture dissociation and fluorination (3), is often in a molten salt containing this oxidant (Ox) during open-circuit corrosion leading to (4) in many studies:

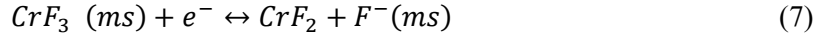


Other relevant oxidizers in spontaneous corrosion studied include dissociated oxygen gas (O₂) via (5) and europium (III) fluoride (EuF₃) via (6)^{13,14}:





Metallic corrosion products, such as CrF₃ or more generally Cr(III), can also act as oxidizers during spontaneous corrosion of structural metals, reducing to a lower oxidation state such as CrF₂ or Cr(II) when a sufficient driving force is present:



The driving forces pertaining to these half-cell redox reactions under non-unity activity can be described by first writing the Nernst equation for each participating half-cell reaction (8):

$$E_{redox} = E_{redox}^0 - \frac{2.303RT}{nF} \log\left(\frac{a_{red}}{a_{ox}}\right) \quad (8)$$

where E_{redox} is the Nernst potential or activity modified standard potential for an half-cell redox reaction, R is the universal gas constant equal to 8.31 J/mol×K, T is temperature in Kelvin, n is the number of e⁻ transferred to complete the reaction a single time, F is the Faraday's constant of 96,500 C/mol e⁻, a_i (= γ_i C_i) is the ion activity, C_i is the molar concentration, and E_{redox}^0 is the standard electrode potential. As an initial estimate, the activity coefficient (γ_i) of all species in this brief manuscript is assumed to be 1.

Table 1 lists the Gibbs energy of formation ($dG_{formation}^o$) between 600°C and 800°C of all the species studied in this work. The Gibbs energy of fusion (dG_{fusion}^o) was also used in calculating the ΔG_{rxn} .^{8,13} Given that most of these dissolved species are in a molten state at the evaluated temperatures, a minor adjustment via (9) was necessary. The ΔG_{rxn} can then be calculated using Equation (10) noting that v_i represents the stoichiometric number of a species, and to calculate using (11)⁹ (note that these thermodynamic data were retrieved from the Factsage 13.1^{TM†} pure substance database):¹⁵

$$\Delta G_f^o = \Delta G_{fusion}^o + \Delta G_{formation}^o \quad (9)$$

$$\Delta G_{rxn}^o = \sum v_i \Delta G_f^o (Red) - \sum v_i \Delta G_f^o (Ox) \quad (10)$$

$$E_{redox}^0 = -\frac{\Delta G_{rxn}^o}{nF} \quad (11)$$

Corrosion is spontaneous when E_{redox} for the proposed cathodic reaction is more positive than that for the corresponding anodic reaction, where upon ΔG is negative, indicating a spontaneous corrosion cell and determining the direction of each reaction (the anode gives up electrons; the cathode gains electrons). This relationship is shown in (12). Note that (12) also applies to the E_{redox}^0 and that the sign of E_{redox} does not change with reaction direction.

$$E_{redox}(Cathodic) - E_{redox}(Anodic) \begin{cases} > 0, \text{spontaneous} \\ = 0, \text{equilibrium} \\ < 0, \text{Not spontaneous} \end{cases} \quad (12)$$

Table 1. Gibbs free energy of select chemical compounds at 600°C¹²

Compound	$\Delta G^{\circ}_{\text{fusion}}$ (kJ/mol)	$\Delta G^{\circ}_{\text{formation}}$ (kJ/mol)
		T = 600°C
F ⁻	-	0
O ²⁻	-	-243.4
HF	-	-277.9
EuF ₃	54.4-32*10 ⁻³ *T(K)	-1351.4
EuF ₂	-	-1046.3
NiF ₂	69 - 41.7*10 ⁻³ *T(K)	-521.9
FeF ₂	47.4 - 38*10 ⁻³ * T(K)	-593.2
CrF ₂	34 - 29.1*10 ⁻³ * T(K)	-665.3
CrF ₃	229.1-183*10 ⁻³ *T(K)	-891.2
KF	28.2 - 25*10 ⁻³ *T(K)	-481.3
LiF	27.2 - 24.254*10 ⁻³ * T(K)	-531.1
NaF	33.3 - 26.277*10 ⁻³ * T(K)	-508.3

Table 2 reports some pertinent half-cell redox reactions, E°_{redox} , and the activity modified or Nernst equation considered in this work. Further discussions are given below about the application of potential-activity diagrams for analysis of the propensity for spontaneous corrosion in molten LiF-NaF-KF salts (or FLiNaK) with various impurities as the assumed predominant cathodic reactions. For thermodynamic reference, it is assumed that the ΔG°_f of F⁻ at 600°C is 0 and the partial pressure of all gaseous species (F₂) to be 1 atm. It was noted that metal fluoride species are represented using the Roman numeral corresponding to the positively charged cation, e.g., Cr(II) as CrF₂ and Eu(III) as EuF₃.

Results and Discussion

To construct a potential-activity diagram, the initial step involves determining an appropriate potential window. This is dictated by selecting a potential range spanning the oxidation of F⁻ to F₂ species and the reduction of molten LiF (or Li⁺), NaF (or Na⁺), and KF (or K⁺) to their respective neutral metal states, as illustrated in Figure 1(a). The lower potential boundary is set by the oxidation of metal salt cation components which will be assumed oxidized under all potentials. There are two different representations in the literature for determining the Nernst potential of salt metal cation reductions: one considers the metal fluoride compound (e.g., KF) as a singular entity, leveraging the more developed thermodynamic data for these species.¹⁰ However, this approach assumes a fluoride-dependent reaction, which remains a subject of debate and requires further experimental validation. The other assumes a fully ionized form (e.g., K⁺).⁶

At the vertical dashed line (representing F⁻ activity of FLiNaK), a substantial difference in potential of roughly 500 mV between KF/K and K⁺/K is observed (Figure 1[a]). This implies that the K⁺/K reaction is thermodynamically more inclined to occur. However, this may not be the case for salts with a low F⁻ activity. Given this comparison, K⁺/K will be considered as the lower potential boundary of FLiNaK salts in the subsequent discussion.

Table 2. A list of half-cell redox reactions, their Nernst potential equation and formal potentials (E^0) calculated at 600°C utilized in this work¹²

Half-Cell Redox Equation	Nernst Equation / Gibbs free energy expression	E^0_{redox} (vs. F_2/F^-)
$F_2 + 2e^- \leftrightarrow 2F^-$	$E = E^0 - \frac{2.303RT}{2F} \log\left(\frac{a_{F^-}^2}{p_{F_2}}\right)$	0
$O_2 + 4e^- \leftrightarrow 2O^{2-}$	$E = E^0 - \frac{2.303RT}{4F} \log\left(\frac{a_{O^{2-}}^2}{p_{O_2}}\right)$	-1.261
$HF + e^- \leftrightarrow \frac{1}{2}H_2 + F^-$	$E = E^0 - \frac{2.303RT}{F} \log\left(\frac{p_{H_2}^{1/2} a_{F^-}}{a_{HF}}\right)$	-2.880
$EuF_3 + e^- \leftrightarrow EuF_2 + F^-$	$E = E^0 - \frac{2.303RT}{F} \log\left(\frac{a_{EuF_2} a_{F^-}}{a_{EuF_3}}\right)$	-2.894
$Ni + 2F^- \leftrightarrow NiF_2 + 2e^-$	$E = E^0 + \frac{2.303RT}{2F} \log\left(\frac{a_{NiF_2}}{a_{F^-}^2}\right)$	-2.536
$Fe + 2F^- \leftrightarrow FeF_2 + 2e^-$	$E = E^0 + \frac{2.303RT}{2F} \log\left(\frac{a_{FeF_2}}{a_{F^-}^2}\right)$	-3.000
$Cr + 2F^- \leftrightarrow CrF_2 + 2e^-$	$E = E^0 + \frac{2.303RT}{2F} \log\left(\frac{a_{CrF_2}}{a_{F^-}^2}\right)$	-3.403
$Cr + 3F^- \leftrightarrow CrF_3 + 3e^-$	$E = E^0 + \frac{2.303RT}{2F} \log\left(\frac{a_{CrF_3}}{a_{F^-}^3}\right)$	-2.430
$CrF_3 + e^- \leftrightarrow CrF_2 + F^-$	$E = E^0 + \frac{2.303RT}{2F} \log\left(\frac{a_{CrF_3}}{a_{CrF_2} a_{F^-}}\right)$	-3.078
$KF + e^- \leftrightarrow K + F^-$	$E = E^0 - \frac{2.303RT}{F} \log\left(\frac{a_{F^-} a_K}{a_{KF}}\right)$	-4.921
$K^+ + e^- \leftrightarrow K$	$E = E^0 - \frac{2.303RT}{F} \log\left(\frac{a_K}{a_{K^+}}\right)$	-4.854
$LiF + e^- \leftrightarrow Li + F^-$	$E = E^0 - \frac{2.303RT}{F} \log\left(\frac{a_{F^-} a_{Li}}{a_{LiF}}\right)$	-5.442
$Li^+ + e^- \leftrightarrow Li$	$E = E^0 - \frac{2.303RT}{F} \log\left(\frac{a_{Li}}{a_{Li^+}}\right)$	-5.379
$NaF + e^- \leftrightarrow Na + F^-$	$E = E^0 - \frac{2.303RT}{F} \log\left(\frac{a_{F^-} a_{Na}}{a_{NaF}}\right)$	-5.159
$Na^+ + e^- \leftrightarrow Na$	$E = E^0 - \frac{2.303RT}{F} \log\left(\frac{a_{Na}}{a_{Na^+}}\right)$	-5.052

Figure 1(b) shows half-cell redox reactions involving gas generation and consumption if present. For instances, F^- is reduced to form F_2 , HF to form H_2 , and O^{2-} to form O_2 . Shaded regions represent stability fields dominated by the evolution of specific gas species. Concentrations of HF and O^{2-} between 10 ppm and 1,000 ppm are considered. These are likely cathodic reactions when coupled with metal oxidation in molten salts. Other cathodic oxidations include the reduction of Cr(III) to Cr(II) or Ni(II) to Ni if NiF_2 is present in the molten fluorides. For spontaneous metal dissolution, the potential should fall within these regions, typically aligned with H_2 gas evolution. Metals with half-cell electrode potentials in the gray region

will not corrode spontaneously unless an additional oxidizer like Eu(III) is present. The role of O₂ as an oxidizer has not been investigated in detail due to uncertainties surrounding its solubility in FLiNaK at 600°C and the possibility for it to be oxidized by F⁻ to form O²⁻.¹⁴

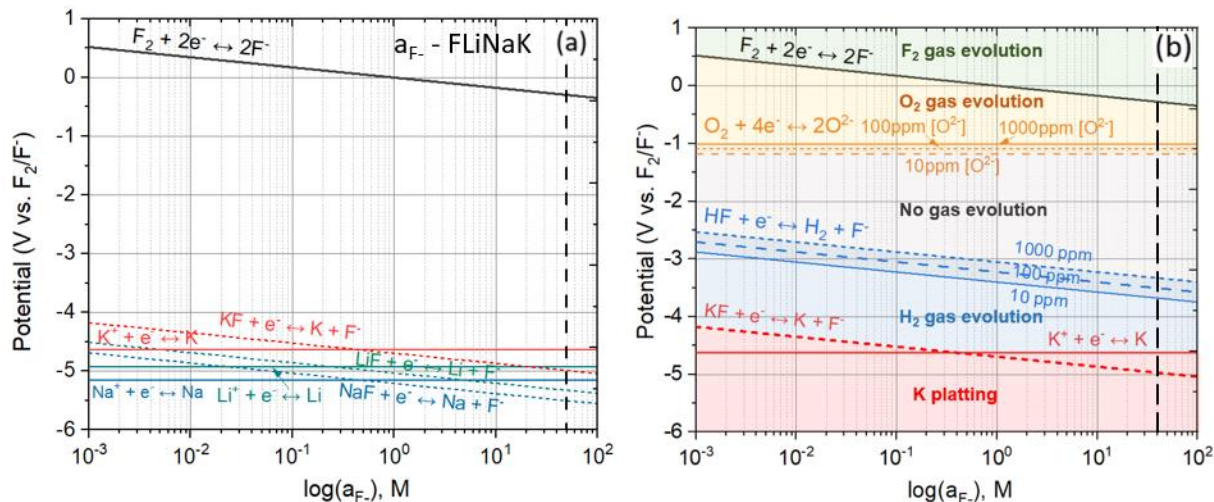


Figure 1. Potential-fluoride activity diagrams at 600°C. (a) shows the potential stability window defined by the fluorine gas evolution (F₂/F⁻) and stability in the oxidized state for Li⁺, K⁺, Na⁺ species salt cation constituents. The vertical dashed line indicates the F⁻ activity in FLiNaK salt at a_{F⁻} = 49.3 M. (b) displays the Nernst potentials of O₂/O²⁻ and HF/H₂ reactions at 10, 100, and 1000ppm. The diagram was shaded with different colors to indicate the type of gas evolution and/or plating of salt cations within the phase stability map.

Figure 2 demonstrates the spontaneity and relative driving forces for the dissolution of pure Ni, Fe, and Cr. As expected, the Nernst potentials of Ni/Ni(II), Fe/Fe(II), and Cr/Cr(II) follow a descending order corresponding to the nobility of each element. Selected cathodic half-cell reactions are included in Figure 2 for this discussion of possible corrosion cells that might form. In order for a reaction to be spontaneous, the cathodic reaction (e.g., HF/H₂, Eu(III)/Eu(II)) must possess a more positive Nernst potential than its anodic counterparts. Fe/Fe(II) and Cr/Cr(II) exhibit lower Nernst potentials compared to HF/H₂ (at 1,000 ppm), indicating the prevalence of impurity-driven corrosion in the presence of trace water.^{1,16} Conversely, Ni/Ni(II) displays a higher potential than HF/H₂, suggesting potential immunity to HF-driven attack.¹⁰ These two observations align with published experimental observations.¹ During spontaneous metal corrosion, the thermodynamic and kinetic factors associated with their respective cathodic and anodic reactions establish a mixed potential, typically termed the corrosion potential. Further interpretation is provided in Pizzini and Morlotti.¹⁴ It should be noted that Fe(III) and Ni(III) were not plotted, but they are other possible species to consider in corrosion cells.

The reduction of higher valence cations, such as Eu(III) and Cr(III), which also act as oxidizers, is hypothetically capable of oxidizing all three elements Ni-, Cr-, or Fe-based on the imposed assumption.

Additionally, for Cr, fluoride complexes such as CrF_3^- for Cr(II) and CrF_6^{3-} in the case of Cr(III) may also form (and change the electrode potential) as suggested by both experimental and computational studies.^{8,17} The effect of fluoride complex formation on these Cr-F phase stability diagrams was investigated in our previous work.⁸

Our discussion herein of this work highlights some of the further research required to address various underlying assumptions. Factors such as activity coefficients, ratios between higher and lower valence states, fluoride complex formation, and the possibility of saturation all require thorough investigation. Moreover, substrate effects can change thermodynamic driving forces. Crystal orientation and nanocurvature can also affect the standard electrode potential.¹⁸⁻¹⁹ However, this work provides a foundation for understanding the spontaneity of metal corrosion in terms of phase stability diagrams. The authors' latest work demonstrates the practicality of these diagrams in understanding experimental polarization curves.⁶ Beyond these insights, the work also establishes a thermodynamic framework that facilitates deeper comprehension of the contributory factors to corrosion, such as radiation.

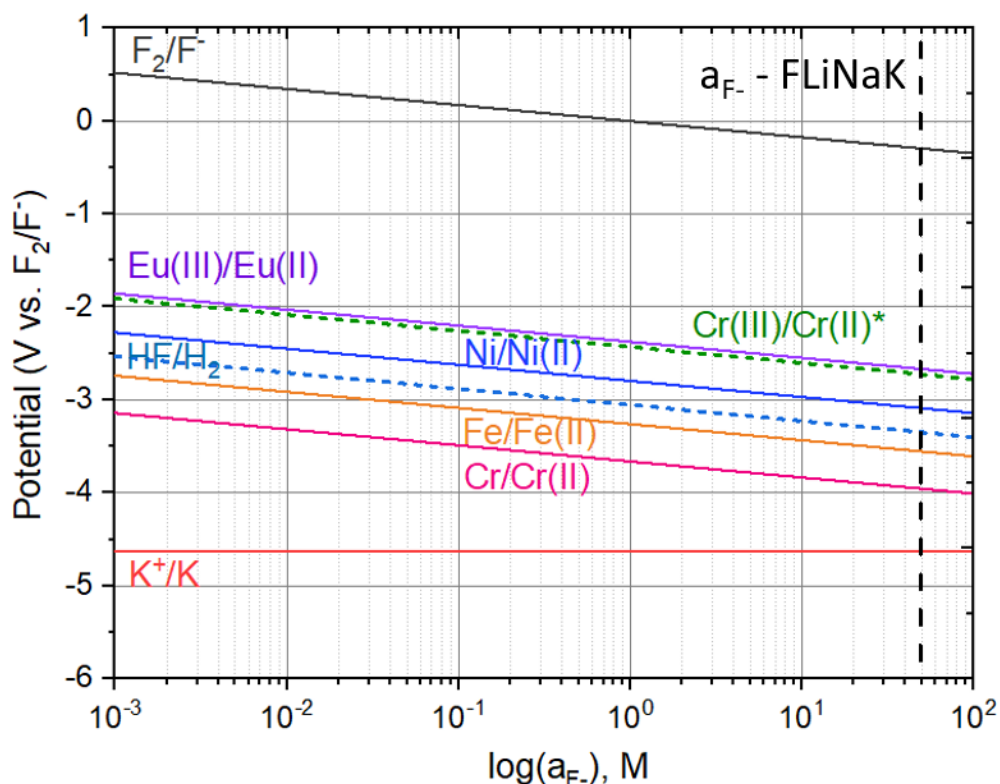


Figure 2. Potential-fluoride activity diagrams displaying the Nernst potentials of F_2/F^- , O_2/O^{2-} , Eu(III)/Eu(II) , Ni/Ni(II) , HF/H_2 , Fe/Fe(II) , Cr/Cr(II) , Cr(III)/Cr(II) , K^+/K , half-cell redox reactions calculated at 600°C . The concentration of O^{2-} and HF was assumed to be 1000 ppm (corresponding to the molar concentration of $1.00 \cdot 10^{-1}\text{M}$ and $1.25 \cdot 10^{-1}\text{M}$), Cr(II) in Cr(III)/Cr(II) and Eu(II) to be 10^{-6}M , while that of Eu(III) , Ni(II) , Fe(II) , Cr(II) in Cr(II)/Cr was assumed to be 10^{-3}M .

Conclusions

This study utilizes potential-activity diagrams tailored for molten fluorides, designed to report in graphical form the driving forces behind various half-cell redox reactions forming a spontaneous corrosion cell involving one or more anodic and cathodic half-cell reactions. Such diagrams enable a comprehensive understanding of phase stability for different metal species and their potential predominant oxidizers during corrosion (e.g., Eu(III), O₂, and HF) assuming a hypothetical range of fluoride activities. However, the study recognizes certain assumptions embedded within this framework and those require further experimental validation. Moreover, the diagram represents an equilibrium condition and does not inform corrosion kinetics. This framework could potentially predict conditions for spontaneous corrosion and serves as a tool for devising strategies for corrosion control and mitigation in these challenging environments, contributing to materials sustainability in fourth generation molten salt reactor technologies.

References

1. Guo, S., J. Zhang, W. Wu, and W. Zhou, *Progress in Materials Science* 97 (2018): pp. 448–487.
2. Wang, Y.L., Q. Wang, H.J. Liu, and C.L. Zeng, *Corrosion Science* 103 (2016): pp. 268–282.
3. McAlpine, S.W., N.C. Skowronski, W. Zhou, G. (Tony) Zheng, and M.P. Short, *Journal of Nuclear Materials* 532 (2020): p. 151994.
4. Hong, M., H.L. Chan, Y. Xie, E. Romanovskaia, J.R. Scully, and P. Hosemann, *Corrosion Science* 212 (2023): p. 110913.
5. Sulejmanovic, D., J.M. Kurley, K. Robb, and S. Raiman, *Journal of Nuclear Materials* 553 (2021): p. 152972.
6. Chan, H.L., E. Romanovskaia, V. Romanovski, M. Hong, D. Sur, P. Hosemann, J.R. Scully, *J. Electrochem. Soc.* (2023), <https://doi.org/10.1149/1945-7111/ace8c0>
7. Hong, M., H.L. Chan, J.R. Scully, and P. Hosemann, *Journal of Nuclear Materials* 584 (2023): p. 154548.
8. Chan, H.L., E. Romanovskaia, J. Qiu, P. Hosemann, and J.R. Scully, *Npj Mater Degrad* 6 (2022): p. 46.
9. Jones, D.A., *Principles and Prevention of Corrosion* (Prentice Hall, 1996).
10. Zhang, J., C.W. Forsberg, M.F. Simpson, S. Guo, S.T. Lam, R.O. Scarlat, F. Carotti, K.J. Chan, P.M. Singh, W. Doniger, K. Sridharan, and J.R. Keiser, *Corrosion Science* 144 (2018): pp. 44–53.
11. Liu, Y., Y. Song, H. Ai, M. Shen, H. Liu, S. Zhao, Y. Liu, Z. Fei, X. Fu, and J. Cheng, *Corrosion Science* 169 (2020): p. 108636.
12. Massot, L., M. Gibilaro, D. Quaranta, and P. Chamelot, *J. Electrochem. Soc.* 168 (2021): p. 026510.
13. Guo, S., N. Shay, Y. Wang, W. Zhou, and J. Zhang, *Journal of Nuclear Materials* 496 (2017): pp. 197–206.
14. Pizzini, S., and R. Morlotti, *Electrochimica Acta* 10 (1965): pp. 1033–1041.
15. Bale, C. W. et al. FactSage thermochemical software and databases—recent developments. *CALPHAD* 33 (2009):p. 295.
16. Liu, Q., H. Sun, H. Yin, L. Guo, J. Qiu, J. Lin, and Z. Tang, *Corrosion Science* 160 (2019): p. 108174.
17. Winner, N., H. Williams, R.O. Scarlat, and M. Asta, *Journal of Molecular Liquids* 335 (2021): p. 116351.
18. Taylor, C.D., P. Lu, J. Saal, G.S. Frankel, and J.R. Scully, *Npj Mater Degrad* 2 (2018): p. 6.
19. Romanovskaia, E., H.L. Chan, V. Romanovski, F. Garfias, M. Hong, S. Mastromarino, P. Hosemann, R. Scarlat, and J.R. Scully, *Corrosion Science* 222 (2023): p. 111389.

Appendix 2: Uncovering Accurate Values of the Polarization Resistance in Molten Fluorides Using Electrochemical Impedance Spectroscopy

Ho Lun Chan^{1,2}, Harjot Singh^{1,2}, Elena Romanovskaia^{1,2}, Valentin Romanovski^{1,2}, Junsoo Han³, John R. Scully^{1,2}

¹ Department of Materials Science and Engineering, University of Virginia, Charlottesville, VA, 22904

² Center for Electrochemical Science and Engineering, University of Virginia, Charlottesville, VA, 22904

³ Laboratoire Interfaces et Systèmes Electrochimiques (LISE), CNRS, Sorbonne Université, F-75005, Paris, France

Abstract

High-temperature operation and the presence of oxidizing impurities in molten chloride and fluoride salts pose significant corrosion risks to structural alloys in molten salt nuclear reactors. Electrochemical impedance spectroscopy (EIS) offers an *operando*, real-time method to study the instantaneous corrosion behavior of these materials non-destructively. However, signal noises may originate from sources extraneous to the electrochemical systems that limit the ability to perform quality impedance measurements in low-frequency regime where polarization resistance (R_p) dominates. Using the exposure of pure Cr in molten LiF-NaF-KF containing 1 wt.% EuF_3 at 600 °C as a model corrosion system, the extent of Non-Uniform Current and Potential (NUCP) distribution during an AC perturbation associate with the disk electrodes is evaluated in terms of two dimensionless correction factors $k_f^{R_{ct}} (= R_{ct}/R_{eff})$ and $k_f^{C_{dl}} (= C_{dl}/C_{eff})$. Results show that a small area Cr disk electrode increases the transition frequency that marks the dominance of R_p to a conventional terminational frequency above 10^{-2} Hz, enabling a reliable charge-transfer resistance (R_{ct}) value to be determined *via* circle fitting an electrical equivalent circuit model (ECM) model. Experimental results were supported by EIS simulations considering commonly used ECM models that factor in the NUCP effect of the bulk rectangular and disk geometries.

Introduction

The pressing need to decrease reliance on petroleum, lower carbon footprints, and satisfy the increasing global energy demands has driven the development of alternative energy technologies. Among them, molten salt-based technology for nuclear power is a growing subcategory that utilizes a blend of molten chloride and fluoride salts¹⁻³, which exhibit high heat capacity, can maintain low vapor pressure, and chemically and thermally stable up to 900 °C. These properties make them ideal for applications in heat storage, transport, cooling, leading to advances in energy technologies such as concentrated solar power (CSP)^{4,5}, molten salt fast reactors (MSFR)⁶, and ionic liquid/molten salt battery^{7,8}.

Corrosion of structural metals and alloys is particularly severe in molten salt environments as compared with conventional atmospheric and aqueous media^{9,10}. The combination of elevated operational temperature (< 500°C), possible radiation, exacerbated by the presence of dissolved hydrochloric or hydrofluoric acids (formed from moisture impurities) pose threats to the lifespan of these structural components 11. Therefore, it is crucial to understand the process of corrosion and accurately quantify its rate, which are essential steps in developing effective corrosion prevention and mitigation strategies. Many published corrosion studies adopt a forensic approach^{9,10}, relying on measuring mass loss and analyzing the post-corrosion morphology of test coupons after immersion in a salt capsule or flow-loop environment. However, this approach fails to provide instantaneous corrosion rates, thus limiting our understanding of the mechanisms involved, given that corrosion is a time-dependent and highly dynamic process depending on the oxidant concentration.

The use of electrochemical impedance spectroscopy (EIS) can provide *in-operando* insights to interrogate corrosion processes in real-time – a well-established method for application in aqueous systems for many years^{12–14}. However, significant challenges remain in extending, evaluating, and validating the applicability of EIS and other electrochemical methods to non-aqueous environments such as molten salts, ionic liquids, and liquid metals^{14–16}.¹ These challenges include designing a working high-temperature electrochemical cell with a low signal-to-noise ratio, proper grounding/cabling, or identifying stable or dynamic reference electrodes¹⁶. Another challenge that is often overlooked is the sensitivity of impedance signals at low frequency to extraneous source, such as environmental noise encompassing physical disturbance from gas flow, vibrations of motor pumps, fridge, furnace if testing is conducted in a glove box, the movement of salts due to natural convection and/or electrode geometry and how the electrode is submerged to the molten salts¹⁶. These factors can still limit the ability to measure, fit and extract accurate electrochemical parameters when they are only accessible at low frequency regime, particularly the charge-transfer resistance (R_{ct}), double layer capacitance (C_{dl}), and/or diffusional impedance¹⁰⁵. To enable a high-quality impedance measurement, four essential requirements must first be met, ranging from causality, stationarity, linearity to reproducibility^{13,16,17}. In the case of the molten salt system, stationarity and reproducibility are of particular concern justified by literature studies.

By analyzing over 90 published EIS data points performed in molten chloride and fluoride salts (Table 1)^{18–86}, significant variability was observed in working electrode geometries (WE), exposure area, and reported values for parameters with variations spanning three orders of magnitude within the same salt system. For instance, the C_{dl} of a eutectic LiF-NaF-KF salt, or FLiNaK, at 700°C has a reported range of values between 0.1 and 1000 mF/cm² and the corresponding R_s also varies between 0.5 and 5 Ω -cm² as

¹ This manuscript primarily focuses on elucidating the use of EIS in molten salts. Our prior work has revisited and discussed the applicability of Pourbaix diagram, Evans diagram, mixed potential theory, as well as extending the use of cyclic voltammetry and chronoamperometry for *in situ* corrosion assessments in molten fluorides.

shown in Table 1. The two parameters here are relatively insensitive to the metallic electrode materials as their surface finish is similar. The large variation in the C_{dl} and R_s values, let alone the R_{ct} values, suggests the complexity of the issues affecting EIS results. To determine these parameters accurately, an experimental EIS scan must cover a sufficient frequency range, *e.g.* R_{ct} typically requires a termination frequency of 10^{-3} Hz or lower. However, many terminated their EIS scan at a frequency of 10^{-2} Hz or higher and then attempted to fit an experimental impedance spectrum with an ECM to determine R_{ct} without sufficient data (*e.g.*, $f < 1/2\pi C_{dl}R_{ct}$). In this instance, accurate fitting is difficult, resulting in possible errors. Some molten salts, particularly fluoride, exhibit a high experimental C_{dl} in the mF scale as compared to the μ F scale typical of aqueous or ionic systems^{41,87-91}. To access a frequency regime where R_{ct} dominates or strongly contributes to the impedance data, it becomes necessary to use a lower frequency range.

One way to overcome this challenge is to simplify the electrode geometry avoiding irregularities such as electrode edges as much as possible as well as to employ microelectrodes to fix the diffusion and ohmic resistance of the electrode⁹⁹⁻¹⁰³. This work explores the use of a disk as the working electrode geometry over a range of electrode radii. Herein, the electrode geometry with an embedded disk geometry is referred to as a flush-mounted disk, which involves embedding a disk within an insulating and chemically stable medium, such as alumina for chloride salts and boron nitride for fluoride salts¹⁰⁴. When considering the WE as a disk, there is a deviation of experimental EIS results from ideal conditions due to the effect of non-uniform current and potential distributions (NUCP) at the center or edges. As shown in Table 1, typical molten salt electrodes often use thin rectangular plates partially submerged in the salt bath, termed “Bulk R”, and the resultant NUCP effect may be very complex. This complexity may be reduced and is recommended⁹⁹⁻¹⁰³ by adopting a mm scale flush-mounted electrode instead.

Disk geometry distorts the primary current distribution due to edge effects affecting ohmic resistance (R_s) measurements^{12,99,105-109}, altering interfacial capacitance due to potential distribution⁹⁹, and changing the concentration profile of relevant redox species that impact the ionic diffusion behavior¹⁵. Each of these phenomena represents the scenarios of time-constant dispersions influencing impedance responses, and which of these becomes predominant depends on factors including disk radius, solution conductivity, and C_{dl} . However, with the disk electrode, these issues can be mathematically quantified as elaborated by Newman *et al.*^{110,111}, Nisancioglu *et al.*⁹⁹, Fleischmann *et al.*^{102,103}, Huang *et al.*^{112,113}, Rotenberg *et al.*¹¹⁴, and by Orazem and colleagues^{12,100,101}. Experimentally, these phenomena often result in a 'shift' in impedance spectra¹¹⁵⁻¹²⁰, allowing the typically low-frequency R_{ct} regime to “shift” and be assessed at higher frequencies. This may, in fact, be useful for conducting impedance measurements in molten salts to access both charge-transfer and diffusional impedance regimes.

However, electrochemical parameters such as R_{ct} and C_{dl} , obtained through this approach, are still prone to errors caused by non-uniform current and potential distributions^{99,105}. Consequently, it is essential to

develop additional correction procedures, thereby improving the reliability and applicability of the disk EIS method for corrosion studies in molten salts. To address these challenges, we propose the following four-step approach in this work: (i) Firstly, quantifying the errors in R_{ct} and C_{dl} measurements as a function of frequency and disk radius, utilizing established mathematical models by Nisancioglu *et al.*⁹⁹ to create impedance simulations with various ECMs pertinent to molten salt corrosion systems (some include diffusional impedance)⁸⁶, enabling systematic sensitivity analysis; (ii) Secondly, comparing these simulations with experimental EIS scans on model corrosion systems, with the corrosion behavior of pure chromium in molten FLiNaK at 600 °C selected as the model system due to extensive prior studies on its corrosion process and rate^{15,92,121–123}. (iii) Thirdly, utilizing results from (i) to correct empirical parameters obtained by ECM fitting in (ii); (iv) Fourthly, evaluating the margin of errors associated with the frequency range selected for ECM fitting as a function of electrode configurations and geometries, which will inform the optimal disk radius, and the minimum frequency required to accurately obtain R_{ct} .

Table 1. Collected electrochemical impedance spectroscopy data in molten salts

Material	Salt	T, °C	Time, h	Electrode geometry**	f_{exp} , Hz	R_s , $\Omega \cdot \text{cm}_2$	R_{ct} , $\Omega \cdot \text{cm}_2$	Q_{dl} , $\text{S} \cdot \text{s}^n \cdot \text{cm}^{-2}$	n_{dl}	$C_{dl,***}$, mF cm^{-2}	Ref
SS316L	FLiNaK	700	1	Bulk R.	$[10^{-2}, 10^4]$	3.70	533	53	1	53	[32]
			10			3.70	519	69.5	1	69.5	
			50			3.80	402	83.8	1	83.8	
			100			3.70	329	195	1	195	
SS316	FLiNaK	650	100	Wire	$[10^{-2}, 10^4]$	0.718	183	15	0.627	39.8	[41]
	FLiNaK + 200 ppm O^{2-}					0.730	271	16.4	0.734	3.37	
	FLiNaK + 500 ppm O^{2-}					0.967	534	12.9	0.753	2.68	
	FLiNaK + 800 ppm O^{2-}					1.03	723	14.3	0.760	3.47	
	FLiNaK + 1000 ppm O^{2-}					0.862	1775	6.23	0.782	1.45	
Fe80Ni20 (wt.%)	45 KF + 50 AlF_3 + 5 Al_2O_3 (wt.%)	700	1	Rod	$[10^{-2}, 10^6]$	7.04	10.8	$5.94 \cdot 10^{-4}$	0.662	$2.80 \cdot 10^{-2}$	[87]
Fe57Ni43 (wt.%)						8.98	6.66	$1.95 \cdot 10^{-3}$	0.640	0.120	
Fe50Ni50 (wt.%)						7.59	2.79	$8.31 \cdot 10^{-3}$	0.601	0.550	
Fe43Ni57 (wt.%)						5.44	2.16	$5.94 \cdot 10^{-3}$	0.619	0.330	
Fe20Ni80 (wt.%)						5.78	16.69	$1.01 \cdot 10^{-3}$	0.656	$5.80 \cdot 10^{-2}$	
Alloy 625	FLiNaK	700	48	Bulk R.	$[10^{-2}, 10^5]$	0.754	253	$4.09 \cdot 10^{-3}$	0.631	0.140	[92]
	FLiNaK + 0.1 wt. % Ta					0.637	4571	$4.65 \cdot 10^{-2}$	0.629	5.83	
	FLiNaK + 0.5 wt. % Ta					1.01	13.9	$7.81 \cdot 10^{-2}$	0.606	14.3	
	FLiNaK + 1 wt. % Ta					0.765	99.8	$5.83 \cdot 10^{-2}$	0.728	18.2	
EDM-3 Graphite	FLiNaK + 5 wt.% H_2O	550	1	Rod	$[10^{-2}, 10^5]$	0.610	13.7	NA	NA	NA	[93]
Cr	48 LiF + 52 BeF_2 (mol%) + 0.2 wt.% CrF_3	600	1	Bulk R.	$[10^{-2}, 10^4]$	0.320	79.2	70.2	0.630	$4.09 \cdot 10^5$	[94]
	FLiNaK + 0.2 wt.% CrF_3					0.570	9.13	3.62	0.889	$3.93 \cdot 10^3$	
OSD Steel	48 LiF + 52 BeF_2 (mol%)	800	1	Disk	$[10^{-2}, 10^5]$	NA	NA	NA	NA	NA	[95]
	FLiNaK					NA	NA	NA	NA	NA	
W	FLiNaK	700	1	Bulk R.	$[10^{-1}, 10^4]$	NA	274	$6.73 \cdot 10^{-3}$	0.725	NA	[96]
Mo						NA	134	$1.40 \cdot 10^{-3}$	0.776	NA	

HfTaTiVZr	FLiNaK	600	60	Bulk R.	$[10^{-3}, 10^5]$	0.785	36.2	19.8	0.605	$1.18 \cdot 10^5$	[28]
TaTiVWZr						0.750	32.2	20.2	0.576	$1.46 \cdot 10^5$	
Inconel 718						0.861	41.8	16.4	0.626	$7.89 \cdot 10^4$	
SS316						0.532	20.4	25.6	0.485	$4.02 \cdot 10^5$	
Ni	FLiNaK	700	50	Bulk R.	$[10^{-2}, 7 \cdot 10^3]$	2.69	319	NA	NA	NA	[97]
Fe			50		$[10^{-2}, 10^3]$	4.93	364	NA	NA	NA	
Cr			18		$[10^{-1}, 10^3]$	2.94	26	NA	NA	NA	
Ni-20Cr (wt.%)	FLiNaK	600	2.78 (@ 1.75V _{K+K})	Bulk R.	$[10^{-2}, 10^4]$	0.891	667	$3.84 \cdot 10^{-3}$	0.821	1.17	[98]
			2.78 (@ 1.90V _{K+K})			0.509	29.6	$9.58 \cdot 10^{-2}$	0.707	27.2	
			2.78 (@ 2.10V _{K+K})			32.4	39.8	$3.59 \cdot 10^{-2}$	0.493	22.7	
Hastelloy N	FLiNaK	700	100	Bulk R.	$[10^{-2}, 10^4]$	3.67	3.93	$4.30 \cdot 10^{-3}$	0.660	11.8	[35]
	FLiNaK + 0.02 wt% graphite					3.24	31.6	$6.50 \cdot 10^{-1}$	0.580	$1.04 \cdot 10^3$	
	FLiNaK + 0.1 wt% graphite					2.89	23.7	$6.85 \cdot 10^{-1}$	0.600	$1.00 \cdot 10^3$	
SS316	13.4 NaCl + 33.7 KCl + 52.9 ZnCl ₂ (mol%)	700	91	Bulk R.	$[10^{-2}, 10^6]$	0.82	2.35	$4.00 \cdot 10^{-2}$	0.800	15.8	[84]
Inconel 625			100			0.59	9.14	$2.20 \cdot 10^{-2}$	0.800	7.31	
Fe40Al0.1B+10Al ₂ O ₃ (at.%)	NaVO ₃	700	24	Rod	$[10^{-3}, 3 \cdot 10^5]$	1.50	156	NA	NA	NA	[47]
Inconel 625	PbSO ₄ + Pb ₃ O ₄ + PbCl ₂ + Fe ₂ O ₃ + ZnO	800	24	Bulk R.	$[10^{-3}, 5 \cdot 10^4]$	185	8.80	0.490	0.620	$1.17 \cdot 10^3$	[66]
		700				124	32.7	1.07	0.670	$5.49 \cdot 10^3$	
		600				$1.23 \cdot 10^3$	142	0.480	1	$4.80 \cdot 10^2$	
SS321H	53 KNO ₃ + 7 NaNO ₃ +40 NaNO ₂ (wt.%)	500	24	Rod	$[10^{-2}, 5 \cdot 10^5]$	3.02	1.68	$1.51 \cdot 10^{-2}$	1.03	17.1	[21]
A36	60 NaNO ₃ + 40 KNO ₃ (wt.%)	390	576	Rod	$[10^{-2}, 10^4]$	2.02	125	$2.07 \cdot 10^{-4}$	0.670	$4.45 \cdot 10^{-3}$	[72]
SS304L						3.90	$1.09 \cdot 10^{40}$	$1.22 \cdot 10^{-2}$	1	12.2	
Ni16Cr13Co4Mo (wt.%)	50 NaCl + 50 KCl (wt.%)	650	2	Bulk R.	$[10^{-2}, 10^4]$	0.982	7.16	$2.63 \cdot 10^{-3}$	0.658	0.110	[83]
	43 NaCl + 43 KCl + 14 Na ₂ SO ₄ (wt.%)					1.04	4.14	$8.98 \cdot 10^{-3}$	0.608	0.380	
Inconel 740H	50 NaCl + 50 KCl (mol%)	700	24	Bulk R.	$[10^{-2}, 10^6]$	2.01	13.4	$6 \cdot 10^{-2}$	1	$6 \cdot 10^{-2}$	[51]
SS316	800	2.85				19.7	$2.20 \cdot 10^{-1}$	1	$2.20 \cdot 10^{-1}$		
DS2205	40 NaCl + 60 Na ₂ CO ₃ (wt.%)	700	1	Bulk R.	$[10^{-1}, 10^6]$	1.03	1.60	0.190	0.470	17.24	[77]
CS1008						0.620	32.1	$5 \cdot 10^{-2}$	0.640	7.01	
SS316	33.4 Na ₂ CO ₃ + 32.1 Li ₂ CO ₃ + 34.5 K ₂ CO ₃ (wt.%)	450	1	Bulk R.	$[10^{-1}, 10^6]$	0.970	0.320	0.110	0.570	7.10	[77]
DS2205						1.61	3.10	$1.24 \cdot 10^{-3}$	0.760	0.15	
CS1008						1.23	544	$3.68 \cdot 10^{-3}$	0.770	0.73	
FeCoNiCrAl HEA	24.5 NaCl + 20.6 KCl + 54.9 MgCl ₂ (wt.%)	650	11	Flush mounted plate	$[10^{-2}, 10^4]$	1.53	20.4	2.35	0.590	$5.43 \cdot 10^3$	[79]
	21		1.42			12.2	3.18	0.610	$7.77 \cdot 10^3$		
	41		1.41			32.5	7.40	0.640	$2.70 \cdot 10^3$		
2.25Cr1Mo steel	44 LiCl + 56 KCl (wt.%)	500	200	Bulk R.	$[10^{-1}, 4.5 \cdot 10^3]$	0.330	9.50	$3.63 \cdot 10^{-3}$	0.710	0.230	[74]
12CrMoV steel	55 ZnCl ₂ + 45 KCl (wt.%)	400	2	Bulk R.	$[10^{-2}, 2 \cdot 10^4]$	2.96	4.08	$5.79 \cdot 10^{-3}$	0.570	0.18	[27]
SS304			10			44.5	22.5	$1.48 \cdot 10^{-2}$	0.940	13.4	
SS316	53 KNO ₃ + 40 NaNO ₂ + 7 NaNO ₃ (wt.%)	450	7	Bulk R.	$[10^{-2}, 10^6]$	0.759	36.5	$4.19 \cdot 10^{-3}$	0.656	0.200	[37]
		600	13			0.629	23.2	$3.80 \cdot 10^{-2}$	1	37.9	
		680	1			0.709	3.54	$4.63 \cdot 10^{-2}$	0.908	32.2	
P91 steel	60 NaNO ₃ + 40 KNO ₃ (wt.%)	580	24	Bulk R.	$[10^{-2}, 5 \cdot 10^5]$	3.79	$2.10 \cdot 10^{-1}$	$3.40 \cdot 10^{-4}$	0.860	$7.10 \cdot 10^{-2}$	[52]
	1000	3	6.67			$2.70 \cdot 10^{-4}$	0.920	0.140			
AA6061	Mg(NO ₃) ₂	120	168	Sheet	$[5 \cdot 10^{-2}, 10^5]$	10.0	181.	$7.70 \cdot 10^{-4}$	0.818	0.260	[42]
CW024A						11.9	4.92	$5.70 \cdot 10^{-6}$	0.921	$2.50 \cdot 10^{-3}$	
1050 steel						14.01	1.80	$1.43 \cdot 10^{-5}$	0.800	$1.70 \cdot 10^{-3}$	
Inconel 718	Na ₂ SO ₄	942	0.5	Rod	$[10^{-3}, 10^5]$	0.620	48.8	0.173	1	173	[81]
	80 V ₂ O ₅ + 20 Na ₂ SO ₄ (wt.%)	637				1.91	5.4	0.647	1	647	
	NaVO ₃	679				1.41	23.7	0.118	1	118	
	Ash (V ₂ O ₅ + Na ₂ O · V ₂ O _{4.5} · V ₂ O ₅ + NaV ₆ O ₁₅)	806				9.21	6.5	0.157	1	157	

P92 steel	62 Li ₂ CO ₃ + 38 K ₂ CO ₃ (mol%)	650	4	Rod	[10 ⁻² , 5·10 ³]	0.79	3.54	3.48·10 ⁻²	0.490	0.670	[67]
SS304						1	1.67	1.07·10 ⁻²	0.470	5.07	
SS310						1	2.85	1.38·10 ⁻²	0.630	36.1	
AISI 309	50 V ₂ O ₅ + 50 Na ₂ SO ₄ (mol.%)	700	0	Bulk R.	[10 ⁻³ , 10 ⁴]	2.7	13.67	6.97·10 ⁻⁷	0.560	1.92·10 ⁻⁸	[44]
			120			4.2	22.8	9.08·10 ⁻⁷	0.640	7.39·10 ⁻⁷	
12CrMoV steel	(52±48) PbCl ₂ + KCl (mol.%)	450	48	Bulk R.	[10 ⁻² , 5·10 ⁴]	34.6	41.6	2.54·10 ⁻⁴	1	0.254	[69]
			72			34.6	41.6	2.54·10 ⁻⁴	1	0.254	
			168			41.9	27.7	5.48·10 ⁻³	1	5.48	
SS304	60 NaNO ₃ + 40 KNO ₃ (wt.%)	550	96	Bulk R.	N/A	2.31	23.7	0.114	0.436	18.0	[63]
SS430						1.84	3.27	9.60·10 ⁻³	0.590	0.430	
HR224						1.92	39.9	0.177	0.713	112	
VM12						2.17	75.5	4.64·10 ⁻²	0.710	17.9	
Inconel 625	60 NaNO ₃ + 40 KNO ₃ (wt.%)	500	1	Bulk R.	[10 ⁻² , 10 ⁵]	4.27	116	1.40·10 ⁻⁴	0.920	7.30·10 ⁻²	[56]
		600				3.28	13.4	2.10·10 ⁻⁴	0.850	5.60·10 ⁻²	
OC4	60 NaNO ₃ + 40 KNO ₃ (wt.%)	390	24	Rod	[10 ⁻² , 10 ⁶]	1.23	4.56	2·10 ⁻⁴	0.840	3.90·10 ⁻²	[38]
304						2.02	2.12	3·10 ⁻³	0.550	2.70·10 ⁻²	
T22						6.43	2.28	2·10 ⁻⁴	0.750	1.40·10 ⁻²	
Fe	60 NaNO ₃ + 40 KNO ₃ (wt.%)	400	16	Bulk R.	[10 ⁻² , 2·10 ³]	4.80	57	1.04·10 ⁻⁴	0.790	1.30·10 ⁻²	[39]
Ni						5.16	805	2.56·10 ⁻⁴	0.870	9.50·10 ⁻²	
Fe-5Cr (wt.%)						10.7	129	3.25·10 ⁻⁴	0.760	5.30·10 ⁻²	
Cr						3.89	6.98	0.280	0.420	170	
VM12	57 KNO ₃ + 30 LiNO ₃ + 13 NaNO ₃ (wt.%)	550	1000	Tensile specimen	[2·10 ⁻² , 10 ³]	NA	NA	7.90·10 ⁻³	0.590	NA	[71]
SS304	57 KNO ₃ + 13 NaNO ₃ + 30 LiNO ₃ (wt.%)	550	2	Bulk R.	[10 ⁻² , 10 ⁶]	2.15	8.10	5·10 ⁻²	0.980	47.6	[23]
			100			2.23	100	1·10 ⁻³	0.990	0.940	
Fe40Al0.5B (at.%)	(Li,K) ₂ CO ₃	650	48	Bulk R.	[10 ⁻² , 1.6·10 ³]	1.40	4.92	2.42·10 ⁻⁴	0.611	1.27·10 ⁻³	[86]
Pt	(Li,K) ₂ CO ₃	700	1	Bulk R.	[10 ⁻¹ , 10 ⁴]	2	176	4.13·10 ⁻³	0.703	0.540	
Ni21.2Al0.1B0.3Cr (at.%)	(Li,NaK) ₂ SO ₄	700	2	Bulk R.	[9·10 ⁻² , 4·10 ³]	0.87	0.5	8.70·10 ⁻²	0.740	24.7	

* R_s, R_{ct}, C_{dl} numerical values are reported with 3 significant digits except for integers. NA means no data available.

** “Bulk R.” is an abbreviation of a bulk rectangular specimen, representing a rectangular-shaped specimen that is partially submerged in molten salts.

*** It is noted that the C_{dl} are calculated using Eq. 19 based on the reported R_s and Q_{dl} values.

Theory

Quantifying Geometrically Induced NUCP Effects in R_{ct} and C_{dl} Measurements

Firstly, it is useful to define several parameters to quantify the non-uniform current and potential distribution effect with various electrode geometries. The Wagner parameter (W), given in Eq. 1, qualitatively describes the extent of non-uniform current distributions¹⁰⁷. When $W < 0.1$, the primary current distribution underlined by geometric factors (*e.g.*, edge effects) becomes predominant; whereas when $W > 10$, a more uniform “termed secondary” current distribution governed by finite Faradaic reactions and a finite comes into effect¹⁰⁷.

$$W = \frac{R_{ct}}{R_s} \quad (1)$$

For disk-shape electrode geometry, the R_s* (R_s that is not normalized by area) and R_s (normalized by area), with the units of Ω·cm², under primary current distribution can be expressed as a function of disk

radius (r_o) with the unit of cm and solution conductivity (κ) with the unit of $\Omega^{-1}\cdot\text{cm}^{-1}$ as indicated in Eq. 2 and Eq. 3 ¹²:

$$R_s^* = \frac{1}{4r_o\kappa} \quad (2)$$

$$R_s = \frac{\pi r_o}{4\kappa} \quad (3)$$

Another quantity is the dimensionless current density (J) ^{12,99}, expressed by Eq. 4. Note that J and W are inversely related as shown in Eq. 5 by combining Eq. 2 to Eq. 4:

$$J = \frac{1}{\pi r_o \kappa R_{ct}} \quad (4)$$

$$\frac{1}{W} = \frac{R_s}{R_{ct}} = \frac{1}{4r_o\kappa R_{ct}} = \frac{\pi J}{4} \quad (5)$$

Moreover, the frequency can also be normalized with respect to C_{dl} with the unit of F/cm^2 , r_o , and κ to produce a dimensionless frequency (K). From this, impedance measurement can be elaborated as a function of geometry, electrode kinetics, and ionic conductivity ^{12,112,113}.

$$K = \frac{2\pi C_{dl} r_o f}{\kappa} = \frac{\omega C_{dl} r_o}{\kappa} \quad (6)$$

Using Eq. 6, a critical frequency ($f_{c,disk}$) can be derived that marks the frequency onset in which the current and potential distribution begins to influence the impedance response derived by setting Eq. 6 to Eq. 1 (i.e. when $K = 1$) ¹²:

$$f_{critical}^{dispersion} = \frac{\kappa}{2\pi C_{dl} r_o} \quad (7)$$

Nisancioglu *et al.* ⁹⁹ developed and outlined a mathematical framework to calculate the errors associated with R_{ct} and C_{dl} on a flat flush mounted disk as a function of frequency. These errors are quantified in terms of the ratio of baseline to effective ECM parameter (*e.g.*, R_{ct}/R_{eff}), shown in Eq. 8 and Eq. 9, and are referred to as k_f^i in this work. The R_{eff} is a frequency-dependent, uncorrected, effective resistance that represents the R_{ct} measured or obtained by ECM fitting under the influence of NUCP distribution.

$$k_f^{Rct}(f) = \frac{R_{ct}}{R_{eff}(f)} = \frac{4}{\pi J} \left[\frac{B_{or}(f) - (B_{or}^2(f) + B_{oi}^2(f))}{(1 - B_{or}(f))^2 + B_{oi}^2(f)} \right] \quad (8)$$

$$k_f^{Cdl}(f) = \frac{C_{dl}}{C_{eff}(f)} = \frac{\pi K(f)}{4} \left[\frac{(1 - B_{or}(f))^2 + B_{oi}^2(f)}{B_{oi}(f)} \right] \quad (9)$$

where B_{or} and B_{oi} are the real and imaginary components of the coefficient B_n that is also frequency dependent. The subscript “o” represents the electrode surface where $z = 0$. B_n can be obtained by solving Eq. 10 using a matrix inversion technique suggested by Nisancioglu *et al.*⁹⁹, providing a series of k_f^{Cdl} and k_f^{Rct} complex coefficients that are frequency dependent.

$$\sum_{n=0}^{\infty} \left[a_{m,n} - \frac{\delta_{m,n}}{jK(f) + J} \frac{M'_{2m}(0)}{4m+1} \right] B_n(f) = a_{o,m} \quad (10)$$

here B_n represents coefficients in a series of complex potentials, $\delta_{m,n}$ as the Kronecker delta, and $M_{2n}(\varepsilon)$ as the Legendre polynomial and function of order $2n$ in which $\varepsilon = 0$, respectively. The mathematical definition of $M'_{2m}(0)$ and $a_{o,m}$ can be found from Nisancioglu *et al.*⁹⁹. In this work, B_n , k_f^{Cdl} , and k_f^{Rct} are solved as a function of r_o at selected disk areas of 10^{-2} , 10^{-1} and 10^0 cm² using the reported C_{dl} of FLiNaK, 600 °C. It is important to note the k_f^{Cdl} and k_f^{Rct} factors are derived based on an ideal and simplified Randles circuit by Nisancioglu *et al.*⁹⁹. Eq. 8 and Eq. 9 can be different when k_f^{Cdl} and k_f^{Rct} are derived based on more complex ECM models. Additionally, the following assumptions are applied¹²⁴: (1) electrode surface is smooth, active, and flush-mounted in an insulating and inert media; (2) the reference electrode is positioned far from the disk; (3) the effect of adsorption, desorption or ionic diffusion effects are neglected and the current density is responsible solely for changing C_{dl} and R_{ct} .

Simulating Impedance Responses Using ECM Models

The global impedance response of the disk electrode given a NUCP distribution effect is predicted. This is accomplished by simulating impedance spectra based on ECM models. To incorporate the effect of NUCP distribution, R_{eff} and C_{eff} in the ECM are calculated from Eq. 8 and Eq. 9, respectively, and expressed as frequency-dependent terms. With a known ECM model, the real (Z_{real}), imaginary (Z_{img}), and the absolute value of the impedance (Z_{mod}) as well as the phase angle can then be calculated. Literature research identified 5 ECM models, shown in Figure 1, used to study the impedance behavior of pure metals (*e.g.*, Cr, Ni, Fe) as well as alloys (316SS, 304SS, *etc.*) in molten chlorides, nitrates, fluorides, and sulfates^{18–86}. For each ECM, simulation is carried out at disk area of 10^{-2} , 10^{-1} , and 10^0 cm².

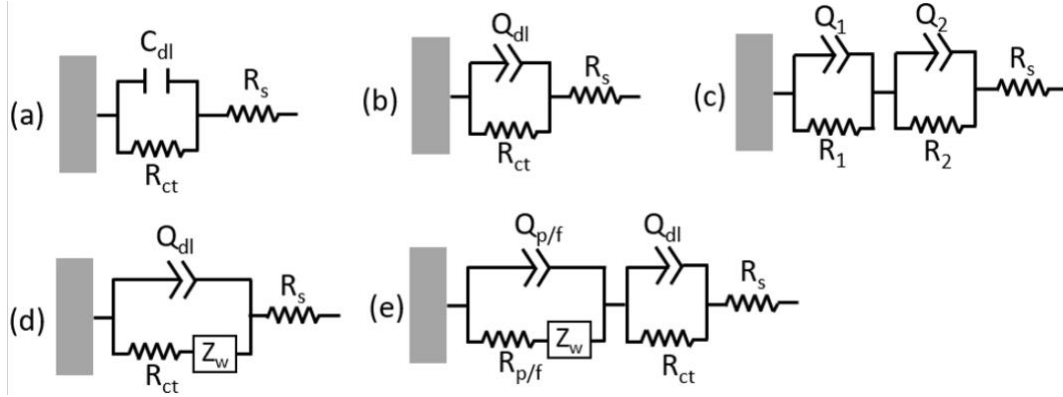


Figure 1. The different equivalent electrical circuits (ECMs) selected for EIS simulation in a molten salt system⁸⁷. (a) shows an ideal and simplified Randles circuit, (b) a simplified Randles circuit with a CPE, (c) shows two-time constants in series, termed “Two-time Constants”, (d) a Randles circuit with a diffusional impedance (Z_w), and (e) a Randles circuit in series with a second-time constant also containing a diffusional element.

Figure 1a, termed the “simplified Randles circuit” consists of a C_{dl} , R_{ct} and R_s . The R_s is calculated based on Eq. 3 at different radii. The global impedance (Z) and phase angle (θ) of Figure 1a can be calculated by Eq. 11 and Eq. 12, respectively:

$$Z = R_s + \frac{R_{ct}}{1 + j\omega R_{ct} C_{dl}} \quad (11)$$

$$\theta = \tan^{-1}\left(\frac{Z_i}{Z_r}\right) \quad (12)$$

where j is the imaginary number, Z_r and Z_i are the magnitude of real and imaginary impedance, respectively. Figure 1b displays the same circuit as Figure 1a except the capacitor is in place of a constant phase element (CPE), quantified by a pseudo resistive-capacitive term Q_{dl} and an unitless exponent α , due to the surface distribution of time constants^{90,113,125}. The Z of Figure 1b can be calculated *via*:

$$Z = R_s + \frac{R_{ct}}{1 + (j\omega)^\alpha R_{ct} Q_{dl}} \quad (13)$$

Both Figures 1a and 1b represent the scenario where the electrode is dissolving relatively uniformly under charge transfer (CT) control without any surface film regulating corrosion (*e.g.*, K_3CrF_6 film on Cr in FLiNaK¹²¹) nor the development of microporosity due to dealloying^{126–128}. Figure 1c, termed “two-time constants”, is used which consists of an additional time constant and is underlined by Eq. 14:

$$Z = R_s + \sum_{i=1}^2 \frac{R_i}{1 + (j\omega)^{\alpha_i} R_i Q_i} \quad (14)$$

It was also reported that, depending on the corrosion potential and salt fluid dynamics, interfacial dissolution can be mass-transport (MT) controlled by the ionic diffusion of corrosion products away from the metal/salt film interface, e.g. Cr(III) in chloride and fluoride salts^{15,97,121,129}. To account for this effect, a diffusional impedance element (Z_w) can be added in series with R_{ct} in both Figures 1b and 1c, resulting in Figures 1d and 1e, respectively. Z_w depends on the concentration profile and geometry of the electrode. Under a semi-infinite condition coupled with a planar concentration profile, the Warburg impedance term^{130–132} (Z_w^{planar}) can be used that is mathematically described by Eq. 15 and Eq. 16. Z_w applies when the diffusion boundary layer δ is much smaller than r_o .

$$Z_w^{planar} = \frac{\sigma}{\sqrt{j\omega}} = \sigma \omega^{-\frac{1}{2}} (1 - j) \quad (15)$$

$$\sigma = \frac{RT}{z^2 F^2 A} \left(\frac{1}{C_{ox} D_{ox}} + \frac{1}{C_{red} D_{red}} \right) \quad (16)$$

where σ is termed the Warburg coefficient with the unit $\Omega s^{-\frac{1}{2}}$, z is the number of oxidation states yielding electrons per ion or mol e^- (2.5 of z is used)¹⁵, F is the Faraday's constant of 96,485 coulomb/mol of e^- , R is the universal gas constant of 8.31 J/(mol·K), T is the temperature in Kelvin, A is the electrode area, C and D are the concentration and diffusivity of the oxidizing (Ox) and reducing (Red) species for each participating half-cell redox reaction during natural corrosion, respectively.

For a disk, the concentration profile of ionic species becomes hemispherical when $r_o < \delta$ and a different Z_w term is required. Fleischmann *et al.*^{102,103} utilize Neumann's integral theorem to solve the equations of diffusion impedance considering a three-dimensional Fick's second law, resulting in Eq. 17:

$$Z_w^{disk} = \frac{4RT}{\pi z^2 F^2 \sqrt{D} \omega r_o^2 C_o} \left(\varphi_4 \left(\frac{r_o^2 \omega}{D} \right) + \varphi_5 \left(\frac{r_o^2 \omega}{D} \right) j \right) \quad (17)$$

where $\varphi_4 \left(\frac{r_o^2 \omega}{D} \right)$ and $\varphi_5 \left(\frac{r_o^2 \omega}{D} \right)$ are frequency-dependent integers, which can be found in¹⁰³. Table 1 shows the ECM simulation parameters selected based on experimental results. The simulated impedance spectra of Figure 1a, 1d, and 1e (Z_w^{planar}) are illustrated in Figure S1. Simulation results are compared with experimental measurements of Cr exposed in FLiNaK, 600 °C when dissolution is CT and MT controlled. Lastly, a baseline is established for each ECM without k_f^i correction to simulate the impedance spectra of a bulk macroelectrode with an area of 1 cm².

Sensitivity Analysis of Fitting Errors

EIS fitting is performed on the simulated spectra in which the lower cutoff frequency (f_{cutoff}) is varied to determine the degree of error due to changing f_{cutoff} . This is performed using a commercially available

software package that adopts the maximum likelihood estimation method for fitting¹³³. For each optimized parameter, errors were assessed by computing a variance-covariance matrix that enables the standard errors to be derived for each optimized parameter¹³³.

$$\text{Percent Deviation} = \frac{R_{ct} \text{ with Fitting Error}}{\text{real}R_{ct}} \times 100 \quad (18)$$

Materials and Methods

Sample and Electrode Preparation

High purity Cr (99.995%, Goodfellow) was selected as the model working electrode (WE). In this work, five different electrode geometries were fabricated as shown in Figure 2: a macroelectrode (Figure 2a, $A = 1.9 \text{ cm}^2$) and two flushed-mounted disk electrodes (Figure 2b, disk A, 0.196 cm^2 and Figure 2c, disk B, 0.0136 cm^2). For the macroelectrode case in which the WE will be partially immersed in the molten salt, the Cr pieces were first machined into a dimension of $20 \pm 2 \times 5 \pm 1 \times 1.5 \pm 0.5 \text{ mm}$, and polished to a 1200 grit surface finish using a SiC paper.

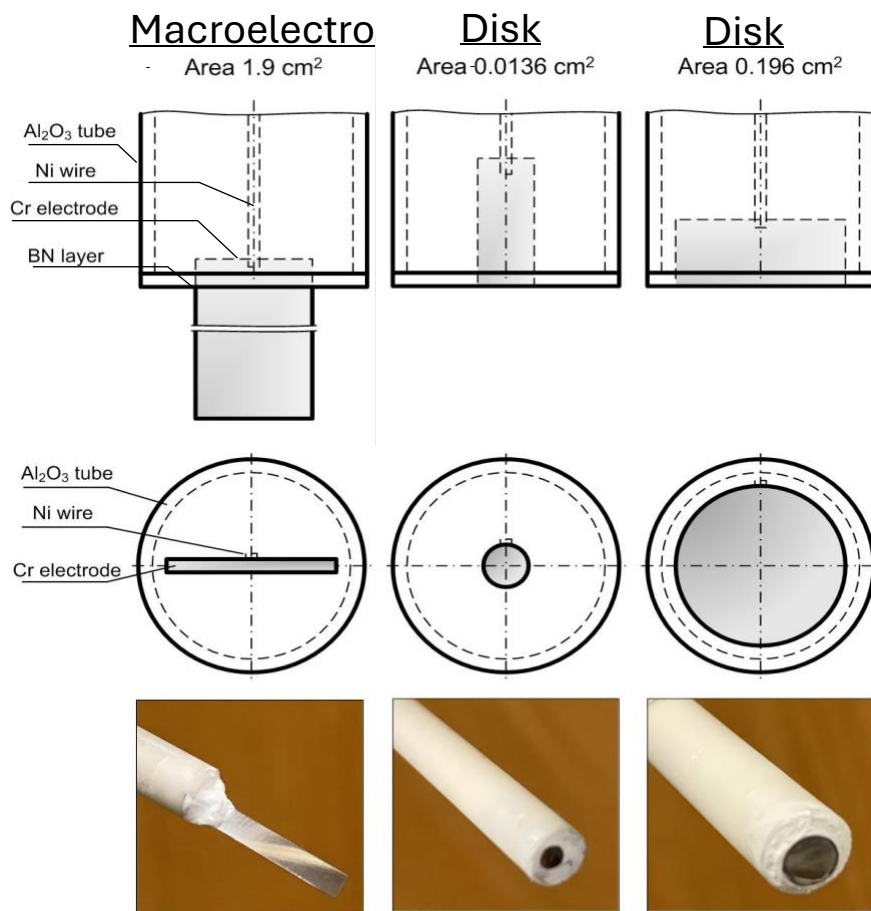


Figure 2. Cross-sectional and plan view schematics and optical micrographs of Cr working electrodes of different areas fabricated for molten FLiNaK electrochemistry.

One end of the electrode was then spot welded to a Ni200 wire, inserted into an alumina tube and sealed with a boron nitride (BN) paste (Graphite Store). The BN paste was subjected to thermal annealing in flowing industry grade N₂ at 100, 200, 300 and 600 °C for 2 h to remove trapped oxygen and moisture. For the disk electrode case wherein full immersion of WE is ensured, cylindrical Cr pieces were flush-mounted in an alumina tube. One end of each piece was spot-welded to a Ni200 wire and sealed with BN paste. Upon thermal annealing of BN paste, the disk electrodes were polished to 1200-grit surface finish using SiC paper. Noted, that a separate immersion test was carried out on as-dried BN paste in molten FLiNaK and no significant mass loss was detected after 24 h.

Salt Preparation

The eutectic LiF-NaF-KF (46.5-11.5-42 mol%) at 600°C, abbreviated as FLiNaK, is used as the model electrolyte. Each salt compound was separately obtained from a commercial vendor: LiF (99.99% purity, Fisher Scientific), NaF (99.9% purity, Fisher Scientific), and KF (>99.5% purity, Fisher Scientific). Each salt compound was first dried in a vacuum oven (Napco, USA) at 100 °C for 48 h and then transferred in a N₂-filled glove box (UNIlab MBraun, USA) controlled under O₂ and H₂O <0.1 ppm. The salt compound was weighted into the molar composition of FLiNaK, mixed, and thermally annealed/melted under the flow of ultra-high purity N₂ (99.999%) thermally at 600 °C for a minimum of 6 h. Additional purification was not performed, as maintaining consistent impurity levels across experiments was sufficient for the purpose of this work. For each electrochemical experiment, 1 wt.% of EuF₃ (99.5% purity, Sigma Aldrich) was added to the FLiNaK, serving as a controlled and common oxidizer to dissolve Cr^{122,134,135}.

Molten salt electrochemical cell

This work utilizes the identical molten salt electrochemical cell as our prior work^{15,123}. All electrochemical experiment is carried out in the glove box environment. A glassy carbon crucible (99.999%, Fisher Scientific) was used as both the salt container and counter electrode. A platinum wire (99.997%, Alfa AesarTM) was used as a quasi-reference electrode relying on a controlled O₂ level in the salt environment (Pt/PtO/O²⁻). Prior to exposing Cr, a separate Pt wire was inserted to measure the equilibrium K⁺/K potential using cyclic voltammetry (CV). The equilibrium K⁺/K potential was utilized as the dynamic reference potential and subsequent potential measurements on Cr were calibrated based on this value (Figure S2). The validation and optimization of CV method on K⁺/K potential measurement, *e.g.* thermodynamic calculation of K⁺/K with respect to F⁻/F₂, electrochemical stability of K⁺/K in FLiNaK, accessing sensitivity to scan rate, identifying optimal scan range, supporting reaction(s) on CE, comparison with galvanostatic studies, have been addressed in our previous work¹²³ as well as in literature¹³⁶⁻¹⁴⁰.

Molten salt electrochemistry

The Cr electrodes are exposed to FLiNaK + 1 wt.% EuF₃ at 600 °C under open-circuit condition for 24 h at 600 °C. EIS scan was performed at a frequency range between 10⁻² and 10⁴ Hz at the open-circuit potential (OCP) condition with an AC amplitude of 20 mV recorded at 10 points/decade. The EIS measurement was carried out at the 1 h and 24 h exposure period, corresponding to the CT and mass-transport controlled regime of Cr dissolution studied in our prior work^{15,92,121–123}. An ECM is utilized to describe the experimental impedance spectra. The C_{dl} is also estimated from each as-fitted EIS results using the Brug's relationship^{14,144}:

$$C_{dl} = Q^{\frac{1}{\alpha}} \left(\frac{1}{R_{ct}} + \frac{1}{R_s} \right)^{\frac{\alpha-1}{\alpha}} \quad (19)$$

Correction to the as-fitted ECM parameters relies on having a separately measured R_{ct} and C_{dl} as the baselines. The reference R_{ct} was calculated by Tafel extrapolation of linear sweep voltammogram¹⁵ of Cr in molten FLiNaK (See Figure S3 and Table S1), estimating a value of 4.74 Ω·cm². A reference C_{dl} was estimated by the differential capacitance method¹⁰⁵. This method relies on calculating the slope of differential current (Δi_{non-faradaic}) versus scan rates over a non-faradaic region. Measurements were carried out on a Pt wire over a scan rate from 5 mV/s to 500 mV/s over a 2 V range (Figure S4a), showing a C_{dl} of 13.3 ± 4.1 mF/cm² (Figure S4b).

Results

Simulated Impedance Under Charge-Transfer Regime

Figure 3 shows the calculated k_f^{Cdl} and k_f^{Rct} values based on the electrochemical properties of FLiNaK salts, 600 °C as a function of frequency and disk electrode area. The $f_{critical}^{dispersion}$ point, calculated *via* Eq. 7, marks the onset frequency above which the effect of NUCP starts having a large effect on R_{eff} deviating from baseline R_{ct}. As the electrode area decreases, $f_{critical}^{dispersion}$ is increased. Below $f_{critical}^{dispersion}$, the k_f^{Rct} stabilizes at approximately 1 (Figure 3a), indicating negligible error in measuring R_{ct}. However, the k_f^{Cdl} values exhibit a systematic error between 10 and 11. An increase in electrode area results in a slightly increased k_f^{Cdl} (despite this effect being-virtually negligible). For $f > f_{critical}^{dispersion}$, both k_f^{Rct} and k_f^{Cdl} values increase due to the decrease in the R_{eff} and C_{eff} values. The decrease in C_{eff} may imply an increased dominance of the capacitive behavior below the $f_{critical}^{dispersion}$, which is expected to contribute to the impedance behavior of the disk electrode. Figure 3 also suggests that in molten FLiNaK, NUCP distributions are likely not significant sources of systematic error in R_{ct} measurements when $f < f_{critical}^{dispersion}$.

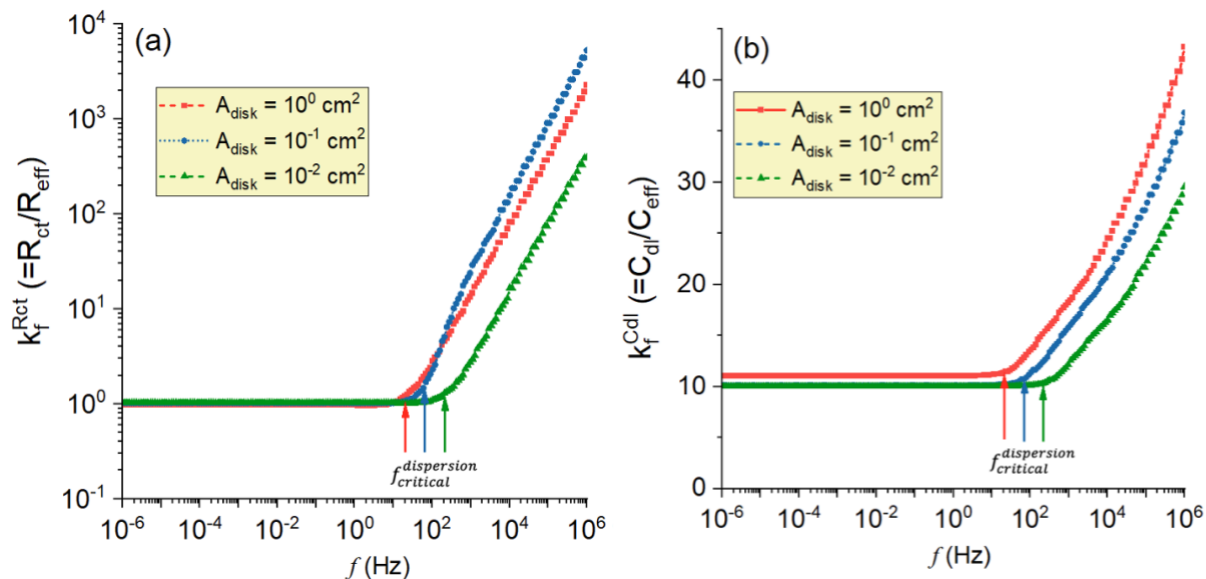


Figure 3. The errors of (a) charge-transfer resistance, R_{ct} and (b) double layer capacitance, C_{dl} calculated as a function of frequency at different disk electrode areas (A_{disk}) and a baseline C_{dl} of 13 mF/cm^2 . The vertical arrows mark the ohmic effect critical frequency ($f_{critical}^{dispersion}$).

Simulated and Experimental Impedance Under Charge-Transfer Regime

Figures 4a and 4b display the simulated Z_{mod} and phase angle response of a simplified Randles circuit (Figure 1b) comparing the behavior of a bulk macroelectrode (without k_f^i correction) and different areas of disk electrodes (with k_f^i correction) between 10^6 and 10^{-6} Hz. The simulated macroelectrode ($A=10^0 \text{ cm}^2$, dashed lines) exhibits a capacitive response due to DL between 10^0 and 10^4 Hz with the frequency of $2 \cdot 10^{-3}$ Hz marking the transition below which impedance is dominated by R_p (this frequency is referred as f_{trans}^{Rp}), which falls in a regime where experimental assessment is challenging^{18–86}. With the same electrode area of 10^0 cm^2 (solid lines) on a disk geometry, Figure 4a shows a three-order magnitude "horizontal shift" in impedance response: resulting in the capacitive regime (*i.e.* time-constant) to adjust to a higher frequency range and decreasing the f_{trans}^{Rp} to an experimentally accessible 10^{-1} Hz across all disk areas. As the electrode area decreases from 10^0 to 10^{-2} cm^2 , the capacitive frequency regime broadens over the medium-high frequency range between 10^1 and 10^4 Hz, with the peak of the phase angle decreasing from -42° to -60° . The increasing dominance of the capacitive response for disk electrodes is due to increasing k_f^{Cdl} and decreasing C_{eff} values, driven by the effects of NUCD. This trend is more pronounced with smaller electrode surface area. This shift also causes the R_s regime to be accessible at a higher frequency.

These observations remain similar when an additional time constant is connected in series (ECM of Figure 1c), as shown in Figures 4c and 4d. The second time constant is incorporated based on the impedance

parameters of a salt film or porous metal substrate layer in molten chlorides and fluorides¹⁵, and is only expected to dominate at a frequency regime lower than $5 \cdot 10^{-2}$ Hz based on simulation (Figure 4b). The presence of a second time constant also slightly decreases the f_{trans}^{Rp} (by a factor of 2 to 3) when comparing the Bode impedance plots between Figure 4a and 4b at each area (Figure S5). One implication for experimental analysis is that a second time constant is likely detectable across the typical experimental frequency range (10^{-2} to 10^4 Hz). However, since most molten salt EIS measurements do not extend below 10^{-2} Hz (See Discussion), ECM fitting based on Figure 1c may not yield an accurate fit with the reasonable physical meaning of each parameter.

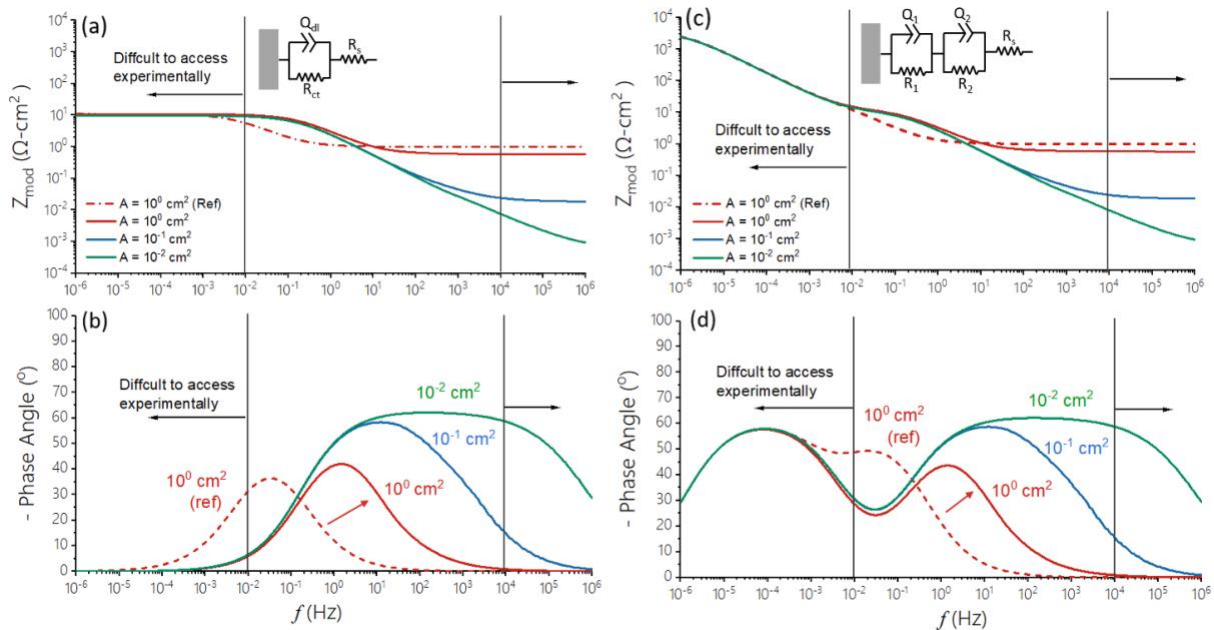


Figure 4. Simulated impedance spectra representing charge-transfer controlled interfacial dissolution of Cr in FLiNaK, 600 °C. The Bode impedance and phase angle plots of the (a,b) simplified Randles circuit and (c,d) two-time constant ECM models are displayed in the case of a disk area of 10^0 , 10^{-1} and 10^{-2} cm^2 . The dashed line shows a baseline case of 10^0 cm^2 with no k_f^i factors correction, labeled as “ref”. The grey vertical lines identify the frequency regime, 10^{-2} to 10^4 Hz, in which experimental measurement is routinely conducted. All simulation parameters are referenced in Table 1.

Figure 5 shows the Bode plots of Cr measured at 1 h after open-circuit exposure in molten FLiNaK containing 1 wt.% of EuF_3 at 600 °C from 10^4 and 10^{-2} Hz. At 1h of OCP exposure, the dissolution of Cr(0) to Cr(II) and then Cr(III) is favorable and charge-transfer regulated based on ref¹⁵. Figure 5a displays the raw Bode plots with different electrode geometries, revealing that the smallest disk ($1.29 \cdot 10^{-2}$ cm^2) exhibits the highest Z_{mod} . Upon normalizing with the surface area (Figure 5b), both disks A and B exhibit overlapping Bode plots in the mid to low-frequency regime (10^1 to 10^2 Hz) and a different R_s as predicted

by Eq. 3 due to ohmic dispersion effect⁹⁹. The contribution of R_s can also be subtracted as shown in Figure 5c, showing that the high to mid-frequency impedance (10^4 to 10^1 Hz) becomes practically identical.

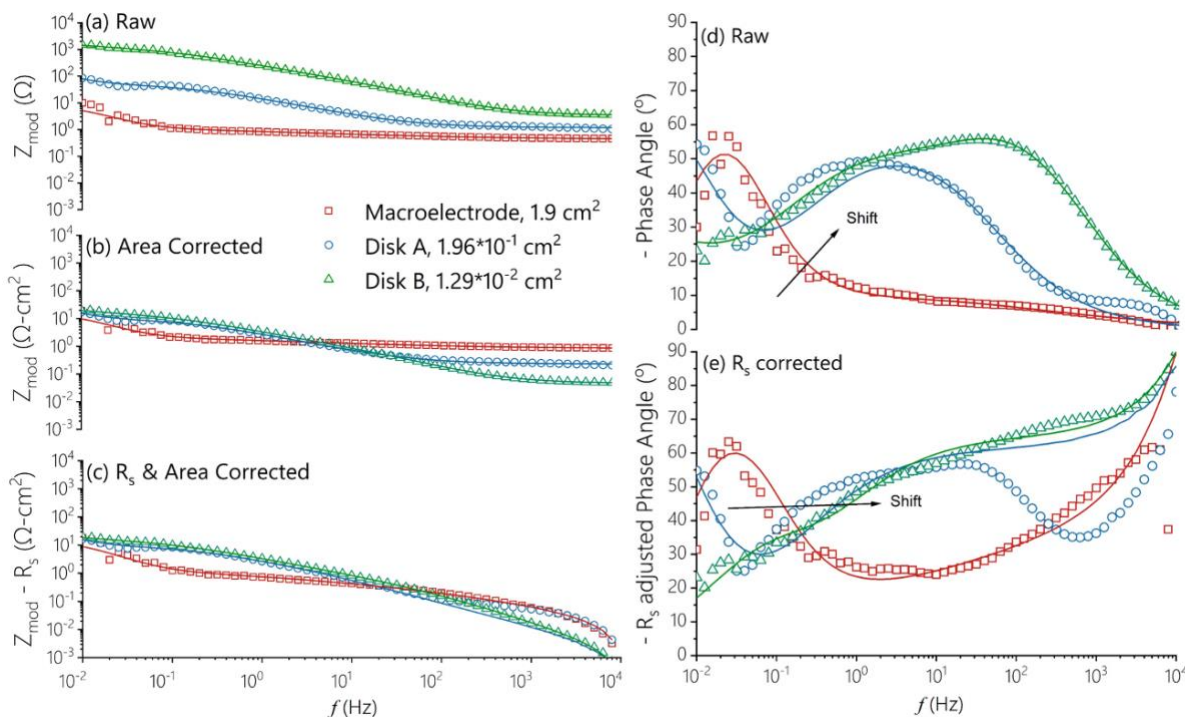


Figure 5. Experimental impedance spectra of Cr exposed in FLiNaK + 1 wt.% EuF_3 , 600 °C for 1 h. The Cr geometries are macroelectrode (1.9 cm^2) and two disk electrodes (Disk A: $1.96 \cdot 10^{-1}$ & Disk B: $1.29 \cdot 10^{-2} \text{ cm}^2$). The Bode impedance plots are shown in (a), (b), and (c), representing the raw, area corrected, and R_s and area corrected curves, respectively. The phase angle plots are shown in (d) and (e) displaying the raw and R_s corrected results, respectively. Symbols are the data and the solid lines are the fits.

As shown in Figures 5a-5c, the Bode modulus of disks A and B is dominated by the R_p regime below 10^{-1} Hz at Z_{mod} of $\sim 10 \text{ }\Omega\cdot\text{cm}^2$ and the phase angle approaches zero. In contrast, that of the macroelectrode is still dependent on frequency until the termination of EIS scan at 10^{-2} Hz (*i.e.* Z increases as f goes down and the phase angle is finite near but below its maximum at 60 degrees). The dependence of Z_{mod} with frequency in Figure 5 is attributed to the large $\sim \text{mF}/\text{cm}^2$ capacitance of the electrochemical double layer, which occurs and the frequency regime over which the dominance of R_p is not reached. Moreover, the phase angle plot (Figure 5d) reveals that the capacitive double layer regime (indicated by a broad peak) is shifted to a higher frequency, from $\sim 10^{-1}$ (macroelectrode) Hz to $\sim 10^0$ Hz (disk A) then to $\sim 10^1$ Hz (disk B), correlating with the EIS simulation performed in Figures 4b and 4d. This observation supports the notion that the use of disk electrodes in both areas enables the interrogation of R_p regime and even some capacitive behavior within the frequency range accessed while meeting the stationarity requirement of EIS. Moreover,

if an ECM is fitted to the macroelectrode spectra in Figure 5, the resulting R_p or R_{ct} value will likely not be reliable, and the capacitive fitting might also be a challenge.

The impedance spectra in Figure 5 can be fitted by the two-time constant ECM model (Figure 1c). The second time constant may be attributed to the formation of a μm -scale K_3CrF_6 salt film¹²¹, detectable but difficult to quantify accurately within the frequency range used in this work, as simulated in Figure 4c. The fitting results are provided in Table 2 along with the calculated R_{ct} , C_{dl} (w & w/o k_f correction) and W values. The k_f factor calculated in Figure 3 for both R_{ct} and C_{dl} can be applied to correct the as-fitted electrochemical parameters to obtain more fitting results. The fitting result of the macroelectrode shows an R_{ct} value of $451 \Omega \cdot \text{cm}^2$, markedly higher than the LSV extracted baseline value of $4.74 \Omega \cdot \text{cm}^2$ (Figure S3). For disks A and B, the post k_f corrected values ($9.77 \pm 2.98 \Omega \cdot \text{cm}^2$ and $5.76 \pm 0.96 \Omega \cdot \text{cm}^2$, respectively) closely align with this baseline. Additionally, the uncorrected C_{dl} values of 136 mF/cm^2 and 352 mF/cm^2 overestimate the baseline of $13.3 \pm 4.14 \text{ mF/cm}^2$. After correction by a k_f factor of 10, the C_{dl} values are adjusted to 13.6 mF/cm^2 and 14.4 mF/cm^2 , closely approximating the reference value. Additionally, the calculated W values: 1.77 for the macroelectrode, 42.2 for disk A, and 186 for disk B. The high W value of disks suggests that the current is primarily dominated by secondary current distributions¹⁰⁷. It is noted that only Q_2 and R_2 are k_f corrected as both likely represent Q_{dl} (*i.e.* C_{dl}) and R_{ct} , respectively, where Eq. 8 and Eq. 9 are applicable. Other ECM components may also be influenced by NUCP distribution, yet the derivation of their respective k_f terms is beyond the scope of this work.

Table 2. EIS fitting parameters for pure Cr in Molten FLiNaK salts + 1 wt.% EuF_3 , 600°C for 1hr under open-circuit condition

EIS Fit Parameters	Macro-electrode	Disk A		Disk B	
	As fitted	As fitted	k_f -corrected	As fitted	k_f -corrected
$R_s (\Omega \cdot \text{cm}^2)$	0.81 ± 0.01	0.23 ± 0.01	-	0.030 ± 0.01	-
a_1	1	1	-	0.55 ± 0.10	-
$Q_1 (\text{S} \cdot \text{s}^{\alpha-1} \cdot \text{cm}^2)$	1.53 ± 0.24	1.46 ± 0.06	-	0.15 ± 0.01	-
$R_1 (\Omega \cdot \text{cm}^2)$	0.40 ± 0.11	$3.78 \cdot 10^8 \pm 7.00 \cdot 10^5$	-	0.84 ± 0.05	-
a_2	0.47 ± 0.09	0.68 ± 0.01	-	0.88 ± 0.02	-
$Q_2 (\text{S} \cdot \text{s}^{\alpha-1} \cdot \text{cm}^2)$	0.32 ± 0.13	$(1.44 \pm 0.04) \cdot 10^{-2}$	$(1.45 \pm 0.04) \cdot 10^{-2}$	0.36 ± 0.17	0.04 ± 0.02
$R_2 (\Omega \cdot \text{cm}^2)$	$4.51 \cdot 10^6 \pm 1.00 \cdot 10^4$	9.67 ± 2.93	9.77 ± 2.98	5.65 ± 0.96	5.76 ± 0.98
$R_{ct} (\Omega \cdot \text{cm}^2)$	451	9.67	9.77	5.65	5.76
$C_{dl} (\text{mF/cm}^2)$	$1.26 \cdot 10^1$	$1.36 \cdot 10^2$	$1.36 \cdot 10^1$	$3.52 \cdot 10^2$	$1.44 \cdot 10^1$
$W = (R_{ct}/R_s)$	1.77	$4.22 \cdot 10^1$		$1.86 \cdot 10^2$	

Impedance Under Mass-Transport Controlled Regime

Figures 6a and 6b show the simulated Bode plots that incorporate the non-uniform current and potential distribution, based on the ECM model (Figure 1e) and use the diffusional impedance element developed for disk electrode ¹⁰³. Even when incorporated with a diffusional element with an ionic species concentration of 10^{-3} M, the spectra in Figures 6a and 6b demonstrate a striking resemblance to that of the two-time constants model (Figures 4c and 4d). Similarly, the NUCP effect associated with the disk geometry shifts the DL capacitive regime to a higher frequency range, resulting in a more negative phase angle (Figure 6b) as the disk electrode area decreases. The simulation also shows that the f_{trans}^{Rp} for the disk electrodes can be between 10^{-2} and 10^0 Hz. The presence of the diffusional element contributes to the Z_{mod} value, possibly leading to a slight overestimation of the R_{ct} value if an ECM analysis is to be performed.

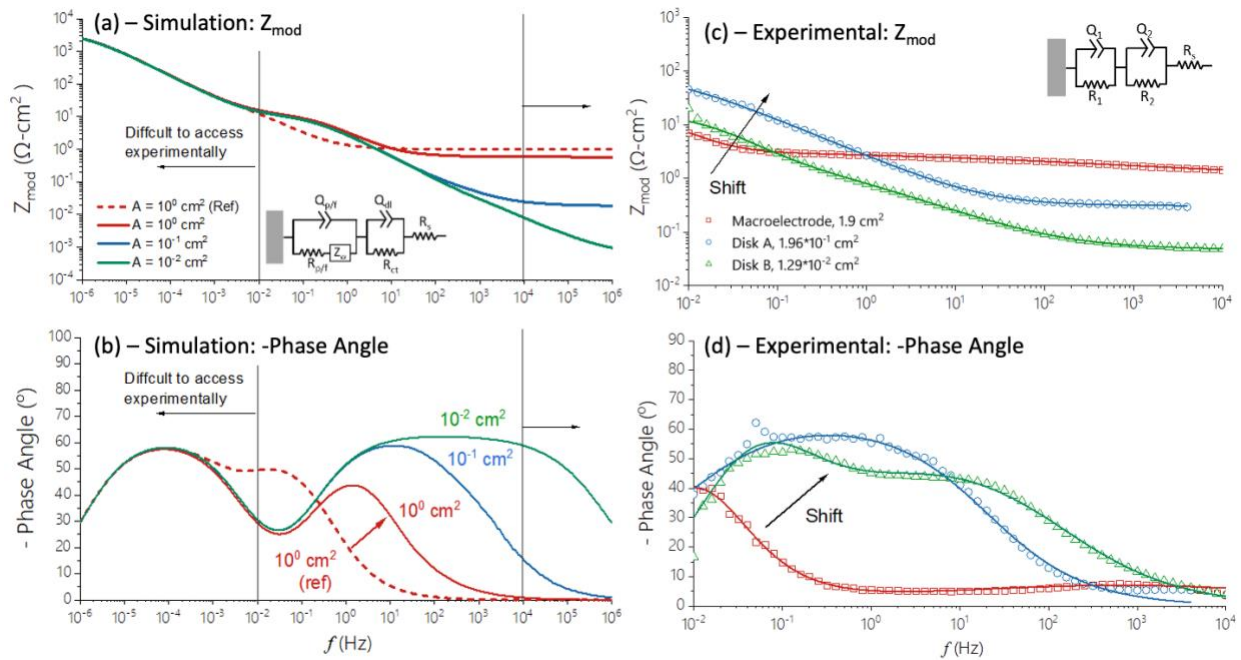


Figure 6. Simulated impedance spectra representing mass transport controlled interfacial dissolution of Cr in FLiNaK, 600 °C. The Bode impedance and phase angle plots in (a,b) are simulated spectra based on an ECM comprising of two-time constants containing the diffusional impedance of a disk (Figure 1e) with an assumed area of 10^0 , 10^{-1} and 10^{-2} cm^2 , and those in (c,d) are experimental measurements of Cr exposed in molten FLiNaK + 1 wt.% EuF_3 for 24h with different electrode geometries and areas. The dashed line reveals a baseline case of 10^0 cm^2 with no k_f^i factors correction, labeled as “ref”. The grey vertical lines the frequency regime, 10^{-2} to 10^4 Hz, in which experimental measurement is feasible

Figures 6c and 6d show the experimental impedance spectra of Cr exposed to molten FLiNaK + 1 wt.% EuF_3 for 24h at open-circuit conditions. Based on our prior work ¹⁵, the OCP of Cr after 24 h of exposure to impure FLiNaK corresponds to the potential regime in which the dissolution of Cr is rate-regulated by mass-transport of Cr(III) due to the presence of a salt film and bulk saturation of Cr(III). The two-time

constants ECM model (Figure 1c) shows good agreement with the experimental data. The as-fitted ECM parameters, along with the C_{dl} calculated with and without k_f correction of Q_{dl} (Q_2) are displayed in Table 3. Figures 6c and 6d show that the macroelectrode spectra are dominated by R_s entirely above 10^{-1} Hz, whereas disks A and B show a broad capacitive regime over the frequency range used. It is important to point out that the R_{ct} and C_{dl} values assumed in Figures 6a and 6b may deviate from practical assumption (e.g., the presence of Cr(III) ions can alter the C_{dl} ¹⁴² and/or a stable salt film may slow down charge-transfer and decrease R_{ct} ¹⁵), and thus the simulation results should only be regarded as a sensitivity analysis to interrogate NUCP effect in the presence of diffusional impedance. Addressing the multitude of variables involved in the case of mass-transport controlled dissolution is beyond of scope of this work and is therefore not discussed further.

Table 3. EIS fitting parameters for pure cr corroded in molten FLiNaK salts + 1 wt.% Euf₃, 600 °C for 24 h under open-circuit condition

EIS Fit Parameters	Macro-electrode	Disk A		Disk B	
	As fitted	As fitted	k_f -corrected	As fitted	k_f -corrected
R_s ($\Omega \cdot \text{cm}^2$)	1.25 ± 0.07	$(3.12 \pm 5.90) \cdot 10^{-1}$	-	$(8.33 \pm 2.22) \cdot 10^{-3}$	-
a_1	0.57 ± 0.08	0.81 ± 1.32	-	$0.64 \pm 4.79 \cdot 10^{-3}$	-
Q_1 ($S \cdot s^{a-1} \cdot \text{cm}^{-2}$)	0.03 ± 0.01	0.46 ± 0.18	-	$0.34 \pm 1.20 \cdot 10^{-2}$	-
R_1 ($\Omega \cdot \text{cm}^2$)	$2.04 \cdot 10^8 \pm 2.40 \cdot 10^6$	$1.17 \pm 2.80 \cdot 10^{-4}$	-	0.53 ± 0.99	-
a_2	0.69 ± 0.19	0.98 ± 0.11	-	$0.81 \pm 1.56 \cdot 10^{-2}$	-
Q_2 ($S \cdot s^{a-1} \cdot \text{cm}^{-2}$)	2.43 ± 1.89	$0.02 \pm 7.99 \cdot 10^{-3}$	$1.70 \cdot 10^{-3} \pm 8.00 \cdot 10^{-4}$	$(0.51 \pm 1.20) \cdot 10^{-2}$	$(0.05 \pm 1.20) \cdot 10^{-3}$
R_2 ($\Omega \cdot \text{cm}^2$)	2.32 ± 0.15	13.30 ± 5.98	13.40 ± 6.01	243 ± 0.99	247 ± 1.01
C_{dl} (mF/cm ²)	5.55	$4.46 \cdot 10^1$	4.27	$2.39 \cdot 10^2$	$1.37 \cdot 10^1$

Discussion

As shown in Table 1, most experimental EIS measurements conducted in the MS research community terminate at 10^{-2} Hz. With the use of a flush-mounted disk electrode, it is feasible to obtain an accurate R_{ct} value *via* ECM fitting over a wide range of disk area ($10^{-2} - 10^0 \text{ cm}^2$) when corrected for NUCP effect using the k_f factors. To enable the quantitative analysis of this process, it may be practical to calculate the transition frequency at which impedance response begins to be dominated by polarization resistance (f_{trans}^{Rct}). For an ideal and simplified Randles circuit (Figure 1a), f_{trans}^{Rct} is located at the point in the Bode impedance plot where $Z_{mod} = R_{CT} = Z_C$. This is illustrated in Figure S6 (analogous to the definition of cutoff frequency in bandpass filter design¹⁴³) and can be calculated *via* Eq. 19 (the derivation is detailed in Supplemental section):

$$f_{trans}^{Rct} = \frac{1}{2\pi\sqrt{3}} \frac{1}{R_{eff}C_{eff}} \quad (19)$$

It is important to point out the inverse relationship between f_{trans}^{Rct} and C_{dl} . As shown in Table 1, molten salts exhibit an experimental C_{dl} ranging from 10^{-1} to 10 mF/cm². Typically, the C_{dl} of room temperature aqueous solution ranges between 10^{-2} and 10^{-1} mF/cm²^{132,144,145}, and that of ionic liquid is even lower in the order of 10^{-3} mF/cm²^{125,146}. Thus, molten salt systems tend to have comparatively low f_{trans}^{Rct} which in some cases as discussed above make experimental studies challenging. When a disk electrode is employed, the R_{eff} and C_{eff} values can be corrected by the pre-determined, constant k_f^i values (below $f_{critical}^{dispersion}$) to incorporate and correct the effect of NUCP distribution, yielding Eq. 20. The same approach can be used to correct for the parameters obtained from ECM fitting as elucidated in later.

$$f_{trans}^{Rct} = \frac{1}{2\pi\sqrt{3}} \frac{1}{R_{ct}C_{dl}} (k_f^{Rct} k_f^{Cdl}) \quad (20)$$

Eq. 20 also shows that the extent of NUCP (*i.e.* the product of k_f^{Rct} and k_f^{Cdl}) also dictates the f_{trans}^{Rct} shift. Corrosion systems with a relatively resistive electrolyte (high R_s) and reactive electrode (low R_{ct}) exhibit a lower Wagner number which may result in a higher k_f^{Rct} and k_f^{Cdl} values^{99,105}. In this work, the Wagner number representing Cr in FLiNaK at 600°C ranges between 10^1 and 10^2 , yielding the values of k_f^{Rct} and k_f^{Cdl} close to 1 and 10, respectively, and thus minimal impact on disk area. An important insight is that flush-mounted disk likely has minimal to negligible “edge-effect” for current distribution in FLiNaK due to the proximity k_f^{Rct} to unity, possibly due to its high electrical conductivity. However, this behavior can be different for another electrode-electrolyte pair. Additionally, if a CPE is in place of an ideal capacitor, Eq. 21 can be used:

$$f_{trans}^{Rct} \approx \frac{1}{2\pi} \left(\frac{\cos(\frac{\alpha\pi}{2})}{R_{ct}Q_{dl}} \right)^{\frac{1}{\alpha}} (k_f^{Rct} k_f^{Cdl})^{\frac{1}{\alpha}} \quad (21)$$

The use of CPE slightly has a negligible effect on the f_{trans}^{Rct} value based on the simulation parameters used for this work (Figure S6). Eq. 21 can be modified for more complex ECMs and can be solved numerically. Experimentally, the EIS scan does not necessarily need to terminate at or below f_{trans}^{Rct} to obtain a R_{ct} value with 10% error, although the margin of errors should be taken into account. As illustrated in section 2.3, numerous commercial software programs adopt an optimization-based statistical parameter estimation based on a selected ECM to yield best-fit values with standard deviations to the entire spectrum. Given this context, it is helpful to quantify the error in terms of percent variations (Eq. 18) as a function of

the lower termination frequency (f_{cutoff}), which is the independent variable for this analysis. This analysis was conducted on the simulated impedance spectra in the charge-transfer controlled dissolution, as depicted in Figure 4, with the results presented in Figure 7.

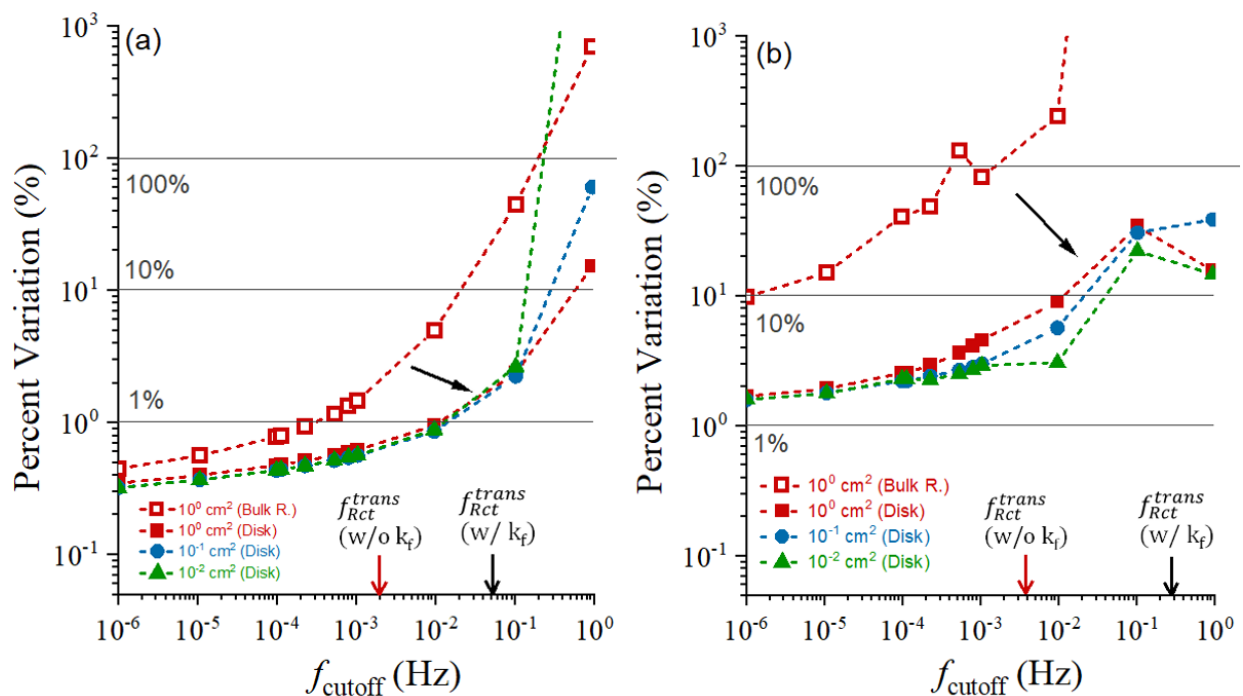


Figure 7. Percent variation as a function of lower termination frequency (f_{cutoff}) selected for ECM fitting analysis. The fitting processes are performed on the simulated impedance spectra constructed based on the (a) simplified Randles circuit (Figures 4a & 4b) and (b) two-time constants (Figure 4c and 4d) ECM models for both bulk rectangular (Bulk R) and disk geometries. The down arrow on (a) and (b) indicates the f_{Rct}^{trans} with and without k_f correction.

Figure 7a shows the percent variations for fitting impedance spectra in Figures 4a and 4b as a function of frequency relative to f_{Rct}^{trans} . For the bulk electrode, with a baseline R_{ct} of 10 $\Omega \cdot \text{cm}^2$ and C_{dl} of 10 mF/cm², a f_{cutoff} of 10⁰, 10⁻¹ and 10⁻² Hz results in 706%, 44.6%, 4.98% of deviation, respectively. Below 10⁻⁴ Hz, the percent deviation falls below 1%. By contrast, when a disk electrode is employed, a discernible rightward shift in the percent variation curve is observed which pushes the cut-off frequency to a higher level. Regardless of disk areas, negligible differences in error are observed among the disk electrode sizes, with errors maintained below 1% until the f_{cutoff} reaches 10⁻² Hz. Even at a relatively moderate frequency of around 10⁻¹ Hz, errors remain below 10%, suggesting a tolerable deviation level. However, beyond this frequency, errors intensify significantly, surpassing 100% at approximately 10⁰ Hz, indicating a substantial deviation from the established reference value. It is noted that the smallest disk electrode size (10⁻² cm²)

exhibits a disproportionately higher error sensitivity to changes in f_{cutoff} compared to the larger sizes. Conversely, the largest disk electrode size (1 cm²) demonstrates less sensitivity to such variation.

Figure 7b displays the percent deviation when the fitting analysis is applied to Figures 4c and 4d (*i.e.* constructed by the two-time constants model). Compared with Figure 7a, the bulk electrode in this case exhibits an overall higher percent deviation, ranging from 10% at 10⁻⁶ Hz to 82.3% at 10⁻³ Hz, with the deviation exceeding 100% above 10⁻² Hz. For disk electrodes, a similar reduction in overall percent deviation is observed, with a more pronounced rightward shift in this case. Notably, the percent deviation remains below 10% at 10⁻² Hz and below 50% even at 10⁰ Hz. Moreover, it also appears that the smaller disk electrodes exhibit increasingly fewer percent deviations.

The analysis presented in Figure 7 demonstrates that using a disk electrode significantly reduces the percent deviation resulting from the optimization-based statistical ECM fitting process which ensures best fits using all the data, maintaining deviations below 10% at the conventional f_{cutoff} of 10⁻² Hz for two commonly used EC< circuits for molten salt corrosion studies. The susceptibility to errors of a bulk electrode depends on the complexity of the corrosion interface behavior, as reflected by the selected ECM models. Particularly in ECM configurations with two-time constants, achieving reliable results is challenging if f_{cutoff} does not extend to 10⁻³ Hz, a condition not typically met in most experimental studies (Table 1). For the selected model molten salt corrosion system (Cr in FLiNaK, 600 °C), which exhibits a high C_{dl} and R_s , the percent deviation appears to not be significantly impacted by the disk area. This finding also provides a critical insight that with a flush-mounted electrode of a wide area range (10⁰–10⁻² cm²), the conventional f_{cutoff} of 10⁻² Hz is possible to yield a relatively reliable R_{ct} value *via* the ECM fitting analysis under these conditions.

Given the rising interest in adopting EIS methods for molten salt corrosion studies (Table 1), developing a metric to evaluate the quality of ECM fitting is beneficial, particularly in guiding the selection of frequency range and electrode geometry optimal for corrosion analysis. Firstly, it is important to independently obtain and/or estimate the values of R_{ct} and C_{dl} using methods such as correlating corrosion rates with mass loss¹²¹, impedance or differential capacitance measurements on planar blocking electrode^{105,125,147}, and/or comparing with computational simulations¹⁴². While these methods also suffer from their respective shortfalls in yielding the exact baseline values of R_{ct} and C_{dl} , they allow f_{trans}^{Rct} (Eq. 19), and thus the necessary f_{cutoff} for polarization resistance measurements to be estimated. In cases where C_{dl} or the product of R_{ct} and C_{dl} are high, a bulk rectangular electrode geometry may be sufficient. An excellent EIS fit can be achieved when f_{cutoff} is lower than f_{trans}^{Rct} . Secondly, depending on the required f_{cutoff} relative to the experimental capability, it may be necessary to employ a flush-mounted electrode to induce a lower effective capacitance, shifting the polarization resistance regime using the effect of NUCP. It is noted that

the mounting medium must be inserted and insulating media, such as alumina for chloride salts and boron nitride for fluoride salts¹⁰⁴. The effect of NUCP can be quantitatively determined by the $k_f^{Rct} (= R_{ct}/R_{eff})$ and $k_f^{Cdl} (= C_{dl}/C_{eff})$ factors obtained by solving the mathematical framework outlined in Nisancioglu *et al.*⁹⁹ (e.g., Eqs. 8-10). The values of k_f^{Rct} and k_f^{Cdl} will above $f_{critical}^{dispersion}$ (Eq.7)¹² but their impacts vary depending on the ECM models. They can also be used to correct the effective electrochemical parameters obtained from conventional ECM fittings. Yet, the k_f^{Rct} and k_f^{Cdl} factors need to be redetermined. Thirdly, if the f_{trans}^{Rct} is experimentally unattainable, it can be useful to perform a sensitivity analysis analogous to that in Figure 7 that correlates the percent variation and experimental terminational frequency to evaluate the acceptability of the fitted data.

Conclusions

In this work, EIS was performed on Cr in molten FLiNaK containing 1 wt% EuF₃ at 600 °C. By aggregating > 95 published molten salt EIS data points and comparing with results from this work, molten salts, particularly FLiNaK, exhibit experimental Cdl in orders of 100 to 101 mF/cm², which is high relative to room temperature aqueous and ionic liquid systems. Such high Cdl when coupling with low Rct renders the Rp dominant regime to below 10⁻² Hz. In this work, a flush-mounted disk WE configuration is proposed, evaluated and validated to facilitate corrosion studies. Based on these results, the following findings can be concluded:

- The use of a flush-mounted Cr disk with areas between 10⁻² and 10⁰ cm² has shown the capability to shift the Rp regime to 10⁻² Hz, enabling the Rp dominant regime to be interrogated experimentally. Experimental results were validated with EIS simulations constructed based on several ECMs commonly used for molten salt corrosion studies, for both bulk rectangular and disk electrode geometries.
- The Rct values can thus be extracted using conventional ECM fitting analysis. However, due to the presence of non-uniform current and potential distribution effects, as-fitted data must be normalized with correction factors, termed $k_f^{Rct} (= R_{ct}/R_{eff})$ and $k_f^{Cdl} (= C_{dl}/C_{eff})$ below $f_{critical}^{dispersion}$, which are detailed by Nisancioglu *et al.*⁹⁹. In the case of Cr in FLiNaK at 600 °C, the k_f^{Rct} and k_f^{Cdl} are found to be nearing 1 and 10, respectively. The influence of primary current distribution on a disk electrode, e.g. edge-effect, is minimal for Cr in FLiNaK at 600 °C due to the high ionic conductivity of FLiNaK, correlating with a Wagner number in the order of 100.

- EIS simulation and experiments were also performed for Cr dissolving under the mass-transport controlled regime in FLiNaK. Simulation results support prior observation and also indicate that the influence of a potential K-Cr-F-based salt film (that gives rise to a second time constant) and ionic diffusional impedance will not be predominant at 10^{-2} Hz, for both bulk rectangular and disk electrodes.
- The simulated EIS spectra were subjected to a sensitivity analysis that correlates the percent deviation of ECM fitted data, obtained via a commercially available optimization-based statistical analysis approach, relative to the frequency in which the EIS scan terminates. Results suggest that using a disk electrode significantly limits percent deviations, maintaining them below 10 % at the conventional termination frequency of 10^{-2} Hz on two commonly used ECM circuits. The bulk rectangular electrode is highly susceptible to fitting errors depending on the ECM complexity.
- Lastly, recommendations were made for the design of EIS experiments in molten salts, notably deriving an equation to estimate the required transition frequency (f_{trans}^{Rct}) below which EIS response is dominated by polarization resistance and by calculating the critical frequency ($f_{critical}^{dispersion}$) above which non-uniform current and potential distribution effects become predominant, informing the optimal point to terminate the EIS scan.

Glossary

Variable	Unit	Equation*	Description
R_{ct}	$\Omega \cdot \text{cm}^2$	Eq. 1	Charge-transfer resistance
R_s	$\Omega \cdot \text{cm}^2$	Eq. 1	Solution resistance normalized by area
R_s^*	Ω	Eq. 2	Solution resistance
r_o	cm	Eq. 2	Disk radius
κ	$\Omega^{-1} \cdot \text{cm}^{-1}$	Eq. 2	Solution conductivity
R_p	$\Omega \cdot \text{cm}^2$	-	Polarization resistance
J	unitless	Eq. 4	Dimensionless current density
W	unitless	Eq. 5	Wagner Number
K	unitless	Eq. 6	Dimensionless frequency
ω	Hz	Eq. 6	Angular frequency
f	Hz	Eq. 6	Frequency
C_{dl}	F/cm ²	Eq. 6	Double-layer capacitance
$f_{critical}^{dispersion}$	Hz	Eq. 7	Critical frequency for ohmic dispersion
k_f^{Rct}	unitless	Eq. 8	Frequency dependent correction factor for R_{ct}
R_{eff}	$\Omega \cdot \text{cm}^2$	Eq. 8	Effective resistance due to NUCP distribution effect
B_{or}	unitless	Eq. 8	Real component of B_n where B.C. is set at electrode surface
B_{oi}	unitless	Eq. 8	Imaginary component of B_n where B.C. is set at electrode surface

k_f^{cdl}	unitless	Eq. 9	Frequency dependent correction factor for C_{dl}
C_{eff}	F/cm ²	Eq. 9	Effective capacitance due to NUCP distribution effect
B_n	unitless	Eq. 10	Frequency dependent complex integer
j	unitless	Eq. 11	Imaginary Number
Z_i	$\Omega \cdot \text{cm}^2$	Eq. 12	Imaginary impedance
Z_r	$\Omega \cdot \text{cm}^2$	Eq. 12	Real impedance
Z_{mod}	$\Omega \cdot \text{cm}^2$	-	Total impedance
Q_{dl}	$\text{S} \cdot \text{cm}^{-2} \cdot \text{sec}^{-1}$	Eq. 13	Constant phase element equivalence capacitance
α or a	unitless	Eq. 13	Constant phase element exponent
Z_w	$\Omega \cdot \text{cm}^2$	Eq. 15	Diffusional impedance
σ	Ω/sec^{-1}	Eq. 16	Warburg coefficient
C	mol/cm ³	Eq. 16	Concentration
D	cm ² /s	Eq. 16	Diffusivity
z	mol e ⁻	Eq. 16	Number of oxidation state yielding electrons per mol of ions
F	coulomb/mol e ⁻	Eq. 16	Faraday's constant
A	cm ²	Eq. 16	Area
φ_4	Unitless	Eq. 17	Frequency dependent integers for disk electrode diffusional impedance
φ_5	Unitless	Eq. 17	Frequency dependent integers for disk electrode diffusional impedance
f_{trans}^{Rct}	Hz	Eq. 19	Transition frequency for polarization resistance regime
f_{cutoff}	Hz	-	Lower end cutoff frequency in which EIS scan is terminated

References

1. J. Braunstein, G. Mamantov, G.P. Smith (Eds.), *Advances in Molten Salt Chemistry*, Springer US, Boston, MA, 1971 <https://doi.org/10.1007/978-1-4757-0504-1>.
2. J. Braunstein, G. Mamantov, G.P. Smith (Eds.), *Advances in Molten Salt Chemistry*, Springer US, Boston, MA, 1973 <https://doi.org/10.1007/978-1-4757-0662-8>.
3. J. Braunstein, G. Mamantov, G.P. Smith (Eds.), *Advances in Molten Salt Chemistry*, Springer US, Boston, MA, 1975 <https://doi.org/10.1007/978-1-4615-8270-0>.
4. S. Bell, T. Steinberg, G. Will, Corrosion mechanisms in molten salt thermal energy storage for concentrating solar power, *Renew. Sustain. Energy Rev.* 114 (2019) 109328, <https://doi.org/10.1016/j.rser.2019.109328>.
5. P. Denholm, M. Mehos, Enabling Greater Penetration of Solar Power via the Use of CSP with Thermal Energy Storage. Technical Report NREL/TP-6A20-52978, November 2011, 2011 <https://www.nrel.gov/docs/fy12osti/52978.pdf>.
6. J. Serp, M. Allibert, O. Beneš, S. Delpech, O. Feynberg, V. Ghetta, D. Heuer, D. Holcomb, V. Ignatiev, J.L. Kloosterman, L. Luzzi, E. Merle-Lucotte, J. Uhlíř, R. Yoshioka, D. Zhimin, The molten salt reactor (MSR) in generation IV: Overview and perspectives, *Prog. Nucl. Energy* 77 (2014) 308–319, <https://doi.org/10.1016/j.pnucene.2014.02.014>.
7. T. Bauer, C. Odenthal, A. Bonk, Molten salt storage for power generation, *Chem. Ing. Tech.* 93 (2021) 534–546, <https://doi.org/10.1002/cite.202000137>.
8. H. Liu, X. Zhang, S. He, D. He, Y. Shang, H. Yu, Molten salts for rechargeable batteries, *Mater. Today* 60 (2022) 128–157, <https://doi.org/10.1016/j.mattod.2022.09.005>.
9. S.S. Raiman, S. Lee, Aggregation and data analysis of corrosion studies in molten chloride and fluoride salts, *J. Nucl. Mater.* 511 (2018) 523–535, <https://doi.org/10.1016/j.jnucmat.2018.07.036>.
10. S. Guo, J. Zhang, W. Wu, W. Zhou, Corrosion in the molten fluoride and chloride salts and materials development for nuclear applications, *Prog. Mater. Sci.* 97 (2018) 448–487, <https://doi.org/10.1016/j.pmatsci.2018.05.003>.

11. R.N. Wright, T.-L. Sham, Status of Metallic Structural Materials for Molten Salt Reactors, Idaho National Lab. (INL), Idaho Falls, ID (United States), 2018. Argonne National Lab. (ANL), Argonne, IL (United States). <https://doi.org/10.2172/1467482>.
12. M.E. Orazem, B. Tribollet, *Electrochemical Impedance Spectroscopy*, John Wiley & Sons Inc, 2008.
13. M.E. Orazem, B. Tribollet, A tutorial on electrochemical impedance spectroscopy, *ChemTexts* 6 (2020) 12, <https://doi.org/10.1007/s40828-020-0110-7>.
14. J. Han, H. Lun Chan, M.G. Wartenberg, H.H. Heinrich, J.R. Scully, Distinguishing interfacial double layer and oxide-based capacitance on gold and pre-oxidized Fe-Cr in 1-ethyl-3-methylimidazolium methanesulfonate room temperature ionic liquid aqueous mixture, *Electrochem. Commun.* (2020) 106900, <https://doi.org/10.1016/j.elecom.2020.106900>.
15. H.L. Chan, E. Romanovskaia, V. Romanovski, D. Sur, M. Hong, P. Hosemann, J.R. Scully, Corrosion electrochemistry of chromium in molten FLiNaK salt at 600°C, *J. Electrochem. Soc.* 170 (2023) 081502, <https://doi.org/10.1149/1945-7111/ad6037>.
16. G.L. Fredrickson, G. Cao, P.K. Tripathy, M.R. Shaltry, S.D. Herrmann, T.-S. Yoo, T.Y. Karlsson, D.C. Horvath, R. Gakhar, A.N. Williams, R.O. Hoover, W.C. Phillips, K.C. Marsden, Review—electrochemical measurements in molten salt systems: a guide and perspective, *J. Electrochem. Soc.* 166 (2019) D645–D659, <https://doi.org/10.1149/2.0991913jes>.
17. M. Mierzejewski, H. Steins, P. Kshirsagar, P.D. Jones, The noise and impedance of microelectrodes, *J. Neural Eng.* (2020) 17 052001, <https://doi.org/10.1088/1741-2552/abb3b4>.
18. L. Crevelt, Investigation of Corrosion Mechanisms Between Molten Eutectic FLiNaK Salt and 316L Stainless Steel, University of Illinois Urbana-Champaign, 2022.
19. W. Doniger, C. Falconer, A. Couet, K. Sridharan, Corrosion of 316L & 316H stainless steel in molten LiF-NaF-KF (FLiNaK), *J. Nucl. Mater.* 579 (2023) 154383, <https://doi.org/10.1016/j.jnucmat.2023.154383>.
20. V. Encinas-Sánchez, M.T. De Miguel, M.I. Lasanta, G. García-Martín, F.J. Pérez, Electrochemical impedance spectroscopy (EIS): An efficient technique for monitoring corrosion processes in molten salt environments in CSP applications, *Sol. Energy Mater. Sol. Cells* 191 (2019) 157–163, <https://doi.org/10.1016/j.solmat.2018.11.007>.
21. V. Encinas-Sánchez, M.I. Lasanta, M.T. De Miguel, G. García-Martín, F.J. Pérez, Corrosion monitoring of 321H in contact with a quaternary molten salt for parabolic trough CSP plants, *Corros. Sci.* 178 (2021) 109070, <https://doi.org/10.1016/j.corsci.2020.109070>.
22. Y. Gu, W. Zhang, Y. Xu, Y. Shi, K. Volodymyr, Stress-assisted corrosion behaviour of Hastelloy N in FLiNaK molten salt environment, *npj Mater. Degrad.* 6 (2022) 90, <https://doi.org/10.1038/s41529-022-00300-x>.
23. A. Mallco, A.G. Fernández, Corrosion Monitoring Assessment on Lithium Nitrate Molten Salts as Thermal Energy Storage Material Applied to CSP Plants, *Oxid. Met.* 94 (2020) 383–396, <https://doi.org/10.1007/s11085-020-09997-0>.
24. L. Olson, K. Sridharan, M. Anderson, T. Allen, Intergranular corrosion of high temperature alloys in molten fluoride salts, *Mater. High Temp.* 27 (2010) 145–149, <https://doi.org/10.3184/096034010X12743509428336>.
25. F.-Y. Ouyang, C.-H. Chang, J.-J. Kai, Long-term corrosion behaviors of Hastelloy-N and Hastelloy-B3 in moisture-containing molten FLiNaK salt environments, *J. Nucl. Mater.* 446 (2014) 81–89, <https://doi.org/10.1016/j.jnucmat.2013.11.045>.
26. F.-Y. Ouyang, C.-H. Chang, B.-C. You, T.-K. Yeh, J.-J. Kai, Effect of moisture on corrosion of Ni-based alloys in molten alkali fluoride FLiNaK salt environments, *J. Nucl. Mater.* 437 (2013) 201–207, <https://doi.org/10.1016/j.jnucmat.2013.02.021>.
27. T.J. Pan, W.M. Lu, Y.J. Ren, W.T. Wu, C.L. Zeng, Electrochemical-Impedance-Spectroscopy Study of Corrosion of Steels 12CrMoV and SS304 Beneath a Molten ZnCl₂-KCl Film at 400 °C in Air, *Oxid. Met.* 72 (2009) 179–190, <https://doi.org/10.1007/s11085-009-9154-1>.
28. K. Patel, C. Mahajan, S. Muskeri, S. Mukherjee, Corrosion behavior of refractory high-entropy alloys in FLiNaK molten salts, *Metals* 13 (2023) 450, <https://doi.org/10.3390/met13030450>.
29. N.S. Patel, V. Pavlík, B. Kubíková, M. Nosko, V. Danielík, M. Bořca, Corrosion behaviour of Ni-based superalloys in molten FLiNaK salts, *Corros. Eng. Sci. Technol.* 54 (2019) 46–53, <https://doi.org/10.1080/1478422X.2018.1525829>.
30. F.J. Pérez, V. Encinas-Sánchez, M.I. Lasanta, M.T. De Miguel, G. García-Martín, Corrosion monitoring of ferritic-martensitic steels in molten salt environments for CSP applications, in: Casablanca, Morocco, 2019: p. 030040.

31. J. Qiu, B. Leng, H. Liu, D.D. Macdonald, A. Wu, Y. Jia, W. Xue, G. Yu, X. Zhou, Effect of SO₂ on the corrosion of 316L stainless steel in molten FLiNaK salt, *Corros. Sci.* 144 (2018) 224–229, <https://doi.org/10.1016/j.corsci.2018.08.057>.
32. J. Qiu, D.D. Macdonald, R. Schoell, J. Han, S. Mastromarino, J.R. Scully, D. Kaoumi, P. Hosemann, Electrochemical study of the dissolution of oxide films grown on type 316L stainless steel in molten fluoride salt, *Corros. Sci.* 186 (2021) 109457, <https://doi.org/10.1016/j.corsci.2021.109457>.
33. K.M. Sankar, P.M. Singh, Effect of Li metal addition on corrosion control of Hastelloy N and stainless steel 316H in molten LiF-NaF-KF, *J. Nucl. Mater.* 555 (2021) 153098, <https://doi.org/10.1016/j.jnucmat.2021.153098>.
34. L. Tao, D. Jiasheng, X. Guang, W. Yisheng, L. Hui, L. Zhijun, Z. Xingtai, L. Langhong, Corrosion behavior of GH3535 superalloy in FLiNaK molten salt. *Acta Metallurgica Sinica* 51(9), 1059-1066. <https://doi.org/10.11900/0412.1961.2014.00357>.
35. Y. Wang, C. Wang, J. Wu, The effect of graphite on the corrosion of Hastelloy N in molten fluorides, *J. Nucl. Mater.* 557 (2021) 153277, <https://doi.org/10.1016/j.jnucmat.2021.153277>.
36. G. Yamazaki, T. Nagasaka, T. Tanaka, T. Goto, J. Shen, K. Saito, M.I. Kobayashi, Corrosion of pure Cr and W in molten FLiNaK with hydrogen fluoride solution, *Fusion Eng. Des.* 172 (2021) 112741, <https://doi.org/10.1016/j.fusengdes.2021.112741>.
37. M. Zhu, S. Zeng, H. Zhang, J. Li, B. Cao, Electrochemical study on the corrosion behaviors of 316 SS in HITEC molten salt at different temperatures, *Sol. Energy Mater. Sol. Cells* 186 (2018) 200–207, <https://doi.org/10.1016/j.solmat.2018.06.044>.
38. A.G. Fern´andez, A. Rey, I. Lasanta, S. Mato, M.P. Brady, F.J. P´erez, Corrosion of alumina-forming austenitic steel in molten nitrate salts by gravimetric analysis and impedance spectroscopy, *Mater. Corros.* 65 (2014) 267–275, <https://doi.org/10.1002/maco.201307422>.
39. G. Zhao, Y. Han, L. Yang, Y. Wang, C. Zeng, Electrochemical impedance study of corrosion of pure Ni, Fe, Cr, and Fe-5Cr alloy in molten nitrides, *Mater. Corros.* 75 (2024) 589–598, <https://doi.org/10.1002/maco.202314166>.
40. H. Ai, S. Liu, X.-X. Ye, L. Jiang, B. Zhou, X. Yang, B. Leng, Z. Li, Metallic impurities induced corrosion of a Ni-26W-6Cr alloy in molten fluoride salts at 850°C, *Corros. Sci.* 178 (2021) 109079, <https://doi.org/10.1016/j.corsci.2020.109079>.
41. H. Ai, M. Shen, H. Sun, K.P. Dolan, C. Wang, M. Ge, H. Yin, X. Li, H. Peng, N. Li, L. Xie, Effects of O₂ additive on corrosion behavior of Fe–Cr–Ni alloy in molten fluoride salts, *Corros. Sci.* 150 (2019) 175–182, <https://doi.org/10.1016/j.corsci.2019.01.040>.
42. L. Calabrese, V. Brancato, V. Palomba, E. Proverbio, An experimental study on the corrosion sensitivity of metal alloys for usage in PCM thermal energy storages, *Renew. Energy* 138 (2019) 1018–1027, <https://doi.org/10.1016/j.renene.2019.02.013>.
43. S. Choi, A.R. Strianese, O. Dale, M.F. Simpson, Electrochemical Measurements for Assessing Corrosion of Metal Alloys in Molten LiF-NaF-KF and MgCl₂-NaCl-KCl, *JOM* 73 (2021) 3544–3554, <https://doi.org/10.1007/s11837-021-04843-3>.
44. E.F. Diaz, C. Cuevas-Arteaga, N. Flores-García, S. Mejía Sintillo, O. Sotelo-Maz´on, Corrosion performance of AISI-309 exposed to molten salts V₂O₅-Na₂SO₄ at 700°C applying EIS and Rp electrochemical techniques, *J. Spectrosc.* 2015 (2015) 1–12, <https://doi.org/10.1155/2015/826759>.
45. W. Ding, A. Bonk, T. Bauer, Corrosion behavior of metallic alloys in molten chloride salts for thermal energy storage in concentrated solar power plants: A review, *Front. Chem. Sci. Eng.* 12 (2018) 564–576, <https://doi.org/10.1007/s11705-018-1720-0>.
46. W. Ding, H. Shi, A. Jianu, Y. Xiu, A. Bonk, A. Weisenburger, T. Bauer, Molten chloride salts for next generation concentrated solar power plants: Mitigation strategies against corrosion of structural materials, *Sol. Energy Mater. Sol. Cells* 193 (2019) 298–313, <https://doi.org/10.1016/j.solmat.2018.12.020>.
47. M.A. Espinosa-Medina, G. Carbajal-De La Torre, H.B. Liu, A. Martínez-Villafañe, J.G. Gonz´alez-Rodríguez, Hot corrosion behaviour of Fe–Al based intermetallic in molten NaVO₃ salt, *Corros. Sci.* 51 (2009) 1420–1427, <https://doi.org/10.1016/j.corsci.2009.03.028>.
48. A.G. Fern´andez, L.F. Cabeza, Corrosion evaluation of eutectic chloride molten salt for new generation of CSP plants. Part 2: Materials screening performance, *J. Storage Mater.* 29 (2020) 101381, <https://doi.org/10.1016/j.est.2020.101381>.
49. J.C. Gomez-Vidal, A.G. Fernandez, R. Tirawat, C. Turchi, W. Huddleston, Corrosion resistance of alumina forming alloys against molten chlorides for energy production. II: Electrochemical impedance spectroscopy

- under thermal cycling conditions, *Sol. Energy Mater. Sol. Cells* 166 (2017) 234–245, <https://doi.org/10.1016/j.solmat.2017.03.025>.
50. M. Gonzalez, U. Nithiyantham, E. Carbó-Argibay, O. Bondarchuk, Y. Grosu, A. Faik, Graphitization as efficient inhibitor of the carbon steel corrosion by molten binary nitrate salt for thermal energy storage at concentrated solar power, *Sol. Energy Mater. Sol. Cells* 203 (2019) 110172, <https://doi.org/10.1016/j.solmat.2019.110172>.
 51. P. Gore, M.P. Singh, D. Suryateja, B. Basu, K. Chattopadhyay, Early-stage corrosion of IN 740H alloy in eutectic NaCl-KCl molten salt at high temperatures, *Sol. Energy* 252 (2023) 330–341, <https://doi.org/10.1016/j.solener.2023.02.010>.
 52. B. Grégoire, C. Oskay, T.M. Meißner, M.C. Galetz, Corrosion mechanisms of ferritic-martensitic P91 steel and Inconel 600 nickel-based alloy in molten chlorides. Part II: NaCl-KCl-MgCl₂ ternary system, *Sol. Energy Mater. Sol. Cells* 216 (2020) 110675, <https://doi.org/10.1016/j.solmat.2020.110675>.
 53. M. Hong, H.L. Chan, Y. Xie, E. Romanovskaia, J.R. Scully, P. Hosemann, Effect of tellurium concentration on the corrosion and mechanical properties of 304 stainless steel in molten FLiNaK salt, *Corros. Sci.* 212 (2023) 110913, <https://doi.org/10.1016/j.corsci.2022.110913>.
 54. M. Hong, S. Samuha, P. Hosemann, Corrosion mechanism of cold forged 316 stainless steel in molten FLiNaK salt, *Corros. Sci.* 232 (2024) 111990, <https://doi.org/10.1016/j.corsci.2024.111990>.
 55. S.J. Keny, V.K. Gupta, A.G. Kumbhar, S. Rangarajan, M.R. Daitkar, N. K. Maheshwari, P.K. Vijayan, B.N. Jagatap, Corrosion tests of various alloys in fluorides of lithium, sodium and potassium (FLiNaK) medium for molten salt reactors in the temperature range of 550–750 °C using electrochemical techniques, *Indian J. Chem. Technol.* 26 (2019) 82–88, <https://doi.org/10.1007/s12182-018-0234-1>.
 56. S. Khorsand, A. Sheikhi, K. Raeissi, M.A. Golozar, Hot Corrosion Behavior of Inconel 625 Superalloy in Eutectic Molten Nitrate Salts, *Oxid. Met.* 90 (2018) 169–186, <https://doi.org/10.1007/s11085-017-9830-5>.
 57. Q. Lei, X. Zhang, M. Gao, W. Wen, Y. Jia, H. Liu, Y. Li, J. Liu, X. Zhou, Inconel 617 corrosion in FLiNaK molten salts: An in situ X-ray diffraction study, *Corros. Sci.* 182 (2021) 109289, <https://doi.org/10.1016/j.corsci.2021.109289>.
 58. H. Li, X. Wang, X. Yin, X. Yang, J. Tang, J. Gong, Corrosion and electrochemical investigations for stainless steels in molten Solar Salt: The influence of chloride impurity, *J. Storage Mater.* 39 (2021) 102675, <https://doi.org/10.1016/j.est.2021.102675>.
 59. X. Li, S. He, X. Zhou, P. Huai, Z. Li, A. Li, X. Yu, High-temperature corrosion behavior of Ni–16Mo–7Cr–4Fe superalloy containing yttrium in molten LiF–NaF–KF salt, *J. Nucl. Mater.* 464 (2015) 342–345, <https://doi.org/10.1016/j.jnucmat.2015.05.007>.
 60. Q. Liu, B. Leng, J. Qiu, H. Yin, J. Lin, Z. Tang, Effect of graphite particles in molten LiF–NaF–KF eutectic salt on corrosion behaviour of GH3535 alloy, *Corros. Sci.* 168 (2020) 108581, <https://doi.org/10.1016/j.corsci.2020.108581>.
 61. Q. Liu, X. Liu, G. Hao, H. Xu, Effect of O₂- additive on the corrosion behavior of Hastelloy N alloy in molten FLiNaK, *Corros. Sci.* 213 (2023) 111001, <https://doi.org/10.1016/j.corsci.2023.111001>.
 62. Q. Liu, H. Sun, H. Yin, L. Guo, J. Qiu, J. Lin, Z. Tang, Corrosion behaviour of 316H stainless steel in molten FLiNaK eutectic salt containing graphite particles, *Corros. Sci.* 160 (2019) 108174, <https://doi.org/10.1016/j.corsci.2019.108174>.
 63. A. Mallco, C. Portillo, M.J. Kogan, F. Galleguillos, A.G. Fernández, A materials screening test of corrosion monitoring in LiNO₃ containing molten salts as a thermal energy storage material for CSP plants, *Appl. Sci.* 10 (2020) 3160, <https://doi.org/10.3390/app10093160>.
 64. M. Maric, O. Muránsky, I. Karatchevtseva, T. Ungár, J. Hester, A. Studer, N. Scales, G. Ribárik, S. Primig, M.R. Hill, The effect of cold-rolling on the microstructure and corrosion behaviour of 316L alloy in FLiNaK molten salt, *Corros. Sci.* 142 (2018) 133–144, <https://doi.org/10.1016/j.corsci.2018.07.006>.
 65. S.W. McAlpine, N.C. Skowronski, W. Zhou, G. Zheng, M.P. Short, Corrosion of commercial alloys in FLiNaK molten salt containing EuF₃ and simulant fission product additives, *J. Nucl. Mater.* 532 (2020) 151994, <https://doi.org/10.1016/j.jnucmat.2020.151994>.
 66. E. Mohammadi Zahrani, A.M. Alfantazi, Molten salt induced corrosion of Inconel 625 superalloy in PbSO₄–Pb₃O₄–PbCl₂–Fe₂O₃–ZnO environment, *Corros. Sci.* 65 (2012) 340–359, <https://doi.org/10.1016/j.corsci.2012.08.035>.
 67. C.S. Ni, L.Y. Lu, Electrochemical impedance and modelling studies of the corrosion of three commercial stainless steels in molten carbonate, *Internat. J. Corr.* 2014 (2014) 1–13, <https://doi.org/10.1155/2014/721208>.
 68. L.C. Olson, J.W. Ambrosek, K. Sridharan, M.H. Anderson, T.R. Allen, Materials corrosion in molten LiF–NaF–KF salt, *J. Fluor. Chem.* 130 (2009) 67–73, <https://doi.org/10.1016/j.jfluchem.2008.05.008>.

69. E. Otero, A. Pardo, F.J. Perez, M.V. Utrilla, T. Levi, Corrosion behavior of 12CrMoV steel in waste incineration environments: hot corrosion by molten chlorides, *Oxid. Met.* 49 (1998) 467–484, <https://doi.org/10.1023/a:1018851029023>.
70. N.S. Patel, V. Pavlik, M. Bořca, High-temperature corrosion behavior of superalloys in molten salts – a review, *Crit. Rev. Solid State Mater. Sci.* 42 (2017) 83–97, <https://doi.org/10.1080/10408436.2016.1243090>.
71. F. Pineda, A. Mallco, F. De Barbieri, C. Carrasco, M. Henriquez, E. Fuentealba, A. G. Fernández, Corrosion evaluation by electrochemical real-time tracking of VM12 martensitic steel in a ternary molten salt mixture with lithium nitrates for CSP plants, *Sol. Energy Mater. Sol. Cells* 231 (2021) 111302, <https://doi.org/10.1016/j.solmat.2021.111302>.
72. F. Pineda, M. Walczak, F. Vilchez, C. Guerra, R. Escobar, M. Sancy, Evolution of corrosion products on ASTM A36 and AISI 304L steels formed in exposure to molten NaNO₃–KNO₃ eutectic salt: Electrochemical study, *Corros. Sci.* 196 (2022) 110047, <https://doi.org/10.1016/j.corsci.2021.110047>.
73. A. Ramu, V. Pavlik, V. Sillikova, M. Boca, Corrosion behavior of incoloy®800H, hastelloy®G35® and 316L stainless steel in the molten eutectic fluoride mixture FLiNaK and its vapors, *Materials* 16 (2023) 2679, <https://doi.org/10.3390/ma16072679>.
74. C.J. Rao, S. Ningshen, High-temperature electrochemical corrosion evaluation of 2.25Cr–1Mo alloy in eutectic LiCl–KCl molten salt, *Corrosion Engineering, Sci. Technol.* 57 (2022) 66–73, <https://doi.org/10.1080/1478422X.2021.1987376>.
75. C.J. Rao, P. Venkatesh, S. Ningshen, Corrosion assessment of 9Cr–1Mo steel in molten LiCl–KCl eutectic salt by electrochemical methods, *J. Nucl. Mater.* 514 (2019) 114–122, <https://doi.org/10.1016/j.jnucmat.2018.11.014>.
76. K.M. Sankar, P.M. Singh, Effect of metal fluorides on the corrosion of structural materials in molten LiF–NaF–KF, *Corros. Sci.* 213 (2023) 110977, <https://doi.org/10.1016/j.corsci.2023.110977>.
77. M. Sarvghad, T.A. Steinberg, G. Will, Corrosion of steel alloys in eutectic NaCl+Na₂CO₃ at 700 °C and Li₂CO₃+K₂CO₃+Na₂CO₃ at 450 °C for thermal energy storage, *Sol. Energy Mater. Sol. Cells* 170 (2017) 48–59, <https://doi.org/10.1016/j.solmat.2017.05.063>.
78. M. Sarvghad, T.A. Steinberg, G. Will, Corrosion of stainless steel 316 in eutectic molten salts for thermal energy storage, *Sol. Energy* 172 (2018) 198–203, <https://doi.org/10.1016/j.solener.2018.03.053>.
79. H. Lu, S. Li, Y. Wang, Corrosion behaviour of FeCoNiCrAl high-entropy alloy in molten NaCl–KCl–MgCl₂ chloride salt, *Corros. Eng. Sci. Technol.* 59 (2024) 345–359, <https://doi.org/10.1177/1478422X241250151>.
80. C.S. Sona, B.D. Gajbhiye, P.V. Hule, A.W. Patwardhan, C.S. Mathpati, A. Borgohain, N.K. Maheshwari, High temperature corrosion studies in molten salt–FLiNaK, *Corros. Eng. Sci. Technol.* 49 (2014) 287–295, <https://doi.org/10.1179/1743278213Y.0000000135>.
81. J.L. Trinstancho-Reyes, M. Sanchez-Carrillo, R. Sandoval-Jabalera, V.M. Orozco-Carmona, F. Almeraya-Calderón, J.G. Chacón-Nava, J. Gonzalez-Rodriguez, A. Martínez-Villafañe, Electrochemical impedance spectroscopy investigation of alloy inconel 718 in molten salts at high temperature, *Int. J. Electrochem. Sci.* 6 (2011) 419–431, [https://doi.org/10.1016/S1452-3981\(23\)15005-X](https://doi.org/10.1016/S1452-3981(23)15005-X).
82. J.L. Trinstancho-Reyes, J.G. Chacón-Nava, D.Y. Peña-Ballesteros, C. Gaona-Tiburcio, J.G. Gonzalez-Rodriguez, A. Martínez-Villafañe, F. Almeraya-Calderón, Hot corrosion behaviour of NiCrFeNbMoTiAl coating in molten salts at 700 °C by electrochemical techniques, *Int. J. Electrochem. Sci.* 6 (2011) 432–441, [https://doi.org/10.1016/S1452-3981\(23\)15006-1](https://doi.org/10.1016/S1452-3981(23)15006-1).
83. J.H. Wang, D.G. Li, T.M. Shao, Electrochemical study on the hot corrosion behavior of Ni₁₆Cr₁₃Co₄Mo alloy in molten NaCl–KCl and NaCl–KCl–Na₂SO₄, *Corros. Sci.* 200 (2022) 110247, <https://doi.org/10.1016/j.corsci.2022.110247>.
84. M. Wang, S. Zeng, H. Zhang, M. Zhu, C. Lei, B. Li, Corrosion behaviors of 316 stainless steel and Inconel 625 alloy in chloride molten salts for solar energy storage, *High Temp. Mater. Processes* 39 (2020) 340–350, <https://doi.org/10.1515/htmp-2020-0077>.
85. H. Yin, J. Qiu, H. Liu, W. Liu, Y. Wang, Z. Fei, S. Zhao, X. An, J. Cheng, T. Chen, P. Zhang, G. Yu, L. Xie, Effect of CrF₃ on the corrosion behaviour of Hastelloy–N and 316L stainless steel alloys in FLiNaK molten salt, *Corros. Sci.* 131 (2018) 355–364, <https://doi.org/10.1016/j.corsci.2017.12.008>.
86. C.L. Zeng, W. Wang, W.T. Wu, Electrochemical impedance models for molten salt corrosion, *Corros. Sci.* 43 (2001) 787–801, [https://doi.org/10.1016/S0010-938X\(00\)00108-6](https://doi.org/10.1016/S0010-938X(00)00108-6).
87. D. Cao, Y. Ma, Z. Shi, J. Xu, X. Hu, Z. Wang, Performance of protective oxide films on Fe–Ni alloy anodes in molten KF–AlF₃–Al₂O₃ salts at 700 °C, *Electrochim. Acta* 347 (2020) 136275, <https://doi.org/10.1016/j.electacta.2020.136275>.

88. D. Inman, Electrode Kinetics and Double Layer in Molten Salts, in: G. Mamantov, R. Marassi (Eds.), *Molten Salt Chemistry: an Introduction and Selected Applications*, Springer, Netherlands, Dordrecht, 1987, pp. 271–278, https://doi.org/10.1007/978-94-009-3863-2_13.
89. A. Kizza, The capacitance of the electric double layer of electrodes in molten salts, *J. Electroanal. Chem.* 534 (2002) 99–106, [https://doi.org/10.1016/S0022-0728\(02\)01148-8](https://doi.org/10.1016/S0022-0728(02)01148-8).
90. A.D. Graves, D. Inman, The electrical double layer in molten salts: Part 2. The double-layer capacitance, *J. Electroanal. Chem. Interf. Electrochem.* 25 (1970) 357–372, [https://doi.org/10.1016/S0022-0728\(70\)80098-5](https://doi.org/10.1016/S0022-0728(70)80098-5).
91. J. Klos, S. Lamperski, Analysis of electrical double layer structure in molten salts, *J. Chem. Phys.* 150 (2019) 064704, <https://doi.org/10.1063/1.5082561>.
92. M. Hong, H.L. Chan, J.R. Scully, P. Hosemann, Corrosion property of Alloy 625 in Molten FLiNaK salt according to the Tellurium Concentrations, *J. Nucl. Mater.* 584 (2023) 154548, <https://doi.org/10.1016/j.jnucmat.2023.154548>.
93. J. Qiu, A. Wu, J. Yao, Y. Xu, Y. Li, R. Scarlat, D.D. Macdonald, Kinetic study of hydrogen transport in graphite under molten fluoride salt environment, *Electrochim. Acta* 352 (2020) 136459, <https://doi.org/10.1016/j.electacta.2020.136459>.
94. Y. Liu, Y. Song, H. Ai, M. Shen, H. Liu, S. Zhao, Y. Liu, Z. Fei, X. Fu, J. Cheng, Corrosion of Cr in molten salts with different fluoroacidity in the presence of CrF₃, *Corros. Sci.* 169 (2020) 108636, <https://doi.org/10.1016/j.corsci.2020.108636>.
95. J. Farmer, B. El-dasher, M.S. de Caro, J. Ferreira, Corrosion of ferritic steels in high temperature molten salt coolants for nuclear applications, *MRS Online Proc. Libr.* 1125 (2009) 609, <https://doi.org/10.1557/PROC-1125-R06-09>.
96. H. Ai, X.-X. Ye, L. Jiang, B. Leng, M. Shen, Z. Li, Y. Jia, J.-Q. Wang, X. Zhou, Y. Xie, L. Xie, On the possibility of severe corrosion of a Ni-W-Cr alloy in fluoride molten salts at high temperature, *Corros. Sci.* 149 (2019) 218–225, <https://doi.org/10.1016/j.corsci.2019.01.012>.
97. Y.L. Wang, Q. Wang, H.J. Liu, C.L. Zeng, Effects of the oxidants H₂O and CrF₃ on the corrosion of pure metals in molten (Li, Na, K)F, *Corros. Sci.* 103 (2016) 268–282, <https://doi.org/10.1016/j.corsci.2015.11.032>.
98. H.L. Chan, E. Romanovskaia, S.H. Mills, M. Hong, V. Romanovski, N. Bieberdorf, C. Peddeti, A.M. Minor, P. Hosemann, M. Asta, J.R. Scully, Morphological evolution and dealloying during corrosion of Ni₂₀Cr in molten FLiNaK Salt, *J. Electrochem. Soc.* 171 (2024) 081501, <https://doi.org/10.1149/1945-7111/ad6037>.
99. K. Nisanc, The error in polarization resistance and capacitance measurements resulting from nonuniform ohmic potential drop to flush-mounted probes, *Corrosion* 43 (1987) 258–265, <https://doi.org/10.5006/1.3583146>.
100. C. You, A. Dizon, M. Gao, V. Vivier, M.E. Orazem, Experimental observation of ohmic impedance, *Electrochim. Acta* 413 (2022) 140177, <https://doi.org/10.1016/j.electacta.2022.140177>.
101. K. Davis, A. Dizon, C.L. Alexander, M.E. Orazem, Influence of geometry-induced frequency dispersion on the impedance of rectangular electrodes, *Electrochim. Acta* 283 (2018) 1820–1828, <https://doi.org/10.1016/j.electacta.2018.07.080>.
102. M. Fleischmann, S. Pons, The behavior of microelectrodes, *Anal. Chem.* 59 (1987) 1391A–A1399, <https://doi.org/10.1021/ac00151a001>.
103. M. Fleischmann, S. Pons, J. Daschbach, The ac impedance of spherical, cylindrical, disk, and ring microelectrodes, *J. Electroanal. Chem.* 317 (1991) 1–26, [https://doi.org/10.1016/0022-0728\(91\)85001-6](https://doi.org/10.1016/0022-0728(91)85001-6).
104. J. Qiu, Y. Zou, G. Yu, H. Liu, Y. Jia, Z. Li, P. Huai, X. Zhou, H. Xu, Compatibility of container materials with Cr in molten FLiNaK salt, *J. Fluor. Chem.* 168 (2014) 69–74, <https://doi.org/10.1016/j.jfluchem.2014.09.010>.
105. J.R. Scully, Polarization Resistance Method for Determination of Instantaneous Corrosion Rates, *Corrosion* 56 (2000) 199–218, <https://doi.org/10.5006/1.3280536>.
106. J. Scully, D. Silverman, M. Kendig (Eds.), *Electrochemical Impedance: Analysis and Interpretation*, ASTM International, 100 Barr Harbor Drive, PO Box C700, West Conshohocken, PA 19428-2959, 1993 <https://doi.org/10.1520/STP1188-EB>.
107. R. Kelly, J. Scully, D. Shoesmith, R. Buchheit, *Electrochemical Techniques in Corrosion Science and Engineering*, CRC Press, 2002, 10.1201/9780203909133.
108. J. Newman, Resistance for flow of current to a disk, *J. Electrochem. Soc.* 113 (1966) 501, <https://doi.org/10.1149/1.2424003>.
109. O. Gharbi, A. Dizon, M.E. Orazem, M.T.T. Tran, B. Tribollet, V. Vivier, From frequency dispersion to ohmic impedance: A new insight on the high-frequency impedance analysis of electrochemical systems, *Electrochim. Acta* 320 (2019) 134609, <https://doi.org/10.1016/j.electacta.2019.134609>.
110. J. Newman, Numerical solution of coupled, ordinary differential equations, *Ind. Eng. Chem. Fundam.* 7 (1968) 514–517, <https://doi.org/10.1021/i160027a025>.

111. K. Nisancioglu, J. Newman, The transient response of a disk electrode, *J. Electrochem. Soc.* 120 (1973) 1339, <https://doi.org/10.1149/1.2403258>.
112. V.-M.-W. Huang, V. Vivier, M.E. Orazem, N. P'eb'ere, B. Tribollet, The apparent constant-phase-element behavior of a disk electrode with faradaic reactions, *J. Electrochem. Soc.* 154 (2007) C99, <https://doi.org/10.1149/1.2398894>.
113. V.-M.-W. Huang, V. Vivier, I. Frateur, M.E. Orazem, B. Tribollet, The global and local impedance response of a blocking disk electrode with local constant-phase-element behavior, *J. Electrochem. Soc.* 154 (2006) C89, <https://doi.org/10.1149/1.2398889>.
114. Z.A. Rotenberg, A.V. Dribinskii, V.P. Lukovtsev, N.S. Khozyainova, Electrochemical impedance of microelectrodes, *Russ. J. Electrochem.* 36 (2000) 879–882, <https://doi.org/10.1007/bf02757062>.
115. Y. Hoshi, M. Ohya, I. Shitanda, M. Itagaki, Diffusion impedance of microband electrode array by FEM, in: Meet. Abstr. (Electrochem. Soc. CD-ROM) MA2013-02, 2013, p. 2686, 10.1149/ma2013-02/48/2686.
116. Y. Hoshi, S. Kawakita, I. Shitanda, M. Itagaki, Diffusion impedance analyzed by equivalent circuit involving CPE using microelectrode, *ECS Trans.* 50 (2013) 9, <https://doi.org/10.1149/05035.0009ecst>.
117. B. Fan, B. Wolfrum, J.T. Robinson, Impedance scaling for gold and platinum microelectrodes, *J. Neural Eng.* 18 (2021) 056025, <https://doi.org/10.1088/1741-2552/ac20e5>.
118. A. Lata, I. Bhar, N. Mandal, Multifunctional electrode polarization impedance-based sensor for calculating flow rate and conductivity of fluid, *IEEE Trans. Instrum. Meas.* 71 (2022) 1–12, <https://doi.org/10.1109/tim.2021.3139704>.
119. A.K. Ahuja, M.R. Behrend, J.J. Whalen, M.S. Humayun, J.D. Weiland, The dependence of spectral impedance on disc microelectrode radius, *IEEE Trans. Biomed. Eng.* 55 (2008) 1457–1460, <https://doi.org/10.1109/TBME.2007.912430>.
120. A. Wang, D. Jung, D. Lee, H. Wang, Impedance characterization and modeling of subcellular to micro-sized electrodes with varying materials and PEDOT coating for bioelectrical interfaces, *ACS Appl. Electron. Mater.* 3 (2021) 5226–5239, <https://doi.org/10.1021/acsaelm.1c00687>.
121. E. Romanovskaia, H.L. Chan, V. Romanovski, F. Garfias, M. Hong, S. Mastromarino, P. Hosemann, R. Scully, J.R. Scully, An In Situ, multi-electrode electrochemical method to assess the open circuit potential corrosion of Cr in unpurified molten FLiNaK, *Corros. Sci.* 222 (2023) 111389, <https://doi.org/10.1016/j.corsci.2023.111389>.
122. H.L. Chan, J.R. Scully, Deciphering when metal corrosion is spontaneous in molten fluorides using potential-activity diagrams, *Corrosion* 79 (2023) 1236–1240, <https://doi.org/10.5006/4401>.
123. H.L. Chan, E. Romanovskaia, J. Qiu, P. Hosemann, J.R. Scully, Insights on the corrosion thermodynamics of chromium in molten LiF-NaF-KF eutectic salts, *npj Mater. Degrad.* 6 (2022) 46, <https://doi.org/10.1038/s41529-022-00251-3>.
124. P.J. Elving (Ed.), *Electrode Kinetics for Chemists, Chemical Engineers, and Materials Scientists*, Wiley, 1997.
125. J. Han, H.L. Chan, M.G. Wartenberg, H.H. Heinrich, J.R. Scully, Distinguishing interfacial double layer and oxide-based capacitance on gold and pre-oxidized Fe-Cr in 1-ethyl-3-methylimidazolium methanesulfonate room temperature ionic liquid aqueous mixture, *Electrochem. Commun.* 122 (2021) 106900, <https://doi.org/10.1016/j.elecom.2020.106900>.
126. R.G. Kelly, A.J. Young, R.C. Newman, The characterization of the coarsening of dealloyed layers by EIS and its correlation with stress-corrosion cracking. ASTM International, STP Paper, 1997, 10.1520/STP18065S.
127. T. Ghaznavi, M.A. Bryk, S.Y. Persaud, R.C. Newman, Alloying effects in high temperature molten salt corrosion, *Corros. Sci.* 197 (2022) 110003, <https://doi.org/10.1016/j.corsci.2021.110003>.
128. T. Ghaznavi, S.Y. Persaud, R.C. Newman, The effect of temperature on dealloying mechanisms in molten salt corrosion, *J. Electrochem. Soc.* 169 (2022) 111506, <https://doi.org/10.1149/1945-7111/aca07e>.
129. K. Bawane, X. Liu, R. Gakhar, M. Woods, M. Ge, X. Xiao, W.-K. Lee, P. Halstenberg, S. Dai, S. Mahurin, S.M. Pimblott, J.F. Wishart, Y.K. Chen-Wiegart, L. He, Visualizing time-dependent microstructural and chemical evolution during molten salt corrosion of Ni-20Cr model alloy using correlative quasi in situ TEM and in situ synchrotron X-ray nano-tomography, *Corros. Sci.* 195 (2022) 109962, <https://doi.org/10.1016/j.corsci.2021.109962>.
130. S.R. Taylor, E. Gileadi, Physical interpretation of the Warburg impedance, *Corrosion* 51 (1995) 664–671, <https://doi.org/10.5006/1.3293628>.
131. V.S. Muralidharan, Warburg impedance - basics revisited, *Anti-Corros. Methods Mater.* 44 (1997) 26–29, <https://doi.org/10.1108/00035599710157387>.
132. H.L. Chan, R. Auguste, E. Romanovskaia, A.L. Morales, F. Schmidt, V. Romanovski, C. Winkler, J. Qiu, Y. Wang, D. Kaoumi, F.A. Selim, B.P. Uberuaga, P. Hosemann, J.R. Scully, Multi-length scale characterization of

- point defects in thermally oxidized, proton irradiated iron oxides, *Materialia* 28 (2023) 101762, <https://doi.org/10.1016/j.mtla.2023.101762>.
133. Gamry Simplex Fit- Algorithm Details Gamry Instruments, (n.d.). <https://www.gamry.com/application-notes/software-scripting/simplex-fit-algorithm/>.
134. S.W. McAlpine, N.C. Skowronski, W. Zhou, G. (Tony) Zheng, M.P. Short, Corrosion of commercial alloys in FLiNaK molten salt containing EuF₃ and simulant fission product additives, *J. Nucl. Mater.* 532 (2020), <https://doi.org/10.1016/j.jnucmat.2020.151994>, 151994.
135. S. Guo, N. Shay, Y. Wang, W. Zhou, J. Zhang, Measurement of europium (III)/europium (II) couple in fluoride molten salt for redox control in a molten salt reactor concept, *J. Nucl. Mater.* 496 (2017) 197–206, <https://doi.org/10.1016/j.jnucmat.2017.09.027>.
136. L. Massot, M. Gibilaro, D. Quaranta, P. Chamelot, Corrosion products electrochemical behaviour into molten LiF-NaF: investigation of Cr(II) system, *J. Electrochem. Soc.* 168 (2021) 026510, <https://doi.org/10.1149/1945-7111/abe088>.
137. Y. Wang, J. Zhang, Electrochemical properties of CrF₂ in FLiNaK molten salt and the new analytical methods for their determination, *J. Electrochem. Soc.* 167 (2020) 086503, <https://doi.org/10.1149/1945-7111/ab8923>.
138. V.V. Zakharova, A.A. Ryzhov, V.A. Volkovich, Electrochemistry of iron, nickel and chromium in LiF-NaF-KF (FLiNaK) eutectic melt: A cyclic voltammetry study, *AIP Conf. Proc.* 2313 (2020) 050039, <https://doi.org/10.1063/5.0032424>.
139. H. Peng, M. Shen, C. Wang, T. Su, Y. Zuo, L. Xie, Electrochemical investigation of the stable chromium species in molten FLiNaK, *RSC Adv.* 5 (2015) 76689–76695, <https://doi.org/10.1039/C5RA09919F>.
140. W. Wu, S. Guo, J. Zhang, Electrochemical behaviors of Cr(III) in molten LiF-NaF-KF eutectic, *Int. J. Electrochem. Sci.* 13 (2018) 225–234, <https://doi.org/10.20964/2018.01.21>.
141. G.J. Brug, M. van Sluyters-Rehbach, J.H. Sluyters, The analysis of electrode impedances complicated by the presence of a constant phase element, *J. Electroanal. Chem.* 176 (1984) 275–295, [https://doi.org/10.1016/s0022-0728\(84\)80324-1](https://doi.org/10.1016/s0022-0728(84)80324-1).
142. L. Langford, N. Winner, A. Hwang, H. Williams, L. Vergari, R.O. Scarlat, M. Asta, Constant-potential molecular dynamics simulations of molten salt double layers for FLiBe and FLiNaK, *J. Chem. Phys.* 157 (2022) 094705, <https://doi.org/10.1063/5.0097697>.
143. I.C. Hunter, *Theory and Design of Microwave Filters*, Institution of Electrical Engineers, London, 2001.
144. R. Auguste, H.L. Chan, E. Romanovskaia, J. Qiu, R. Schoell, M.O. Liedke, M. Butterling, E. Hirschmann, A.G. Attallah, A. Wagner, F.A. Selim, D. Kaoumi, B.P. Uberuaga, P. Hosemann, J.R. Scully, A multimodal approach to revisiting oxidation defects in Cr₂O₃, *npj Mater. Degrad.* 6 (2022) 1–13, <https://doi.org/10.1038/s41529-022-00269-7>.
145. C. Zhong, Y. Deng, W. Hu, J. Qiao, L. Zhang, J. Zhang, A review of electrolyte materials and compositions for electrochemical supercapacitors, *Chem. Soc. Rev.* 44 (2015) 7484–7539, <https://doi.org/10.1039/c5cs00303b>.
146. A.J. Lucio, *The Electrochemical Double Layer in Ionic Liquids*, University of Iowa, Doctor of Philosophy, 2018 <https://doi.org/10.17077/etd.0wj158yg>.
147. V. Lockett, M. Horne, R. Sedev, T. Rodopoulos, J. Ralston, Differential capacitance of the double layer at the electrode/ionic liquids interface, *PCCP* 12 (2010) 12499, <https://doi.org/10.1039/c0cp00170h>.

Supplemental A Tables, Appendix #2

Table S1. Electrochemical kinetic parameters obtained from graphical analysis of LSV scans of Cr in FLiNaK salts w/ 1wt.% EuF₃ at 600 °C.

Test	E _{oc}	β_a	β_c	B	i _{corr,}	R
#	V _{K⁺/K}	V/dec		V	mA/cm ²	Ω -cm ²
1	1.27	0.0452	0.351	0.173	3.65	4.74

Supplemental A Figures, Appendix #2

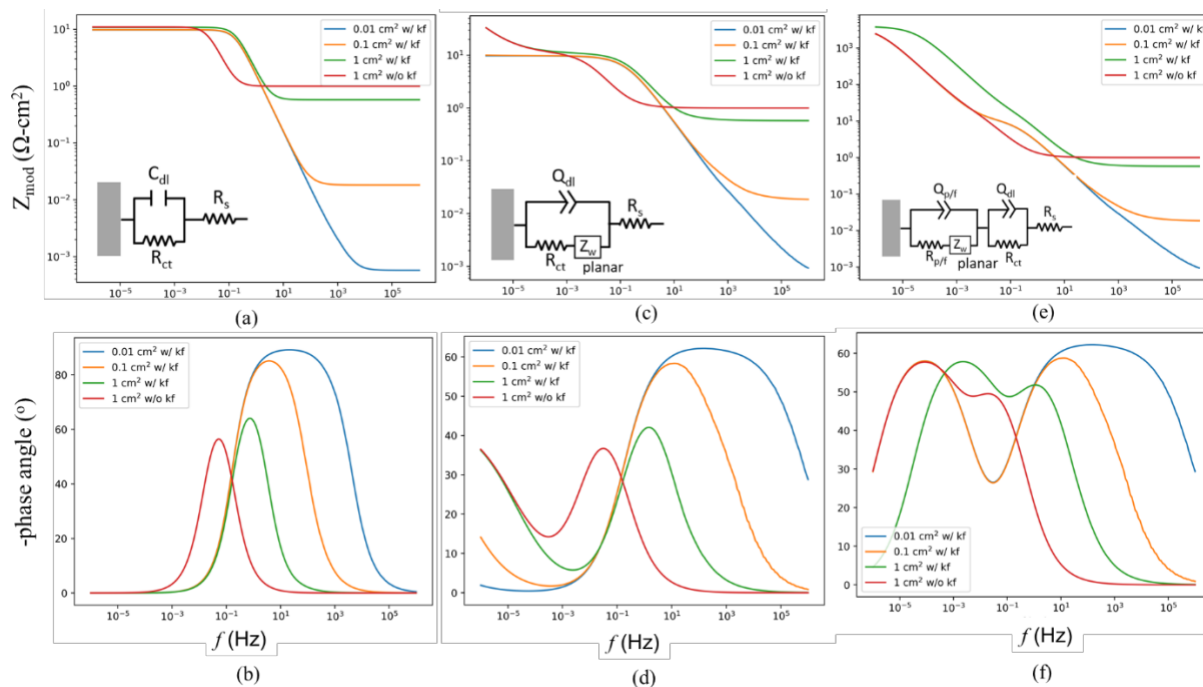


Figure S1. Simulated impedance spectra representing the interfacial dissolution of Cr in FLiNaK, 600°C calculated using (a,b) the simplified Randles circuit with an ideal capacitor, or Figure 1a, (c,d) a Randles circuit with a Warburg diffusional element, or Figure 1d, and (e,f) a two-time constant model with a Warburg diffusional element, or Figure 1e. The EEC model is included as an inset for each case. The simulation parameters are based on Table 1. Three disk areas of 10^0 (green), 10^{-1} (gold) and 10^{-2} cm^2 (blue) as well as a macroelectrode baseline of 10^0 cm^2 are simulated (red curve).

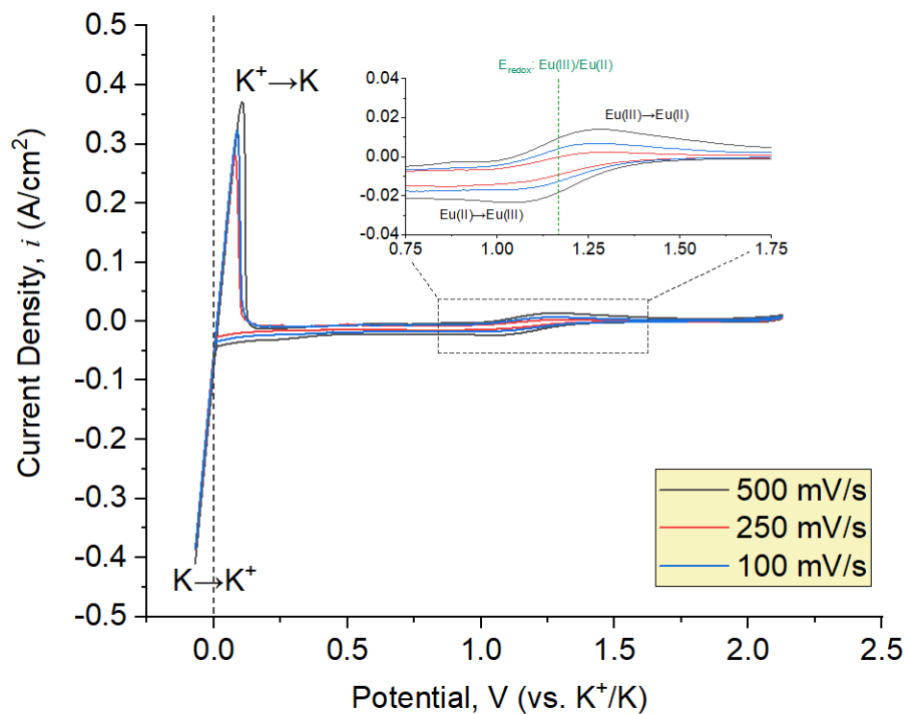


Figure S2. Cyclic voltammogram of Pt wire in molten FLiNaK + 1 wt.% EuF₃ at 600 °C measured at a scan rate of 500, 250, and 100 mV/s.

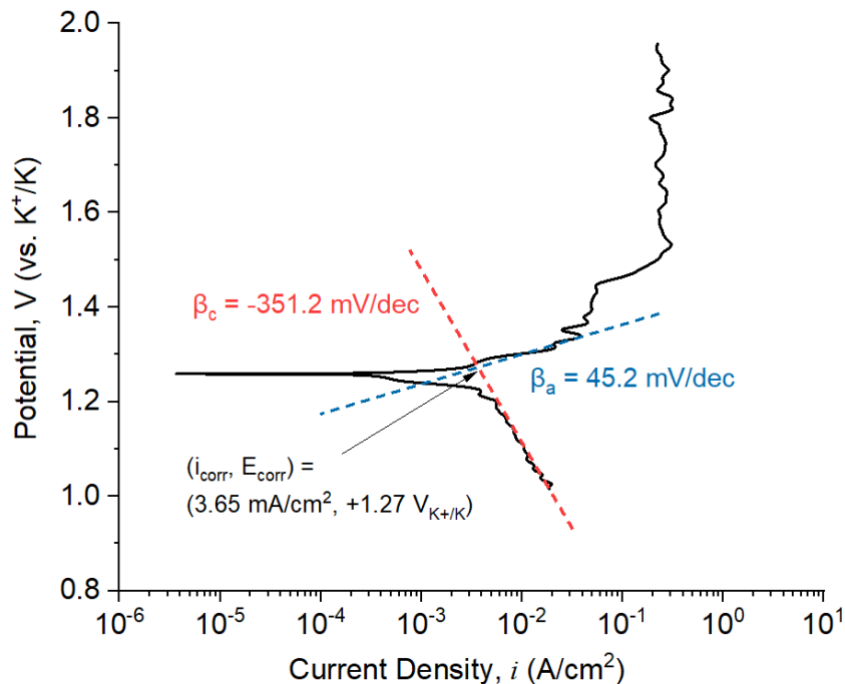


Figure S3. Linear sweep voltammogram (LSV) of Cr measured at a scan rate of 1 mV/s in molten FLiNaK + 1 wt.% EuF₃ at 600 °C using the macroelectrode geometry.

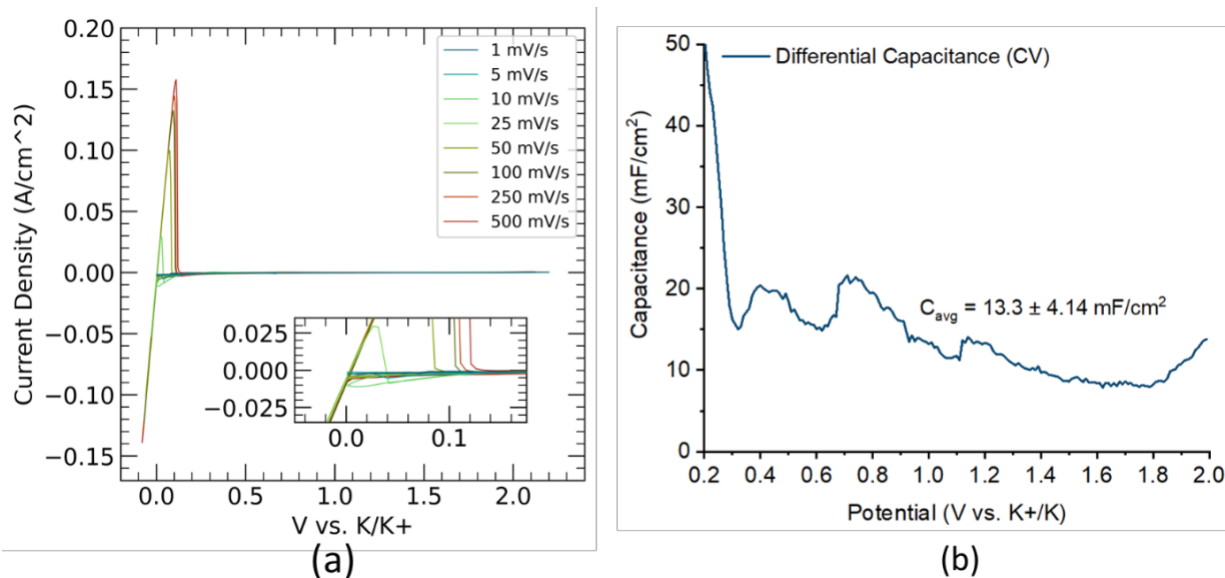


Figure S4. Differential capacitance analysis on a Pt wire in molten FLiNaK at 600 °C. (a) shows the cyclic voltammogram measured at a scan rate between 1 and 500 mV/s. (b) shows the differential capacitance calculated using Eq. S2.

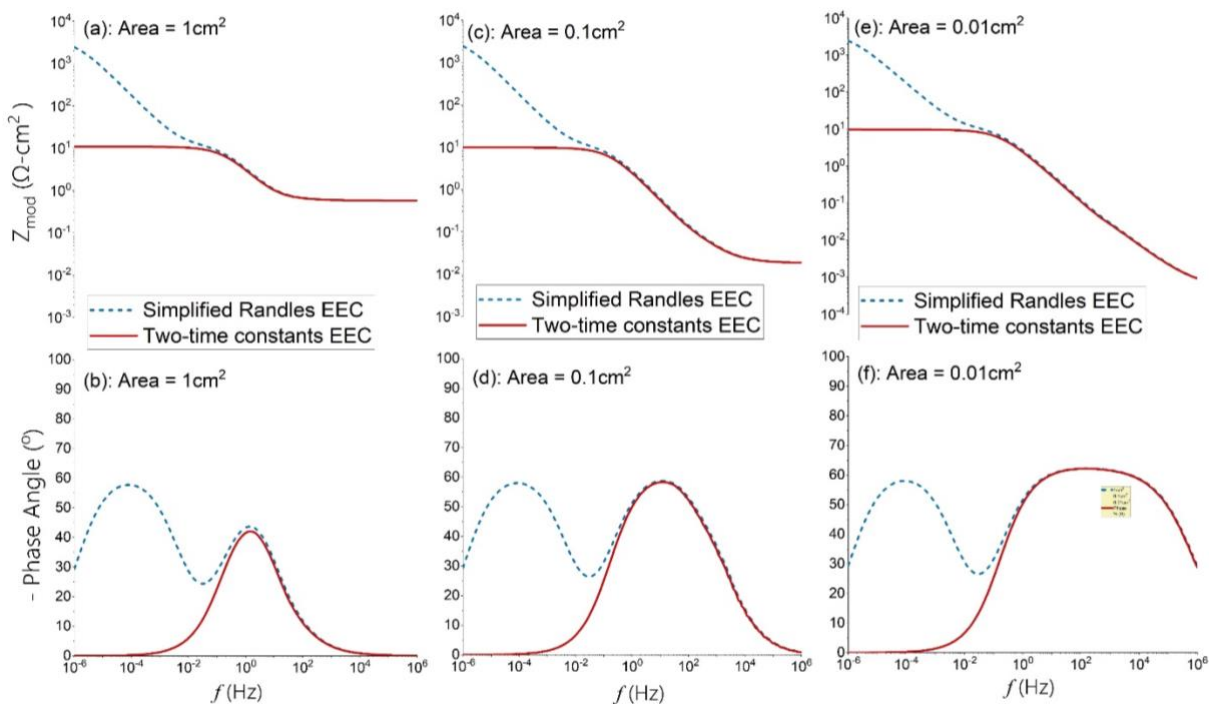


Figure S5. Simulated Bode plots of Cr disk electrode in FLiNaK, 600 °C using the simplified Randles circuit (Figure 1b) and two-time constants EEC (Figure 1d) models. The disk electrode areas are (a,b) 1 cm², (c,d) 0.1 cm² and (e,f) 0.01 cm².

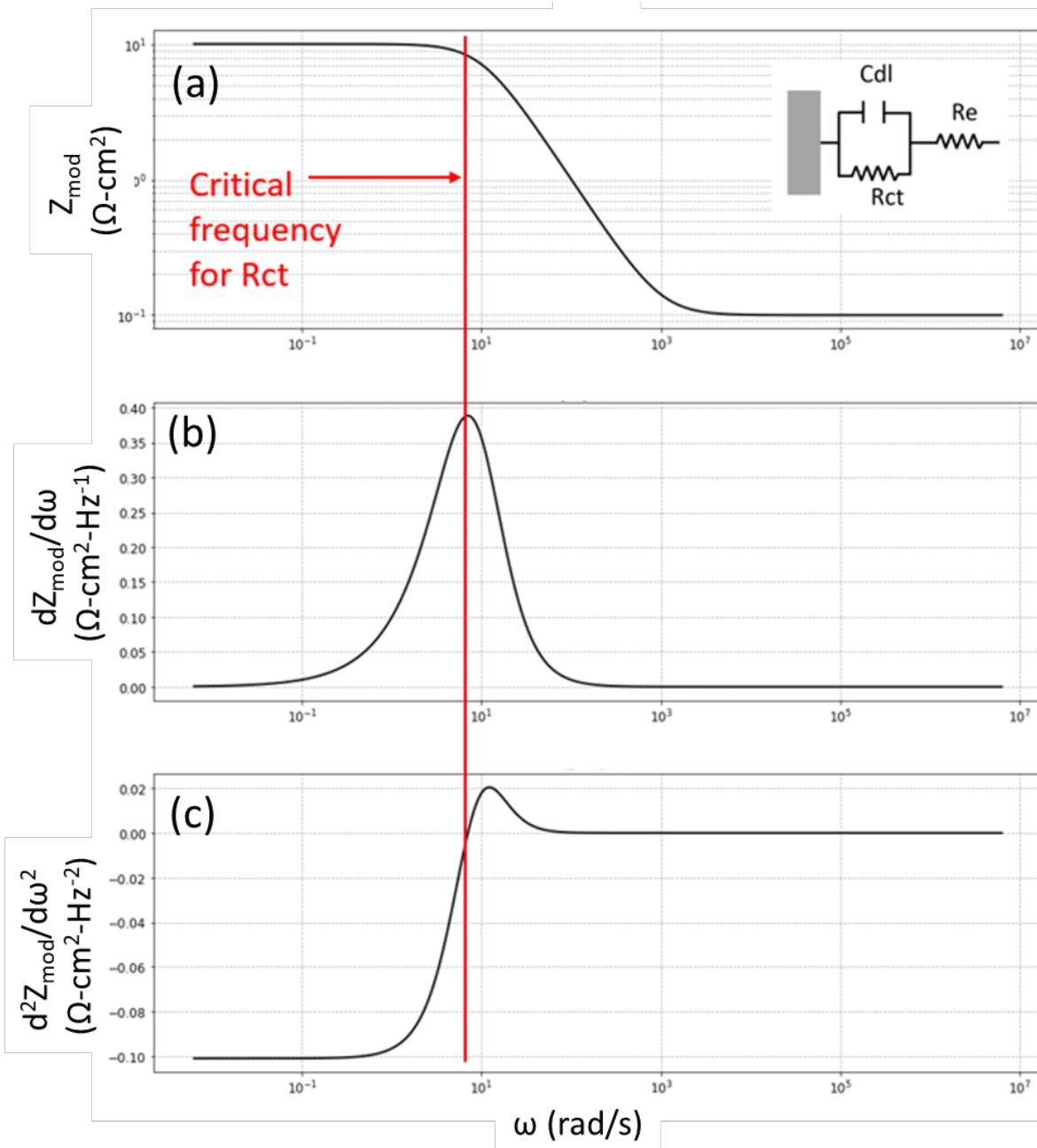


Figure S6. Impedance simulation constructed using a simplified Randles circuit with an ideal capacitor (Figure 1a). The assumed EEC parameters are as follows: $C_{dl} = 10 \mu\text{F}/\text{cm}^2$, $R_{ct} = 10 \Omega\text{-cm}^2$, and $R_e = 0.1 \Omega\text{-cm}^2$. (a) shows the as simulated Bode impedance plot. (b) and (c) shows the first and second derivatives of (a), respectively.

Supplemental Section B: Equation derivations

Derivation of f_{trans}^{Rct} for the simplified Randles circuit with an ideal capacitor

Eq. S1 shows the complex impedance modulus based on the electrical equivalent circuit model (ECM) in Fig. 1a, which shows a simplified Randles circuit model with an ideal capacitor. The real and imaginary components of Eq. S1 can also be separated and expressed in terms of the magnitude of Z_{mod} in Eq. 2:

$$Z = R_s + \frac{R_{ct}}{1+j\omega R_{ct}C_{dl}} \quad (\text{Eq. S1})$$

$$Z_{mod}(f) = \sqrt{\left(R_e + \frac{R_{ct}}{1+(w)^2 R_{ct}^2 C_{dl}^2}\right)^2 + \left(\frac{-(w)R_{ct}^2 C_{dl}}{1+(w)^2 R_{ct}^2 C_{dl}^2}\right)^2} \quad (\text{Eq. S2})$$

As shown in Fig. S7, f_{trans}^{Rct} can be solved by identifying the maxima of $dZ_{mod}/d\omega$ vs. ω plot (Fig. S7b) or solving ω or f when $d^2Z_{mod}/d\omega^2$ equals zero (Fig. S7c). However, the derivative of Eq. S1 and Eq. S2 is difficult to solve analytically. A simpler way to find f_{trans}^{Rct} is to take the derivative of Z_{real} with respect to ω instead since the Z_{real} vs. ω plot and Z_{mod} vs. ω plot are identical in shape and Z_{real} has a simpler analytical expression. The first and second derivatives of Z_{real} are shown in Eq. S3 and Eq. S4, respectively:

$$\frac{\partial Z_{real}}{\partial w} = \frac{-2wR_{ct}^3 C_{dl}^2}{(1+w^2 R_{ct}^2 C_{dl}^2)^2} \quad (\text{Eq. S3})$$

$$\frac{\partial Z_{real}^2}{w^2} = \frac{-2R_{ct}^3 C_{dl}^2 (1-3w^2 R_{ct}^2 C_{dl}^2)}{(1+w^2 R_{ct}^2 C_{dl}^2)^3} \quad (\text{Eq. S4})$$

Setting Eq. S4 to zero at f_{trans}^{Rct} ($w = 2\pi f_{trans}^{Rct}$), Eq. S5 can be derived:

$$f_{trans}^{Rct} = \frac{1}{2\pi\sqrt{3}} \frac{1}{R_{eff} C_{eff}} \quad (\text{Eq. S5})$$

Applying Eq. 8 and Eq. 9 to Eq. 5 to account for the NUCP effect, Eq. S6 (or Eq. 20) can be formulated:

$$f_{trans}^{Rct} = \frac{1}{2\pi\sqrt{3}} \frac{1}{R_{ct} C_{dl}} (k_f^{Rct} k_f^{Cdl}) \quad (\text{Eq. S6 or Eq. 20})$$

Derivation of the f_{trans}^{Rct} for a simplified Randles circuit with a constant phase element

Similarly, with a constant phase element is in place of a capacitor for the same circuit (Fig. 1b), Eq. S1 and Eq. S2 can be modified to Eq. S7 and Eq. S8, respectively:

$$Z = R_s + \frac{R_{ct}}{1+(j\omega)^\alpha R_{ct} Q_{dl}} \quad (\text{Eq. S7})$$

$$Z_{mod} = \sqrt{\left(R_e + \frac{R_{ct}(1+(w)^\alpha R_{ct} Q_{dl} \cos(\frac{\alpha\pi}{2}))}{1+2(w)^\alpha R_{ct} Q_{dl} \cos(\frac{\alpha\pi}{2}) + (w)^{2\alpha} R_{ct}^2 Q_{dl}^2}\right)^2 + \left(\frac{(w)^\alpha R_{ct}^2 Q_{dl} \sin(\frac{\alpha\pi}{2})}{1+2(w)^\alpha R_{ct} Q_{dl} \cos(\frac{\alpha\pi}{2}) + (w)^{2\alpha} R_{ct}^2 Q_{dl}^2}\right)^2} \quad (\text{Eq. S8})$$

The real component of Z_{mod} is displayed in Eq. S9:

$$Z_{real} = R_e + \frac{R_{ct}(1+(w)^\alpha R_{ct} Q_{dl} \cos(\frac{\alpha\pi}{2}))}{1+2(w)^\alpha R_{ct} Q_{dl} \cos(\frac{\alpha\pi}{2}) + (w)^{2\alpha} R_{ct}^2 Q_{dl}^2} \quad (\text{Eq. S9})$$

In the denominator term, the component $(w^{2\alpha} R_{ct}^2 Q_{dl}^2) > 2(w)^\alpha R_{ct} Q_{dl} \cos(\frac{\alpha\pi}{2}) > 1$ when $R_{ct} = 10\Omega\text{-cm}^2$, $C_{dl} = 10^{-2} \text{ F/cm}^2$, and $\alpha = 0.7$ (parameters comparable to experimental data in Table 2 and Table 3). This enables Eq. S9 to be simplified to Eq. 10:

$$Z_{real} = R_e + \frac{R_{ct}(1+(w)^\alpha R_{ct} Q_{dl} \cos(\frac{\alpha\pi}{2}))}{w^{2\alpha} R_{ct}^2 Q_{dl}^2} = R_e + \frac{1}{w^{2\alpha} R_{ct} Q_{dl}^2} + \frac{\cos(\frac{\alpha\pi}{2})}{w^\alpha Q_{dl}} \quad (\text{Eq. S10})$$

The first and second derivatives of the real component of Eq. S10 can be shown Eq. 11 and Eq. 12:

$$\frac{\partial Z_{real}}{\partial w} = \frac{-2\alpha}{w^{2\alpha+1} R_{ct} Q_{dl}^2} - \frac{\alpha \cos(\frac{\alpha\pi}{2})}{w^{\alpha+1} Q_{dl}} \quad (\text{Eq. S11})$$

$$\frac{\partial^2 Z_{real}}{\partial w^2} = \frac{2\alpha(2\alpha+1)}{w^{2\alpha+2} R_{ct} Q_{dl}^2} + \frac{\alpha(\alpha+1) \cos(\frac{\alpha\pi}{2})}{w^{\alpha+2} Q_{dl}} \quad (\text{Eq. S12})$$

Setting Eq. S12 to zero, f_{trans}^{Rct} can be solved as shown in Eq. S13:

$$f_{trans}^{Rct} \approx \frac{1}{2\pi} \left(\frac{\cos(\frac{\alpha\pi}{2})}{R_{eff} Q_{eff}} \right)^{\frac{1}{\alpha}} \quad (\text{Eq. S13})$$

Similarly, the NUCP can be accounted for by correcting R_{eff} and Q_{eff} with the k_f^{Rct} and k_f^{Cdl} factors:

$$f_{trans}^{Rct} \approx \frac{1}{2\pi} \left(\frac{\cos(\frac{\alpha\pi}{2})}{R_{ct} Q_{dl}} \right)^{\frac{1}{\alpha}} (k_f^{Rct} k_f^{Cdl})^{\frac{1}{\alpha}} \quad (\text{Eq. S14})$$